Direct and flanking transmission across timber concrete composite floors with cross laminated timber walls

Thesis submitted in accordance with the requirements of the

University of Liverpool for the degree of Doctor in Philosophy

by

Claire Churchill

School of Architecture, University of Liverpool

January 2018

Direct and flanking transmission across timber-concrete composite floors with cross laminated timber walls

Claire Churchill

Timber-concrete composite (HBV) floors are widely manufactured by many construction companies. Cross laminated timber (CLT) elements are an effective way to produce more homogenised timber building elements. In this thesis, the applicability of measurement-based prediction methods to calculate the apparent sound reduction index (*R*') for these two types of elements was investigated.

A prediction model using Statistical Energy Analysis (SEA) was developed and validated to calculate the airborne sound transmission of a HBV floor. There was additional complexity in modelling this floor system compared with other SEA models found in the literature therefore two types of model were compared. To determine the stiffness of the floor it was proposed that bending stiffness predicted using the theories of Huffington and Troitsky provide a more suitable and flexible approach than that of Kimura and Inoue. All SEA models predicted a weighted sound reduction index to within 2.0dB of the measurements.

For CLT plates, an accurate measure of the elastic moduli was sought to determine direct sound transmission. A low-frequency stiffness can be determined by modal measurement and optimisation of the material constants (≤ 100Hz a thin plate model is adequate). At mid to high frequencies (>300Hz) sound transmission of CLT was predicted using a frequency-dependant modulus determined from directly measuring the bending wavespeed. Elastic moduli were extracted from wavespeed data (the Young's modulus was measured to be approximately 50% less stiff than the low-frequency stiffness) and in the y-direction the value of the shear modulus G_{yz} determined that a thick plate model should be applied in this direction.

Finite Element Method (FEM) models of CLT plates and junctions using the elastic moduli determined using the methods described above were validated using measurements of freely and simply supported plates and three simple junctions (L-junction, rotated L-junction and T-junction). The contribution of residual modes (higher than the frequency range of interest) to the calculated point mobility was assessed. The transition to thick plate theory occurs within the frequency range of interest (100-5000Hz). This resulted in a modal density which increases with frequency and some implications of this are discussed. The best agreement between FEM model and measured data was obtained for the simplest (unrotated) L-junction.

Finally, measurement based prediction methods to assess the flanking performance of CLT combined with the HBV floor were investigated. Agreement was obtained between the structure-borne and airborne methodologies if a correction factor, which accounts both for the thick plate properties of the CLT and the fit of measured results to the HBV model, was used. The Df path was the strongest transmission path and the most accurately predicted and hence it was possible to predict the apparent sound reduction index (R') by summing the paths.

Acknowledgements

I would like to thank my supervisors for their support throughout the work. Prof Carl Hopkins, Dr Luboš Krajči, Kurt Eggenschwiler, the University of Liverpool and EMPA for financial backing and technical support. I would also like to thank colleagues at Berner Fachhochschule, Lignum and the industrial partners ERNE, Schuler AG, and Ampack, for testing material and other support. The constructions presented were selected from a comprehensive list of all types of Swiss lightweight and lightweight-heavyweight construction compiled by Berner Fachhochschule, and Lignum.

For the work in chapter 3, I would like to additionally thank Rudolf Buetikover for laboratory commissioning, quality control and technical support, Markus Studer, Hans Martin Troebs, Urs Hintermueller, Robert Widman, Rolf Diggleman for technical support and Simon Huggler, Mica Kraus, Dominika Malkowska, and Stefano Pedersoli for their assistance carrying out the measurements.

Use of the ultrasonic longitudinal wavespeed measurement data in chapter 4 from the paper by Krajči et. al [1] is gratefully acknowledged. Driving-point mobility measurements on the panel (presented in chapter 5) were carried out by Dr Luboš Krajči, and Rudolf Buetikover. Additional data for chapter 5 was also obtained from the following sources: The analysis of recorded impulse responses of the CLT plate to obtain the T_5 measurement was carried out by Dr Mathew Robinson. These were used to calculate the internal loss factors of the CLT plate. The measurement of the total loss factor of the plate when installed in the transmission suite was carried out by Hans Martin Troebs.

Much of the planned data required for chapter 6 was collected by Dr Stefan Schoenwald, Hans Martin Troebs, and Dominika Malkowska in my unforeseen absence. The possibility of airborne flanking through the laboratory space in the newly commissioned laboratory when measuring CLT plates in T-junctions (discussed in section 6.3.5 and confirmed in section 6.6.2 of this thesis) was first posited by colleagues at Berner Fachhochschule. Structure-borne radiation efficiency of the HBV floor and radiation efficiencies of the CLT plate included in APPENDIX D were measured by Hans Martin Troebs.

Finally, I would like to thank my family for their unwavering strength and support throughout the long and difficult process to complete this work. At times when I thought I couldn’t continue, their belief in me carried me forward.

"*To some extent, sanity is a form of conformity. And to some extent, people who are insane are non-conformists, and society and their family wish that they would live what appear to be useful lives.*"

John Forbes Nash, Jr. (quoted from "Words to the Wise: A Medical-Philosophical Dictionary")

Contents

3 Prediction of airborne sound transmission across a timber concrete composite floor using Statistical Energy Analysis (SEA)

4 Prediction of airborne sound transmission across a cross laminated timber plate

5 Prediction of structure-borne sound transmission across junctions of cross laminated timber plates

6 Prediction of direct and flanking transmission across a timber-concrete composite floor and cross laminated timber flanking walls

7 Conclusions

List of figures

List of tables

List of symbols

a	Radius of circular excitation area (m^2)
a_i, a_j	Acceleration at measurement point i (ms^{-2}), absorption length (m^{-1})
a, b	Plate dimensions (m)
c, d	Constants (-)
d	Subscript indicating diffuse incidence
c_0	Speed of sound in air (ms^{-1})
$c_{B,p}$	Bending wave phase velocity (ms^{-1})
$c_{B,thick,p}$	Thick plate bending wave phase velocity (ms^{-1})
$c_{D,p}$	Dilatational wave phase velocity (ms^{-1})
$c_{B,eff}$	Effective bending phase velocity for a plate (ms^{-1})
$c_{R,p}$	Rayleigh wave phase velocity for a plate (ms^{-1})
$c_{g(B)}$	Bending wave group velocity for a plate (ms^{-1})
$c_{g(B,thick)}$	Thick plate bending wave group velocity for a plate (ms^{-1})
c_L	Quasi-longitudinal phase velocity (ms^{-1})
c_S	Shear wave phase velocity (ms^{-1})
$c_{i,thin}$	Thin plate bending wave phase velocity in direction i (ms^{-1})
$c_{i,thick}$	Thick plate bending wave phase velocity in direction i (ms^{-1})
d_{ij}	Velocity ratio between plates i and j (-)
d_R	Length of the repeating cross-section of the plate (m)
d_y	Thickness of the beam in a ribbed plate (m)
d_z	Total combined thickness of the beam and plate in a ribbed plate (m)
e	Volume expansion (-)
f	Frequency (Hz)
f_L	Frequency parameter (Hz)
f_R	Measured modal frequency parameter (Hz)
f_{Ri}	Measured modal frequency number i used to determine elastic moduli (Hz)
f_c	Critical frequency of plate (Hz)
f_{c1}, f_{c2}	Lowest and highest critical frequency of an orthotropic plate, respectively (Hz)
$f_{n,symm}$, $f_{n,anti}$	Symmetric and antisymmetric modal frequencies of dilatational waves (Hz)
f_{ref}	Reference frequency (1000Hz)
f_S	Shear wave cross-over frequency (Hz)
$f_{resonance}$, $f_{anti\text{-}resonance}$	Resonance and anti-resonance frequencies respectively (Hz)
h	Plate thickness (m)

h_{eq}	Equivalent plate thickness (m)
h_i	Thickness of layer i (m)
h_a	Thickness of the actual plate (m)
i	Denotes complex value $\sqrt{-1}$
i, j, k, m, n	Subscript denoting index or layer
k, k'	Coefficients
k	Dynamic stiffness (Nm^{-1}), Wavenumber (m^{-1})
k_B	Bending wavenumber (m^{-1})
$k_{B,i}$	Bending wavenumber in the i^{th} direction (m^{-1})
k_L	Quasi-longitudinal wavenumber (m^{-1})
k_S	Rayleigh wave (corrected shear wave) wavenumber (m^{-1})
l	Length of the junction (m)
m_i	Mass of subsystem i (kg), mass of body i (kg)
$n(\omega)$, $n(f)$	Modal density as a function of angular frequency (rad^{-1}) or frequency (Hz^{-1})
n_i, n_j	Modal density of subsystem i (Hz^{-1}), modal density of subsystem j (Hz^{-1})
$n_{B,thick}(\omega)$	Modal density for bending waves on a thick plate as a function of angular frequency (rad^{-1})
$n_{B,b}(f)$, $n_{B,p}(f)$	Modal density for bending waves on a beam or plate respectively as a function of frequency (Hz^{-1})
$n_{1D}(f)$, $n_{2D}(f)$, $n_{3D}(f)$	Modal density of a 1D, 2D or 3D cavity respectively (Hz^{-1})
p	Subscript indicating phase velocity
$\langle p_R^2 \rangle$, $\langle p_S^2 \rangle$	Mean-square sound pressure in receiving and source rooms respectively (Pa)
q	Arbitrary force (N)
q_i	Arbitrary force in the i^{th} direction (Hz^{-1})
r	Subscript indicating radial co-ordinate
r_0	Radius of hammer tip (m)
r_d	Reverberation distance (m)
Δr	Distance between two points (m)
t	Time (s)
u, v, w	Displacement (m)
$\ddot{u}$	Acceleration (ms^{-2})
v(x,y)	Velocity at position x,y (ms^{-1})
w	Weighting in the weighted least squares method (-)
$w(x,t)$, $w(x,y,t)$	Wave function for a beam or plate at position x (beam) (-), position x,y (plate) and time, t (-)
x, y, z	x-, y-, or z-coordinate (m)
z_y	Distance from the mid-plane of the plate to the neutral axis (m)

A	Area of the cross-section (m^2), Absorption area (m^2)
A_{ij}	Bending beam amplitude coefficient in Warburton's equation (m)
$[A]$, $[B]$	Decomposed matrices of the compliance matrix (Nm^{-2})
A, B, C	Correction factors in Ljunggren's calculation of thick plate airborne transmission (-)
$C_{95\%}$	95% confidence limits (*units of measurement*)
C_{OB}, C_{BC}	Constants denoting baffle orientation and boundary conditions respectively (-)
C_{ij}, C_{in}, C_{mj}	Coefficients in Warburton's equation in i^{th} direction (-)
$[C]$	Stiffness matrix (Nm^{-2})
D_i, D_{ij}	Bending stiffness in the i^{th} direction (Nm), Bending stiffness in the ij plane (Nm)
D_{eff}	Effective bending stiffness (Nm)
$D_{v,ij}$	Velocity level difference between plate i and j (dB)
$\overline{D_{v,ij}}$	Direction-averaged velocity level difference (dB)
D_{fmax}	Maximum measurable flanking reduction index for the Df path (dB)
E_L, E_T, E_R	Young's modulus in the direction longitudinal, tangential or radial to the wood grain (Nm^{-2})
$E_{\parallel}$	Young's modulus parallel to the wood grain (Nm^{-2})
$E_{\perp}$	Young's modulus perpendicular to the wood grain (Nm^{-2})
E	Young's modulus (Nm^{-2})
E_a	Young's modulus of the actual plate (Nm^{-2})
E_i	Young's modulus in the i^{th} direction, Energy in subsystem i (Nm^{-2})
E_{Li}	Young's modulus of the layer L in the i^{th} direction (Nm^{-2})
E_{Leff}	Effective Young's modulus of the layer L (Nm^{-2})
$E_{eff,i}$	Effective Young's modulus in the i^{th} direction (Nm^{-2})
E_{eq}	Equivalent Young's modulus (Nm^{-2})
E_z	Young's modulus in the z-direction (Nm^{-2})
$E_{z,i}$	Young's modulus in the z-direction of layer i (Nm^{-2})
F	Coefficient in Warburton's equation (-)
F_0	Force at the origin (N)
F_i	Force at measurement point i (N)
Fd_{max}	Maximum measurable flanking reduction index for the Fd path (dB)
Ff_{max}	Maximum measurable flanking reduction index for the Ff path (dB)
G_i	Coefficient in Warburton's equation in i^{th} direction (-)
G_{Bessel}	Constant (-)
G_{ij}	Shear constant in plane ij (Nm^{-2})
$G_{ij,k}$	Shear constant in plane ij of layer k (Nm^{-2})
G'	Corrected shear constant (Nm^{-2})

H	Coefficient in Warburton's equation (-)
H_i	Coefficient in Warburton's equation in i direction (-)
I_a	Moment of inertia of the actual plate (m^4)
I_i	Moment of inertia of layer i (m^4)
I_{0i}	Moment of inertia of layer i with respect to its own neutral plane (m^4)
I_{total}	Total moment of inertia of a cross-section (m^4)
$J_0(x)$	Zeroth order Bessel function of the first kind (-)
J_i	Coefficient in Warburton's equation in the i^{th} direction (-)
K	Contact stiffness for plate material (Nm^{-1})
K_{ij}	Direction-averaged vibration reduction index (dB)
K_i	Coefficient in Warburton's equation in the i^{th} direction (-)
L_i	Coefficient in Warburton's equation in the i^{th} direction (-)
L_p	Sound pressure level in the receiving room (dB)
L_T	Total edge length for a room or cavity (m)
L_V	Velocity level of the partition in the receiving room (dB)
L_1, L_2	Smaller and larger of the plate dimensions respectively, sound pressure levels in the source and receiving rooms respectively (m)
L_x, L_y, L_z	Length in the x, y or z direction (m)
L_{p1}, L_{p2}	Sound pressure level in the source and receiving rooms respectively (dB)
M_i	Coefficient in Warburton's equation in i^{th} direction (-)
M	Total mass of plate (kg), Modal overlap (-)
M_i	Bending moment in the i^{th} direction (Nm)
M_{ij}	Bending moment in the ij plane (Nm)
M_I	Bending moment of a repeating section (Nm)
N	Number of connectors (-), Number of modes in a third octave band (-), Number of measurements (-)
$N_{statistical}$	Number of modes in a one-third octave band calculated from the statistical modal density (-)
R	Damping constant (-)
R_Q	Summed residuals (-)
R	Sound reduction index (dB)
R'	Apparent sound reduction index (dB)
R_c	Thin plate sound reduction index (dB)
R_M	Total sound reduction index for a thick plate (dB)
ΔR	Thick plate correction to the sound reduction index (dB)
ΔR_i,	Correction to the sound reduction index for shielding of wall i or j respectively (dB)
R_{max}	Maximum measurable sound reduction index of a facility (dB)

S	Surface area (m^2)
S_{ij}	Compliance component (m^2N^{-1})
S_0	Area of the separating partition (m^2)
S_T	Total surface area of a room or cavity (m^2)
$[S]$	Compliance matrix (m^2N^{-1})
T, T_5, T_{20}, T_{30}	Reverberation time (s), reverberation time determined from the time taken for the sound pressure level to decay 5dB, 20dB or 30dB (s)
T_{max}	Maximum kinetic energy (J)
U	Plate perimeter (m)
U_a	Strain energy of the actual plate (J)
U_x	Strain energy of the equivalent plate (J)
$U(L_x/L_y)$	Function of the rectangular shape of the plate (-)
V_{max}	Maximum potential energy (J)
V	Volume (m^3)
$W(x,y)$	Spatial part of the wave function of a plate (-)
$Y(x,y)$	Wave mobility of a plate ($mN^{-1}s^{-1}$)
Y_{dp}, Y_i, Y_j, Y_c	Driving-point mobility ($mN^{-1}s^{-1}$), driving-point mobility of subsystem i ($mN^{-1}s^{-1}$), driving-point mobility of subsystem j ($mN^{-1}s^{-1}$), mobility of a connector ($mN^{-1}s^{-1}$)
$<Y_j>$	Mean wave mobility of subsystem j ($mN^{-1}s^{-1}$)
Z	Surface impedance (Nsm^{-1})
γ, γ'	Solutions to the transcendental equations (-)
γ_{ij}	Transmission coefficient for a junction (-)
δ	Residual (-)
δ_κ	Residual (index κ) (-)
ε_i	Strain component in direction i (-)
$[\varepsilon]$	Strain component matrix (-)
η	Loss factor (-)
η_i	Total loss factor in subsystem i (-)
$\eta_{diss,i}$	Internal loss factor in subsystem i (-)
η_{ij}	Coupling loss factor between subsystems i and j (-)
θ_i	Beam function in direction i (-)
κ	Shear correction factor (-)
κ_i	Shear correction factor in direction i (-)
κ_{DS}	Ratio of the dilatational to transverse shear wave (-)
λ	Lamé constant (Nm^{-2})
λ	Wavelength (m)
λ_S	Wavelength of the Rayleigh (corrected shear) wave (m)

μ	Lamé constant (Nm^{-2}), square root of ratio of critical frequency to frequency of interest (-)
ν	Poisson's ratio (-)
ν_{Li}	Poisson's ratio of layer *i* (-)
ν_{eff}	Effective Poisson's ratio (-)
ν_{ij}	Poisson's ratio in the *ij* plane (-)
$\nu_{ij,k}$,	Poisson's ratio in the *ij* plane of the *k*th layer (-)
$\nu_{section}$	Section Poisson's ratio (-)
ξ	Transverse shear wavenumber (m^{-1})
ξ'	Dimensionless transverse shear wavenumber (-)
ρ	Density (kgm^{-3})
ρ_0	Density of air (kgm^{-3})
ρ_S	Surface density of a plate (kgm^{-2})
ρ_{eq}	Equivalent density (kgm^{-3})
ρ_i	Density of a layer (kgm^{-3})
σ	Standard deviation (*units of measurement*)
σ_i	Stress component in the i^{th} direction (Nm^{-2})
σ_i, σ_j	Radiation efficiency of panel *i*, radiation efficiency of panel *j* (-)
σ_{f_c}	Radiation efficiency of the plate assuming the wavespeed in the plate is always equal to that in air (-)
σ_a, σ_s	Measured radiation efficiency due to airborne excitation, measured radiation efficiency due to structure-borne excitation (-)
σ_r, σ_{nr}	Resonant airborne radiation efficiency, non-resonant radiation efficiency (-)
$[\sigma]$	Stress components matrix (Nm^{-2})
τ_{ij}	Shear stress component in plane *ij* (Nm^{-2})
τ	Transmission coefficient (-)
τ'	Apparent transmission coefficient (-)
τ_d	Sound power ratio in the receiving room due to sound directly coming from the partition (Dd and Fd paths) (-)
τ_f	Sound power ratio in the receiving room from the Ff and Df flanking paths (-)
τ_e	Sound power ratio in the receiving room due to small elements mounted in the partition (-)
τ_s	Sound power ratio due to airborne flanking outside the rooms (-)
τ_{NR}	Non-resonant transmission coefficient (-)
ϕ_i	Beam function in the i^{th} direction (-)
$\{\Phi\}$	Eigenvectors (-)
$\Delta\phi_{ij}$	Phase difference between points *i* and *j* (rad)
$\Delta\varphi_{ij}$	Corrected phase difference between two points *i* and *j* (rad)

ψ_i	Plate rotation in direction i (-)
ω	Angular frequency (rad)
ω_i	Angular eigenfrequency (rad)
$\Pi_{\text{in},i}$	Power input to subsystem i (W)
$\Pi_{\text{diss},i}$	Power dissipated in subsystem i (W)
Π_{ij}	Power transfer from subsystem i to j (W)
Ω	Dimensionless frequency parameter (-)
$\langle ... \rangle$	Denotes mean value or column matrix
$\{ ... \}$	Denotes column matrix
$[...]$	Denotes square matrix

1 Introduction

1.1 Modern timber building systems

Three main types of timber building system exist in the marketplace [2, 3]: Timber-frame lightweight construction, solid wood and wood fibre construction and timber-frame heavyweight construction. It is the latter two which are considered in more detail in this thesis however all three types are discussed here to provide context.

1.1.1 Timber-frame lightweight construction

Timber-frame lightweight structures are a very versatile method of construction, and often incorporate cavity wall constructions. They may be assembled in the factory as plate or volume modules or the raw materials may be assembled on site. Examples of construction materials include Holzwerkstoffe (HWS) (e.g. wood board, Plywood /Veneer OSB, MDF Particleboard /Melamine) and plasterboard. Point connections (e.g. nails, screws) between materials with or without glue are common. There has also been a return to traditional methods to connect joints which exclude metal nails, screws, or glues alongside increased use of wood soaking or heating methods to minimise use of glues, wood preserving, waterproofing and fireproofing products which can be environmentally problematic.

Several studies have examined models for sound transmission across timber-frame lightweight walls or floors [4, 5, 6, 7]. For heavyweight constructions, Statistical Energy Analysis (SEA) models are commonly used but SEA has also been considered for lightweight constructions [8]. Beams forming a timber supporting framework can be modelled as individual subsystems. Craik and Galbrun [9] showed that connections between timber beams can be assumed to be pinned (also called hinged). Galbrun [10] extended this work to connections between plates and

structural supporting frameworks where deep beams tended to follow a pinned junction model, whereas shallow beams followed a rigid junction model [10, 11].

Incorporating a timber framework into SEA is potentially problematic because the low modal overlap factors of timber beams can produce system dependant results at low frequencies. (i.e. high peaks and troughs in frequency regions of low modal density) [12, 9]. To address this problem Craik *et al*. [12] and Craik and Galbrun [9] proposed a correction factor for the Coupling Loss Factors (CLFs) between coupled beams based on the measured mobility to determine an "envelope" of the expected response at low frequencies.

1.1.2 Heavyweight timber-frame construction

Heavyweight timber-frame construction is used in multi-storey buildings to satisfy fire-safety and earthquake-proofing requirements. These structures require deeper beams compared to lightweight timber-frame structures. Solid timber or glulam products are often used as they provide more uniform strength properties throughout the beam. These constructions are typically prescribed in conjunction with floating floors, shielding elements and suspended ceilings. An example of a basic Swiss timber-frame heavyweight construction is the Holzbetonverbund (HBV) floor. Concrete is cast over lightweight OSB panels which are glued and nailed to deep timber beams (Figure 1-1).

There are few papers concerning modelling of the sound insulation for heavyweight timber-frame construction [13]. However, much of the theory which applies to lightweight panels with a timber structural framework could also apply to heavyweight panels with a similar framework.

1.1.3 Solid wood and wood fibre construction

Wood is a highly orthotropic raw material with elastic moduli ratios of the order 24:1 comparing the direction longitudinal to the wood grain with the direction tangential to the growth rings [14]. Solid wood and wood fibre construction can often be simplified to a specially orthotropic description if the wood grain is symmetrically oriented about the mid-plane of the plate. An example of a multilayer specially

orthotropic laminate in which the alternate layers are rotated by the angles $+\theta$ and $-\theta$ is presented in [14]. However, unusual angles and curvatures sometimes mean that this simplification is not appropriate. Modular construction methods are making unusual geometries more economical and more common; hence the theory of generalised orthotropic plates and shells can be applied in these cases. A "general" [15] orthotropic material description requires additional elastic coefficients and shear-shear or shear-extension coefficients may be required. If the orientation of the material is known the anisotropic behaviour can be estimated by a calculation involving transformation matrices of the measured orthotropic moduli [15].

Failure properties of the raw material can be highly variable due to the distribution of early and late wood throughout sawn timber and imperfections such as knots. Failure grading of the raw material is done by visual inspection so that the elastic properties of the material can be homogenised and failure characteristics can be removed prior to the manufacture of finished wood products. For example, this can be achieved by including laminates where thin sheets of wood are combined in layers (e.g. plywood), or aligning thicker strips of wood, such as finger joints free of imperfections in layers (e.g. glulam or Cross Laminated Timber (CLT)).). The simplest case is where the material fibres are aligned with the edges of the beam or plate. Smaller pieces of wood or wood chip disperse defects more readily, randomly distributing the fibres which can result in a more homogeneous material. However, the bending stiffness and nature of the constitutive relations of the finished material is also dependant on the thickness and bonding of the adhesive product.

Placing weaker material closer to the neutral plane in a beam or panel, and stronger material on the upper and lower surfaces is common practice when an improvement in bending properties is required [14]. A side effect of manufacturing processes such as these is a change in the stiffness characteristics of the finished material compared with solid wood products, which may need to be considered when modelling the vibrational and acoustic properties of the finished material. As a simplifying assumption, the glue between laminae is often assumed to be perfectly bonded which may occur with a thermosetting resin but not with other adhesives. For laminated products, the quality of glue-lines may affect the failure properties of the finished

material however they are not believed to affect the elastic behaviour [14]. The elastic properties of glue are often close to the wood product [14].

As a subtype of solid wood construction CLT panels are usually made from an odd number of layers of material (e.g. 3 or 5 are common). They are assembled from thin strips of timber during the manufacturing process which results in a material with more homogenised material properties than lumber. Some examples of Swiss CLT construction are shown in Figure 1-2 and Figure 1-3.

A large variety in technologies, working practices and workmanship can result in different field sound insulations for nominally identical constructions [2]. Solid wood and wood fibre construction products are ideal materials for modular construction owing to the assembly that is possible in the factory and the fact that materials are lightweight in comparison to masonry/concrete. This means fast site assembly with a high degree of flexibility and reduced costs. Modern machining techniques have improved precision and tolerances and thus broadened the variety of architectural structures possible with these materials [16].

1.2 Statement of objectives

The main aim in this thesis was to determine the applicability of measurement-based prediction methods to combined HBV/CLT junctions as shown in Figure 1-3. Chapter 2 introduces the approaches to prediction (analytical methods, SEA, FEM and measurement-based SEA methodologies) that were considered and used in the work. Four intermediate goals were identified and a single chapter, of the subsequent chapters of the thesis, was devoted to each. The intermediate goals were:

Develop an appropriate SEA model for direct transmission across a timber-frame heavyweight (HBV) floor (shown in Figure 1-1) with experimental validation in a test laboratory. The model should consider some of the more difficult aspects of the floor construction such as appropriate modelling of the supporting beams and suspended ceiling structure. An assessment of the appropriateness of current methodologies; clarifying the underlying energy transfer processes and mechanisms in the airborne sound transmission, where possible, is described in chapter 3.

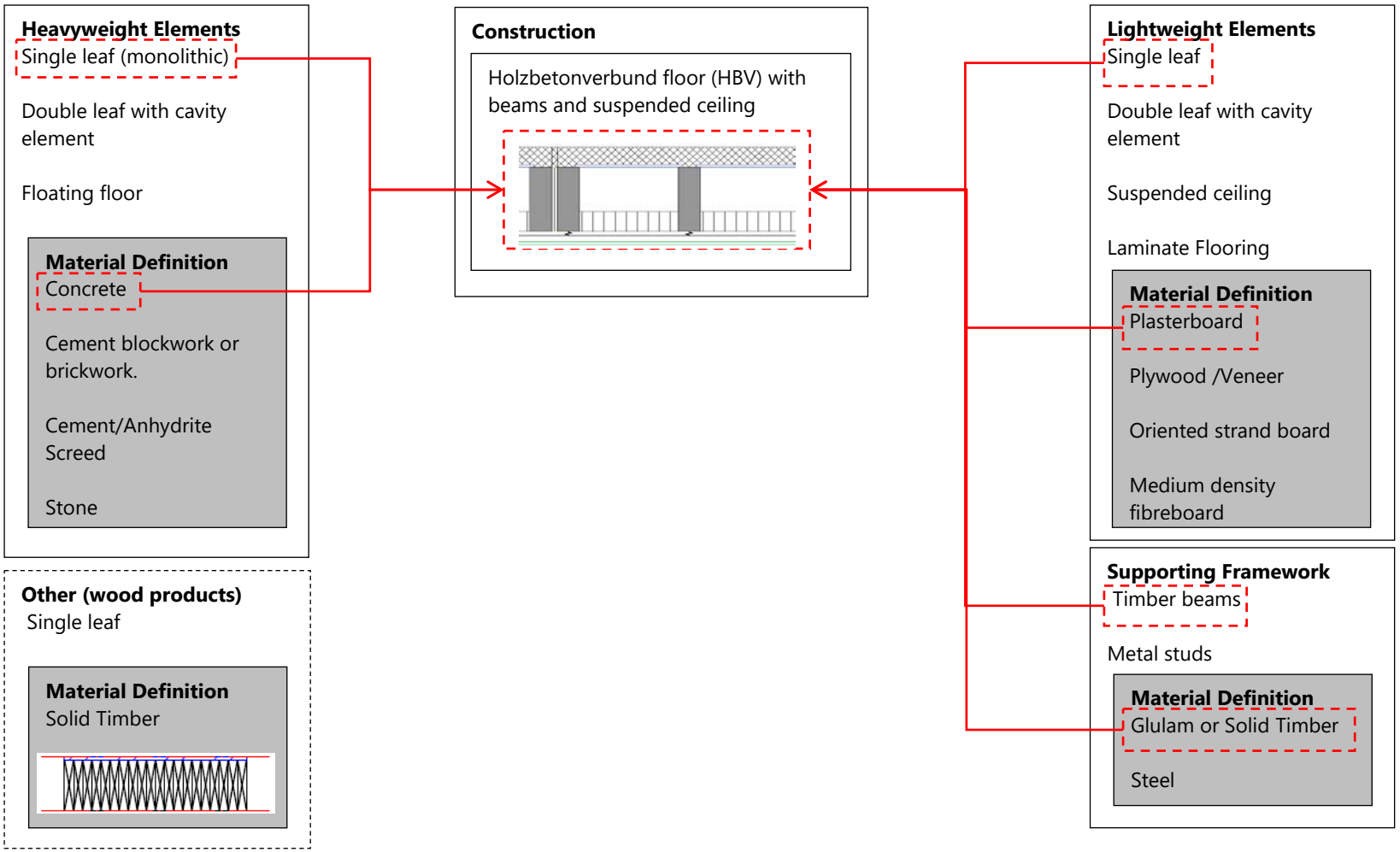

Figure 1-1 Some examples of Swiss construction types; floor examples (sketches reproduced from [3]).

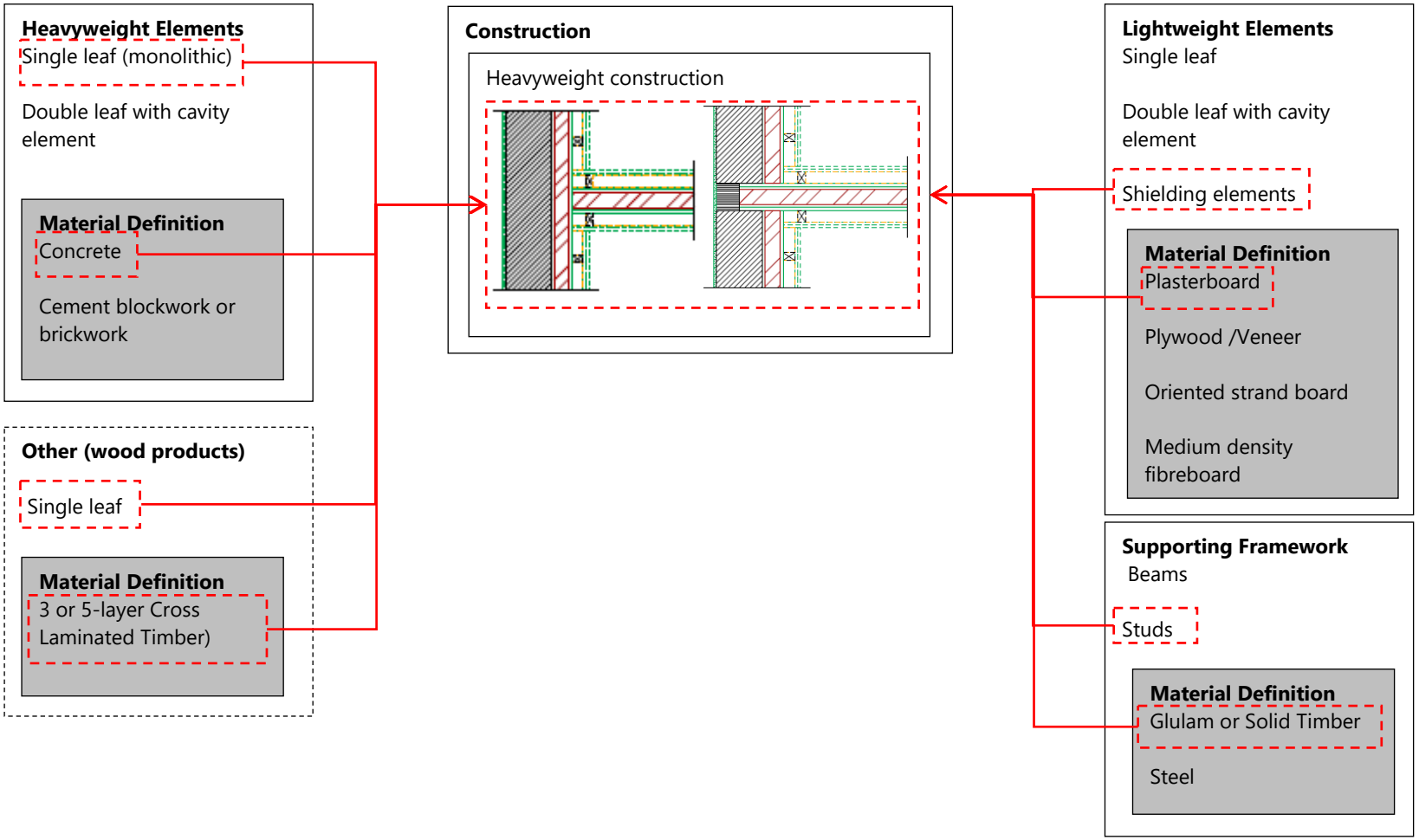

Figure 1-2 Some examples of Swiss Construction types; façade wall/wall junction examples (sketches reproduced from [3]).

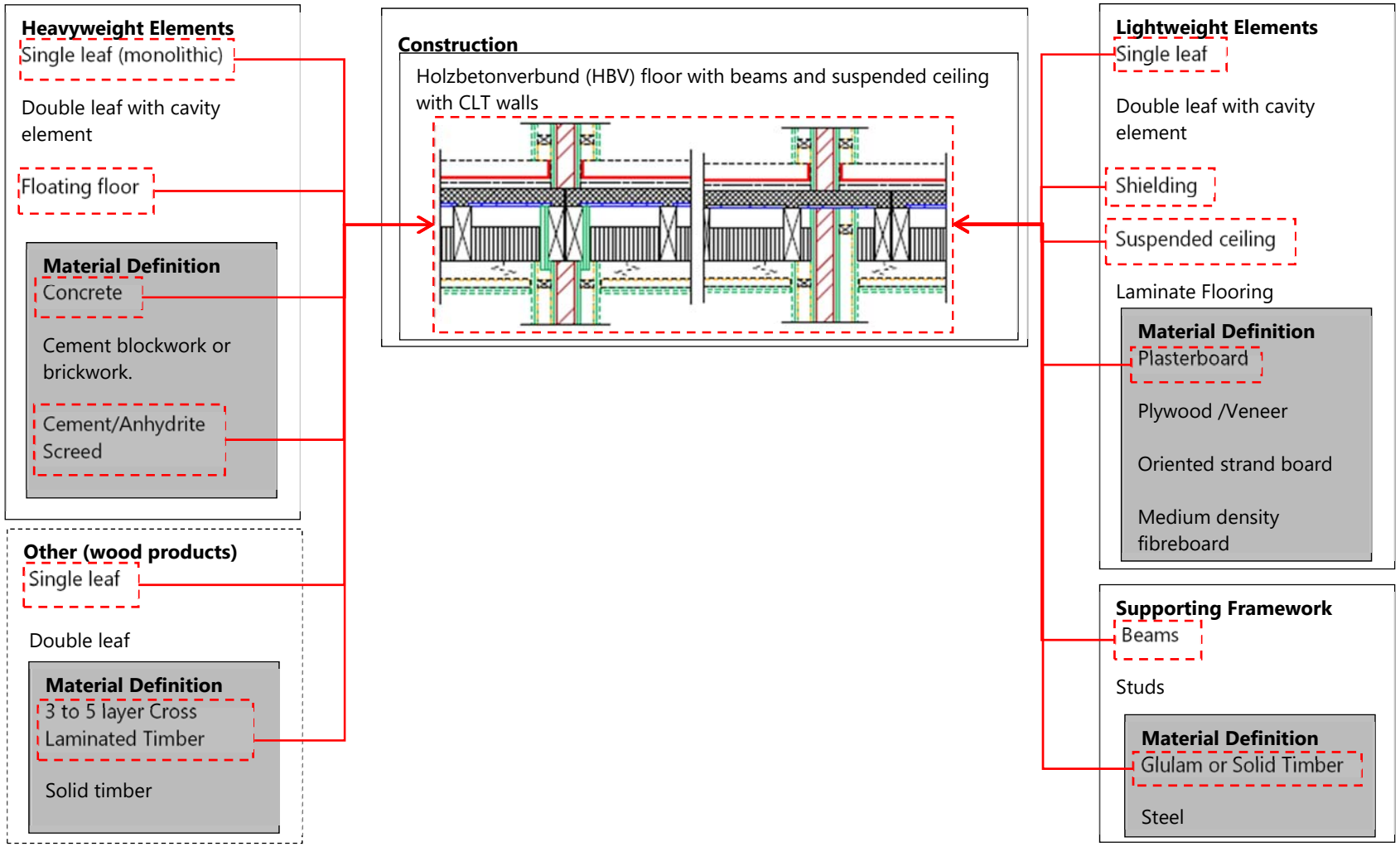

Figure 1-3 Some examples of Swiss construction types; floor/wall junction examples (sketches reproduced from [3]).

Overcome known difficulties to predict the sound insulation models of timber panels (e.g. plywood [17] and CLT [1, 18]) by assessing techniques to determine the elastic moduli of a CLT plate for implementation in sound transmission models. The focus is on a methodology to determine the frequency-dependant elastic moduli of CLT plates to improve prediction of airborne transmission. A review and validation of models with the improved input parameters to test the appropriateness of the different measurement procedures is described in chapter 4.

Investigate the structural dynamics of CLT plates and the structure-borne sound transmission for CLT junctions (shown in Figure 1-2). Identify appropriate finite element method (FEM) models, and assess the appropriateness of boundary conditions and coupling conditions between CLT plates. Chapter 5 describes the application of FEM to determine the point mobility and flanking transmission of a CLT wall and three simple junctions using the elastic moduli determined in chapter 4.

Execute and validate laboratory measurements of combined HBV/CLT junctions. Compare structure-borne and airborne methodologies and, where possible, justify appropriate methodological selections. Chapter 6 uses a flanking laboratory facility to bring together the findings of chapters 3, 4 and 5 and assesses measurement-based prediction methods for the overall sound insulation performance of a timber-frame heavyweight floor with CLT walls.

Finally, chapter 7 summarises the main findings and impact of the research outlining areas for further work.

1.3 Novel applications

Novel aspects of this thesis include the application of methods by Huffington [19] and Troitsky [20] to determine bending stiffness in the directions parallel and perpendicular to a rib-stiffened plate where the ribs consist of a different material from the plate. This is applied to the prediction of airborne sound insulation for the timber-frame heavy-weight floor. In addition, improvements to prediction methods to determine airborne sound transmission of a CLT plate are sought by incorporating measured wavespeed data. To date, accurate models of CLT rely on the intelligent

manipulation of the plate material parameters (e.g. elastic modulus and/or loss factor data [18, 21]) by an experienced designer to obtain close agreement with measured results. The incorporation of measured plate material properties does not work for some plate configurations and agreement with the airborne sound transmission prediction [1] is not achieved. Implementation of FEM highlights the influence of residual modes [22] on the predicted mobility of freely hanging and simply supported CLT plates. The modal density is also shown to be problematic when trying to estimate the low-frequency accuracy of the flanking transmission of T- and L-shaped CLT junctions, due to the fluctuations caused by prominent modal peaks in the data. Finally, development of a measurement regime to validate laboratory based prediction methods of a combined CLT and HBV junction highlights difficulties in the application of methods to junctions of combinations of these plates.

2 Theory

2.1 Introduction

This chapter gives the background theory for the modelling methodologies used in the thesis, these were: analytical methods, SEA, FEM and measurement-based SEA.

Analytical methods describing the fundamentals of the dynamic behaviour of isotropic and orthotropic plates are covered in section 2.2; this provides background to the modelling of the timber-concrete composite floor and CLT walls in later chapters 3 and 4. Statistical models based on SEA to predict sound and vibration transmission in built-up structures are described in section 2.3, as SEA was used in chapter 3 to predict the airborne sound insulation of a timber-concrete composite floor. Potential issues with statistical approaches occur when components of walls and floors lack high modal densities and modal overlap. In these cases, a potential solution is a deterministic method such as FEM as described in section 2.4 which was used in chapters 4 and 5 for CLT plates. When using SEA to model airborne and flanking transmission the complexity of modern building constructions is such that not all transmission coefficients or loss factors can be determined from material properties. Hence not all information is available for an SEA model and the incorporation of some measured parameters becomes inevitable [8]. For this reason, a measurement-based approach to SEA is introduced in section 2.5 that combines laboratory measurements and SEA to determine sound and vibration transmission. This was used in chapter 6 to predict the combination of direct and flanking transmission across the timber-concrete composite floor and CLT walls.

2.2 Fundamental theory for individual plates

2.2.1 Constitutive relations of an isotropic material

From Hooke's law, the properties of a material are fully described by the stiffness (or compliance) matrix which relates stress to strain

$$\{\sigma\} = [C]\{\varepsilon\} \tag{2-1}$$

where $[\sigma]$ is the stress component matrix, $[C]$ is the stiffness matrix. and $\{\varepsilon\}$ is the strain component matrix. An isotropic material is fully described by two independent constants [23]:

$$\begin{Bmatrix} \sigma_x \\ \sigma_y \\ \sigma_z \\ \tau_{yz} \\ \tau_{zx} \\ \tau_{xy} \end{Bmatrix} = \begin{bmatrix} \lambda+2\mu & \lambda & \lambda & 0 & 0 & 0 \\ \lambda & \lambda+2\mu & \lambda & 0 & 0 & 0 \\ \lambda & \lambda & \lambda+2\mu & 0 & 0 & 0 \\ 0 & 0 & 0 & \mu & 0 & 0 \\ 0 & 0 & 0 & 0 & \mu & 0 \\ 0 & 0 & 0 & 0 & 0 & \mu \end{bmatrix} \begin{Bmatrix} \partial_x u \\ \partial_y v \\ \partial_z w \\ \partial_y w + \partial_z v \\ \partial_z u + \partial_x w \\ \partial_x v + \partial_y u \end{Bmatrix} \tag{2-2}$$

where σ_x, σ_y, σ_z are the stress components, τ_{yz}, τ_{zx}, τ_{xy} are the shear stress components, λ, μ are the Lamé constants, $\partial_x u$, $\partial_y v$, $\partial_z w$ are the strain components and $\partial_y w + \partial_z v$, $\partial_z u + \partial_x w$, $\partial_x v + \partial_y u$ are the shear strain components. Hooke's law together with the differential equations of equilibrium for a three-dimensional body [23] gives:

$$\partial_x \sigma_x + \partial_y \tau_{xy} + \partial_z \tau_{xz} - q_x = 0 \tag{2-3}$$

$$\partial_y \sigma_y + \partial_x \tau_{xy} + \partial_z \tau_{yz} - q_y = 0 \tag{2-4}$$

$$\partial_z \sigma_z + \partial_x \tau_{xz} + \partial_y \tau_{yz} - q_z = 0 \tag{2-5}$$

where q_x, q_y, and q_z are in this case the d'Alembert forces in the x, y and z directions, gives the Poisson equations [23] for a three-dimensional body:

$$(\lambda + \mu)\partial_x e + \mu \nabla^2 u - \rho \partial_{tt} u = 0 \tag{2-6}$$

$$(\lambda + \mu)\partial_y e + \mu\nabla^2 v - \rho\partial_{tt} v = 0 \tag{2-7}$$

$$(\lambda + \mu)\partial_z e + \mu\nabla^2 w - \rho\partial_{tt} w = 0 \tag{2-8}$$

where the volume expansion $e = \partial_x u + \partial_y v + \partial_z w$, ∇^2 is the three-dimensional operator $\nabla^2 = \partial_{xx} + \partial_{yy} + \partial_{zz}$. Eqns. (2-6) to (2-8) can be decoupled [23, 24] into transverse shear waves where the change in volume is assumed to be zero:

$$\mu\nabla^2 u - \rho\partial_{tt} u = 0 \tag{2-9}$$

$$\mu\nabla^2 v - \rho\partial_{tt} v = 0 \tag{2-10}$$

$$\mu\nabla^2 w - \rho\partial_{tt} w = 0 \tag{2-11}$$

For shear waves the phase velocity is [23]

$$c_{\mathrm{S}} = \sqrt{\frac{\mu}{\rho}} \tag{2-12}$$

and dilatational waves where the rotation of an element is assumed to be zero [23]

$$(\lambda + 2\mu)\nabla^2 u - \rho\partial_{tt} u = 0 \tag{2-13}$$

$$(\lambda + 2\mu)\nabla^2 v - \rho\partial_{tt} v = 0 \tag{2-14}$$

$$(\lambda + 2\mu)\nabla^2 w - \rho\partial_{tt} w = 0 \tag{2-15}$$

For dilatational waves, the phase velocity is [23]

$$c_{\mathrm{D},p} = \sqrt{\frac{\lambda + 2\mu}{\rho}} \tag{2-16}$$

The ratios between the phase velocities of the different wave types (which are functions of the Poisson ratio) are commonly used in computations. The ratio of the dilatational to transverse shear wave velocities is given by

$$\kappa_{\mathrm{DS}} = \frac{c_{\mathrm{D},p}}{c_{\mathrm{S},p}} = \sqrt{\frac{\lambda + 2\mu}{\mu}} = \frac{2(1-\nu)}{(1-2\nu)} \tag{2-17}$$

Dilatational waves in a solid produce a rolling motion at a surface boundary known as Rayleigh waves [23]. The ratio of the Rayleigh wave to transverse shear wave velocities is given in section 2.2.5.

The symmetric modal frequencies of dilatational waves (a.k.a. thickness-stretch modes [24]) can be calculated using [8]:

$$f_{n,symm} = \frac{nc_{D,p}}{2h} \tag{2-18}$$

and the antisymmetric modal frequencies of dilatational waves (thickness-stretch modes [24]) are given by

$$f_{m,anti} = \frac{mc_{D,p}}{h} \tag{2-19}$$

where *n* and *m* take integer values, and *h* is the thickness.

The simplicity of the isotropic (also transversely isotropic and specially orthotropic) stiffness matrix is such that it can be decomposed into two separate matrices *A* and *B*

$$[S] = [C]^{-1} = \begin{bmatrix} [A]^{-1} & 0 \\ 0 & [B]^{-1} \end{bmatrix} \tag{2-20}$$

where [*S*] is the compliance matrix

$$[A]^{-1} = \begin{bmatrix} S_{11} & S_{12} & S_{13} \\ S_{12} & S_{22} & S_{23} \\ S_{13} & S_{23} & S_{33} \end{bmatrix} \tag{2-21}$$

$$[B]^{-1} = \begin{bmatrix} S_{44} & 0 & 0 \\ 0 & S_{55} & 0 \\ 0 & 0 & S_{66} \end{bmatrix} \tag{2-22}$$

Inverting the stiffness matrix to obtain the decomposed compliance matrix for an isotropic material gives [25]:

$$[A]^{-1} = \begin{bmatrix} S_{11} & S_{12} & S_{12} \\ S_{12} & S_{11} & S_{12} \\ S_{12} & S_{12} & S_{11} \end{bmatrix}$$

$$\text{where } S_{11} = \frac{(\lambda + 2\mu)^2 - \lambda^2}{(\lambda + 2\mu)^3 - 3(\lambda + 2\mu)\lambda^2 + 2\lambda^3} \tag{2-23}$$

$$\text{and } S_{12} = \frac{\lambda^2 - (\lambda + 2\mu)}{(\lambda + 2\mu)^3 - 3(\lambda + 2\mu)\lambda^2 + 2\lambda^3}$$

$$[B]^{-1} = \begin{bmatrix} 1/\mu & 0 & 0 \\ 0 & 1/\mu & 0 \\ 0 & 0 & 1/\mu \end{bmatrix} \tag{2-24}$$

and comparing with the terms of the compliance matrix [15]:

$$\begin{Bmatrix} \partial_x u \\ \partial_y v \\ \partial_z w \\ \partial_y w + \partial_z v \\ \partial_z u + \partial_x w \\ \partial_x v + \partial_y u \end{Bmatrix} = \begin{bmatrix} 1/E & -\nu/E & -\nu/E & 0 & 0 & 0 \\ -\nu/E & 1/E & -\nu/E & 0 & 0 & 0 \\ -\nu/E & -\nu/E & 1/E & 0 & 0 & 0 \\ 0 & 0 & 0 & 2(1+\nu)/E & 0 & 0 \\ 0 & 0 & 0 & 0 & 2(1+\nu)/E & 0 \\ 0 & 0 & 0 & 0 & 0 & 2(1+\nu)/E \end{bmatrix} \begin{Bmatrix} \sigma_x \\ \sigma_y \\ \sigma_z \\ \tau_{yz} \\ \tau_{zx} \\ \tau_{xy} \end{Bmatrix} \tag{2-25}$$

where *E* is the Young's modulus and *ν* is Poisson's ratio. It is observed that only extension, shear and extension-extension coupling [15] are required. The relations to the Lamé constants [26] are given by:

$$\mathrm{E} = \frac{\mu(2\mu + 3\lambda)}{(\mu + \lambda)} = 2\mu(1 + \nu) \tag{2-26}$$

$$\lambda = \frac{\nu E}{1 - \nu - 2\nu^2} = \frac{\nu E}{(1 + \nu)(1 - 2\nu)} \tag{2-27}$$

$$\mu = \frac{E}{2(1 + \nu)} \tag{2-28}$$

2.2.2 Transversely isotropic material

The diagonally symmetric strain-stress relationship for a transversely isotropic material is described using the following compliance matrix [15]

$$\begin{Bmatrix} \partial_x u \\ \partial_y v \\ \partial_z w \\ \partial_y w + \partial_z v \\ \partial_z u + \partial_x w \\ \partial_x v + \partial_y u \end{Bmatrix} = \begin{bmatrix} 1/E & -\nu/E & -\nu_{zx}/E & 0 & 0 & 0 \\ -\nu/E & 1/E & -\nu_{zy}/E & 0 & 0 & 0 \\ -\nu_{xz}/E & -\nu_{yz}/E & 1/E & 0 & 0 & 0 \\ 0 & 0 & 0 & 1/G_{yz} & 0 & 0 \\ 0 & 0 & 0 & 0 & 1/G_{xz} & 0 \\ 0 & 0 & 0 & 0 & 0 & 2(1+\nu)/E \end{bmatrix} \begin{Bmatrix} \sigma_x \\ \sigma_y \\ \sigma_z \\ \tau_{yz} \\ \tau_{zx} \\ \tau_{xy} \end{Bmatrix} \quad (2\text{-}29)$$

where $\nu_{xz}=\nu_{yz}$ is the section Poisson's ratio and G_{xz} and G_{yz} are the shear constants in the *xz*- and *yz*- planes. The material is fully described by five independent elastic moduli. In a thin laminate, it can be assumed that $\sigma_z=\tau_{yz}=\tau_{zx}=0$ and the material description is that of an isotropic material.

For a transversely isotropic (or orthotropic) material Eqns. (2-18) and (2-19) is difficult to implement because the stiffness matrix is a more complex combination of the engineering constants than for isotropic plates (the Lamé constants in Eqn. (2-2) no longer apply). Numerical methods are therefore needed and in this thesis, estimates are based on measured wavespeed data.

2.2.3 Specially orthotropic material

A material may be classified as specially orthotropic if there is a symmetric organisation of the laminate. The diagonally symmetric strain-stress relationship for a specially orthotropic material is described using the following compliance matrix [15]

$$\begin{Bmatrix} \partial_x u \\ \partial_y v \\ \partial_z w \\ \partial_y w + \partial_z v \\ \partial_z u + \partial_x w \\ \partial_x v + \partial_y u \end{Bmatrix} = \begin{bmatrix} 1/E_x & -\nu_{yx}/E_y & -\nu_{zx}/E_z & 0 & 0 & 0 \\ -\nu_{xy}/E_x & 1/E_y & -\nu_{zy}/E_z & 0 & 0 & 0 \\ -\nu_{xz}/E_x & -\nu_{yz}/E_y & 1/E_z & 0 & 0 & 0 \\ 0 & 0 & 0 & 1/G_{yz} & 0 & 0 \\ 0 & 0 & 0 & 0 & 1/G_{xz} & 0 \\ 0 & 0 & 0 & 0 & 0 & 1/G_{xy} \end{bmatrix} \begin{Bmatrix} \sigma_x \\ \sigma_y \\ \sigma_z \\ \tau_{yz} \\ \tau_{zx} \\ \tau_{xy} \end{Bmatrix} \quad (2\text{-}30)$$

Six different Poisson ratios are shown in the matrix. Poisson's ratio is defined as the ratio of passive strain to active strain [14]. The Poisson's ratios related by the equations

$$\frac{\nu_{yx}}{E_x} = \frac{\nu_{xy}}{E_y} \quad (2\text{-}31)$$

$$\frac{\nu_{zx}}{E_x} = \frac{\nu_{xz}}{E_z} \quad (2\text{-}32)$$

$$\frac{\nu_{yz}}{E_z} = \frac{\nu_{zy}}{E_y} \quad (2\text{-}33)$$

These sets of equations in combination with the orientation of the fibres and symmetry of the elastic moduli in a specially orthotropic laminate (shown in Figure 2-1) describe the behaviour.

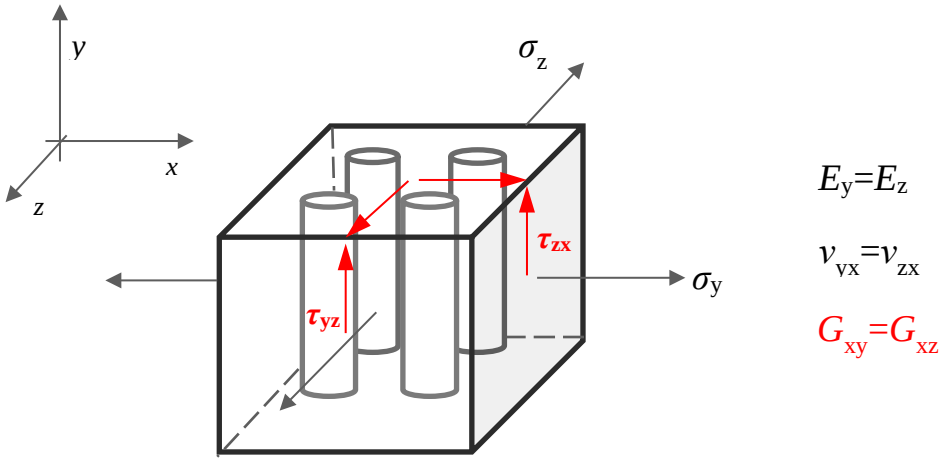

Figure 2-1 The orientation and symmetry of the fibres in a specially orthotropic laminate [15].

The material is fully described by eight independent elastic moduli. In a thin laminate, it can be assumed that $\sigma_z=\tau_{yz}=\tau_{zx}=0$. In this thesis, these relations are assumed to hold within the CLT panel and to determine the elastic moduli for the complete CLT panel.

2.2.4 Free bending vibration

2.2.4.1 Frequency range of applicability of the theories

The frequency ranges of applicability of thin plate theory or Mindlin's first order shear deformation theory can be estimated using [24]

$$\Omega^2 = \frac{f^2}{f_{1,\text{anti}}^2} = \pi\xi'^2\left[\frac{1}{3}\left(1+\frac{1}{\kappa_{DS}^2}\right)\right]^{1/2} \tag{2-34}$$

where Ω is the ratio of frequency to the frequency of the lowest antisymmetric thickness-shear wave (see Eqn. (2-19)), ξ' is the transverse shear wave number converted to a dimensionless form $\xi'=h\xi/\pi$ and κ_{DS}^2 is the ratio between the dilatational and transverse shear wave velocities (see Eqn. (2-17)). The range of applicability is estimated to lie in the range $0\leq\Omega\leq0.1$ for thin plate theory, in the range $0\leq\Omega\leq1.5$ [24] for Mindlin's first order shear deformation theory.

2.2.4.2 Thin plates

The definition of a thin plate is that the neutral plane traces a straight line thorough the material which remains straight and normal and its length is unchanged under load [15]. The principle material directions of the plate are shown in Figure 2-2.

In the case of a specially orthotropic material the moments per unit width (M_x, M_y, M_{xy}) for a thin laminate in bending can be determined reducing the compliance matrix to give

$$\begin{Bmatrix} M_x \\ M_y \\ M_{xy} \end{Bmatrix} = \int_{-h/2}^{h/2} \begin{Bmatrix} \sigma_x \\ \sigma_y \\ \tau_{xy} \end{Bmatrix} z\,\mathrm{d}z = \begin{bmatrix} S_{11} & S_{12} & 0 \\ S_{12} & S_{22} & 0 \\ 0 & 0 & S_{66} \end{bmatrix} \int_{-h/2}^{h/2} \begin{Bmatrix} \partial_{xx}w(x,y,t) \\ \partial_{yy}w(x,y,t) \\ 2\partial_x\partial_y w(x,y,t) \end{Bmatrix} z^2\,\mathrm{d}z \tag{2-35}$$

where *w(x,y,t)* is the wave function (where ∂_{ii} denotes $\frac{\partial^2}{\partial i^2}$, and ∂_{ij} denotes $\frac{\partial^2}{\partial i \partial j}$), which results in the following relations between the moments and curvatures

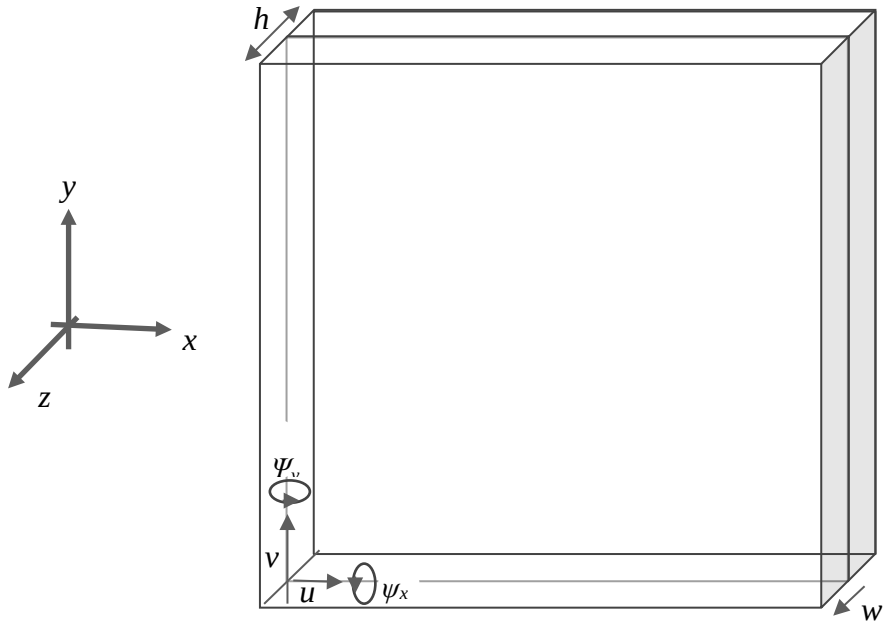

Figure 2-2 Sketch of the principle coordinate directions, thickness, displacements and rotation of the mid plane of the plate

$$\begin{Bmatrix} M_x \\ M_y \\ M_{xy} \end{Bmatrix} = \begin{bmatrix} {E_x h^3}/{12(1-\nu_{xy}\nu_{yx})} & \nu_{xy}{E_y h^3}/{12(1-\nu_{xy}\nu_{yx})} & 0 \\ \nu_{xy}{E_y h^3}/{12(1-\nu_{xy}\nu_{yx})} & {E_y h^3}/{12(1-\nu_{xy}\nu_{yx})} & 0 \\ 0 & 0 & {G_{xy} h^3}/{12} \end{bmatrix} \begin{Bmatrix} \partial_{xx} w(x,y,t) \\ \partial_{yy} w(x,y,t) \\ 2\partial_x \partial_y w(x,y,t) \end{Bmatrix} = \begin{bmatrix} D_x & \nu_{xy} D_y & 0 \\ \nu_{xy} D_y & D_y & 0 \\ 0 & 0 & D_{xy} \end{bmatrix} \begin{Bmatrix} \partial_{xx} w(x,y,t) \\ \partial_{yy} w(x,y,t) \\ 2\partial_x \partial_y w(x,y,t) \end{Bmatrix} \quad (2\text{-}36)$$

where D_x, D_y and D_{xy} are bending stiffness. The equilibrium equation is given by [15]

$$\partial_{xx}M_x + 2\partial_{xy}M_{xy} + \partial_{yy}M_y = -q \tag{2-37}$$

where -q in this case is the d'Alembert force, therefore the thin plate equation of motion for free vibration is [27]

$$\begin{aligned} D_x\partial_{xxxx}w(x,y,t) + 2\left(\nu_{xy}D_y + 2D_{xy}\right)\partial_{xxyy}w(x,y,t) + D_y\partial_{yyyy}w(x,y,t) \\ = -\rho_s\partial_{tt}w(x,y,t) \end{aligned} \tag{2-38}$$

where ρ_s is the surface density of the plate and $w(x,y,t)$ is the plate displacement. This relation reduces to the following equation in the case of isotropy [8, 24, 28]

$$D\nabla^4 w(\mathrm{x},\mathrm{y}) = -\rho_s\partial_{tt}w(x,y,t) \tag{2-39}$$

where $\nabla^4 = \nabla^2\nabla^2$ ($\nabla^2$is the two-dimensional differential operator $\nabla^2 = \partial_{xx} + \partial_{yy}$).

2.2.4.3 Thick plates

Mindlin's first order shear deformation theory for a thick plate considers the rotation and shear motion of a normal to the neutral plane of the plate. To implement this the bending moments per unit width are altered to account for shear deformation by introducing functions ψ_x and ψ_y describing the rotations about the *x* and *y* axes which correspond to the plate displacement components $u = z\psi_x(x,y,t)$, $v = z\psi_y(x,y,t)$ and $w = w(x,y,t)$. The bending moments are described similarly to Eqn. (2-35)

$$\begin{Bmatrix} M_x \\ M_y \\ M_{xy} \end{Bmatrix} = \int_{-h/2}^{h/2} \begin{Bmatrix} \sigma_x \\ \sigma_y \\ \tau_{xy} \end{Bmatrix} z\mathrm{d}z = \begin{bmatrix} S_{11} & S_{12} & 0 \\ S_{21} & S_{22} & 0 \\ 0 & 0 & S_{66} \end{bmatrix} \int_{-h/2}^{h/2} \begin{Bmatrix} \partial_x\psi_x(x,y,t) \\ \partial_y\psi_y(x,y,t) \\ \partial_x\psi_y + \partial_y\psi_x \end{Bmatrix} z^2\mathrm{d}z \tag{2-40}$$

which results in the following relations between the bending moments and plate displacement components

$$\begin{Bmatrix} M_x \\ M_y \\ M_{xy} \end{Bmatrix}$$

$$= \begin{bmatrix} {E_x h^3}/{12(1-\nu_{xy}\nu_{yx})} & \nu_{yx}{E_x h^3}/{12(1-\nu_{xy}\nu_{yx})} & 0 \\ \nu_{xy}{E_y h^3}/{12(1-\nu_{xy}\nu_{yx})} & {E_y h^3}/{12(1-\nu_{xy}\nu_{yx})} & 0 \\ 0 & 0 & {G_{xy} h^3}/{12} \end{bmatrix} \begin{Bmatrix} \partial_x \psi_x \\ \partial_y \psi_y \\ \partial_x \psi_y + \partial_y \psi_x \end{Bmatrix} \quad (2\text{-}41)$$

$$= \begin{bmatrix} D_x & \nu_{yx} D_x & 0 \\ \nu_{xy} D_y & D_y & 0 \\ 0 & 0 & D_{xy} \end{bmatrix} \begin{Bmatrix} \partial_x \psi_x \\ \partial_y \psi_y \\ \partial_x \psi_y + \partial_y \psi_x \end{Bmatrix}$$

and accounting for the additional moment relations

$$\begin{Bmatrix} M_{xz} \\ M_{yz} \end{Bmatrix} = \int_{-h/2}^{h/2} \begin{Bmatrix} \tau_{xz} \\ \tau_{yz} \end{Bmatrix} dz = \begin{bmatrix} S_{44} & 0 \\ 0 & S_{55} \end{bmatrix} \int_{-h/2}^{h/2} \begin{Bmatrix} \partial_x w(x,y,t) + \psi_x \\ \partial_y w(x,y,t) + \psi_y \end{Bmatrix} z dz \quad (2\text{-}42)$$

In a first order theory, the integrals in Eqn. (2-42) are replaced by constants κ_1^2, κ_2^2 [29]. The shear correction factor is discussed in more detail in section 2.2.5. This results in the following relations between the moments and curvatures

$$\begin{Bmatrix} M_{xz} \\ M_{yz} \end{Bmatrix} = \begin{bmatrix} \kappa_1^2 G_{xz} h & 0 \\ 0 & \kappa_2^2 G_{yz} h \end{bmatrix} \begin{Bmatrix} \partial_x w(x,y,t) + \psi_x \\ \partial_y w(x,y,t) + \psi_y \end{Bmatrix} \quad (2\text{-}43)$$

The equilibrium equations in this case are [29]

$$\partial_x M_x + \partial_y M_{xy} - M_{xz} = q_x \quad (2\text{-}44)$$

$$\partial_x M_{xy} + \partial_y M_y - M_{yz} = q_y \quad (2\text{-}45)$$

$$\partial_x M_{xz} + \partial_y M_{yz} = q_z \quad (2\text{-}46)$$

For a specially orthotropic material in the case of free vibrations the bending wave equations are [29]

$$\frac{D_x(1-\nu)}{2} \nabla^2 \psi_x + \frac{h^3}{12} G_{xy} \partial_x \Phi - \kappa_1^2 G_{xz} h (\psi_x + \partial_x w(x,y,t)) = \frac{\rho h^3}{12} \partial_{tt} \psi_x \quad (2\text{-}47)$$

$$\frac{D_y(1-\nu)}{2}\nabla^2\psi_y + \frac{h^3}{12}G_{xy}\partial_y\Phi - \kappa_2^2 G_{yz}h\big(\psi_y + \partial_y w(x,y,t)\big) = \frac{\rho h^3}{12}\partial_{tt}\psi_y \tag{2-48}$$

$$\kappa_1^2 G_{xz}h(\partial_{xx}w(x,y,t) + \partial_x\psi_x) + \kappa_2^2 G_{yz}h\big(\partial_{yy}w(x,y,t) + \partial_y\psi_y\big) = \rho_s\partial_{tt}w(x,y,t) \tag{2-49}$$

$$\Phi = \partial_x\psi_x + \partial_y\psi_y \tag{2-50}$$

where κ_1^2, κ_2^2 are the shear correction factors (discussed in section 2.2.5), ∇^2 is the two-dimensional operator $\nabla^2 = \partial_{xx} + \partial_{yy}$. When there is isotropy or transverse isotropy (see section 2.2.2) then $D=D_x=D_y=6G_{xy}(1+\nu)$ and there is an apparent shear modulus G' for which

$$G'h = \kappa_1^2 G_{xz}h = \kappa_2^2 G_{yz}h \tag{2-51}$$

Equations (2-47), (2-48) and (2-49) then reduce to [29]:

$$\frac{D}{2}[(1-\nu)\nabla^2\psi_x + (1+\nu)\partial_x\Phi] - G'h(\psi_x + \partial_x w(x,y,t)) = \frac{\rho h^3}{12}\partial_{tt}\psi_x \tag{2-52}$$

$$\frac{D}{2}\big[(1-\nu)\nabla^2\psi_y + (1+\nu)\partial_y\Phi\big] - G'h\big(\psi_y + \partial_y w(x,y,t)\big) = \frac{\rho h^3}{12}\partial_{tt}\psi_y \tag{2-53}$$

$$G'h(\nabla^2 w(x,y,t) + \Phi) = \rho_s\partial_{tt}w(x,y,t) \tag{2-54}$$

In the case of isotropy (see section 2.2.1) (but not transverse isotropy, see section 2.2.2):

$$G'h = \frac{\kappa^2 Eh}{2(1+\nu)} \tag{2-55}$$

A single differential equation for $w(x, y, t)$ was obtained by Mindlin by combining equations (2-52) to (2-54) to give respectively [29]:

$$\left(\nabla^2 - \frac{\rho}{G'}\partial_{tt}\right)\left(D\nabla^2 - \frac{\rho h^3}{12}\partial_{tt}\right)w(x,y,t) = -\rho_s\partial_{tt}w(x,y,t) \tag{2-56}$$

In this case there are parallels with one dimensional (beam) theory from Timoshenko theory [30].

2.2.5 Dispersion relations for thin and thick plates

To determine the common expression for the phase velocity of a plane wave on a thin isotropic plate, the solution $w(x,t) = \cos\left(\frac{\omega}{c_{\mathrm{B,p}}}x - i\omega t\right)$ is substituted into Eqn. (2-39)

$$D\left(\frac{\omega}{c_{\mathrm{B,p}}}\right)^4 = \rho h\omega^2 \tag{2-57}$$

where ω is the angular frequency, D is the isotropic bending stiffness. Rearranging, the bending wave phase velocity is given by [8]:

$$c_{\mathrm{B,p}} = \sqrt[4]{\frac{\omega^2 D}{\rho h}} \tag{2-58}$$

The critical frequency of the plate can be determined by setting the phase velocity equal to the speed of sound in air to give [8]

$$f_c = \frac{c_0^2}{2\pi}\sqrt{\frac{\rho h}{D}} \tag{2-59}$$

In the case of a thick isotropic plate Mindlin obtained equations for the modified phase velocities in the according to Eqn. (2-56) by substitution of the wave solution $w(x,t) = \cos\frac{2\pi}{\lambda}\left(x - c_{\mathrm{B,thick,p}}t\right)$ [29] which can be rearranged to give:

$$\frac{c_{\mathrm{B,thick,p}}^6}{c_{\mathrm{L}}^2\kappa^2 c_{\mathrm{S}}^2} - \left[\frac{1}{\kappa^2 c_{\mathrm{S}}^2} + \frac{1}{c_{\mathrm{L}}^2}\right]c_{\mathrm{B,thick,p}}^4 + c_{\mathrm{S}}^4 c_{\mathrm{B,thick,p}}^2 - \omega^4 = 0 \tag{2-60}$$

where c_L is the quasi-longitudinal phase velocity

$$c_L = \sqrt{\frac{12D}{\rho h^3}} \tag{2-61}$$

An alternative method for calculating the modified phase velocity is proposed by Kurtze and Watters [31]. In this the modified phase velocity of a thick sandwich panel is derived using an equivalent circuit model where the stiffness term of the impedance for the bending waves in the outer layers and the stiffness term of the impedance for shear waves in the core are connected "in parallel". This approach could be useful for modelling vertical (*y*-) direction of layered CLT panels where the material contribution to stiffness of the panel comes mainly from the outer layers but not for modelling horizontal (*x*-) direction where the material contribution to the stiffness of the panel comes mainly from the core (see Table 4-3). The resulting equation is [31]:

$$\frac{c_{\mathrm{S}}^4}{c_{\mathrm{B,p}}^4} c_{\mathrm{B,thick,p}}^6 + c_{\mathrm{S}}^2 c_{\mathrm{B,thick,p}}^4 - c_{\mathrm{S}}^4 c_{\mathrm{B,thick,p}}^2 - c'^4_{\mathrm{B,p}} c_{\mathrm{S}}^2 = 0 \tag{2-62}$$

where at high frequencies $c'_{\mathrm{B,p}} \approx c_{\mathrm{B,thick,p}}$. An approximate solution to equations (2-60) and (2-62) is proposed in [32, 33]:

$$c_{\mathrm{B,thick,p}} \approx \left(\frac{1}{c_{\mathrm{B,p}}^3} + \frac{1}{\kappa^3 c_{\mathrm{S}}^3} \right)^{-1/3} \tag{2-63}$$

where the ratio $\kappa = c_{\mathrm{B,thick,p}}/c_S$ defines the upper limit of the modified phase velocity. In the literature, there are two views on the physical significance of the correction term, κ, in these equations. Firstly, it can be thought of as a correction due to the distribution of the shear strain through the plate, [34, 35]; this assumption is demonstrated in Eqn. (2-43). Secondly it aligns the upper limit of the corrected phase velocity at high frequencies with the phase speed of the Rayleigh surface wave. Mindlin gives the following equation for calculating κ, which is derived by making a comparison with three-dimensional theory, and indicates that the values of $\kappa^2 = 5/6$ or $\pi^2/12$ correspond to a Poisson's ratio of 0.176 [29],

$$\sqrt{16\left(1 - \frac{(1-2\nu)\kappa^2}{2(1-\nu)}\right)(1-\kappa^2)} = (2-\kappa^2)^2 \tag{2-64}$$

where $0<\kappa<1$. Magrab suggests the following approximate solution [36]:

$$\kappa \approx \frac{(0.87 + 1.12\nu)}{(1 + \nu)} \tag{2-65}$$

Equations (2-64) and (2-65) are plotted alongside some commonly used values for the correction factor in Figure 2-3.

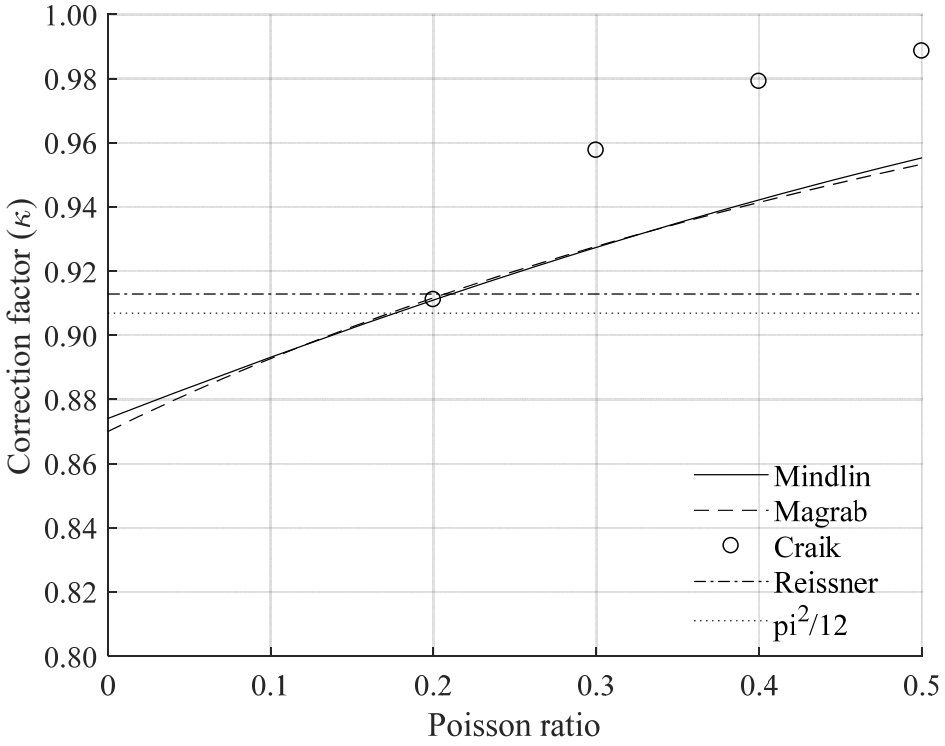

Figure 2-3 Values of the correction factor κ (solid line) Mindlin Eqn. (2-64) [29], (dashed line) Magrab Eqn. (2-65) [36] (circles) Craik ($\kappa^2 = \sqrt{\gamma}$) [32], (dash dot line) κ^2=5/6 Reissner [29], or (dotted line) $\kappa^2=\pi^2/12$ Reissner [29]

A rule of thumb is that the resulting $G'=\kappa^2 G$ is approximately 10-20% lower than G [23]. (To compare the data from Craik [32] it has been assumed that although $\gamma \equiv \kappa$ in Eqn. (3.6) [32, p. 52] the tabulated values are actually $\gamma=(c_{B,thick,p}/c_S)^4=\kappa^4$.)

Eqn. (2-63) can be used to calculate the bending wave speed phase velocity from the material constants or it can be rearranged to determine the elastic modulus and apparent shear modulus (G') from measured bending phase velocity data using a weighted least squares fit, and it is this latter method which is used in this thesis. The corresponding group velocity is [32]:

$$c_{\mathrm{g(B,thick)}} = \left(\frac{c_{\mathrm{B,thick,p}}^2}{c_{\mathrm{B,p}}^2 c_{\mathrm{g(B)}}} + \frac{c_{\mathrm{B,thick,p}}^2}{\kappa^3 c_{\mathrm{S}}^3} \right)^{-1} \tag{2-66}$$

In the isotropic case the shear wave crossover frequency, f_s, is defined by Rindel [33] as the frequency where the bending phase velocity is equal to the shear phase velocity. Neglecting Poisson's ratio this can be calculated by equating (2-12) with (2-58):

$$f_{\mathrm{S}} \approx \frac{\mu}{2\pi} \sqrt{\frac{h}{D\rho}} \tag{2-67}$$

2.2.6 Solving finite thin plate equations to obtain the eigenfrequencies

The solution to the equation of vibration of a thin plate is assumed to be of the form $w(x, y, t) = \mathrm{W}(x, y)\cos(i\omega t)$. Considering Eqn. (2-39) and Eqn. (2-58)

$$D\nabla^4 w(x, y, t) = \mathrm{D}\nabla^4\, \mathrm{W(x, y)}\cos(i\omega t) \tag{2-68}$$

$$-\rho h \partial_{tt} w(x, y, t) = -\omega^2 \rho h\, \mathrm{W(x, y)}\cos(i\omega t) \tag{2-69}$$

which gives

$$\nabla^4 \mathrm{W(x, y)} - \frac{\omega^4}{c_{B,p}^4} \nabla^4 \mathrm{W(x, y)} = 0 \tag{2-70}$$

There is a useful subset of idealised finite boundary conditions for thin plates that are commonly considered in the literature which relate to realistic edge conditions. These are commonly referred to as free, simply supported, or clamped edges. An exact solution to the free vibration equation of thin plates has only been specified for simply supported edge conditions. To determine solutions for other edge conditions requires a numerical approach. The difficulty with plates that have free edges is that the natural boundary conditions (concerning the moments) are only approximately fulfilled. The solutions for plates with simply supported and clamped edges are found to be independent of Poisson's ratio [28]. In subsequent chapters of this thesis only simply supported and free boundaries are considered. Statement of the

boundary conditions is only relevant for modal analysis of the plates and does not affect the SEA. The boundary conditions of a plate only affect the locations of the modes at low frequencies. Above the tenth mode, or so, the statistical mode count is unaffected [37] by conditions at the boundaries.

Three commonly used methods for modelling the dynamic behaviour of a thin rectangular plate are: FEM (discussed in section 2.4), Rayleigh's method, and the Rayleigh-Ritz technique. The Rayleigh-Ritz technique is preferred because of higher accuracy when compared with Rayleigh's method and low computational requirements when compared with FEM. Ritz's contribution to the technique is the assumption of orthogonal trial functions, a list of possible functions is given below. Other energy methods include Hamilton's variational principle and Galerkin's method.

The (not necessarily exhaustive) list of functions which can be used to model the vibration of a plate includes characteristic beam functions [28], trigonometric and hyperbolic series using the method of superposition [38, 39] simply supported plate functions [40], beam characteristic orthogonal polynomials [24, 41], plate characteristic orthogonal polynomials and simplified (non-orthogonal) polynomials. Leissa [42] is one example from a vast literature, reviewing available methodologies in 1969 to solve the vibration equations for different plate types, aspect ratios and boundary conditions. To implement the Rayleigh-Ritz method in this thesis the characteristic beam functions are used as they are relatively simple to implement and provide sufficient accuracy.

Warburton [28] comprehensively applied the thin beam functions to simply supported, clamped and free edge combinations. The characteristic beam functions (specifically for free edge conditions) are detailed in the next section (2.2.6.1). The plate deflection amplitude is represented by the beam functions $\theta_i(x)$ $\phi_j(y)$ in the series

$$W(x,y) = \sum_{i=1}^{m}\sum_{j=1}^{n} A_{ij}\theta_i(x)\phi_j(y) \qquad (2\text{-}71)$$

The expressions for the maximum potential and kinetic energies of a harmonically vibrating plate are given by

$$V_{\max} = \frac{1}{2}\int_0^a \int_0^b \left[D_{11}(\partial_{xx}W)^2 + 2D_{12}\partial_{xx}W\partial_{yy}W + D_{22}\left(\partial_{yy}W\right)^2 + 4D_{66}\left(\partial_{xy}W\right)^2\right]\mathrm{d}x\mathrm{d}y \tag{2-72}$$

$$T_{\max} = \frac{1}{2}\rho h\omega^2 \int_0^a \int_0^b W^2 \mathrm{d}x\mathrm{d}y \tag{2-73}$$

and the Rayleigh principle is stated as follows§

$$\omega^2 = \frac{V_{\max}}{T_{\max}/\omega^2} \tag{2-74}$$

Kim and Dickenson [43] improved the accuracy of this method for applicability to orthotropic plates with free boundary edge conditions using multiple thin beam functions consisting of the natural frequency of interest and a proportion of the next higher modes. The proportion of the next higher modes required to improve agreement with the natural boundary condition are given by the constants *c* and *d* described in section 2.2.6.2.

2.2.6.1 Characteristic beam functions

The characteristic beam functions proposed by Warburton [28] are of the given form

$$W(x,y) = A_{ij}\theta_i(x)\phi_j(y) \tag{2-75}$$

The beam functions for a bar which has free edge conditions at both ends are given by [28]

$$\theta(x) = \begin{cases} 1, & \text{for } m = 0 \\ 1 - \dfrac{2x}{a}, & \text{for m} = 1 \\ \cos\gamma\left(\dfrac{x}{a} - 1/2\right) + k\cosh\gamma\left(\dfrac{x}{a} - 1/2\right), & \text{for m} = 2, 4, 6 \text{ etc.} \\ \sin\gamma'\left(\dfrac{x}{a} - 1/2\right) + \mathrm{k}'\sinh\gamma'\left(\dfrac{x}{a} - 1/2\right), & \text{for m} = 3, 5, 7 \text{ etc.} \end{cases} \tag{2-76}$$

where a is the beam length, γ and γ' are the corresponding numbered solutions to the transcendental equations [28]

$$\tan\frac{\gamma}{2}+\tanh\frac{\gamma}{2}=0 \text{ and } \tan\frac{\gamma'}{2}-\tanh\frac{\gamma'}{2}=0 \tag{2-77}$$

The solutions to the transcendental equations are shown in Figure 2-4, and k and k' are determined by [28]

$$k=-\frac{\sin\frac{\gamma}{2}}{\sinh\frac{\gamma}{2}} \text{ and } k'=\frac{\sin\frac{\gamma'}{2}}{\sinh\frac{\gamma'}{2}} \tag{2-78}$$

The trial function given in Eqn. (2-76) is substituted into the expressions for the V_{max} (Eqn. (2-72)) which is the total potential energy of the system and T_{max} (Eqn. (2-73)) which is the total kinetic energy of the system. Applying the Rayleigh principle results in the frequency expression [43]

$$C_{ij}=\frac{b^2}{a^2}\frac{D_x}{H}G_i^4+\frac{a^2}{b^2}\frac{D_y}{H}G_j^4+2\left[H_iH_j+2\frac{D_{xy}}{H}\left(J_iJ_j-H_iH_j\right)\right]=\frac{\omega^2\rho h a^2b^2}{\pi^4H} \tag{2-79}$$

where a and b are the dimensions of the plate and

$$H=\nu_{xy}D_y+2D_{xy} \tag{2-80}$$

The coefficients of Eqn. (2-79) [43] are

$$G_i^4=\frac{a^4}{\pi^4}\int_0^a(\partial_{xx}\theta_i)^2dx\Big/\int_0^a(\theta_i)^2dx \tag{2-81}$$

$$H_i=-\frac{a^2}{\pi^2}\int_0^a\theta_i\partial_{xx}\theta_i\,dx\Big/\int_0^a(\theta_i)^2dx \tag{2-82}$$

$$J_i=\frac{a^2}{\pi^2}(\partial_x\theta_i)^2dx\Big/\int_0^a(\theta_i)^2dx \tag{2-83}$$

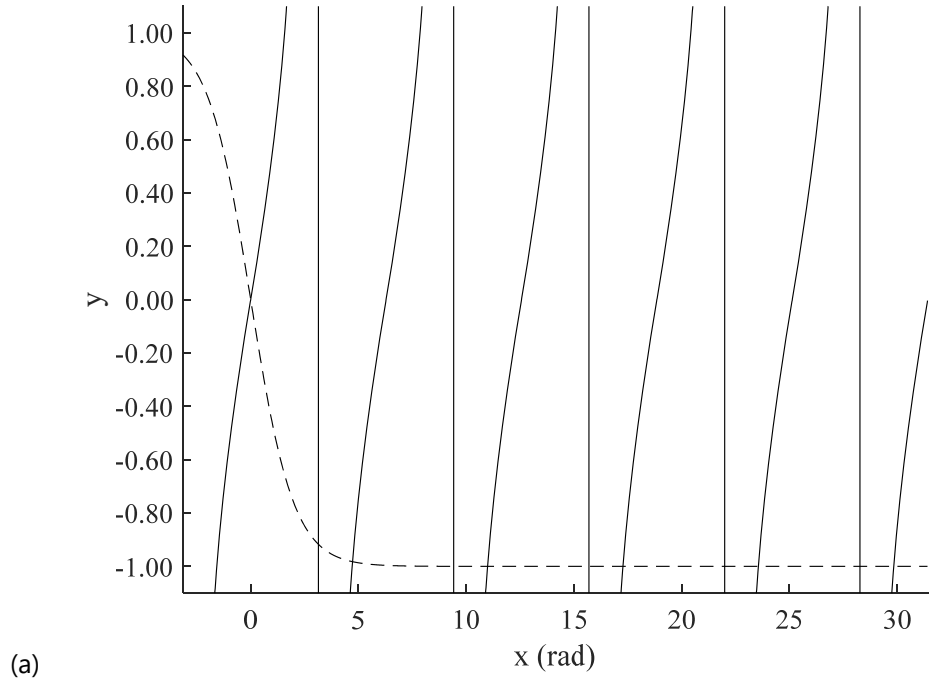

(a)

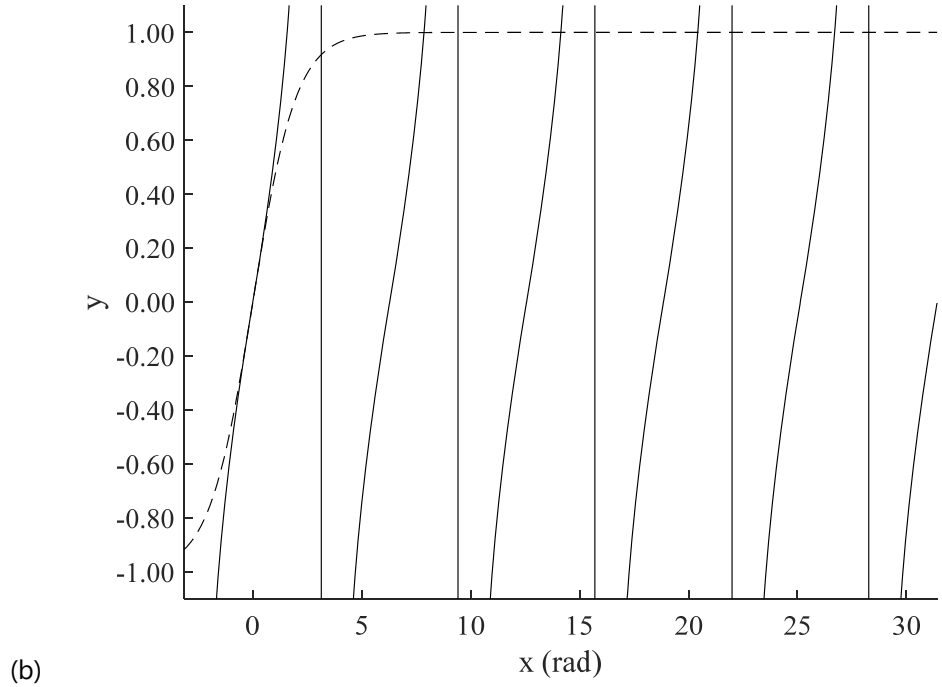

(b)

Figure 2-4 The solutions to the transcendental equations (a) γ and (b) γ' (dashed lines represent the hyperbolic functions $y = \pm\tanh\frac{\gamma}{2}$ and solid lines represent the trigonometric function $y = \tan\frac{\gamma}{2}$)

where the values for G_j, H_j and J_j can also be determined by exchanging a to b, and θ_i to ϕ_j. These coefficients can be calculated using series which are tabulated for easy reference (e.g. G_x, G_y, H_x, H_y and J_x, J_y in [27, 28, 43]). In the absence of a free edge Warburton [28] demonstrated that $H_x=J_x$ and $H_y=J_y$ therefore in equation (2-79) the term containing Poisson's ratio cancels and the frequency parameter is independent of Poisson's ratio. For at least one free edge Poisson's ratio does not cancel out.

2.2.6.2 Using multi-term characteristic beam functions

Without resorting to a full calculation of many additional terms of the deflection series, which could involve considerably more work, the method of Kim and Dickenson aimed to improve accuracy by a plate deflection amplitude which is represented by a beam function comprising an optimal combination of the mode of interest and the next two higher modes given by [43]

$$W(x,y) = A\left[\theta_i(x)\phi_j(y) - c\theta_i(x)\phi_n(y) - d\theta_j(x)\phi_j(y)\right] \tag{2-84}$$

This trial function results in an extended frequency expression [43]

$$\frac{\omega^2 \rho h a^2 b^2}{\pi^4} = \frac{H\left(C_{ij} + c^2 C_{in} + d^2 C_{mj} - 2cE_{ij} - 2dE_{ji} + 2cdF\right)}{1 + c^2 + d^2} \tag{2-85}$$

where c, d are constants, $H=\nu_{xy}D_y+2D_{xy}$ and using the simplified constants G_i^4, G_j^4, G_n^4, G_m^4, H_i, H_j, H_n, H_m and J_i, J_j, J_n and J_m which are obtained by substituting i, a, and θ with j, b and ϕ respectively (or i with n or m). The additional terms are given by [43]

$$C_{in} = \left(\frac{D_x}{H}\right) G_i^4 \left(\frac{b^2}{a^2}\right) + \left(\frac{D_y}{H}\right) G_n^4 \left(\frac{a^2}{b^2}\right) + 2\left[H_i H_n + 2\left(\frac{D_{xy}}{H}\right)(J_i J_n - H_i H_n)\right] \tag{2-86}$$

$$C_{mj} = \left(\frac{D_x}{H}\right) G_m^4 \left(\frac{b^2}{a^2}\right) + \left(\frac{D_y}{H}\right) G_j^4 \left(\frac{a^2}{b^2}\right) + 2\left[H_m H_j + 2\left(\frac{D_{xy}}{H}\right)(J_m J_j - H_m H_j)\right] \tag{2-87}$$

$$E_{ij} = H_i(K_j + L_j)\left[2\left(\frac{D_{xy}}{H}\right) - 1\right] + 4\left(\frac{D_{xy}}{H}\right) J_i M_j \tag{2-88}$$

$$E_{ji} = H_j(K_i + L_i)\left[2\left(\frac{D_{xy}}{H}\right) - 1\right] + 4\left(\frac{D_{xy}}{H}\right) J_j M_i \tag{2-89}$$

$$F = -\left(K_i K_j + L_i L_j\right)\left[2\left(\frac{D_{xx}}{H}\right) - 1\right] + 4\left(\frac{D_{xy}}{H}\right) M_i M_j \qquad (2\text{-}90)$$

Additional coefficients K_i, K_j, L_i, L_j, M_i, and M_j are given by [43]

$$K_i = -\frac{a^2}{\pi^2}\int_0^a \theta_i \partial_{xx}\theta_m \,\mathrm{d}x \Big/ \int_0^a (\theta_i)^2 \mathrm{d}x \qquad (2\text{-}91)$$

$$L_i = -\frac{a^2}{\pi^2}\int_0^a \partial_{xx}\theta_i \,\theta_m dx \Big/ \int_0^a (\theta_i)^2 \mathrm{d}x \qquad (2\text{-}92)$$

$$M_i = -\frac{a^2}{\pi^2}\int_0^a \partial_x\theta_i \,\partial_x\theta_m dx \Big/ \int_0^a (\theta_i)^2 \mathrm{d}x \qquad (2\text{-}93)$$

With appropriate substitution of *i*, *a*, θ, and *m* with *j, b,* ϕ and *n* respectively. The three-term plate deflection amplitude expression has been applied by Ayorinde and Gibson [27] to determine the elastic moduli of isotropic (aluminium), and orthotropic (glass, glass/epoxy, E-glass/vinylester and graphite/epoxy) plates, with orthotropy ratios between 1 and 13 and aspect ratios between one (i.e. square) and two, by examining the eigenfrequencies extracted from modal analysis measurement data. However increased term expressions are also available (e.g. the six-term expression of Ayorinde and Yu [44]). These functions, which use increased numbers of terms, are generally thought to result in improved accuracy in the case of free boundary conditions. However, it is also possible to decrease accuracy under certain conditions [45]. One and two term expressions are compared in chapter 4.

2.2.7 Finite plate (resonant and non-resonant) transmission

The equations of Leppington *et al.* [46, 47] model the energy transmission through a finite panel. The transmission coefficients are categorised by whether they are defined by a total contribution from the resonant modes of the panel or if the transmission is due to off-resonance excitation of the modes (a forced contribution). The modes radiate efficiently at frequencies higher than the critical frequency of the panel and inefficiently at frequencies lower than the critical frequency, where the off-resonance excitation becomes more important.

The resonant contribution can be described by defining a resonant frequency-average radiation efficiency which is calculated using $\mu = \sqrt{f_c/f}$ as follows:

$$\sigma = \frac{U}{2\pi\mu k S\sqrt{\mu^2-1}}\left[\ln\left(\frac{\mu+1}{\mu-1}\right)+\frac{2\mu}{\mu^2-1}\right]\left[C_{\mathrm{BC}}C_{\mathrm{OB}}-\mu^{-8}(C_{\mathrm{BC}}C_{\mathrm{OB}}-1)\right] \quad \text{for } f < f_c \tag{2-94}$$

$$\sigma = \frac{1}{\sqrt{1-\mu^2}} \quad \text{for } f > f_c \tag{2-95}$$

$$\sigma \approx \left(0.5-\frac{0.15L_1}{L_2}\right)\sqrt{k}\sqrt{L_1} \quad \text{for } f = f_c \tag{2-96}$$

where U is the plate perimeter, S is the plate area, C_{BC} is a constant for the plate boundary conditions (C_{BC}=1 for simply supported boundaries, C_{BC}=2 for clamped boundaries), C_{OB} is a constant for the orientation of the baffle that surrounds the edges of the plate (C_{OB}=1 when the plate lies within the plane of an infinite rigid baffle, C_{OB}=2 when the rigid baffles along the plate perimeter are perpendicular to the plate surface L_1 is the smaller and L_2 is the larger of the rectangular plate dimensions, L_x and L_y (for square plates, L_1=L_2=L_x=L_y). The radiation efficiency for the frequency band that contains the critical frequency in Eqn. (2-96) can be calculated using $k=2\pi f_c/c_0$ (where f_c is the critical frequency of the plate and c_0 is the speed of sound in air).

The non-resonant transmission coefficient which is only defined below the critical frequency is calculated according to Leppington *et al.* [47].

$$\tau_{NR} = \left(\frac{2\rho_0}{\rho_s k(1-\mu^{-4})}\right)^2\left\{ln\left(k\sqrt{S}\right)+0.16-U\left(\frac{L_x}{L_y}\right)+\frac{1}{4\mu^6}\left[(2\mu^2-1)(\mu^2+1)^2 ln(\mu^2-1)+(2\mu^2+1)(\mu^2-1)ln(\mu^2+1)-4\mu^2-8\mu^6 ln(\mu)\right]\right\} \tag{2-97}$$

where $U\left(L_x/L_y\right)$ is a function of the rectangular shape of the plate. These equations are used to calculate the coupling loss factors for SEA calculations, described in

section 2.3. They are useful for application to thin plates because the resonant and non-resonant contributions to the transmission coefficients are considered separately. The relationship between sound reduction index (R) and transmission coefficient (τ) is given by

$$R = 10\lg\left(\frac{1}{\tau}\right) \tag{2-98}$$

2.2.8 Driving-point mobility

2.2.8.1 Thin plates

The driving-point mobility is the ratio of velocity to the force applied at the excitation point. If the plate is thin and the force acts at a point which is small when compared with the dimensions (specifically the thickness) of the plate the driving-point mobility, Y_{dp}, in the central part of a plate can be stated as [48]

$$Y_{\mathrm{dp}} = \frac{\omega}{8Dk_{\mathrm{B}}^2} = \frac{1}{8\sqrt{D\rho h}} \tag{2-99}$$

2.2.8.2 Thick plates

The calculation of the real part of the driving-point mobility in the central part of thick infinite plate uses the assumptions of Mindlin [29]. From Bulhert [49] the driving-point mobility for a thick plate in the central part of the plate is given by

$$Y_{\mathrm{dp}} = \left(\frac{\omega}{8Dk^2}\right) + \left(\frac{\omega}{8G'h}\right) + j\left(\frac{\omega}{4\pi G'h}\right)[0.768 - \ln(ka)^2] \tag{2-100}$$

where a is the radius of the excitation area, $G'=\kappa^2 G$ is the apparent shear modulus corrected for the shear distribution through the material thickness. The correction factor, κ, is a function of Poisson's ratio and is given by Eqn. (2-65). The imaginary part of the driving-point mobility for a thick plate is governed by the size of the area on which the force acts.

Alternatively, the driving-point mobility can be calculated from the average modal density [50] where a modified modal density which considers the shear contribution

to the modes for the real part of the driving-point mobility can be inserted to determine the real part

$$\mathrm{Re}\left(Y_{\mathrm{dp}}\right) = \frac{\pi}{2}\frac{\langle n_{B,\mathrm{thick}}(\omega)\rangle}{M} \tag{2-101}$$

$n_{\mathrm{B,thick}}(\omega)$ can be determined from the group velocity for thick plates (Eqn. (2-66)) using [32]

$$n_{\mathrm{B,thick}}(\omega) = \frac{\omega S}{2\pi c^2_{\mathrm{g(B,thick)}}} = \frac{\omega S}{2\pi}\left(\frac{c^2_{\mathrm{B,thick},p}}{c^2_{\mathrm{B,p}} c_{\mathrm{g(B)}}} + \frac{c^2_{B,\mathrm{thick},p}}{\kappa^3 c^3_{\mathrm{S}}}\right)^2 \tag{2-102}$$

To simplify and obtain the same result as Eqn. (2-100) the following bandwidth approximation is used

$$\langle n_{B,\mathrm{thick}}(\omega)\rangle \approx \frac{\omega S}{2\pi}\left(\frac{1}{c^2_{\mathrm{g(B)}}} + \frac{1}{2\kappa^2 c^2_{\mathrm{S}}}\right) \tag{2-103}$$

This gives the real part of the thick plate mobility

$$\mathrm{Re}\left(Y_{dp}\right) = \frac{\omega}{8Bk^2_{\mathrm{B}}} + \frac{\omega}{8G'h} \tag{2-104}$$

The real part of Eqn. (2-100) or (2-104) is equivalent to Eqn. (2-99) for a thin plate at low frequencies. If necessary the imaginary part of the point mobility can be determined in a similar manner [50].

2.2.9 Infinite plate airborne sound transmission

2.2.9.1 Heckl's orthotropic infinite plate airborne transmission model

For an infinite plate, airborne transmission model Cremer's equation describes the transmission coefficient as the integral over relevant angles of incidence of the angle dependant transmission coefficient [8, 51].

$$\tau_{\infty,d} = \frac{2}{\pi}\int_0^{\pi/2}\int_0^1 \frac{\mathrm{d}(\sin^2\theta)\mathrm{d}\phi}{\left|1 + \frac{Z\cos\theta}{2\rho_0 c_0}\right|^2} \tag{2-105}$$

where $\tau_{\infty,\mathrm{d}}$ is the diffuse incidence transmission coefficient, Z is the surface impedance.

Heckl [52] extends this theory from a thin isotropic plate to a thin orthotropic plate. The surface impedance is given in terms of the bending stiffness in the principle directions [8, 52].

$$Z = i\omega\rho_{\mathrm{s}}\left[1 - \left(\frac{B_x\cos^2\phi}{\omega^2\rho_{\mathrm{s}}} + 2\,\frac{(B_{\mathrm{y}}\nu_{\mathrm{xy}} + {}^1\!/_6\,G_{\mathrm{xy}}h^3)\sin^2\phi\cos^2\phi}{\omega^2\rho_{\mathrm{s}}} + \frac{B_{\mathrm{y}}\sin^2\phi}{\omega^2\rho_{\mathrm{s}}}\right)k^4\sin^4\theta\right] \tag{2-106}$$

where it is assumed that

$$B_{\mathrm{eff}} = B_{\mathrm{y}}\nu_{\mathrm{xy}} + {}^1\!/_6\,G_{\mathrm{xy}}h^3 \approx \sqrt{B_{\mathrm{x}}B_{\mathrm{y}}} \tag{2-107}$$

Therefore, in terms of the bending wavenumber

$$Z = i\omega\rho_{\mathrm{s}}\left[1 - \left(\frac{\cos^2\phi}{k_{\mathrm{B,x}}^2} + \frac{\sin^2\phi}{k_{\mathrm{B,y}}^2}\right)^2 k^4\sin^4\theta\right] \tag{2-108}$$

The wave numbers ($k_{\mathrm{B,x}}$ and $k_{\mathrm{B,y}}$) are calculated from the complex bending stiffness $D_{\mathrm{p,x}}(1+i\eta)$ and $D_{\mathrm{p,y}}(1+i\eta)$ using an estimated total loss factor, η, calculated from summing the internal loss factor and the coupling loss factors in each third octave band. The integral in Eqn. (2-105) can be performed numerically.

Although infinite plate equations can give accurate results for laboratory and field situations they often require empirical correction to reduce the contribution from grazing angles of incidence [8, 53]. Finite plate equations to determine airborne transmission coefficients from room to room through a plate have been shown to give closer agreement with measurement than wave impedance models [8, 46, 47]. In this thesis use is made of an estimate for the frequency-average radiation efficiency for one-third octave bands between the two critical frequencies of the orthotropic plate from Heckl [52]

$$\sigma = \frac{1}{\pi^2}\sqrt{\frac{f_{c1}}{f_{c2}}}\left(\ln\frac{4f}{f_{c1}}\right)^2 \tag{2-109}$$

where f_{c1} and f_{c2} are the two critical frequencies of the orthotropic plate for which $f_{c1}<f_{c2}$. This radiation efficiency can be used in conjunction with finite plate (resonant) transmission calculations (such as Leppington's equations given in section 2.2.7).

2.2.9.2 Thick plate airborne transmission

Ljunggren [54] provides a method to calculate the sound reduction index of a thick plate in the form of a correction to the thin plate calculation. The thick plate model for isotropic plates is based on the correction of a resonant thin plate airborne transmission coefficient. As such it is only meaningful at frequencies higher than the critical frequency of the plate. The total sound reduction index (R_M) is given by.

$$R_{\mathrm{M}} = R_{\mathrm{c}} - \Delta R \tag{2-110}$$

where the correction is calculated by.

$$\Delta R = 10\lg(A/BC) \tag{2-111}$$

$$A = [1 + (h^2/12)(\frac{k_{\mathrm{c}}^2 k_{\mathrm{S}}^2}{k_{\mathrm{L}}^2} - k_{\mathrm{S}}^2)]^2 \tag{2-112}$$

$$B = \frac{(k_{\mathrm{S}}h)^2}{12} + \frac{k_{\mathrm{c}}^2(k_{\mathrm{S}}^2 + k_{\mathrm{L}}^2)^2}{k_{\mathrm{B}}^2} \tag{2-113}$$

$$C = [1 - \frac{(k_{\mathrm{S}}h)^2}{12} + (k_{\mathrm{S}}^2 + k_{\mathrm{L}}^2)^4/(4k_{\mathrm{B}}^4)]^{1/2} \tag{2-114}$$

where k_{L} is the quasi-longitudinal wavenumber, k_{S} is the wave number of a hypothetical Rayleigh wave, and k_{c} is the wavenumber at coincidence. The quasi-longitudinal wavenumber can be obtained from Eqn. (2-61),

$$k_{\mathrm{L}} = \omega \sqrt{\frac{\rho h^3}{12D}} \tag{2-115}$$

The Rayleigh wavenumber (referred to as a corrected shear wave in [54]) can be obtained from,

$$k_{\mathrm{S}} = \omega \sqrt{\frac{\rho}{\kappa^2 G}} = \frac{\omega}{\kappa} \sqrt{\frac{E}{2\rho(1+\nu^2)}} \tag{2-116}$$

There are several possible ways to determine the wavenumber at coincidence. The method used in this thesis is to rearrange Eqn. (2-62) to give (like Cremer *et al.* [48] but retaining the shear correction factor, κ)

$$k_{\mathrm{B,thick}}^4 - k_{\mathrm{B,thick}}^2 \omega^2 \left[\frac{1}{\kappa^2 c_{\mathrm{S}}^2} + \frac{1}{c_{\mathrm{L}}^2}\right] + \frac{\omega^4}{c_{\mathrm{L}}^2 \kappa^2 c_{\mathrm{S}}^2} - k_{\mathrm{B,p}}^4 = 0 \tag{2-117}$$

then setting the phase velocity equal to the speed of sound in air ($c_{B,\mathrm{thick},p}$=c_0=343ms^{-1}) and solving for the wavenumber (e.g. using the MATLAB "solve" function). To simplify this equation, the shear correction factor may be assumed to equal one (κ=1). Ljunggren recommends that the shear correction factor (κ) given by Magrab [36] (Eqn. (2-65)) be used.

2.2.10 Equivalent plate models for bending vibration

When considering rib-stiffened or multilayer plates, the integrals in Eqns. (2-35) and (2-40) become more complicated. One solution is to determine equivalent plate parameters [14, 19, 20, 55, 56] such that the behaviour of the plate can be described using a homogenous model, reducing the complexity of the multilayer plate problem. When there is no bend-twist coupling such as in the case of special orthotropy equivalent material models are applicable. Equivalent models for rib-stiffened plates can be determined by considering the plate as a series of strips of equal width, in effect, dividing the plate into beams. The strips are selected appropriately by examining the repeating pattern; for beams attached to a plate this may be a T- or inverted L-shape, for a multilayer plate the width of the whole plate may be

considered. Equivalent models for multilayer plates can be determined by summing the partial contribution to bending stiffness of the layers.

Plates which are symmetrical about their mid-plane, such as CLT or rib-stiffened plates with ribs on both sides of the plate are simpler to analyse because the neutral axis lies at the mid-plane of the plate. There are fundamental difficulties to determine the appropriate behaviour of layered plates with asymmetries about the mid-plane such as stiffeners located on only one side of the plate [23] therefore alternative models rely on different simplifying assumptions. There are few available models which address both complicated geometry and different material properties within each layer. Two equivalent models for rib-stiffened plates and one equivalent model for layered plates are investigated in this thesis.

In the first method for ribbed plates, Kimura and Inoue [56] propose a set of empirical equations for solid plates and plates which contain cavities using the second moment of area to calculate an equivalent density, ρ_{eq}, equivalent Young's modulus, E_{eq}, and equivalent thickness, h_{eq}. For solid plates, the basic equations are

$$\rho_{\mathrm{eq}} = \frac{\sum_{i=1}^{n} \rho_i h_i}{\sum_{i=1}^{n} h_i} \tag{2-118}$$

$$E_{\mathrm{eq}} = \sum_{i=1}^{n} E_{L_i} I_i \, / I_{\mathrm{total}} \tag{2-119}$$

$$h_{\mathrm{eq}} = h_i + \sum_{j=1}^{n} h_j \left(\frac{\rho_j}{\rho_i}\right) \tag{2-120}$$

$$I_{\mathrm{total}} = \iint_A z^2 \mathrm{d}x\mathrm{d}z \tag{2-121}$$

where the subscripts i, or j indicate the various material layers. For plates which include cavities an equivalent thickness is determined

$$h_{\mathrm{eq}} = \sqrt[3]{12 I_{\mathrm{total}}} \tag{2-122}$$

The second approach considers Huffington's approach [19] for the direction perpendicular to the beams and Troitsky [20] in the direction parallel to the beams. In Huffington's approach, each repeating cross-section of length, d_R, the strain energy of the equivalent plate is assumed equal to the strain energy of the actual plate. The strain energy of the equivalent plate, U_x, is

$$U_x = \int_{-d_R/2}^{d_R/2} \frac{d_R M_I^2}{2D_x} \mathrm{d}x \tag{2-123}$$

and the strain energy of the actual plate, U_a, is

$$U_a = \int_{-d_R/2}^{d_R/2} \frac{d_R M_I^2}{2E_a(x)I_a(x)} \mathrm{d}x \tag{2-124}$$

where the bending moment, M_I, is the same for each repeating section and $E_a(x)$ and $I_a(x)$ are the Young's modulus and second moment of area as functions of x respectively. Setting Eqns. (2-123) and (2-124) to be equal gives

$$\frac{D_x}{d_R} = \left[\int_{-d_R/2}^{d_R/2} \frac{1}{E_a(x)I_a(x)} \mathrm{d}x\right]^{-1} \tag{2-125}$$

For a floor with simple geometry this can be calculated using a summation. However, if the floor geometry is more complex, then an 'effective thickness' from Huffington [19] can be used to calculate the bending stiffness in the x-direction perpendicular to the beams. Setting Eqns. (2-123) and (2-124) to be equal, keeping $E_a(x)$ constant (in this case setting it to E_1, the Young's modulus of the concrete) and varying $I_a(x)$ results in a general equation for D_x, given by

$$D_x = \frac{E_i I_1}{\frac{h^3}{d_R}\int_{-d_R/2}^{d_R/2} \frac{\mathrm{d}x}{h_a^3(x)}} \tag{2-126}$$

where $h_a(x)$ is a continuously-variable effective plate thickness which is equivalent to the actual ribbed plate. An advantage with this approach is that it can be used for unusual cross-sections and in situations where the plate and beams consist of different materials.

In the second method for ribbed plates Troitsky's [20] approach is adapted to account for a plate and stiffeners of two different materials E_1 and E_2 and is a summation of the partial bending stiffness contributions of the plate and stiffener

$$D_y = \frac{E_1 h^3}{12(1-\nu^2)} + \frac{E_1 h z_y^2}{(1-\nu^2)} + \frac{E_2 I_2}{d_\mathrm{R}} \tag{2-127}$$

where z_y is the distance from the mid-plane of the plate to the neutral axis which is calculated according to

$$z_y = \frac{\iint_A E(z) z \mathrm{d}y\mathrm{d}z}{\iint_A E(z) \mathrm{d}y\mathrm{d}z} \tag{2-128}$$

where $E(z)$ is the elastic modulus as a function of z. When there are many stiffeners per unit length the assumption of a plane neutral surface and equation (2-128) may not be satisfactory [20]. Parallel axis theorem is included in the definition explicitly for the plate and implicitly for the stiffener within the definition of I_2. Parallel axis theorem can be stated as follows:

$$I_i = I_{0_i} + A_i (d_i)^2 \tag{2-129}$$

where I_{0i} is the moment of inertia of layer i, A_i is the cross-sectional area of layer i and d_i is the distance between the neutral plane of each lamina and the neutral plane of the whole plate.

For symmetrically layered orthotropic plates such as CLT the neutral surface lies at the mid-plane of the plate therefore z_y=0. An effective modulus of elasticity E_{Leff} can therefore be determined in a single direction (x or y) by summing the partial contributions to bending stiffness for the layers of one half of the plate, multiplying by two and dividing by the second moment of area of the total combined cross-section [14].

$$E_{L_\mathrm{eff}} = \frac{2}{I} \sum_{i=1}^{n} E_{L_i} I_i \tag{2-130}$$

where I is the total second moment of area of the beam or plate, E_{Li} is the elastic modulus of layer i and I_i is the moment of inertia of each lamina, given by parallel axis theorem, Eqn. (2-129). The layers (i) are numbered from the middle surface and the thickness of the first layer h_1 is one half the thickness of the middle layer (see Figure 2-5),

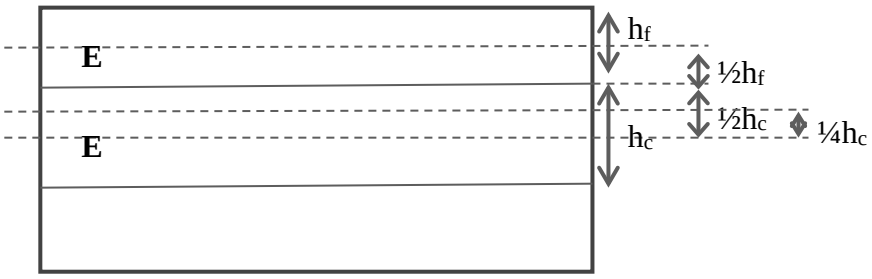

Figure 2-5 Three-layer symmetric glulam.

Regarding the remaining constants, in a similar manner a calculation approach to determine Poisson's ratio of an equivalent single layered shell from the individual layers is provided by Jones and Klein [55]. A weighted mean Poisson's ratio is calculated from the sum of partial contributions of the layers to the bending stiffness which are symmetric about the middle surface the equivalent Poisson's ratio is defined as

$$\nu_{\text{eff}} = \frac{\sum_{i=1}^{n} \nu_{L_i} E_{L_i} I_i}{\sum_{i=1}^{n} E_{L_i} I_i} \tag{2-131}$$

where ν_{Li} is the relevant Poisson's ratio of the layer, E_{Li} is the elastic modulus of the relevant layer and I_i is the moment of inertia of each lamina, given by parallel axis theorem, Eqn. (2-129). Similarly, to Eqn. (2-130), the layers (i) are numbered from the middle surface and the thickness of the first layer h_1 is one half the thickness of the middle layer. As a rule of thumb when the stiffness is dominant for one of the layers then Poisson's ratio for that layer is also dominant [55]. Finally, for isotropic (but not orthotropic) materials the shear modulus can be calculated from an effective modulus of elasticity [8]:

$$G_{xy} = \frac{E_{\text{eff}}}{2(1+\nu)} \tag{2-132}$$

For orthotropic plates, this is calculated from the effective bending stiffness and is approximated by (from [8, 32]):

$$E_{\text{eff}} \approx \sqrt{E_{\text{eff,x}} E_{\text{eff,y}}} \tag{2-133}$$

In all the above calculations, the layers are assumed to be thin, isotropic and perfectly bonded.

2.2.11 Equivalent plate models using the law of mixtures

The Young's modulus (E_z) the shear moduli (G_{xz} and G_{yz}) and Poisson's ratios (ν_{xz}, ν_{zx}, ν_{yz}, ν_{zy}) in the thickness (z) direction of a layered plate can be determined by a calculation method. For thick plates volume change and shear distortion of an element is considered in the thickness direction rather than bending motion. In this case, it is intuitive to use the law of mixtures of a symmetric laminate (which would normally be applied in the case of longitudinal waves) as an appropriate method to calculate effective moduli of layered systems. The Young's modulus in the thickness direction can be calculated from the material constants of the layers using [14].

$$E_z = \frac{h}{2\sum_{i=1}^{n}\left(h_i / E_{z,i}\right)} \tag{2-134}$$

where h is the total thickness of the plate, h_i are the thickness of the individual layers, n and $E_{z,i}$ are the elastic moduli of the layers, n in the z-direction. The shear moduli are calculated from the material constants using [14].

$$G_{xz} = \frac{h}{2\sum_{i=1}^{n}\left(h_i / G_{xz,i}\right)} \tag{2-135}$$

$$G_{yz} = \frac{h}{2\sum_{i=1}^{n}\left(h_i / G_{yz,i}\right)} \tag{2-136}$$

where $G_{xz,i}$ and $G_{yz,i}$ are the elastic moduli of the layers, n in the z-direction. Poisson's ratios are calculated using [14].

$$\nu_{xz} = \frac{2}{h}\sum_{i=1}^{n} \nu_{xz,i} h_i \tag{2-137}$$

$$\nu_{yz} = \frac{2}{h}\sum_{i=1}^{n} \nu_{yz,i} h_i \tag{2-138}$$

where $\nu_{xz,i}$ and $\nu_{yz,i}$ are Poisson's ratios of the layers, n in the z-direction. Additionally, the upper limits for Poisson's ratios can be calculated from the Young's moduli [15]:

$$|\nu_{xz}| < \sqrt{\frac{E_x}{E_z}} \tag{2-139}$$

$$|\nu_{yz}| < \sqrt{\frac{E_y}{E_z}} \tag{2-140}$$

2.3 Statistical energy analysis (SEA)

2.3.1 Introduction

SEA models are used to predict sound and vibration transmission in engineering structures such as buildings, cars, aeroplanes and spacecraft [50]. The SEA framework has been used to determine the sound insulation of single and cavity walls by Crocker and Price [57] and Price and Crocker [58]. It provides a framework of analysis based on a statistical description of power flow which [50]: Firstly, is proportional to the difference in decoupled energy. For multi degree of freedom systems this is proportional to the actual vibrational energy of the systems, and is from greater energy to lesser energy, Power flow is thus described according to [50]

$$\Pi_{12} = \omega\eta_{12}\left(\frac{E_1}{n_1} - \frac{E_2}{n_2}\right) \tag{2-141}$$

Secondly follows a reciprocal relationship, this is the consistency relationship given by [8, 57, 58]

$$\frac{\eta_{ij}}{n_j} = \frac{\eta_{ji}}{n_i} \tag{2-142}$$

where n_i is the statistical modal density (see section 2.3.3). And thirdly excludes the possibility that the maximum possible energy for coupled subsystems can exceed that of the excited subsystem (when only one subsystem is excited).

In these models, the whole system is divided into subsystems. Subsystems differ enough to have separate randomly distributed modal energies. The actual location of modes is not required; but instead is expressed by an even statistical distribution of modes with the same modal density. A uniform distribution of modes with several modes per band and a high modal overlap factor [8] is considered ideal to predict a band average response, in contrast to FEM which is tied to the modal responses of the subsystems. For plates and beams at least five modes per frequency band and the geometric mean of the modal overlap factors of subsystems *i* and *j* of at least one are considered necessary [8]. Lyon [50] states that the modes are approximated by rectangular filters of an equivalent bandwidth (Δ_e) to those in the actual system described by [50]

$$\Delta_e = \frac{\pi}{2}\eta f_0 \tag{2-143}$$

Coupling between subsystems is determined by factors such as whether the systems are structural or fluid filled, the number of dimensions in a subsystem that support the modes and the nature of structural coupling connections.

2.3.2 Fundamentals

The power balance equations for two coupled subsystems are

$$\Pi_{in,1} = \Pi_{diss,1} + \Pi_{12} \tag{2-144}$$

$$\Pi_{in,2} = \Pi_{diss,2} - \Pi_{12} \tag{2-145}$$

where $\Pi_{in,I}$ is the power input to subsystem i, $\Pi_{diss,i} = \omega\eta_{diss,i}E_i$ is the power dissipated in subsystem i, $\eta_{diss,i}$ is the internal loss factor, E_i is the total energy in the subsystem i, and $\Pi_{ij} = \omega\eta_{ij}n_i\left(\frac{E_i}{n_i} - \frac{E_j}{n_j}\right)$ is the power transfer between the subsystems i and j, η_{ij} being the coupling loss factor between the two subsystems. This can be extended to larger systems (e.g. three and five coupled subsystems which include one or two panels [57, 58]).

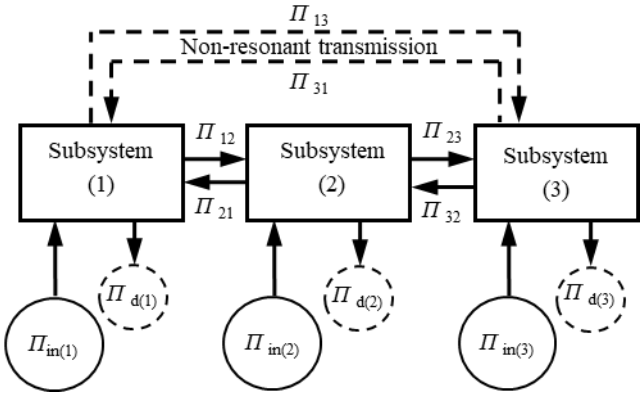

Figure 2-6 A three-subsystem SEA model.

For three coupled subsystems that are all coupled to each other (see Figure 2-6), the power balance equations are

$$\Pi_{in,1} = \Pi_{diss,1} + \Pi_{12} + \Pi_{13} \tag{2-146}$$

$$\Pi_{in,2} = \Pi_{diss,2} - \Pi_{12} + \Pi_{23} \tag{2-147}$$

$$\Pi_{in,3} = \Pi_{diss,3} - \Pi_{13} - \Pi_{23} \tag{2-148}$$

and for five coupled subsystems (connected as shown in Figure 2-7)

$$\Pi_{in,1} = \Pi_{diss,1} + \Pi_{12} + \Pi_{13} \tag{2-149}$$

$$\Pi_{in,2} = \Pi_{diss,2} - \Pi_{12} + \Pi_{23} \tag{2-150}$$

$$\Pi_{in,3} = \Pi_{diss,3} - \Pi_{13} - \Pi_{23} + \Pi_{34} + \Pi_{35} \tag{2-151}$$

$$\Pi_{in,4} = \Pi_{diss,4} - \Pi_{34} - \Pi_{45} \tag{2-152}$$

$$\Pi_{in,5} = \Pi_{diss,5} - \Pi_{35} + \Pi_{45} \tag{2-153}$$

Note that for these three and five coupled system models, the non-resonant component 'bypasses' the plate. This results in non-resonant loss factors directly between the rooms or the rooms and the cavity. The strength of this method to determine the resonant vibration response of thin heavyweight single leaf panels is apparent in many applications and is a strong basis upon which models for more complicated systems can be designed. The mechanisms of non-resonant transmission are required to adequately explain energy coupling between thin lightweight plate and room subsystems. However not all mechanisms of non-resonant transmission "bypass" the plate (e.g. transmission which occurs due to the stiffness contribution for thick plates which usually occurs at high frequencies >>f_c). Thick plates are generally regarded as uncommon in acoustics compared to other fields (e.g. geophysics) and where they occur an *ad hoc* empirical correction (involving a frequency dependant elastic modulus, E) is applied (e.g. thick concrete plates).

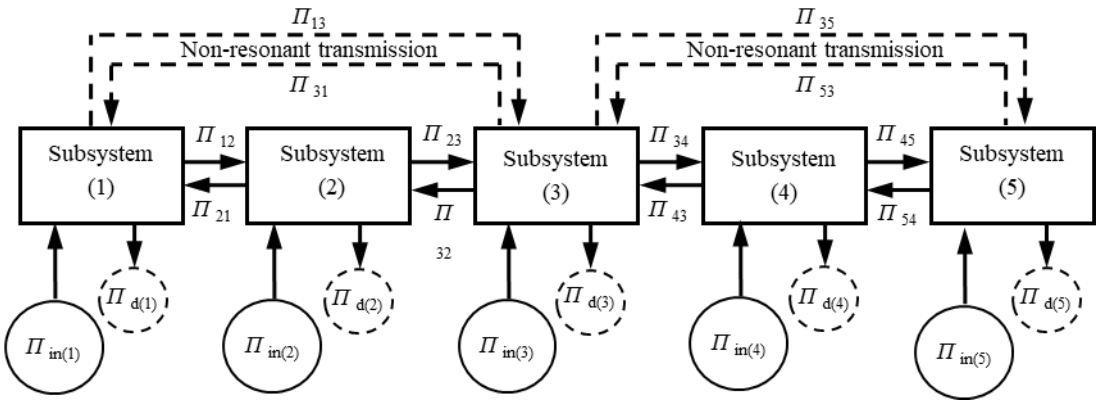

Figure 2-7 A five-subsystem SEA model.

The work of Crocker and Price in [57, 58] also demonstrates the capacity to adopt classical methods (such as empirical mass law [59]) into the SEA framework e.g. by making use of non-resonant coupling loss factors determined from non-resonant transmission coefficients.

In all models, the SEA matrix is solved by inverting the loss factor matrix to give the energies in each subsystem [8].

$$\begin{bmatrix} E_1 \\ E_2 \\ \vdots \\ E_n \end{bmatrix} = \begin{bmatrix} \eta_1 & -\eta_{21} & \cdots & -\eta_{n1} \\ -\eta_{12} & \eta_2 & \cdots & -\eta_{n2} \\ \vdots & \vdots & \ddots & \vdots \\ -\eta_{1n} & -\eta_{2n} & \cdots & \eta_n \end{bmatrix}^{-1} \begin{bmatrix} \frac{\Pi_{\mathrm{in},1}}{\omega} \\ \frac{\Pi_{\mathrm{in},2}}{\omega} \\ \vdots \\ \frac{\Pi_{\mathrm{in},n}}{\omega} \end{bmatrix} \tag{2-154}$$

where η_i are the total loss factors.

SEA path analysis is also used to compare the relative strengths of transmission paths. The basic equations of path analysis in acoustics are usually derived using a first order SEA chain (see e.g. Craik [32] for a derivation) although it is possible to construct higher order chains. The basic equations can be derived for a simple three subsystem chain shown in Figure 2-8.

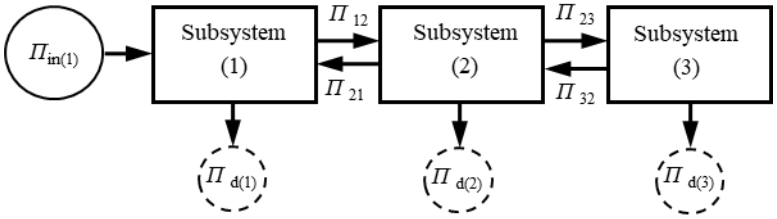

Figure 2-8 A three-subsystem chain.

The power balance equations for this chain are

$$\Pi_{diss,2} - \Pi_{12} + \Pi_{23} = 0 \tag{2-155}$$

$$\Pi_{diss,3} - 0 - \Pi_{23} = 0 \tag{2-156}$$

which gives

$$E_2\eta_{diss,2} = \eta_{12}E_1 - (\eta_{21} + \eta_{23})E_1 + \eta_{32}E_3 \tag{2-157}$$

$$E_2 = E_3\frac{(\eta_{diss,3} + \eta_{32})}{\eta_{23}} \tag{2-158}$$

The solution gives

$$\frac{E_1}{E_3} = \frac{(\eta_{diss,2} + \eta_{21} + \eta_{23})(\eta_{diss,3} + \eta_{32})}{\eta_{12}\eta_{23}} - \frac{\eta_{32}}{\eta_{12}} \tag{2-159}$$

The first term of Eqn. (2-159) dominates when $\eta_{12} > \eta_{32}$. Provided this condition holds Eqn. (2-159) approximates to the first order analysis

$$\frac{E_1}{E_3} \approx \frac{\eta_2\eta_3}{\eta_{12}\eta_{23}} \tag{2-160}$$

and the energy level difference in the *n* subsystem model is given by

$$\frac{E_1}{E_n} \approx \frac{\eta_j \dots \eta_n}{\eta_{1i}\eta_{ij} \dots \eta_{kn}} \tag{2-161}$$

where *i, j* and *k* indicate intermediate subsystems in the transmission path.

Both the matrix solution and path analysis give the energies in the source room (subsystem 1) and receiving room (subsystem 5) which is converted into the sound reduction index, *R*, using

$$R = 10\lg\left(\frac{E_1}{E_n}\right) + 10\lg\left(\frac{V_1}{V_n}\right) + 10\lg\left(\frac{S}{A}\right) \tag{2-162}$$

where *V* is the room volume, *S* is the surface area of the floor and *A* is the absorption area in the receiving room which can be calculated from the Sabine formula

$$A = \frac{0.161V}{T} \tag{2-163}$$

where *T* is the reverberation time.

2.3.3 Modal densities

The bending wave statistical modal densities of each subsystem can be defined by the equations shown in Table 2-1. In regions of low modal density (such as the first few modes of a system) these statistical quantities do not provide accurate estimates. The coupling loss factors between the subsystems can be calculated from the basic

material properties of the subsystems or from measured parameters and indicate the degree of connectivity between subsystems.

Subsystem type	Sound field	Equation	
Thin Beam (simply supported ends[1])	1D	$n_{B,b}(f) = \frac{2L_x}{c_{B,p}}$	(2-164)
Thin Plate (simply supported edges[1])	2D	$n_{B,p}(f) = \frac{\pi f S}{c_{B_p}^2}$	(2-165)
Cavity	1D	$n_{1D}(f) = \frac{2L_x}{c_0}$	(2-166)
Cavity	2D	$n_{2D}(f) = \frac{2\pi f S}{c_0^2} + \frac{L_x + L_y}{c_0}$	(2-167)
Room/Cavity	3D	$n_{3D}(f) = \frac{4\pi f^2 V}{c_0^3} + \frac{\pi f S_T}{2c_0^2} + \frac{L_T}{8c_0}$ where $S_T = 2(L_x L_y + L_x L_z + L_y L_z)$ and $L_T = 4(L_x + L_y + L_z)$	(2-168)

Table 2-1 Modal densities of different subsystems [8] ([1]Beyond about the tenth mode the statistical mode count is unaffected by the boundary conditions [37])

In each case the loss factors in the forward and reverse directions are related by the modal density (n_i), by means of the consistency relationship (Eqn. (2-141)). Note the thin plate modal density has been defined using the bending wave phase speed to maintain applicability even in the case of a transition to thick plate theory. (For thin plates, statistical modal density is a constant and is therefore often defined with respect to the speed of sound in air [26].)

2.3.4 Application of SEA to the prediction of sound insulation

The prediction of direct and flanking transmission in heavyweight buildings is well-established with validations [8, 32]. Solid heavyweight walls and floors often have low mode counts and low modal overlap at low frequencies. Hence while SEA tends to predict smooth curves, measurements can have large fluctuations in vibration level differences between walls and floors; these fluctuations were shown by Craik *et al.* to correspond to the mobility of the receiving plate subsystem [12]. However, with airborne sound insulation this is less problematic because although a heavyweight wall or floor has only a few modes in the low-frequency bands, the rooms have many modes and there tends to be reasonable agreement between SEA and measurements [8].

In contrast to heavyweight constructions, plates that form lightweight constructions usually have higher modal densities which result in uniform vibration fields. In addition, non-resonant transmission often plays an important role in determining the airborne sound insulation at low frequencies and this is less affected by plate modal counts in the frequency bands. However, there is often significant complexity in the fixings of the panels to the structurally supporting framework which can add periodicity and orthotropy to the plate system. Although timber beams forming this framework often have low modal density, the large fluctuations are predictable based on the receiving beam mobility [9]. Some examples of SEA being used for lightweight buildings include airborne transmission across timber frame walls [60] a timber floor [8, 61] and flanking transmission on a timber frame [9].

To model the cavities inside lightweight walls and floors at low-frequencies, they need to be treated as one or two dimensional subsystems [60, 62], and to determine non-resonant vibration into and out of a shallow space such as a cavity, different modelling approaches need to be adopted in contrast to large volumes such as rooms [63].

Hongisto [61] gives an overview of modelling sound transmission across double panel models. These methodologies place an emphasis on physical factors categorised as (1) without studs and cavity absorbent, (2) without studs and with absorbent, (3) rigid studs with absorbent, and (4) flexible studs with absorbent. It is

possible to adopt many of these methods for use in SEA models to determine the sound insulation [8, 32, 58, 62]. Studs or battens can act as structural bridges between the leaves [59], and can also increase the number or strength of acoustic flanking paths [2, 64]. Although metal studs often have little or no stiffening effect on a panel [65, 66] timber ribs attached to a plate can sometimes act to stiffen it [8, 65]. The simplest model for vibration transmission across a rib between two plates assumes a rigid point connection model which has an analogy in circuit theory [10, 59, 60, 62] or a “rigid massless” empirical line connection model [10, 59, 60]. Work on point and line connections have been developed over many of years [10]. It is possible to model a line connection using an analytical approach of wave theory on semi-infinite plates this allows the rib to be modelled as a beam or plate [62]. Cross over frequencies between models can depend on the connection and stud spacing [7]. Many connections are sufficiently complicated that idealised models may not be appropriate for which it is possible to incorporate measured coupling data.

Structural requirements primarily determine beam spacing, depth, geometry and connection details, and a constant rib-spacing is usually used. In the low-frequency range where the bending wavelength (λ_B) is very much greater than the rib spacing (d_R) [8] ribs can act to stiffen a plate in the direction parallel to the studs (which can result in an orthotropic plate). When $\lambda_B >> d_R$ a combined bending stiffness for the plate and rib can be used. In the mid-frequencies, there is a transition phase where parallel to the beams different plate stiffness on and between the beams can be observed and in the perpendicular direction there is little or no stiffening [8, 65]. Finally, at high frequencies where the beam and plates are weakly coupled, little or no stiffening in the plate is observed. In this latter case, it is possible that the plate moves independently of the beams.

Accurate solutions involving the second moment of area to determine the combined stiffness of a panel with ribs rely on the panel being symmetrical about the panel midline (which is then the neutral plane). However, more commonly in building constructions ribs are located on one side of the panel and the exact location of the neutral plane unknown which makes determining the combined stiffness of the panel with ribs more difficult and approximate solutions involving the second moment of

area of the panel cross-section are required [19]. Stiffening elements with cross-sections that are a complex geometry can be simplified. When examining the stiffening properties of the beams on the panel, the full depth of the beam need not necessarily be considered and instead a more appropriate shape that is judged to better account for the “resistance” to the bending moment may be used [19].

In this thesis, the SEA model of the timber-concrete floor in chapter 3 needs to consider the relatively complex connections between the floor plate and the supporting beams. Since beams are known to act to stiffen a plate and separate the plate into sub-plates at high frequencies [67] methodologies for determining the rib-stiffening effect of narrowly spaced deep beams attached to a thin (0.07m) floor plate are tested. In the literature, the depth of the beams can be shown to affect whether coupling between them and the other building elements should be modelled using rigid or pinned coupling [9, 10]. Where the beams are of substantial depth they could also be modelled as a separate subsystem. The beam itself could be modelled as a beam or plate system [10, 11], this latter possibility is also treated in more detail in section 3.4.3. Resilient point hangers were used to connect the beam to the suspended ceiling. Brunskog and Hammer [68] propose a methodology for measuring the stiffness of suspended ceiling hangers and resilient channels in a manner which can be easily adopted into SEA modelling methodologies, and this is explored in more detail in section 3.5.3. The stiffening effect of the beams on the plate is also examined in detail in sections 3.7.3 and 3.7.4.

2.4 Finite element method (FEM)

2.4.1 Introduction

The two main approaches to numerically solve the coupled equations of motion [69] are the direct or modal approach. In the direct approach, FEM is used to obtain the output parameters (such as velocity) using an iterative procedure given a set of coupled equations of motion and a specific type of excitation. In the modal approach, the modes of the system are determined and then the loading is applied to obtain the velocities. For steady-state excitation and an approximately linear material the modal

approach is less computationally expensive [34] and this is the approach adopted for this work.

The FEM software was ABAQUS/CAE 6.14-2 [34]. ABAQUS's "explicit" method obtains the output parameters from the known initial displacements or velocities and adjusts them incrementally, returning the solution after a few iterations. The "explicit" tool is useful to capture non-linear behaviour such as in the case of high force, transient excitation such as impact sources. For this thesis, linear behaviour was assumed sufficient and steady state analysis only performed. For short duration excitation, such as a hammer, the high computational cost of the explicit method becomes justifiable. The short increment time steps required to perform an explicit calculation becomes a reasonable condition when the excitation is an impulse. An explicit numerical method, however, particularly when the input signal is of sufficient duration for a steady state analysis to accurately capture the low-frequency response is considered too computationally costly and was not applied in this thesis.

Alternatively, the "implicit" method uses matrix inversion, modal analysis is one such application of the "implicit" method [34]. In the "implicit" method the problem is formulated as an eigenvalue matrix. Modal analysis is a well-known and widely implemented "implicit" method in which the eigenfrequencies are determined as functions of the system coordinates. A general statement of the free vibrations of a multidegree of freedom system is [69, 70]

$$[M]\{\ddot{u}\} + [C]\{u\} = 0 \tag{2-169}$$

and the eigenvalue problem in modal analysis is given by [69, 70]

$$([C] - \omega_i^2[M])\{\Phi\} = 0 \tag{2-170}$$

where [C] and [M] are the stiffness and mass matrices, ω_i are the eigenfrequencies and <Φ> the eigenvectors or mode shapes ($\{u\}=\{\Phi\}\cos(i\omega t)$). When the eigenfrequencies have been determined, they can then be combined by superposition to give the dynamic response of the system. Obtaining the system response becomes a two-step method in which the eigenfrequencies are first extracted and secondly used to determine the system response. Modal analysis can be regarded as a sub-type

of the FEM and as such is a deterministic approach which is most effective at low frequencies. This is the method implemented in this work.

2.4.2 Elements

Several element types and geometries are available in ABAQUS to model plates. The STRI3 ABAQUS element used in section 4.4.3 is a 3-node triangular thin shell element based on the Kirchhoff plate FEM equations. The limitation of these elements is that convergence and accuracy do not always coincide. In these circumstances, thick plate theory is recommended. Section 4.4.3 and 5.3 of the thesis use S4 and S8 thick plate elements (of the Mindlin type). S4 elements are available with (S4R elements) and without (S4 elements) reduced integration and S8R elements are only available in the reduced integration form. A schematic of the three different element types is shown in Figure 2-9. This shows the difference between the fully integrated (S4) element and the reduced integration (S4R) element in that the S8R mesh has an extra 4 nodes which increases the number of (reduced) integration points from one in the S4R element to four in the S8R.

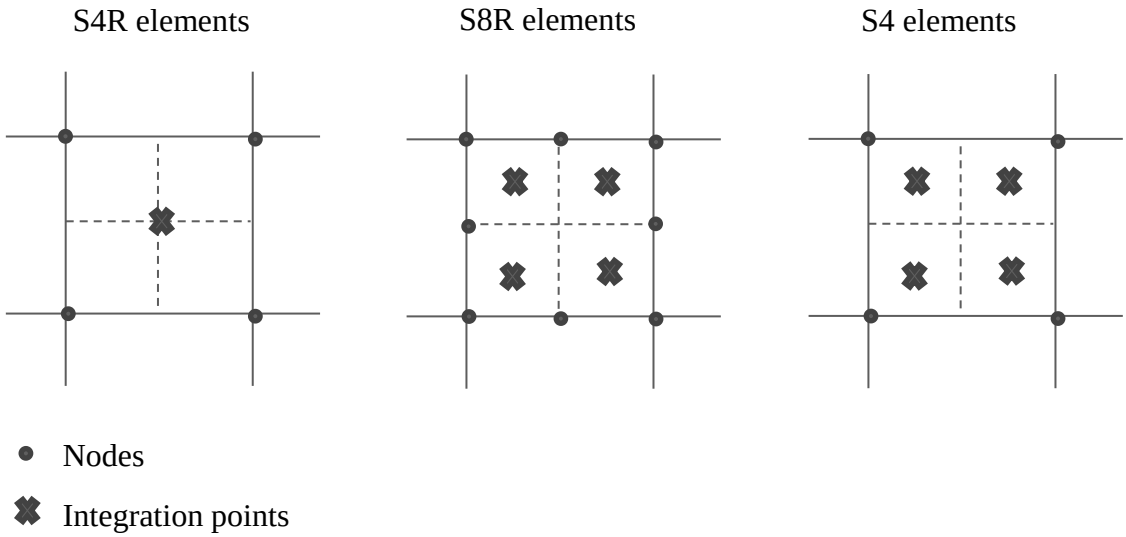

Figure 2-9 Schematic of the S4R and S8R elements

The S4R ABAQUS element is a 4-node rectangular general shell element based on Mindlin first order shear deformation plate theory [34, 35]. Higher order shear deformation elements are not available in ABAQUS and were judged to be

unnecessary for this work. General shell elements use mixed interpolation methods which determine the tensor components by separating the bending (determined by the displacements) and the shear strains [69] thus providing an accurate calculation method with relatively few element nodes.

Reduced integration elements suffer from reduced stiffness due to the collapse (termed “hourglassing”) of the elements which can result in inaccuracy or increasingly expensive computation due to zero-energy modes. For this reason, the results from the reduced integration elements are compared with fully integrated elements in section 5.5.1. Where differences in the results are observed fully integrated S4 elements were preferred. This is found to be true at higher frequencies (>100Hz).

Calculation of the shear correction factor (κ^2) in ABAQUS is based on a calculation of the strain energies through the thickness of the plate and a comparison with the strain energy due to shear in the three-dimensional case [34, 35]. The estimate for a homogeneous plate element is quoted as $\kappa^2=5/6$ [34].

2.4.3 Application of FEM to modelling CLT panels

In this thesis, modal analysis is used as part of an inverse problem to determine the material properties of whole panels and to determine the modal frequencies and structural response of CLT panels and junctions. Much of the literature on layered panels considers alternate layers of hard and soft material (e.g. sandwich structures with a soft deformable core [31, 71] and floating floors). In materials with increased numbers of alternating soft and hard layers when subjected to incident oblique plane waves such as investigated by Guyader and Leseuer [72, 73] it is thought that increasing the number of layers sees the model tend towards a combined modulus determined by the law of mixtures (see section 2.2.11). Their work has also been extended to include excitation over all angles of incidence [74].

CLT panels are unusual in that they consist of alternating hard layers which are perfectly bonded [14]. There are only a few works which discuss hard layers, these include carbon epoxy composites [15], and timber composites [14]. Models of laminates with few layers based on the variational principle show that perfectly

bonded laminates can be modelled using a finite plate approach without considering the shear distribution through the layers. The shear distribution through the profile only becomes an integral part of the problem if the shear constants (G_{xz}, G_{yz}) are very different in adjacent layers [75]. Plates with orthotropic layers that are symmetric about the mid-plane exhibit special orthotropy (described in section 2.2.3) and are a much simplified class of problems (see also sections 2.2.10 and 2.2.11).

Analytical studies verified by measurement of orthotropic layered plates such as plywood have shown that panel assembly can smooth the coincidence notch (e.g. see Ordubadi and Lyon [17]). The dip in sound insulation between critical frequencies can be widened in thin plates whereas thick plates are thought to reduce the orthotropic nature of the wood and hence little or no widening is observed.

A comprehensive survey of FEM models and the kinematic assumptions available in ABAQUS to model the free vibrations of homogenous and composite plates is found in Burlayenko *et al.* [76]. Results obtained using ABAQUS are compared with analytical and numerical solutions in the literature to establish "benchmark" solutions for certain problems. The following points were noted:

(1) First order shear deformation elements should be used with a finer mesh than thin plate elements
(2) S4(R) elements were found to be less accurate than S8R elements especially at high frequencies for thick plates.
(3) The thin shell elements S8R5 were found to be inadequate for modelling layered plates and were only recommended for very thin plates.
(4) S8R elements give satisfactory results for moderately thick elements however performed poorly with an increased E_1:E_2 ratio for single layer laminates.

Modal analysis is used in section 4.4.3 in an inverse method to determine the whole panel elastic moduli of a CLT plate from the measured modes, in section 5.5.1 to determine the point mobility of CLT plates and in section 5.5.6 to determine the vibration reduction index of CLT plate installed in L- and T- junctions. When considering the junctions, a numerical method based on global modal analysis (i.e. of the whole junction) was considered necessary as modes could not be easily identified from measurements made on a single plate.

2.5 Measurement-based SEA methodologies

2.5.1 Introduction

The EN 12354 standards [77] are calculation procedures for determining in situ acoustic parameters in buildings and are primarily based on laboratory measurements of sound insulation from individual building elements. The early work on which these standards were based is discussed briefly in APPENDIX C. For the prediction of airborne sound insulation, EN 12354-1 is considered in this thesis. The aim is to incorporate measured data from the ISO 10140 and ISO 10848 standards which are used to measure airborne and flanking transmission respectively to calculate the apparent sound reduction index (R'). EN12354-1 is intended for adjoining rooms of heavyweight and other selected types of construction as indicated in the literature [78] [79].

Since 2006 work has been carried out to apply the method to lightweight elements [5, 6, 7, 80, 81, 82, 83]. Flanking transmission measurements in an accredited laboratory test stand enables room-to-room measurements to be made more easily from a practical point of view than installing a free-standing junction in an open laboratory space. Structure-borne sound measurements of flanking transmission measured in an open laboratory space may be limited by airborne flanking through the reverberant space. This issue is discussed in sections 6.3.5 and 6.6.2.

Various issues have been identified with EN12354. As it is a simplified form of SEA path analysis, it only considers first order flanking paths [7, 84], although it has been shown that this is insufficient for heavyweight constructions [85, 86]. In addition, standards are not able to provide accurate estimates of the low-frequency performance of a partition [87, 88, 89]. Ongoing research in this area calls for the standards to be more explicit in how to estimate the accuracy of the measurement and calculation regimes [90], and how to improve it [9].

2.5.2 EN12354 calculation approach

The basic premise of EN12354 [77] is that the path transmission coefficients can be added to give a total transmission coefficient τ'

$$\tau' = \tau_{\mathrm{d}} + \sum_{\mathrm{f}=1}^{\mathrm{n}} \tau_{\mathrm{f}} + \sum_{\mathrm{e}=1}^{\mathrm{m}} \tau_{\mathrm{e}} + \sum_{\mathrm{s}=1}^{\mathrm{k}} \tau_{\mathrm{s}} \tag{2-171}$$

where τ_{d} is the sound power ratio in the receiving room due to sound directly coming from the partition (Dd and Fd paths, see Figure 2-10), τ_{f} is the sound power ratio in the receiving room from the Ff and Df flanking paths (see Figure 2-10) (for a monolithic construction twelve first order flanking paths are considered for airborne sound insulation between adjacent rooms [86]), τ_{e} is the sound power ratio in the receiving room due to small elements mounted in the partition and τ_{s} is the sound power ratio due to airborne flanking outside the rooms.

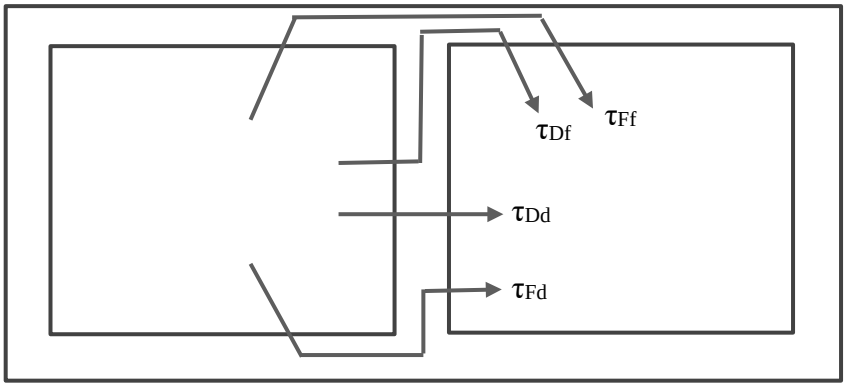

Figure 2-10 The direct (τ_{Dd}) and first order flanking paths (τ_{Ff}, τ_{Df} and τ_{Fd})

2.5.3 Direct airborne sound insulation

For laboratory, airborne sound insulation measurements ISO 10140-1 [91] gives the laboratory requirements and ISO 10140-2 [92] describes the methodology. The sound reduction index is given by

$$R = L_{\mathrm{p1}} - L_{\mathrm{p2}} + 10\mathrm{lg}\left(\frac{S}{A}\right) \tag{2-172}$$

where L_1 and L_2 are the sound pressure levels in the source and receiving rooms respectively, S is the area of the separating element, and A is the sound absorption area in the receiving room.

2.5.4 Flanking transmission

The apparent sound reduction index can also be calculated using Eqn. (2-172) given the relevant sound pressure level measurements. The sound reduction indices of each flanking path can be determined by appropriate shielding of partition walls thus ensuring appropriate sound pressure level measurements. Alternatively, flanking may be determined by structure-borne measurements. The velocity ratio of source and receiving plates *i* and *j* respectively is given by [8]

$$d_{\mathrm{ij}} = \frac{\langle v_j^2 \rangle}{\langle v_i^2 \rangle} \tag{2-173}$$

and the vibration level difference between the two plates (*i* and *j*) is given by [8]

$$D_{\mathrm{v,ij}} = -10lgd_{\mathrm{ij}} \tag{2-174}$$

The energy level difference is related to the vibration level difference as follows [8]

$$D_{\mathrm{v,ij}} = 10\mathrm{lg}\left(\frac{E_i}{E_j}\right) + 10\mathrm{lg}\left(\frac{m_j}{m_i}\right) \tag{2-175}$$

The coupling loss factor between adjacent plates can thus be determined [8]

$$D_{\mathrm{v,ij}} = 10\mathrm{lg}\left(\frac{\eta_j}{\eta_{\mathrm{ij}}}\right) + 10\mathrm{lg}\left(\frac{m_j}{m_i}\right) \tag{2-176}$$

Making use of the reciprocity relationship (Eqn. (2-142)) the following relation can also be determined

$$D_{\mathrm{v,ij}} = 10\mathrm{lg}\left(\frac{\eta_j n_i}{\eta_{ji} n_j}\right) + 10\mathrm{lg}\left(\frac{m_j}{m_i}\right) \tag{2-177}$$

The coupling loss factor between two plates (of differing thicknesses and bending wave phase speeds) can be determined from Eqns. (2-165) (2-176) and (2-177)

$$10\mathrm{lg}\left(\eta_{\mathrm{ij}}\right) = 10\mathrm{lg}\left(\eta_{\mathrm{j}}\right) - D_{\mathrm{v,ij}} + 10\mathrm{lg}\left(\frac{m_{\mathrm{j}}}{m_{\mathrm{i}}}\right) \tag{2-178}$$

$$10\lg(\eta_{\mathrm{ji}}) = 10\lg(\eta_{\mathrm{j}}) - D_{\mathrm{v,ij}} + 10\lg\left(\frac{c_{\mathrm{Bp,j}}^2}{c_{\mathrm{Bp,i}}^2}\frac{\rho_{\mathrm{s,j}}}{\rho_{\mathrm{s,i}}}\right) + 10\lg\left(\frac{S_{\mathrm{i}}}{S_{\mathrm{j}}}\right) \tag{2-179}$$

The velocity level difference in the reverse direction can also be determined by [8]

$$D_{\mathrm{v,ji}} = 10\lg\left(\frac{\eta_{\mathrm{i}}}{\eta_{\mathrm{ji}}}\right) + 10\lg\left(\frac{m_i}{m_{\mathrm{j}}}\right) = 10\lg\left(\frac{\eta_{\mathrm{i}}}{\eta_{\mathrm{ij}}}\frac{n_j}{n_i}\right) + 10\lg\left(\frac{m_i}{m_{\mathrm{j}}}\right) \tag{2-180}$$

Hence the direction averaged velocity level difference by [8]

$$\overline{D_{\mathrm{v,IJ}}} = \frac{D_{\mathrm{v,ij}} + D_{\mathrm{v,ji}}}{2} = 10\lg\left(\frac{1}{\eta_{\mathrm{ij}}}\right) + 5\lg\left(\eta_{\mathrm{i}}\eta_j\frac{n_j}{n_i}\right) \tag{2-181}$$

If the flanking reduction indices can be determined from a first order path analysis [8]

$$R_{\mathrm{ij}} = 10\lg\left(\frac{\eta_{\mathrm{i}}\eta_{\mathrm{j}}\eta_{\mathrm{R}}}{\eta_{\mathrm{Si}}\eta_{\mathrm{ij}}\eta_{\mathrm{jR}}}\right) + 10\lg\left(\frac{V_{\mathrm{R}}S}{V_{\mathrm{S}}A_R}\right) \tag{2-182}$$

$$R_{\mathrm{ji}} = 10\lg\left(\frac{\eta_{\mathrm{j}}\eta_{\mathrm{i}}\eta_{\mathrm{S}}}{\eta_{\mathrm{Rj}}\eta_{\mathrm{ji}}\eta_{\mathrm{iS}}}\right) + 10\lg\left(\frac{V_{\mathrm{S}}S}{V_{\mathrm{R}}A_S}\right) \tag{2-183}$$

Note that

$$\begin{aligned} R_{\mathrm{ij}} = R_{\mathrm{ji}} = \overline{R_{\mathrm{IJ}}} = \frac{R_{\mathrm{ij}} + R_{\mathrm{ji}}}{2} \\ = 5\lg\left(\frac{\eta_{\mathrm{i}}\eta_{\mathrm{j}}\eta_S\eta_{\mathrm{R}}}{\eta_{\mathrm{Si}}\eta_{\mathrm{iS}}\eta_{\mathrm{Rj}}\eta_{\mathrm{jR}}}\right) + 5\lg\left(\frac{S^2}{A_RA_S}\right) + 10\lg\left(\frac{1}{\eta_{\mathrm{ij}}}\right) + 5\lg\left(\eta_{\mathrm{j}}\eta_{\mathrm{i}}\frac{n_j}{n_i}\right) \end{aligned} \tag{2-184}$$

The resonant sound reduction indices for flanking partition i is defined as [8]

$$R_{\mathrm{Resonant,i}} = 10\lg\left(\frac{\eta_{\mathrm{i}}\eta_{\mathrm{R}}}{\eta_{\mathrm{Si}}\eta_{\mathrm{iR}}}\frac{V_{\mathrm{R}}S_{\mathrm{i}}}{V_{\mathrm{S}}A_R}\right) \tag{2-185}$$

and for flanking partition j

$$R_{\mathrm{Resonant,j}} = 10\lg\left(\frac{\eta_{\mathrm{j}}\eta_{\mathrm{S}}}{\eta_{\mathrm{Rj}}\eta_{\mathrm{jS}}}\frac{V_{\mathrm{S}}S_{\mathrm{j}}}{V_{\mathrm{R}}A_S}\right) \tag{2-186}$$

which results in

$$\frac{R_{\mathrm{Resonant,i}}}{2}+\frac{R_{\mathrm{Resonant,j}}}{2}=5\lg\left(\frac{\eta_{\mathrm{i}}\eta_{\mathrm{j}}\eta_{\mathrm{S}}\eta_{\mathrm{R}}}{\eta_{\mathrm{Si}}\eta_{\mathrm{iS}}\eta_{\mathrm{Rj}}\eta_{\mathrm{jR}}}\right)+5\lg\left(\frac{S_{\mathrm{i}}}{A_R}\frac{S_{\mathrm{j}}}{A_S}\right) \tag{2-187}$$

Substituting Eqn (2-187) into Eqn. (2-184)

$$\begin{aligned}\overline{R_{\mathrm{ij}}}=\frac{R_{\mathrm{ij}}+R_{\mathrm{ji}}}{2}=\frac{R_{\mathrm{Resonant,i}}}{2}+\frac{R_{\mathrm{Resonant,j}}}{2}+10\lg\left(\frac{1}{\eta_{\mathrm{ij}}}\right)\\+5\lg\left(\eta_{\mathrm{i}}\eta_{\mathrm{j}}\frac{n_j}{n_i}\right)+10\lg\left(\frac{S}{\sqrt{S_{\mathrm{i}}S_{\mathrm{j}}}}\right)\end{aligned} \tag{2-188}$$

and substituting Eqn. (2-181) into Eqn. (2-188)

$$\overline{R_{\mathrm{ij}}}=\frac{R_{\mathrm{ij}}+R_{\mathrm{ji}}}{2}=\frac{R_{\mathrm{Resonant,i}}+R_{\mathrm{Resonant,j}}}{2}+\overline{D_{\mathrm{v,ij}}}+10\lg\left(\frac{S}{\sqrt{S_{\mathrm{i}}S_{\mathrm{j}}}}\right) \tag{2-189}$$

The relationship between the airborne measurement and the direction-averaged velocity level difference ($\overline{D_{v,ij}}$) (including shielding such as a plasterboard ceiling) is given in [93]:

$$\overline{R_{\mathrm{ij}}}=\frac{R_{\mathrm{Resonant},i}+R_{\mathrm{Resonant},j}}{2}+\overline{D_{v,ij}}+\Delta R_i+\Delta R_j+10\lg\left(\frac{S_s}{\sqrt{S_iS_j}}\right) \tag{2-190}$$

and as described in section 2.5.4, resonant sound reduction indices (R_{i} and R_{j}) of the junction plates are required.

2.6 Summary

This chapter introduced four types of modelling of structural dynamics and sound and vibration transmission: analytical approaches, SEA, FEM, and measurement-based SEA. A breakdown summary of the modelling strategies applied in the thesis in each chapter is shown in Table 2-2. Additional measurement methods to determine the plate properties which are described in later chapters are also included

	Prediction of airborne sound transmission across a timber-concrete composite floor using Statistical Energy Analysis (SEA)	transmission across a cross laminated timber (CLT) plate	Structure-borne sound transmission across junctions of cross laminated timber plates	Direct and flanking transmission across a timber concrete composite floor and cross laminated timber plate junction
CHAPTER	**3**	**4**	**5**	**6**
Panel type				
HBV	x			x
CLT		x	x	x
Model type				
Thin plates - Kirchhoff type (section 2.2.2.1)	x	x		
Thick plates - Mindlin type (section 2.2.2.2)		x	x	
Material model				
Isotropic plates (section 2.2.1.1)	x	x		
Transversely isotropic plates (section 2.2.1.2)		x		
Specially orthotropic plates (section 2.2.1.3)	x	x		
Numerical model (Specially orthotropic thick plate)			x	
Measurement or calculation method to determine plate properties				
Equivalent plate models for bending only (section 2.2.6)	x	x	x	
Equivalent plate models using the law of mixtures (section 2.2.7)			x	
Time of flight measurement (section 4.5.2)	x	x		
Modal analysis measurement with a laser vibrometer (sections 4.5 & 6.4.2)		x	x	
Extracting moduli from modal analysis and an inverse method (section 4.6)		x		
Measurement of the bending wavespeed (section 4.5.6)		x		
Mobility measurement (section 6.4.1)			x	
Analytical calculation methods				
Dispersion relations for thin and thick plates (section 2.2.3)		x		
Characteristic beam functions (sections 2.2.4.1 & 2.2.4.2)		x		
Finite plate (resonant and non-resonant) transmission (section 2.2.4.3)	x	x		
Heckl's orthotropic infinite plate sound transmission model (section 2.2.5.3)	x	x		
Thick plate sound transmission (section 2.2.5.4)		x		
Driving point mobility of thin plates (section 2.2.5.1)	x	x		
Driving point mobility of thick plates (section 2.2.5.2)				
Statistical energy analysis (SEA)				
Matrix Inversion (section 2.3.2)	x	x		
Path analysis (section 2.3.2)	x			
Finite element method (FEM)				
Kirchhoff plate finite element method (section 2.4.2)		x		
Mindlin first order plate finite element method (section 2.4.2)		x	x	
Poisson's ratio in bending (section 2.4.2.4)		x		
Measurement based SEA methodologies				
Direct sound transmission (section 2.5.3.1)	x	x		
Flanking transmission - Airborne methodology (section 2.5.3.2)				x
Flanking transmission - Structure-borne methodology (section 2.5.3.2)	x		x	x

Table 2-2 Overview of prediction methods used in the thesis chapters.

to complete the list. To model the airborne sound insulation of the combined heavyweight-lightweight floor in chapter 3 only thin isotropic or orthotropic floors need be considered and time of flight measurements can be used to determine the elastic moduli of the material. An equivalent plate model to determine the bending stiffness may be applied.

SEA models are used to determine the airborne transmission. The CLT panel described in chapter 4 is more complex therefore four different ways to determine the plate elastic moduli are compared. To achieve this calculation and measurement strategies are required with thick and thin plate models using isotropic and orthotropic plate constants. Different strategies are then trialled to determine airborne transmission. Following this the CLT wall junctions are modelled numerically using FEM in chapter 5. In chapter 6 measurement based SEA methodologies are applied to combined junctions of the two construction types.

3 Prediction of airborne sound transmission across a timber concrete composite floor using Statistical Energy Analysis (SEA)

3.1 Introduction

This chapter concerns the development and validation of a prediction model for airborne transmission across a timber-concrete composite floor. Prediction models based on SEA to determine the airborne sound transmission are experimentally validated. Compared to modelling a basic timber joist floor, the timber-concrete composite floor has the added complexity of having (1) a multilayer upper plate formed from concrete and Oriented Strand Board (OSB), (2) multiple types of rigid connector between the upper plate and the timber joists and (3) a resiliently suspended ceiling. Whilst it is relatively straightforward to identify beam and plate subsystems for an SEA model of a basic timber joist floor, the timber-concrete composite floor is sufficiently complex that it is necessary to consider different approaches to describe the dynamic behaviour of the structural elements. A combination of measured and predicted loss factors are used to determine the dominant transmission paths across this floor and to predict the SRI measured in accordance with ISO 10140-2 [92] in a transmission facility.

3.2 Timber-concrete composite floor construction

A timber-concrete composite floor was built in two steps into a transmission facility to measure the airborne transmission. In the first step, the basic floor was constructed without a suspended ceiling. A cross-section through the basic floor construction is shown in Figure 3-1. (Drawings of the HBV floor are also shown in APPENDIX F.)

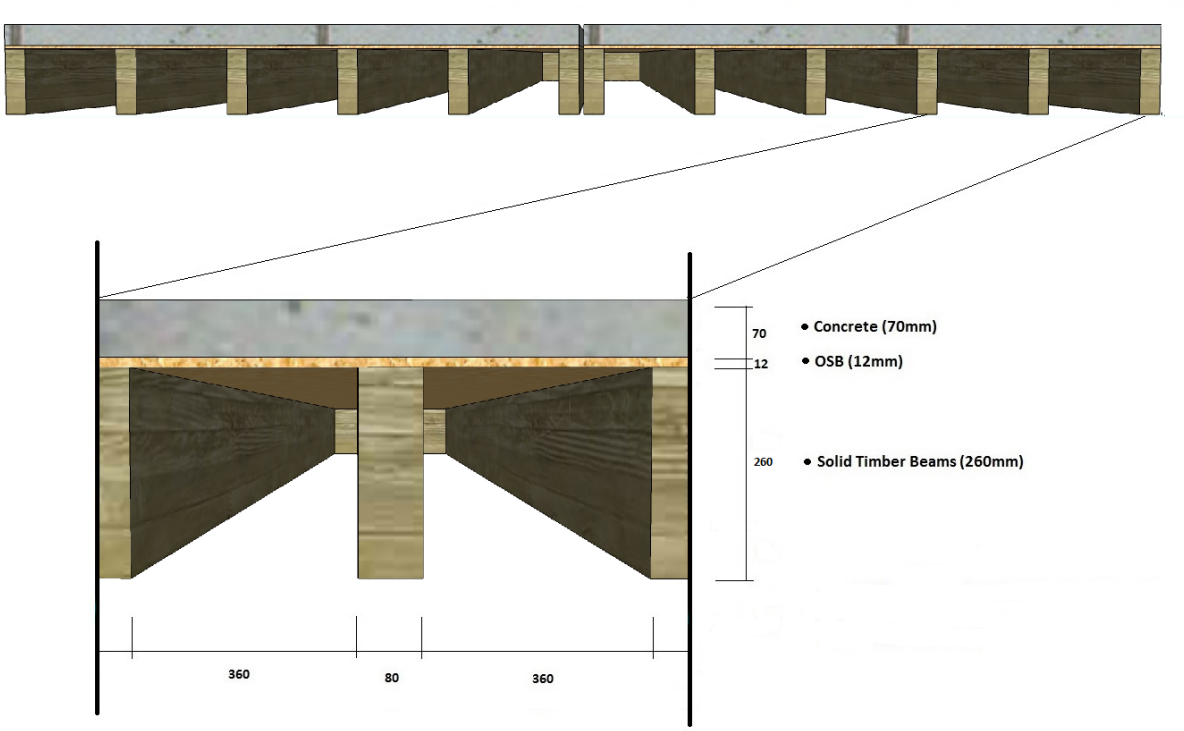

Figure 3-1 Cross section through the basic floor construction.

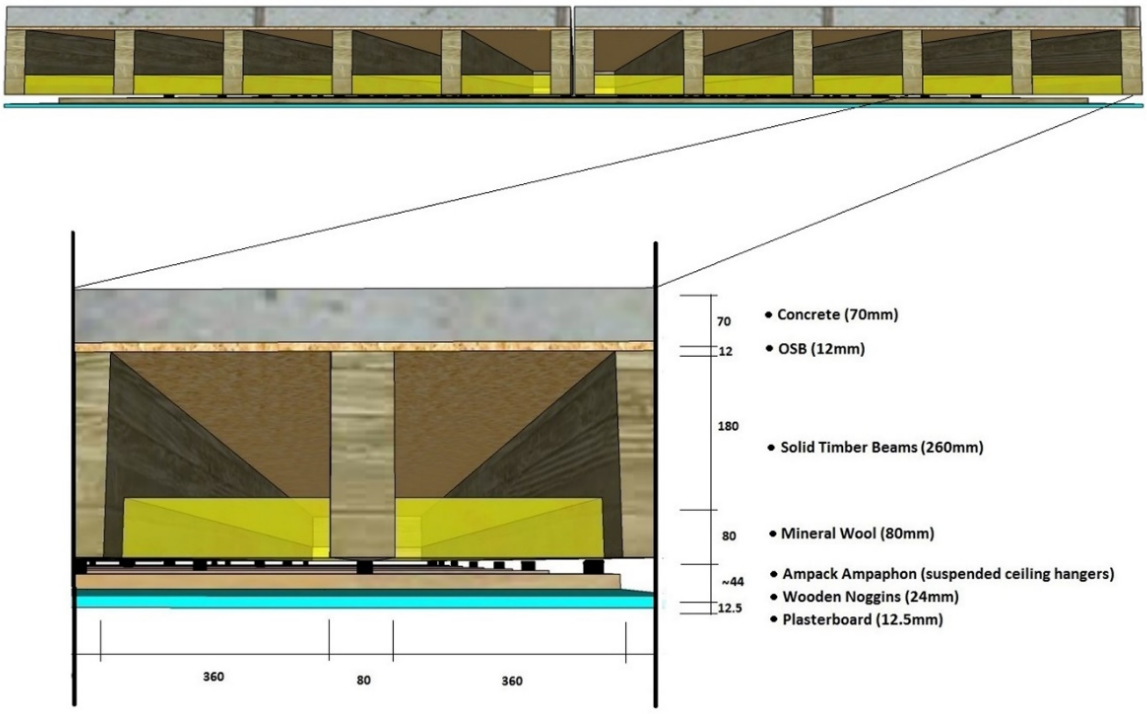

Figure 3-2 Cross section through the floor and suspended ceiling construction.

In the second step, a suspended ceiling was added to the floor. A cross-section through the floor and suspended ceiling construction is shown in Figure 3-2. The dimensions of the full floor are 5670mm x 4590mm. The base floor is formed from two factory-built composite slabs which consist of 70mm concrete cast on top of 12mm OSB. Each slab is supported by solid timber joists (5670mm long, 260mm deep, 80mm wide) with a joist spacing of 440mm. For structural reasons, the two slabs are rigidly connected using two welded steel plates (120mm x 60mm) with a gap of ~20mm between the slabs. Circular foam tubes (40mm diameter) are compressed into this gap and a cement skim is applied on top. Before the concrete is cast, nails are used to connect the OSB to the timber joists at 100mm centres. There are additional "shear" connecting strips (~180mm long, 90mm wide) formed from 2mm thick perforated metal connecting the concrete slab to the timber joists (seven strips per joist). These strips are aligned along the centre line of the joist as shown in Figure 3-3 and penetrate the concrete by ~40mm and the joists by ~40mm. Figure 3-4 shows that the concrete slab is in contact with one-third of the top of the joist.

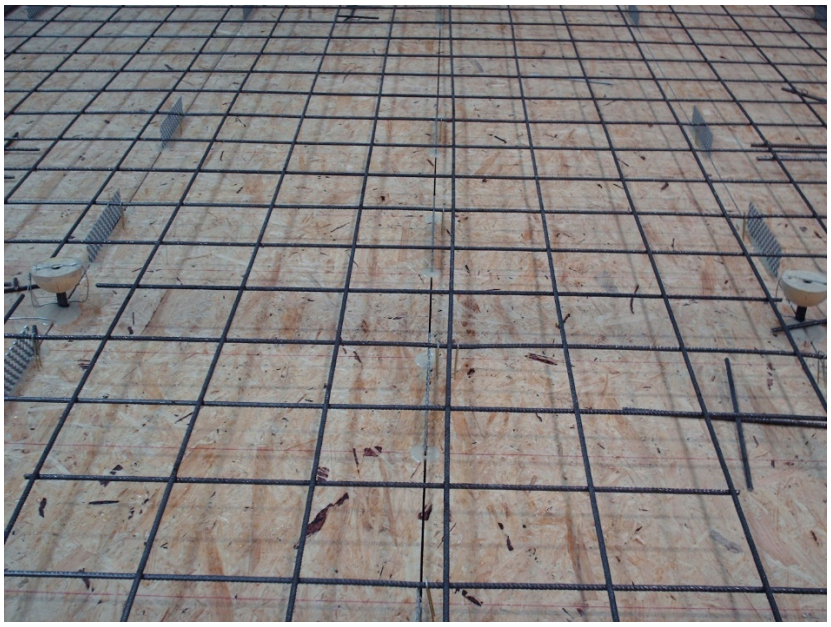

Figure 3-3 Lines of shear connecting strips protruding through the OSB before the concrete is cast on a nominally identical floor (NB This photo also shows the steel reinforcement mesh.).

Figure 3-4 Timber joist in contact with the concrete.

The suspended ceiling consisted of 12.5mm plasterboard which is screwed to 24mm thick, 48mm wide, timber noggins at 200mm centres. These noggins are spaced 500mm to 550mm apart (except at the edges where a smaller spacing is needed to support the plasterboard). The noggins are connected to the joists using resilient hangers (Ampack Ampaphon) as shown in Figure 3-5. The hanger comprised two metal brackets isolated from each other by 6.5mm of rubber where the rubber is in compression under static load. Most hangers are fixed at 440mm centres (except where the two slabs are connected where this increased to ≈520mm). This resulted in a total of 56 hangers. In the cavities above the plasterboard, 120mm rock wool (38kg/m^3) is installed between the joists just above the plasterboard by cutting it to a size such that it is held in place by friction.

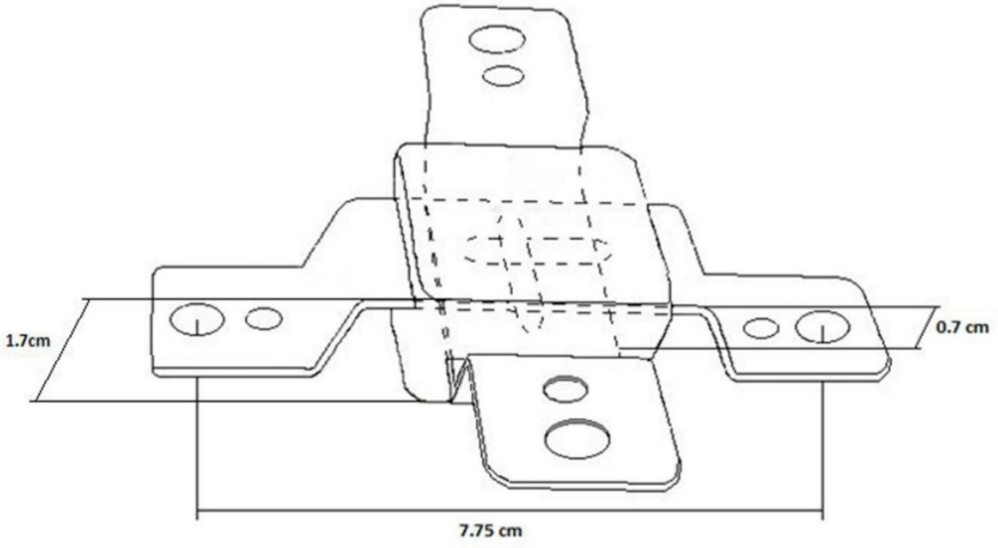

(a)

(b) (c)

Figure 3-5 Resilient hanger. (a) sketch with dimensions (b) photo of actual hanger (c) photo of hanger installed between a joist and a noggin.

In countries such as Switzerland these types of floor are cast in the factory and transported to site for installation. The separate elements are then attached together on site usually in real dwellings the gaps between elements fall at the edges between rooms and at the door thresholds. In the laboratory measurement, the floor area was unusually large to ensure sufficient bending modes on each slab and was cast in two pieces. The material properties are given in Table 3-1. The quasi-longitudinal wavespeed, c_L, of nine nominally identical sample beams were measured in the factory prior to floor installation, using an ultrasound probe. Because it was not

possible to attach the ultrasound probe to the concrete or plasterboard the quasi-longitudinal wave speed was measured in these cases using a force hammer (PCB 086B03 (200g)) at one end of the sample and accelerometer (PCB M352C65) at the other. For the plasterboard, a flat headed nail was driven into the edge of the plasterboard as a target for the force hammer to ensure a short duration delivery of the pulse. The time for a pulse to cross the length of the sample was recorded and used to calculate the wavespeed.

Floor component	**Type of element**	**Thickness (mm)**	**Quasi-longitudinal wavespeed, c_L (m/s)**	**Density (kg/m^3)**	**Poisson's ratio (-)**	**Internal loss factor (-)**
Concrete	Plate	70	3690[a]	2200[c]	0.2[c]	0.01[b]
OSB	Plate	12	2570[c]	590[c]	0.3[c]	0.01[c]
Plasterboard	Plate	12.5	2375[a]	1024[d]	0.3[c]	0.0125[c]
Timber joist	Beam	260	5775[a]	440[c]	0.3[c]	0.0156[b]

Table 3-1 Material properties for the floor components that form plates and beams in the SEA model.

[a] Measured using time-of-flight (see section 3.11.3.5 in [8])

[b] Determined from measured structural reverberation times (see section 3.11.3.4 in [8]).

[c] From Table A2 in [8].

[d] Datasheet provided by manufacturer.

The internal losses of a timber joist and a sample of concrete were measured by suspending the sample in the laboratory and measuring structural reverberation times using a shaker (Gearing and Watson Electronics Type 6WV46), MLS signal, a pair of accelerometers (PCB M352C65) were fixed to the concrete with beeswax and a dual channel RTA (Norsonic 840). Three source positions were used and four decays per source position were measured. This resulted in a mean 95% confidence interval of 0.9dB over the frequency range 50-5000Hz (0.2dB, 2.8dB minimum and maximum). For comparison the number of measurement positions recommended for panels in EN ISO 10848-1 [94] is a minimum of nine to measure structural

reverberation times for vibration reduction index measurement and in ANNEX E EN ISO 140-3 [95] (superseded by 10140-2 [92]) to measure loss factor with sound insulation is twelve for an area 10 m^2 to 20 m^2 “typically two measurement points × three excitation points × two decays per point”.

3.3 Laboratory measurement of airborne transmission

The test floor was built into a laboratory to measure the airborne transmission. The two test rooms either side of the floor have volumes of 64m^3 and 69m^3. These volumes vary slightly according to the exact installation and specification of the junction e.g. floor and temporary shielding thicknesses. The SRI was measured in both directions according to ISO 10140-2 [92] and the direction-average value is used for comparison with the SEA models.

The laboratory walls are lined to suppress flanking transmission. The flanking limit of the laboratory was assessed in terms of the SRI, R, in one-third octave bands between 50Hz and 5kHz using the maximum achievable sound reduction index, R'_{max}. The results show that (R+15.0dB)≤R'_{max} although at 4kHz, (R+10.0dB)≤R'_{max} and at 5kHz, (R+7.0dB)≤R'_{max}. Hence between 50Hz and 3.15kHz it can be assumed that flanking transmission was negligible.

3.4 SEA prediction model

In the first step the basic floor construction is modelled using a three-subsystem model shown in Figure 3-6. However, in the second step the complexity of the floor and suspended ceiling construction, was such that different SEA models were developed to model the floor construction for comparison with the measurements. In total, the floor comprised twelve beams, ten cavities, two concrete/OSB plates, one plasterboard plate, plus the source and receiver rooms. However, assuming the total sum of the coupling loss factors for each subsystem are much greater than the internal loss factor of the building element the floor can be simplified by an SEA model with a single subsystem for each element type to which the coupling loss

factors can be scaled up to represent the strength of the total number of connections in the floor. A summary of all the basic models is shown in Table 3-2.

	50-5000Hz	50-5000Hz	63-200Hz	80-5000Hz	80-5000Hz	80-5000Hz	80-200Hz
FEM model	**(i)a**	**(ii)b**	**(ii)c**	**1(a)**	**2(a)**	**2(b)**	**2(c)**
Number of subsystems							
Three	x	x	x				
Five				x			
Six					x	x	x
Methodology							
Kimura & Inoue (OSB & concrete)	x			x			
Kimura & Inoue (concrete & beams)					x		
Huffington & Troitsky (concrete & beams)		x	x			x	x

Table 3-2 Summary of all basic SEA models

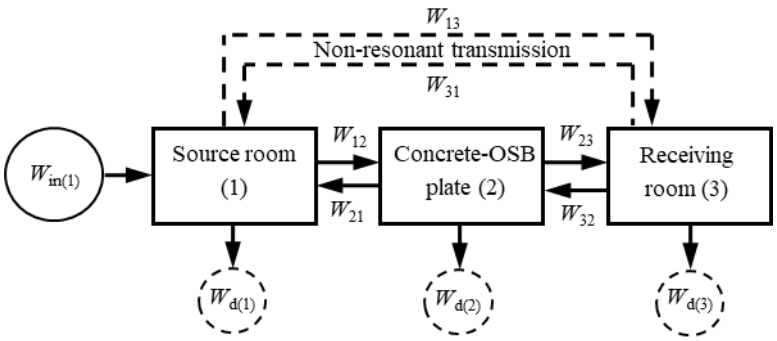

Figure 3-6 SEA modelling of the basic floor construction.

3.4.2 Three subsystems

The three-subsystem model was used to compare the different methodologies to calculate the coupling loss factors for sound radiation from the plate to the room (these models are identified using the Roman numerals (i) and (ii)). It is of the type implemented by Crocker and Price [57] the subsystems are labelled (1), (2) and (3). The concrete-OSB plate were modelled as a single subsystem (described in section 3.7.2) and the SEA matrix is given by

$$\begin{bmatrix} \eta_1 & -\eta_{21} & -\eta_{31} \\ -\eta_{12} & \eta_2 & -\eta_{32} \\ -\eta_{13} & -\eta_{23} & \eta_3 \end{bmatrix} \begin{bmatrix} E_1 \\ E_2 \\ E_3 \end{bmatrix} = \begin{bmatrix} \frac{\Pi_{\text{in},1}}{\omega} \\ 0 \\ 0 \end{bmatrix} \tag{3-1}$$

Model (a) treats the concrete-OSB plate as an isotropic plate with equivalent thickness, density and Young's modulus as described in section 3.7.2 following the approach of Kimura and Inoue [56]. Model (b) treats the concrete-OSB plate and the timber joists as an isotropic plate with an effective bending stiffness for the orthotropic plate as described in section 3.7.4 using the approaches of Huffington [19] and Troitsky [20]. Model (c) treats the concrete-OSB plate and the timber joists as an orthotropic plate using the approaches of Huffington [19] and Troitsky [20]. This model only applies below the higher of the two critical frequencies (in directions perpendicular and parallel to the joists) and is described in section 3.7.4. The orthotropic model of Heckl [52] described in section 2.2.9.1 was also calculated (using the MATLAB "integral2" function) for comparison.

3.4.3 Model 1: Six subsystems

The six-subsystem SEA model shown in Figure 3-7 was used (with the five-subsystem model described in section 3.4.4) to compare the different methodologies to calculate the mechanical coupling loss factors across the point connections. It is formed by considering the concrete-OSB plate as a single subsystem (described in section 3.7.2) for which the SEA matrix is given by

$$\begin{bmatrix} \eta_1 & -\eta_{21} & -\eta_{31} & 0 & 0 & 0 \\ -\eta_{12} & \eta_2 & -\eta_{32} & 0 & 0 & -\eta_{62} \\ -\eta_{13} & -\eta_{23} & \eta_3 & -\eta_{43} & -\eta_{53} & 0 \\ 0 & 0 & -\eta_{34} & \eta_4 & -\eta_{54} & -\eta_{64} \\ 0 & 0 & -\eta_{35} & -\eta_{45} & \eta_5 & 0 \\ 0 & -\eta_{26} & 0 & -\eta_{46} & 0 & \eta_6 \end{bmatrix} \begin{bmatrix} E_1 \\ E_2 \\ E_3 \\ E_4 \\ E_5 \\ E_6 \end{bmatrix} = \begin{bmatrix} \frac{\Pi_{\text{in},1}}{\omega} \\ 0 \\ 0 \\ 0 \\ 0 \\ 0 \end{bmatrix} \tag{3-2}$$

Similarly, to the three-subsystem (model a) described above, model 1 treats the concrete-OSB plate as an isotropic plate with equivalent thickness, density and Young's modulus as described in section 3.7.2 following the approach of Kimura and Inoue [56].

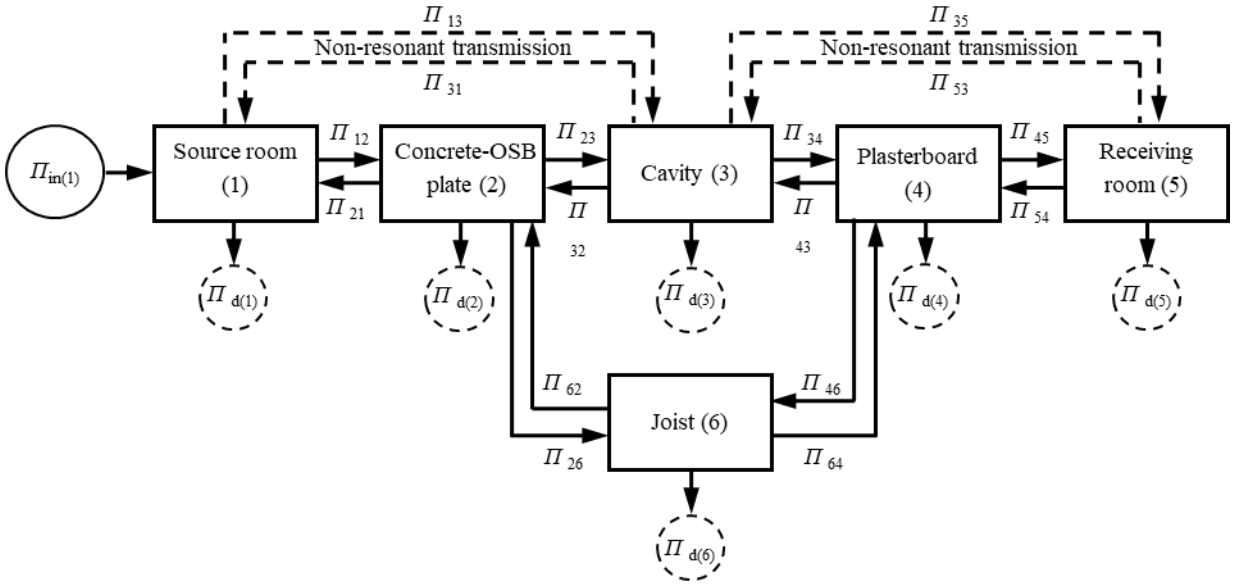

Figure 3-7 SEA modelling of the floor and suspended ceiling construction: Model 1 (six subsystems)

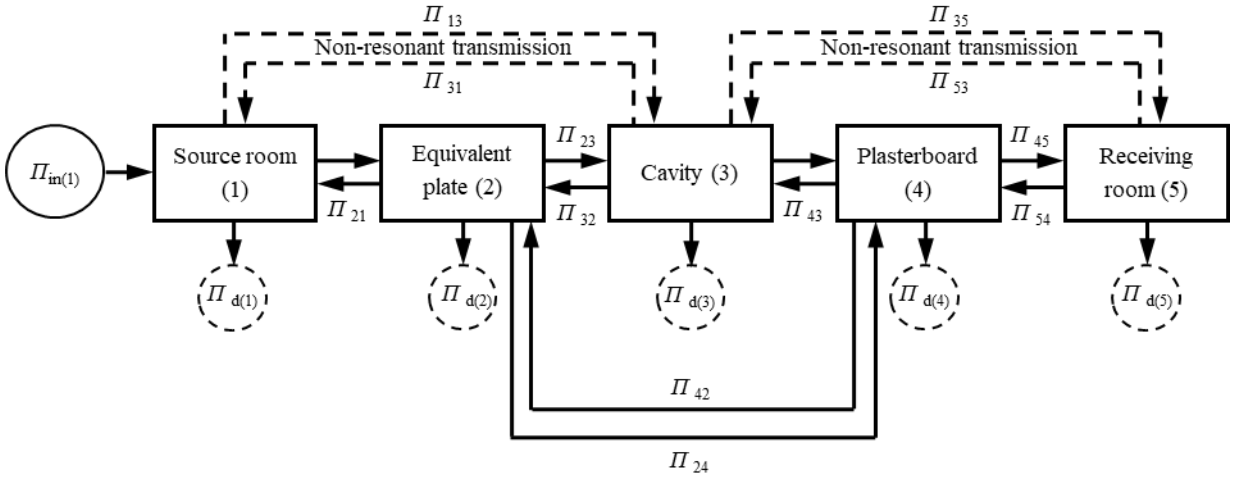

Figure 3-8 SEA modelling of the floor and suspended ceiling construction: Model 2 (five subsystems)

3.4.4 Model 2: Five subsystems

The five-subsystem SEA model shown in Figure 3-8 was used (with the six-subsystem model described in section 3.4.3) to compare the different methodologies to calculate the mechanical coupling loss factors across the point connections. It is formed by considering the concrete-OSB plate and the timber joists as a single subsystem with equivalent plate properties. This is considered due to the large number of nails and shear connectors that connect the concrete, OSB and timber joists together. The five-subsystem model requires solution of the following matrix

$$\begin{bmatrix} \eta_1 & -\eta_{21} & -\eta_{31} & 0 & 0 \\ -\eta_{12} & \eta_2 & -\eta_{32} & -\eta_{42} & 0 \\ -\eta_{13} & -\eta_{23} & \eta_3 & -\eta_{43} & -\eta_{53} \\ 0 & -\eta_{24} & -\eta_{34} & \eta_4 & -\eta_{54} \\ 0 & 0 & -\eta_{35} & -\eta_{45} & \eta_5 \end{bmatrix} \begin{bmatrix} E_1 \\ E_2 \\ E_3 \\ E_4 \\ E_5 \end{bmatrix} = \begin{bmatrix} \frac{\Pi_{\text{in},1}}{\omega} \\ 0 \\ 0 \\ 0 \\ 0 \end{bmatrix} \tag{3-3}$$

Model 2a treats the concrete-OSB plate and the timber joists as an isotropic plate with equivalent thickness, density and Young's modulus as described in section 3.7.3 following the approach of Kimura and Inoue [56]. Model 2b treats the concrete-OSB plate and the timber joists as an isotropic plate with an effective bending stiffness for the orthotropic plate as described in section 3.7.4 using the approach of Huffington [19] and Troitsky [20].

Model 2c treats the concrete-OSB plate and the timber joists as an orthotropic plate using the approach of Huffington [19] and Troitsky [20]. This model only applies below the higher of the two critical frequencies (in directions perpendicular and parallel to the joists) and is described in section 3.7.4.

3.5 Calculation of coupling loss factors

3.5.1 Radiation coupling

For all SEA models, the coupling loss factor that accounts for sound radiation from a plate (e.g. subsystems 2 and 4) to a space (e.g. subsystems 1, 3 and 5) is calculated using

$$\eta_{ij} = \frac{\rho_0 c_0 \sigma}{\omega \rho_s} \tag{3-4}$$

where ρ_0 is the density of air, c_0 is the speed of sound in air, ρ_s is the mass per unit area of the plate and for SEA models 1, 2a, and 2b, σ is the frequency-average radiation efficiency from Leppington *et al.* [46].

For SEA model 2c, an estimate for the frequency-average radiation efficiency is needed for one-third octave bands between the two critical frequencies of the orthotropic plate and this is calculated using Heckl [52] (see section 2.2.9.1). At f_{c1} there is no validated approach in the literature to calculate the radiation efficiency, therefore measured data using the methodology outlined in [6] with mechanical excitation (see APPENDIX D) is used to obtain data for this one-third octave band.

Calculation of the radiation efficiency from Leppington *et al.* requires knowledge of the plate boundary conditions (simply supported or clamped) and the orientation of the baffles that affect sound radiation around the edges of the plate. For sound radiation from the concrete-OSB and plasterboard, the calculations assume that the plate boundaries are simply supported and that the walls of the laboratory represent perpendicular baffles.

The concrete-OSB plate was installed such that one end of the timber joist rested directly on an individual angle iron whereas the other end rested on rubber isolating mounts on a continuous angle iron connected to the flanking laboratory. The empirical approach for masonry/concrete described by Hopkins [8] (Method No.3) is used in which all calculated values of the radiation efficiency greater than one are set to a value of one.

Separate sheets of plasterboard were joined together with gypsum skim and tape so the plasterboard can be assumed to act as one large plate. For plasterboard, the radiation efficiency near the critical frequency tends to be overestimated; hence all calculated values of the radiation efficiency greater than one are set to a value of one [8].

3.5.2 Non-resonant coupling between the cavities and the rooms

To calculate non-resonant transmission from the cavity to a room across a plate it is necessary to identify the frequency ranges over which the cavity sound field can be described as one-, two- or three-dimensional [8]. These mode counts in the cavity, separated by sound field type is shown in Figure 3-9.

The lowest cavity mode is an axial mode which occurs in the 31.5Hz one-third octave band. The first tangential mode occurs across the cavity width (360mm) because the width is larger than the depth, and occurs in the 500Hz one-third octave band. The first cross-cavity mode is the tangential mode across the cavity depth (260mm) which occurs in the 630Hz one-third octave band (the mode falls in this band regardless of whether the depth occupied by the noggins and hangers is included in the definition of the cavity depth or not). The first oblique mode occurs in the 800Hz one-third octave band.

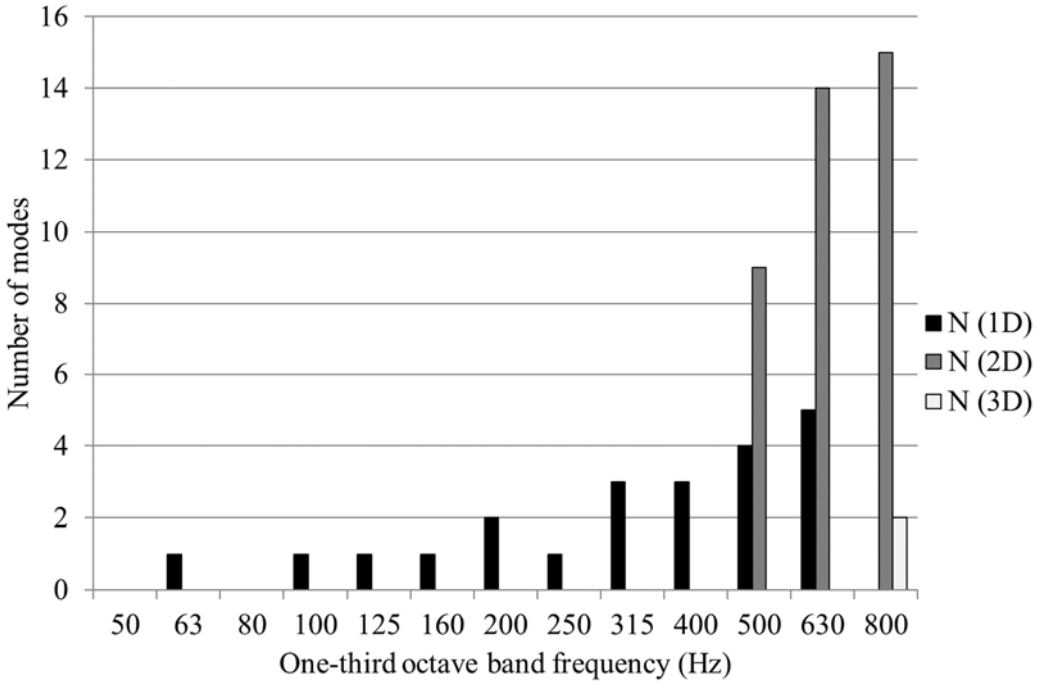

Figure 3-9 Mode count in the cavity, (subsystem 3 in models 1 and 2), up to the third octave band which contains the first cross cavity mode (50Hz-800Hz).

For a one- or two-dimensional sound field in the cavity, the coupling loss factor for non-resonant transmission from a cavity (subsystem *i*) to a room (subsystem *j*) is given by [63]

$$\eta_{ij} = \frac{\rho_0^2 c_0^3 S \sigma_{f_c}}{\omega^3 V_i \rho_s^2} \tag{3-5}$$

where S is the surface area of the plate that faces into the cavity, V_i is the volume of subsystem i, and σ_{fc} is the radiation efficiency of the plate assuming the wavespeed in the plate is always equal to that in air which is calculated using Leppington *et al.* [46]. An empirical correction is applied in which all calculated values of the radiation efficiency greater than one are set to a value of one [8].

For a three-dimensional sound field in the cavity, the coupling loss factor for non-resonant transmission from a cavity (subsystem *i*) to a room (subsystem *j*) is given by [58]

$$\eta_{ij} = \frac{c_0 S}{4\omega V_i} \tau_{\mathrm{NR}} \tag{3-6}$$

where τ_{NR} is the non-resonant transmission coefficient for the plate and is calculated according to Leppington *et al.* [47] (see section 2.2.7). (The plate perimeter, U is calculated using the dimensions L_1 and L_2 for the whole floor.)

The coupling loss factor for non-resonant transmission from the room to the cavity is calculated from the consistency relationship in Eqn. (2-142). To assess the transition from Eqn. (3-5) to Eqn. (3-6), both have been used to estimate the coupling loss factor in the 500Hz one-third octave band. The transition from a one- to two- or three-dimensional sound field in the cavity means that there is a discontinuity in the predictions at 500Hz. Taking the average of the two different models from the SEA matrix solution at 500Hz is used as a pragmatic solution to this problem.

For SEA model 2c which uses an orthotropic plate model, the non-resonant coupling loss factor between the two critical frequencies is also required. For this floor, Eqn. (3-5) is used because both critical frequencies are below the first cross-cavity mode of the floor.

The other potential forms of non-resonant coupling correspond to mass-spring-mass resonances. The mass-spring-mass resonance of the system formed by the concrete-OSB (acting as a mass), cavity (acting as an air spring) and the plasterboard (acting as a mass) occurs below 50Hz and therefore it is not included in the SEA model as it is below the frequency range of interest. The mass-spring-mass resonance of the concrete-OSB and joists, resilient hangars and plasterboard is inside the 50Hz one-third octave band; however, this band is still considered in the SEA model.

3.5.3 Mechanical coupling at point connections

For point connections between plates and/or beams, the coupling loss factor is given by [32]

$$\eta_{ij} = \frac{N}{\omega m_i} \frac{Re\{Y_j\}}{\left|Y_i + Y_j + Y_c\right|^2} \tag{3-7}$$

where Y_i and Y_j are the driving-point mobilities of subsystems i and j, and Y_c is the mobility of the connector.

Note that Eqn. (3-7) requires the mass of the source subsystem (i.e. a combination of concrete, OSB, and timber joists). For SEA model 2a, an equivalent density and thickness is used to give m_i=3280kg and for SEA models 2b and 2c, the thickness and density of the concrete is used to give m_i=5528kg.

Infinite plate mobilities are commonly used in SEA to give a frequency-independent value for plates where the actual boundary conditions are not known with sufficient accuracy to use an analytical model.

These calculations were made assuming that there were only point connections in the model. There were also shear connecting strips between the concrete and the beams, the effects of which were neglected to simplify to a point model. Considering only the point connections the crossover point for substitution of a line model should occur when the connection spacing is approximately half the bending wavelength [60]: Comparison of the calculated bending wavelengths for the concrete and OSB shows that this occurs at a frequency greater than 5kHz for the combined concrete-OSB.

For the concrete-OSB plate, there are nails connecting the OSB to the joists at 100mm centres. To determine the coupling loss factors η_{26} and η_{62} for SEA model 1 these are considered as rigid point connections for which Y_c=0 in Eqn. (3-7).

The plasterboard ceiling was suspended by resilient hangers. Assuming each hanger can be represented as a spring with dynamic stiffness, k, the mobility of the connector for use in Eqn. (3-7) is

$$Y_c = \frac{i\omega}{k} \tag{3-8}$$

The dynamic stiffness of the resilient hangers is measured in the laboratory. For resilient devices used in suspended ceilings, Brunskog and Hammer [68] developed a test rig to quantify the input stiffness and transfer stiffness of devices ranging from hangers to resilient channel systems that are under static load. This measurement system is adopted for the measurements and is shown in Figure 3-10. (Drawings of the suspended ceiling apparatus components are also shown in APPENDIX E.)

It is essentially a mass-spring-mass system where the upper mass is resiliently supported on a separate frame and the lower mass provides a representative static load. The upper mass includes the masses of the wooden noggins. This arrangement accounts for the noggins themselves; hence they are not included as separate subsystems in the SEA model. The upper mass, m_1, weighs 2.56kg and the lower mass, m_2, weighs 10.84kg. This lower mass represents the typical static load applied by one to two layers of plasterboard when suspended by four hangers to ensure that the result is representative of in situ. Excitation is applied to the upper mass using an electrodynamic shaker (Ling Type 201). Broadband noise is used because resonance measurements on resilient elements are prone to non-linear response when using a force hammer [96]. The input force is measured using a force Transducer (PCB Type 208 A04) and the response is measured using accelerometers (PCB Type M352C65) on the underside of the lower and upper masses.

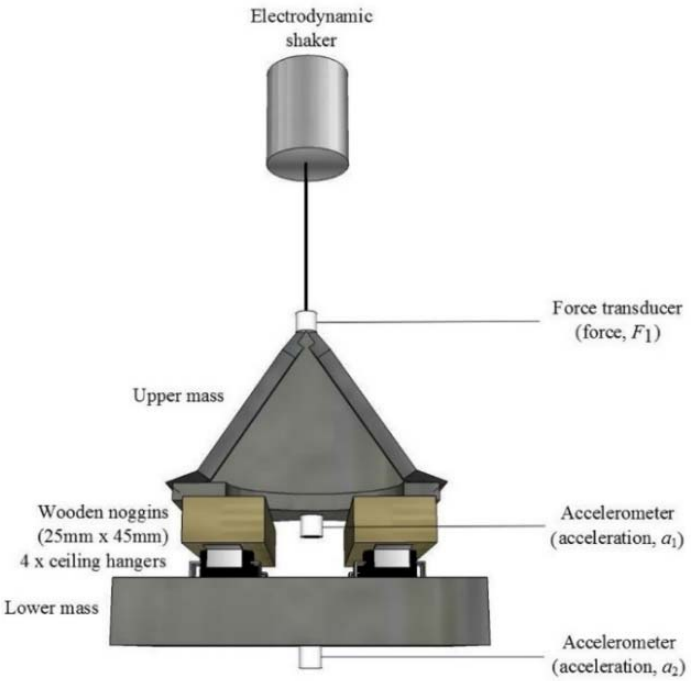

(a)

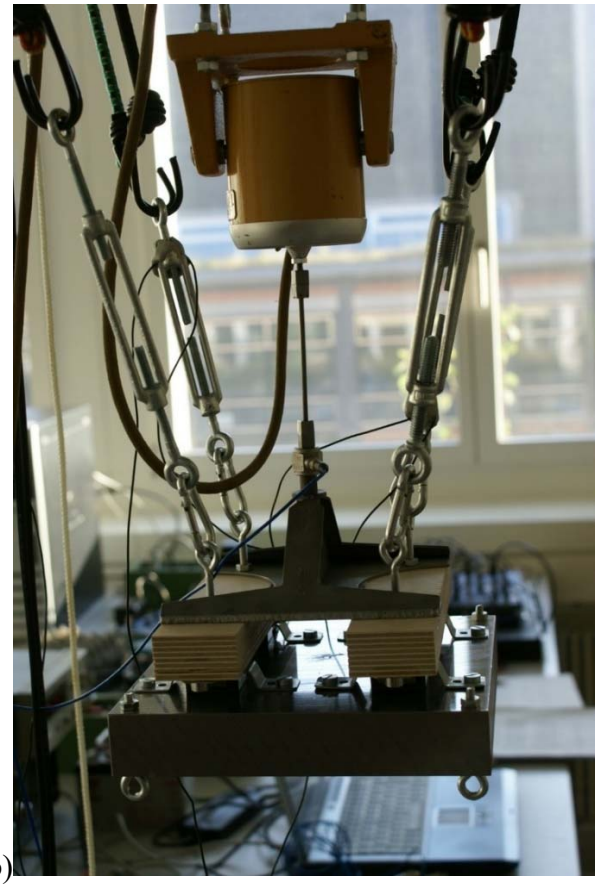

(b)

Figure 3-10 Test rig used to determine the spring stiffness (a) sketch with labels, (b) photograph.

As with measurements of dynamic stiffness using mass-spring-mass systems for wall ties [96], two Frequency Response Functions (FRF) are measured. For these experiments, these are the direct and transfer accelerance. Using equivalent circuit theory for lump mass and spring elements for a mass-spring-mass system gives the direct accelerance as [8]

$$\frac{a_1}{F_1} = \frac{k + i\omega R - \omega^2 m_2}{\left[i\omega m_1 \left(i\omega m_2 + \frac{k}{i\omega} + R\right)\right] + \left[i\omega m_2 \left(\frac{k}{i\omega} + R\right)\right]} \tag{3-9}$$

and the transfer accelerance as [8]

$$\frac{a_2}{F_1} = \frac{k + i\omega R}{\left[i\omega m_2 \left(i\omega m_2 + \frac{k}{i\omega} + R\right)\right] + \left[i\omega m_2 \left(\frac{k}{i\omega} + R\right)\right]} \tag{3-10}$$

where a is the acceleration, F is the force, k is the dynamic stiffness of the resilient device, R is the damping constant of the resilient device, and m is the mass. The subscripts 1 and 2 refer to the upper and lower masses respectively.

For the mass-spring-mass resonance, the damping constant, R, is related to the loss factor, η, by

$$R = \eta \sqrt{k \frac{m_1 m_2}{m_1 + m_2}} \tag{3-11}$$

Both the direct and transfer accelerance can be used to identify the mass-spring-mass resonance frequency which occurs at

$$f_{\text{resonance}} = \frac{1}{2\pi} \sqrt{\frac{k}{\left(\frac{m_1 m_2}{m_1 + m_2}\right)}} \tag{3-12}$$

with an anti-resonance that is present in the direct accelerance at

$$f_{\text{anti-resonance}} = \frac{1}{2\pi} \sqrt{\frac{k}{m_2}} \tag{3-13}$$

(a)

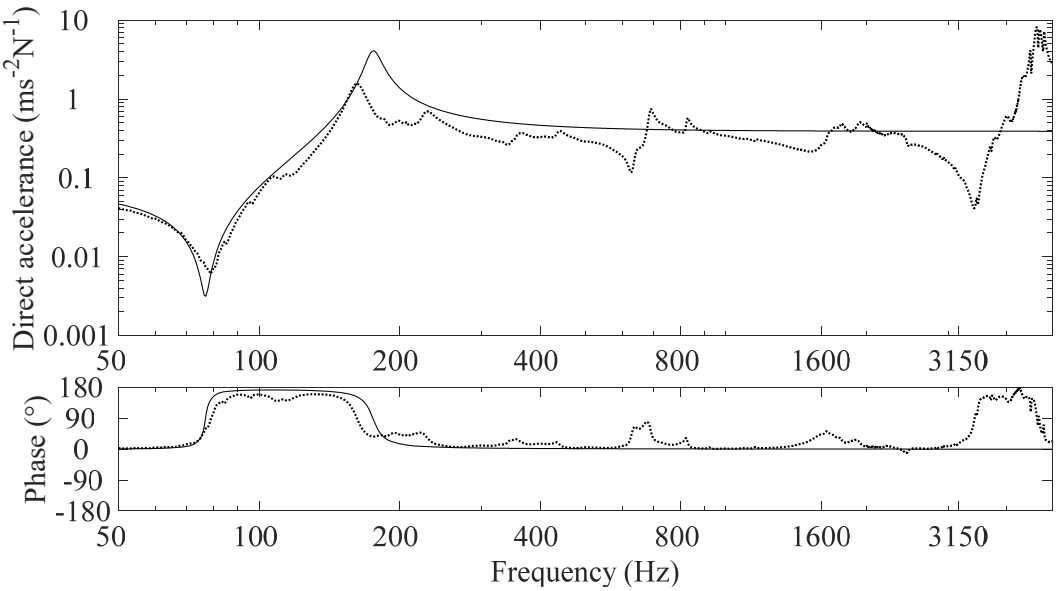

(b)

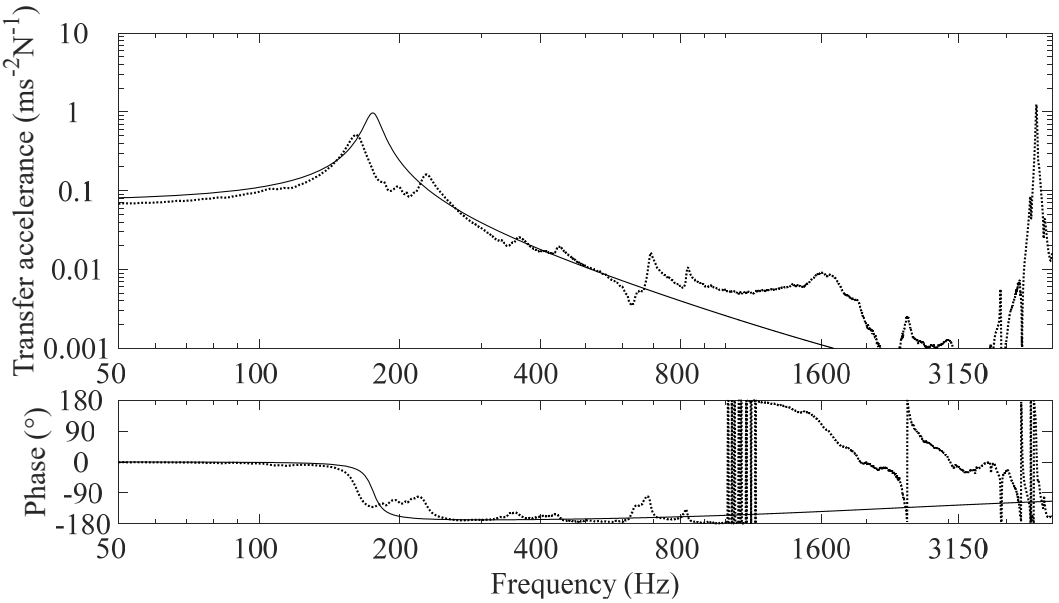

Figure 3-11 Measurements with the resilient hanger in the mass-spring-mass test set-up (a) direct accelerance, (b) transfer accelerance. The dashed line indicates measured data. The solid line indicates calculated results from Eqns. (3-9) and (3-10) for (a) and (b) respectively using estimated values of dynamic stiffness and damping constant from the measured data.

Estimates of the dynamic stiffness, k, can be determined by using Eqns. (3-9) and/or (3-10)) with the resonance or anti-resonance frequencies identified from the magnitude and/or phase of the direct and/or transfer accelerance.

The measured direct and transfer accelerance are shown on Figure 3-11. The anti-resonance occurs in the direct accelerance at 79Hz. The first peak in the direct and transfer accelerance corresponds to the mass-spring-mass resonance frequency and occurs at 162Hz. The model described by equivalent circuit theory for the direct accelerance. Eqn. (3-9) is fitted to the measured data by measuring the half-power bandwidth to obtain the damping loss factor at resonance and minimising the differences between the measured and predicted resonance and anti-resonance frequencies to estimate the spring constant, k. This resulted in the stiffness of the four hangers in parallel as k=2.52MN/m, and a value of R corresponding to a loss factor, η=0.077. These values are then inserted into Eqns. (3-9) and (3-10) and plotted on Figure 3-11. The discrepancy between the two curves indicates that the resilient hanger does not behave exactly as a simple, linear spring, but that it is a reasonable approximation.

Small displacements and hence a linear spring response is a reasonable assumption when predicting airborne sound insulation [8, 96]. However, this would not necessarily be true for impact sound insulation; where higher forces, including impacts, may be responsible for sound transmission. When the upper mass in the apparatus was changed the resonance peak was measured at different frequencies, and hence different spring constants, k were calculated, although the anti-resonance trough was unchanged [97]. Emphasis was therefore placed on determining the spring stiffness from the antiresonance to give more consistent results (regardless of upper mass). The sensitivity of the loss factor was such that a difference in spring constant, k of ±0.15MN/m altered the coupling loss factor (according to Eqn. (3-7)) by ~±0.5dB.

(a)

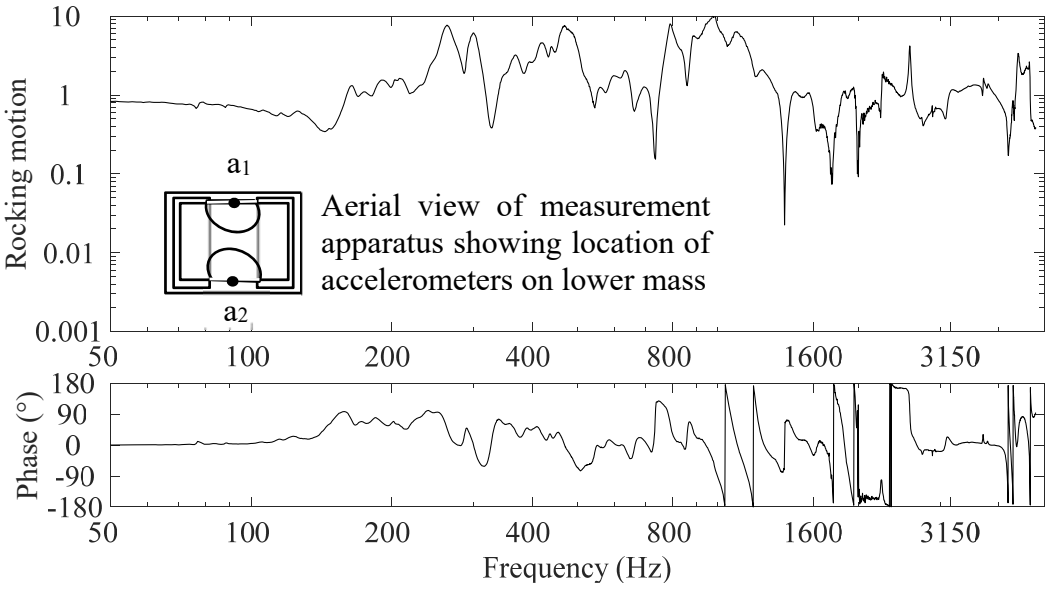

(b)

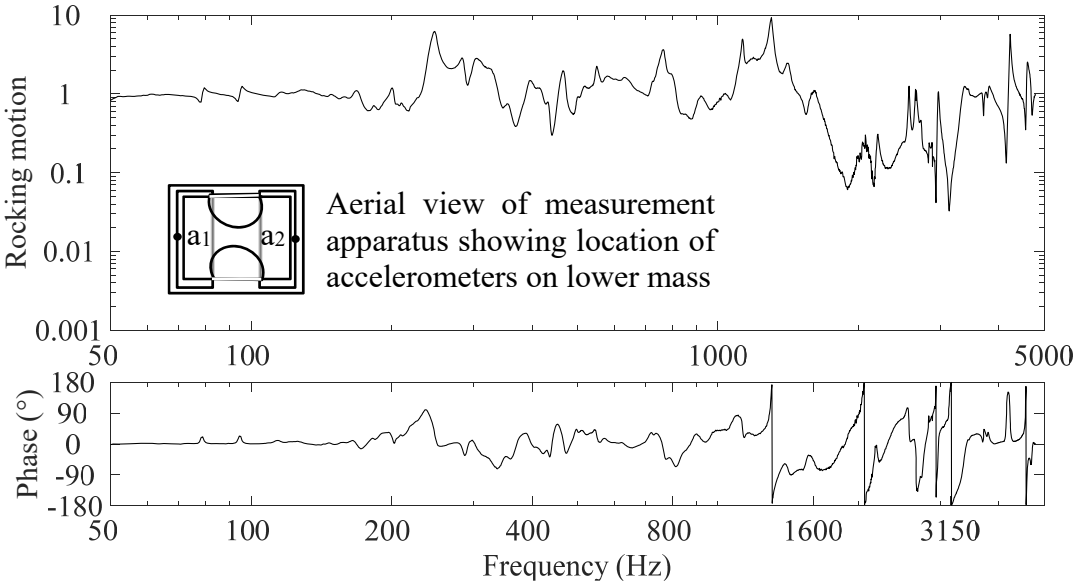

Figure 3-12 An example of the rocking motion (a) in the direction parallel to the wooden noggins (b) in the direction perpendicular to the wooden noggins (M_1=0.810kg and M_2=10.84 kg)

Above 1000Hz the rocking motion of the apparatus is assessed for each of the masses. The rocking motion for the small upper mass in the directions perpendicular and parallel to the wooden noggins is shown in Figure 3-12. The first phase change from -180º to 180º occurs at 1000Hz in the direction parallel to the beams and 1300Hz in the direction perpendicular to the noggins. Therefore, the rocking motion did not affect the calculation of the stiffness from the mass-spring-mass resonance frequency. However, the rocking motion does prevent use of the high frequency accelerances to determine a frequency-dependent stiffness in the high frequency range.

Brunskog and Hammer [68] used their experimental set-up to improve estimates of the spring stiffness at high frequencies when it acts as a one-dimensional wave continuum. For the resilient hanger in this work, additional measurements are therefore carried out with different upper masses and the model is fitted to the data for the largest upper mass. These additional measurements indicate that above the mass-spring-mass resonance frequency the high frequency peaks shift as the magnitude of the upper mass is altered. However, the high frequency model from Brunskog and Hammer predicts resonance peaks which do not vary when using different upper masses. Hence it is not possible to find realistic values for the Helmholtz number corresponding to rubber that would give good agreement between measurements and the high frequency model. It is therefore considered unlikely that a model for a one-dimensional wave continuum would be applicable to this resilient hanger because the metal fixing braces are only separated by 6.5mm thick rubber. An additional complication is that above 1kHz there is rocking motion in the test set-up which prevents use of the accelerance data to determine a frequency-dependent stiffness. For this reason, only the mass-spring-mass resonance frequency is used to estimate the dynamic stiffness of the resilient hanger and this is applied across the entire frequency range used in the SEA models.

3.6 Experimental determination of loss factors

Due to the complexity of the timber-concrete composite floor it is necessary to incorporate some measured loss factors in the SEA models as described in this section.

3.6.1 Total loss factor for the rooms

The reverberation times for the rooms are measured according to ISO 10140-2 [92] from which the TLFs are calculated using [8]

$$\eta_i = \frac{2.2}{fT_i} \tag{3-14}$$

where T_i is the reverberation time of subsystem i.

For the plate and beam subsystems the internal loss factor is summed with the coupling loss factors of the system to give a total loss factor. In the case of the concrete and timber beam, the measured internal loss factor is used, and in the case of the plasterboard a typical internal loss factor for plasterboard is taken from the literature [8].

3.6.2 Total loss factor for the floor cavity

Previous reverberation time measurements on cavities inside timber joist floors [8] and wall cavities [26] have shown that it is difficult to accurately predict the cavity TLF and that it is usually necessary to use measured reverberation times to calculate the TLF. One of the cavities in the floor is used for the reverberation time measurements. A loudspeaker (Fostex 6301B) is placed inside the cavity and the measured decay times averaged from two source positions and eight receiver positions for each source position, with signal processing carried out using M-Reverb with an MLS signal.

3.6.3 Coupling loss factor between a timber joist and the plasterboard ceiling across the resilient hangers

An alternative method to determine the CLF between the timber joist (subsystem *i*) and plasterboard ceiling (subsystem *j*) across the resilient hangers is considered with a two-subsystem SEA model. The coupling loss factor is determined using Eqn. (2-178). A small mock-up of the ceiling is built in the laboratory as shown in Figure 3-13. It comprises two 4000mm long, 260mm deep, 80mm wide timber joists that are attached to four timber noggins on a 2000mm x 980mm sheet of 12.5mm plasterboard using four suspended ceiling hangers on each joist. The beam width and depth are the same as those of the actual floor. The dimensions of the plasterboard are chosen to represent the static load that is supported by each hangar in the actual floor. The material properties are given in Table 3-1.

Figure 3-13 Laboratory mock-up for measuring the CLF between the timber joists and the plasterboard ceiling across the resilient hangers.

As there are four resilient hangers per beam, Eqn. (3-7) is scaled up to represent the total number of hangers in the floor, by dividing by four and multiplying by the number of resilient hangers for the whole floor (i.e. 56).

The timber joist is excited with an electrodynamic shaker (Gearing and Watson Electronics Type 6WV46) and the vibration level difference is measured between the timber joist and the plasterboard using accelerometers (PCB Type M352C65). All signal analysis is carried out using a Norsonic 840 analyser. The structural reverberation times of the plasterboard sheet are measured using the Norsonic 840 analyser with an MLS signal and time reversal to determine the total loss factor of the plasterboard.

3.7 Subsystem properties for the combination of concrete, OSB and timber joists

To form the concrete-OSB plate, the concrete is cast directly onto the OSB. However, it is not known whether the concrete and OSB would undergo bending vibration as a homogeneous unit over the frequency range from 50Hz to 5kHz. For this reason, the vibration level difference is measured between the concrete and the OSB as described in section 3.7.1 to assess whether the concrete-OSB plate can be considered as a single SEA subsystem.

For SEA model 1, a single subsystem is used to represent the combination of concrete and OSB using the equivalent properties described in section 3.7.2. For SEA model 2a, a single subsystem is used to represent the combination of concrete, OSB and timber joists as described in section 3.7.3 using the approach of Kimura and Inoue. For SEA model 2b and 2c, a single subsystem represents the combination of concrete, OSB and timber joists as described in section 3.7.4 using the approach of Huffington and Troitsky.

3.7.1 Velocity level difference between the OSB and concrete

The velocity level difference between the concrete and OSB is measured using (1) mechanical excitation with an electrodynamic shaker (B&K Type 4809) attached using a threaded stud at three positions on the concrete and three positions on the

OSB (these positions are at least 1m apart) and (2) airborne excitation with two loudspeaker positions in the room facing the concrete surface and in the room facing the OSB surface (before the suspended ceiling was installed). Acceleration levels are measured using accelerometers (B&K Type 4513-B-002) at twelve random positions on both the source and receiving subsystems using a multi-channel analyser (Müller BBM PAK). These accelerometers weigh 8.7g but the effect of mass loading from the accelerometer on the OSB is estimated to change the measured vibration levels by less than 1.0dB up to 5kHz [8].

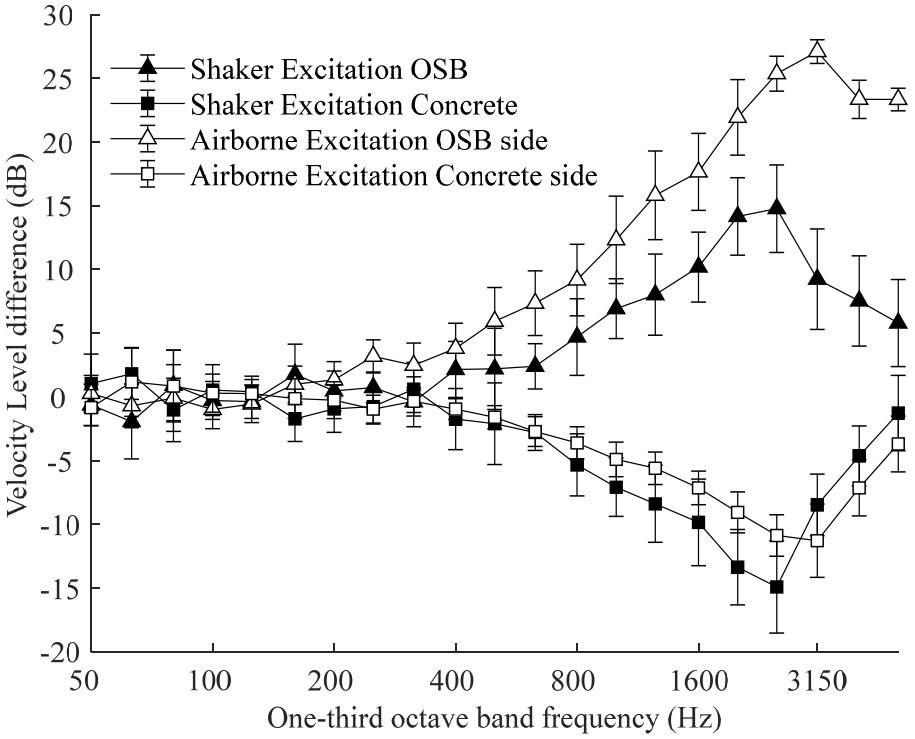

Figure 3-14 Velocity level difference between the concrete and the OSB with excitation on either the OSB or the concrete (95% confidence limits are indicated).

Velocity level differences between the excited side and the other side of the concrete-OSB plate are shown in Figure 3-14. Between 50Hz and 630Hz the velocity level difference between the OSB and the concrete is <6.0dB. Above 630Hz the differences rapidly increase which indicates that the OSB and concrete do not behave as a single subsystem supporting bending wave vibration.

The above findings indicate that SEA model 1 is appropriate up to 630Hz, but errors might occur at higher frequencies due to the assumption that the concrete-OSB acts as a single plate. However, there are two reasons why the vibration could be primarily transmitted from the concrete to the joists, rather than from the OSB to the joists. Firstly, the concrete, OSB and timber joists are all connected by shear connectors. Secondly, for the connection between the concrete and OSB, approximately one-third of the top of each joist is in contact with the concrete and two-thirds is in contact with the OSB (see Figure 3-4). For these reasons, any errors in the predicted transmission due to the velocity level difference between the concrete and OSB are expected to be negligible and this is confirmed by the results presented in Section 3.8.

3.7.2 SEA model (i) and model 1: Concrete-OSB plate with equivalent thickness, density and Young's modulus

The combination of concrete and OSB can be modelled to give an equivalent density, ρ_{eq}, equivalent Young's modulus, E_{eq}, and equivalent thickness, h_{eq}, following the approach of Kimura and Inoue [56]. Considering the second moment of area for the concrete and OSB (I_1 and I_2 respectively) and combined cross-sections (I_{total}) in Eqn. (2-121) gives these values as:

$$\rho_{eq} = \frac{\rho_1 h_1}{h_1 + h_2} + \frac{\rho_2 h_2}{h_1 + h_2} \tag{3-15}$$

$$E_{eq} = (E_1 I_1 + E_2 I_2)/I_{total} \tag{3-16}$$

$$h_{eq} = h_1 + h_2 \left(\frac{\rho_2}{\rho_1}\right) \tag{3-17}$$

where ρ is the density, h is the thickness, E is the Young's modulus, subscript 1 indicates the concrete and subscript 2 indicates the OSB. These equivalent values are used to calculate the driving-point mobility of the plate, Y_{dp}. Eqn. (2-99) is used (see section 3.5.3) to determine mechanical coupling across the point connections for model 1. (In models (i), 1 and 2 they are also used to calculate the coupling loss factors for sound radiation from the plate to the room.)

3.7.3 SEA model 2a: Combination of concrete, OSB and timber joists with equivalent thickness, density and Young's modulus

Following the approach of Kimura and Inoue [56] it is possible to model the combination of concrete, OSB and timber joists to give an equivalent density, equivalent Young's modulus and equivalent thickness. The limitations of this approach are that it only considers the stiffness in the direction parallel to the beams; hence caution must be exercised when using equivalent values to calculate parameters other than the point impedance because the calculated equivalent parameters may differ significantly from the actual values.

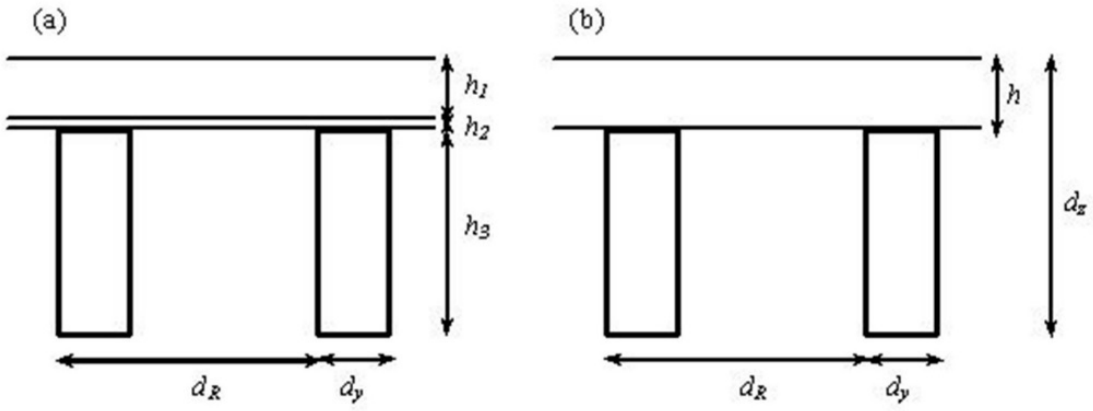

Figure 3-15 Cross-section of the concrete-OSB and timber joists showing dimensions for calculation of (a) equivalent thickness, density, Young's modulus and (b) equivalent bending stiffness.

For the cross-section of the floor shown on Figure 3-15(a), the equivalent density, equivalent Young's modulus and equivalent thickness for the combination of concrete, OSB and timber joists are given by

$$\rho_{\mathrm{eq}} = \frac{\rho_1 S_1}{S_1 + S_2 + S_3} + \frac{\rho_2 S_2}{S_1 + S_2 + S_3} + \frac{\rho_3 S_3}{S_1 + S_3 + S_3} \tag{3-18}$$

$$E_{\mathrm{eq}} = (E_1 I_1 + E_2 I_2 + E_3 I_3)/I_{\mathrm{total}} \tag{3-19}$$

$$h_{\mathrm{eq}} = \sqrt[3]{12 I_{\mathrm{total}}} \tag{3-20}$$

where S is the cross-sectional area of the materials, I_{total} is the second moment of area, subscript 1 indicates the concrete, subscript 2 indicates the OSB and subscript 3 indicates the timber joists. As in section 3.7.2, these values can be used to determine the driving-point mobility using Eqn. (2-99). A drawback of this approach is that if the equivalent values are very different to the concrete plate values, then they may not be appropriate to calculate the coupling loss factors for sound radiation from the plate to the room.

3.7.4 SEA models, (ii)b, (ii)c, 2b and 2c: Equivalent isotropic plate and orthotropic plate

For the timber-concrete composite floor, the bending wavelength, λ_B, on the concrete-OSB plate is equal to the beam spacing, d_R, in the 3.15kHz one-third octave band. Hence $d_R<\lambda_B$ over most the building acoustics frequency range (50Hz to 5kHz) therefore it is reasonable to consider a model for an equivalent orthotropic plate based on the bending stiffness in the directions parallel and perpendicular to the beams.

When the beam spacing is smaller than the bending wavelength ($d_R<\lambda_B$), the approach from Huffington [19] (see section 2.2.10) can be used to calculate an upper bound for the bending stiffness, D_x, in the x-direction perpendicular to the beams. For the timber-concrete composite floor the cross-section is a simple T-section; hence the integral (2-125) can be separated into parts where $E_a(x)$ and $I_a(x)$ are constant to estimate the upper bound for D_x by considering the concrete (subscript 1) forming the plate and the timber joists (subscript 2) where

$$\frac{D_x}{d_R} = \left[\int_{-d_R/2}^{-d_y/2} \frac{1}{E_1 I_A}\mathrm{d}x + \int_{-d_y/2}^{d_y/2} \frac{1}{E_1 I_C - E_2 I_D + E_2 I_E}\mathrm{d}x + \int_{d_y/2}^{d_R/2} \frac{1}{E_1 I_B}\mathrm{d}x\right]^{-1} \quad (3\text{-}21)$$

where $I_A = I_B = I_C = I_D = \frac{h^3}{12}$ and $I_E = \frac{d_z^3}{12}$, h is the thickness of the concrete and OSB plate (see Figure 3-15(b)) and d_z is the full depth of the floor as indicated in Figure 3-15(b).

For the timber-concrete composite floor it is possible to consider only the concrete and the timber joists because the OSB has negligible influence on the resulting bending stiffness. Hence D_x can be calculated from

$$D_x = \frac{d_{\mathrm{R}} h^3}{12}\left[\frac{E_1\left(E_1 h^3 + E_2(d_z^3 - h^3)\right)}{\left(d_{\mathrm{R}} - d_y\right)E_2(d_z^3 - h^3) + d_{\mathrm{R}} E_1 h^3}\right] \tag{3-22}$$

where subscript 1 indicates the concrete and subscript 2 the beams. The geometry for the calculations is shown in Figure 3-15(b).

The estimate of the upper bound of the bending stiffness in the *y*-direction parallel to the beams is calculated from Troitsky [20] using equations (2-127) and (2-128) (see section 2.2.10). In this case E(z) can be expressed with respect to the central plane of the plate as

$$E(z) = E_1 \text{ where } -\frac{h}{2} < z < \frac{h}{2} \tag{3-23}$$

$$E(z) = E_2 \text{ where } \frac{h}{2} \leq z \leq \left(d_z - \frac{h}{2}\right) \tag{3-24}$$

For the concrete plate (subscript 1) with timber joists (subscript 2), D_y is given by

$$D_y = \frac{E_1 h}{(1-\nu^2)}\left[\frac{h^3}{12} + z_y^2\right] + d_y \frac{E_2}{d_{\mathrm{R}}}(d_z - h)\left[\frac{(d_z - h)^2}{12} + \left(\frac{d_z}{2} - z_y\right)^2\right] \tag{3-25}$$

where

$$z_y = \frac{E_2(d_z^2 - d_z h)d_y}{2\left(E_1 h d_{\mathrm{R}}/(1-\nu^2) + E_2(d_z - h)d_y\right)} \tag{3-26}$$

An effective bending stiffness can be calculated from D_x and D_y which allows the orthotropic plate to be modelled as an equivalent isotropic plate using

$$D_{\mathrm{eff}} = \sqrt{D_x D_y} \tag{3-27}$$

Eqn. (3-27) can be used to estimate the driving-point mobility of the plate by replacing D with D_{eff} in Eqn. (2-99) to determine mechanical coupling across the

point connections for models 2b and 2c. In model (ii)b this value of D_{eff} is also used to calculate the coupling loss factors for sound radiation from the plate to the room. Finally, in models (ii)c and 2c they are used to determine the radiation efficiencies between the critical frequencies using Eqn. (2-109) (and hence coupling loss factors for sound radiation from the plate to the room).

3.7.5 Comparison of calculated subsystem properties

Table 3-3 gives the properties for (1) the concrete plate, (2) the combination of concrete and OSB and (3) the combination of concrete and timber joists.

Method	Bending stiffness (Nm)	Equivalent thickness (m)	Equivalent density (kg/m^3)	Equivalent Young's modulus (N/m^2)	Difference in bending stiffness[1] (%)
Concrete plate	8.57x10^5	-	-	-	0
Concrete-OSB plate (Kimura and Inoue)	7.03x10^5	0.0732	1964	2.06x10^{10}	-18
Concrete-OSB-timber joist T-section (Kimura and Inoue)	1.03x10^7	0.1845	1407	1.88x10^{10}	1097
Orthotropic plate parallel to beams (Troitsky)	1.51x10^7	-	-	-	1665
Orthotropic plate perpendicular to beams (Huffington)	1.00x10^6	-	-	-	17
D_{eff} for an equivalent isotropic plate	3.89x10^6				354

Table 3-3 Calculated bending stiffness, thickness, density, Young's modulus.
([1]Relative to the value for the concrete plate)

The difference between the bending stiffness for the combined concrete-OSB plate and the concrete by itself is 18%. However, the percentage difference is significantly larger for the combination of concrete, OSB and timber joist T-section (Kimura and Inoue), the orthotropic plate parallel to the beams (Troitsky) and the equivalent isotropic plate (Huffington and Troitsky). The bending stiffness calculated using Troitsky may also be regarded as an upper limit because it considers the full depth of the beams.

The orthotropic plate calculations according to Huffington and Troitsky result in bending stiffness for directions parallel and perpendicular to the beams that differ by more than a factor of ten; this gives rise to two critical frequencies of 63Hz and 232Hz. The bending stiffness parallel to the beams differs from the concrete by 1662% when calculated according to Troitsky, and 1102% for the combination of concrete, OSB and timber joist T-section when calculated according to Kimura and Inoue. The equivalent and effective bending stiffness can be used to calculate the mobility of the combination of concrete, OSB and timber joists using Eqn. (2-99) and thus the coupling loss factor across the resilient hangers to the plasterboard according to Eqn. (3-7). For SEA models 2a and 2b these coupling loss factors are shown on Figure 3-16. Using the Kimura and Inoue model results in a coupling loss factor that is ≈2.3dB lower than the Huffington and Troitsky model.

The fundamental mode of the concrete-OSB plate is estimated as being below 50Hz using both the Huffington and Troitsky and Kimura and Inoue models. For this reason, the SEA model can be used to predict the performance over the building acoustics frequency range from 50Hz to 5kHz.

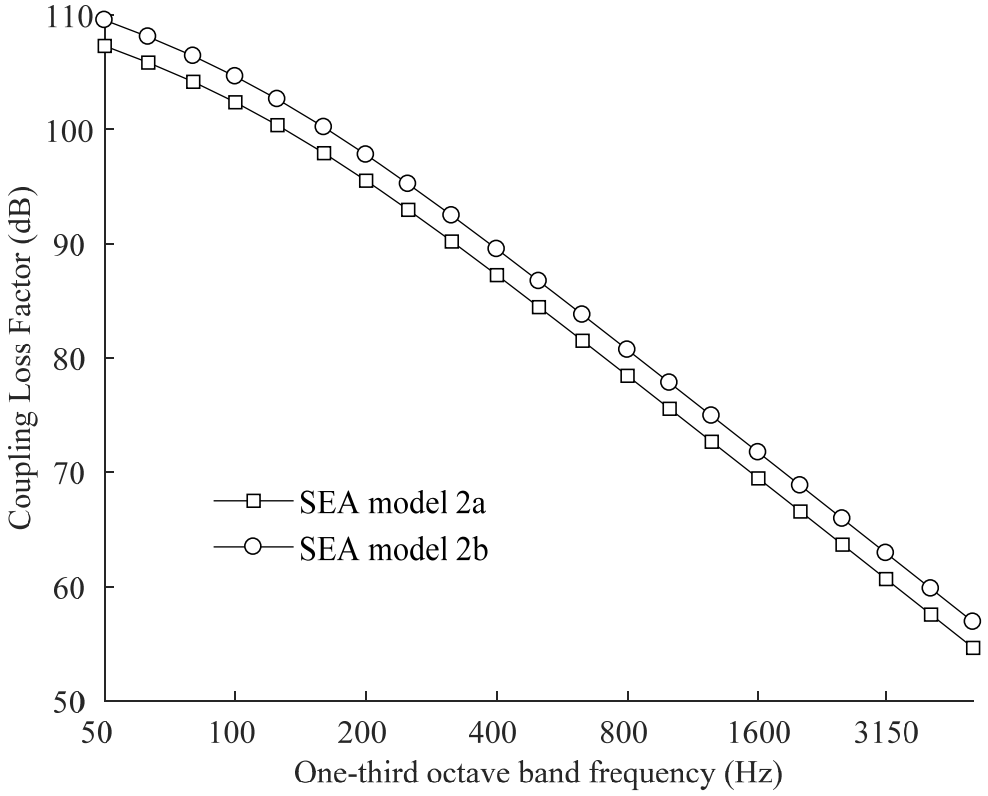

Figure 3-16 SEA model 2. Calculated coupling loss factors from the plate subsystem for model 2a and 2b representing the combination of concrete, OSB and timber joists to the plasterboard subsystem.

3.8 Results

3.8.1 Total loss factor for the cavity

The measured cavity reverberation times are shown in Figure 3-17 for one cavity inside the floor that was installed into the transmission facility. The first cross-cavity mode occurs in the 630Hz one-third octave band, and above this frequency band the average reverberation time is shorter than the average reverberation time of the frequency bands below 630Hz.

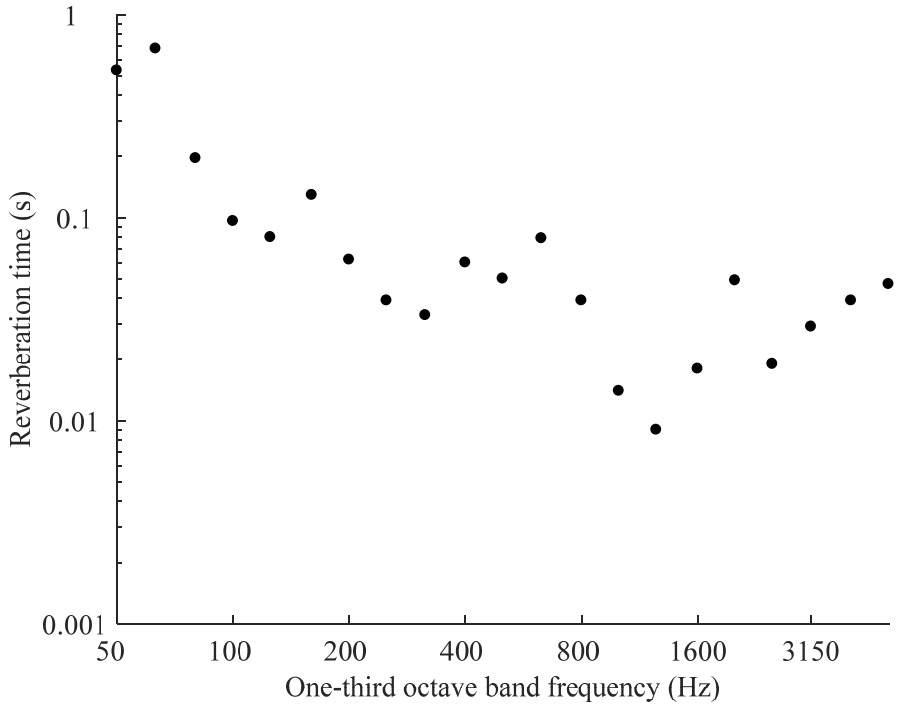

Figure 3-17 Measured reverberation times in one floor cavity.

3.8.2 Coupling loss factor between a timber joist and the plasterboard ceiling across the resilient hangers

In SEA model 1, the timber joists are modelled as a single subsystem; hence it is beneficial to validate the predicted coupling across the resilient hangers from the timber joists to the plasterboard. This coupling loss factor is calculated from the measured dynamic stiffness of the resilient hanger as described in sections 3.5.3, and measured as described in section 3.6.3

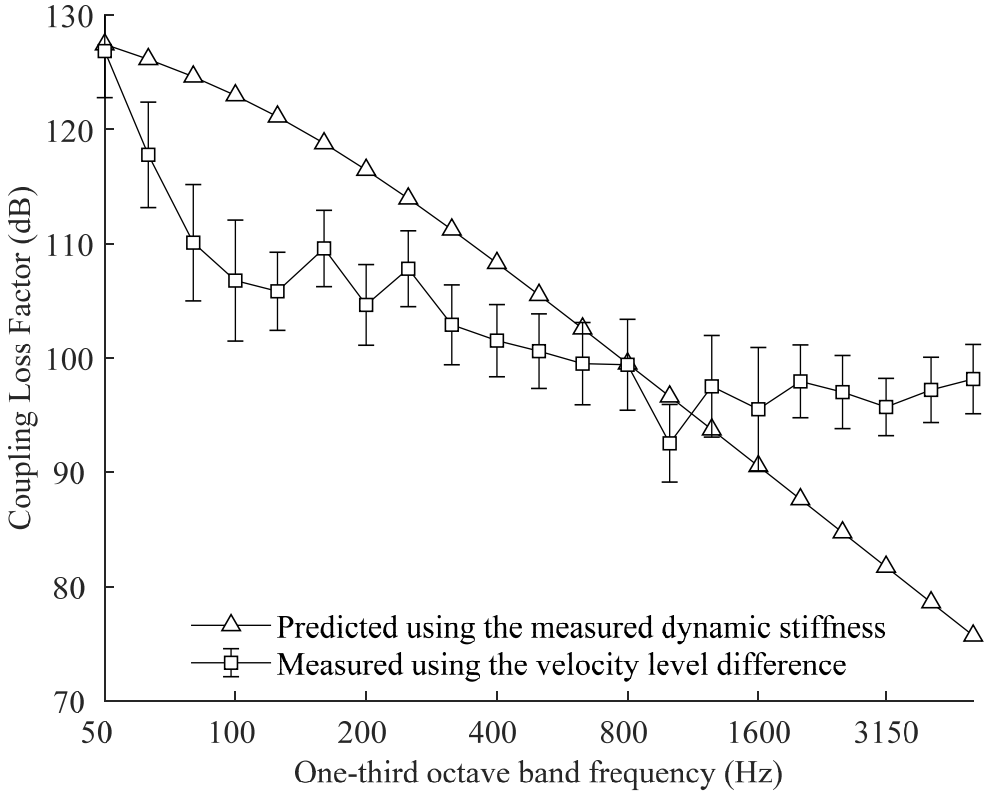

Figure 3-18 Coupling loss factors from a timber joist (beam) to the plasterboard ceiling (plate): (a) predicted using the measured dynamic stiffness for the resilient hanger as described in section 3.5.3 using Eqn. (3-7) and (b) measured using the velocity level difference as described in section 3.6.3 (95% confidence limits are indicated).

Figure 3-18 shows that below 160Hz the measured coupling loss factor is significantly lower than predicted (which might be attributed to strong coupling from the first two beam modes) but that there is reasonable agreement between 160Hz and 1kHz. Above 1kHz the measured coupling loss factor tends to plateau and this feature is not evident in the predicted coupling loss factor. This is likely to be due to the difficulty in accurately measuring the structural reverberation time in the region of the critical frequency of the plasterboard [8]. Due to the agreement in the mid-frequency range it is therefore considered appropriate to use the coupling loss factor calculated from the measured dynamic stiffness of the resilient hanger across the entire frequency range for all SEA models.

3.8.3 Comparison of SEA models with measurements

3.8.3.1 Basic floor (without suspended ceiling): Three subsystems

SEA models (i), (ii)b, and (ii)c, are compared against measured data and Heckl's [52] orthotropic infinite plate model (based on the equations described in section 2.2.7) in Figure 3-19.

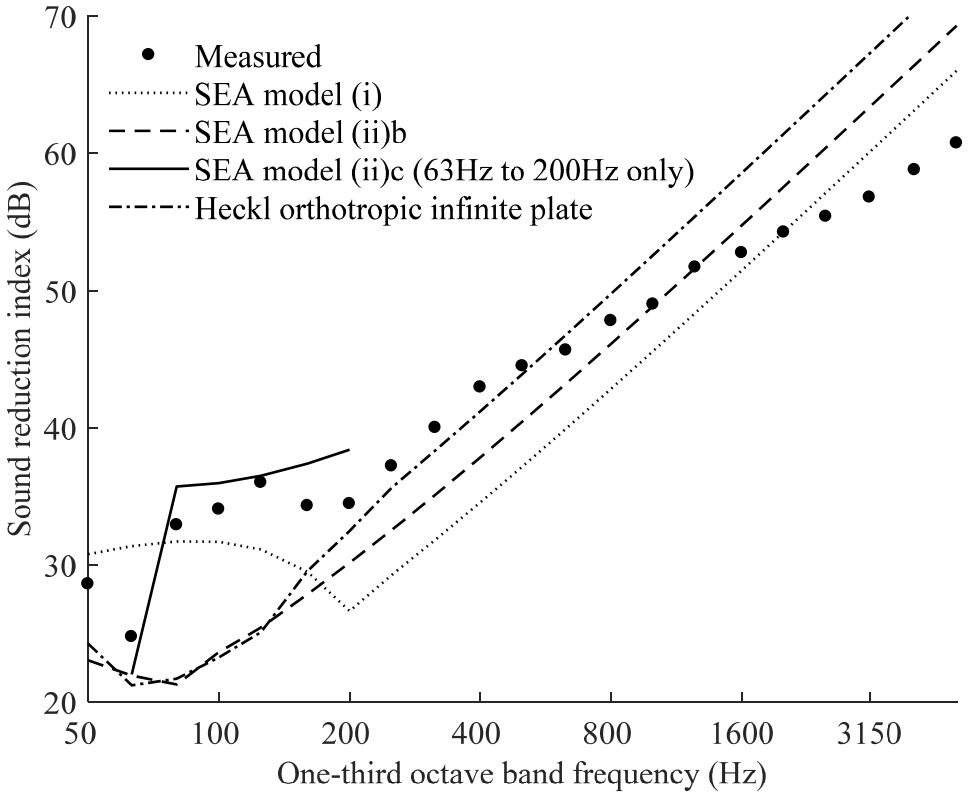

Figure 3-19 Comparison of the measured and predicted SRI (without suspended ceiling) from the different three subsystem SEA models; concrete plate, effective bending stiffness and orthotropic plate model

Above the critical frequencies all three models show a steeper trend with frequency than the measurements. It is difficult to explain the trend with any certainty however, one possible interpretation of this data could be that below 800Hz the floor is behaving as an orthotropic rib-stiffened plate, then there is a transition phase 800Hz to 1250Hz above which the ribs and plate act independently and a thin plate model may be more appropriate. However above 2500Hz the measured data also falls

below model (i) data; this may be due to radiation from the beams or because the concrete floor is transitioning to a thick plate model.

For SEA models (i) (100Hz to 500Hz), (ii)b (100Hz to 500Hz), (ii)c (Heckl, radiation factor $f_1<f<f_2$) (100 to 200Hz) and Heckl's orthotropic infinite plate model the average difference in terms of magnitudes between measurements and predictions from the one-third octave band data were 6.5dB, 6.3dB, 2.4dB and 4.3dB respectively, and the average difference considering positive and negative values were -6.5dB, -6.3dB, 2.4dB and -4.3dB. The differences below 250Hz between SEA model (i), compared with SEA models (ii)b, (ii)c and the orthotropic infinite plate are due to the different critical frequencies. Only model (ii)c (Heckl, radiation factor $f_1<f<f_2$) captures the two critical frequency dips (63Hz and 250Hz) appropriately and shows the closest agreement within its limited frequency range. Although the weaknesses of this model are: It uses a measured radiation efficiency at 63Hz, because there are currently no recommendations of how to calculate radiation efficiency (or SRI) of an orthotropic plate at its lowest critical frequency. Using a prediction model such as Leppington *et al.* [98] which can model an orthotropic plate below, between and above the critical frequencies instead of separating the frequency ranges could be an improvement on this model.

3.8.3.2 Floor and suspended ceiling construction: Five and six subsystems

The suspended ceiling was added to the basic floor. SEA models 1, 2a, 2b and 2c are compared against measured data in Figure 3-20. Note that the matrix inversion for SEA did not yield values for the 50Hz and 63Hz one-third octave bands. All four SEA models show the same general trend with frequency as the measurements. For SEA models 1 (100Hz to 500Hz), 2a (100Hz to 500Hz), 2b (100Hz to 500Hz) and 2c (100Hz to 250Hz), the average differences in terms of magnitudes between measurements and predictions from the one-third octave band data are 3.0dB, 2.3dB, 2.8dB and 3.1dB respectively, and the average differences considering positive and negative values are 2.1dB, 1.5dB, 0.4dB and -3.1dB. These differences in terms of magnitude indicate that the average error is similar to those using SEA to predict airborne transmission with heavyweight building elements [8]. The differences in terms of positive and negative values are sufficiently close to 0.0dB that it is

reasonable to expect that when the single-number quantities are calculated there is close agreement between measurements and SEA.

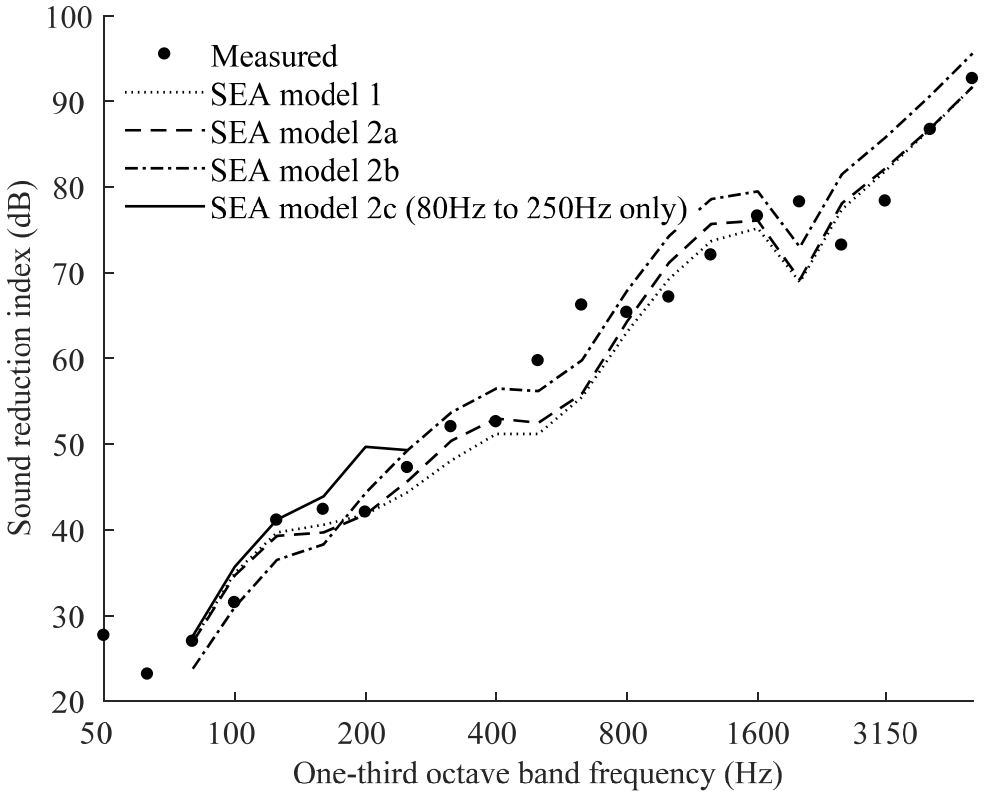

Figure 3-20 Comparison of the measured and predicted SRI (with suspended ceiling) from the different SEA models.

The differences between models 1, 2a, 2b, and 2c at frequencies below 250Hz are due to the different critical frequencies (and hence radiation efficiencies) of subsystem 2. The models therefore have different plate to room resonant coupling loss factors, and subsystem 2 also has a lower modal density in models 2b and 2c. At and above 250Hz the differences between the models are due to the lower modal density of subsystem 2 in model 2b.

For lightweight cavity walls, Hongisto [61] compared seventeen different prediction models described in the literature. The average prediction errors for individual frequencies were as high as 20.0dB for most of the models, and less than 10.0dB for the best models. One of the main criticisms of these models is that they have limited application to actual building elements. Hence not only are the predictions for the

timber-concrete composite floor with SEA significantly more accurate, but they also demonstrate that real floors (which are relatively complex constructions) can be modelled using SEA by incorporating some measured loss factors in the model.

The single-number quantities in terms of $R_w(C;C_{tr})$ are rated using ISO 717-1 [99] over the frequency range from 100Hz to 3.15kHz. $R_w(C;C_{tr})$ is 58(-2;-9) dB for the laboratory measurement, and 56(-1;-6) dB, 57(-2;-7) dB and 58(-3;-10) dB for SEA models 1, 2a and 2b respectively; hence the maximum error of the SEA models in predicting R_w is 2dB. The adverse deviations that occur in the calculation of the single-number quantity are between 100Hz and 400Hz for the measurement, between 100Hz and 630Hz for SEA models 1 and 2a, and between 100Hz and 500Hz for model 2b. Hence for single-number quantities it is more important for the SEA model to provide accurate predictions at and below 630Hz rather than in the high-frequency range.

The trends predicted by SEA models 1, 2a and 2b agree with measurements over the entire frequency range from 100Hz to 3.15kHz, and SEA model 2c agrees between 80Hz and 250Hz. Model 2b predicts the closest single figure values due to close agreement over the low-frequency range (100-500Hz). For SEA model 2c the Huffington and Troitsky model for the combination of concrete, OSB, and timber joists indicates that the plate is highly orthotropic with two critical frequencies of 63Hz and 232Hz; in fact, the measurements do indicate slight dips in the SRI in the 63Hz and 200Hz bands which are near these two critical frequencies. In practice, SEA model 2c provides a reasonable estimate of the upper bound to the SRI when compared with the measured data because it uses an upper bound to determine the bending stiffness.

When considering the application of the orthotropic plate models to other similar framed or ribbed plate constructions there are some limitations to be considered. SEA model 2a does not take account of the bending stiffness perpendicular to the joists and a potential disadvantage of using effective thickness, density and Young's modulus is that unusual shapes and deep beams could result in effective values that cannot be used to determine an appropriate radiation efficiency. For this reason, model 2b is preferred because the approach of Huffington and Troitsky is well-suited

to multi-layer plates with complex geometric cross-sections. To apply model 2c to other floors, the applicable frequency range might need to be extended. This could be achieved above and below the two critical frequencies by applying a more generally applicable model such as proposed by Leppington *et al.* [98]. Additional theory could be developed to improve the prediction of non-resonant transmission between the critical frequencies; for the double wall Eqn. (3-5) was used.

For simple SEA models with only a few dominant transmission paths where the combination of all the other paths is negligible, the sum of the dominant transmission paths from the source room (subsystem 1) to the receiving room (subsystem 5) is approximately equal to the matrix solution to within 0.1dB [32]. This situation does not occur with SEA model 1 because of the strong coupling between the concrete and the timber beam subsystems. However, this does occur for SEA models 2a, 2b and 2c. Hence for SEA model 2b, Figure 3-21(a) allows comparison of the relative strengths of different transmission paths from SEA path analysis. The crossover between the 1D and 3D non-resonant models for transmission into and out of the cavity occurs at 500Hz and therefore two predicted data points occur in this one-third octave band. Figure 3-21(b) shows the corresponding matrix SEA results for model 2b.

From 50Hz to 100Hz the dominant transmission path is 1→3→5. Unfortunately, the matrix solution is invalid for the 50Hz and 63Hz one-third octave bands; hence no values are shown in these bands although path 1→3→5 gives an indication of the overall SRI. From 125Hz to 400Hz the strongest paths are 1→2→3(1D)→5 and 1→2→4→5. From 500Hz to 1.6kHz the main paths are 1→2→3(2D/3D)→5 and 1→2→4→5. At and above 2kHz the strongest paths are 1→2→3(2D/3D)→4→5 and 1→2 →4→5.

Based on SEA model 2b, identification of the dominant paths indicates how the airborne transmission could be increased. Below 100Hz this would require increasing the mass of the concrete-OSB and/or the plasterboard to reduce non-resonant transmission from the rooms to the cavities along path 1→3→5. Above 100Hz, an extra layer of plasterboard on the ceiling and completely filling the cavity

with porous material would reduce the strength of paths 1→2→3→5, 1→2→4→5 and 1→2→3→4→5.

The predicted dip in the SRI near the 2kHz one-third octave band due to the critical frequency of the plasterboard is not evident in the measured data although there is a shallow dip in the 2.5kHz band. However, it is common for measured and predicted transmission to differ near the critical frequency, partly due to uncertainty in the range of angles of incidence that exist near grazing and partly because of the empirical approach used to limit all the radiation efficiency values to a value of one [8]. The dotted line on Figure 3-21(b) indicates the upper range for the calculated radiation efficiency of the plasterboard and whilst this overestimates the sound radiation at the critical frequency it provides slightly closer agreement with measured data above the critical frequency.

In addition to the simple paths for the six-subsystem model there are more complicated paths where there is a backwards flow of power likely due to the strong coupling between the concrete floor slab and timber beams. These paths revisit the subsystems and when summed make a significant contribution to the total sum of paths. The solution proposed to account for this is to take an infinite sum of all the backward flowing paths. These paths are shown in Eqns. (3-28) to (3-30):

$$\frac{E_1}{E_5} = \sum_{n=1}^{\infty} \frac{\eta_2 \eta_6 (\eta_2 \eta_6)^n \eta_4 \eta_5}{\eta_{12} \eta_{26} (\eta_{62} \eta_{26})^n \eta_{64} \eta_{45}} \tag{3-28}$$

$$\frac{E_1}{E_5} = \sum_{n=1}^{\infty} \frac{\eta_2 (\eta_6 \eta_2)^n \eta_3 \eta_4 \eta_5}{\eta_{12} (\eta_{26} \eta_{62})^n \eta_{23} \eta_{34} \eta_{45}} \tag{3-29}$$

$$\frac{E_1}{E_5} = \sum_{n=1}^{\infty} \sum_{m=1}^{\infty} \frac{\eta_2 (\eta_6 \eta_2)^n \eta_3 (\eta_5 \eta_3)^m \eta_5}{\eta_{12} (\eta_{26} \eta_{62})^n \eta_{23} (\eta_{35} \eta_{53})^m \eta_{35}} \tag{3-30}$$

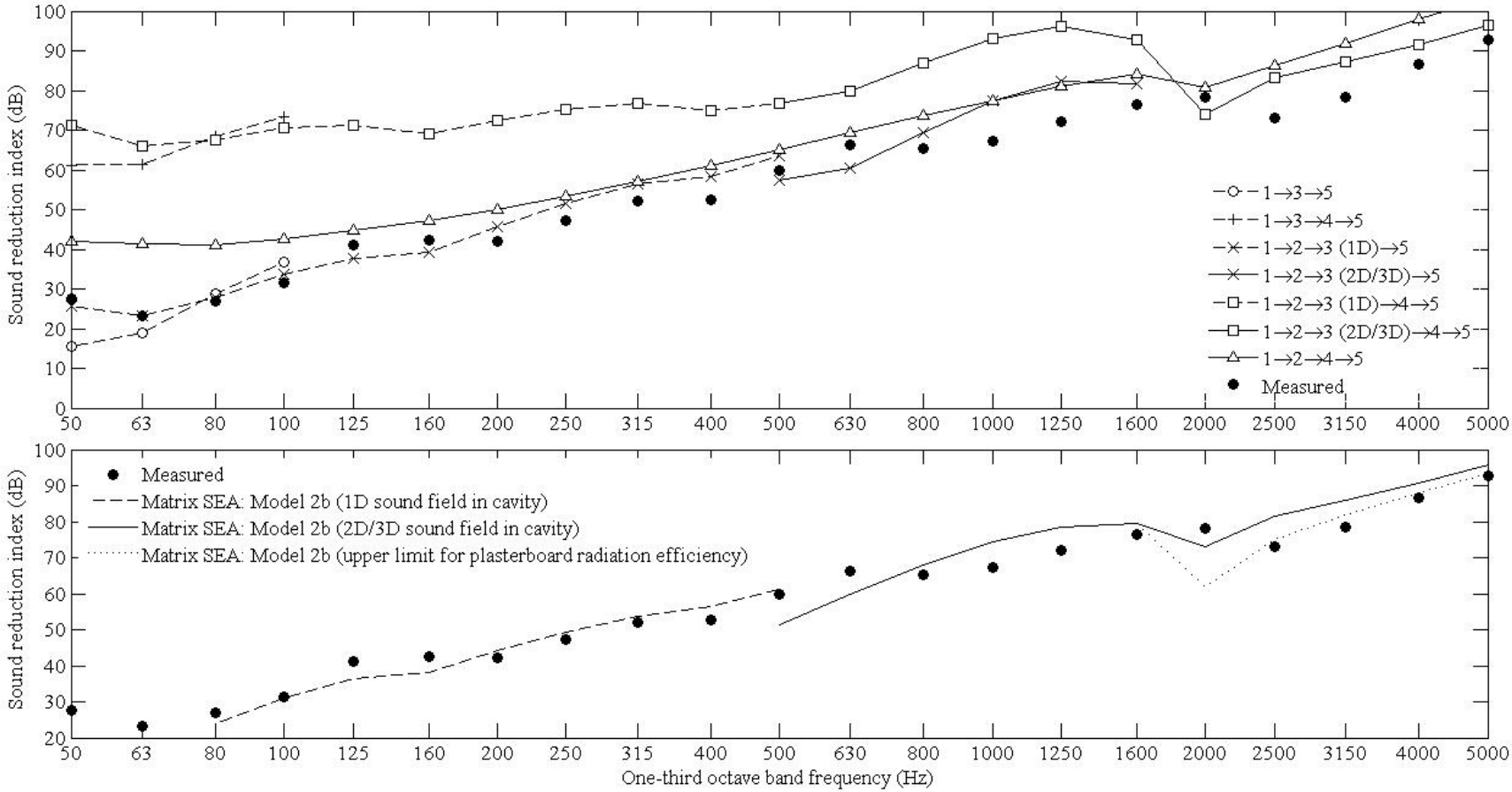

Figure 3-21 SEA model 2b. Upper graph: comparison of the different path strengths with measured data, all the primary paths are indicated in the legend to the right. Lower graph: Comparison of measurement with matrix SEA. The dotted line(s) indicates the SEA prediction at and above the critical frequency of the plasterboard by using the upper limit for the calculated radiation efficiency.

These paths were summed numerically to within 0.1dB or less contribution to the sum of all paths. The sum of all paths shown in Figure 3-21(b) is within 0.5 dB of the matrix solution at high frequencies (250Hz and above) and within 1.4 dB at low frequencies (below 250Hz) this indicates that there are additionally more complicated paths which contribute to the total sum of paths at low frequencies, not presented in the results shown.

However in parallel with the five subsystem model the most significant paths through this floor are up to and including 160 Hz the non-resonant path 1→3→5, between 200 Hz and 1.6 kHz the sum of the resonant paths 1→2→6→ [6→2] →4→5 indicated by Eqn. (3-28) and the sum of the partially resonant (across the concrete/OSB) and partially non-resonant (across the plasterboard) paths 1→2→ [6→2] →3→5 indicated by Eqn. (3-29), and finally above 2 kHz the resonant paths 1→2→6→ [6→2] →4→5 indicated by Eqn. (3-29) and 1→2→[6→2] →3→4→5 indicated by Eqn. (3-30).

3.9 Conclusions

SEA models have been developed to predict airborne transmission across a timber-concrete composite floor with a suspended ceiling. The large number of nails and shear connectors connecting the concrete, OSB and timber joists in this floor required consideration of two different types of SEA model. A six-subsystem model which treated the concrete-OSB plate as a single subsystem with point connections to the joist and three different five-subsystem models which treated the combination of concrete, OSB and timber joists as a single subsystem. All the models were experimentally validated against laboratory measurements and could predict the weighted SRI to within 2.0dB. For the comparison of measurements and predictions in one-third octave bands, the average difference (magnitude) was up to 4.3dB. These results add to a growing body of evidence [8, 26, 60] indicating that SEA can be used to model airborne transmission across realistic cavity wall/floor constructions found in buildings with greater accuracy than many analytical models. However, this requires the inclusion of some measured parameters in the SEA model and the theory for non-resonant transmission between widely spaced critical frequencies of an orthotropic plate requires further validation. For the timber-

concrete composite floor, measured data was needed for the dynamic stiffness of the resilient isolators and the reverberation time in the cavity. Compared to some analytical or deterministic models, path analysis with SEA provides straightforward insights into the dominant transmission mechanisms and this simplifies the process of identifying design changes to improve the airborne transmission.

To model similar ribbed plates with SEA when it is ambiguous whether the upper plate and the ribs should be modelled as separate subsystems or as a single orthotropic plate subsystem, it is recommended that both models are created and compared with measurements. For the orthotropic plate model, it is suggested that bending stiffness predicted using the theories of Huffington and Troitsky provide a more suitable and flexible approach than that of Kimura and Inoue. This is primarily because (1) the latter does not take account of the bending stiffness perpendicular to the joists, (2) it is not suited to modelling the stiffening effect of the beams when predicting sound radiation and (3) the approach of Huffington and Troitsky is better suited to multi-layer plates with complex geometric cross-sections. Further work could investigate the application of these models to impact insulation.

4 Prediction of airborne sound transmission across a cross laminated timber plate

4.1 Introduction

This chapter concerns the prediction of the airborne sound transmission of cross laminated timber (CLT) panels. Previous work by Krajči *et al.* [1] indicated problems in predicting the direct airborne sound insulation of CLT panels over the mid- and high-frequency range. Previous work on prediction models identified material parameters such as elastic moduli and loss factors to obtain a best fit with measured sound transmission data [18], [21]. Augustsson [18] rules out the use of static or dynamic laminate calculations and adjusts the solid wood constants (adjusted loss factors are also required) whereas Wareing *et al.* [21] use a frequency-dependant elastic modulus. However, evidence that these adjusted properties match the material properties of the panel or indeed are within an allowable parametric range is lacking. This can lead to difficulties as selecting particularly stiff elastic moduli or low loss factors, for example, affects the principal modes or modal overlap factors of the panel [18]. Such models also have limited applicability to more complicated panel designs which include CLT layers [18].

To predict direct and flanking transmission with CLT, models incorporating measured material properties are a potential solution. Work by Van Damme *et al.* [100] and Santoni *et al.* [101] represents a move in this direction. This chapter investigates methods to determine the elastic moduli of CLT plates as input data for prediction models of airborne transmission. There are a variety of static and dynamic measurement methods available to determine the elastic moduli of these plates, such as (1) static measurement using a four point bending stiffness method [102], (2) time

of flight measurements of the longitudinal wavespeed and calculation of the moduli [1], (3) determination of elastic moduli from measured eigenfrequencies using an optimisation process [27, 102, 103, 104] (this method can also be carried out on strip samples as described in [100]), and (4) in situ measurements of the bending wavespeed [105].

Steiger *et al.* [102] carried out static measurements on CLT alongside dynamic tests on small panels. This study concluded that determining the stiffness of whole panels is preferable to strip samples (e.g. for four-point bending stiffness tests) because the bending stiffness varies within a single panel. (Methods (2), (3) and (4) described above can be performed on a complete CLT panel.) For panels with large lamellae, local non-homogeneities, and defects, stiffness can depend on the grading method of the raw material. Therefore, strip sample testing requires many narrow (e.g. 100mm) or several wider (e.g. 300mm) strips [102] to achieve a representative result. One of the panels measured in this study was nominally identical to the panel described in this thesis and the values determined for G_{xz} and G_{yz} are used in section 4.4.3 to determine the validity of a thin plate model at low frequencies (<100Hz) for this panel. In which case, the eigenfrequencies can be assumed to be independent of the shear constants G_{xz} and G_{yz}.

In this chapter, methods based on (2), (3) and (4) are implemented and compared for the panel described in section 4.2. Section 4.3 describes the measurement of the internal loss factor. Section 4.4 examines the various measurement methodologies to determine the elastic moduli. The laboratory measurement and prediction of airborne sound insulation are described in sections 4.5 and 4.6. Prediction models are used which consider a finite plate isotropic method, an infinite plate orthotropic method and an infinite plate isotropic thick plate method (introduced in sections 2.2.7, 2.2.9.1 and 2.2.9.2 respectively). To improve the methods frequency-dependant Young's moduli based on measured properties of the panel are implemented where possible. An appropriate frequency range for the models is estimated from direct measurement of the bending wavespeed. Results and conclusions are presented in sections 4.7 and 4.8.

4.2 CLT plate description

4.2.1 Assembly and basic properties

CLT is assembled from crosswise layers of lamellae into whole panels. The panel under test consisted of three glued layers of small strips of visually graded Norwegian Spruce of density 438 kgm^{-2} (Figure 4-1 shows a sketch including the laminae) The surface layers were built up from wood strips, 15 mm thick by 27 mm wide with the middle layer from wood strips 50 mm thick by 27 mm wide. Panel dimensions and properties are summarized in Table 4-1.

x (mm)	4180
y (mm)	2890
z (mm)	80
Weight (kg)	455
Density (kgm^{-3})	438

Table 4-1 Panel dimensions, weight and density.

4.2.2 Principle material directions of wood composites

In wood products such as CLT, glulam, and some plywood products, the orientation of the wood fibres is such that principle material directions of the wood are aligned with the edges of the plates and therefore the principle axes of the load distributions. In this work, it is assumed that the orientation of the principle material directions (designated in wood to be longitudinal (L), radial (R), and tangential (T)) are aligned with the principle axis directions (x, y and z), though aligned with different co-ordinates in different layers.

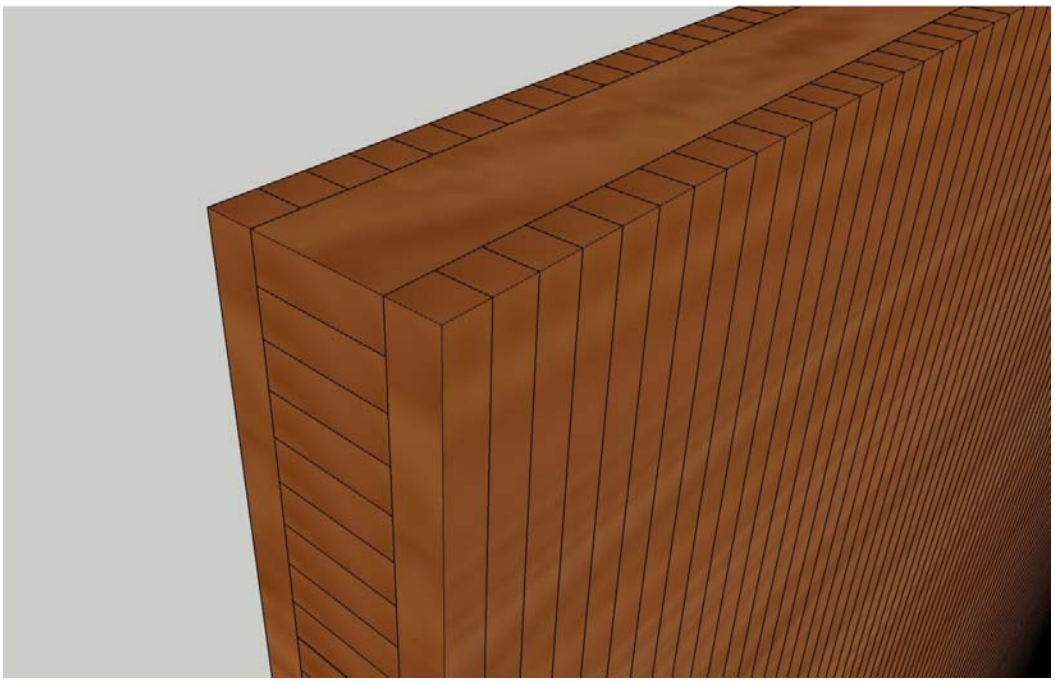

Figure 4-1 Sketch of the CLT panel showing the lamellae.

The similar magnitude of the elastic moduli in the R and T directions means that manufacturers of wood products often simplify this assumption further describing the elastic moduli simply in the longitudinal ($\parallel$) and transverse ($\perp$) directions. Thus, if $E_{\parallel} = E_L$ and that $E_{\perp} = E_R = E_T$. The raw material of the tested panel was of strength class C24 [105] with elastic moduli in the parallel and perpendicular directions of $E_{ll} = 12.0 \times 10^9$ Nm^{-2}, $E_{\perp} = 4.0 \times 10^8$ Nm^{-2} respectively.

4.2.3 Calculation of an effective modulus of elasticity (for thin plates)

The elastic moduli of the wood (according to the timber specification for the panels) provided by the manufacturer are used to calculate elastic moduli of an equivalent single plate according to the Eqn. (2-130) in terms of global co-ordinates *x*- and *y*- which correspond to the horizontal and vertical directions respectively (see Table 4-2). Examining the contributions of each layer in Eqn. (2-130) to the total stiffness of the panel, the *E* modulus in the parallel direction of the wood $E_{\parallel}$ gives the greatest contribution to the overall stiffness of the panel in both the vertical and horizontal directions. These are the outer layers of the panel in the *y*-direction and the middle layer of the panel in the x-direction. The percentage contributions of these layers to the total value of the elastic moduli are presented in Table 4-3.

Layer	Thickness (mm)	E_x (N/m^2)	E_y (N/m^2)
Outer	15	1.2 x10^{10}	4 x10^8
Middle	50	4 x10^8	1.2 x10^{10}
Outer	15	1.2 x10^9	4 x10^8
Equivalent	80	3.23 x10^9	9.17 x10^9

Table 4-2 Material properties provided by the manufacturer and calculated combined properties of the panel.

Elastic modulus	Layer with the greatest contribution to bending stiffness	Percentage contribution to bending stiffness from E‖ (%)
E_x	**Middle**	90.6
E_y	**Outer**	98.9

Table 4-3 Percentage contribution to the bending stiffness of the middle and outer layers of the panel.

4.2.4 Poisson's ratio

For a panel subjected to pure bending, the Poisson's ratios are described by Eqn. (2-131). The rule of thumb is that when the stiffness of one of the layers dominates the Poisson's ratio for that layer also dominates (see section 2.2.10). Dominant layers are shown in Table 4-3. Literature on Poisson's ratio for spruce in tension is extensive; hence mean values are shown in Table 4-4 [106, 107]. However, the literature also indicates that all values of the elastic moduli for timber are dependent on whether the wood is in tension or compression [108]. Elastic moduli in the material directions are also shown.

Elastic modulus in the material directions	**Voichita and Bucur[1]** [109] **(GPa)**	**Bodig and Jayne[2]** [14] **(GPa)**	**Poisson's ratios**	**Kohlhauser** [107]
E_L **(N/mm²)**	15900	10300	ν_{LR}	0.394
E_R **(N/mm²)**	690	690	ν_{RL}	0.036
E_T **(N/mm²)**	390	410	ν_{LT}	0.486
G_{LR} **(N/mm²)**	750	620	ν_{TL}	0.026
G_{LT} **(N/mm²)**	770	620	ν_{TR}	0.350
G_{RT} **(N/mm²)**	36	50	ν_{RT}	0.470

Table 4-4 Elastic moduli in the material directions and Poisson's ratios of spruce, given in the literature. [1]Spruce unspecified, [2]Engleman spruce related species to Norwegian spruce.

Figure 4-2(a) and (b) show the alignment of the lamellae in the CLT with respect to the grain. If there is little or no cross-grained wood the elastic moduli of the wood can be assumed to be aligned with the grain direction. The L direction (aligned with the grain) and R direction (along the growth rings) (Figure 4-2(b)) are assumed to lie in the plane of the plate. Poisson's ratios used for calculation were set to the mean of the values for Spruce in the L and R directions, ν_{LR}=0.486 and ν_{RL}=0.036 (first subscript denotes the passive direction). The material was graded prior to assembly, therefore material constants provided by the manufacturer were used to perform Poisson's ratio calculation in accordance with Eqn. (2-131) with the assumptions that $E_L=E_\parallel$, and $E_R=E_T=E_\perp$. Examining the elastic moduli in Table 4-4 in the material directions $G_{LR}\approx G_{LT}$ and $\nu_{RL}\approx\nu_{TL}$. The approximation $E_R\approx E_T$ is not as close, however, the whole panel constants E_x and E_y are mainly dependant on the Young's modulus in the E_L direction so this is less critical. Correct determination of ν_{xy} is crucial to obtain agreement with the higher modes [110]. Values were found to be ν_{xy}=0.04, and ν_{yx}=0.07. The relation between the orthotropic elastic moduli is given by

$$\frac{\nu_{yx}}{\nu_{xy}} \approx \frac{E_y}{E_x} \tag{4-1}$$

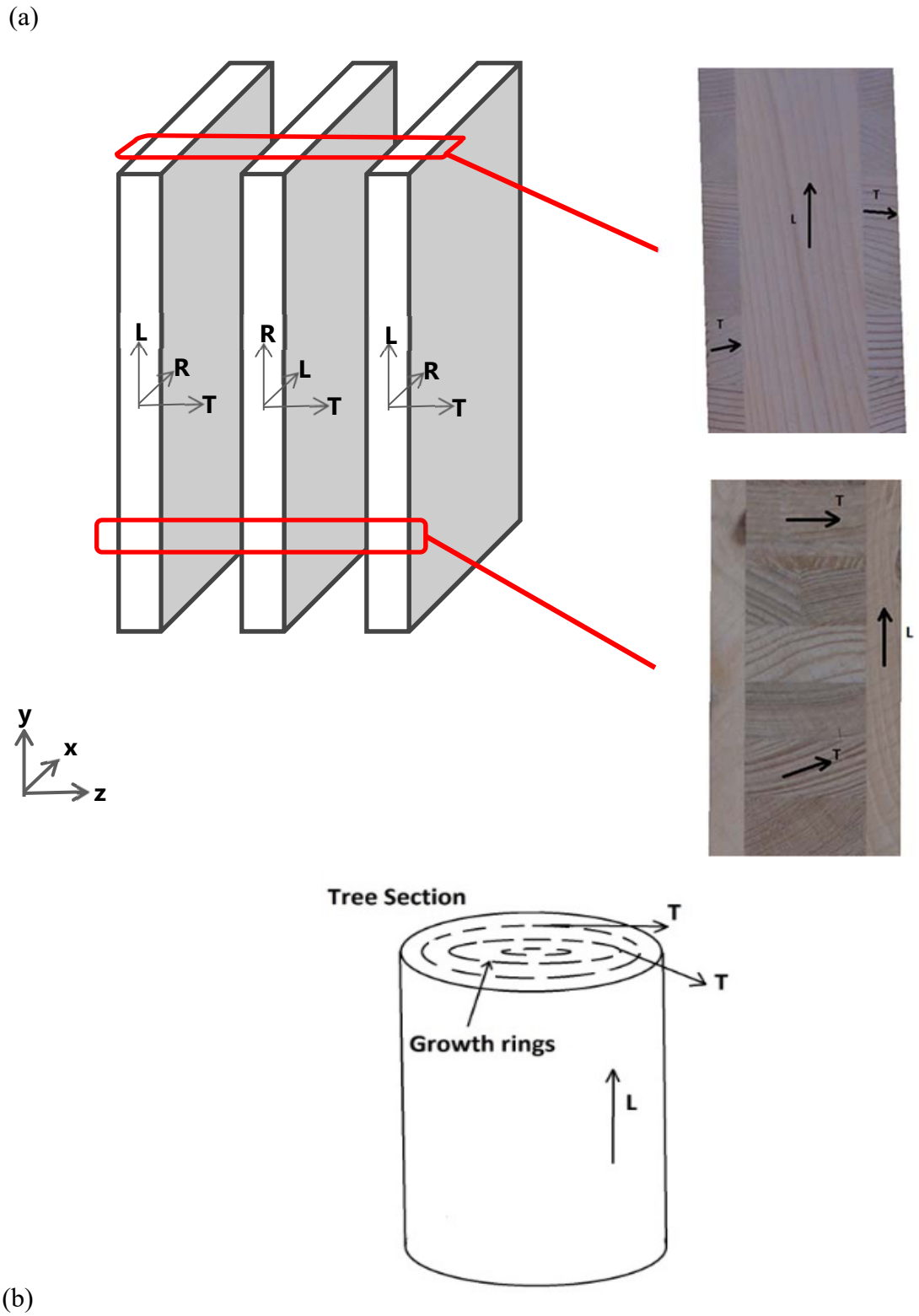

Figure 4-2 (a) Material orientation in the CLT layers; Top and side view of the panel (b) L and T directions in a tree section.

Eqn. (4-1) using the described approximations yields 1.75 and 2.48 for the ratios of Poisson's values and elastic moduli respectively. The poor agreement here is most likely to be due to the assumption that $E_R=E_T=E_\perp=4.0\text{x}10^8$Pa. However, the behaviour of Poisson's ratio is believed to be described with sufficient accuracy for the purposes described in this thesis. (If the actual value for $E_T=6.9\text{x}10^8$ is taken from Table 4-2 the Poisson's ratios are found to be ν_{xy} =0.04, and ν_{yx}=0.09 and the ratio using Eqn. (4-1) gives 2.11 and 2.48 for the ratios of Poisson's ratio and elastic moduli respectively). There is insufficient contribution to the bending stiffness of the overall panel from the fibres in the R and T directions (see Table 4-3) to assess whether assumptions involving the elastic moduli E_R, or E_T are appropriate by means of measurement of a fully assembled panel. The calculated values for ν_{xy} and ν_{yx} are weakly dependant on $E_\perp$. Remaining Poisson's ratios in the other directions are calculated in section 2.2.11 in accordance with the "law of mixtures" (Eqns. (2-137) and (2-138)).

Moarcas [111] outlines a measurement method to determine Poisson's ratio in pure bending for particle board, however Poisson's ratios of CLT are calculated to be very small and this measurement method is not deemed to be sufficiently accurate. The elastic moduli of timber in the static case have also been demonstrated to be dependent on moisture content of the wood and creep [112]. An alternative methodology for Poisson ratio measurement, based on aspect ratios and transition points of a plate material [113] could be considered for future work.

4.3 Loss factor measurement

The internal (or total) loss factor of the CLT plate is required to calculate the airborne transmission at frequencies above the critical frequency. Accurate total loss factor measurements were not made at the time of measuring the sound reduction index of the plate therefore an estimate of internal loss factor was made from the measured structural reverberation times of the plate. The plate was suspended in the laboratory space from a single point using a hole drilled in the top of the plate 20cm from the upper edge. This was attached to the laboratory crane. The suspension of the plate was to minimise coupling losses, although plate to room coupling losses are

unavoidable in this situation, which may increase measured losses. Acceleration decays from an impulse measurement were recorded with a two-channel digital recorder (Sound Devices 702T) and analysed to obtain the structural reverberation time from a T_5 measurement as described in [114]. Two accelerometers (B&K Type 4513-B) were used to record the decay signal. Comparison was made between excitation with a large hammer (4.78kg) and a small hammer (0.58kg). The results of this measurement are presented in section 4.7.1.

4.4 Methods to measure the elastic moduli

4.4.1 Time of flight measurement

The quasi-longitudinal wavespeed was measured in each laminate in each direction using two methods. Method 1 used an ultrasonic apparatus (see Figure 4-4) and Method 2 used a combination of force transducer and accelerometer.

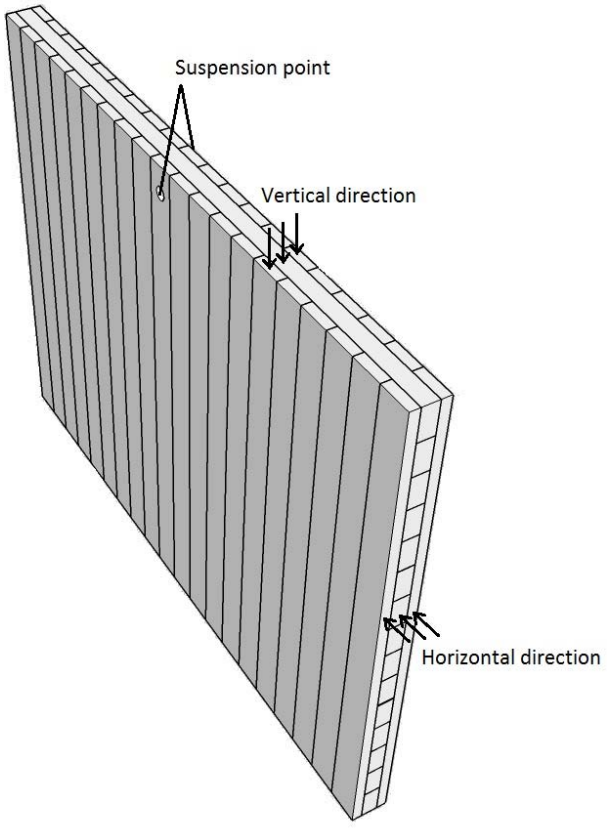

Figure 4-3 Sketch indicating the measurement of the longitudinal wavespeed in the layers.

These methods were applied to see if the wavespeed of each of the layers could be measured individually. The CLT plate was suspended in the laboratory for the duration of the measurements (Figure 4-3). For layer *i* the modulus of elasticity is calculated from the quasi-longitudinal wavespeed [8]:

$$E_i = \frac{c_{\mathrm{L}i}^2 \rho_s (1 - \nu^2)}{h} \tag{4-2}$$

Figure 4-4 One half of the transducer pair of the ultrasonic measurement apparatus attached at one end of a timber beam.

For method 1, measurement positions were drilled at suitable points in each of the layers and the ultrasonic probe was attached at pairs of points on either side of the plate. The time taken for the pulse to travel across the plate in each layer in the *x*- and *y*- directions was recorded. For method 2, a force hammer incorporating a force transducer was used to excite the beam at one end, and an accelerometer was fixed using beeswax to record the signal at the other end. The time taken between the rising edge of the force pulse and the rising edge of the received pulse at the accelerometer was recorded. The drawback of these approaches is that inhomogeneity is known to limit the applicability of the measurement method [109]. Cracks or discontinuities can scatter the pulse at interfaces, deforming the pulse

shape which results in inaccuracies. The results of these measurements are presented in section 4.7.2.

4.4.2 Identifying eigenfrequencies with laser vibrometer measurements

The literature indicates different methods to determine the modal frequencies by locating the nodal lines using a force hammer and accelerometer [27], a force hammer and microphone [104], or a force hammer and a non-contacting eddy current proximity probe [103]. Another possibility is to locate nodal lines using a scanning laser vibrometer. This allows the modes to be easily located and visualized. From a visual inspection of the mode shapes the assumed boundary conditions could also be approximately verified. Ideal nodal lines for rectangular plates should be straight and parallel to the edges, and are therefore easy to identify with the mode numbers. The images obtained with the laser vibrometer would also make it easy to identify curved or diagonal nodal lines which could be produced due to a poor choice of aspect ratio (for free or clamped edges) or imperfections in the plate.

For the measurement of thin plates, there are three feasible options for the edge conditions: clamped, free, or simply supported boundaries. A fourth option is guided ends, however these are difficult to achieve in practice and were therefore ruled out. The difficulty of obtaining experimentally exact clamped boundary conditions for substantial wood products such as plywood plates and CLT is highlighted in [115], where it is shown that a frame used to clamp the edges is less effective with thicker plates and plates with smaller lateral dimensions. Simply supported boundaries give the advantage that for square or rectangular plates nodal lines are always parallel to the sides, curved or diagonal lines should not occur. However, these conditions are difficult to accurately realize in the laboratory given the thickness of the plate. Results for free edge conditions are given in [27, 103, 104]. Ayorinde and Gibson [27] found that free edges are the easiest to achieve in practice, whereas Moussu and Nivoit [104] argue that they are difficult to achieve in practise even though they describe apparatus to successfully achieve them. An advantage of free edges is that the modes occur at lower frequencies than with clamped or simply supported edges. Therefore, more modes can be measured in the thin plate region before having to consider more complicated thick plate models.

Elastic moduli were determined from a freely hanging plate in the laboratory by suspending it from a single point attached to the laboratory crane. The wall surface was scanned with the laser vibrometer (Polytec PSV-400 scanning head) to measure out-of-plane velocity with an average from five measurements used at each measurement position. A grid of 13 x 9 measurement positions was used. Based on calculation of the bending wavespeed there were more than six grid points per wavelength up to ~100Hz A continuous pink noise source was used to excite the wall and two shaker positions were used to capture all the eigenfrequencies. For a linear system with low structural damping the eigenfrequencies and mode shapes determined by the forced response would be expected to approximately equal those determined from the free (i.e. unforced) vibrations of the plate. The results of these measurements are presented in section 4.7.3.

4.4.3 Estimating the elastic moduli of the CLT panel from the eigenfrequencies using FEM

Eigenfrequencies obtained from FEM can be used to obtain the elastic moduli of a panel through comparison with experimentally measured eigenfrequencies. FEM allows both thin and thick plate solutions to be implemented and compared. However, the methodology is computationally expensive compared to the Rayleigh-Ritz technique described in section 4.4.4 and can be complex to implement in an inverse methodology. A simple algorithm using three eigenfrequencies was used. The plate modes measured using the laser vibrometer (see section 4.4.2) were compared with a FEM model constructed using ABAQUS. Thin plate elements (STRI3), which enforce the Kirchhoff constraint analytically, were compared with thick plate elements based on a Mindlin first order theory (S4R). The mesh size was based on the thin plate bending wavespeed with at least six elements per wavelength up to ~1000Hz.

ABAQUS provides the option to use continuum shell elements (where nodes are assigned directly through the thickness) or conventional shell elements. The conventional element was used as the elastic moduli of the plate are fully described by the reduced stiffness matrix (see Eqn. (2-35) or (2-40)). The shear moduli G_{xz} and G_{yz} are required to model transverse shear deformation through the thickness (see

Eqn. (2-42)) (a shell section is used to assign material properties through the thickness). Values of the shear constant were taken from nominally identical panels in the literature (G_{xz}=6.78x10^8 and G_{yz}=1.39x10^8) [102]. Wood has non-linear properties at large displacements however linear elasticity was assumed because only small displacements are relevant for airborne sound insulation. When linearity is assumed, displacements through the thickness are calculated before the analysis.

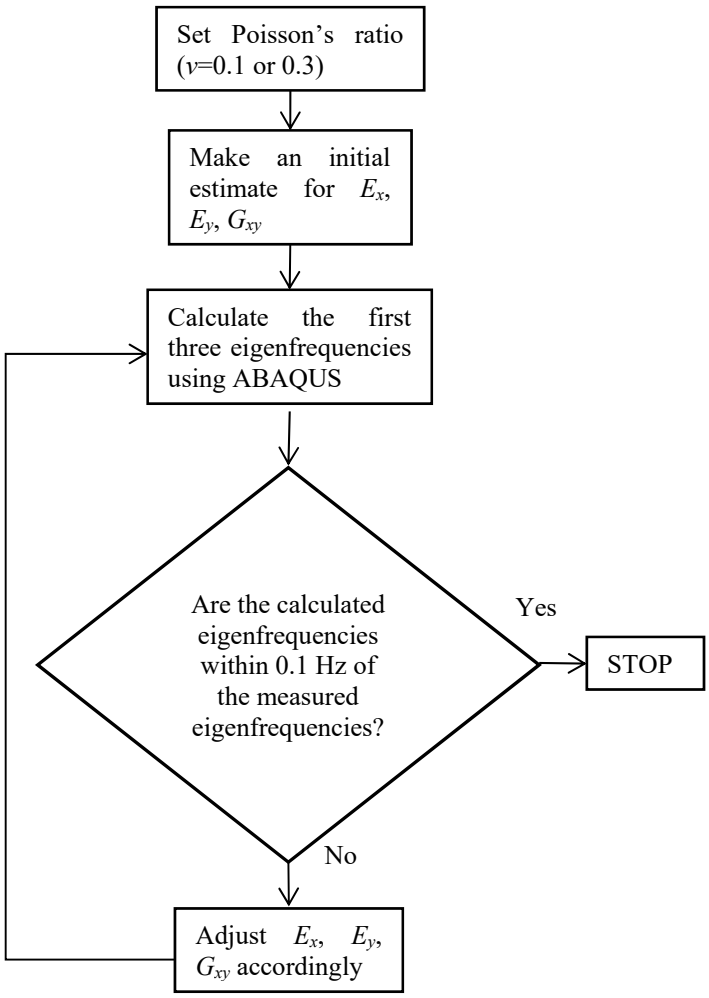

Figure 4-5 Optimisation process.

A simple iterative process (Figure 4-5) was used to optimise values for E_x, E_y and G_{xy} for three measured eigenfrequencies: f_{11}, f_{20}, and f_{02} to within 0.1Hz. It is not possible to determine the wood material constants from this process because the whole panel stiffness is only weakly dependant on some properties (e.g. $E_\perp$ as shown in Table 4-3, section 4.2.3 and, if the panel can be modelled using a thin plate, the

shear constants through the material thickness) making it difficult to determine less sensitive parameters. Instead effective values of the elastic moduli and an estimation of Poisson's ratio of a single layered composite possessing equivalent vibroacoustic properties is sought. The results of high and low Poisson's ratios were compared (v_{xy}=0.04, v_{xy}=0.1 and v_{xy}=0.3). The calculated elastic moduli for the panel from Eqns. (2-130) and (2-132) were used as a starting point for optimisation. The results of these measurements are presented in section 4.7.4.

4.4.4 Determining the elastic moduli of the CLT panel from the eigenfrequencies using a Rayleigh-Ritz technique

The proposed methodology for this work is an improved version of Warburton's method [28] for calculating the eigenfrequencies which employs the characteristic beam functions and the Rayleigh-Ritz technique. The free vibrations of thin plates are described in sections 2.2.4.2 and the solutions to finite thin plate equations are described in section 2.2.6. The advantages of a Rayleigh-Ritz technique are that it is less computationally expensive than FEM and the methodology is straightforward to implement in an inverse method to obtain the elastic moduli from the experimentally measured eigenfrequencies. This methodology therefore, allowed many permutations of the eigenfrequencies to be examined to determine averaged values of the elastic moduli. The effect of using different Poisson's ratios was also investigated. Two alternative methods using the characteristic beam functions were implemented in MATLAB.

Warburton's [28] method using single term characteristic beam functions was compared with the improved method using multi-term characteristic beam functions proposed by Ayorinde and Gibson [27]. Free boundary conditions were chosen due to the difficulty in achieving exact clamped or simply supported boundary conditions (as noted in section 4.4.2). The modes were measured as described in section 4.4.2. For the purposes of determining the elastic moduli the frequency expression of Warburton (Eqn. (2-79)) can be rearranged to

$$f_{\mathrm{L}} = \frac{\rho h a^2 b^2}{\pi^4} = HC_{ij} = f_{\mathrm{R}} \tag{4-3}$$

where f_L is the calculated frequency parameter which is only dependent on the plate dimensions and material parameters and f_R is the measured modal frequency parameter returned by the boundary conditions and nodal lines. Ayorinde and Gibson [27] rearrange the frequency expression (Eqn. (2-85)) to

$$f_L = \frac{\rho h a^2 b^2}{\pi^4} = \frac{H\left(C_{ij} + c^2 C_{in} + d^2 C_{mj} - 2cE_{ij} - 2dE_{ji} + 2cdF\right)}{\omega^2(1 + c^2 + d^2)} = f_R \qquad (4\text{-}4)$$

Since in each case f_L comprises the mass density and geometry of the plate a dimensionless residual may be defined for the modal frequencies (i=1, 2, etc.) according to

$$\frac{f_{Ri}}{f_L} - 1 = \delta_\kappa \qquad (4\text{-}5)$$

This results in a set of simultaneous equations. The total residual can be determined from the modal values by

$$R_Q = \sum_{\kappa}^{3} {\delta_\kappa}^2 \qquad (4\text{-}6)$$

A cut-off of R_Q<0.1 was used to ensure that the elastic constants had converged. Four independent elastic moduli are sufficient to define the behavior of a thin specially orthotropic plate (see section 2.2.4.2): Young's modulus in the x and y directions (E_x and E_y) the shear modulus (G_{xy}) and Poisson's ratio (υ_{xy}). The set of equations for the constants are linear therefore they can be determined using the Newton-Raphson multivariate method. Poisson's ratio (ν_{xy}) can potentially be determined in the same manner as the other moduli, however, the large difference in magnitude between it and the other elastic moduli results in an ill-conditioned matrix. When the matrix is ill-conditioned the Newton-Raphson multivariate method is not suited to finding the solution to the inverse matrix problem. Ayorinde and Gibson [27] avoid this problem by using a least squares method to calculate the four constants. Instead of adopting Ayorinde and Gibson's approach the method was modified slightly to specify, rather than optimize Poisson's ratio.

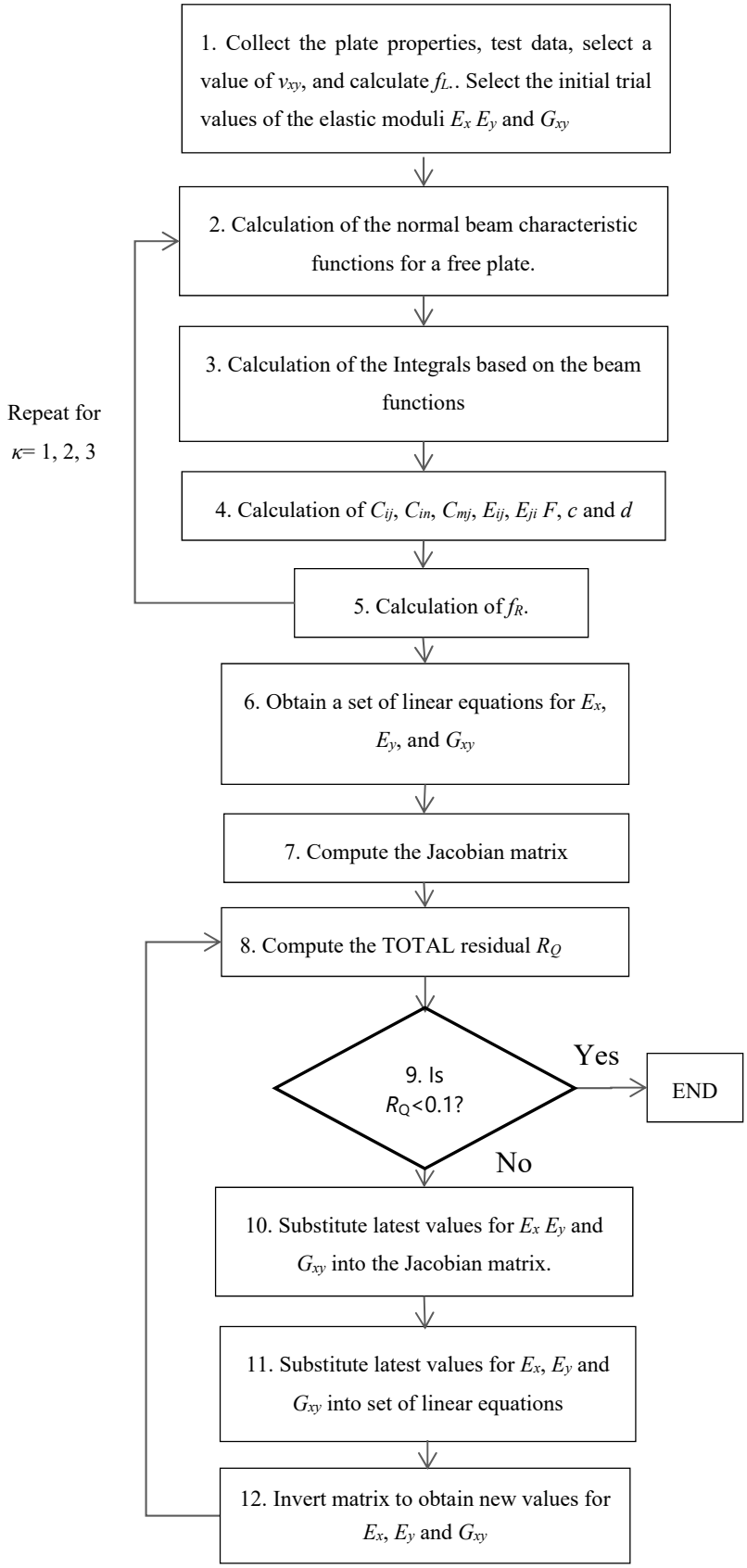

Figure 4-6 Algorithm used to determine the elastic moduli.

Poisson's ratio, υ_{xy}, was set to a range of values between 0.05 to 0.4 and the elastic constants E_x, E_y and G_{xy} were determined for each υ_{xy}. In each calculation, the matrix converged within four to five iterations, for υ_{xy} >0.4 the matrix did not converge within ten iterations and this data was discarded. The problem phrased using the Newton-Raphson multivariate method f_R the first (and subsequent iterations) becomes

$$\begin{Bmatrix} E_x(1) \\ E_y(1) \\ G_{xy}(1) \end{Bmatrix} = \begin{Bmatrix} E_x(0) \\ E_y(0) \\ G_{xy}(0) \end{Bmatrix} - \begin{bmatrix} \partial_{E_x}\delta_1(E_x,E_y,G_{xy}) & \partial_{E_y}\delta_1(E_x,E_y,G_{xy}) & \partial_{G_{xy}}\delta_1(E_x,E_y,G_{xy}) \\ \partial_{E_x}\delta_2(E_x,E_y,G_{xy}) & \partial_{E_y}\delta_2(E_x,E_y,G_{xy}) & \partial_{G_{xy}}\delta_2(E_x,E_y,G_{xy}) \\ \partial_{E_x}\delta_3(E_x,E_y,G_{xy}) & \partial_{E_y}\delta_3(E_x,E_y,G_{xy}) & \partial_{G_{xy}}\delta_3(E_x,E_y,G_{xy}) \end{bmatrix}^{-1} \begin{Bmatrix} \delta_1(E_x,E_y,G_{xy}) \\ \delta_2(E_x,E_y,G_{xy}) \\ \delta_3(E_x,E_y,G_{xy}) \end{Bmatrix} \quad (4\text{-}7)$$

The values of E_x, E_y and G_{xy} are found by inverting the matrix. A simple block diagram showing the basic algorithm used to extract the elastic constants from the measured natural frequencies is shown in Figure 4-6. The first eleven eigenfrequencies were implemented for 24 values of Poisson's ratio $0.01 \leq \nu_{xy} \leq 0.3$. Since only three eigenfrequencies are required to determine the unknowns; all three from eleven combinations and thus a total of 165 combinations were trialled. All the values of E_x, E_y and G_{xy} where the error converged to <0.1 within ten iterations were recorded. The results of these measurements are presented in section 4.7.4.

4.4.5 Direct measurement of the bending wavespeed

The bending wavespeed in the *x*- and *y*- direction were measured directly using a method proposed by Roelens *et al* [116].. Advantages of this measurement method are that it can be performed in situ and it can be used to determine the high frequency elastic moduli. The methodology was checked by measuring a 160mm concrete floor, the Young's and shear moduli were determined for the concrete floor to within approximately ±20% and ±10% respectively of values from Hopkins [8]. (Young's modulus, *E*, and shear modulus, *G*, were determined from longitudinal wavespeed tables; for an isotropic material, such as concrete, the shear constant can be determined from the relation $G=E/2(1+\nu)$).

The CLT panel was supported in a concrete-filled steel frame in the laboratory. Direct measurement was made using a force hammer and two accelerometers. The phase difference between the two accelerometers was recorded using a three channel RTA (B&K Photon II). The distance between the excitation position (hammer) and the first receiver position was based on an estimate of the expected bending wavelengths. Optimum measurement positions should be out of the nearfield but sufficiently far from the edges and sufficiently close to the source point to capture the direct field; this distance was chosen to be 0.33m although frequencies <400Hz in the horizontal direction and <630Hz in the vertical direction may be affected by the nearfield.

The possibility to use a draw away line for a moving source was trialled on the CLT but the result was poorer than a static source with a much noisier output than a single source position and was therefore abandoned. This was thought to be due to the reflections at the glue lines between the constituent pieces of timber in the CLT plates. Phase matching of the accelerometers was verified by placing them on top of each other. Accelerometer spacing of 0.02m to 0.32m were trialled and the optimum distance for the accelerometers was found to be 0.04m for the CLT (a wider spacing of 0.16m is possible with other materials e.g. concrete). Wavelengths shorter than this distance show a 2π phase shift, therefore the upper bound for the CLT data was expected to be ~3150 Hz (using thick plate assumptions). The signal was windowed using a short flat topped steep exponential window (damping factor 20). A variety of window sizes were tried; from only a few samples wide to no window and the optimal window length was found to be 14 samples wide (0.683ms) with a pre-trigger of 10 samples. Measurements were made in the horizontal and vertical directions parallel to the plate edges with 20 measurements averaged at each point. Five different measurement positions were used.

The bending wavenumber was calculated from the phase difference between the accelerometers using [116].

$$\mathrm{Re}(k_B(f)) = -\frac{\Delta\phi_{12}(f)}{\Delta r} \tag{4-8}$$

where $\Delta\phi_{12}(f)$ is the phase difference and Δr is the distance between the accelerometers, then the phase velocity can be determined from the real part of the bending wavenumber according to [116]

$$\mathrm{Re}\left(c_{\mathrm{B,p}}(f)\right) = -\frac{\omega}{\mathrm{Re}\left(k_{\mathrm{B}}(f)\right)} \tag{4-9}$$

where $\mathrm{Re}\left(k_B(f)\right)$ is the real part of the bending wavenumber calculated in Eqn. (4-8).

The phase difference between the accelerometer pairs can be affected by phase fluctuations due to the diffuse field. A correction is proposed by Roelens *et al.* [116] (based on [117]) to correct for the diffuse phase component $G_{\mathrm{Bessel}}J_0(\mathrm{Re}(k_{\mathrm{B}})\Delta r)$

$$\Delta\varphi_{12}(f) = \tan^{-1}\left(\frac{sin(\mathrm{Re}(k_{\mathrm{B}})\Delta r)}{cos(\mathrm{Re}(k_{\mathrm{B}})\Delta r) + G_{\mathrm{Bessel}}J_0(\mathrm{Re}(k_{\mathrm{B}})\Delta r)}\right) \tag{4-10}$$

where G_{Bessel} is a coefficient which determines how much the phase measurement is affected by the diffuse phase component, and $J_0(x)$ is a zeroth order Bessel function of the first kind. Estimating the value of the coefficient G_{Bessel} determined the sensitivity of the measurement to the diffuse vibration field. The results of these measurements are presented in section 4.7.5.

Frequency-dependent moduli for substitution into the airborne transmission models can be determined from a back calculation of Eqn. (2-58). Two different frequency-dependant moduli were determined. $E_1(f)$ was determined using the directly measured data which was uncorrected for diffuse phase i.e. without applying Eqn. (4-10), and $E_2(f)$ was determined using the corrected data i.e. applying Eqn. (4-10).

4.5 Laboratory measurement of airborne transmission

Airborne sound insulation measurements were made in EMPA's accredited transmission facility (see Figure 4-7). The walls of the laboratory are lined and the flanking limit of the laboratory is 78 dB (-3; -8 dB) $R_{\mathrm{w,max}}$. In this facility test walls are installed between the rooms using a sliding frame system, the frames are

constructed from concrete filled steel and are clamped together using fluid-filled cushions to seal off airborne paths between the frame and laboratory rooms. Flanking transmission is suppressed by the cushions which act as isolators for the frame, and linings on the walls of the source and receiving rooms. Reverberation times are between 1.0−2.0s in the frequency range 100Hz-5000Hz. The two test rooms either side of the wall have volumes of 101m^3 and 73m^3. The CLT panel was installed in the frame on a felt lining and was sealed at the perimeter between the wall and frame with Prestik Kitt (a reusable putty). The test wall that was built into the laboratory to measure the airborne transmission had dimensions of 2.9m high x 3.9m wide. The SRI was measured in both directions according to ISO 10140-2 [92] and the direction-average value was used for comparison with the SEA models.

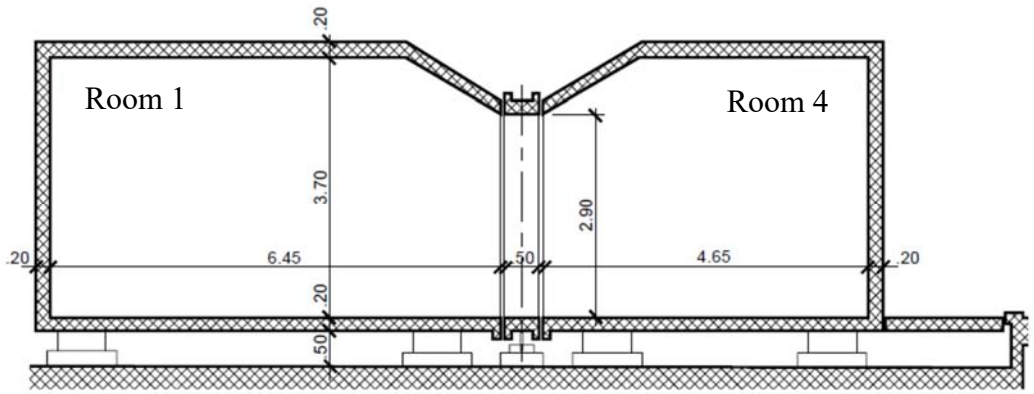

(a)

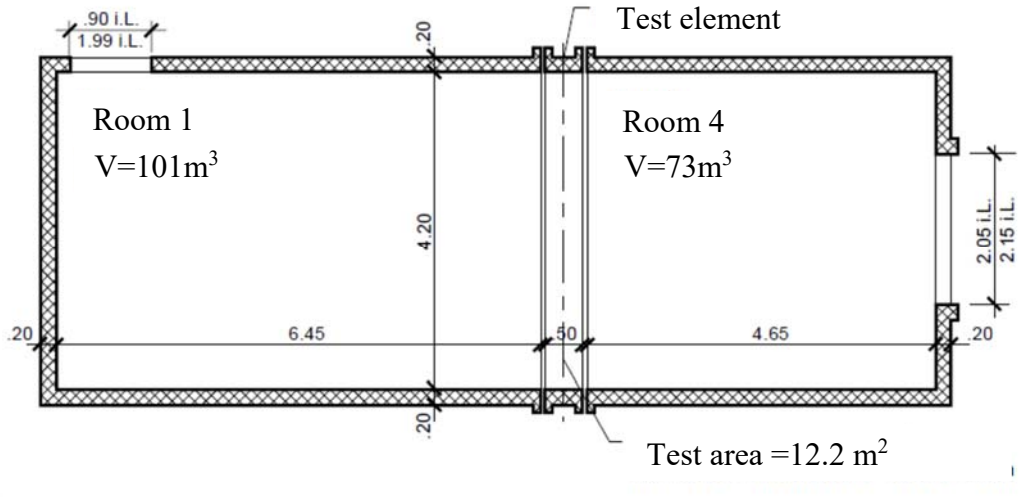

(b)

Figure 4-7 EMPA transmission facility (a) Cross section (b) Aerial view (reproduced from EMPA drawings)

4.6 Predicting airborne sound insulation

4.6.1 Prediction models

The aim is to draw conclusions about how to develop an accurate model for the airborne transmission of CLT using elastic constants determined by the methods described in sections 4.4.3 to 4.4.5 in prediction models for comparison with the measured SRI. A comparison is made between the elastic constants determined from the eigenfrequencies below 100Hz with elastic constants determined at frequencies above 300Hz from the bending phase speed measurements. Three models were introduced in sections 2.2.7, 2.2.9.1 and 2.2.9.2 and are labelled models 1, 2 and 3 as follows:

Model 1 is Leppington's [47] finite, isotropic, thin plate theory which was shown in chapter 3 to be effective to construct an approximate model of the orthotropic properties of a concrete floor with deep rigidly attached beams when using a calculated effective bending stiffness. The model is appropriate for modelling an isotropic or mildly orthotropic plate. (Here mildly orthotropic is used to denote orthotropic plates with critical frequencies separation of less than an octave.) This model can also be applied using a frequency-dependant high-frequency modulus. Frequency-dependant models could also be applied to more recently developed models such as [21] which implement a frequency-dependant Young's modulus to model orthotropic panels such as plywood.

Model 2 is Heckl's [52] infinite orthotropic thin plate model. This can be applied in two ways; calculation of the radiation factor between the critical frequencies to determine resonant transmission or application of the full model to determine the airborne transmission. In this chapter, only the latter approach is applied; the integral was calculated numerically using the "integral2" function in MATLAB. Applicability of the first approach is limited to between the critical frequencies and is relevant only when the plate is highly orthotropic with critical frequencies that are widely separated. These models were also applied in chapter 3 to calculate the airborne transmission of the HBV floor without a suspended ceiling and to calculate the radiation efficiency between the two critical frequencies.

Model 3 is Ljunggren's [54] isotropic thick plate model, although the mild orthotropy of the material means that it does not fit thick plate isotropic or transverse isotropic assumptions. The method separates the airborne transmission index calculation into two parts, a thin plate calculation and a thick plate "correction term". Currently no methodology exists to incorporate this into an SEA model. One limitation of this calculation is that Eqn. (2-110) is not appropriate for third octave bands at and below the critical frequency (f_c) so ΔR was set to zero at these frequencies.

4.6.2 Elastic modulus input data

Three sets of elastic moduli from those measured in this chapter were used to make the airborne transmission models. Dataset "a" was the frequency-independent elastic moduli determined from measured modal analysis data described in sections 4.4.2 to 4.4.4. For the isotropic models, Eqn. (2-133) can be used to determine the effective modulus. For the orthotropic models, E_x and E_y can be used directly. Datasets "b" and "c" are frequency-dependant elastic moduli determined respectively from the uncorrected (Eqn. (4-9)) and corrected (Eqn. (4-10)) directly measured bending wavespeed data described in section 4.4.5. For use in the isotropic models Eqn. (2-133) can be used to determine the effective modulus in each third octave band. For the orthotropic models, the frequency-dependant (or independent) moduli $E_x(f)$ and $E_y(f)$ can be used directly.

4.6.3 Modal density

The modal density of a plate was given in section 2.3.3 by Eqn. (2-165), for thin plates this is constant across the whole frequency range. However, for thick plates the bending phase velocity plateaus and this results in a modal density which increases with increasing frequency. To demonstrate this effect the results from four methods to calculate the model density are plotted and compared. The modal density determined using the two frequency dependant elastic moduli $E_1(f)$ and $E_2(f)$ (in the frequency range 50-5000Hz) obtained from the bending wavespeed measurement are compared with numerically determined modal density data from the FEM

calculations (in the frequency range <1000Hz) using thick plate and thin plate elements averaged over 200Hz intervals.

4.6.4 Frequency ranges of applicability for the Kirchhoff thin plate and Mindlin's thick plate first order shear deformation theories

An estimate of the frequency range of applicability of the thin plate and first order shear deformation theories is made. The common acoustic method would be to calculate the shear wave (2-67) cross-over frequency described in section 2.2.5. The major problem to determine this cross-over frequency is that the material has different G_{xz} and G_{yz} moduli in the *xz*- and *yz*-planes, however the equation assumes strict isotropy (i.e. that the shear moduli are identical $G_{xy}=G_{xz}=G_{yz}$, the Young's moduli are identical $E_x=E_y=E_z$ and that the relationship between E and G is defined according to G=2(1+ν)/E, as can be seen in the derivation starting from section 2.2.1 and ending in Eqn. (2-67) in section 2.2.5). Which is not the case for the input data used; a more complicated derivation using the elastic constants starting from sections 2.2.2 (transverse isotropy) or 2.2.3 (specially orthotropic material) may be possible. Instead, for simplicity, the calculations were performed using the Young's and shear moduli for the *y*-direction which gave the lowest cross-over frequency.

An alternative method is to determine the frequency ranges of applicability using equations (2-19) and (2-34) in section 2.2.1. This latter method was applied by directly using a numerically estimated asymptote to which the wavespeed was plateauing in the *y*-direction and applying a correction to obtain the dilatational wavespeed using Eqns. (2-17) and (2-65)

$$\frac{\kappa_{DS}}{\kappa} = \frac{c_{\mathrm{D},p}}{c_{\mathrm{R},p}} \approx \frac{2(1-\nu)}{(1-2\nu)} \cdot \frac{(1+\nu)}{(0.87+1.12\nu)} \tag{4-11}$$

For a low Poisson's ratio, this correction approximates to $\kappa_{D,s}/\kappa \approx 2.3$.

4.7 Results and Analysis

4.7.1 Loss factor

The estimated internal loss factor was calculated from the T_5 measurement using Eqn. (3-14). Structural reverberation times measured over a longer period (such as a T_{20} or a T_{30} measurement) are not recommended for heavyweight structures [114]. Unsuitable T_{20} or T_{30} measurements include a double decay, often occurring in the region of the critical frequency where the radiation coupling loss factor is high. This has the apparent effect of an increased decay time as the loss factor is determined over the double decay and thus reduces the calculated loss factor. The measured loss factors are presented in Figure 4-8. A sum of the coupling losses from both sides of the plate are also included for comparison, these are calculated using Eqn. (3-4) and model 1a. The plate to room coupling losses are close enough to the measured values of loss factor to increase them more than 2.0dB (by simply adding the loss factors) in the frequency range 200-400Hz.

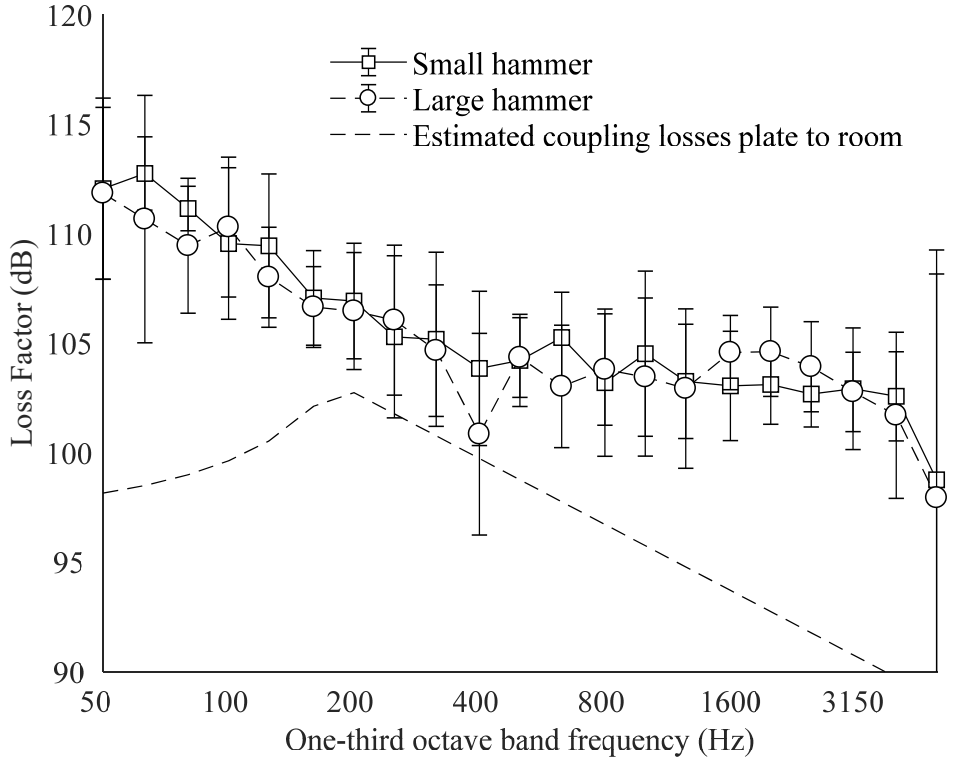

Figure 4-8 Internal loss factor of the CLT plate measured using a large hammer (4.8kg) and a small hammer (~0.6kg) (95% confidence limits are indicated).

Measurement of structural reverberation times using an impulse source such as a hammer can be problematic, if the force of the hammer is high, large deflections of the wall might occur introducing nonlinearity into the decay resulting in different measured structural reverberation times [8]. Different test operators may excite the wall with very different force magnitudes. However, for one operator using hammers of different sizes there was little difference between the measured loss factors. The measured internal loss factor for the CLT was significantly higher than the internal loss factors of other wood products e.g. 100.0dB for chipboard, medium density fibreboard (MDF), oriented strand board (OSB) or 102.0dB for plywood (Birch) [8]. A higher loss factor may be beneficial when carrying out a direct measurement of the bending wave phase velocity (described in section 4.4.5) as we wish to measure the phase change of the direct field rather than the reverberant field between two points on the panel.

The relationship between the loss factor and the reverberation distance, r_d, (the distance from the excitation point where the direct and reverberant fields have equal energy densities) can be estimated using [8, 50]:

$$r_d \approx \frac{Sf}{c_{\mathrm{g(B)}}}\eta \tag{4-12}$$

The mean reverberation distance across the building acoustics frequency range (50-5000Hz) was calculated to be ~42cm. Therefore, a distance <40cm between source and measurement positions would be expected to be appropriate to ensure measurement of the direct field with little or no contribution from the diffuse field. Note however that a measurement of the direct field very close to the source would also not be recommended due to the contribution from the near field. Measuring outside both the near field and diffuse field is rarely achievable in practice.

4.7.2 Time of flight measurement

Elastic constants calculated from an effective modulus obtained using time-of-flight measurements are shown in Table 4-5, assuming a Poisson's ratio of 0.3 [8]. The values of E_x and E_y suggested isotropic behaviour therefore G_{xy} was also calculated using Eqn. (2-132).

	Method 1	Method 2
E_x	5.54×10^9 Nm^{-2}	7.71×10^9 Nm^{-2}
E_y	5.37×10^9 Nm^{-2}	6.22×10^9 Nm^{-2}
G_{xy}	2.08×10^9 Nm^{-2}	2.66×10^9 Nm^{-2}

Table 4-5 Elastic constants obtained using time-of-flight measurement data.

These values of the elastic constant do not yield a more accurate airborne transmission calculation [1]. When substituted into a FEM model they do not accurately predict the correct eigenfrequencies. The measurement result had been verified using similar materials with comparable distances between transmitter-receiver probe pairs which suggests that the problem did not lie in the attenuation of the pulse across the measurement distance of the material. Measurements on solid timber beams show correlation between the ultrasound and accelerometer method, however this is not the case with the CLT. For layered materials assembled in a cross-wise fashion such as CLT, significantly different longitudinal wavespeeds in the two orthogonal directions make it impossible to identify whether the measured pulse is distorted by propagation through a faster adjacent layer. Indeed, time of flight measurement methods are known to rely on the homogeneity of the material which suggests that the measurement method is not appropriate for this type of panel, therefore it was not investigated further.

4.7.3 Comparison between measured eigenfrequencies and FEM using ABAQUS

The simple optimisation process was sufficient to optimise values for E_x, E_y and G_{xy} for three measured eigenfrequencies: f_{11} = 8.2 Hz, f_{20} = 12.5 Hz, and f_{02} = 41.9 Hz (to within 0.1Hz). The 131 lowest eigenfrequencies (bending only, <1000Hz) are plotted in Figure 4-9 for the thin and thick plate models. For the first 11 frequencies (<100Hz) the thin plate model is adequate and the shear moduli G_{xz} and G_{yz} can be assumed to have little influence on the eigenfrequencies. Above the 16th mode (>120 Hz) the thin plate model additionally calculates 674 consecutive (zero energy)

modes due to shear locking which slows the calculation procedure. Further refinement of the mesh has no effect on this phenomenon. The location of these zero energy modes can be adjusted by the altering the value of G_{yz}. (These modes are not included in Figure 4-9.) Other thin plate elements may present an option to avoid such problems, by enforcing the Kirchhoff constraint numerically, such as quadratic STRI65 or S9R5 elements. However, a better solution is to use thick plate elements. The eigenfrequencies calculated using S4R elements can be seen to diverge from the eigenfrequencies calculated using STRI3 elements at frequencies >300Hz and the number of modes calculated using the S4R elements is larger than the number calculated using the STRI3 elements in the same frequency range. Optimised values for elastic constants obtained using modal analysis are shown in Table 4-6.

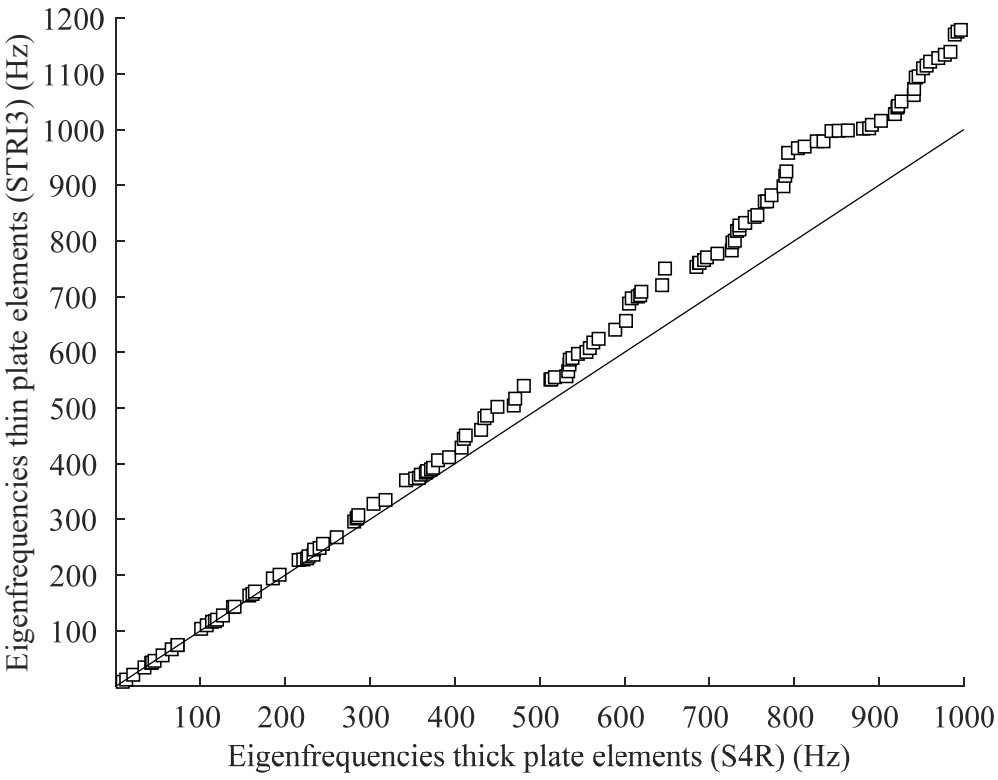

Figure 4-9 Eigenfrequencies of the thin CLT plate predicted using thin and thick plate FEM models.

Poisson's Ratio	**0.04**	**0.1**	**0.3**
E_x	$3.13\text{x}10^9$ Nm^{-2}	$3.15\text{x}10^9$ Nm^{-2}	$3.13\text{x}10^9$ Nm^{-2}
E_y	$8.48\text{x}10^9$ Nm^{-2}	$8.04\text{x}10^9$ Nm^{-2}	$7.13\text{x}10^9$ Nm^{-2}
G_{xy}	$6.20\text{x}10^8$ Nm^{-2}	$6.20\text{x}10^8$ Nm^{-2}	$6.20\text{x}10^8$ Nm^{-2}

Table 4-6 Elastic constants obtained using optimisation.

	Poisson's Ratio v_{xy} = 0.1			
	0	**1**	**2**	**3**
0			2.18	5.88
1		1.41	1.42	2.14
2	2.58	3.62	4.11	2.57
	Poisson's Ratio v_{xy} = 0.3			
	0	**1**	**2**	**3**
0			2.69	12.0
1		1.42	1.44	2.21
2	3.34	6.00	5.05	3.34

Table 4-7 Sum of the squared residuals (SSQR) (where v_{xy}=0.1, E_x=3.15x109 Nm^{-2}, E_y=$8.04\text{x}10^9$ Nm^{-2}, G_{xy}=$6.2\text{x}10^8$ Nm^{-2}, and where v_{xy}=0.3, E_x=$3.13\text{x}10^9$ Nm^{-2}, E_y=$7.13\text{x}10^9$ Nm^{-2}, G_{xy}=$6.2\text{x}10^8$ Nm^{-2})

Using these elastic constants, the FEM model gives accurate eigenfrequencies (<5%) for the first eleven measured eigenfrequencies. The optimised values for elastic constants with Poisson's ratio of ν_{xy}=0.04 (to agree with the calculation procedure in section 4.2.4), were found to be within 3% and 8% of the calculated elastic constants from the raw materials in Table 4-2 in the x- and y- directions respectively. The CLT plate is not highly orthotropic; the ratio of the Young's moduli E_x: E_y is ~1:4.

	Model (Poisson's ratio v_{xy}=0.1)	Model (Poisson's ratio v_{xy}=0.3)	Measurement
f_{11}	8.2 Hz	8.2 Hz	8.2 Hz
	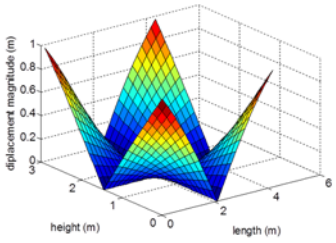	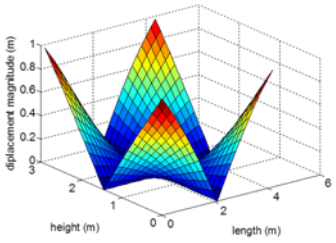	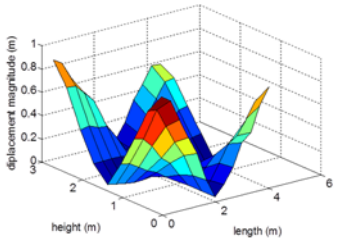
f_{20}	12.5 Hz	12.5 Hz	12.5 Hz
	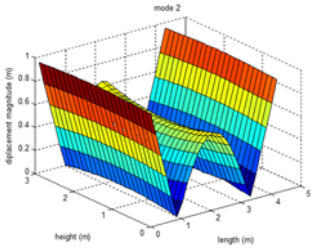	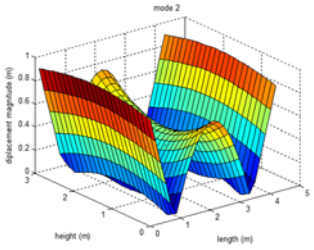	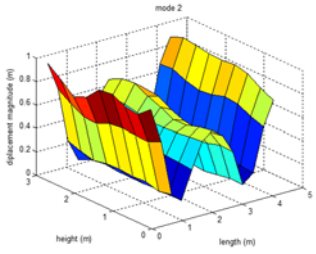
f_{21}	20.9 Hz	21.1 Hz	20.8 Hz
	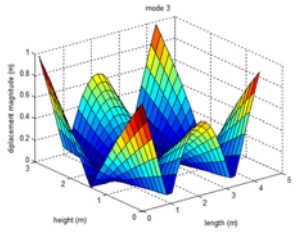	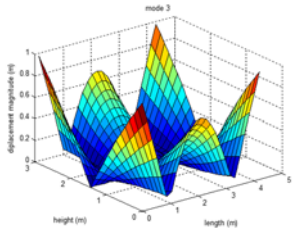	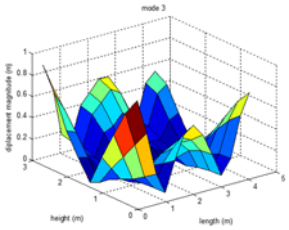
f_{30}	34.5 Hz	33.8 Hz	34.2 Hz
	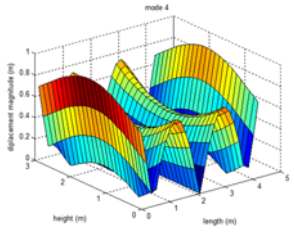	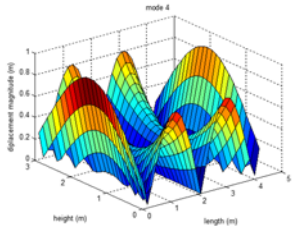	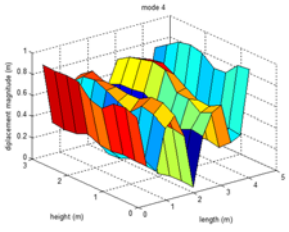
f_{40}	69.0 Hz	73.4 Hz	67.0 Hz
	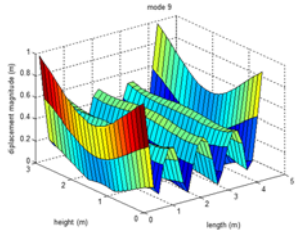	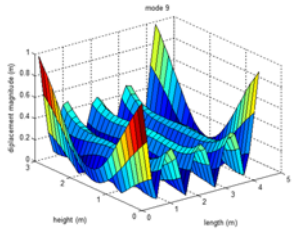	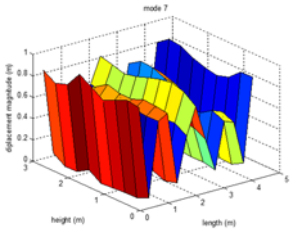

Table 4-8 Comparison of predicted and measured mode shapes (where v_{xy}=0.1, E_x=3.15x10^9 Nm^{-2}, E_y=8.04x10^9 Nm^{-2}, G_{xy}=6.2x10^8 Nm^{-2}, and where v_{xy}=0.3, E_x=3.13x10^9 Nm^{-2}, E_y=7.13x10^9 Nm^{-2}, G_{xy}=6.2x10^8 Nm^{-2})

If the plate behaves as a single layer specially orthotropic material G_{xy} of the whole plate is a good approximation for G_{xz} but not G_{yz}, as was shown in section 2.2.3 (see Figure 2-1). The optimised G_{xy} ($6.20 \times 10^8 Nm^{-2}$) is within 9% of the value of G_{yz} (6.78×10^8 Nm^{-2}) for a nominally identical panel taken from the literature [102]. The ratio of the three shear moduli G_{xy}: G_{yz} : G_{xz} was shown to be 11: 10: 49 (G_{yz} and G_{xz} are taken from the literature [100, 102]). This ratio is not significant enough to warrant a model which considers the shear distribution through the layers of the plate [75].

Adjusting Poisson's ratio to between 0.04 and 0.3 results in a range of values of the elastic constants. Better agreement was obtained between measured and modelled eigenfrequencies and mode shapes when 0.04 was used (<1.7% with the first eleven measured eigenfrequencies). The nodal lines are almost straight, also indicating that Poisson's ratio is small, and that the beam functions are likely to provide an effective approximation for the fitting function. The sum of squared residuals (SSQR) obtained from fitting mode shapes for Poisson's ratios of 0.1 and 0.3 are shown in Table 4-7. Example mode shapes are shown in Table 4-8. For certain modes (e.g. f_{30} and f_{40}) the mode shape changes according to whether Poisson's ratio of 0.1 or 0.3 is used.

4.7.4 Comparison between measured eigenfrequencies and modes calculated using a Rayleigh-Ritz technique

4.7.4.1 Characteristic beam functions

Mean values for the elastic constants E_x, E_y and G_{xy} for the single term (alongside multi-term) characteristic beam methodologies are presented for different Poisson's ratios in Figure 4-10. The data was assembled in the following manner: Negative values were removed from the dataset. Eight datasets were also removed as they did not converge for more than one value of the Poisson's ratio and yielded elastic constants far from the values for natural wood products. After this data cleaning, ~116 converged datasets remained (from the original 165 eigenfrequency permutations) to determine the mean elastic constants for each value of the Poisson's ratio. The mean values of the elastic constants for two Poisson's ratios are presented in Table 4-9.

Poisson's ratio	**0.005**	**0.1**
$\boldsymbol{E_x}$	3.1×10^9 Pa	3.1×10^9 Pa
$\boldsymbol{E_y}$	7.7×10^9 Pa	7.5×10^9 Pa
$\boldsymbol{G_{xy}}$	5.4×10^8 Pa	5.4×10^8 Pa

Table 4-9 The elastic constants determined using the beam functions (v_{xy}<0.1).

The elastic constants do not vary considerably with the value of the Poisson's ratio when $v_{xy} \leq 0.1$. Figure 4-10 also shows that at Poisson's ratios v_{xy}>0.1 the trend is that values of E_x and E_y decrease with increasing Poisson's ratio as indicated by FEM.

4.7.4.2 Multi-term characteristic beam functions

Mean values for the elastic constants E_x, E_y and G_{xy} for the multi-term (alongside single term) characteristic beam methodologies are presented for different Poisson's ratios in Figure 4-10. Similarly, to Warburton's method, the negative values were removed. One dataset was also removed as it did not converge to elastic constants close to the values for natural wood products. After data sorting, ~124 converged datasets remained (from the original 165 eigenfrequency permutations) to determine the mean elastic constants for each value of the Poisson's ratio. The mean values of the elastic constants for two Poisson's ratios are presented in Table 4-10.

Only E_y varies considerably with the value of the Poisson's ratio when $v \leq 0.1$. Figure 4-10 also shows the trend that at Poisson's ratios v>0.1 the values of E_x, E_y and G_{xy} decrease with increasing Poisson's ratio. The values constants c and d governing the additional functions are shown in Figure 4-11.

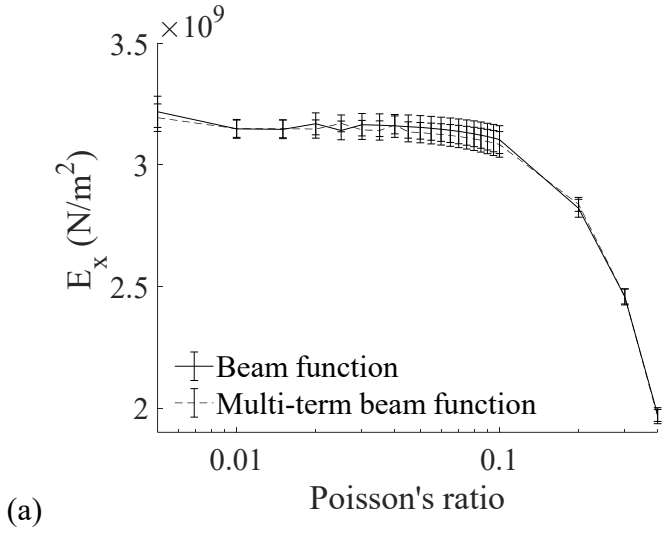

(a)

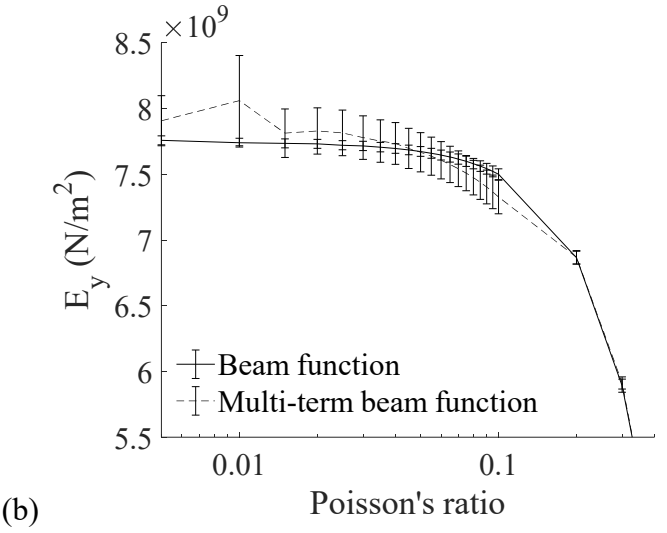

(b)

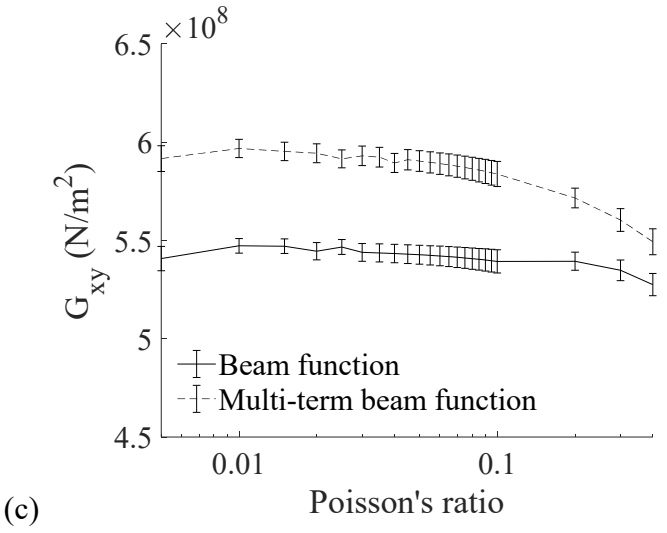

(c)

Figure 4-10 Values of the elastic constants (a) E_x (b) E_y and (c) G_{xy} as functions of Poisson's ratio.

Poisson's ratio	**0.005**	**0.1**
E_x	3.1×10^9 Pa	3.1×10^9 Pa
E_y	8.1×10^9 Pa	7.3×10^9 Pa
G_{xy}	5.9×10^8 Pa	5.8×10^8 Pa

Table 4-10 The elastic constants using multi-term beam functions.

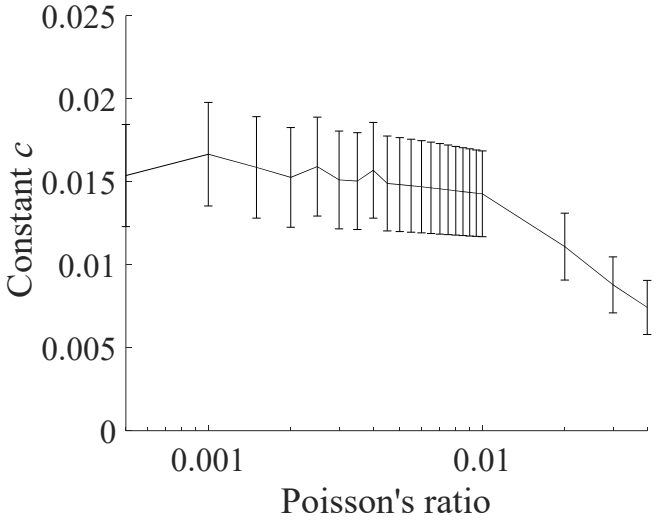

(a)

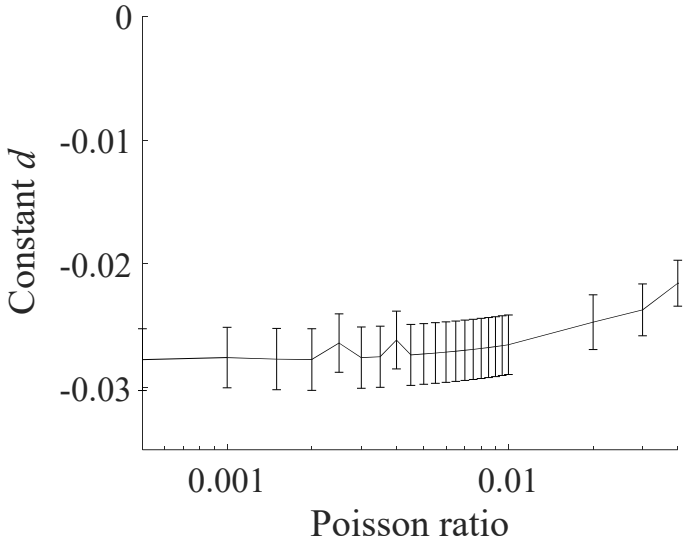

(b)

Figure 4-11 Values of the coefficients of the multiple terms (a) *c* and (b) *d* with 95% confidence intervals

The mean values of the constants c and d are small (c=0.0137 and d=-0.0264). However, a range of values of c and d were determined to fit the elastic constants depending on the dataset of modes used for optimisation, this is reflected in the relatively large 95% confidence limits.

4.7.4.3 Shear modulus G_{xy} and the upper limit for Poisson's ratio

The values for the shear modulus G_{xy} determined using the characteristic beam functions (5.4×10^8 Pa at a Poisson's ratio of 0.04) were slightly lower than those determined using multi-term characteristic beam functions (5.9×10^8 Pa with a Poisson's ratio of 0.04) which were slightly lower than those determined using FEM (6.2×10^8 Pa with all Poisson's ratios tested) It is thought that the value of the optimised value for G_{xy} is likely to converge towards the FEM solution when more terms are added to the multi-term characteristic beam functions.

There is no evidence to indicate that the value for the Poisson's ratio calculated in section 4.2.4 is correct. However, the upper limit for Poisson's ratio based on ideal two-dimensional thin plate behaviour is given in [15, 27]

$$\nu_{xy} = \left(\frac{E_x}{E_y}\right)^{1/2} \tag{4-13}$$

where E_x and E_y are the elastic moduli in the x and y directions. Using the values for E_x and E_y determined by optimisation this gives an upper limit of ν_{xy}=3.15/8.04=0.391. Correspondingly for values of Poisson's ratio >0.39 it was difficult to find mode groups that converged.

4.7.5 Direct measurement of the bending wavespeed

The measured phase differences between the accelerometer pairs in the x- and y-directions are shown in Figure 4-12 (black dots). However, applying a minor correction (to account for modification of the measured phase difference due to a diffuse field) to the data using Eqn. (4-10) for example G_{Bessel}=0.17 in the x-direction, G_{Bessel}=0.12 in the y-direction causes large changes in the elastic moduli extracted from the data. The corrected phase difference for these values of the G_{Bessel} coefficients are also shown in Figure 4-12 (black open circles).

The measured and corrected data (using Eqn. (4-10)) were fitted to the thin and thick plate phase velocities (Eqns. (2-58) and (2-63)) using a weighted least squares method. The default "bisquare" weighting available in MATLAB (where δ is the residual) was applied [118].

$$\begin{aligned} w &= (1-\delta^2)^2 \qquad \text{for } |\delta| < 1 \\ w &= 0 \qquad\qquad\ \ \text{for } |\delta| \geq 1 \end{aligned} \tag{4-14}$$

For the uncorrected phase data for $E_{x,thin,}$=1.66x10^{9}Pa and $E_{y,thick}$=3.94x10^{9}Pa in the x- (100Hz<f<3000Hz) and y- directions (100Hz<f<3000Hz) and G'_{yz}=1.21x10^{8}Pa for the CLT were determined. A value for G'_{xz} could not be determined because the x-direction data better fitted a thin plate model and did not fit a thick plate model with sufficient accuracy. The values of Young's modulus are approximately 50% lower than those obtained in sections 4.7.3 and 4.7.4 and the value of G_{yz} is approximately 90% of that found in the literature [102]. The fit to thin and thick plate models for the uncorrected data is shown in Figure 4-13.

For the corrected (G_{Bessel}=0.17 in the x-direction, G_{Bessel}=0.12 in the y-direction) phase data $E_{\text{x,thin,}}$=2.83x10^{9}Pa and $E_{\text{y,thick}}$=6.92x10^{9}Pa in the x- (100Hz<f<3000Hz) and y-directions (100Hz<f<3000Hz) and G'_{yz}=1.81x10^{8}Pa for the CLT were determined. Similarly, a value for G'_{xz} could not be determined. The values of Young's modulus are approximately 90% (E_x) and 80-100% (E_y) of the values obtained in sections 4.7.3 and 4.7.4 and the value of G'_{yz} is approximately 130% of that found in the literature [102]. The fit to thin and thick plate models for the uncorrected data is shown in Figure 4-14. Eqn. (2-60) from Mindlin is also plotted in Figure 4-13(b) and Figure 4-14(b) using the MATLAB "solve" function. A comparison is also made between calculated bending phase speed determined from elastic moduli obtained in in sections 4.7.3 and 4.7.4 and from the literature. It is difficult to conclude from the measurement whether the low values of the Young's modulus should be corrected for diffuse phase or are due to some other physical effect. Diffuse phase may be introduced by multiple reflections from the edges of the plate and gluelines or the inhomogeneous nature of the material.

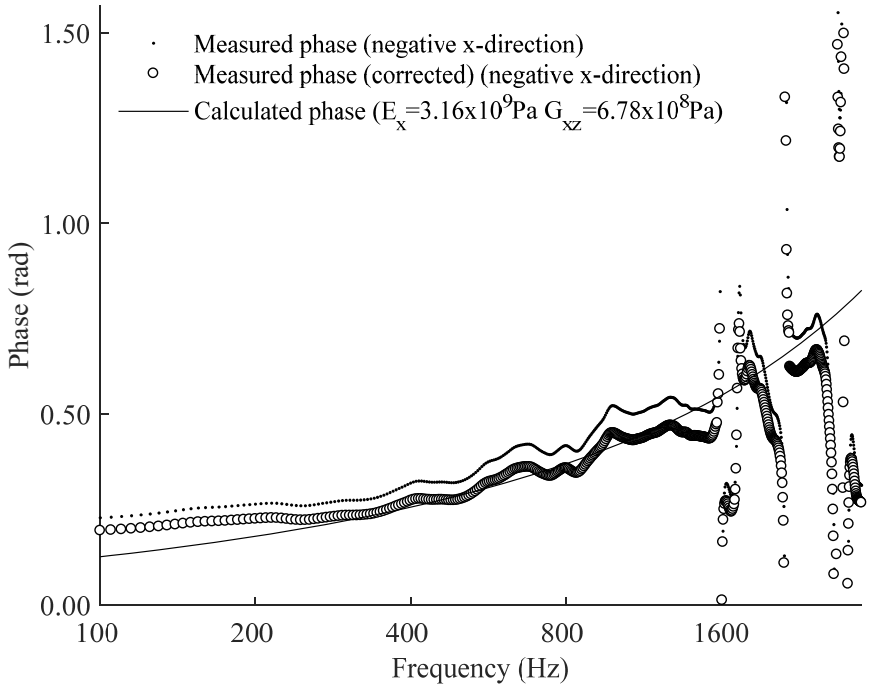

(a)

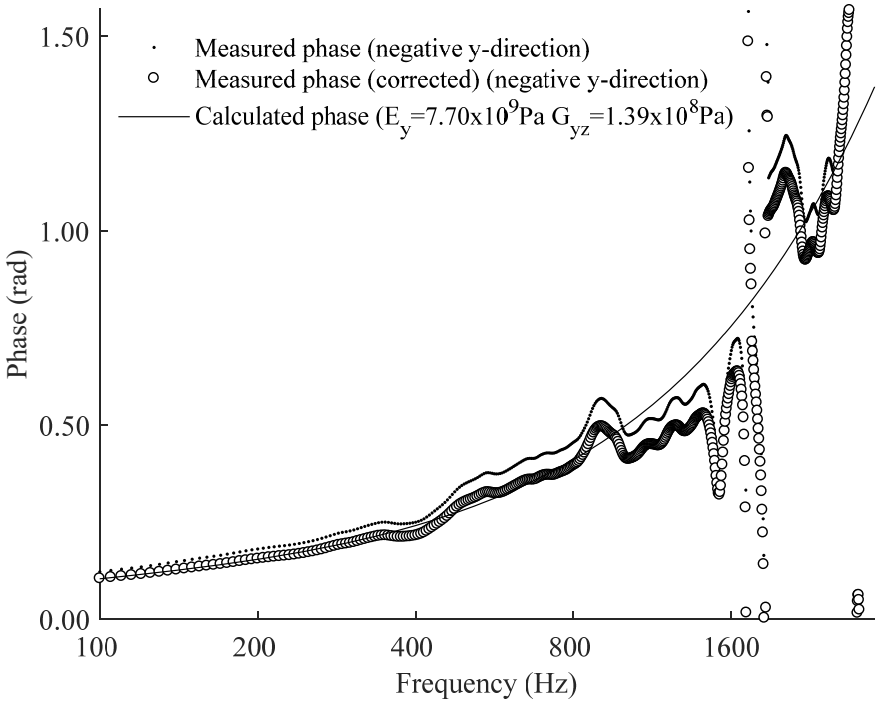

(b)

Figure 4-12 Measured phase differences (a) x-direction (b) y-direction.

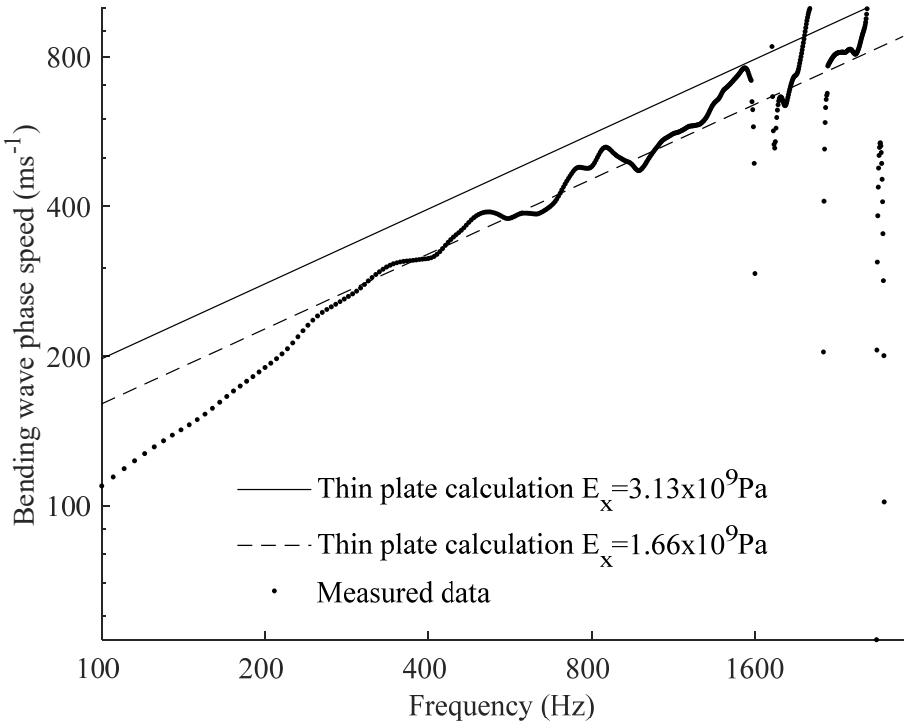

(a)

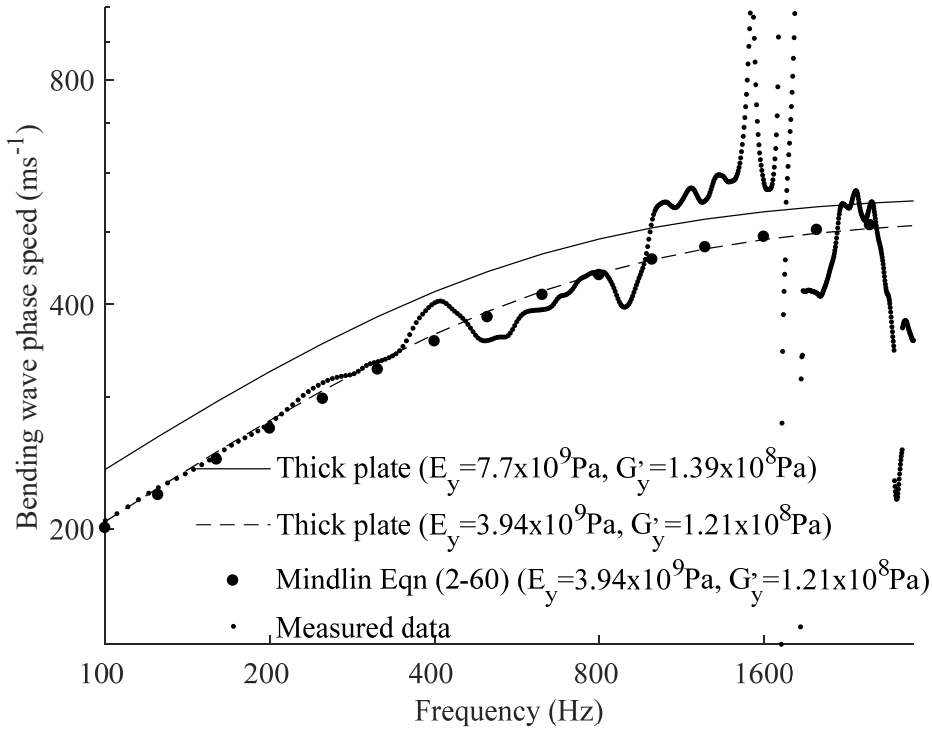

(b)

Figure 4-13 Phase velocity of the bending wave for 80mm CLT in the (a) horizontal and (b) vertical directions (uncorrected phase data).

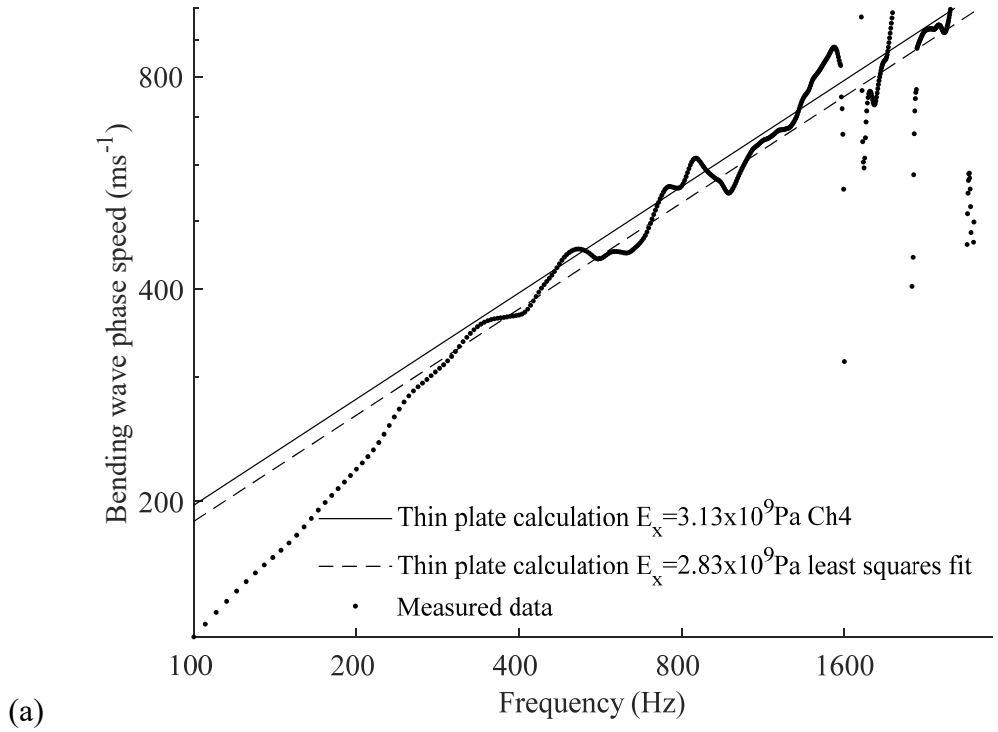

(a)

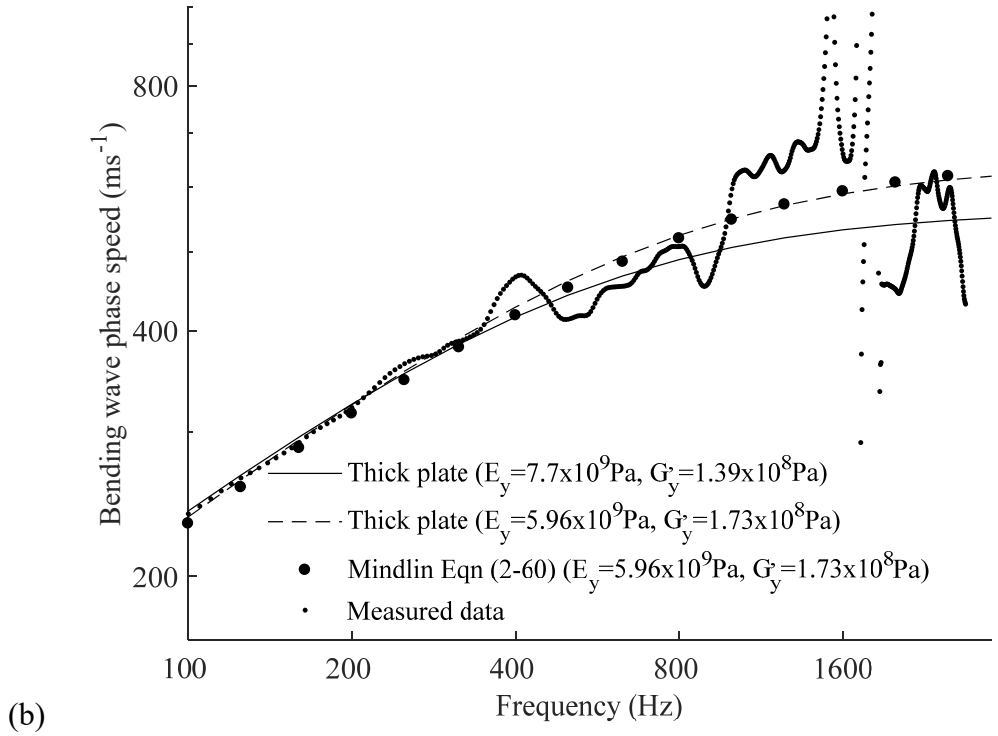

(b)

Figure 4-14 Phase velocity of the bending wave for 80mm CLT in the (a) horizontal and (b) vertical directions (corrected phase data).

For both the uncorrected and corrected data the upper cut off frequency was >3000Hz. This cut-off is likely to be determined by the accelerometer spacing compared with the bending wavelength especially in the vertical (*y*-direction) (see also Figure 4-16 which compares the 0.04m cut-off with the bending wavelengths). It was more problematic to obtain smooth results on a discontinuous material such as CLT than on a homogeneous material such as concrete. This is clearest above 1250Hz. The "noise" in the data could be due to specular reflections at the interfaces between the wood strips in the panel. Evidence for this can be found in the observation that there appears to be more noise in the horizontal direction where the wood strips are narrow (27mm) rather than in the vertical direction where the wood strips are long. A zoom of the uncorrected data plot of frequency against the wavelength in the measured horizontal (*x*) direction showing strip width (27mm) indicates that the location of the phase changes appears to lie in a regular pattern (see Figure 4-15).

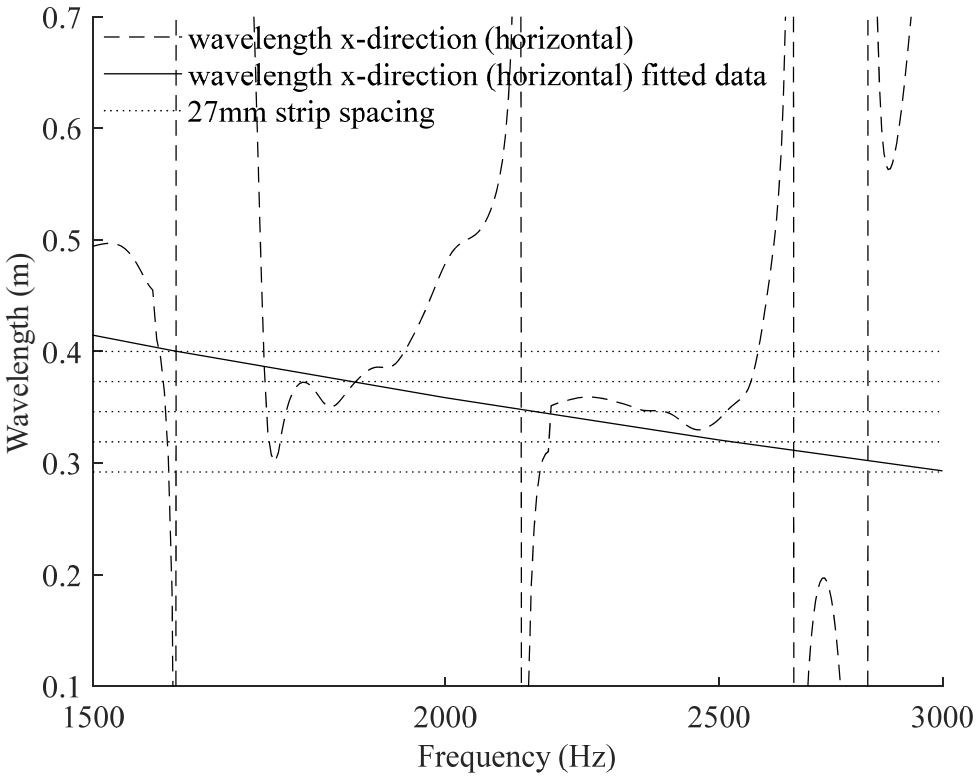

Figure 4-15 Bending wavelength for 80mm CLT in the horizontal direction.

The poor quality of the fit of the data in the x-direction below 250Hz (see Figure 4-13(a) and Figure 4-14(a)) is likely to be due to the short window length used to remove waves reflected from the edges of the plate. The choice of window length is a trade-off between accuracy at low frequencies and noise at high frequencies, a compromise which is not always achievable [116]. The short distance between the accelerometers can also reduce the accuracy of measured data at low frequencies. The calculated bending wavelengths are plotted and the 0.04m accelerometer spacing is shown as a cut-off in Figure 4-16.

The bending wavelength coincides with the wavelength in air for the uncorrected data in the 315Hz and 500Hz octave bands. The bending wavelength coincides with the wavelength in air for the corrected data in the 250Hz and 315Hz octave bands. The former corresponds most closely with the dip observed in the measured airborne transmission (see Figure 4-20).

The directly measured wavespeed data was used to calculate a frequency-dependant Young's modulus *E(f)* which can be substituted into the thin plate calculation for the SRI. This acts as a "thick plate" correction for the prediction equations. The frequency-dependent moduli for substitution in an isotropic model are shown in Figure 4-17 from Eqn. (2-58). $E_1(f)$ was determined using an effective bending phase speed from the uncorrected data determined by:

$$c_{\text{eff}} = \sqrt{c_{\text{x,thin}} c_{\text{y,thick}}} \tag{4-15}$$

where $c_{x,\text{ thin}}$ is the calculated thin plate bending phase speed in the horizontal (x-) direction and $c_{y,\text{ thick}}$ is the calculated thick plate bending phase speed in the vertical (y-) direction; using the elastic moduli determined from the direct measurement of the bending wavespeed. $E_2(f)$ was determined in a similar manner using the corrected data.

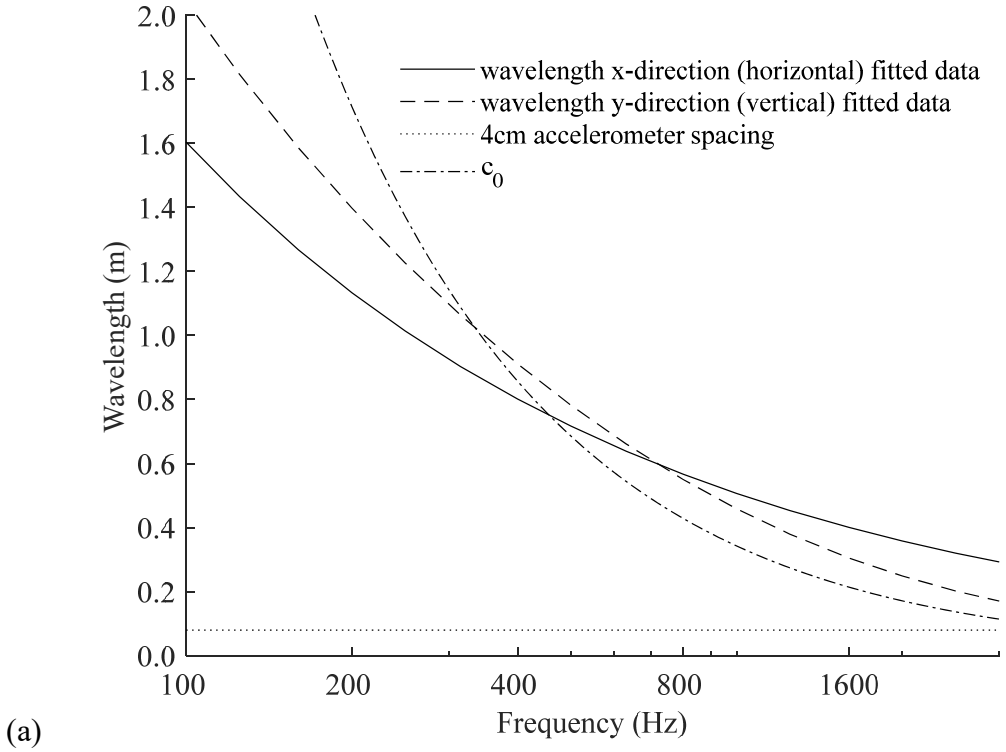

(a)

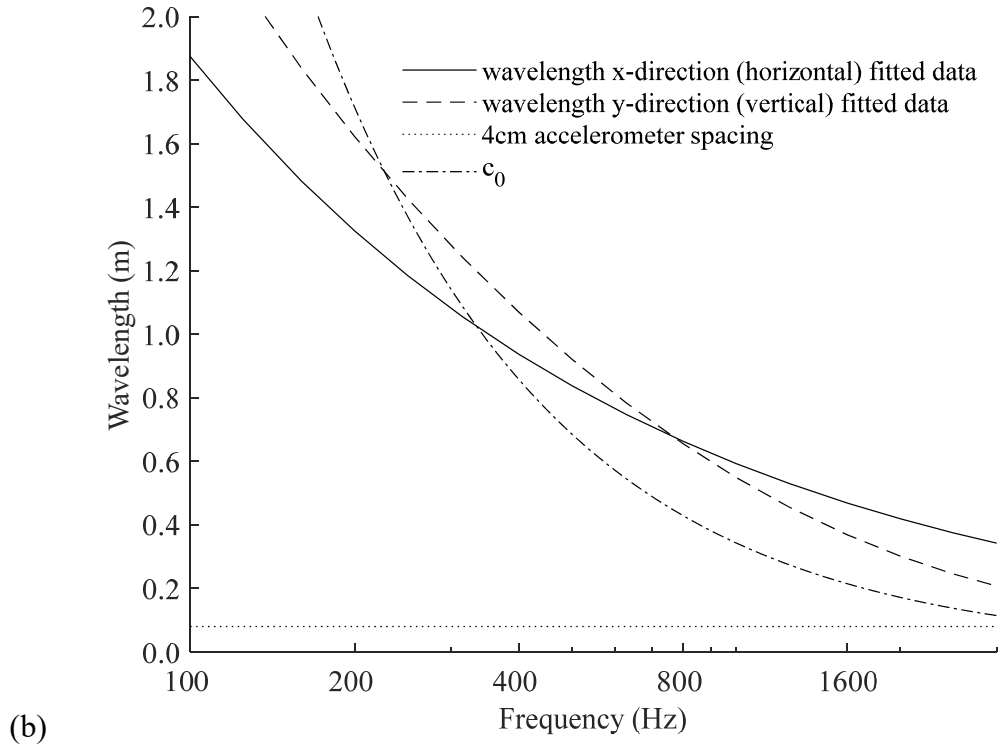

(b)

Figure 4-16 Bending wavelength for 80mm CLT in the horizontal and vertical directions (a) uncorrected data (b) corrected data.

The calculated moduli provide a smoother function than the measured data and can be extrapolated below 250Hz and above 2500Hz (frequency limits for the measured direct bending wavespeed). The frequency-dependant moduli are reduced in comparison with the frequency-independent values. The frequency-dependant moduli can be substituted into an isotropic thin plate calculation. For an orthotropic model, the frequency-independent modulus in the *x*-direction (E_x) can be used together with a frequency-dependant modulus determined from a back calculation of Eqn. (2-58) of the bending phase speed ($c_{y,\text{thick}}$) in the *y*-direction.

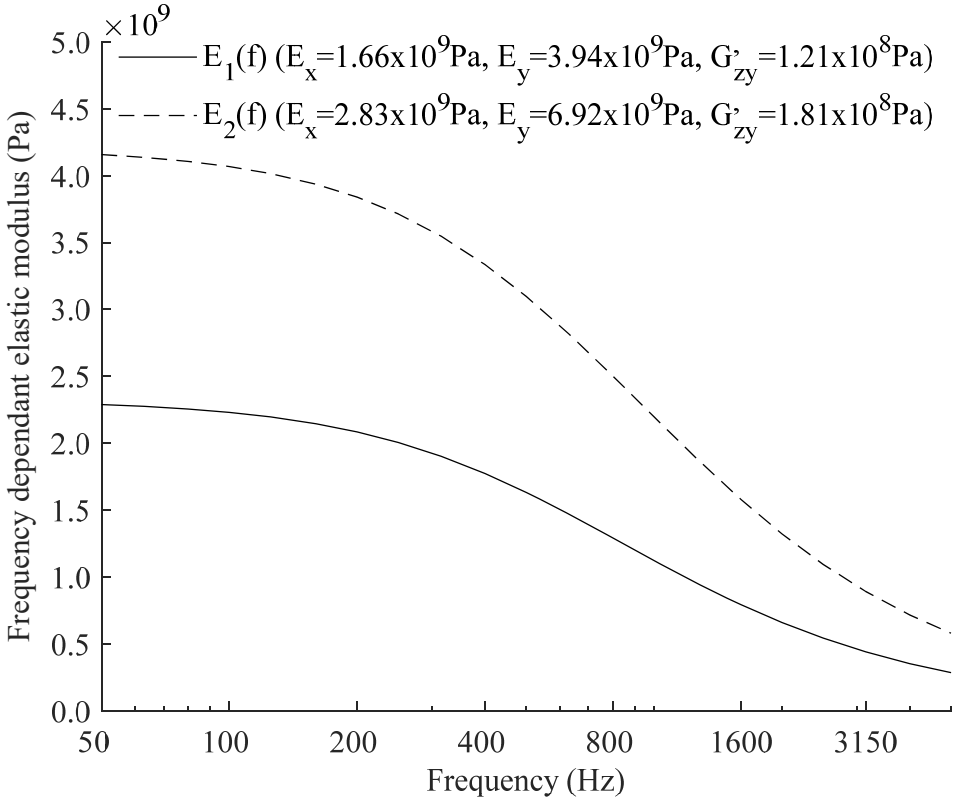

Figure 4-17 Frequency-dependant elastic moduli.

4.7.6 Modal density

The calculated modal densities are presented in Figure 4-18. Thin plates result in a frequency independent modal density. The modal densities determined from the bending wavespeed measurement rise with frequency because of the frequency dependant modulus. The modal densities determined from the numerical data

calculated using FEM are a limited data set and it's difficult to conclude that there is a significant rise in the modal density when using S4R elements (No change in modal density would be expected when using the STRI3 elements). The rise in modal density may need to be considered in a SEA model of CLT plates, for example where the consistency relationship is used. In general care must be taken when dealing with thick plates not to inappropriately implement equations which rely on the assumption of the plate being thin.

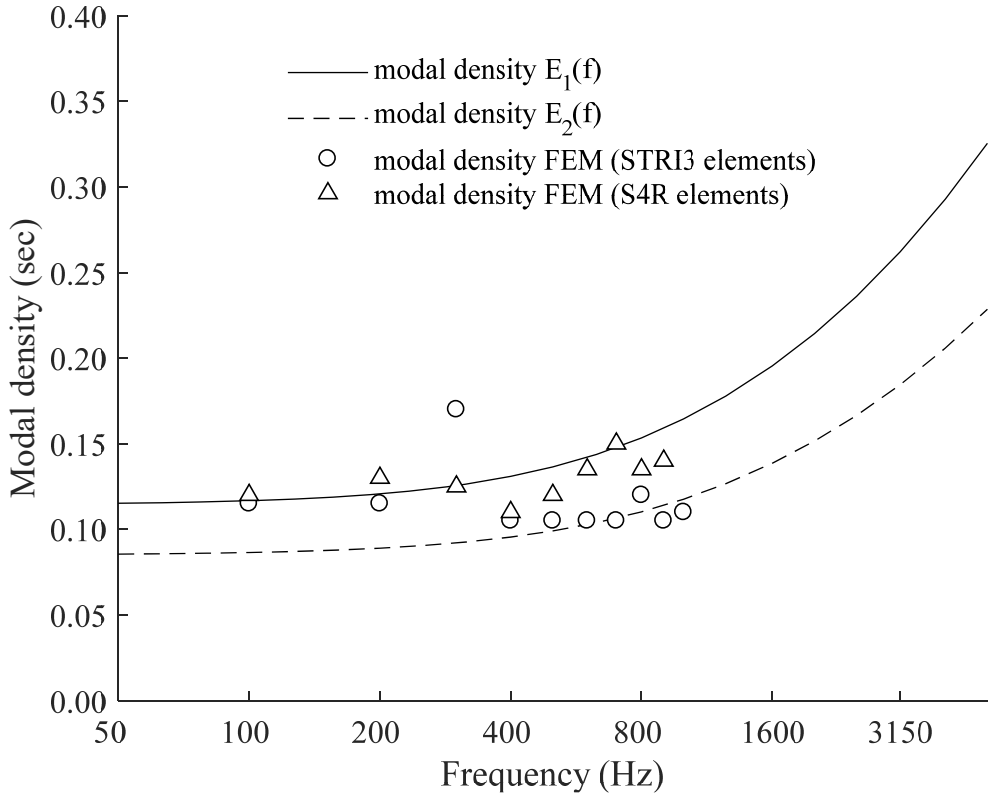

Figure 4-18 Comparison of calculated modal densities.

4.7.7 Frequency ranges of applicability of the Kirchhoff thin plate and Mindlin's first order shear deformation theories

The results in section 4.7.3 show that thin plate elements in the FEM model are inefficient at frequencies above ~123Hz for the CLT plate. The limitation of the thin plate elements is such that they are likely to fail within the range of applicability of the equivalent analytical model [69] (i.e. the upper frequency of applicability is reduced for FEM compared to the equivalent analytical model). The shear wave

cross-over frequency was made for the elastic constants in the *y*-direction was calculated to be in the 500Hz third octave band. Transitions between the thin and thick plate theories and between Mindlin's first order theory and higher order theories occur slowly and the lower order analytical theories are expected to give reasonable estimates for the airborne transmission of a plate at frequencies greater than f_S.

The expected ranges of applicability of the Kirchhoff thin plate and Mindlin's first order shear deformation theories were described in section 4.6.4. The plateau of the bending wavespeed in the *y*-direction was calculated (by inserting infinity in to the fitted function) to be 526ms^{-1} for the uncorrected data and 642ms^{-1} for the corrected data in section 4.7.5. This results in an estimated mean dilatational wavespeed of ~1343±114ms^{-1}. Therefore, the calculated first antisymmetric resonance is 16780±1425Hz. The frequency range of applicability was $0 \leq f_{t,\text{thin}} \leq 1678 \pm 143$Hz for thin plate theory and $0 \leq f_{t,\text{thick}} \leq 25170 \pm 2138$Hz for Mindlin's first order theory.

The low shear modulus (G_{yz}) means that there is a transition to a thick plate model (at least in the y-direction) within the building acoustics range (50-5000Hz). Subsequent sections address the question of how to determine airborne transmission of the CLT panel. There is a considerable body of work devoted to higher order shear deformation theories [119]. However, given the calculated frequency ranges of applicability of the theories, Mindlin first order theory is a sufficiently high order theory for this thesis.

4.7.8 Airborne transmission results

4.7.8.1 Isotropic airborne transmission models

The SRI of the isotropic models is compared with laboratory measured data in Figure 4-19. For SEA models 1a (315Hz to 1.6kHz), 1b (315Hz to 1.6kHz), and 1c (315Hz to 1.6kHz), the average difference in terms of magnitudes between measurements and predictions from the one-third octave band data are 5.2dB, 2.4dB and 3.9dB respectively (and the average differences considering positive and negative values are the same). Model 1a uses a frequency-independent elastic modulus but fails to predict the SRI at 200Hz and above 400Hz. The dip in the

predicted data due to the critical frequency is much lower than the apparent dip in the measured data. This confirms the findings of Krajči *et al.* [1].

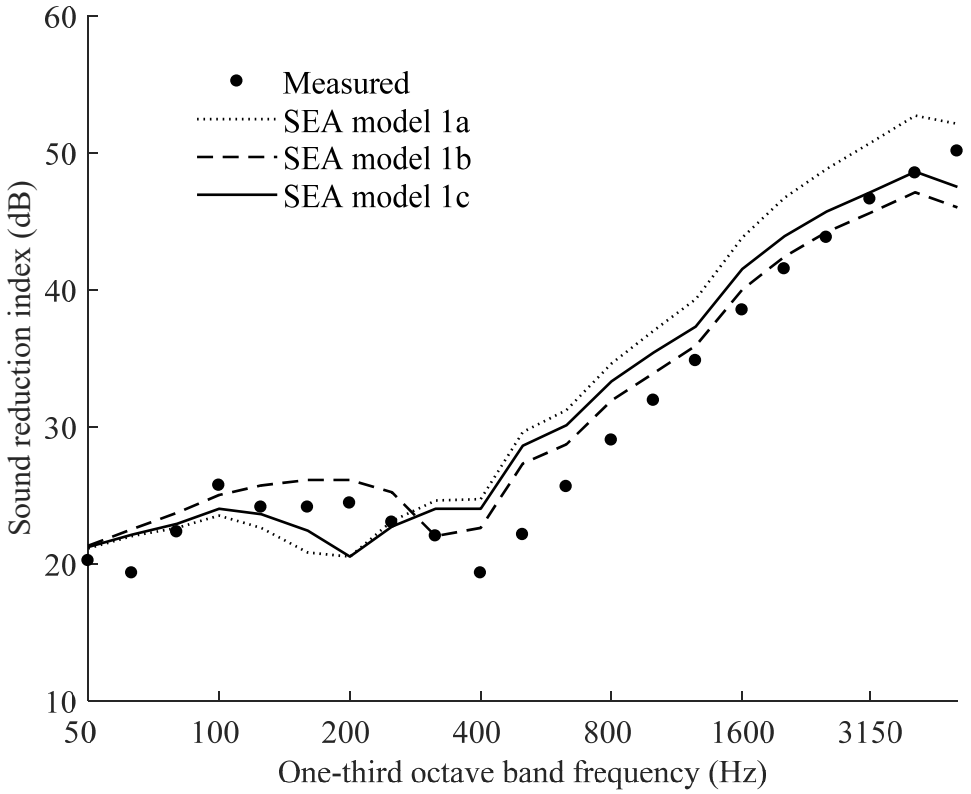

Figure 4-19 Comparison of measured airborne transmission with isotropic prediction models.

The closest agreement is obtained by model 1b using the frequency-dependant modulus $E_1(f)$ obtained using the uncorrected measured data in section 4.7.5. In this case the frequency-dependant modulus has the effect of increasing the width of the critical dip and shifting it upwards. Model 1c using the frequency-dependant modulus $E_2(f)$ obtained using the corrected measured data agrees slightly less. At 5000Hz the airborne sound insulation reaches a plateau for all the prediction models but not the measurements. The frequency-dependant modulus affects the resonant transmission only. Non-resonant transmission (apart from the increased critical frequency) changes little between the models. Models 1b and 1c capture a frequency-dependant effective modulus of a panel that is thick in "one direction" only (the *y*-direction). To apply this model to other panels it seems likely that each

new CLT panel would have to be measured individually to determine the frequency dependency for that specification.

The single-number quantities in terms of $R_w(C;C_{tr})$ are rated using ISO 717-1 [99] over the frequency range from 100Hz to 3.15kHz. $R_w(C;C_{tr})$ is 30(-1;-3) dB for the laboratory measurement, 34(-1;-5) dB, 32(-1;-3) dB and 33(-1;-4) dB for SEA models 1a, 1b and 1c respectively; the difference is therefore 2.0dB for the best performing model. The adverse deviations that occur in the calculation of the single-number quantity are between 315Hz and 1.0kHz for the measurement, between 160Hz and 800Hz for model 1a, between 315Hz and 1.25kHz for model 1b, and between 200Hz and 1.0kHz for model 1c.

4.7.8.2 Orthotropic transmission models

The SRI of the orthotropic models is compared with laboratory measured data in Figure 4-20.

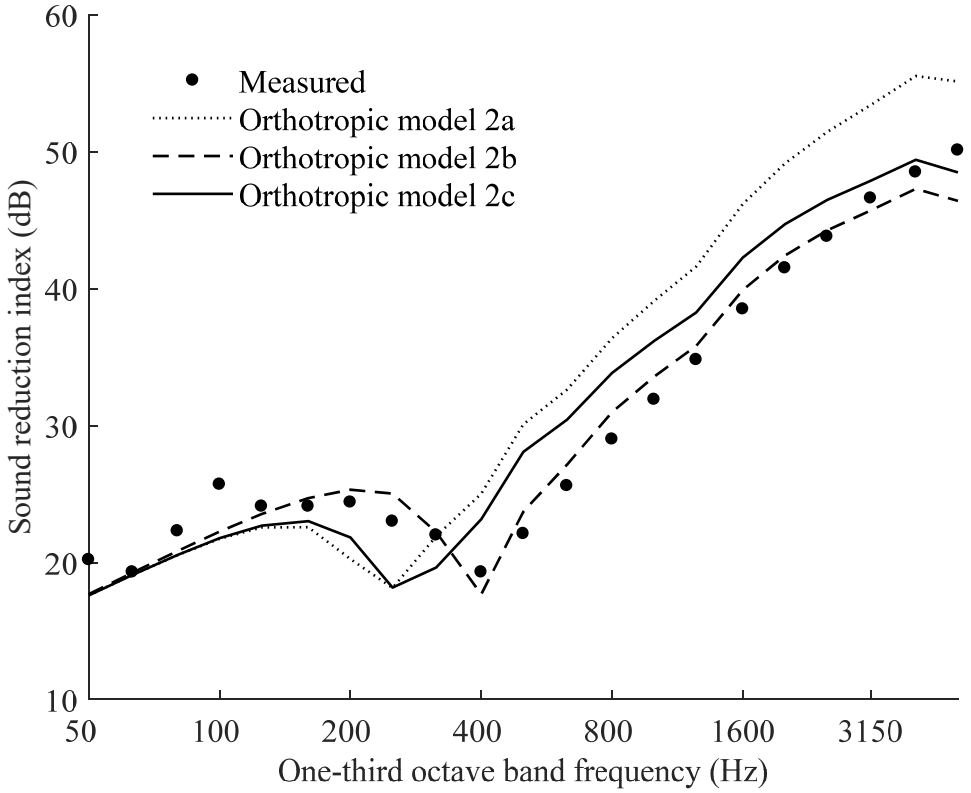

Figure 4-20 Comparison of measured airborne transmission with an orthotropic prediction model.

For orthotropic models 2a (315Hz to 1.6kHz), 2b (315Hz to 1.6kHz), and 2c (315Hz to 1.6kHz), the average differences in terms of magnitudes between measurements and predictions from the one-third octave band data are 6.2dB, 1.4dB and 4.2dB respectively, and the average differences considering positive and negative values are 6.2dB, 1.0dB and 3.6dB. Orthotropic model 2a shows less agreement with measured SRI when compared with the isotropic models. In this application, frequency-independent elastic moduli are also shown to be deficient in predicting airborne transmission. This also agrees with the findings of Krajči *et al.* [1]. Model 2b relies on an uncorrected frequency-dependant modulus calculated from direct measurement of the bending wavespeed data and this shows a significantly improved agreement with measurements. Model 2c which relies on a corrected frequency-dependant modulus calculated from direct measurement of the bending wavespeed data shows a slightly improved agreement with measurements.

The single-number quantities in terms of $R_w(C;C_{tr})$ are rated using ISO 717-1 [99] over the frequency range from 100Hz to 3.15kHz. $R_w(C;C_{tr})$ is 30(-1;-3) dB for the laboratory measurement, 33(-1;-5) dB, 31(-2;-4) dB and 32(-1;-5) dB for orthotropic models 2a, 2b and 2c respectively; the difference is therefore 1.0dB for the best performing model. The adverse deviations that occur in the calculation of the single-number quantity are between 200Hz and 630Hz for model 2a, 315Hz and 1kHz for model 2b and between 200Hz and 800Hz for model 2c.

4.7.8.3 Thick plate transmission models

The SRI of the thick plate models is compared with laboratory measured data in Figure 4-21. Applying the correction of Ljunggren [54] to SEA model 1a in the bands above the critical frequency (>250Hz) slightly improves the airborne transmission prediction. This is model 3a shown in Figure 4-21; there is only a slight improvement at frequencies above 2kHz. Below the critical frequency of the plate and in the 315Hz to 1.6kHz range (important for the single number rating) these results show little or no deviation from the isotropic thin plate model.

From thick plate theory, the airborne transmission would be expected to plateau towards the first thickness resonances (symmetric 8390Hz, anti-symmetric 16780Hz)

and then at some higher frequency to resume an increase with frequency again [54]. This was not observed as this was above the frequency range of measurements. An isotropic thick plate theory is not adequate to explain the reduced airborne transmission in the measurement.

The single-number quantities in terms of $R_w(C;C_{tr})$ are rated using ISO 717-1 [99] over the frequency range from 100Hz to 3.15kHz. $R_w(C;C_{tr})$ is 30(-1;-3) dB for the laboratory measurement, 34(-1;-5) dB and 33(-1;-4) dB for orthotropic models 1a and 3a respectively; the difference is therefore 3.0dB for the best performing model. The adverse deviations that occur in the calculation of the single-number quantity are between 200Hz and 800Hz for model 3a.

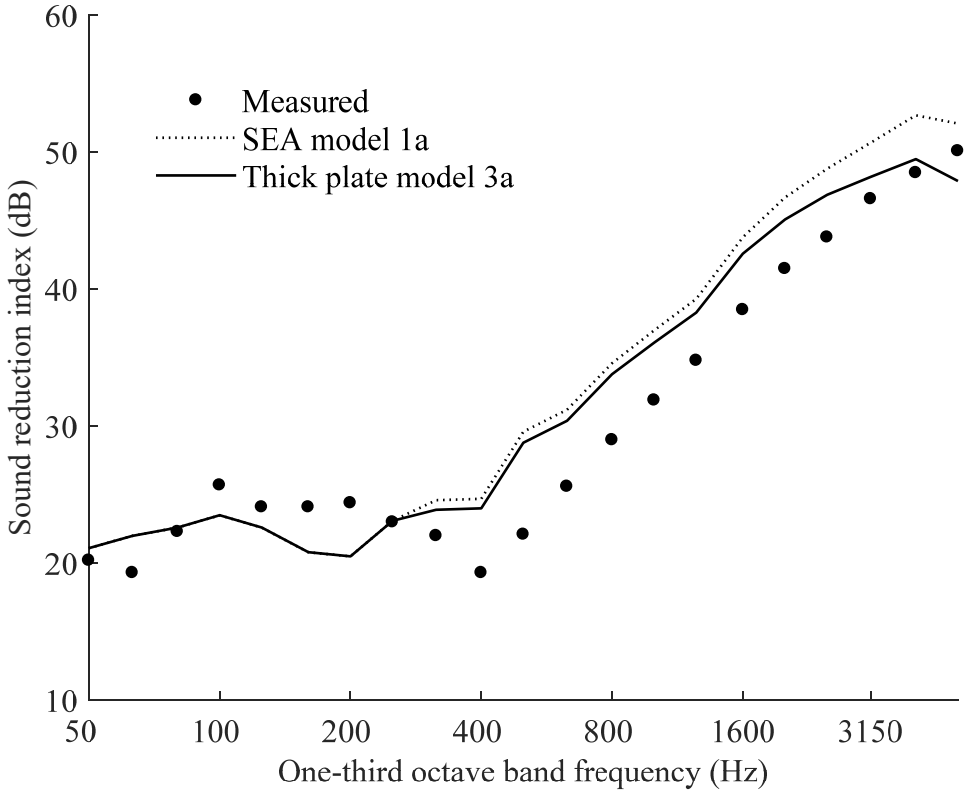

Figure 4-21 Comparison of measured airborne transmission with a thick plate prediction model.

4.8 Conclusions

Four methods to determine the elastic constants of a CLT plate were assessed from which a frequency-dependant elastic modulus (uncorrected for diffuse phase) determined by direct measurement of the bending wavespeed resulted in isotropic and orthotropic airborne transmission models which gave the closest agreement with measured airborne transmission. The method using time of flight measurements was not suited to measurement of multilayer specially orthotropic panels (such as CLT), and is not considered further.

The methods to measure the modal frequencies of a CLT panel and optimise the elastic constants using FEM or a Rayleigh-Ritz technique gave optimised elastic constants which were reasonably close to those calculated from the raw material. The optimised E_x is within 3% of that calculated from the material constants of the raw material and the optimised E_y is within 8-29% of that calculated from the raw material depending on Poisson's ratio used to optimise the constants.

In a CLT panel the ratio of the low-frequency elastic constants of the whole panel (E_x:E_y~1:4) is reduced as compared with the raw material (E_T :E_L ~1:30 using data provided by the manufacturer). Optimisation to frequency-independent moduli is accurate for the first eleven measured eigenfrequencies. The low G_{yz} modulus meant that the FEM thin plate elements failed due to shear locking in the frequency range >123Hz. The value of the elastic modulus determined in the y-direction (E_y) is affected by the assumed Poisson's ratio (ν_{xy}) in bending. The Poisson's ratio (ν_{xy} =0.04) in bending for CLT was calculated from the values in tension provided in the literature. The value of the G_{xy} modulus obtained using the Rayleigh-Ritz method is affected by the number of terms used to define the characteristic beam functions.

The fourth method to determine the elastic constants of the CLT plate is the direct measurement of the bending wave speed. This was carried out at higher frequencies (315-3150Hz). The aim of this measurement is to measure the phase of the direct field; however nearfield and diffuse fields are also present on the plate. The nearfield presents a problem at low frequencies because of the long distances required to remain out of it. The estimated mean reverberation distance across the building

acoustics range (50-5000Hz) was ~42cm. A distance between the receiver and source positions within this limit could be expected to contain little or no diffuse field contribution. However, a correction by applying only a small amount of diffuse phase using Eqn. (4-10) (with a low G_{Bessel} coefficient) dramatically affects the values of the elastic moduli extracted from the data. Before diffuse phase correction values of Young's modulus (E_x and E_y) are approximately 50% lower than those obtained in sections 4.7.3 and 4.7.4 and the value of G_{yz} is approximately 90% of the value in the literature [102]. The physical mechanism, such as whether measurement is affected by diffuse phase described by Roelens *et al.* [116], remains an open question. However, the numerical correction can be used to match the high frequency elastic coefficients determined from directly measured propagating phase data to the low frequency coefficients. After diffuse phase correction Young's modulus are approximately 90% (E_x) and 80-100% (E_y) of the values obtained in sections 4.7.3 and 4.7.4 and the value of G'_{yz} is approximately 130% of the value in the literature. In the horizontal (x-) direction, reasonable agreement is obtained with thin plate theory up to 2500Hz. In the vertical (y-) direction, a thick plate theory is required to model the bending wavespeed.

Although direct measurement of the bending wavespeed data is used in this chapter the main problems are setting the measurement parameters like distance from the source, distance between the accelerometers, window length and correction coefficients due to the diffuse field contribution without biasing the results. Difficulties of measurement are compounded by the inhomogeneity of the plate. Noise in the data, thought to be due to specular reflections at glue-lines, also limits the accelerometer spacing. Consequently, the resulting elastic constants have large uncertainties. There is also subjectivity when examining the data in selecting what frequency range to use in the least squares fitting of a thin or thick plate modelling curve to determine the Young's and shear modulus.

It is not possible to make accurate predictions of the airborne sound insulation of CLT panels from the elastic constants of the timber provided by the manufacturer ($E\parallel$, $E\perp$, and G) such as those usually determined during the grading process or values determined from measurement of the low-frequency modes of the plate. As a

minimum requirement, the values of the shear constants G_{xz} and G_{yz} are also required particularly at high frequencies (>250Hz). The shear constants can be determined from small panel tests [102], testing of large panel higher modes (in the case of the panel tested here modes >250Hz), strip tests [100] or direct measurement of the bending wavespeed. CLT has low shear moduli values compared to other building materials such as concrete or masonry.

The results of isotropic, orthotropic and thick plate theory were compared. The frequency-dependant moduli determined from uncorrected bending wavespeed data were found to give improved values of airborne transmission compared with those determined from the modal frequencies (or the corrected bending wavespeed data). The model which gave the closest agreement with the measured airborne sound insulation was orthotropic model 2b. In this model, the Young's modulus was measured to be approximately 50% less stiff than the modulus calculated from the modes.

Elastic modulus input data "b" is closest to the laboratory measurement single number quantity (in the isotropic and orthotropic models). This is because the weighting curve places emphasis on the low to mid frequencies whereas much of the disagreement between the laboratory measurement and models is due to the mid to high frequency range. Therefore, the single number quantities, R_w [99] were not an adequate reflection of the accuracy. The adverse deviations for determining the R_w occur around the region of the critical frequencies of the plate. Increased emphasis on the low frequencies such with the implementation of the A-weighted urban traffic noise spectrum (C_{tr}) results in a significant reduction (-3dB to -5dB) in the single figure values compared to the ISO 717-1 [99] standard spectrum adaptation term.

Orthotropy in a plate is known to cause a widening in the dip in the airborne sound insulation because there are effectively two critical frequencies [17]. Also, the shear motion of thick plates can act to shift the critical frequency dip to higher frequencies [17]. The orthotropic and thick plate behaviour of CLT plates is likely to be found in other layered products including those with a relatively thick core or products with many layers [17] and may also be observable in other similar materials including but not limited to wood products. The point mobility of a freely suspended and simply

supported CLT plate and prediction of the transmission coefficients of CLT installed in simple L- and T-junctions is investigated in chapter 5.

5 Prediction of structure-borne sound transmission across junctions of cross laminated timber plates

5.1 Introduction

The aim of this chapter is to apply FEM to predict the point mobility of a CLT panel and to determine the coupling loss factors for flanking transmission across T- and L-junctions of connected CLT panels. The applicability of the elastic moduli determined in chapter 4 are considered (except those determined from time of flight measurements) even though the low-frequency constants did not result in accurate values for the airborne sound insulation when incorporated in existing theories. This is carried out because it is anticipated that the low-frequency elastic moduli determined from the modal data (or high frequency constants estimated from the directly measured phase data after a correction for diffuse phase has been applied) would be most appropriate to model the flanking transmission across simple junctions in the frequency range 50-800Hz.

For the plate mobility, the effect of the plateau in the bending wavespeed in the y-direction is assessed. The plateau of the bending wavespeed at high frequencies for thick plates affects the modal density. As the bending wavespeed plateaus the modal density is no longer constant but increases as a function of frequency. A linear elastic model is used to study the plate. The first few modes (<50Hz) and a convergence analysis of the calculated mobility of a freely hanging plate (<100Hz c.f. 600Hz-1000Hz), simply supported plate (<100Hz c.f. 600Hz-1000Hz) and T-junction (500-700Hz) is carried out to determine if an increasing number of modes at frequencies higher than the range of interest affects the calculated point mobility due to a stiffness contribution from higher modes. This is known as the contribution of

"residual modes" [22]. For thin plates, residual modes only affect the stiffness contribution between sparsely populated modes when the modal density is low. Unlike thin plates the contribution of residual modes to the peak mobility in the problems presented are not thought to be negligible.

L- and T-junctions are modelled with point and line connections and compared with laboratory measurements. An assessment is made to determine the error envelope due to the modal rather than the statistical distribution of energy [12]. The difficulty to model boundary conditions was assessed by comparing models with and without the inclusion of springs to the edges of the plates.

Previous work [120] on CLT indicates that the EN12354 methodology is appropriate for CLT panels when using a measured airborne transmission coefficient. It would indeed be useful if this standard could be applied to other materials which fall less clearly into heavyweight or lightweight categories (such as CLT or combined heavyweight and lightweight elements such as HBV).

5.2 Test Samples

The single CLT panel used for measuring point mobility is described in detail in section 4.2. Additionally, two L-junctions were built using two 80mm thick CLT plates (4.0m x 3.0m and 3.4m x 3.0m) connected using 160mm long screws to connect the plates at 400mm centres. Two lines of adhesive were also used to ensure a strong connection at the edge of the two plates (see Figure 5-2). This method of connection would be used in normal practice. The specification of the plates was nominally identical to that described in section 4.2. L-junction No. 1 (see Figure 5-1) was formed by cutting the T-junction described below.

L-junction No. 2 was created by cutting the first L- junction and rotating the 3m x 4m plate by 90° so that the outside laminate was in the horizontal rather than vertical direction and cutting it to size to form a second L-junction with one vertically oriented plate of size 3.25m x 3.0m and one horizontally oriented plate of size 3.0m x 3.0m. The plates were connected in the same way described above.

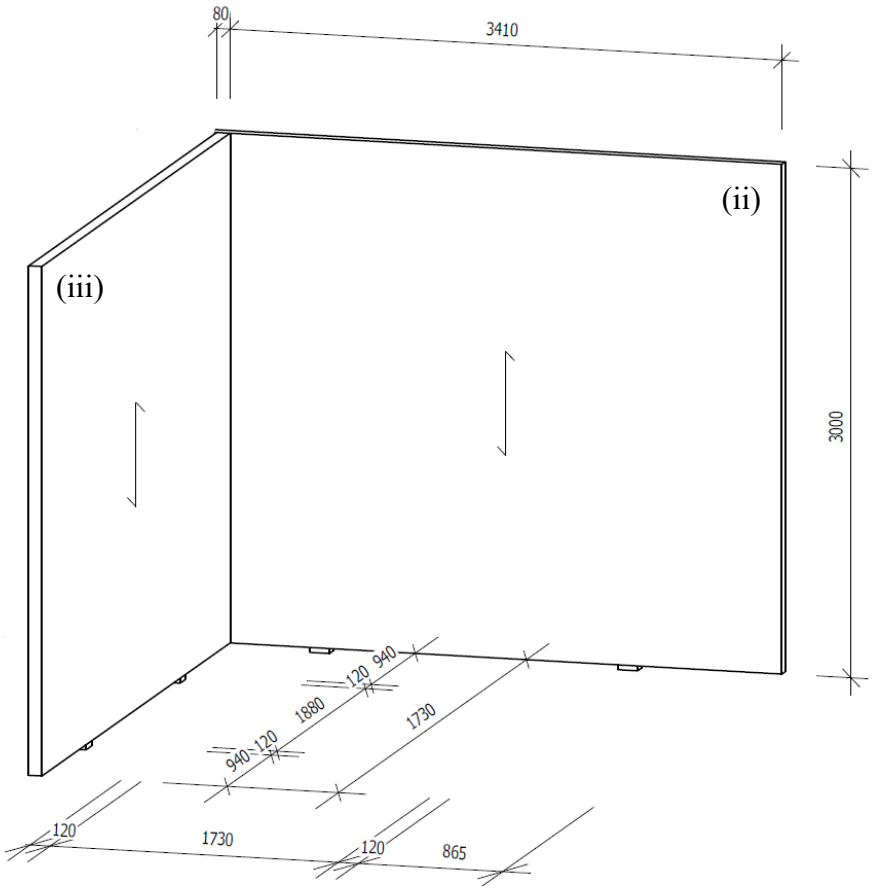

Figure 5-1 L-junction No. 1 installed in the laboratory space (the walls are labelled (ii) and (iii)) (adapted from Lignum drawings, Adrian Burkhardt)

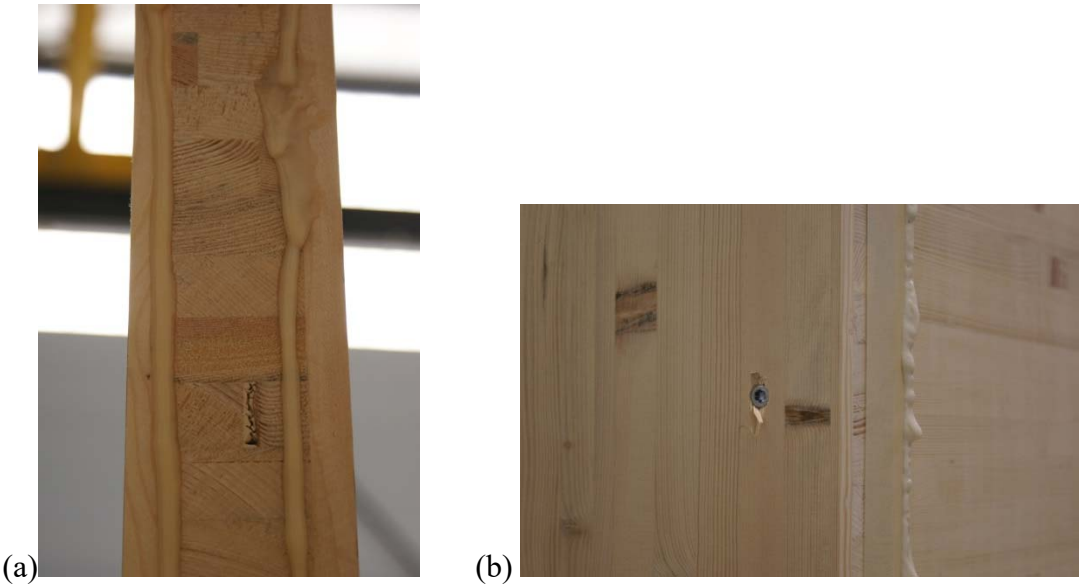

Figure 5-2 Photos showing assembly of the measured T- and L- junctions (a) lines of adhesive (b) point connections (160mm long screws)

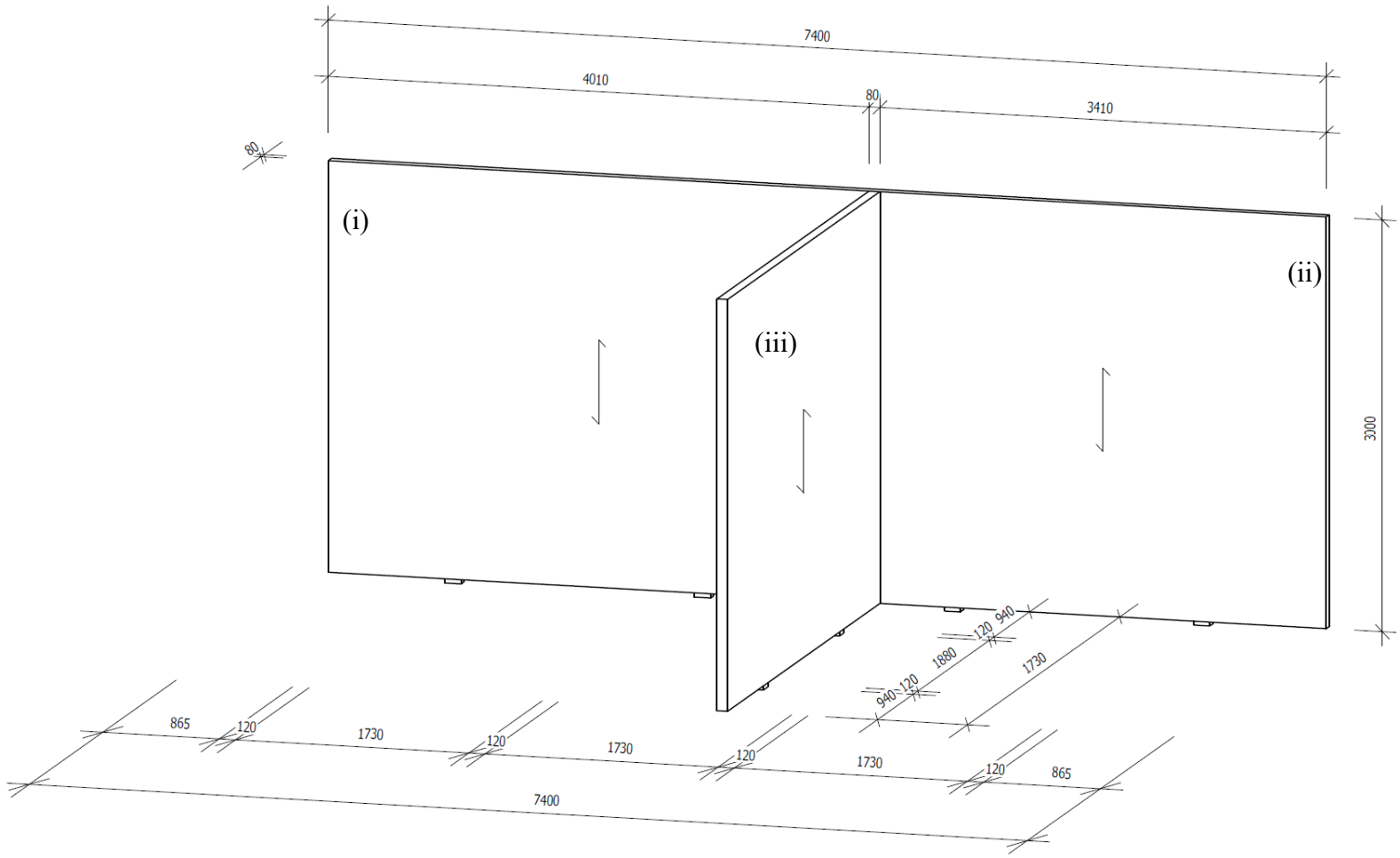

Figure 5-3 T junction installed in the laboratory space (the walls are labelled (i), (ii) and (iii)) (reproduced from Lignum drawings, Adrian Burkhardt)

The T-junction (Figure 5-3) was also built with 80mm thick CLT plates. The 7.48m x 3.0m plate was connected to a cantilever plate with dimensions 4.0 m x 3.0 m. Thus, segmenting the larger plate into 4.0m and 3.4m length plates (not counting the 80mm width of the junction). The plates were connected as described above for the L-junction. All junctions were free standing in the laboratory. One pair of rubber mounts was located under each of the walls and a single rubber mount under the junction line itself to isolate the junction from the concrete floor.

5.2.2 Material input parameters

Material properties	Value
Young's modulus (E_x)[1]	3.1×10^9 Nm^{-2}
Young's modulus (E_y)[1]	7.7×10^9 Nm^{-2}
Young's modulus (E_z)[2]	3.9×10^8 Nm^{-2}
Shear modulus (G_{xy})[1]	5.9×10^8 Nm^{-2}
Shear modulus (G_{yz})[3]	1.39×10^8 Nm^{-2}
Shear modulus (G_{xz})[3]	6.78×10^8 Nm^{-2}
Poisson's ratio (v)[4]	0.03
Section Poisson's ratio ($v_{section}$)[5]	0.3

Table 5-1 Material properties of the CLT plate implemented in the FEM models. [1]Selected from Figure 4-10, [2] calculated mean taking the lowest Young's modulus values from the literature see Table 4-4 (this value would be calculated for a whole panel of different material layers using the "law of mixtures" (Eqns. (2-134), section 2.2.11) however since E_z is assumed to be the same for each layer the calculation is trivial), [3]for a nominally identical panel taken from [102], [4]estimated equivalent in bending [5]estimated from the literature see Table 4-4 (also note "law of mixtures", Eqns. (2-137) and (2-138), section 2.2.11)

Material properties were obtained from the modal analysis of suspended CLT plates described in sections 4.7.3 and 4.7.4 with additional required properties obtained

from the literature as indicated in Table 5-1. Note that Poisson's ratio in bending calculated in section 4.2.3 was used for the material definition however ABAQUS makes provision for a different Poisson's ratio to be assigned by the section definition and this was activated for these calculations. The section Poisson's ratio was determined by the "Law of Mixtures" described in section 2.2.11.

5.3 FEM modelling

5.3.1 Methodologies

5.3.1.1 General

ABAQUS was used to perform the FEM calculation using a two-step process. In the first step, the free modes of the plate and the mass-normalised mode shapes were determined. A subspace based method was used to extract the modes. The eigenfrequencies were calculated using the Lanczos solver and the SIM architecture was activated (these are default options in ABAQUS). This method extracts the modes in blocks and is a highly efficient algorithm for medium to high numbers of modes. In the second step, the modes were superposed to obtain the mobility and/or random response. In all cases, rigid body motions were excluded from the calculation. The models investigated are small and relatively uncomplicated one, two or three plate system structures with a relatively low number of output sampling points. In the investigated junction, the data collection points are physically close to the source (on the same or an adjacent panel).

The contribution of "residual modes" was assessed. To obtain the correct mobility, for some plates, a methodology to take account of the effects of residual modes is necessary. For a given frequency range, f_1 to f_2, where $f_1<f_2$, there are an infinite number of modes with resonance peaks at frequencies $>f_2$ in any system. The contribution within the range f_1 to f_2, from the stiffness region of the higher modes can be assessed by convergence analysis for the models; successively adding the contribution from modes with resonant frequencies $>f_2$.

5.3.1.2 FEM model 1: Driving-point mobility

ABAQUS mode-based steady-state dynamic analysis was used to determine the mobility of the freely hanging and simply supported plates for comparison with measurements. This method is appropriate for determining phase and magnitude data of the response of a system. This was used because it was computationally cheaper than the direct solution although it can be less accurate. It was assumed that a linear elastic model would be sufficient to model the plate behaviour. A frequency sweep loading is applied and the force is linear across the spectrum. Driving-point mobility is obtained using the velocity at the input node from the definition of point mobility. The transfer mobility for a plate can be stated as

$$Y(x,y) = \frac{v(x,y)}{F_0} \tag{5-1}$$

and the point mobility

$$Y_{dp} = Y(0,0) = \frac{v(0,0)}{F_0} \tag{5-2}$$

The damping was identified based on measured data. However, it was difficult to accurately determine the critical damping fraction of the modes from the peaks in the measured data for the two sets of boundary conditions. Improved agreement at low frequencies (<50Hz) between measured and modelled results was obtained when the critical damping fraction for the freely hanging plate was capped at 0.06. The simply supported plate had few peaks where the half power bandwidth could be ascertained to achieve an accurate measure. Instead an estimate of the critical damping fraction was made based on the envelope traced by the modal peaks. The estimates are compared against the measured data (determined using the peak picking method) for the freely hanging and simply supported plate in Figure 5-4 and Figure 5-5.

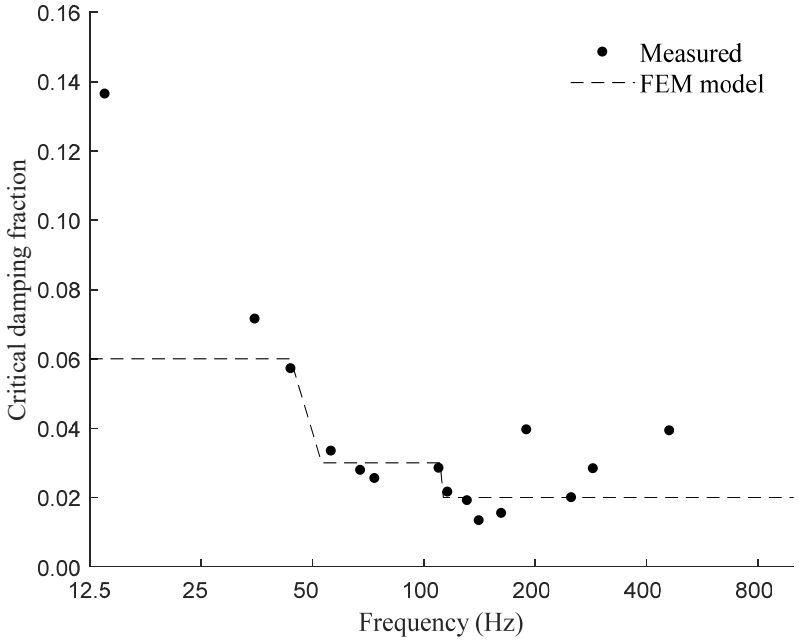

Figure 5-4 Critical damping fractions for the freely hanging plate

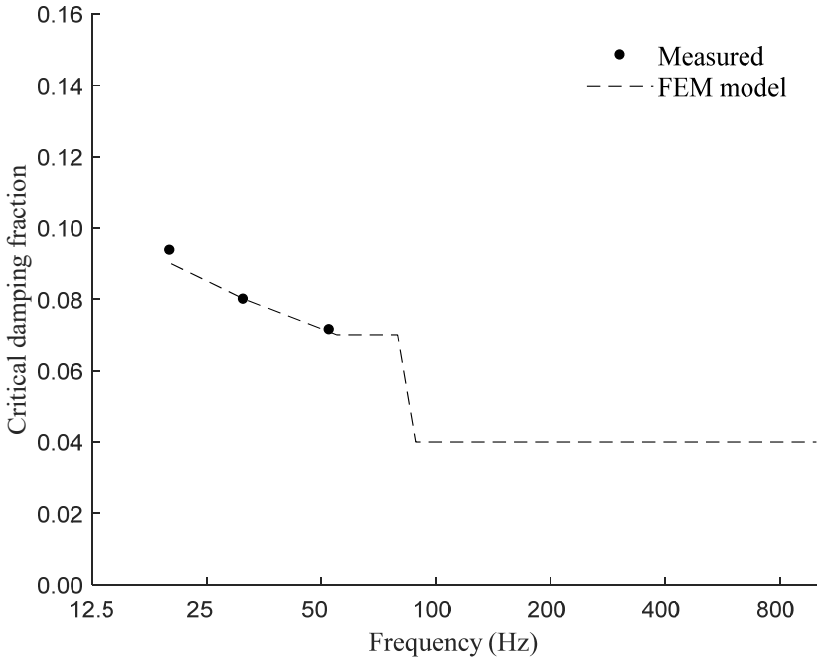

Figure 5-5 Critical damping fractions for the simply supported plate.

5.3.1.3 FEM models 2 and 3: Forced response of the T- junction

The random response analysis in ABAQUS was selected to model the junctions and determine the mean forced response for the long panel (walls (i) and (ii) combined) and short panel (wall (iii)) of the junctions as a preliminary and calculate the velocity level differences between the walls (i), (ii) and (iii). It was not possible to match the modes for the three walls separately because of the strong coupling between wall (i) and wall (ii). Unfortunately, the long panel (walls (i) and (ii)) was slightly undersized in the model (7.3m rather than 7.4m). For the low forces involved an approximation to a linear system is assumed to be reasonable. A flat Power Spectral Density (PSD) function using the same magnitude of the measured data in the frequency range 20-50Hz was specified as input at a single node (see Figure 5-6 for measured and modelled input forces). Any errors due to the frequency-dependent measured force input at low frequencies are expected to be negligible as the velocity is divided by the force to determine the measured mobility. Likewise, for the frequency-dependent force input above 600Hz (only the frequency range <700Hz is examined).

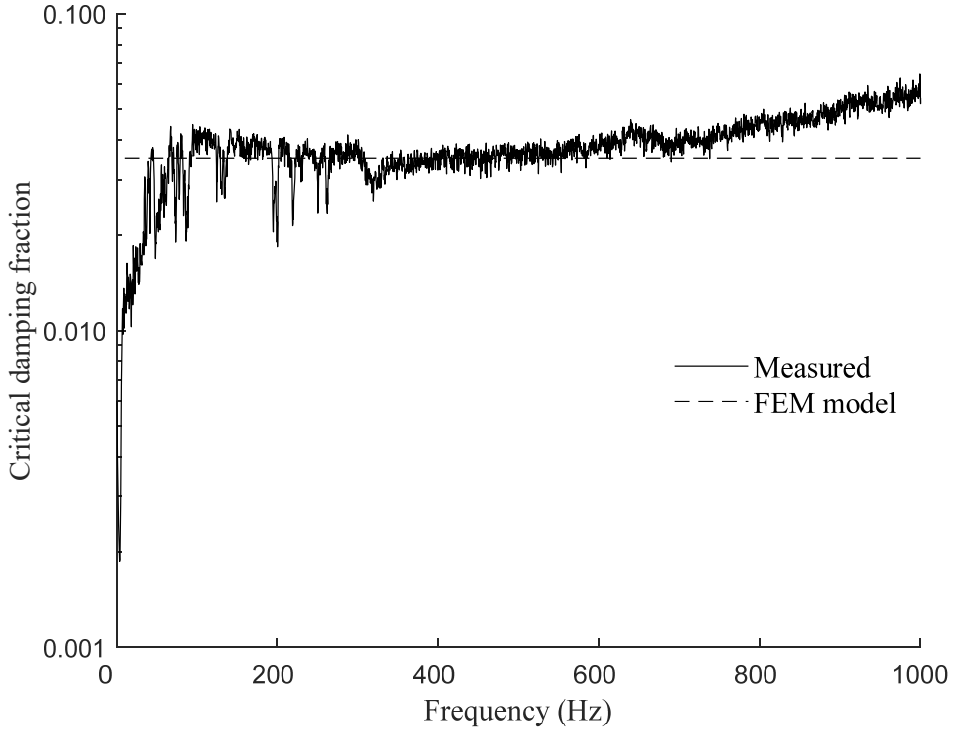

Figure 5-6 Measured force input compared with the modelled force input.

The critical damping fraction of the modes in the frequency range <50Hz was determined from measured data points using a peak picking method. The half peak bandwidth of individual modes in this frequency range was determined and the data interpolated to obtain estimated critical damping fractions for the first 24 modes. For the remaining modes, the critical damping fraction was set at 0.014 (to correspond with measured mean total loss factor). A plot of the critical damping fractions in the frequency range 0-50Hz is shown in Figure 5-7.

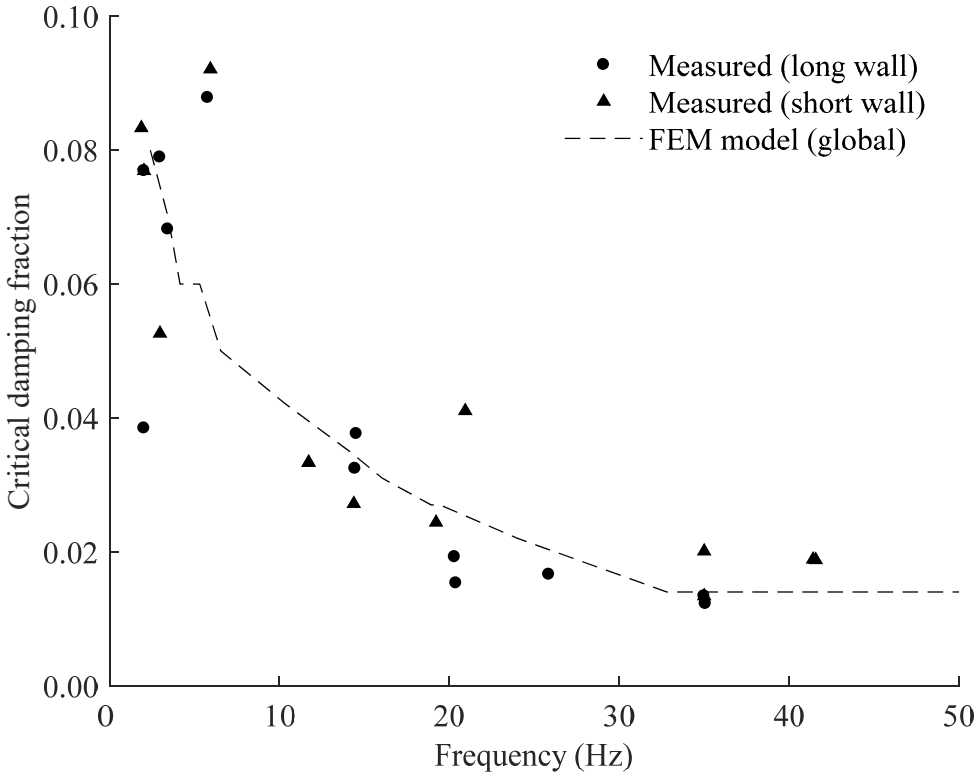

Figure 5-7 Estimated critical damping fraction in the frequency range 0-50Hz determined from measured data points using a peak picking method.

At low frequencies, it is possible to pick out individual modes of the whole junction or the long panel (walls (i) and (ii) combined) and short panel (wall (iii)) (<50Hz). The transfer mobility averaged over the entire modelled surface of each panel was compared with measured data averaged over the surface of each panel. Thirty-three modes were extracted for this purpose. In this frequency range (<50 Hz) a thin plate model is more appropriate and the modal density is constant across the frequency range. At higher frequencies (>50Hz) the accuracy of the calculated

eigenfrequencies was poor and the modal overlap too high to match individual modes.

The transfer mobility at each node of the long panel (walls (i) and (ii) combined) and the short panel (wall (iii)) is determined from the velocity using Eqn. (5-1). This is averaged over the surface of the wall to give the mean forced response (driving-point mobility) of the long panel (walls (i) and (ii) combined) and short panel (wall (iii)) from the alternative definition,

$$Y_{\mathrm{dp}} = \frac{\langle v(x,y) \rangle}{F_0} \tag{5-3}$$

5.3.1.4 FEM model 4: Velocity level difference of T- and L-junctions

The random response analysis in ABAQUS is applied as this is comparable to the measurement method. An identical excitation force and PSD function to that described in section 5.3.1.3 was used. All modes were calculated within the frequency range 50Hz-800Hz with the critical damping fraction set to 0.014. The upper frequency limit was set by the frequency at which modelling flaws due to the overly stiff behaviour of the mesh are observed for the in-plane modes. This becomes computationally expensive (>800Hz) as increased numbers of these modes are observed with increasing frequency.

Twenty nodes were selected with an even distribution over the plate surface (>0.5m of plate boundaries to avoid regions with higher energy density) to determine the average mean-square response. As noted in section 5.3.1.3 the long panel (walls (i) and (ii)) was slightly undersized in the model (7.3m rather than 7.4m).

5.3.2 Boundary conditions of thin plates and coupling conditions at the junction

In a FEM model, the plate boundary conditions are applied by restricting the degrees of freedom of individual edge nodes. For most calculations described in this chapter the junction was installed in a free space and no constraints at the boundaries were applied. The exception is the simply supported boundary condition for which the following restrictions were used at the plate edges.

$$u = v = w = 0 \tag{5-4}$$

Free boundary conditions for the lower plate edges are unlikely to exist in the experimental situation because of the rubber supporting mounts. Hence the actual boundary conditions of the plate were simulated by adding horizontal springs acting between one node on the plate and a rigid ground point at the locations of the rubber mounts. A comparison of the modes below 50Hz was made with and without these spring point connections. The FEM model did not include additional conditions due to the thickness of the plate.

The CLT junction was connected using long screw point connections at 500mm centres and glued. In the model, translational motion at the junction was not restricted. At the junction from one side of the long panel to the other (walls (i) and (ii)) the options are limited and all degrees of freedom are coupled. However, to join the perpendicular wall (iii) there are several possibilities. The junction could be modelled as a line or point junction and only translational or both translational and rotational degrees of freedom could be coupled. Four options were therefore tried to identify the appropriate connection in the FEM model.

Connection (a): All degrees of freedom of all the coincident nodes along the junction are coupled. Coincident nodes were coupled using the "TIE" constraint in ABAQUS with and without rotational degrees of freedom to model the two junctions. For each node:

$$\{u\}_{\text{plate i}} = \{u\}_{\text{plate j}} \tag{5-5}$$

$$\{v\}_{\text{plate i}} = \{v\}_{\text{plate j}} \tag{5-6}$$

$$\{w\}_{\text{plate i}} = \{w\}_{\text{plate j}} \tag{5-7}$$

$$\{\partial_{\text{x}} u\}_{\text{plate i}} = \{\partial_{\text{x}} u\}_{\text{plate j}} \tag{5-8}$$

$$\{\partial_{\text{y}} v\}_{\text{plate i}} = \{\partial_{\text{y}} v\}_{\text{plate j}} \tag{5-9}$$

$$\{\partial_{\text{z}} w\}_{\text{plate i}} = \{\partial_{\text{z}} w\}_{\text{plate j}} \tag{5-10}$$

Connection (b): Only translational degrees of freedom of all the coincident nodes along the junction are coupled; Eqns. (5-8) to (5-10) only.

Connection (c): All degrees of freedom at connection points corresponding to the point connection spacing are coupled. To model a point junction ABAQUS makes provision for point fasteners that are independent of the mesh and these were used to represent the screw point connections along the length of the junction. For the point junction, connections with a radius of 5mm were used in the FEM model. For each point connection:

$$\{u_{\text{point n}}\}_{\text{plate i}} = \{u_{\text{point n}}\}_{\text{plate j}} \tag{5-11}$$

$$\{v_{\text{point n}}\}_{\text{plate i}} = \{v_{\text{point n}}\}_{\text{plate j}} \tag{5-12}$$

$$\{w_{\text{point n}}\}_{\text{plate i}} = \{w_{\text{point n}}\}_{\text{plate j}} \tag{5-13}$$

$$\{\partial_{\text{x}} u_{\text{point n}}\}_{\text{plate i}} = \{\partial_{\text{x}} u_{\text{point n}}\}_{\text{plate j}} \tag{5-14}$$

$$\{\partial_{\text{y}} v_{\text{point n}}\}_{\text{plate i}} = \{\partial_{\text{y}} v_{\text{point n}}\}_{\text{plate j}} \tag{5-15}$$

$$\{\partial_{\text{z}} w_{\text{point n}}\}_{\text{plate i}} = \{\partial_{\text{z}} w_{\text{point n}}\}_{\text{plate j}} \tag{5-16}$$

Connection (d): Only translational degrees of freedom at connection points corresponding to the point connection spacing are coupled; Eqns. (5-14) to (5-16) only. Note that these connections only apply to wall (iii) because walls (i) and (ii) are modelled as a single panel.

5.3.3 FEM mesh

General element (thick or thin plate) S4R and (thick plate) S8R conventional elements were (both with reduced integration) compared with fully integrated S4 elements to model the freely hanging and simply supported CLT plates. For all other models only S4 elements were used. S4 elements could model a transition from thin to thick plate (at least in one direction if not both, see sections 4.7.5 and 4.7.7) within the building acoustics range (50 Hz to 5000Hz). In principle, S4R or S4 elements

could be used for the whole frequency range of interest. S8R elements are more accurate for modelling thick plates.

An element mesh density of 0.1m was used which corresponds to at least one-sixth of a bending wavelength up to approximately 700-1000Hz (depending on which measured bending wavespeed from section 4.7.5 is applied). A visual inspection of the modes was made to determine if the mesh density was sufficient. Hourglassing was controlled using the default settings in ABAQUS; a small amount of hourglassing can be permitted. Conventional plate elements were used to model the plate(s) and for this work a homogenous shell section is defined. Integration through the section is carried out before the analysis because it is assumed that the plate behaviour is linear. The moduli from Table 5-1 were implemented.

5.3.4 Outputs

The FEM output was compared against measured data. Four main models were constructed (summarized in Table 5-2):

Model 1: The driving-point mobility of the freely hanging and simply supported plates was calculated between 10 and 1kHz. The calculated driving-point mobilities from different element types were compared against measurements. Third octave band data was also compared against the analytical calculation model (described in section 2.2.8.2). A convergence analysis was performed to illustrate the influence of residual modes.

Model 2: Forced response of the T-junction (<50Hz) is examined. The outputs were the mean response including all nodes over the whole surface area of each of the two panels (the long panel (walls (i) and (ii) combined) and the short panel (wall (iii))). A comparison of the calculated modal frequencies was made with measured modal frequencies. Coupling conditions (a) and (b) at the junction were compared, as were completely free boundary conditions with boundary conditions which included a point spring to model the pairs of rubber mounts underneath the junction. The actual spring constant of the rubber mounts when acting in the direction specified was unknown and therefore estimated to be k=1.0x10^6 Nm^{-1}. (The actual spring constant data available for the mount was specified in the vertical rather than the horizontal

direction; which likely involved some shear movement of the mount and therefore was not used.)

Model 3: Forced response of the T-junction in the frequency range between 50 and 700Hz is examined. A convergence analysis of residual modes is performed.

	10-1000Hz	<50Hz	50-700Hz	50-800Hz
FEM model	**1**	**2**	**3**	**4**
Test object(s)				
Plate	x			
T-junction		x	x	x
L-junctions				x
Method				
Mode-based steady-state response	x			
Random response analysis		x	x	x
Boundaries				
Free	x	x	x	x
Simply supported	x			
Free with point springs		x		
Elements				
S4R shell	x			
S8R shell	x			
S4 shell	x	x	x	x
Junction				
(a)	-	x	x	x
(b)	-	x	x	x
(c)	-			x
(d)	-			x
Outputs				
Eigenfrequencies		x		
Driving-point mobility/ mean response	x	x	x	
Velocity level difference				x

Table 5-2 Summary of the four FEM models used in chapter 5.

Model 4: Vibration transmission across between the pairs of walls between 50 and 800Hz is investigated. To determine the velocity level difference twenty measurement points randomly selected from the regular rectangular nodal grid and

distributed evenly over each measurement surface (>0.5m from the edges of the plate) of the three walls (i), (ii) and (iii) were calculated.

5.3.5 Assessment of low frequency fluctuations

The frequency below which peaks may occur in the vibration level difference data due to the modal properties of the receiving subsystem is estimated by $M<2/\pi$ [12], where M is modal overlap (third octave band frequencies less than ~500Hz). The upper limit of the peaks is estimated using [12]

$$\text{upper limit} = 20\text{lg}\left(\frac{N}{N_{\text{statistical}}}\right) \tag{5-17}$$

where N is the number of modes for each third octave band (in this case calculated from FEM, the number of global modes within the third octave band is used), $N_{\text{statistical}}$ is the number of modes per third octave band calculated from a statistical modal density and $<Y_j>$ is the mean wave mobility of the receiving subsystem j. The lower limit of the troughs is estimated using [12]

$$\text{lower limit} = 20\text{lg}\left(\frac{4M}{\pi}\right) \tag{5-18}$$

5.4 Measurement Methods

5.4.1 Driving-point mobility

Values of the driving-point mobility measured in the central part of a freely hanging and a simply supported CLT plate were measured. The measured upper frequency limit was 1000Hz. At this limit the bending wavelength (taken from Figure 4-16) is 0.46-0.59m (depending on which measured bending wavespeed from section 4.7.5 is applied) therefore (assuming $a\approx10$mm) the requirement that $k_B a<<1$ [49] is fulfilled although at the shorter wavelength the factor of ten that is usually implied by use of "<<" is not satisfied. The cut-off frequency above which the force spectrum of the impulse hammer is no longer flat is ~600Hz (see Figure 5-6).

5.4.1.1 Freely hanging plate

To try and achieve free boundary conditions around all edges the CLT plate was suspended from a crane in the laboratory via a single hole at the top of the plate which was 20cm from the upper edge (see Figure 4-3). To ensure stability and prevent rotational movement, the lower left and right corners rested on 10cm thick glass wool. The weight compressed the glass wool by about 2cm. The point mobility of the CLT plate was measured at 13 measurement points over the central part of the plate (>0.40m from the plate edges). A 200g impulse hammer (PCB 086803) was used as the excitation source, (the "blue Elastomer" tip was used). One accelerometer (PCB 352C22) was used to record the measurement signal. The impulse hammer was used to strike the wall as close to the accelerometer as possible. The excitation area of the source was assumed to be a circle with a radius equal to the distance between the force hammer and accelerometer, the distance was not measured however it was estimated to be approximately 10mm. A three channel RTA (B&K photon II) was used to record the mobility magnitude, phase and the coherence between the measured signal from the force hammer and the accelerometer. The signal was windowed using an exponential window and an average from ten measurements was made at each measurement point. The results of these measurements are presented in section 5.5.1.1.

5.4.1.2 Simply supported plate

The CLT plate was installed in the horizontal transmission suite described in section 4.5. It was installed in the concrete filled steel test aperture as would normally be used for testing and the gap between the wall and frame was sealed with a roll of Prestik Kitt putty. The mobility was measured in the same manner as described in the previous section 5.4.1.1. The distance between the force hammer and accelerometer was not measured. The results of these measurements are presented in section 5.5.1.2.

5.4.2 Modal analysis of the T-junction

A similar methodology to that described in section 4.4.2 for a CLT plate was used to determine the response of the long panel (walls (i) and (ii) combined) and short panel

(wall (iii)) in the T-junction. In this case, however the dimensions of the T-junction meant it was difficult to suspend it so the same support conditions (i.e. rubber mounts) were used as described in section 5.2.

A scanning laser vibrometer (Polytec PSV-400 scanning head) was used to measure orthogonal surface velocity with an average of five measurements at each grid position. A grid of 40 x 25 positions was used on the large (7.48m x 3.0m) plate and a grid of 25 x 25 positions on the smaller (4.0m x 3.0m) plate corresponding to six grid points per wavelength up to approximately 700-1000Hz (depending on which measured bending wavespeed from section 4.7.5 is applied). A continuous pink noise source was used as the excitation signal. The results from two source positions were compared. Only the panel onto which the source was mounted was measured at each source position. One laser scanning head was available so the panels were scanned consecutively. A reference accelerometer was used at the bottom corner of the plate and the force input from the shaker was recorded using a PCB type 208 A04 force transducer. A high pass filter is used by the scanning software with a cut-off set at 2Hz and this is thought to be one reason for the poor agreement between measured and modelled mobility at very low frequencies (up to ~12Hz). However, the generation of sufficient vibration by the shaker at such low frequencies is also a problem (see Figure 5-6). The modes and mode shapes were compared with a FEM modal model as a first check to verify the validity of the FEM prediction model. With a low source amplitude and structural damping, the eigenfrequencies can be satisfactorily compared to those determined for the free (i.e. unforced) plate. The results of these measurements are presented in sections 5.5.2 to 5.5.4.

5.4.3 Total loss factors

The total loss factor for each wall in junction (i), (ii), and (iii) was calculated from the measured structural reverberation times between 50Hz and 5000Hz. A shaker (B&K Type 4809) and MLS signal was used as the excitation source with a pair of accelerometers (Type 4513-B-002) connected to a Norsonic 840 RTA to capture the acceleration level decay. Reverse filtering and time reversal was used to minimise the decay times of the filters so that short reverberation times could be adequately measured, the reverberation time was derived from a T_{20} measurement in each third

octave band. For the rotated L-junction a repeat measurement was made with a two-channel analyser (Dirac software version 5) to obtain T_5 and T_{10}. Additionally, the reverberation times were measured after increasing the absorption in the vicinity (>1m from the plates) of the junction. The result of this measurement is presented in section 5.5.5.

5.4.4 Coupling loss factors and flanking reduction index

To calculate the coupling loss factors the acceleration level differences on pairs of plates were measured. (This is equivalent to the velocity level difference.) A pink noise source and (B&K Type 4809) shaker were used to supply the input signal. Pairs of accelerometers (B&K Type 4513-B-002) and a Norsonic RTA was used to record the vibration level difference. Three source points and twelve accelerometer positions per source point were used. For comparison the number of measurement positions recommended for panels in EN ISO 10848-1 [94] is a minimum of nine for vibration reduction index measurement. This was estimated to reduce the 95% confidence limits ($C_{95\%}$) by a factor of two (see Eqn. (5-19), N=9, compared with N=36) [121].

$$C_{95\%} = 1.96\frac{\sigma}{\sqrt{N}} \tag{5-19}$$

where σ is the standard deviation and N is the number of measurements.

There was >0.5m distance between source and measurement positions with all evenly distributed measurement positions >0.5m from the plate edges. The signal-to-noise ratio was >6.0dB where a background correction was applied (in the range 50-125Hz), or >10.0dB (in the range 160-5000Hz, 125Hz). The coupling loss factors were calculated in the forward and reverse directions according to Eqns. (2-178) and (2-179), and the flanking reduction index according to Eqn. (2-188). To calculate R_{ij} for this data the standard partition area $S_s=S_0=10m^2$ was used. Note that where the resonant sound reduction index (R_i) is used to calculate the flanking transmission coefficient (R_{ij}), the radiation efficiency at and below the critical frequency (calculated using Leppington), used to determine the resonant sound reduction index (R_i), is shown to depend on the exact dimensions of the plate. However, as an

approximation the dimensions of the CLT plate (measured in chapter 4, 4.2m x 2.9m) is consistently used to make R_i calculations for all CLT plates in the thesis (with insignificant error).

Three main measurements were made:

(1) L-junction No. 1
(2) L-junction No. 2
(3) T-junction.

To test the effect of the plate layers on the methodology, measurements on L-junction No. 1 were made in each direction from inner to inner layers and from inner to outer layers to see if there was any difference in recorded acceleration levels. (Inner denoting the surface that would be visible from inside the room, and outer the surface that would be visible from outside the room.) The junction excitation is always on the outer layer. L-junction No. 2 was a modified junction in which one of the attached plates was rotated by 90°. (The reverberation time measurements were also repeated in this case.) For the T-junction, the vibration level difference of the Ff, Fd and Df paths were determined. The results of these measurements are presented in section 5.5.6.

5.5 Results

5.5.1 Model 1: Driving-point mobility of a freely hanging and simply supported plate

5.5.1.1 Freely hanging plate

For the freely hanging plate Figure 5-8 allows comparison of the measured and FEM driving-point mobility at a single excitation point (1.5m from the side edge and 1.0m from the bottom edge of the plate) using three different element types. There is reasonable agreement between measured and modelled data regarding the location of the data peaks up to ~150Hz. At higher frequencies (i.e. above the 12th mode) there is less agreement in the peaks which is to be expected in the comparison of a deterministic model with measurements when the wavelengths are small; this is where statistical models can be advantageous. Note that the depth of the troughs in

the measured data is affected by the signal processing (although very deep troughs may also indicate anti-resonances in the data).

Above 150Hz the general trend of the modelled data follows the measurements however agreement with the exact location of the peaks is lacking. In this frequency range (>150Hz) there are differences between the three FEM elements. Although S4 fully integrated elements might be expected to give the closest agreement with measurements the combination of imprecise elastic constants and small wavelengths means that there is no clear indication of this. Above 880Hz there are distorted in-plane mode shapes in the FEM model, likely due to overly stiff behaviour (shear locking) of the fully integrated elements or overly flexible behaviour (hourglassing) of the reduced integration elements. Thus, slowing the calculation procedure but not necessarily affecting the calculated perpendicular motions. At frequencies above 800Hz differences between the measured result and FEM could be due to truncation of the higher (residual) modes because only 200 modes were used in this FEM model.

For one of the three types of element (S4) the effects of modal truncation are shown in the convergence analysis in Figure 5-9. The large error at high frequencies due to truncation of the residual modes shows the contribution to the data peaks (and troughs) from the stiffness-controlled region of higher modes. using only the S4 element. This is interesting because only a small amount of phase interference is required to lower the measured phase difference between two points on the CLT plate (see section 4.7.5) and hence reduce calculated values of the elastic constants determined from directly measured bending phase speed. A similar, but not identical, effect is observable when the modes are truncated at low frequencies (<100Hz). Where the plate behaves as a thin plate, the modal overlap is low and truncated modes only affect the troughs, not the peaks, in the data. This is illustrated in the convergence analysis shown in Figure 5-10. In this region (<100Hz) there would be expected to be little or no phase interference.

Figure 5-11 compares the measured third octave band values for the real and imaginary parts of the mobility against the analytical model (Eqn. (2-100)) and the FEM model averaged over third octave bands. Reasonable agreement is obtained for

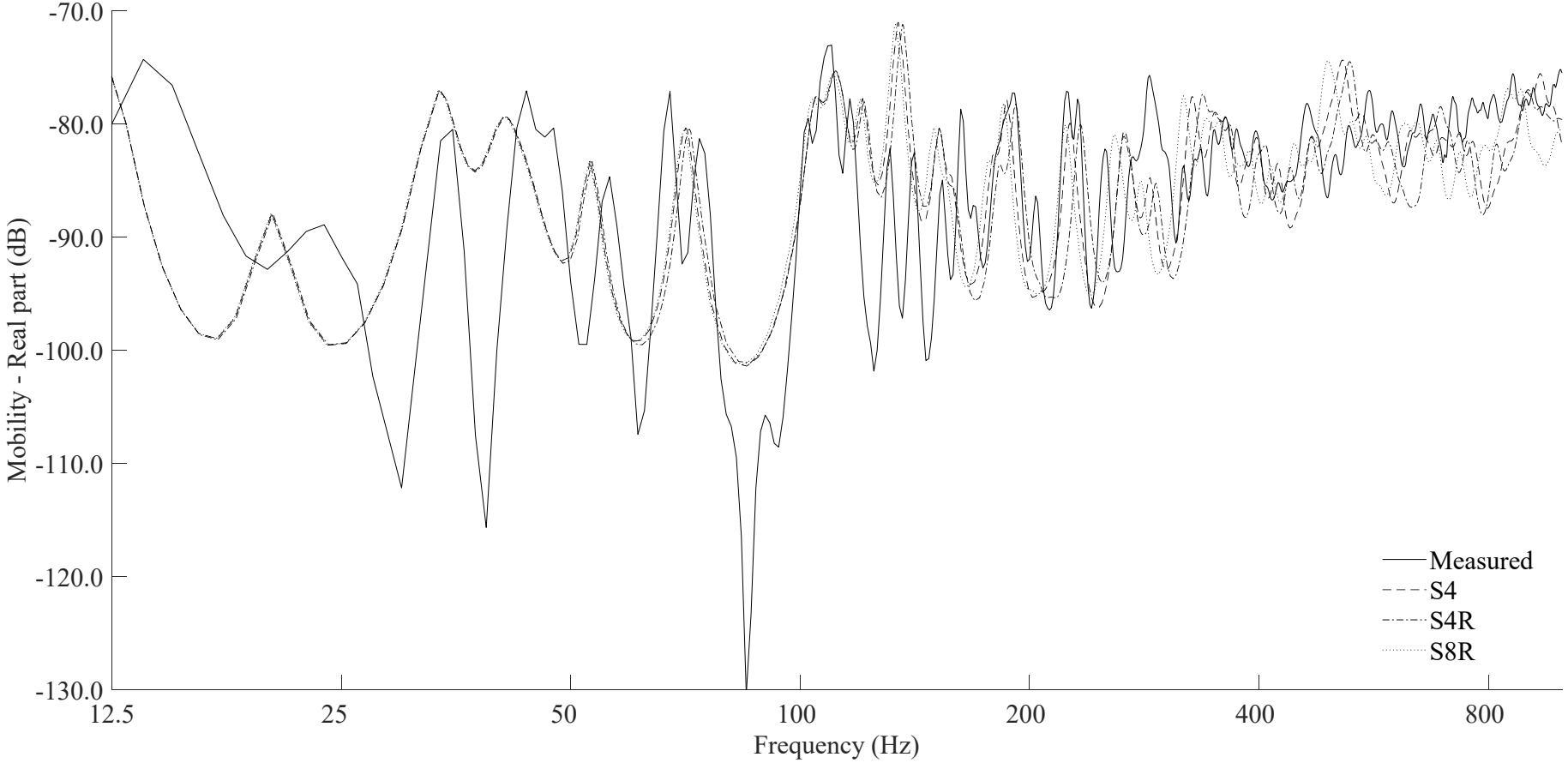

Figure 5-8 (a) Real part of the mobility using a coarse mesh (0.1m) compared with FEM three different element types (200 modes).

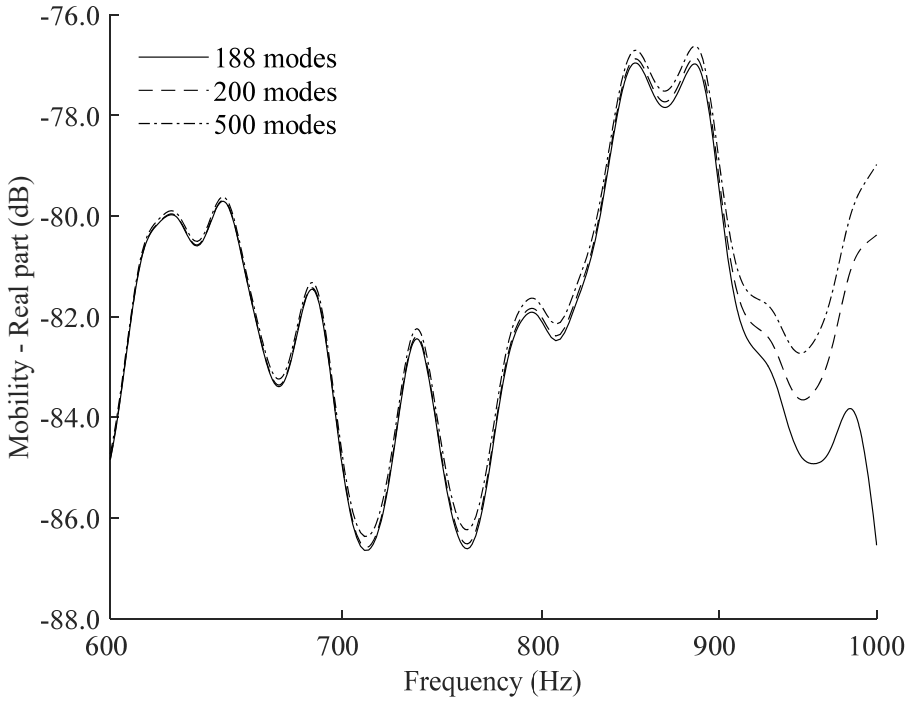

(a)

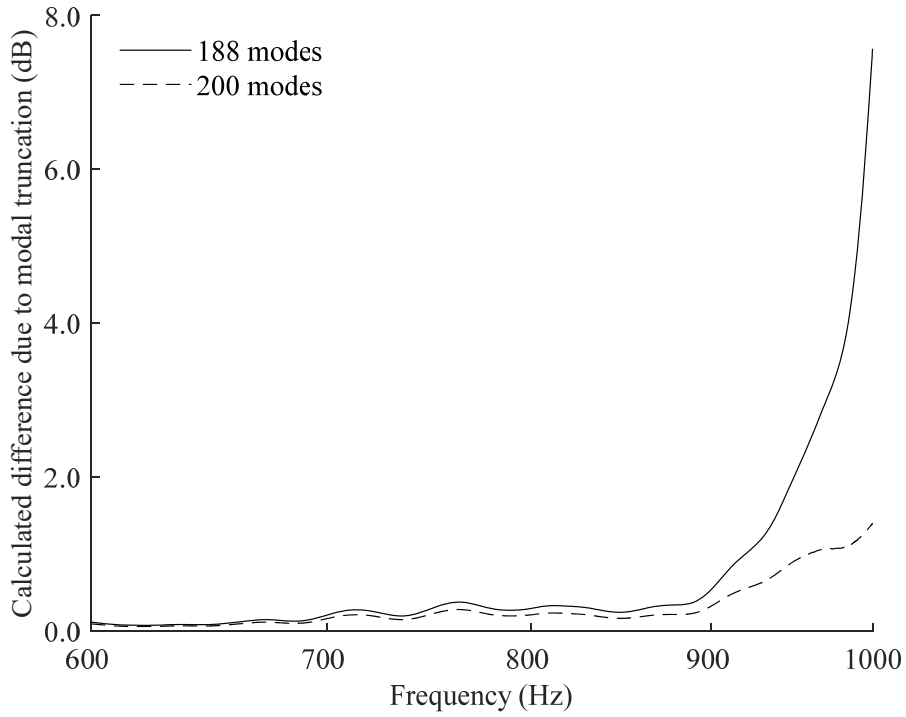

(b)

Figure 5-9 Convergence analysis showing (a) The contribution to mobility from residual (i.e. higher frequency) modes (b) estimated error (500 modes taken as the baseline) at high frequencies due to modal truncation (A mesh size of 0.025m was used)

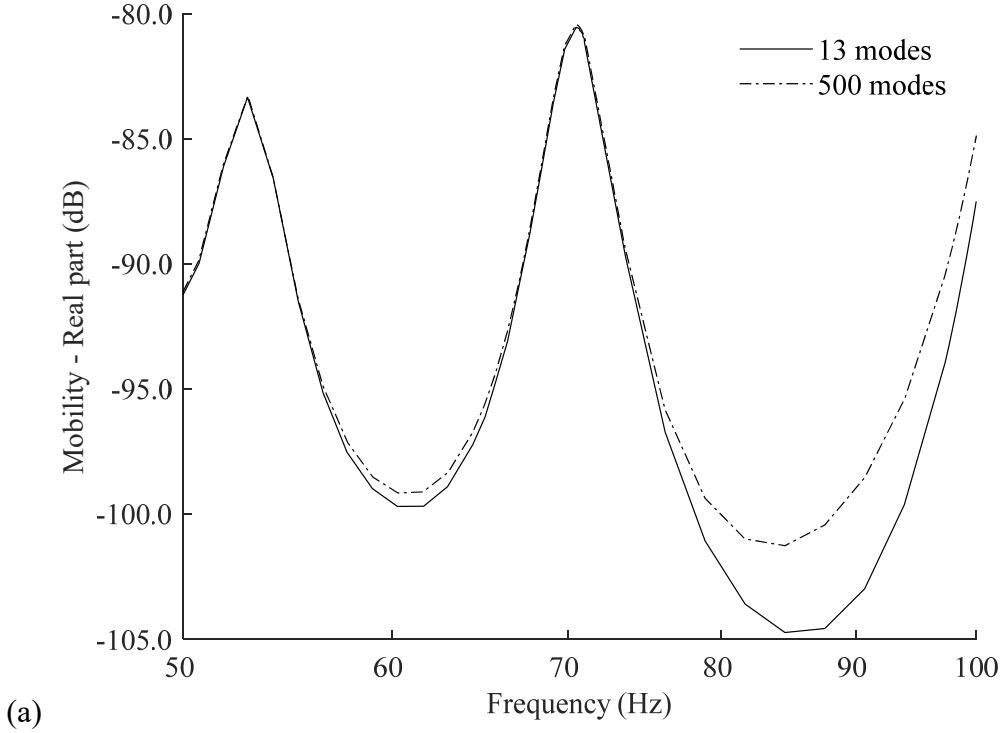

(a)

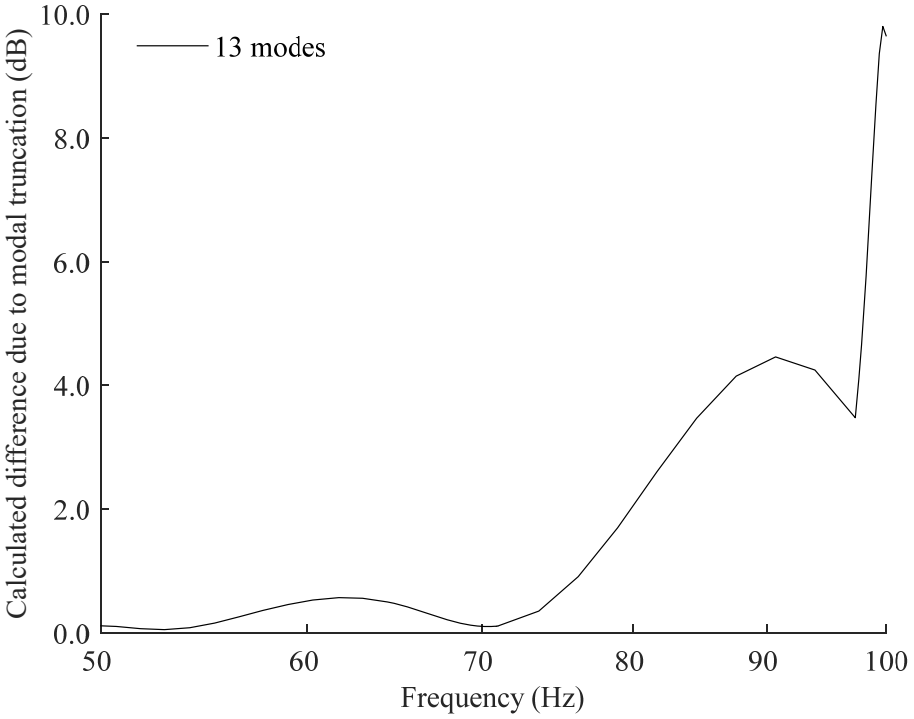

(b)

Figure 5-10 Convergence analysis for the S4 element showing (a) contributions to mobility from residual (i.e. higher frequency) modes (b) estimated error (500 modes taken as the baseline) at low frequencies (<100Hz) due to modal truncation (A mesh size of 0.025m was used)

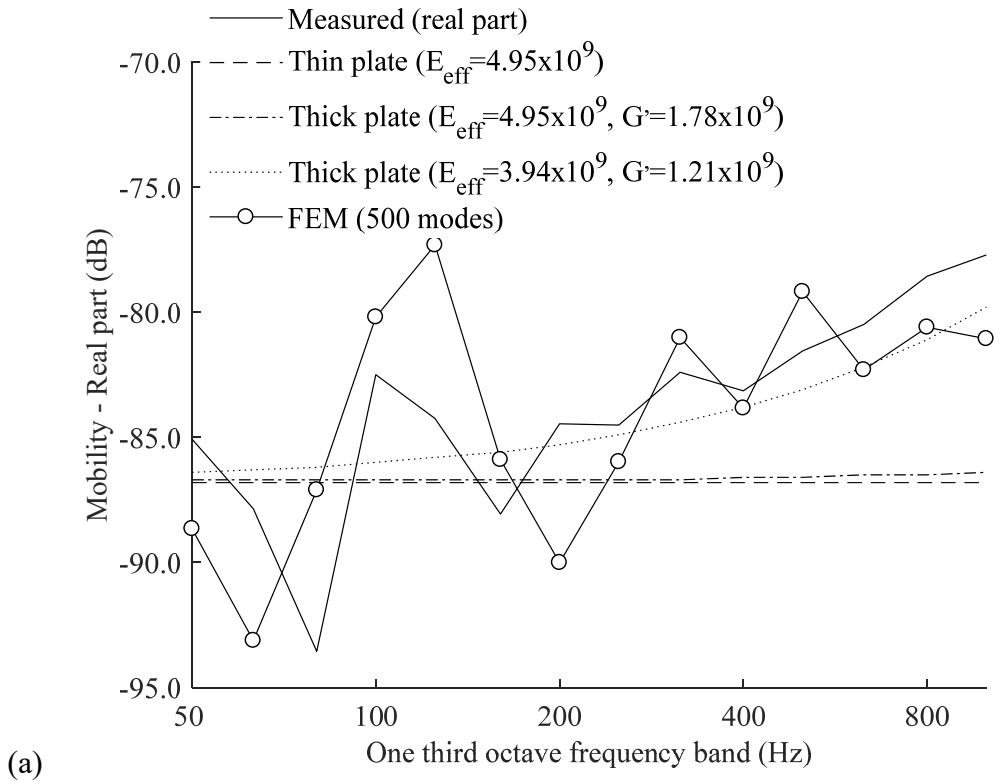

(a)

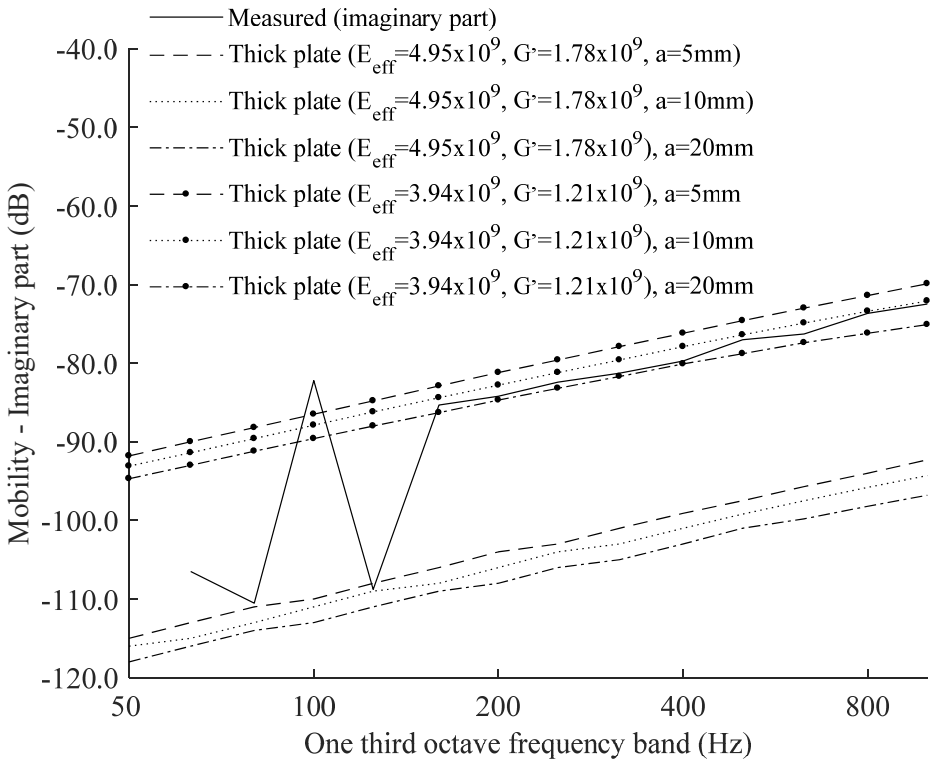

(b)

Figure 5-11 Measured (a) real and (b) imaginary point mobility for freely supported CLT plate compared with calculated point mobility for a thick infinite plate.

both real and imaginary parts using the constants determined from uncorrected directly measured bending wavespeed data (see section 4.7.5), but there is poor agreement when using the low-frequency constants determined in section 4.7.4. In contrast, agreement with the trend of the FEM model and the measured real part when using the low-frequency constants (determined in section 4.7.4) can be achieved if an adequate number of residual modes are included in the calculation.

5.5.1.2 Simply supported plate

For the simply supported plate, Figure 5-12 allows comparison of the measured and FEM driving-point mobility at a single excitation point (1.5m from the side edge and 1.0m from the bottom edge of the plate) using three different element types. The peaks of the measurements and FEM only agree for the first two modes which (as noted in section 4.4.2) could be due to simply supported edge conditions being difficult to achieve in practice, especially when the plate has a substantial thickness. The three FEM models give consistent results up to ~500Hz. Distorted in-plane mode shapes in the FEM model, likely due to overly stiff behaviour (shear locking) of the fully integrated elements or overly flexible behaviour (hourglassing) of the reduced integration elements, are observed above 1275Hz. Thus, slowing the calculation procedure but not necessarily affecting the calculated perpendicular motions. At frequencies, up to 1000Hz it is sufficient to consider up to 200 modes. Using only the S4 element this is illustrated in the convergence analysis shown in Figure 5-13.

Similarly, to the freely supported plate the relatively large error at high frequencies shows the contribution of the stiffness-controlled region of higher modes. For the simply supported plate the error due to modal truncation can also be reduced by using a "method of residual modes" [122] which is computationally less costly than calculating many additional modes. The results from this method are also shown in Figure 5-13, although this requires estimating the damping of the residual mode; here this was estimated to be 0.04. The "method of residual modes" extends the upper frequency bound (to 983Hz) where the 134 modes (plus one residual mode) gives an answer within 3.0dB of the non-truncated result (taken to be equal to the result from 400 modes), but could not account for all the truncated modes.

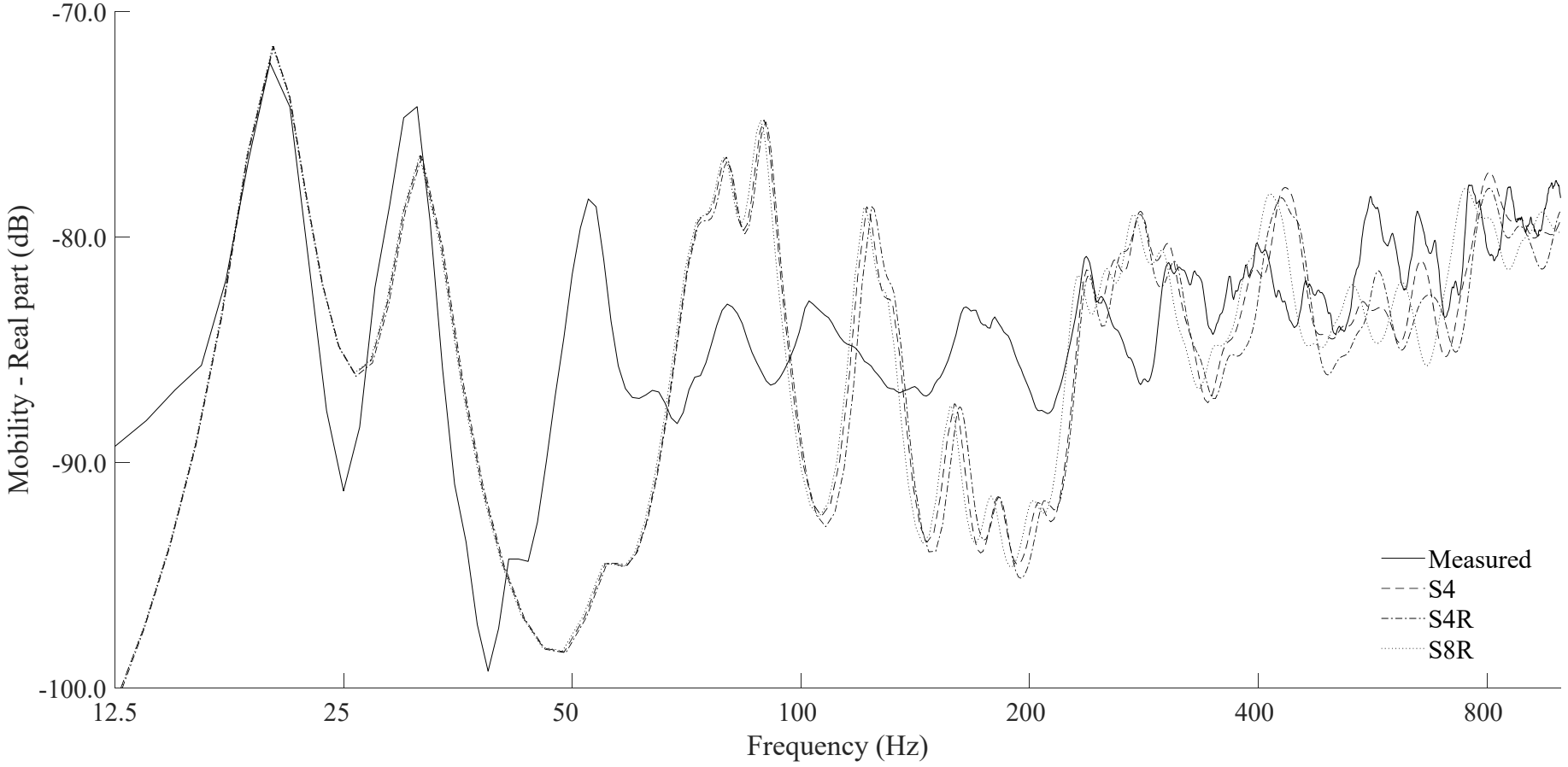

Figure 5-12 Real part of the mobility using a coarse mesh (0.1m) compared with FEM three different element types (200 modes).

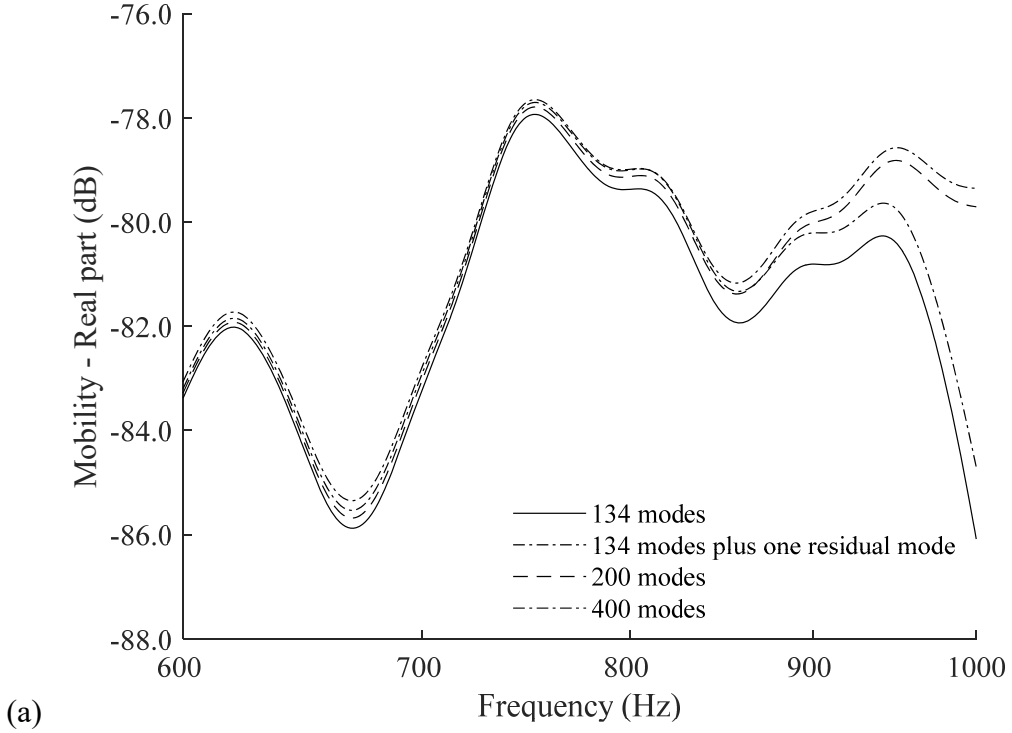

(a)

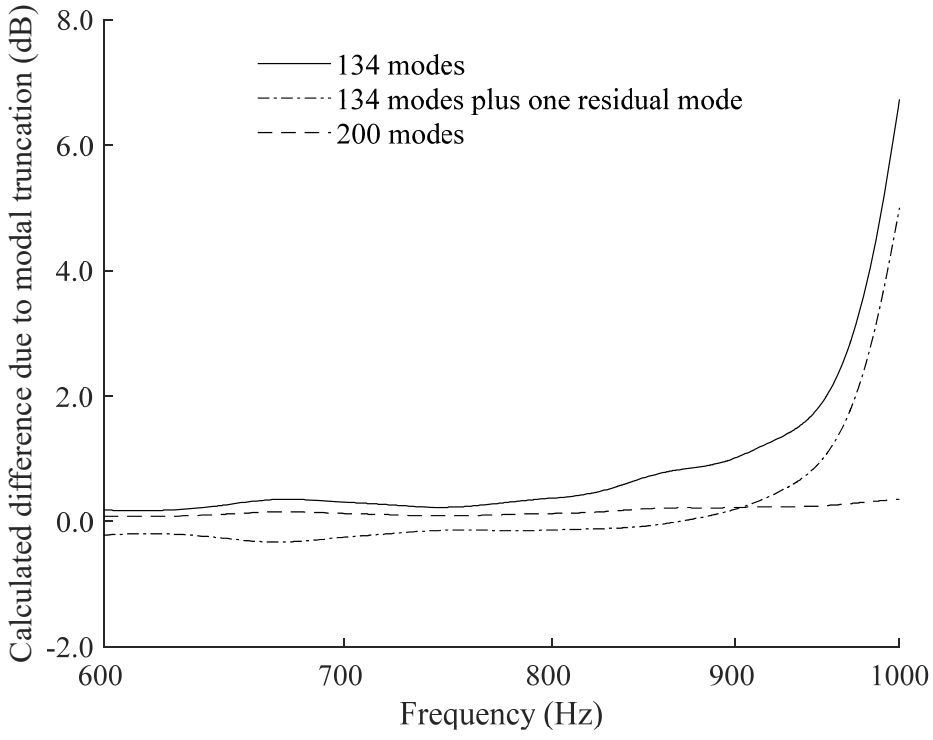

(b)

Figure 5-13 Convergence analysis for the S4 element showing (a) The contribution to modelled mobility from residual (i.e. higher frequency) modes (b) estimated error (400 modes taken as the baseline) at high frequencies due to modal truncation (A mesh size of 0.025m was used)

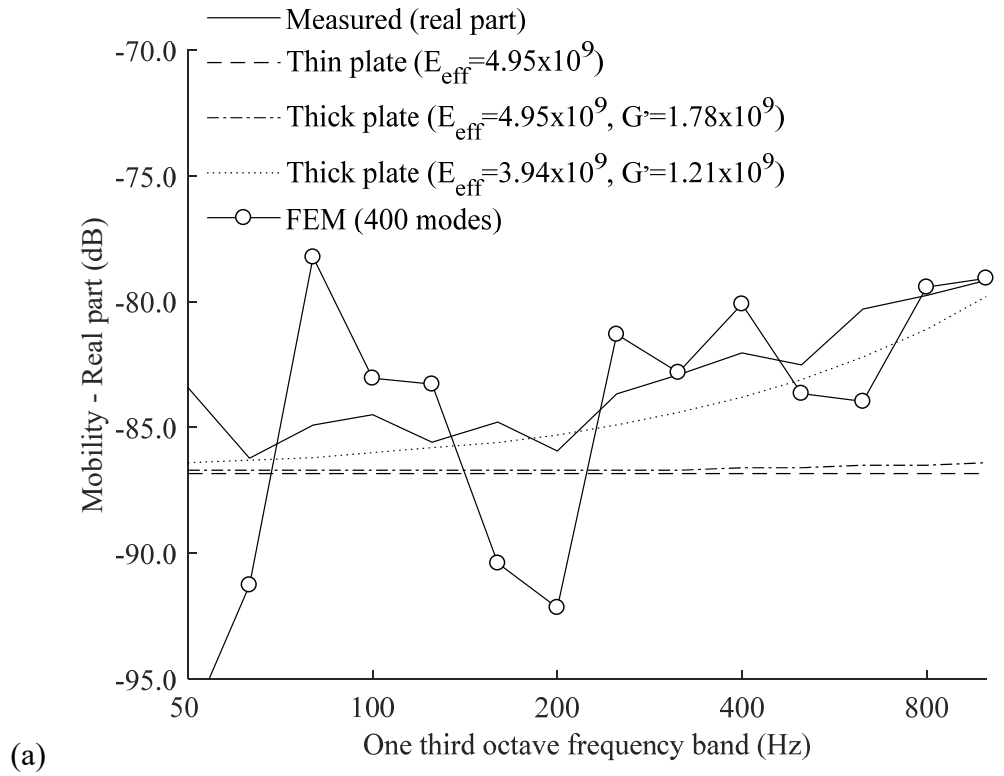

(a)

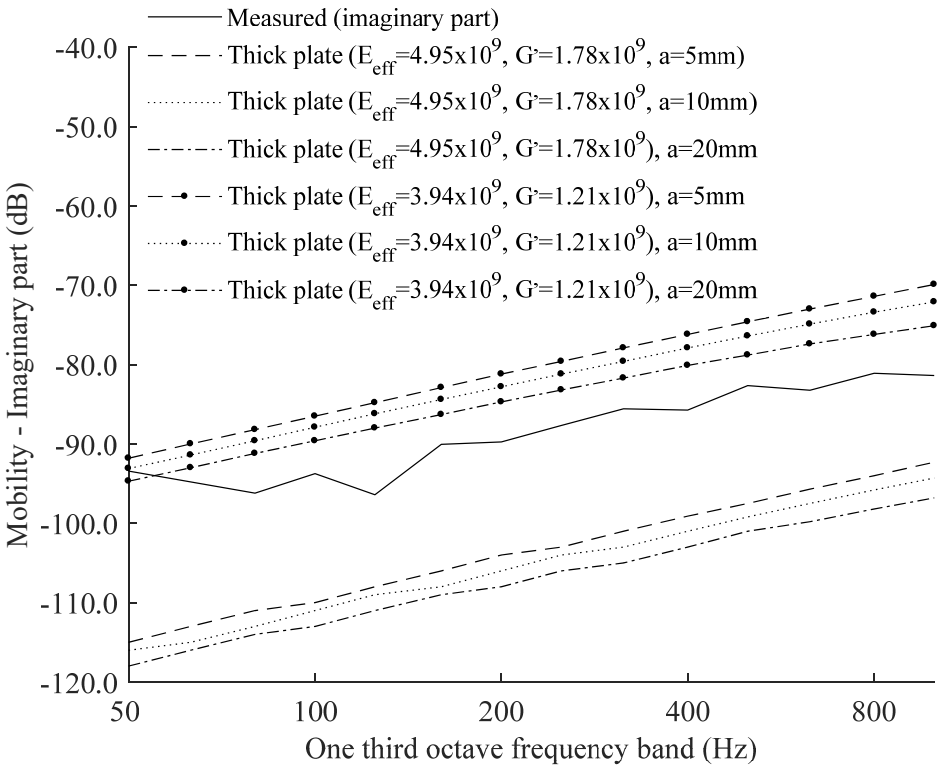

(b)

Figure 5-14 Measured (a) real and (b) imaginary driving-point mobility for simply supported CLT plate compared with the analytical model for a thick infinite plate.

Analytical calculations for thin and thick plates can be found in sections 2.2.8.1 and 2.2.8.2. Figure 5-14 compares the measured third octave band values for the real and imaginary parts of the mobility against the analytical model and the FEM model averaged over third octave bands. Agreement is obtained for the real but not the imaginary parts using the constants determined from uncorrected directly measured bending wavespeed data (see section 4.7.5), but there is poor agreement when using the low-frequency constants determined in section 4.7.4. As in the case of the freely supported plate, there is agreement with the trend of the measured real part when using the low-frequency constants (determined in section 4.7.4) when the residual modes are included in the calculation.

In conclusion, the results from the freely hanging and simply supported plate indicate that the low-frequency constants from section 4.7.4 are sufficient when used with S4 elements and an increased number of modes to eliminate any error due to truncated modes. The contact stiffness or size of the force excitation area likely do not explain the frequency dependency of the mobility because the upwards trend starts at such a low frequency (<100Hz).

5.5.2 Model 2: Modal analysis of the T-junction below 50Hz (Coupling conditions at the junction)

The measured and modelled modes were compared for the long panel (walls (i) and (ii) combined) and short panel (wall (iii)). A comparison between the measured data for the long panel (walls (i) and (ii) combined) and short panel (wall (iii)) and the calculated data for junctions with connection (a) or connection (b) was made. Modes with displacement primarily along the horizontal axis are the easiest to identify and compare. These are shown in Table 5-3. Below 10Hz it was not always possible to identify mode shapes, and it was also not possible to identify a mode at 14.5Hz for connection (b). The data is noisy at low frequencies due to the high pass filter although the most likely cause for the absence of these modes is thought to be due to the difficulty of exactly defining the boundary conditions of the test junction; they are not precisely described by freely hanging edges.

	FEM			FEM	
Measured data	**Connection (a)**	**Connection (b)**	**Measured data**	**Connection (a)**	**Connection (b)**
(Unable to identify in dataset)	2.4 Hz 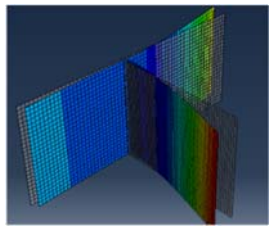	9.7Hz 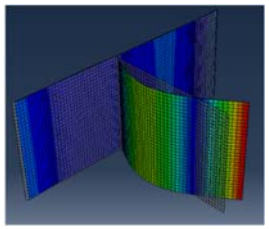	14.5Hz 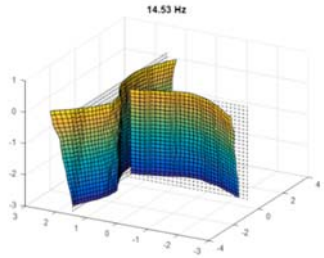	14.1Hz 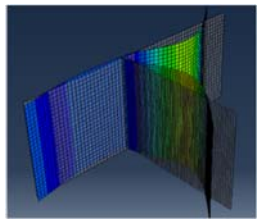	No equivalent
(Unable to identify in dataset)	3.6Hz 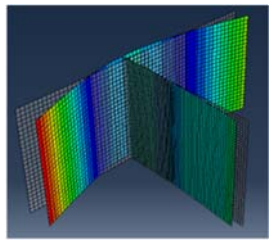	3.4Hz 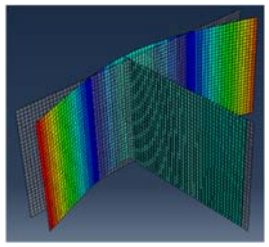	20.3Hz 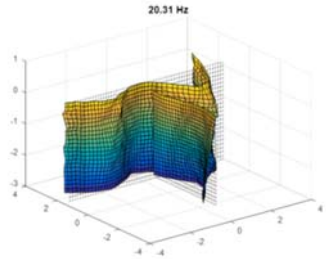	19.5Hz 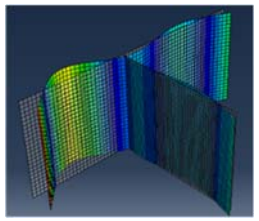	18.8Hz 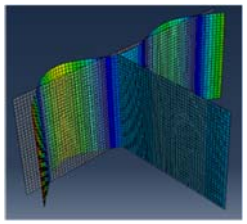
11.3Hz 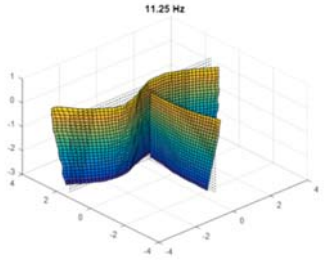	10.4Hz 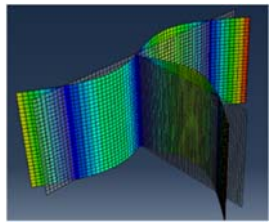	10.9Hz 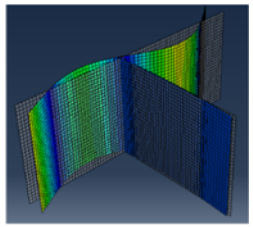	35.0Hz 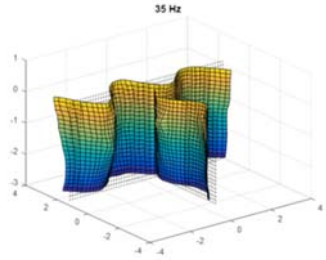	32.8Hz 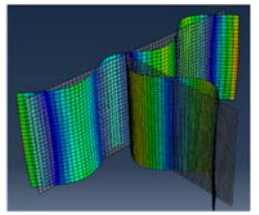	34.1Hz 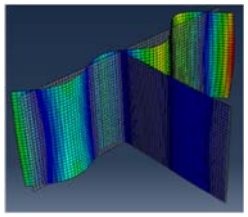

Table 5-3 Measured horizontal axis mode shapes compared with FEM (excitation is on the long panel (walls (i) and (ii) combined))

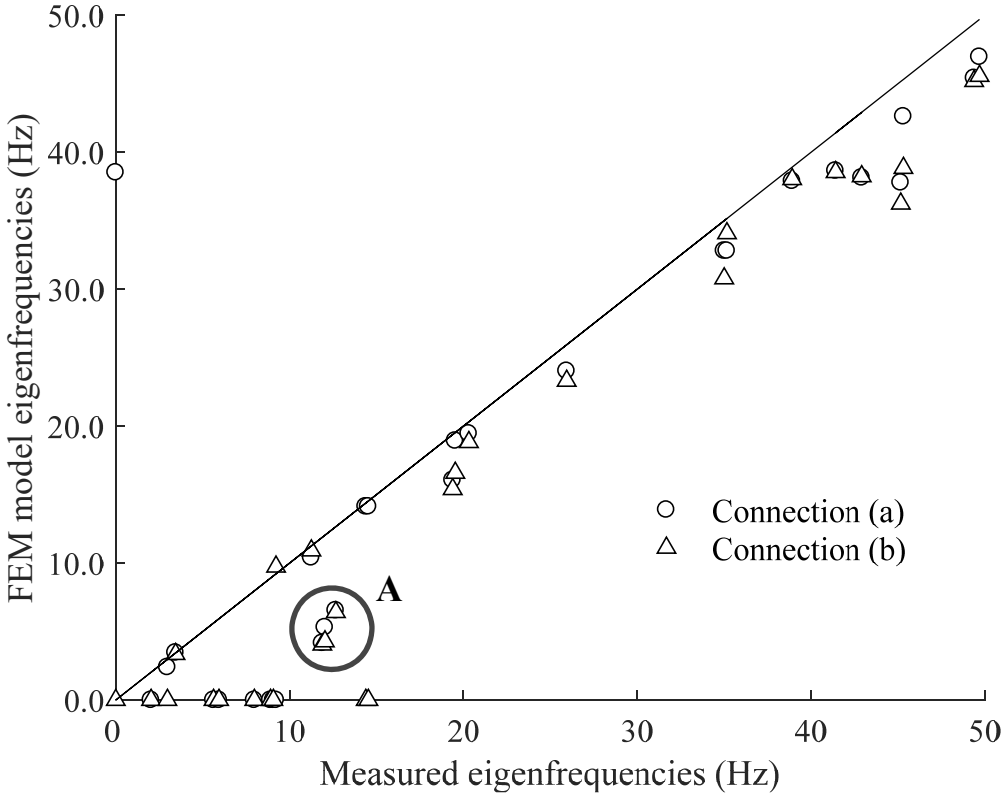

Figure 5-15 Comparison of measured and FEM eigenfrequencies ("A" indicates a group of modes where the FEM eigenfrequency is approximately half the measured eigenfrequency)

For other mode shapes below 50Hz, measurements and FEM using connection (a) or (b) are compared in Figure 5-15. It is difficult to conclude from this data whether the junction with connection (a) or connection (b) is the more appropriate model at low frequencies. However, of note are the number of measured modes below 10Hz that cannot be identified in either FEM model, and the group of modes labelled "A" in Figure 5-15 where the FEM eigenfrequencies are approximately half of the measured eigenfrequencies. These are all twisting modes and the mismatch is most likely due to the imperfect bottom boundary condition where the junction is resting on rubber mounts.

5.5.3 Model 2: Modal analysis of the T-junction below 50Hz (Boundary conditions)

Seven horizontally acting springs, motion perpendicular to the plane of each plate (with estimated spring constant k=1x10^{6}Nm^{-1}) were added to the bottom edge of the plate to model the boundary condition due to the rubber mounts underneath the junction. Below 50Hz, a comparison of measured and FEM modes calculated using connection (a) or connection (b) with the addition of these springs is shown in Figure 5-16. It is difficult to estimate what the horizontal stiffness of the springs underneath the panels should be and whether this should be a constant or frequency-dependant. However, the fit of the modelled twisting modes to the measured data at frequencies <30Hz is improved by the addition of springs with stiffness k=1x10^{6}Nm^{-1}, although some of the measured modes are absent. Below 30Hz the comparison of modelled to measured modal shape of the twisting modes is shown in Table 5-4. At frequencies above 30Hz it is difficult to identify modes from their mode shape.

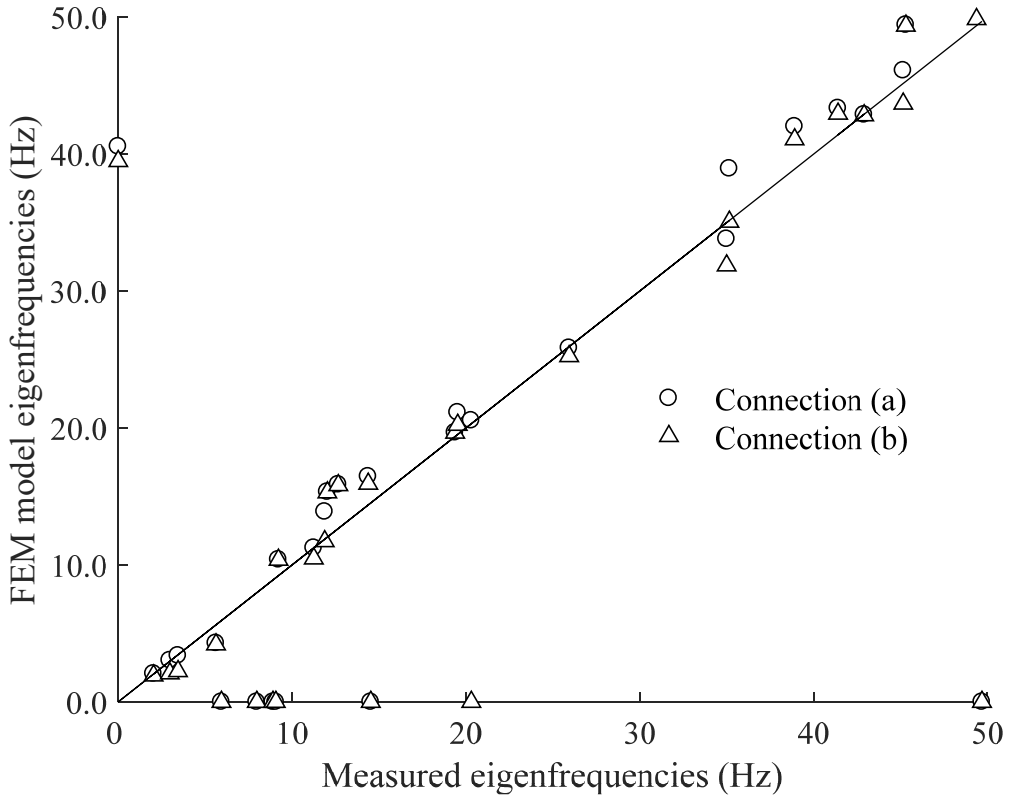

Figure 5-16 Comparison of measured and calculated modes with springs added to the base of the panels to represent the mounts

	FEM	
Measured data	**Connection (a)**	**Connection (b)**
2.0Hz 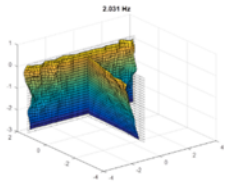	2.1 Hz 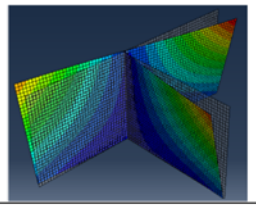	1.9Hz 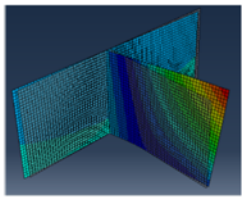
3.0Hz 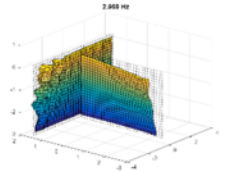	3.0Hz 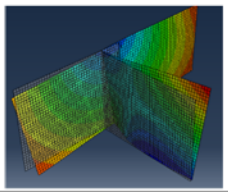	2.1Hz 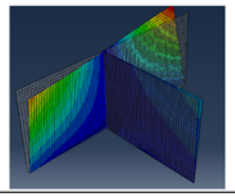
3.4Hz 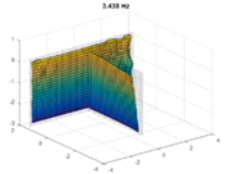	3.4Hz 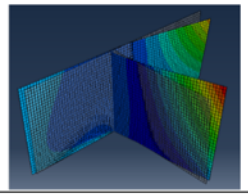	2.2Hz 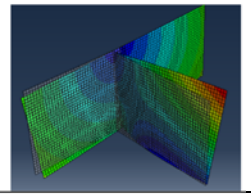
5.6Hz 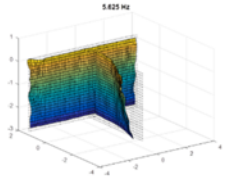	4.3Hz 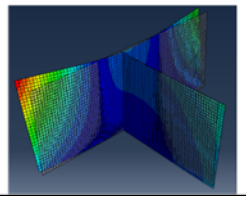	4.2Hz 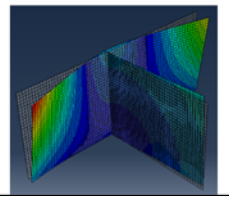

	FEM	
Measured data	**Connection (a)**	**Connection (b)**
9.2Hz 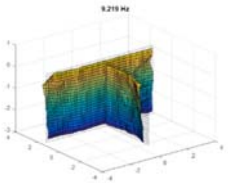	10.4Hz 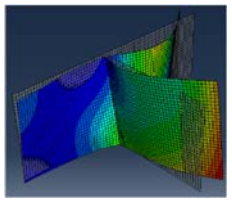	10.4Hz 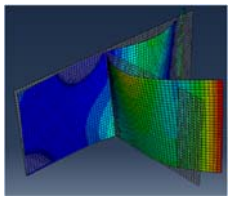
11.9Hz 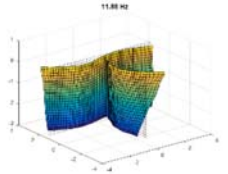	13.9Hz 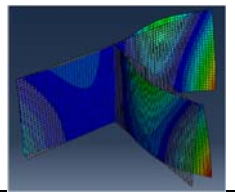	11.7Hz 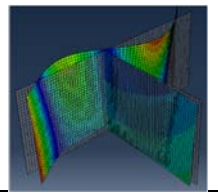
12.0Hz 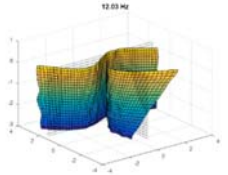	15.3Hz 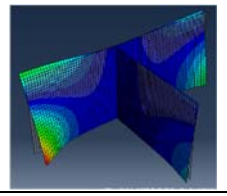	15.3Hz 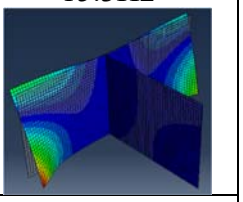
12.7Hz 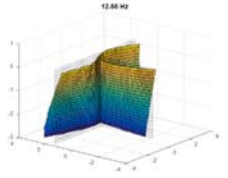	15.9Hz 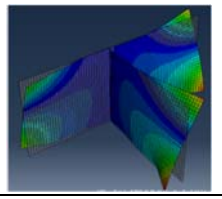	15.8Hz 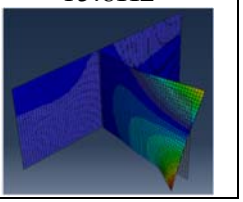

Table 5-4 Measured twisting mode shapes below 30Hz compared with FEM (excitation is on the long panel (walls ((i) and (ii) combined))

Unidentified measured modes are 5.94Hz, 7.97Hz, 8.91Hz and 9.06Hz. This may be due to noise in the data. An additional measurement could have been made on the short panel (wall (iii)) exciting the long panel (walls (i) and (ii) combined) and vice versa instead only the panel contacted with the source was measured, which limits the data set. The two-dimensional modes are also affected by the lower boundary condition but are less clearly identifiable. The modes along the horizontal axis do not change significantly with the addition of the horizontal springs. It is often difficult to predict the exact coupling conditions at a junction or boundary conditions and hence the exact location of the modal frequencies.

5.5.4 Model 3: Modal analysis of the T-junction (50Hz-700Hz)

Convergence analysis was carried out for each wall of the junctions with connection type (a) to show the problem of truncating higher modes on the calculated mobility. In these FEM models, wall (i) is the source wall and walls (ii) and (iii) are the receiving walls. The driving-point mobility of the source wall, normalised to the mean value, is shown in Figure 5-17. In all the following diagrams, the driving-point mobility (Y_{dp}) is determined from mean mobility of all nodes of the wall (or for the source wall only, from mobility at the input node).

The excited wall clearly shows the contribution from the residual modes. For connection (a) there are 325 modes below 700Hz. As the number of modes increases the FEM mobility increases at high frequencies. The upper cut-off for this mesh density is approximately 440 modes, beyond which FEM does not perform efficiently, likely due to overly stiff behaviour of the mesh. The receiving walls, however, show a different trend; where an increased number of modes results in a decreased mobility. The mechanism for this is unclear, perhaps it is caused by inaccuracy of the element size (0.1m) or mesh geometry (the normalised mobilities are shown in Figure 5-18 and Figure 5-19). The velocity level on the receiving walls is due to the coupling at the junction rather than a forcing function at an input node. If the total energy within each model (with and without residual modes) is identical and adding residual modes has the effect of increasing the energy density on the source wall than this “extra” energy may be balanced by an energy loss on the receiving wall(s).

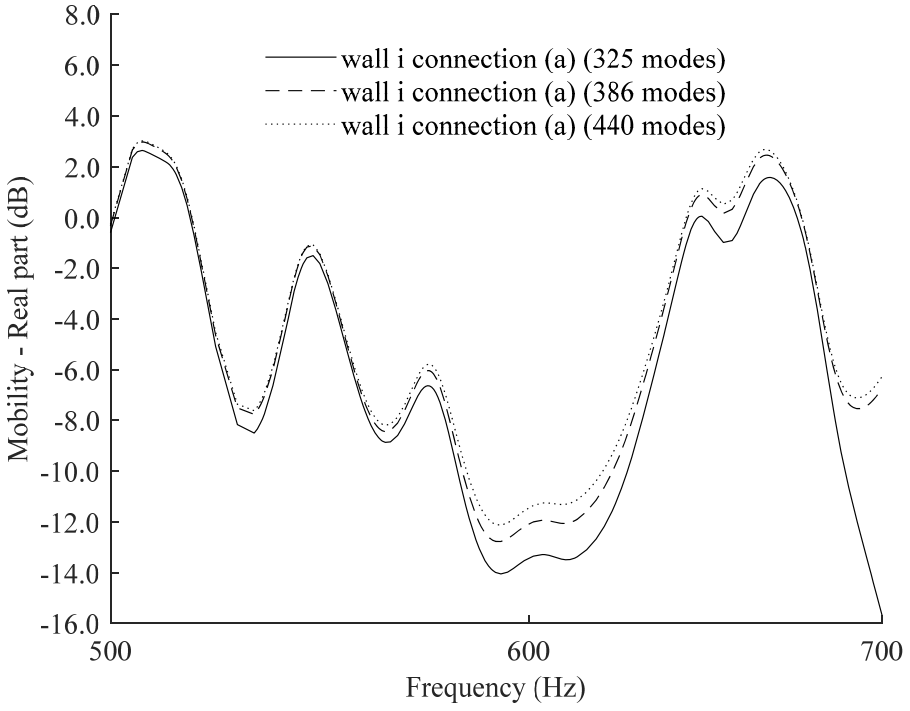

(a)

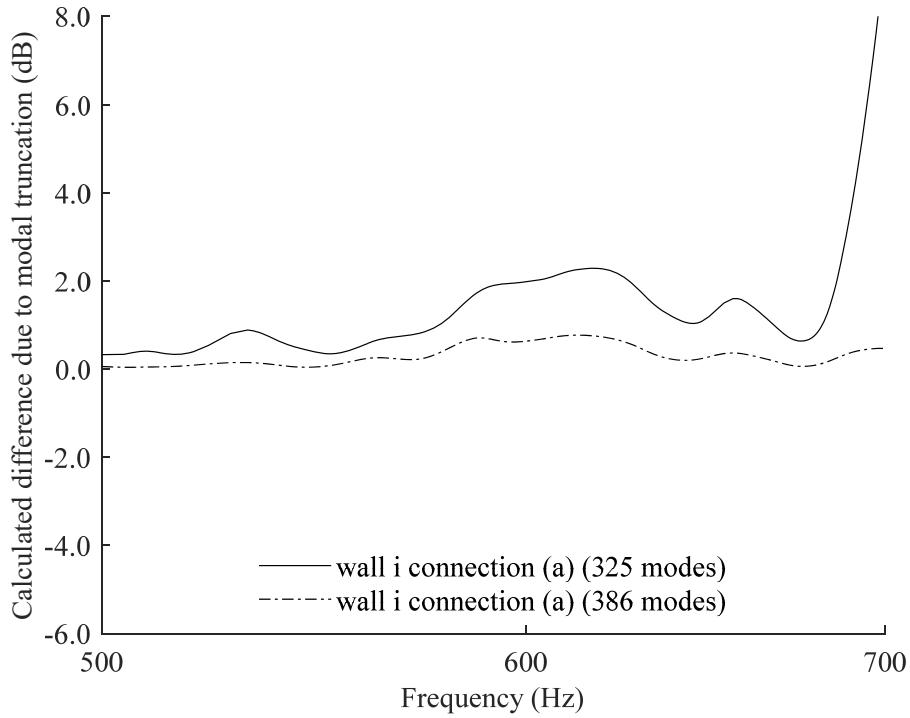

(b)

Figure 5-17 (a) The contribution to FEM mobility from residual (i.e. higher frequency) modes (b) estimated error (440 modes taken as the baseline) at high frequencies due to modal truncation. (Excitation: wall i.)

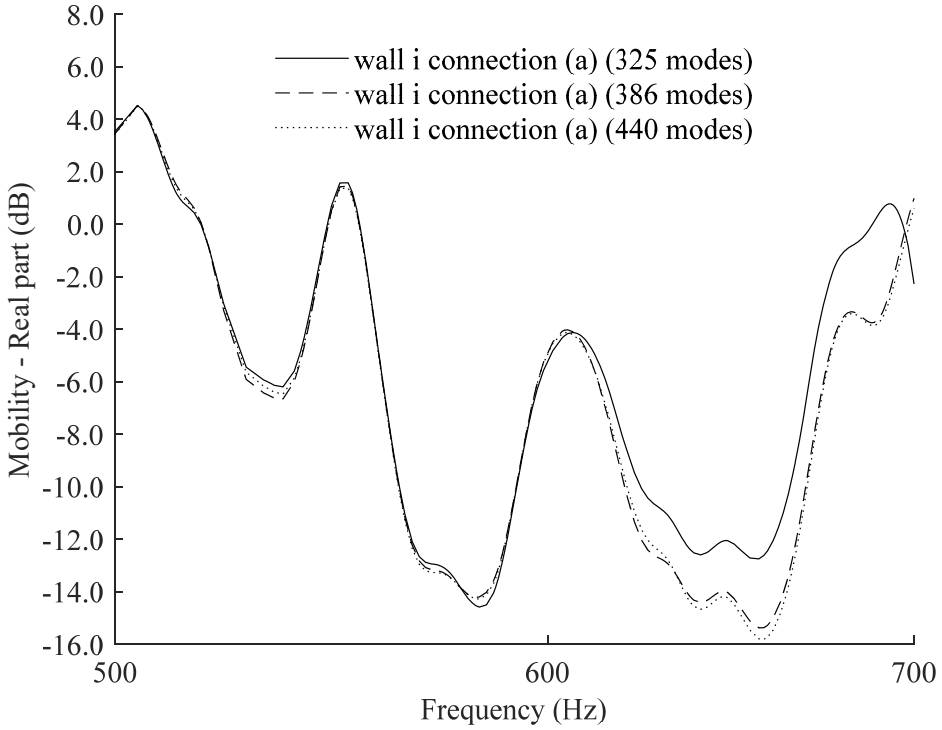

(a)

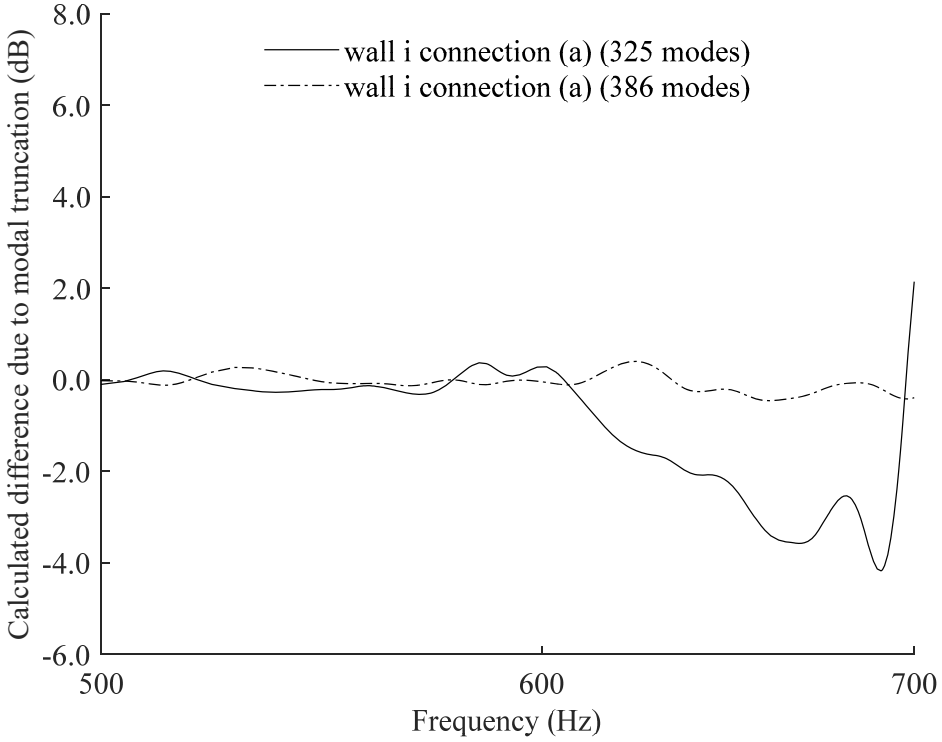

(b)

Figure 5-18 (a) The contribution to FEM mobility from residual (i.e. higher frequency) modes (b) estimated error (440 modes taken as the baseline) at high frequencies due to modal truncation. (Excitation: wall i.)

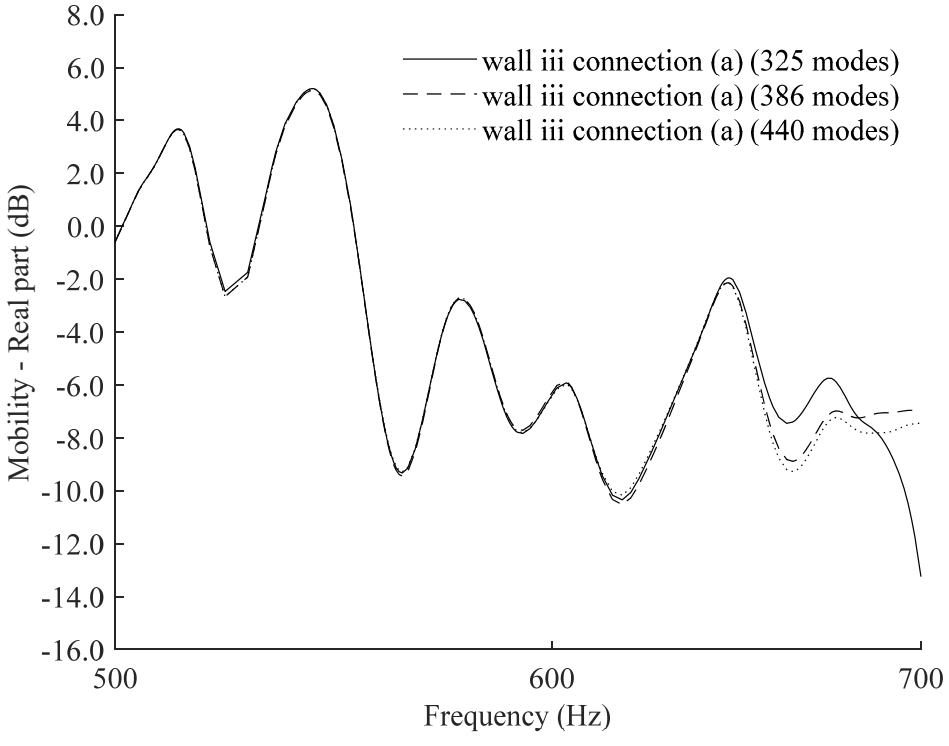

(a)

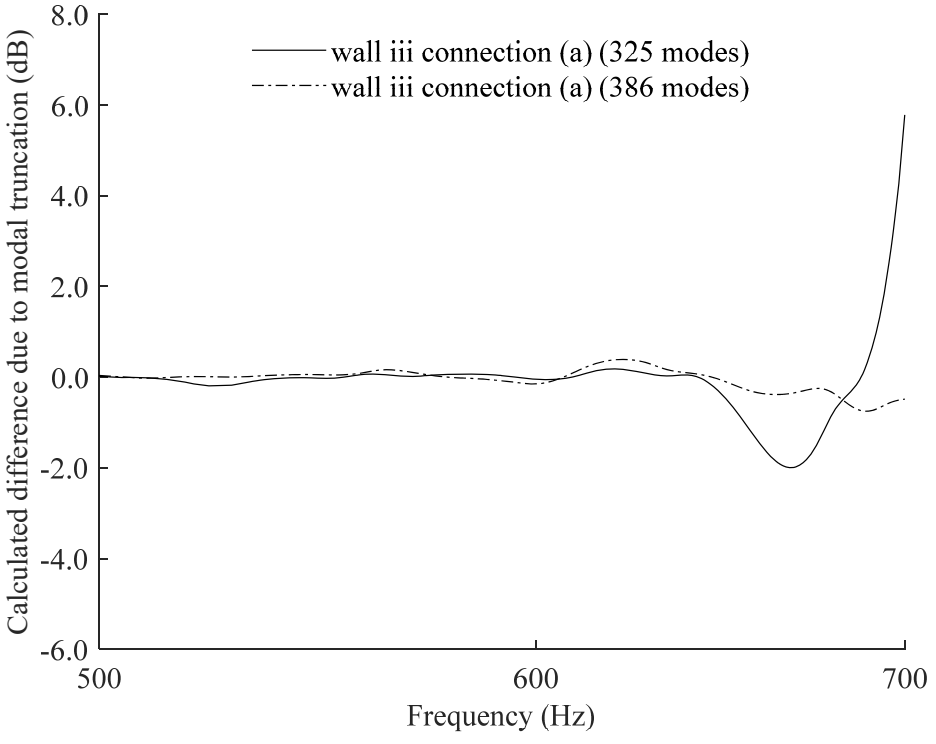

(b)

Figure 5-19 (a) The contribution to modelled mobility from residual (i.e. higher frequency) modes (b) estimated error (440 modes taken as the baseline) at high frequencies due to modal truncation (Excitation: wall i.).

Implementing an algorithm of residual modes in ABAQUS would be a computationally efficient way to correct for the modal truncation. However, due to the way the Lanczos solver in ABAQUS implements the algorithm of residual modes, with a static perturbation step of the same load and boundary conditions as the frequency extraction step, it is not possible to use this method in the case of a freely supported plate or junction (but it could be used in the case of other boundary conditions). This is because the boundary condition magnitudes are required to be zero [35] which is not true in the case of free boundary conditions. The Automatic Multilevel Sub-structuring (AMS) Eigensolver in ABAQUS could be another option but was not available.

In theory, there are an infinite number of modes with eigenfrequency values greater than the frequency band of interest. Therefore, to accurately predict point mobility one of the following options is required; an analytical approach, a numerical approximation of the sum to infinity such as an algorithm of residual modes, or by numerically including the stiffness contribution of a specified number of modes above the frequency range of interest.

5.5.5 Total loss factor measurement

The structural reverberation times were used to calculate the total loss factor of each of the plates in each of the junctions. The total loss factors are shown in Figure 5-20. A sum of the coupling losses from both sides of the plate are also included for comparison, these are calculated using Eqn. (3-4) and model 1a (as described in section 4.7.8.1, despite poor agreement with direct airborne transmission). The measured total loss factors were very similar for each of the plates and in both junctions. This is to be expected since each of the plates have three free edges and only one 3m connected edge. The connecting edge should increase the loss factors slightly when compared with a freely hanging plate. (Note that only one edge on each plate is connected to a junction therefore total coupling losses at the plate edges are low although this would be increased when all four plate edges are connected.) However, at low frequencies these total loss factors were shown to be less than the internal loss factor measured on a nominally identical freely hanging plate (see section 4.7.1). The internal loss factors might vary considerably from plate to plate

or there could be a systematic error in one or more of the methods. The comparison of the measured loss factor with estimated coupling losses indicates that at low frequencies it is the coupling loss factor only which is measured here. An improved fit between estimated coupling losses and the measured data could perhaps be obtained by developing a way to determine the plate to room coupling loss factor from the measured radiation efficiency or SRI of the CLT plate.

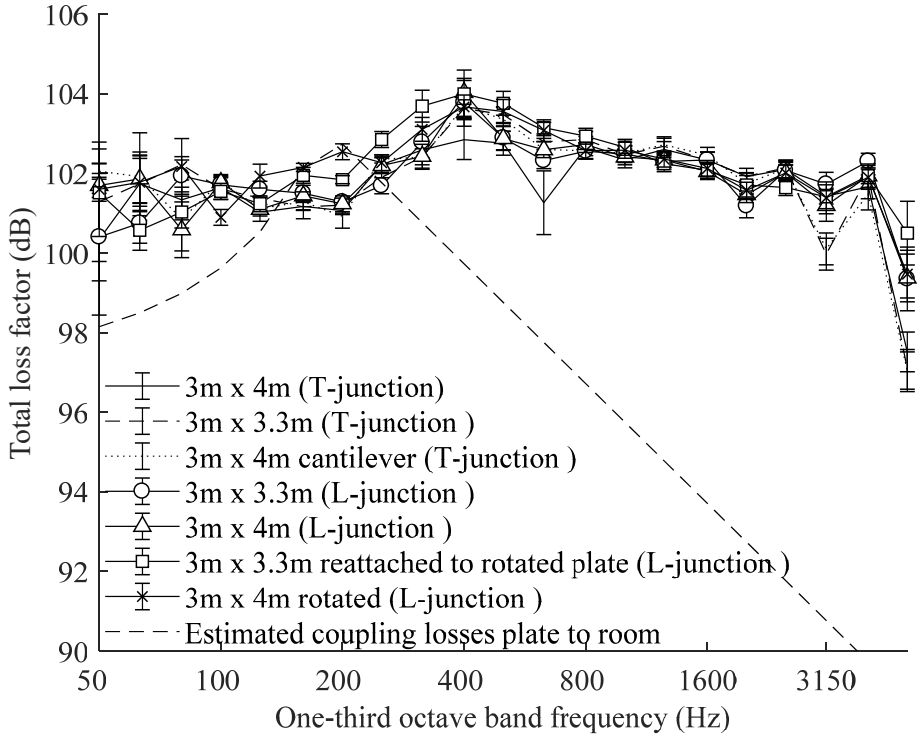

Figure 5-20 Total loss factor of each CLT plate in the L- and T- junctions T_{20} measurements.

For the rotated L-junction a repeat measurement was made, firstly to compare a T_5 and T_{10} measured with the a two-channel analyser (Dirac software version 5) with the T_{20} and T_{30} measured with the 840 and secondly to increase the absorption in the vicinity (>1m from the plates) of the junction to see if this would change the measured loss factor thus indicating coupling through the room and decreased measured loss factors due to double decays. A small difference (mostly within 95% confidence limits) is observed in the loss factors of the plate in either case (Figure 5-21 and Figure 5-22). The mean total loss factor is 0.014 (50-250Hz) and is used in FEM to determine the velocity levels on the plates.

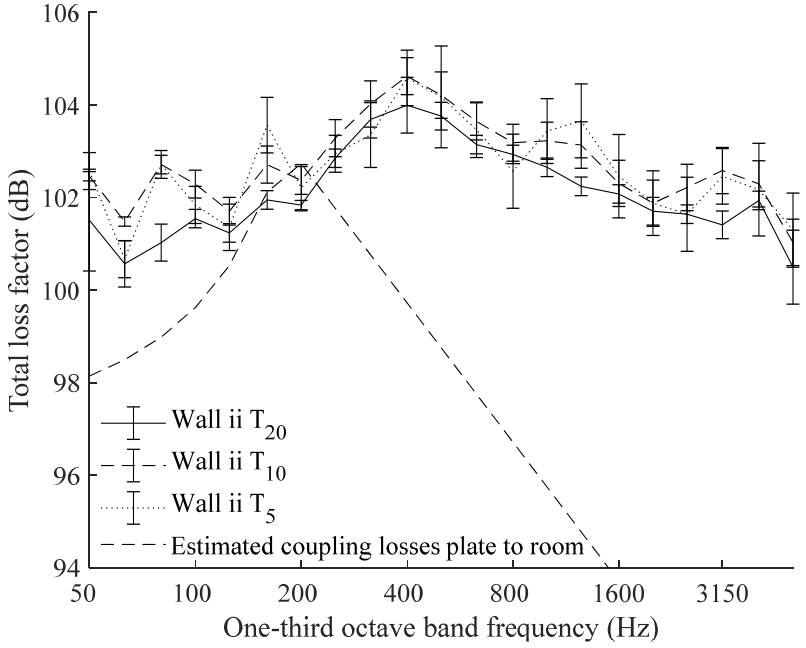

Figure 5-21 Total loss factor of plate (i i) in the L- junction; comparison of T_{20}, T_{10} and T_5.

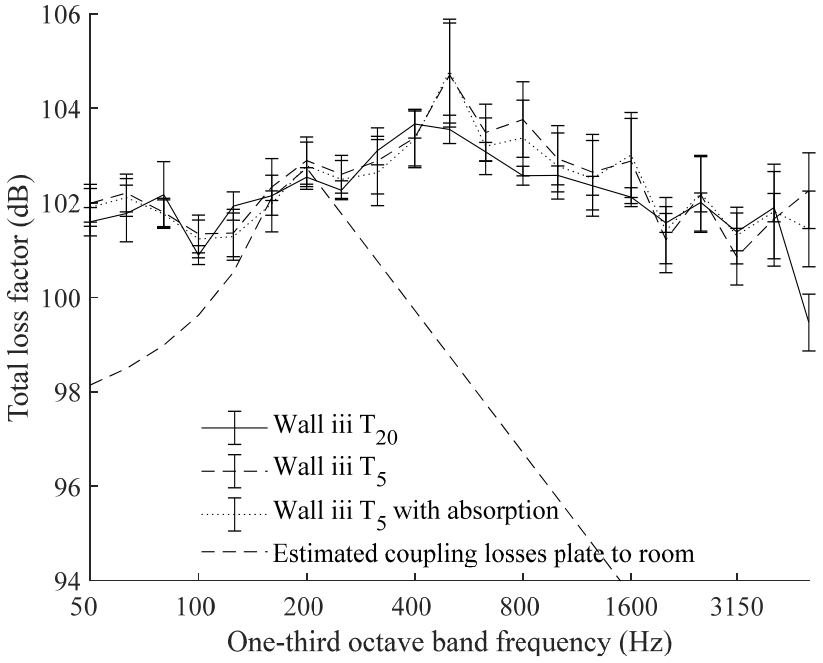

Figure 5-22 Total loss factor of plate (iii) in the L- junction; comparison of T_{20}, T_5, and T_5 with extra absorption.

5.5.6 Model 4: Comparison between measured coupling loss factors and FEM

5.5.6.1 L-junction

The measured coupling loss factors in the forward and reverse directions and from the inner surface to inner surface or inner surface to the outer surface of the wall are shown alongside FEM model for junctions with connection type (a) and (b) in Figure 5-23. The FEM model with connection (a) at the junction shows the best fit to measurements. The mean difference between measurements (inside wall to inside wall) and FEM in this frequency range (50-800Hz) is -2.9dB (minimum -7.1dB, maximum 0.3dB) from wall ii to wall iii and 0.3dB (minimum -2.0dB, maximum 3.5dB) from wall iii to wall ii. The coarse (0.1m mesh) of plate elements used for the FEM model is sufficient to model the 50Hz-800Hz frequency range. However, the measured data includes the whole frequency range of interest (50-5000Hz). A different model may be required to extend the FEM modelled data above 800Hz.

The mean difference obtained by measuring in the forwards or backwards direction is ±1.3dB (±8.4dB and ±3.6dB minimum and maximum depending on direction). The mean difference obtained by comparing measurements on the inside or outside of the wall is 0.1dB (minimum −1.3dB, maximum 1.7dB) from wall ii to wall iii and 0.2dB (minimum -1.7dB, maximum 1.4dB) from wall iii to wall ii. The mean difference obtained by measuring in the forwards or backwards direction is therefore larger than the mean difference obtained by comparing measurements on the inside or outside of the wall and is an indicator that the CLT can be treated as a homogeneous material.

The measured and FEM model data for the L junction with one rotated plate is shown in Figure 5-24. The connection type (a) at the junction for the L-junction with a rotated plate is used to obtain modelled values of coupling loss factor. The mean difference between measurements and FEM in this frequency range (50-800Hz) is -3.1dB (minimum -7.7dB, maximum 1.0dB) from wall ii to wall iii and -4.1dB (minimum -10.3dB, maximum 1.5dB) from wall iii to wall ii. The mean difference obtained by measuring in the forwards or backwards direction is ±0.2dB (±9.0dB and ±10.5dB minimum and maximum depending on direction). Rotating one of the plates of the L-junction increases the coupling loss factor. It is possible that the

output data sampling (using a randomly selected number of data points, in this case twenty points) obscures subtle changes (i.e. ~2.5dB, see below) in the coupling loss factor.

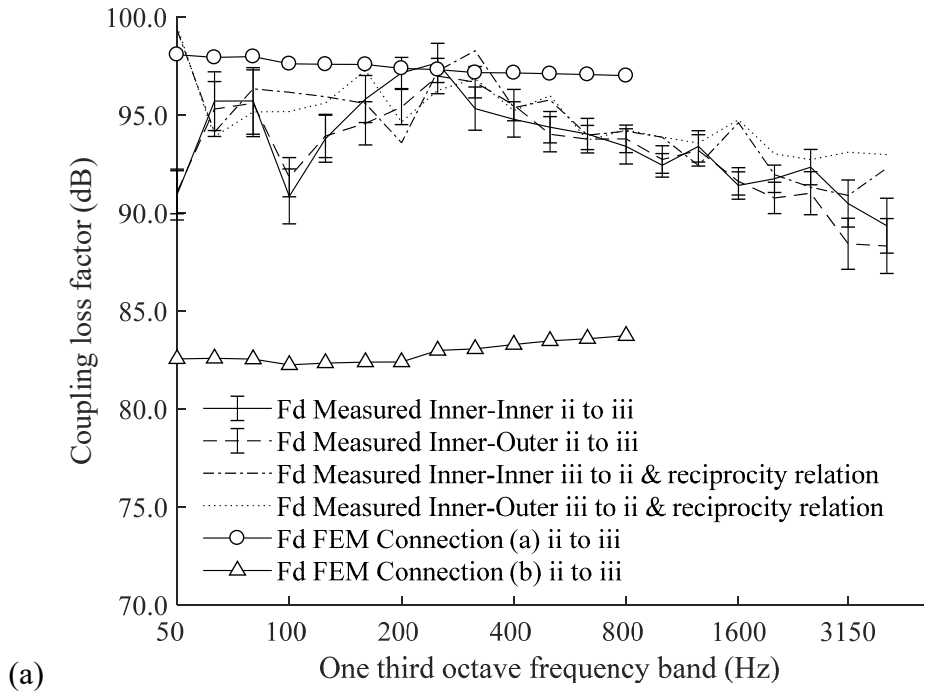

(a)

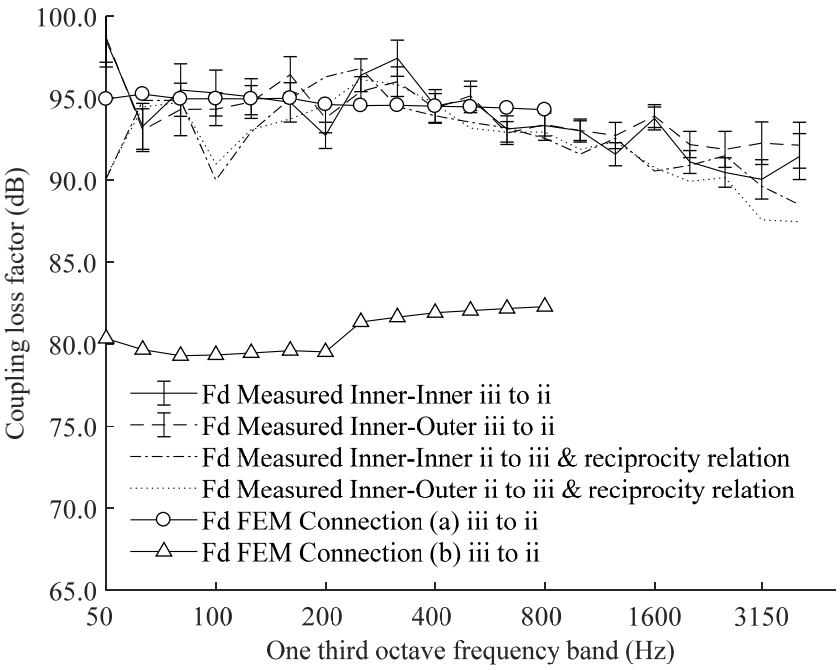

(b)

Figure 5-23 Coupling loss factors for the L-junction (a) wall ii to wall iii (b) wall iii to wall ii.

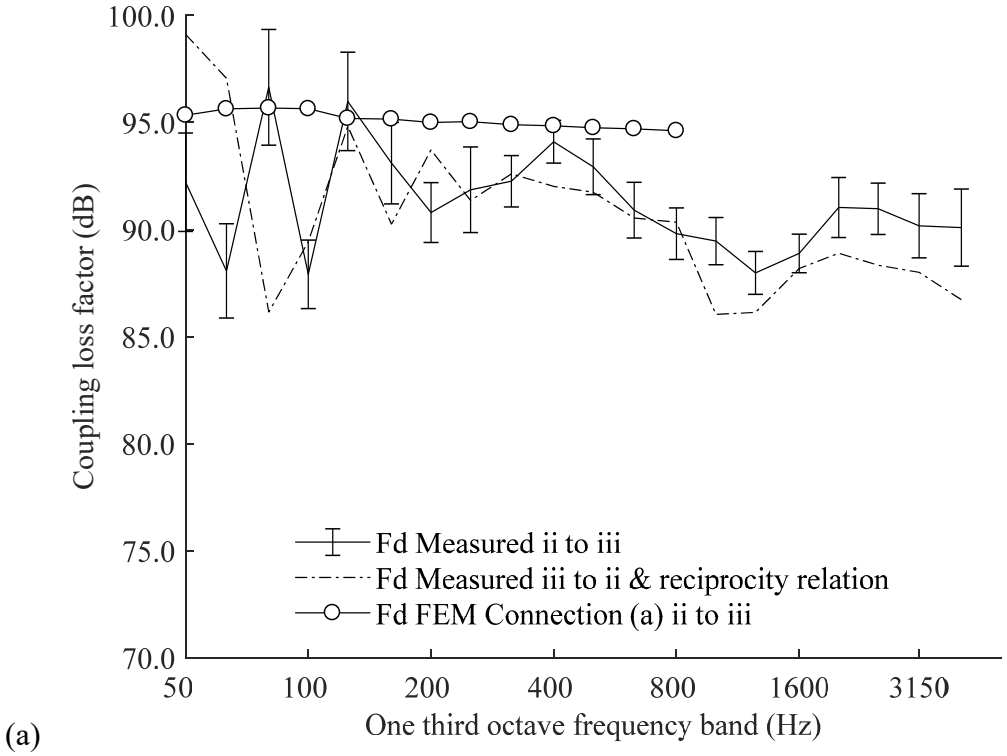

(a)

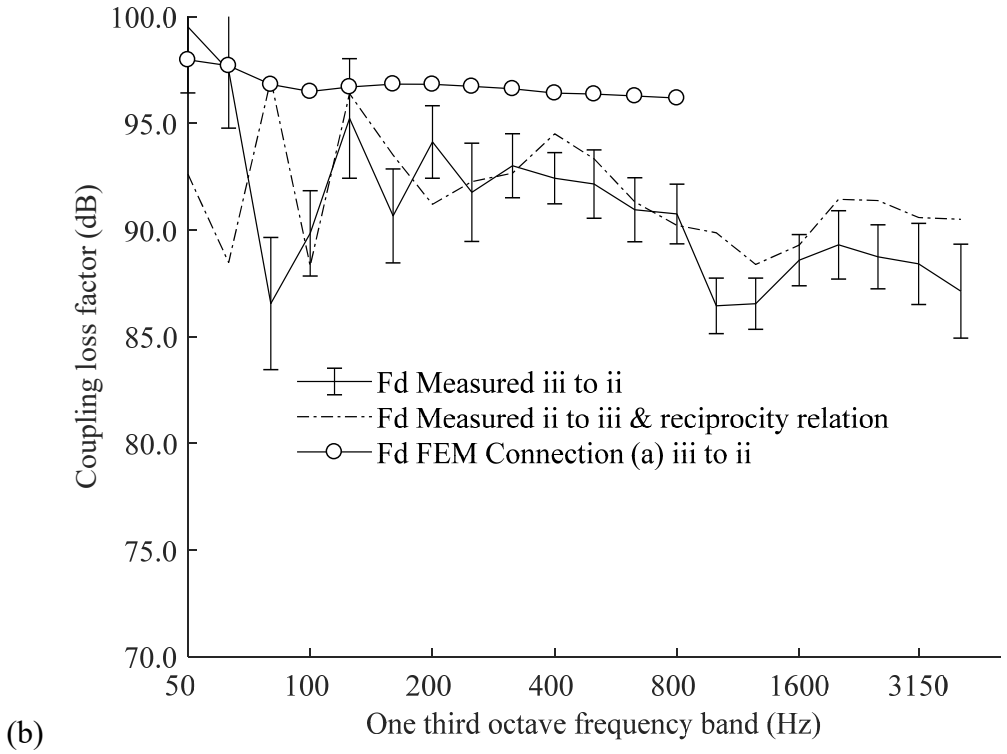

(b)

Figure 5-24 Coupling loss factors for the rotated L-junction (a) wall ii to wall iii (b) wall iii to wall ii.

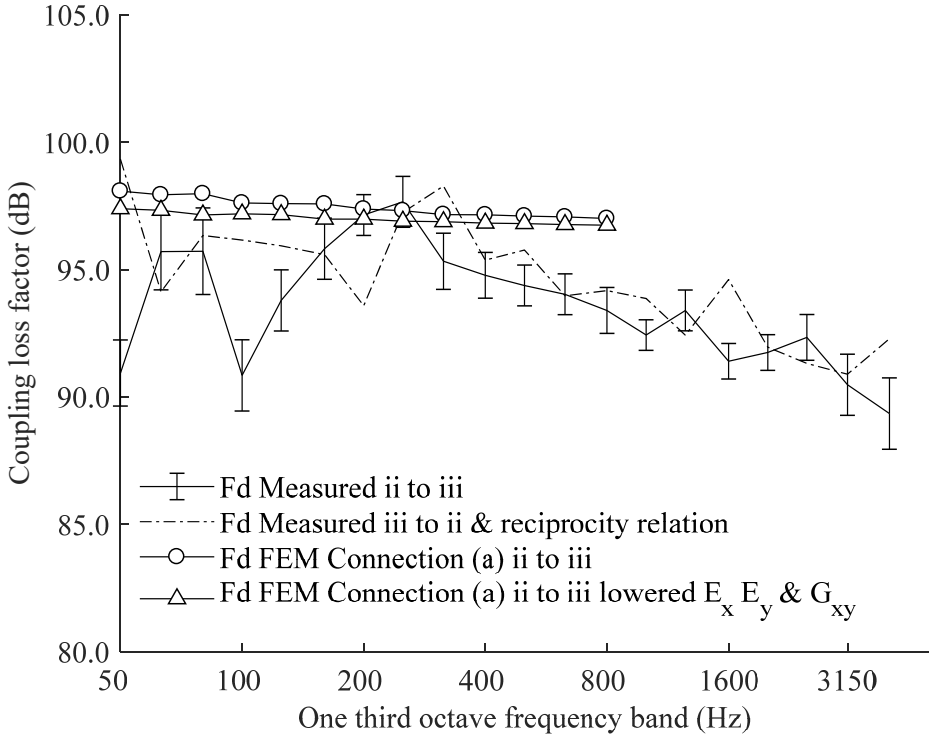

(a)

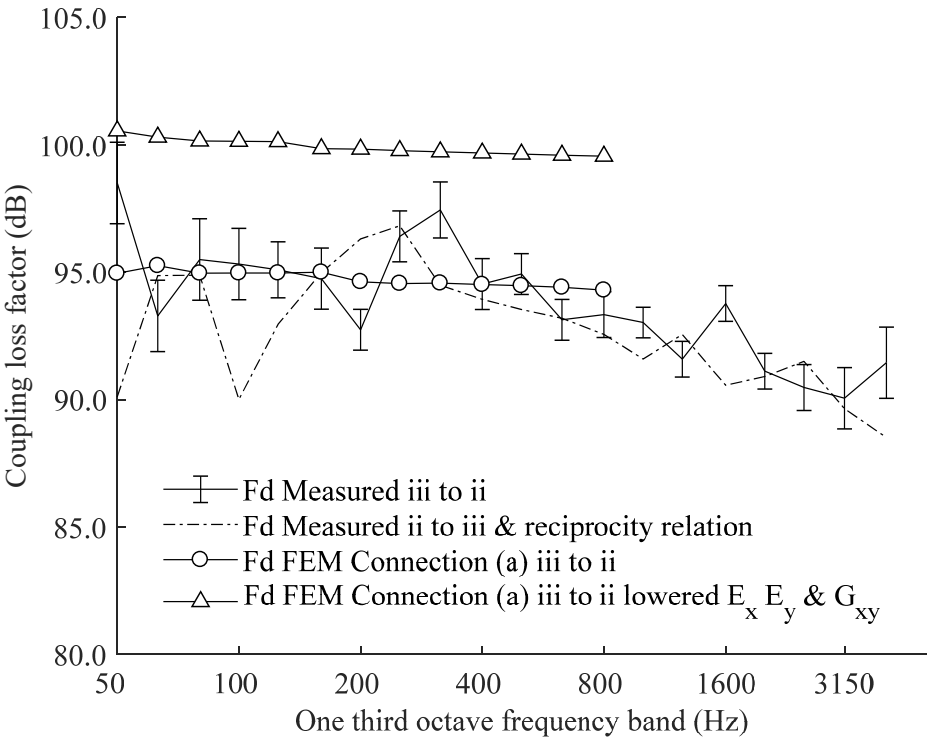

(b)

Figure 5-25 Coupling loss factors for the L-junction with E_x= 1.66x10^{9}Pa, E_y= 3.94x10^{9}Pa, and G_{xy}=1.21x10^{8}Pa (see section 4.7.5) (a) wall ii to wall iii (b) wall iii to wall ii.

Note that there are significant fluctuations in the measurements below 160Hz for the rotated L-junction. The T- junction was cut to form the L-junction and to form the rotated junction the plates were detached, cut to size and then glued and screwed to reattach them in the same manner as for the previous T- and L- junctions. The variation across the frequency range in the rotated L-junction could therefore be due to workmanship in the reassembly process.

An investigation was also made into the effect of lowering the elastic constants on the coupling loss factor. The elastic constants were lowered to E_x= 1.66x10^{9}Pa, E_y= 3.94x10^{9}Pa, and G_{xy}=1.21x10^{8}Pa (see section 4.7.5). G_{yz}' was used as an approximation for G_{xy}. The results are shown in Figure 5-25. Lowering the elastic constants by using the values obtained from the uncorrected measured wavespeed data, does not achieve a better fit between measured and modelled data.

5.5.6.2 T-junction

In Figure 5-26 the coupling loss factors in the forward and reverse directions for the Ff path are compared with FEM using connection types (a), (b), (c) and (d) to connect the perpendicular plate which subdivides the longer plate into two plates at the junction. The coupling loss factors of the Fd and Df paths of the T-junction in the forward and reverse directions are compared with FEM in Figure 5-27 and Figure 5-28 respectively.

All the models for the Ff path are similar because whichever FEM model is used to connect the perpendicular plate (wall (iii)) the other walls are always coupled by connection (a) and this reflects the fact that walls (i) and (ii) are essentially a single plate. The variation between the different FEM models is 1.4dB in the direction wall i to wall ii (Figure 5-26(a)) and 3.3dB, in the direction wall ii to wall i (Figure 5-26(b)). (Some of this is likely due to the random sampling of the FEM model output data points, see below). Comparing measurements with the FEM model with connection (a) at the junction between 50 and 800Hz, the mean difference in the coupling loss factors is -3.1dB (minimum -6.8dB, maximum 1.9dB) from wall i to wall ii and -4.6dB (minimum -7.7dB, maximum -2.7dB) from wall ii to wall i. Comparing measurements with the FEM model with connection (c) at the junction

between 50 and 800Hz, the mean difference in the coupling loss factors is -3.4dB (minimum -7.3dB, maximum 1.4dB) from wall i to wall ii and -2.9dB (minimum -6.1dB, maximum -0.7dB) from wall ii to wall i.

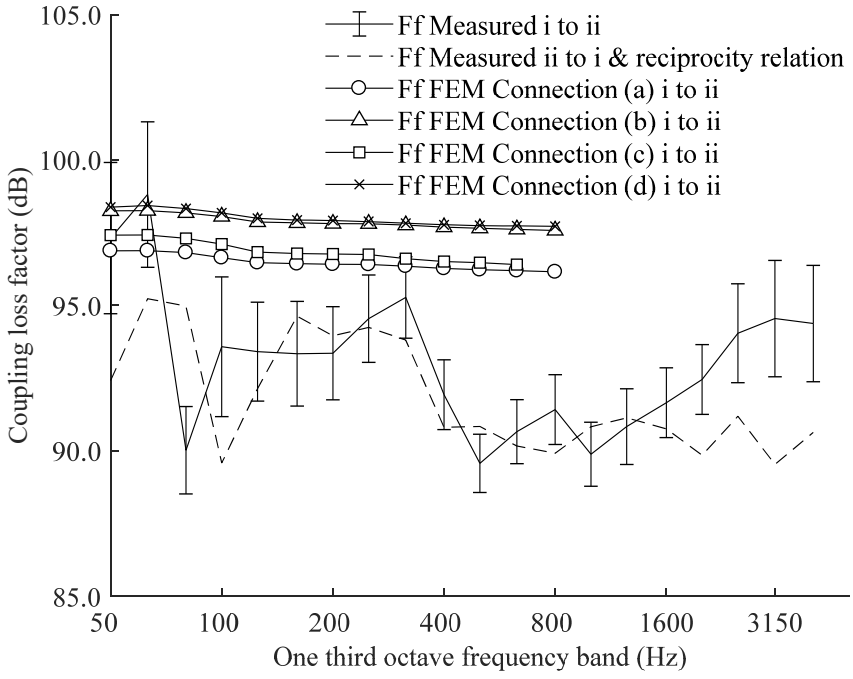

(a)

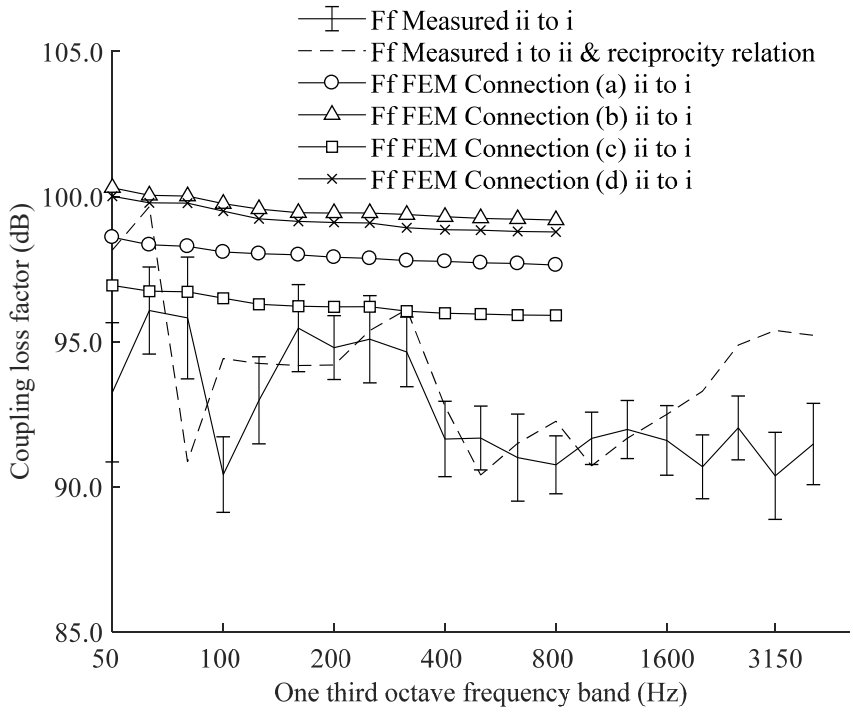

(b)

Figure 5-26 Coupling loss factors for the T-junction in each direction for the Ff path (a) wall i to wall ii (b) wall ii to wall i

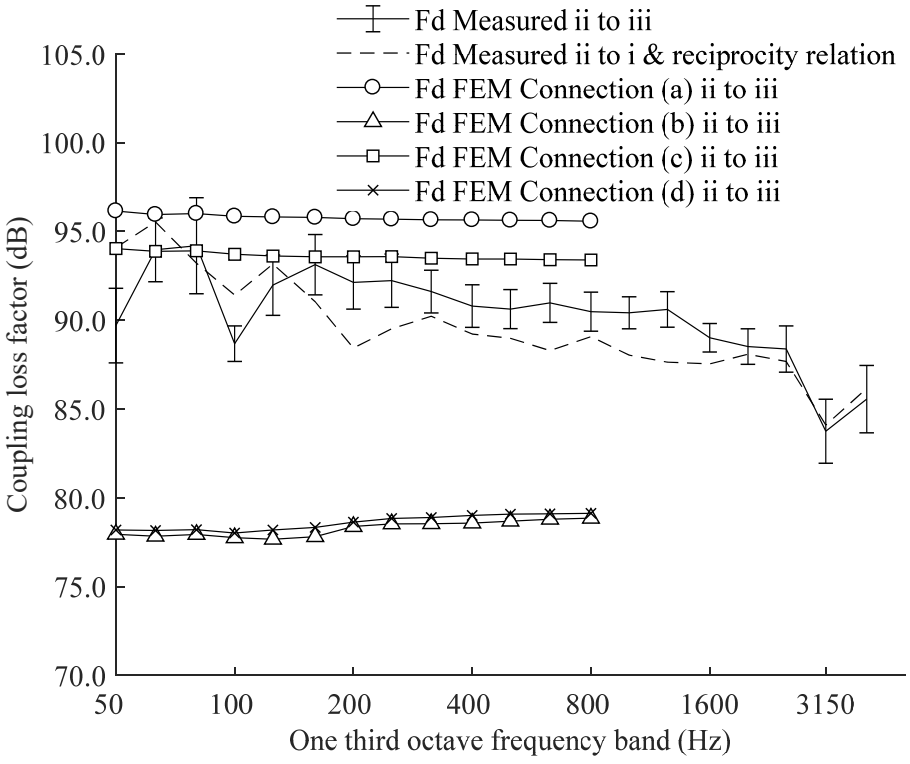

(a)

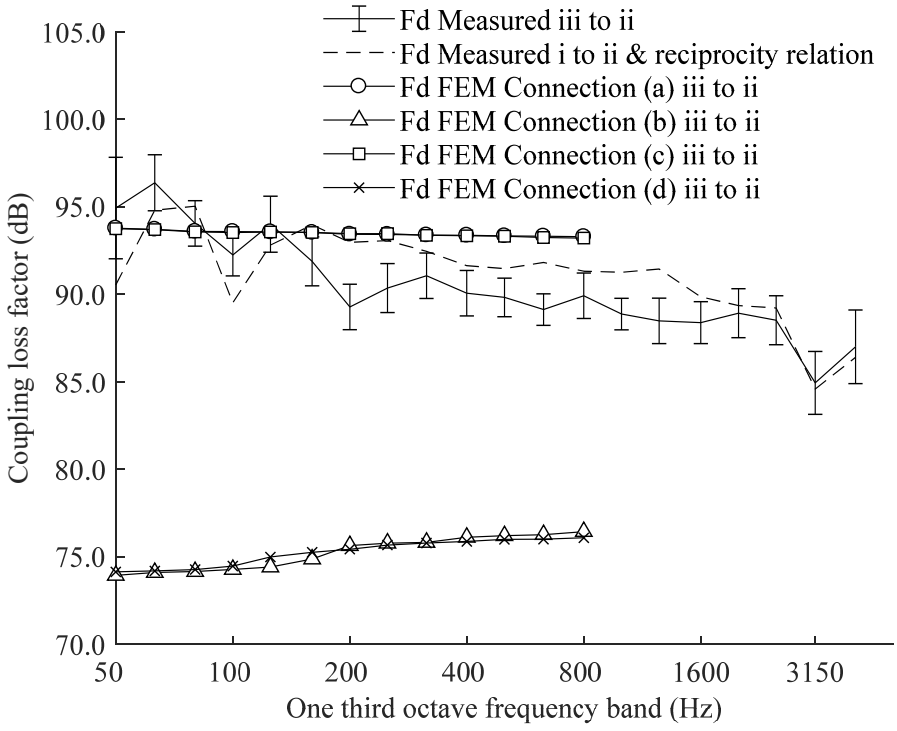

(b)

Figure 5-27 Coupling loss factors for the T-junction in each direction for the Fd path (a) wall ii to wall iii (b) wall iii to wall ii

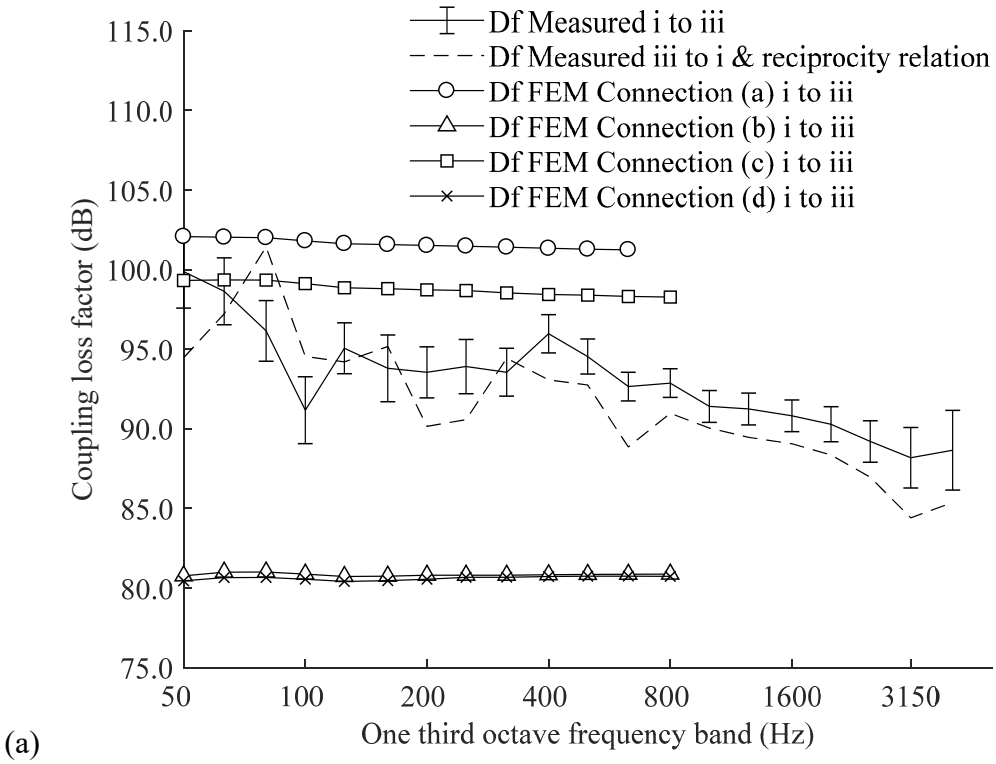

(a)

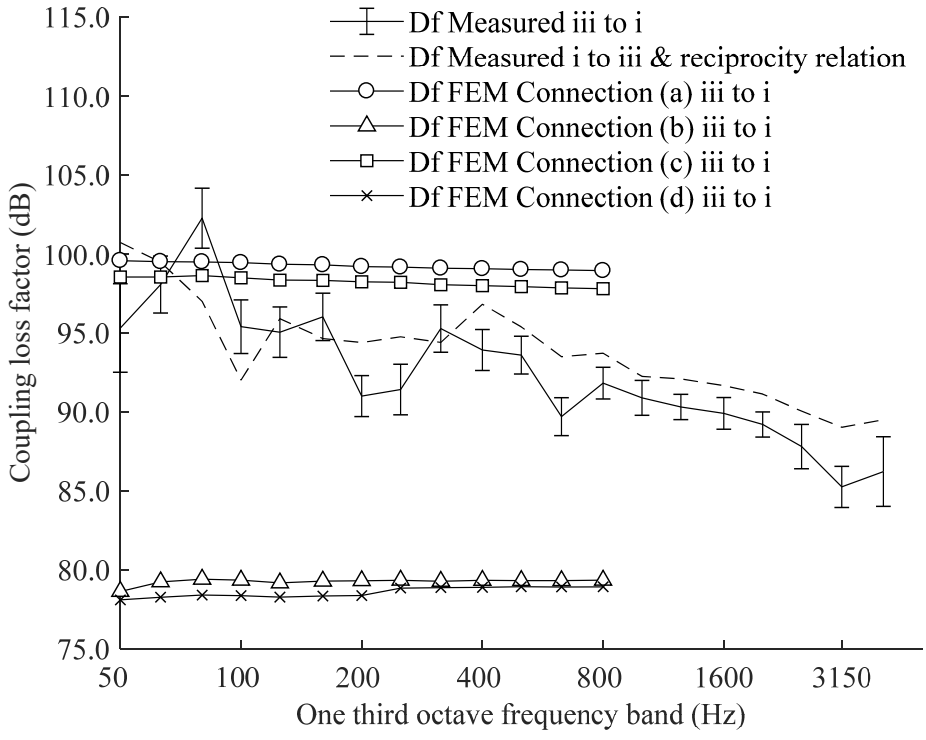

(b)

Figure 5-28 Coupling loss factors for the T-junction in each direction for the Df path (a) wall i to wall iii (b) wall iii to wall i

For the Fd and Df paths (Figure 5-27 and Figure 5-28) the FEM models with connection types (a) and (c) give the closest agreement with measurements. Connection (c) gives slightly better agreement than connection (a). Comparing measurements with the connection (c) FEM model (between 50 and 800Hz), the mean difference in the coupling loss factors for the Fd path is -2.0dB (minimum -5.0dB, maximum 0.3dB) from wall ii to wall iii and -1.7dB (minimum -4.2dB, maximum 2.7dB) from wall iii to wall ii. The mean difference between 50 and 800Hz for the Df path is -4.0dB (minimum -8.0dB, maximum 0.6dB) from wall i to wall iii and -3.7dB (minimum -8.1dB, maximum 3.6dB) from wall iii to wall i.

All coupling loss factor measurements show good agreement between the forwards and reverse directions with mean differences of ±0.8dB, ±0.6dB, and ±1.1dB for the Ff, Fd and Df paths respectively across the frequency range 50-5000Hz. Though there is some disagreement between the forwards and reverse directions for the Ff path at very high frequencies (≥3150Hz). The differences between the coupling loss factors in the forwards and reverse directions can be quoted as a measure of reciprocity of the measurements.

For a given set of coupling condition at the junction (i.e. all degrees of freedom or only rotational degrees of freedom) the calculated results show little variation (50-800Hz) between point and line connections. Comparing connections (a) and (c) the mean differences are 0.4dB, 2.2dB and 2.8dB (50-800Hz) for the Ff, Fd and Df paths respectively and comparing connections (b) and (d) the mean differences are 0.1dB, 0.3dB and 0.2dB (50-800Hz) for the Ff, Fd and Df paths respectively. Which are mostly within the estimated error for a limited number of sampling points, see below. A clearly defined crossover frequency from a point (connections (c) and (d)) to line (connections (a) and (b)) for all models is not clearly visible. Subtle trends are likely to be obscured by the random sampling of twenty nodes for the FEM models. This number of nodes is estimated to give a velocity level difference within 2.5dB of the whole wall values (all nodes are at a distance >0.5m from the edges of the plate). This error value is estimated by comparing the results for selected models with twenty and forty data collection points.

5.5.6.3 Assessment of low frequency fluctuations

A plot of the estimated fluctuations using Eqns. (5-17) and (5-18) and the actual fluctuations (connecting peaks and troughs) in the FEM mobility data for walls (i) and (iii) (large, 12m^2) and wall (ii) (small, 9m^2) are shown in Figure 5-29 and Figure 5-30.

The problem with the estimated upper limit is that when a thin plate modal density is used for the statistical mode count the estimated fluctuations diverge due to the increasing modal density at high frequencies. Even when a frequency-dependant modulus ($E_1(f)$, see section 4.7.5) is used to calculate the number of modes per band the error is constant over the frequency range and does not appear to converge towards ~500Hz. This is unlikely to reflect the actual behaviour of the plate. The upper and lower fluctuation bounds are too wide (±15.0dB) to be meaningful. Note that because of the way the FEM model is constructed the number of global modes are used to perform the calculation rather than the number of modes on the receiving plate [12]. A better estimate at high frequencies (where the coupling between subsystems is weak) could be obtained by dividing the number of global modes equally between the number of subsystems, in this case three, though this does not affect the problem of non-convergence. In addition, the lower limit does not reflect the troughs in the data but this is likely because the data is normalised to linearly fitted mean mobility (because a flat PSD function is used) rather than a thin plate calculated value.

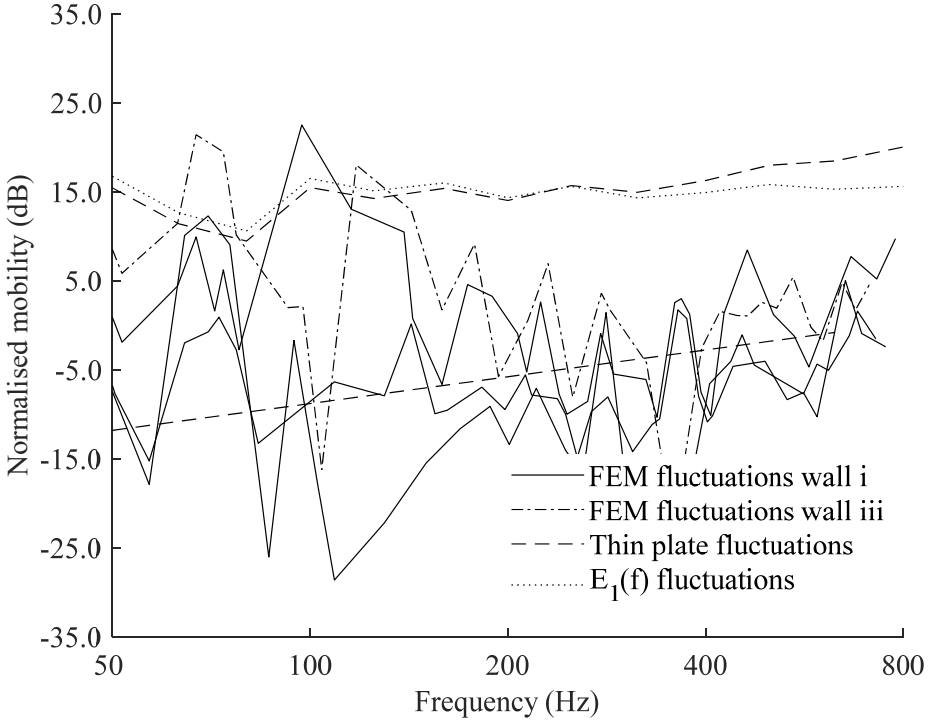

Figure 5-29 Estimated and calculated fluctuations of peak mobility for the $12m^2$ walls (i and iii).

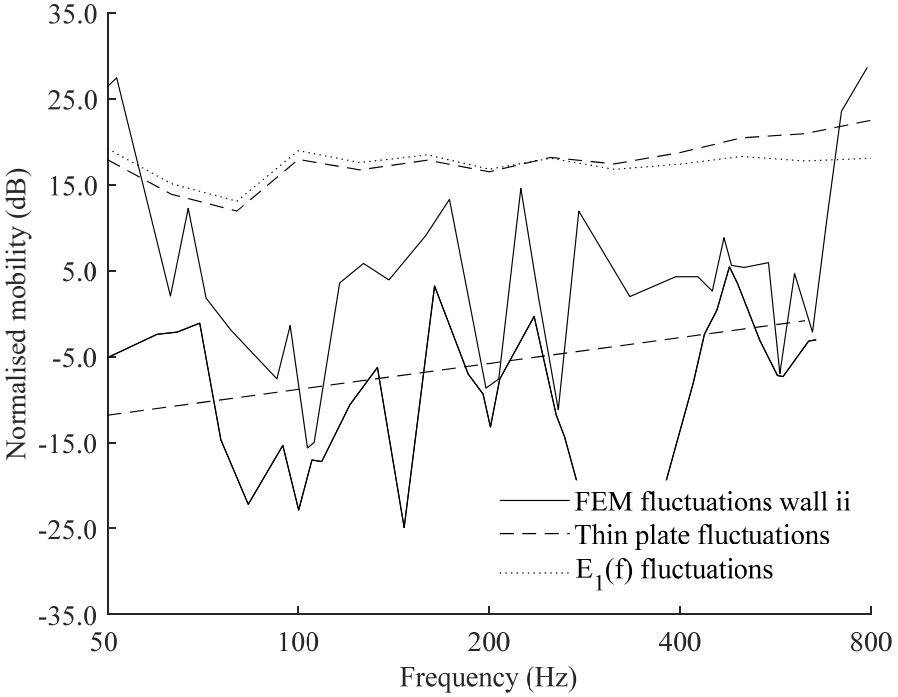

Figure 5-30 Estimated and calculated fluctuations of peak mobility for the $9m^2$ wall (ii).

5.5.7 Comparison between measured and modelled flanking reduction index (R_{ij})

5.5.7.1 L-junction

The flanking reduction index (R_{ij}) is compared with the FEM model for a type (a) connection L-junction and the rotated L-junction in Figure 5-31. The sound reduction index of a nominally identical plate is also shown for comparison. The mean difference between the flanking reduction index and FEM over the modelled frequency range (50-800Hz) were 2.7dB (inner to inner), 2.8dB (inner to outer) and 4.7dB (rotated junction). Where the flanking walls of the junction are identical R_{max} (due to flanking through the room/laboratory space) can be approximated as twice the measured sound reduction index of a nominally identical CLT plate. (The significance of this criterion when measuring with structure-borne sound is discussed further in sections 6.4.2 and 6.6.2.) The plot shows that the R_{max} could have only affected the measurements at 50Hz, 63Hz, 400Hz and 500Hz.

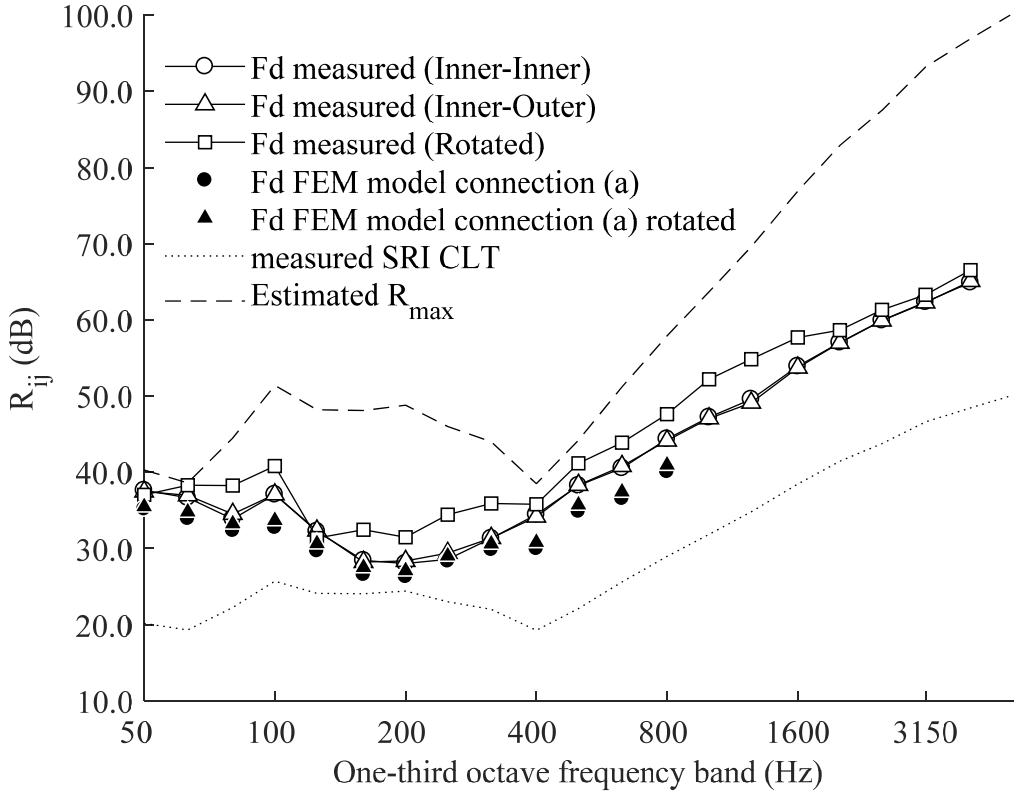

Figure 5-31 Flanking reduction index data for the L- and rotated L-junctions.

Agreement between measured values and the FEM model using a type (a) connection is reasonably good for the inner-inner and inner-outer L-junction measurements (though not within the 95% confidence limits which are too narrow to be shown in Figure 5-31) but not for the rotated L-junction. A comparison of the measured sound reduction index with the flanking reduction index shows that the apparent sound reduction index (R', for this simple CLT junction) is unlikely to be affected by flanking for all but a few third octave bands (e.g. 160Hz and 200Hz).

5.5.7.2 T-junction

The flanking reduction index is compared with the FEM calculation for connection type (c), which gave the closest agreement of all models, for the T-junction in Figure 5-32. The sound reduction index of a nominally identical plate is also shown for comparison. The mean difference between the flanking reduction index and FEM over the modelled frequency range (50-800Hz) were 4.2dB, 5.1dB and 6.2dB for the Ff, Fd and Df paths respectively. The R_{max} of the measurement is formulated in a similar way to section 5.5.7.1 and is found to be of possible significance for frequency bands 50Hz, 63Hz, 400Hz and 500Hz only.

The agreement between measured values and the FEM model using a type (c) connection is poor for flanking paths Ff, Fd and Df; flanking is overestimated. The best agreement is obtained at low frequencies (<200Hz). The models were assembled using the global modes of the junction and agreement with measured results may be improved in the mid frequency range by a model which instead uses only the local modes of individual panels.

Lack of agreement with the FEM model could also be due to the emphasis on the coupling between bending waves using conventional plate elements. For CLT plates there might be different types of wave (e.g. transverse shear waves). These could possibly be modelled using continuum plate elements, however this might be at the expense of bending coupling accuracy. Further work would be required to determine the effect of other wave types.

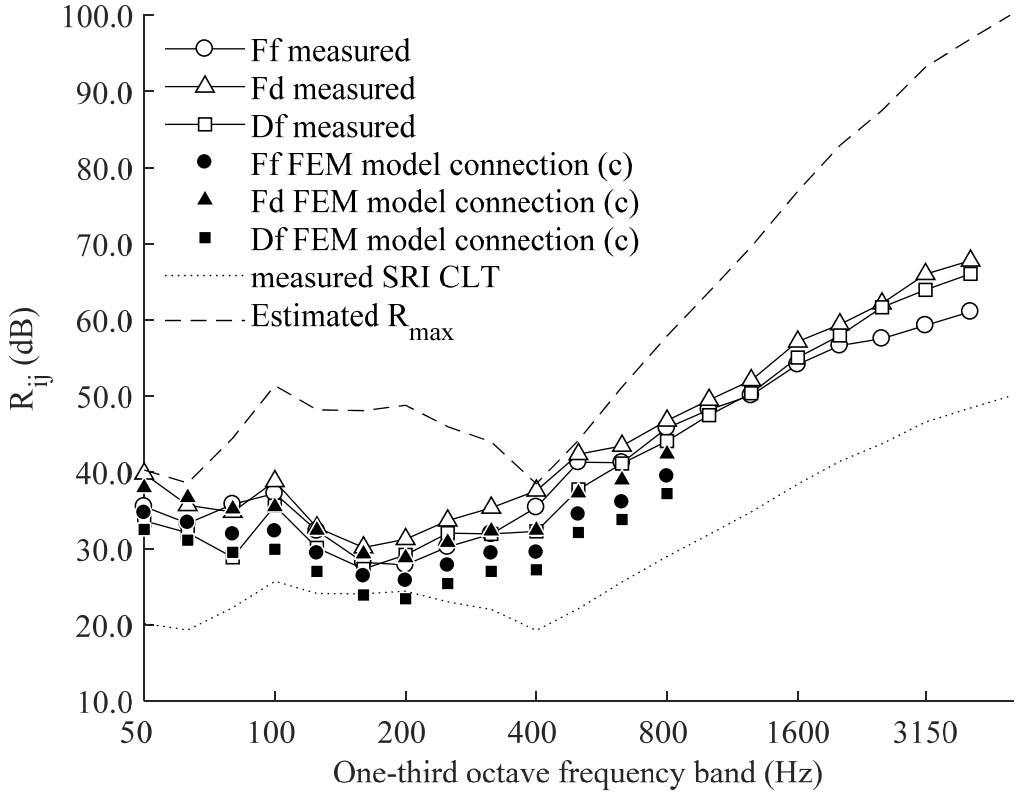

Figure 5-32 Flanking reduction index data for the T-junction.

5.6 Conclusion

Experimental modal analysis indicated that it was only possible to match the first few modes of a freely supported plate/junction or "simply supported" plate. For the latter, it is possible that the mounting conditions of the plate were not reasonable approximations to simply supported. It was also difficult to model the boundary conditions of the plates in the junctions; however, improvements were made by inserting horizontal springs in the model along the bottom edge of the plates to represent the rubber mounts.

Low-frequency and high frequency convergence analysis show the effect of the stiffness contribution from truncated higher modes. At low frequencies where the modal overlap is also low only the troughs between modes are affected but at high frequencies the peak mobility is also affected. It would be computationally more cost effective to be able to calculate the stiffness contribution from truncated higher

modes using a method of residual modes (such as described in section 0 for simply supported plates). However, these methods are limited by suitable boundary conditions and the appropriateness of available calculation methods. An alternative explanation for the increased phase differences between two points when directly measuring bending wavespeed on a CLT plate, encountered in section 4.7.5, is to attribute it to the stiffness contribution from higher modes. This is increased at the high end of the spectrum because of the increasing modal density towards higher frequencies as the bending phase velocity levels off to the Rayleigh wavespeed.

A variety of connection methodologies for CLT plates are available on the market. For the methodology described here (glued and screwed at 500mm centres) the type (a) connection at the L-junction and type (c) connection at the T-junction are the models selected to match most closely to the measured data. Measurable differences between the type (a) and (c) connections (line or point) were obscured by the method of outputting r.m.s. velocity which relied on a random selection of (twenty) output nodes. The L-junction gives the closest agreement between the FEM model and measured results. The relatively poor agreement with the results of the T-junction might require other FEM elements to accurately model coupling between bending modes only and other wave types.

It is noteworthy that different connection types gave the best predictions for different junction types. There were no significant changes to the method of connection as elements were taken away; the T-junction was simply cut to form the L-junction. One possible explanation is that the total sum of moments acting on the junction as elements were removed would be lower and perhaps this affected the properties of the glue line. The results were also contrary to the expectation that connection (b) or (d) would match most closely to the measured data. Hinged or pinned connections have proven successful in previous work involving timber components, such as deep beams [9, 10, 11] .

Fully integrated elements were selected to model the junctions and it is possible to model only a limited part of the building acoustics range (50-800Hz). FEM models are limited by the specific methodology which determines the wave types that are most accurately predicted such as bending waves, transverse shear, or dilatational

waves. Other modal families than bending waves may need to be considered and expressions for cross coupling between families obtained. All models were constructed using the global modes of the junction, further work could include constructing a model in ABAQUS using the local modes of the separate panels to see if similar results are obtained. (It may be possible to achieve this using the SIM architecture [122].)

A method described by Craik and Galbrun [9] or Craik *et al*. [12] (which uses the thin plate statistical mode count) was used to estimate upper and lower fluctuation limits to determine an error envelope at low frequencies. However, this did not result in a converging error estimation of the upper fluctuation limit of CLT, and might need to be revised to allow for the thick plate properties to give a meaningful limit.

Additional material properties of the panel required for modelling were estimated by calculation using an equivalent plate model for bending or the "law of mixtures" appropriately. Using elastic constants obtained from a direct measurement of the bending wavespeed uncorrected for diffuse phase from section 4.7.5 did not result in an improved prediction.

Results involving the measured data indicate that the application of the prediction standard (EN12354) to CLT plates could be expected to work well when using measured data for the inputs. EN12354 has the potential to provide an effective model for CLT plates of the whole building acoustics range (50-5000Hz). Modal overlap is high for all but the lowest frequencies. With respect to applicability of the measurements; the plates behave in a homogenous manner and the principle of reciprocity can be applied to plate systems. Precision is reduced when using detached and reattached plates. A comparison between structure-borne and airborne measurement methods is made for a more complicated junction in chapter 6.

6 Prediction of direct and flanking transmission across a timber-concrete composite floor and cross laminated timber flanking walls

6.1 Introduction

In buildings, it is common that the flanking transmission between two rooms is more significant than the direct path (Dd path see Figure 2-10) to determine the apparent SRI (R') in situ [86]. In this chapter, two methodologies to measure flanking for the combined heavyweight timber floor and CLT junction are considered. The methods can be found in ISO 10848 [94]. In method No. 1, the flanking vibration reduction index is determined from the velocity level difference measured using structure-borne excitation. Individual pathways may be evaluated by measuring the velocity levels of selected pairs of elements. Method No. 2 measures the normalised flanking transmission directly using airborne sound where individual paths are measured by selective shielding of the direct and flanking elements. The limiting factors for this method are based on the practical installation requirements and the degree to which the elements can be appropriately shielded. This is particularly apparent at low frequencies. Three flanking paths were considered separately (Ff, Fd and Df paths, see Figure 2-10, although an additional flanking path outside the laboratory was shown to limit the Ff measurement and the Df path was limited by the R_{max} of the laboratory).

The applicability of EN12354 to determine apparent SRI in the laboratory is discussed in terms of practical considerations, qualification of the laboratory test stand to quantify flanking transmission, the precision of the measurement and accuracy of the methods. Preliminary measurements were used to qualify the test

stand including: Flanking of the test stand, level differences between the measured junction and all adjacent test elements, airborne flanking outside the laboratory and R_{max} values. The additional concepts of "build stage" and measurement direction (investigating the reciprocity) were also noted. The build stages are described in section 6.4.1. The test specimen was not remounted and the source and accelerometer positions were not altered between tests.

Accuracy in this chapter is defined by the standard error calculation on the measurement data. (95% confidence limits are plotted on graphs.) However, nominally identical partitions perform differently when installed in different situations, (e.g. due to factors such as the low modal density of the partitions and rooms of different sizes, the curing and ageing of samples or the mounting method used to attach the measured structure to the surrounding structure).

The measurement methodologies used in the chapter were designed with the guidance of published standards and carried out using newly commissioned laboratory facilities. However, (at the time of measurement) they were not accredited using quality and competence standards.

6.2 Test junction description

The vertical T-junction was installed in a flanking test stand. This CLT junction is more complex than the CLT junctions modelled in chapter 5 although it is simpler than in an actual building. The junction consisted of the HBV floor described in section 3.2 combined in a vertical T-junction with two 80mm CLT walls consisting of three 15mm-50mm-15mm layers. It is nominally identical to that described in section 4.2. Sketches of the test junction are shown in APPENDIX B.

The junction was simplified based on the following considerations: Usually the cavity size on this floor is dictated by the beam spacing, which in turn depends on the static load on the floor and the manufacturer, ERNE, advised that the optimum beam spacing for this floor span was 600mm. However, a narrower beam spacing of 360mm was retained from the pilot project. This means the floor is over-engineered with more beams and suspended ceiling hangers than in normal practice. The size of CLT wall is limited to a maximum of 3m in height or width to allow transportation

to site (height was selected to be the smaller dimension). However, the minimum floor height installation in the lightweight facility did not permit such a short (or narrow) wall therefore a concrete step running the length of the wall was used to raise the floor installation to the required level for testing (see Figure 6-1).

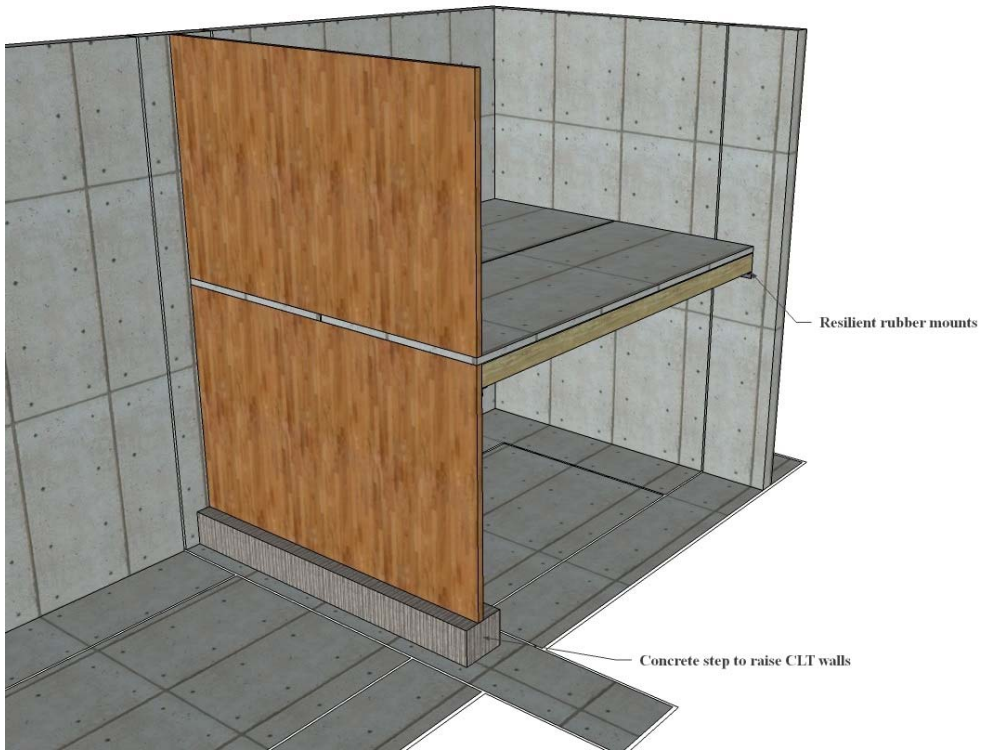

Figure 6-1 Sketch showing installation of the junction in the flanking laboratory.

Figure 6-2 Beams located on rubber isolators at the concrete default element.

The CLT walls were fixed with twelve angle brackets on the underside (each located at the supporting timber beams) and two angle brackets one on each HBV floor segment on the upper side (see Figure 6-3). The beams run in the direction of the long span (5.75m). At the concrete default element, the beams sit on rubber isolators (see Figure 6-1 and Figure 6-2) on the angle as described in section 3.5.1.

(a)  (b) 

(c) 

Figure 6-3 Angle brackets (a) dimensions (b) fixed on the upper side (c) supporting the beams on the underside.

The concrete floor was sandwiched between the CLT walls. In practice, the beams would usually be installed between the CLT walls. However, this junction was assembled to represent a simplified version of what would be used in practice. A suspended ceiling on resilient hangers was attached to the beams as would be installed in practice. A floating floor would usually be installed but this was omitted to simplify the installation. Also in practice, an assembly of gypsum board would be installed to shield the CLT. This would be fixed directly onto the CLT with or without timber battens, but again this was omitted to simplify the installation. Sketches of the floor can also be found in APPENDIX B. It was important to maintain an acoustic break between default elements and the junction (see section 6.3). The default ceiling was therefore supported by the CLT wall at the top of the junction and opposite concrete element (E2 in Figure 6-5) as the load bearing walls (Figure 6-4).

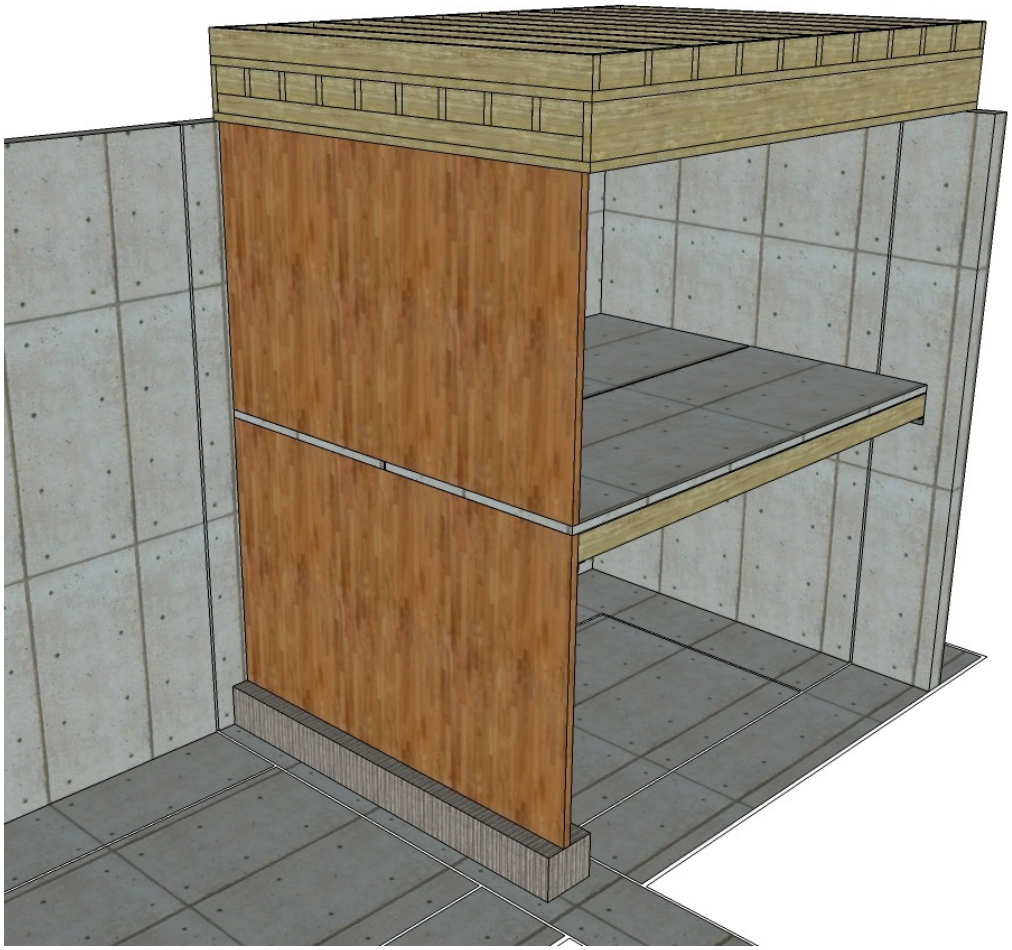

Figure 6-4 Sketch showing the load bearing of the roof default element.

6.3 Description and qualification of the test stand

6.3.1 The laboratory base structure

The test stand (LK106) at EMPA Acoustic laboratories was partially commissioned to facilitate the flanking measurements of a vertical T-junction. It consists of structurally isolated concrete floor plates and 250mm thick concrete L-support walls with a structurally decoupled test aperture which enables structural connection or decoupling as required by the test junction and elements. A sketch of the test stand indicating the labels used to identify the concrete elements is shown in Figure 6-5. This structure supports both airborne and structure-borne methodologies.

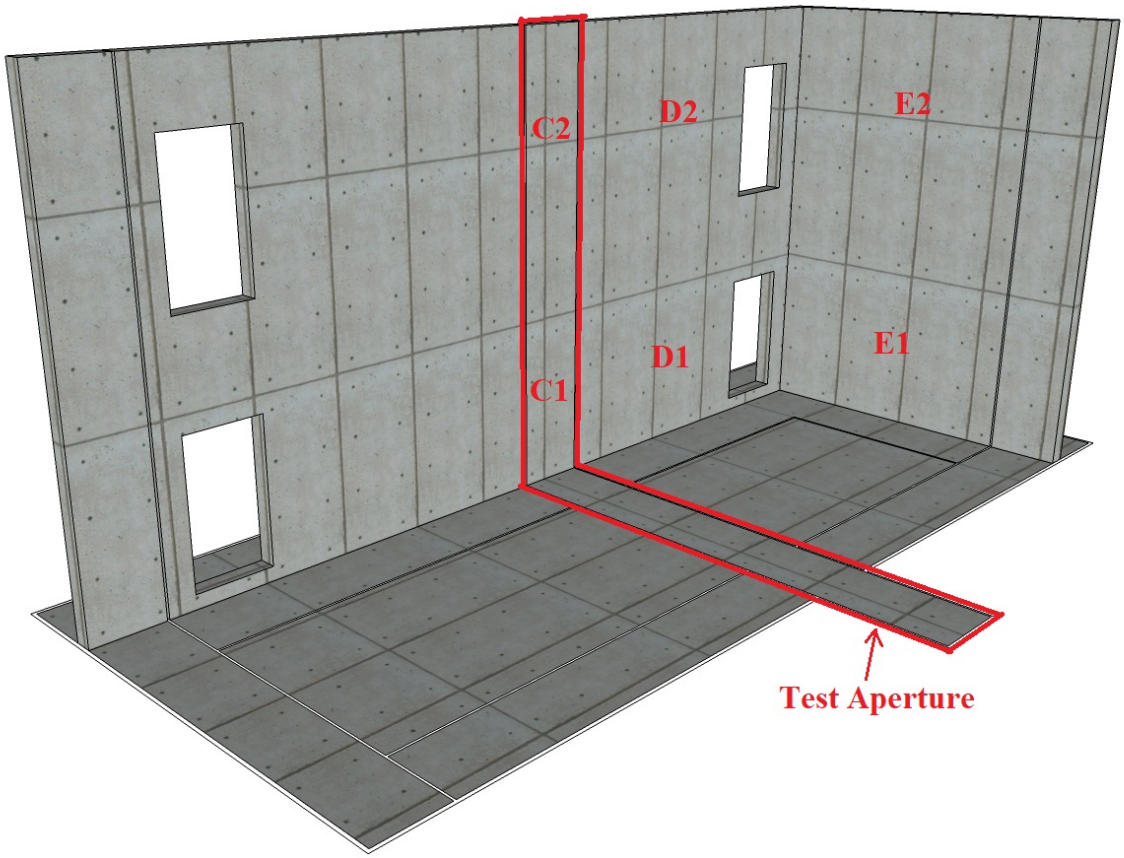

Figure 6-5 Idealised sketch of the test stand (LK106), showing the labelling of the concrete base elements.

6.3.2 Default elements

Asymmetric CLT triple wall "default elements" (sketched and photographed in Figure 6-6) with permanent shielding of depth 200mm were added to close off the rooms. The concrete walls described above also include permanently placed shielding with a depth of 200mm to suppress flanking transmission. The permanent shielding consists of a double layer of 12mm particleboard which has a removable upper layer which can be fitted to different thicknesses of floor or shaped around beams as necessary. The cavity is filled with mineral wool, and the particleboard is fixed to the face of the default elements using resilient fixings.

(a) (b)

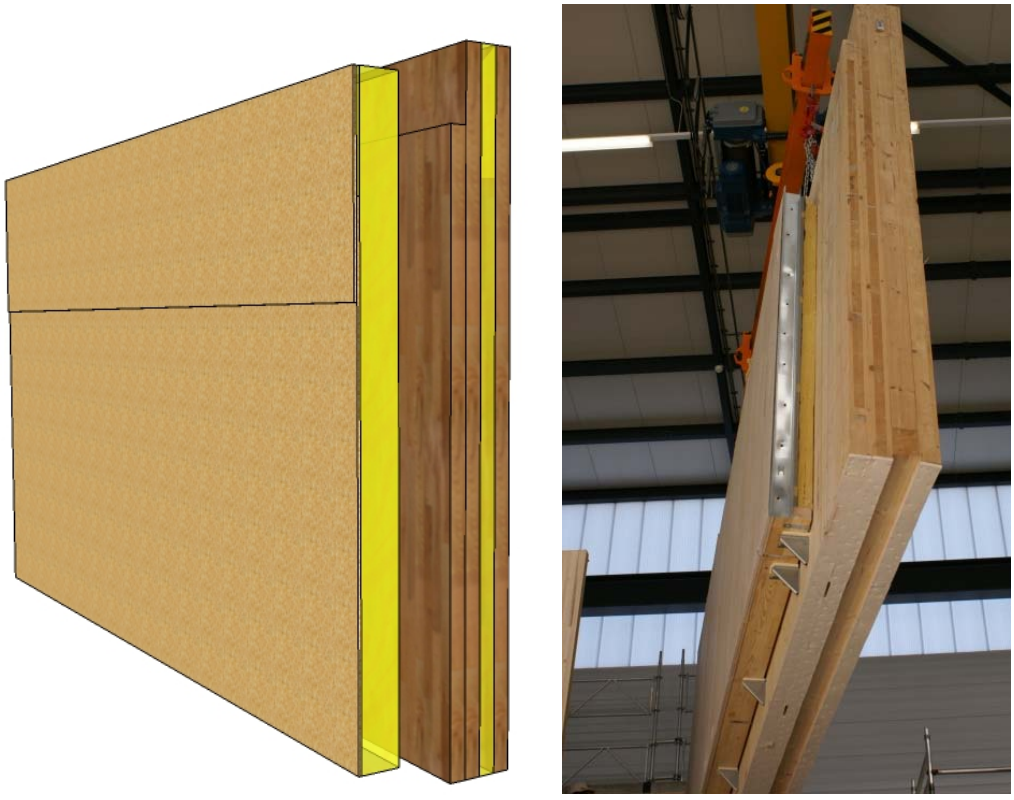

Figure 6-6 Default elements for LK106: (a) idealised sketch and (b) photograph.

The geometry of the default elements is such that they do not need to be structurally coupled to the test elements thus supressing the additional flanking paths by providing an acoustic break. Structure-borne tests can be carried out with or without

closure of the rooms. This enables direct comparison of the available methodologies for flanking tests. Figure 6-7 shows the test stand and the default elements which would be used to close off the rooms and the labelling system used to reference the elements.

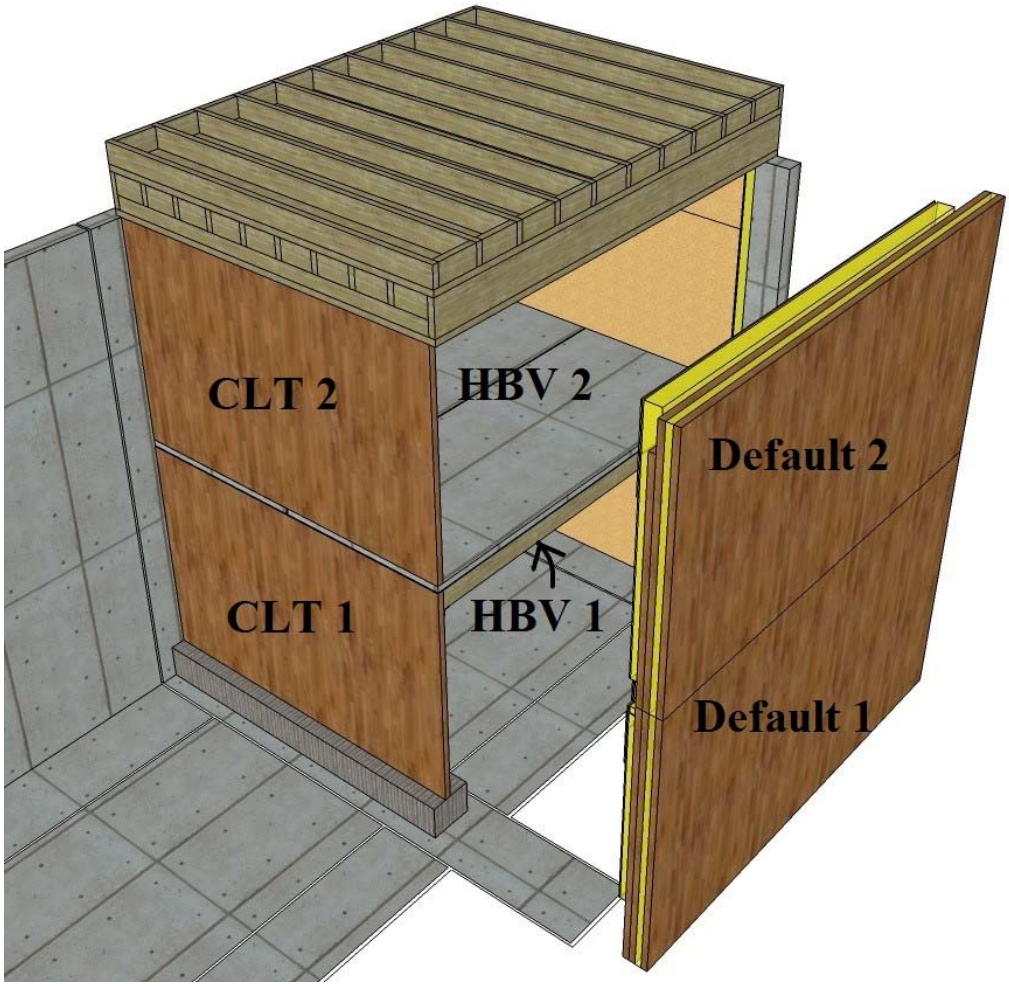

Figure 6-7 Sketch indicating the test and default elements.

6.3.3 Shielding of the measured junction elements

To determine the contribution of paths using airborne sound, the test element walls that should not be included in a specific path must be shielded. To achieve shielding of the CLT walls a double layer of 12.5mm plasterboard was mounted on 60mm x 80mm timber battens in front of the elements. The cavity depth was 280mm to the backside of the first plasterboard layer and the cavity was filled with absorptive material (2 x 100mm layers of Caruso, density 2.0kg/m^2). Three timber battens were

used and they were hung from the default wall shielding at each end using resilient elements so that they were not in contact with the test element (see Figure A-3 in APPENDIX A). All perimeters were sealed with silicone to provide an airtight seal, and taped.

To shield the floor element a double layer of 15mm OSB was placed on two layers of denser absorptive material (2 x 100mm Caruso, density 4.0kg/m^2). The higher density material was to ensure less compression from the weight of the OSB layers (see Figure A-7 in APPENDIX A). The ceiling was shielded by attaching steel U-profiles to the default shielding on the default and concrete walls and pairs of metal studs were used in the direction perpendicular to the beams to mount a double layer of 12.5mm plasterboard, again the cavity was filled with absorptive material (2 x 100mm layers of Caruso, density 2.0kg/m^2), see Figure A-7 in APPENDIX A. All shielding could be assembled as required (Figure A-1 to Figure A-8 in APPENDIX A) to measure the various pathways and estimate R_{max}. As with the wall shielding all perimeters were sealed with silicone to provide an airtight seal, and taped.

6.3.4 Junction installation requirements

In ISO 10848-1 [94] requirements to eliminate (or at least minimise) systematic errors are described. This is to ensure that the measurement of flanking is an accurate reflection of the junction and is not instead due to a strong flanking path within the test stand. When measuring flanking transmission with combinations of heavyweight and lightweight elements there are conflicting practical considerations. The first is the physical installation of the junction in the test space to ensure an accurate measurement without additional (unwanted) flanking transmission through the laboratory structure. The easiest way to achieve this is by isolating the junction (i.e. ensuring an acoustic break between the junction and flanking laboratory). The second consideration is that the installation should be representative of in situ. ISO 10848 states that for junctions where the coupling losses of the connected elements (e.g. concrete, CLT) primarily determine the total loss factor, the junction should be installed as it is usually installed in practice. For other panel types (e.g. plasterboard) where the internal losses primarily determine the total loss factor, the method of

installation is less important. However, when either junction is installed as in practice there may be a conflict with the first practical consideration.

To ensure that the default elements were installed in such a manner that avoid any "short-circuits" to eliminate unwanted flanking paths via the test stand (e.g. see Figure 6-8) an acoustic break was maintained between the test laboratory or default elements and the junction. Air gaps (closed with mastic where necessary) and resilient elements were used to help fulfill this requirement. For example, an airgap between the test junction and test laboratory or default elements was used to prevent energy transfer via the paths AB and CD.

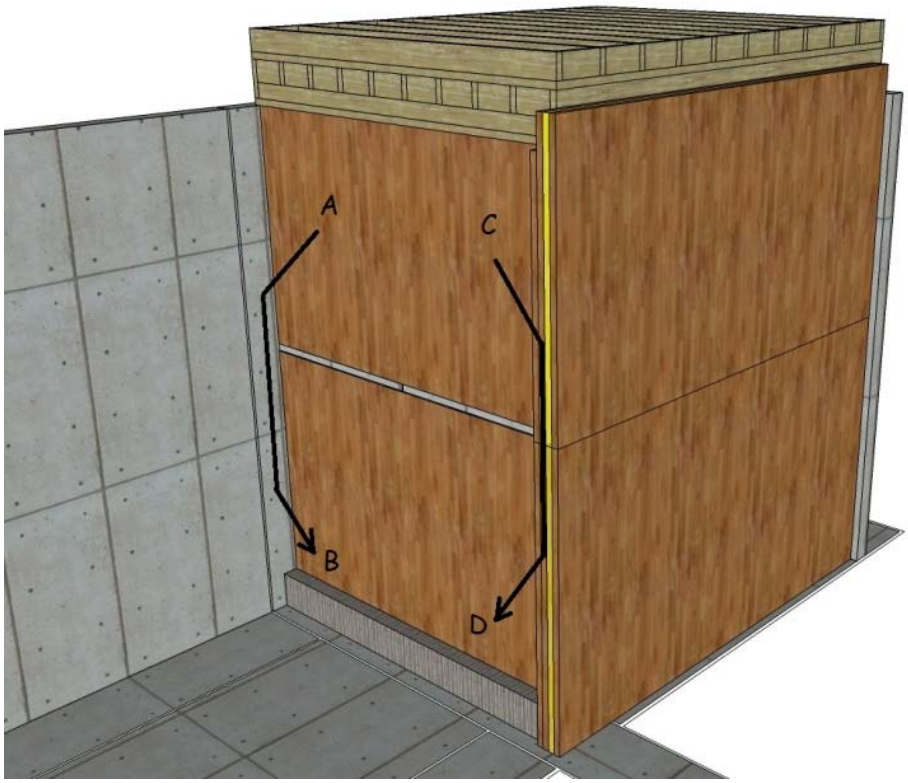

Figure 6-8 No structural connection at the test stand and default walls to supress flanking paths AB and CD.

Preliminary measurements were made to assess the decoupling between the junction and default elements, or shielding. These include vibration reduction index of the test stand concrete L-support (i.e. elements D1 to E1, D2 to E2, D1 to D2 and E1 to E2, see also Figure 6-5) and velocity level differences between the vertical T-junction and the test aperture (i.e. CLT1 to C1 and CLT2 to C2), the structurally decoupled

concrete elements (i.e. C1 to D1 and C2 to D2, see also Figure 6-5) and between the vertical T-junction and the timber default elements (e.g. CLT1 to Default 1, HBV2 to Default 1) or shielding elements (e.g. CLT1 to shielding on Default 1, CLT1 to shielding on D1, HBV2 to shielding on Default 1, or HBV2 to shielding on D2, see also Figure 6-7).

The acoustic breaks between all separated elements of the laboratory, also between the junction and laboratory elements were judged to be adequate. The prescribed limit (see Eqn. (6-1)) was fulfilled in most cases except in selected cases between the CLT elements and the shielding and, at high frequencies (>1000Hz) only, between the HBV floor and the shielding.

$$D_{\mathrm{v,ij}} + 10\lg\left(\frac{\rho_{\mathrm{s,i}} n_{\mathrm{j}}(f)}{\rho_{\mathrm{s,j}} n_{\mathrm{i}}(f)}\right) > 10 \qquad (6\text{-}1)$$

However, certainly in the latter case, this was shown to be coupling through the room rather than structural coupling. Which demonstrates a drawback of this method to indicate whether structural coupling is present between adjacent elements. (Especially when a lightweight element such as shielding is being measured.) Difficulties were also encountered to demonstrate that an adequate acoustic break was implemented when segments of shielding were excited indirectly from another shielding segment (on the same wall) rather than directly by the shaker.

It was demonstrated that the addition of silicone sealant to seal gaps between elements and at shielding edges did not compromise acoustic breaks. The validity of subsequent measurements, and the maximum measurable values of each test stand configuration were determined by measuring flanking due to noise breakout from the test stand and back into the receiver room and R_{max} values. This measurement regime was not sufficiently comprehensive to ensure accurate results which are transferable to “in situ” for all partition types. However, it was sufficient to determine the validity of the data in this case.

6.3.5 Airborne flanking outside the test stand

During measurements of the velocity levels for shielding configurations (g) Ff and (h) Df path (Figure A-7 and Figure A-8 in APPENDIX A) with airborne excitation, the sound pressure level in the surrounding laboratory outside the test stand was monitored. This was achieved by mounting two microphones, one of each at 2m distance from the CLT faces. The sound pressure level difference between inside the rooms and outside in the laboratory space were then converted to a sound pressure level in the receiving room with a back calculation of Eqn. (2-172) to give:

$$L_{\mathrm{p2}} = L_{\mathrm{p1}} - R + 10\mathrm{lg}\left(\frac{S}{A}\right) \tag{6-2}$$

This predicted sound pressure level was then used to determine a flanking R_{ij} due to the sound outside the laboratory using Eqn. (2-172) and is reported where relevant.

6.3.6 R_{max} values

The R_{max} of the facility for measurement of Ff, Df and Fd flanking were made according to ISO 10140-2 [92]. The shielding configurations to obtain the R_{max} of the facility and for measurement of $\mathrm{Df_{max}}$ or $\mathrm{Fd_{max}}$ are shown in Figure A-2, Figure A-3 and Figure A-4 respectively in APPENDIX A). This was achieved by shielding the surfaces of the sample as described in section 6.3.3 with layers of 12.5mm Knauff fireboard or 15mm OSB on the floor. The cavities were filled with absorptive material. The fully shielded case (b) in Figure A-2 was required for the measurement of the R_{max}, the walls and ceiling (c) in Figure A-3 for the $\mathrm{Df_{max}}$ and just the floor and walls (d) in Figure A-4 in the case of the $\mathrm{Fd_{max}}$.

To achieve sufficiently high R_{max} values, new sliding doors were installed in the test stand. The radiation from the doors was checked by intensity measurement. The next weakest path through the test stand identified for further remedial work was found to be the floor strips at the base of the concrete default walls. Additional floor shielding strips could be added when required, however it is shown to be unnecessary for the T-junction described. A junction box was also added to allow the convenient conveyance of wires into and out of facility.

A comparison of Df_{max}, and Fd_{max} for the different pathways are shown in the results section 6.6.2 alongside the measured values for flanking in Figure 6-24, and Figure 6-25. This shows where the measured values are affected by the limits of the test stand and highlights the strengths and weaknesses of the test stand flanking suppression. The shielding to suppress test stand flanking is effective for all but low frequencies (<125Hz), (and high frequencies in the case of high SRI (e.g. the Fd path, >3150Hz).

6.3.7 Build stages

Measurements for the structure-borne paths were taken at all the following three stages of the build process. These build stages were:

- Build stage (1) When the junction was first installed in the lab and the lab was open to the laboratory space (Figure 6-4).
- Build stage (2) When the default elements were first installed.
- Build stage (3) When the suspended ceiling was installed and shielding was fully installed on the inside of the default elements.

Some measurements could only be performed at the final stage, when all default elements and shielding were fully installed.

6.4 Measurement methods

6.4.1 Method No. 1: Structure-borne path measurements

6.4.1.1 Structural reverberation time

Measurements of structural reverberation times were made on the CLT walls, the suspended plasterboard ceiling, the concrete upper surface and the OSB lower surface of the HBV floor. Measurements were made at build stage (2) and (3) using a pair of accelerometers (B&K Type 4513-B-002), a two-channel analyser (Dirac software version 5) and a shaker source (B&K Type 4809) using swept sine as the excitation signal. There were three source positions and twelve measurement positions per source position. A T_5 value for structural reverberation time, was recorded. For comparison the number of measurement positions recommended for

panels in EN ISO 10848-1 [94] is a minimum of nine for vibration reduction index measurement. This was estimated to reduce the 95% confidence limits by a factor of two (see Eqn. (5-19), N=9, compared with N=36). An alternative methodology was implemented at build stage (1) (which used longer averaging times T_{20} or T_{30}) however this data was discarded (see the discussion in section 6.6.1.1). The shaker was fixed to the walls, ceiling and floor using a screw thread attachment which was drilled into a metal plate that was glued in place.

6.4.1.2 Velocity level difference

The velocity level difference between all walls of the junction (CLT1, CLT2, HBV1 and HBV2, see Figure 6-7) were measured simultaneously using accelerometers placed on each of the CLT walls, the topside of the floor and the underside on the OSB or on the suspended ceiling when it was installed. Eight channels were available for simultaneous data acquisition using a Müller-BBM PAK system; hence, two accelerometers per surface could be measured simultaneously. For the measurements with a structure-borne source, a shaker (B&K, type 4829) supplied by a pink noise from the analyser was used as the excitation source and fixed to the walls, ceiling and floor using a screw thread attachment (described in section 6.4.1.1). For the measurements with an airborne source, dodecahedron loudspeakers supplied by a pink noise source were used. Three source positions were used and measurements at each source position were repeated six times to obtain twelve measurement positions over the surface of the elements.

The velocity level difference measurements were measured at all three stages of the build process described in the previous section 6.3.7 and once during the airborne measurement described in section 6.4.2.

6.4.1.3 Coupling loss factors

Coupling loss factors were calculated from the measured total loss factors and velocity level differences using Eqns. (2-178) and (2-179). The coupling losses in the forwards and backwards directions were compared to verify compliance with the consistency relationship (Eqn. (2-142)).

6.4.2 Method No. 2: Airborne path measurements

The airborne path measurements could only be carried out in the fully completed laboratory (build stage (3)). Details of the temporary shielding for this measurement can be found in section 6.3.3. Each flanking path was measured in turn by shielding appropriate pairs of elements. The measurements of airborne sound insulation were carried out according to EN ISO 10140-2 [92]. Dodecahedron loudspeakers were used at two source positions with rotating microphones at two locations in each of the rooms to measure the sound pressure level and the reverberation times. (With a rotating microphone the requirement in EN ISO 10140-2 [92] is only one position.) Measurements were made in both directions.

6.4.2.1 Resonant sound reduction indices (R_i and R_j) of HBV and CLT plates

The comparison of methods No. 1 and No. 2 to measure flanking requires that the velocity level difference measured using a structure-borne source to be converted to a sound transmission coefficient (R_{ij}). This can be done using Eqn. (2-189) (where no additional shielding is present) or Eqn. (2-190) (which includes the shielding of the suspended ceiling). Note that where the resonant sound reduction index (R_i) is used to calculate the flanking transmission coefficient (R_{ij}), the radiation efficiency at and below the critical frequency (calculated using Leppington), used to determine the resonant sound reduction index (R_i), is shown to depend on the exact dimensions of the plate. However, as an approximation the dimensions of the CLT plate (measured in chapter 4, 4.2m x 2.9m) is consistently used to make R_i calculations for all CLT plates in the thesis.

The correction factors to obtain the resonant SRI are estimated by comparing the resonant SRI with the measured SRI and the difference is plotted. For the HBV, the resonant part of the SRI is calculated using model (ii)c shown in section 3.8.3. This model is implemented between the critical frequencies (63Hz to 200Hz) and for the rest of the frequency range (250-5000Hz) model (ii)b (which uses a calculated D_{eff}) showing marginally better agreement over model (i) (which is for the concrete plate only) is applied. For the CLT the resonant part of the SRI is calculated from model 1a (which uses a calculated D_{eff}, and does not agree with measured SRI obtained for

the CLT plate, see section 4.7.8.1) and the elastic constants from section 4.7.4. The resulting correction factors for the Ff, Df, and Fd path are shown in Figure 6-9. In the case of the Ff path, flanking outside the laboratory is measured and the correction factor is not relevant.

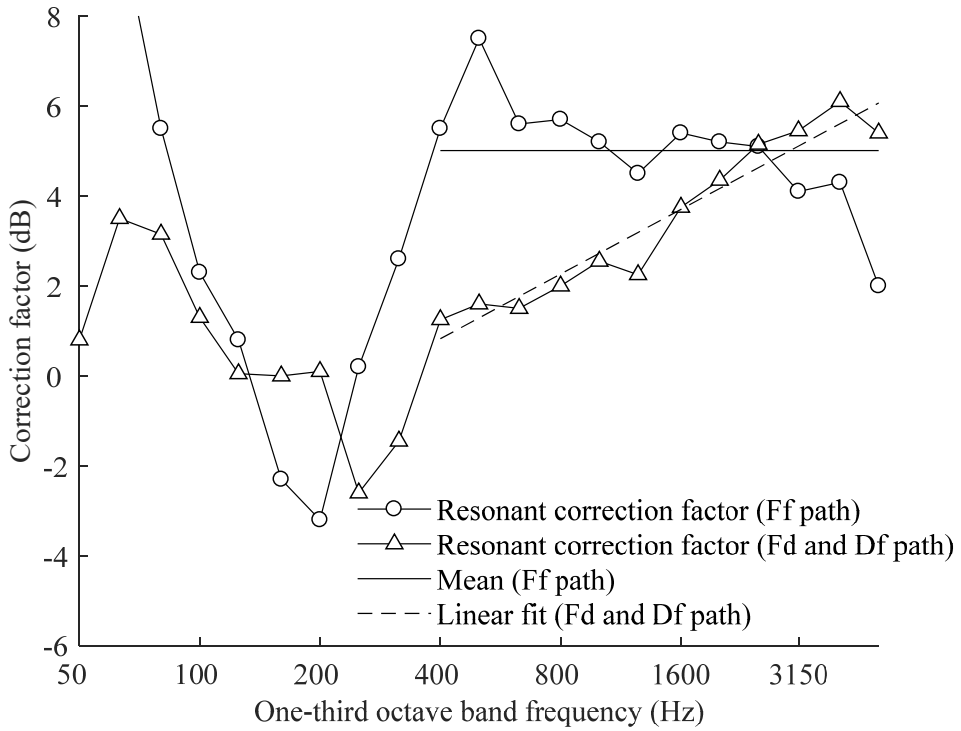

Figure 6-9 Correction factors for the Ff, Df and Fd paths.

The solid line shows the mean correction factor for the Ff path related to the thick plate properties of the CLT (≥400Hz). It is determined by the fit of measured data to the calculated thin plate isotropic model 1a shown in Figure 4-19. The dotted line shows a correction factor (smoothed by a linear fit) for the Df and Fd paths. This is partially due to the thick plate properties of the CLT (≥400Hz) and partially due to the fit of measured results to the HBV floor model (ii)b (≥250Hz) shown in Figure 3-19. Because of the difference in slopes between the measured data and the HBV floor model (ii)b (≥250Hz) this correction factor is frequency dependant.

In this case the cross-over to a thick plate for the CLT occurs within an octave band of the critical frequency however this may not hold for all CLT plates. If there exist other thick plates in which the cross-over frequency is at a frequency much lower

than the critical frequency the correct application of correction factors is likely to be more complicated. In the cases described EN12354 guidance is required to adequately deal with orthotropic and thick plates.

The correction factors for lightweight plates are given (for comparison) in Figure D-3, APPENDIX D. Significant lightweight corrections for the Ff, Fd, and Df paths are not apparent. The application of a lightweight correction coefficient is not necessarily recommended near the critical frequency because this is the region in which it is most difficult to accurately determine the radiation losses (see Hopkins [8] on radiation efficiency measurement and the radiation efficiency calculation for lightweight plates). With respect to the lightweight correction, it would be expected that the usual requirements of a heavyweight plate apply for the frequency range above the highest (assuming orthotropy) critical frequencies (>250Hz) for both the HBV floor and the CLT plate.

6.4.2.2 Sound reduction improvement index of the plasterboard suspended ceiling

The sound reduction improvement index, ΔR, due to the plasterboard suspended ceiling was estimated by an insertion loss measurement of the direct (Dd path) transmission. The improvement was measured using a sound insulation measurement in accordance with ISO 10140-2 [92] as described in section 6.4.2 before and after installation of the plasterboard ceiling. However, for logistical reasons, the insertion loss of the Fd flanking path (as recommended in EN12354 ANNEX D [77]) was not measured.

6.5 SEA Models

Model 2b of the HBV floor (from section 3.4.4) which treats the concrete-OSB plate and the timber joists as an isotropic plate with an effective bending stiffness for the orthotropic plate determined as described in section 3.7.4 using the approach of Huffington [19] and Troitsky [20] was extended to form the T-junction flanking model. The CLT walls are added using model 1a as described in section 4.7.8.1 despite poor agreement with direct airborne transmission. (Models of type 1, see section 4.7.8.1, can be easily incorporated into a larger SEA model.) In these

prediction models, it is assumed that there is no connection between the flanking walls and the suspended ceiling. Two models are proposed; Model 1 excludes the flanking from the Ff path and model 2 includes it.

6.5.1 Model 1: Excluding airborne flanking outside the laboratory (Ff path)

In model 1 of the T-junction (shown in Figure 6-10) the flanking from the Ff path was not included because this was not accurately measured in the lightweight facility due to flanking outside the laboratory. This results in a seven-subsystem model requiring the following matrix

$$\begin{bmatrix} \eta_1 & -\eta_{21} & -\eta_{31} & 0 & 0 & -\eta_{61} & 0 \\ -\eta_{12} & \eta_2 & -\eta_{32} & -\eta_{42} & 0 & -\eta_{62} & -\eta_{72} \\ -\eta_{13} & -\eta_{23} & \eta_3 & -\eta_{43} & -\eta_{53} & 0 & 0 \\ 0 & -\eta_{24} & -\eta_{34} & \eta_4 & -\eta_{54} & 0 & 0 \\ 0 & 0 & -\eta_{35} & -\eta_{45} & \eta_5 & 0 & -\eta_{75} \\ -\eta_{16} & -\eta_{26} & 0 & 0 & 0 & \eta_6 & 0 \\ 0 & -\eta_{27} & 0 & 0 & -\eta_{57} & 0 & \eta_7 \end{bmatrix} \begin{bmatrix} E_1 \\ E_2 \\ E_3 \\ E_4 \\ E_5 \\ E_6 \\ E_7 \end{bmatrix} = \begin{bmatrix} \frac{\Pi_{\text{in},1}}{\omega} \\ 0 \\ 0 \\ 0 \\ 0 \\ 0 \\ 0 \end{bmatrix} \quad (6\text{-}3)$$

This result requires a correction to account for airborne flanking outside the lightweight facility.

6.5.1 Model 2: Including airborne flanking outside the laboratory (Ff path)

In model 1 of the T-junction (shown in Figure 6-11) the flanking from the Ff path is included as a coupling loss factor which is determined from the velocity level difference between the two CLT plates. This model requires solution of the following matrix

$$\begin{bmatrix} \eta_1 & -\eta_{21} & -\eta_{31} & 0 & 0 & -\eta_{61} & 0 \\ -\eta_{12} & \eta_2 & -\eta_{32} & -\eta_{42} & 0 & -\eta_{62} & -\eta_{72} \\ -\eta_{13} & -\eta_{23} & \eta_3 & -\eta_{43} & -\eta_{53} & 0 & 0 \\ 0 & -\eta_{24} & -\eta_{34} & \eta_4 & -\eta_{54} & 0 & 0 \\ 0 & 0 & -\eta_{35} & -\eta_{45} & \eta_5 & 0 & -\eta_{75} \\ -\eta_{16} & -\eta_{26} & 0 & 0 & 0 & \eta_6 & -\eta_{76} \\ 0 & -\eta_{27} & 0 & 0 & -\eta_{57} & -\eta_{67} & \eta_7 \end{bmatrix} \begin{bmatrix} E_1 \\ E_2 \\ E_3 \\ E_4 \\ E_5 \\ E_6 \\ E_7 \end{bmatrix} = \begin{bmatrix} \frac{\Pi_{\text{in},1}}{\omega} \\ 0 \\ 0 \\ 0 \\ 0 \\ 0 \\ 0 \end{bmatrix} \quad (6\text{-}4)$$

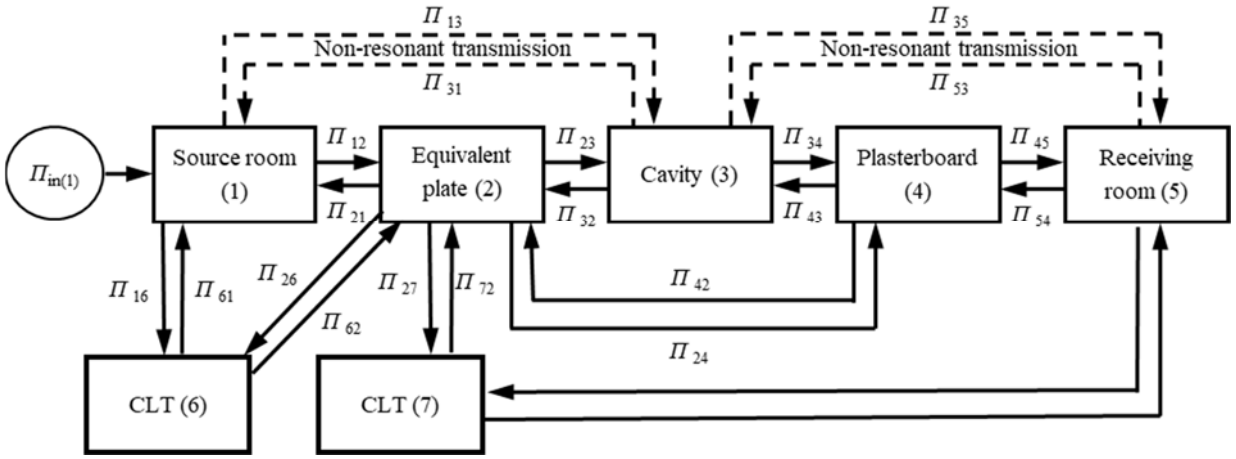

Figure 6-10 Seven-subsystem model 1 (circles indicating internal losses have been removed for clarity)

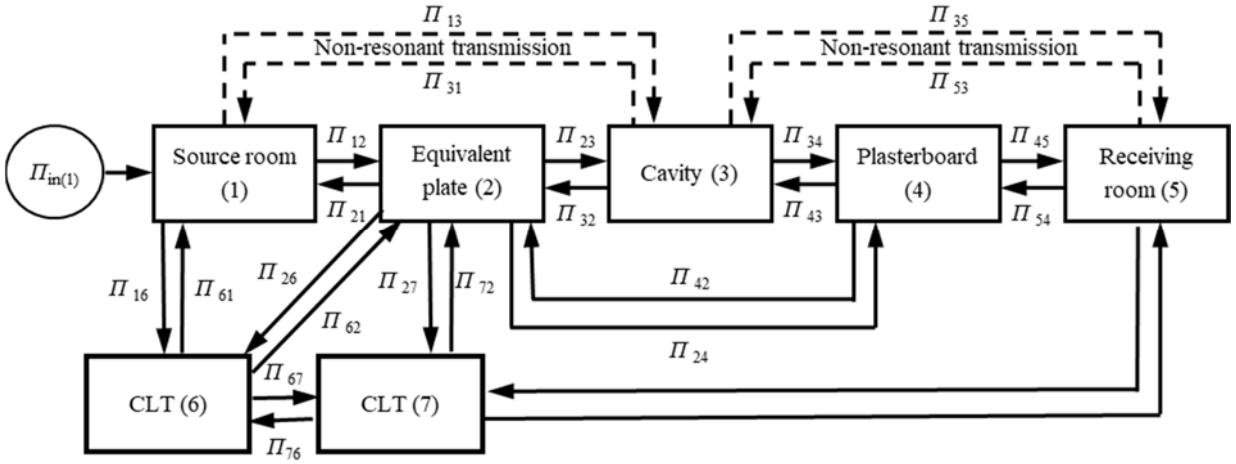

Figure 6-11 Seven-subsystem model 2 (circles indicating internal losses have been removed for clarity)

6.6 Results

6.6.1 Method No. 1: Flanking path measurements using a structure-borne methodology

6.6.1.1 Total loss factors

The structural reverberation time data is used to calculate total loss factors using Eqn. (3-14) [8]. Loss factors were found to be higher when measuring T_5 rather than T_{20} (or T_{30}) particularly in the region of the critical frequency (in this case 160-1000Hz). Combining the means of these different data sets was therefore deemed inappropriate (particularly at these frequencies) because combined results were shown to be bimodal distributions. Data which recorded a reverberation time based on averaging times >5s was therefore discarded; as described in section 4.7.1 a structural reverberation time determined from a T_5 is an improved methodology and preferred [114].

There was also found to be an increase in the coupling loss factor at frequencies <630Hz between build stages (1) and (2), however the data for build stage (1) was discarded as was the comparable data at build stage (2) as they were based on averaging times >5s. It would be intuitive to attribute the increase to additional coupling due to connections to the other elements. However, the evidence to support this is lacking, as in this case there are no additional structural connections because there is an airgap between the default walls and shielding wall and the test element (see section 6.3.4). The cause of the increase was not established.

The mean loss factors for build stages (2) and (3) of the CLT walls are shown in Figure 6-12. The total loss factor of a homogenous panel is the sum of the internal loss factor and the coupling losses. The internal loss factor of a nominally identical CLT wall described in section 4.7.1 should therefore be lower than the measured total losses, however this was not observed (particularly at low frequencies). The coupling losses with only one connected junction are low and would make a small difference to the measured total loss factor, however, this would of course be increased if all four edges of the panel were connected. An alternative explanation for the decrease in loss factor with increased coupling is required. It could be that

this wall had a particularly high internal loss factor compared with the nominally identical wall examined in chapter 4 or there could be a systematic error in one or more of the methods.

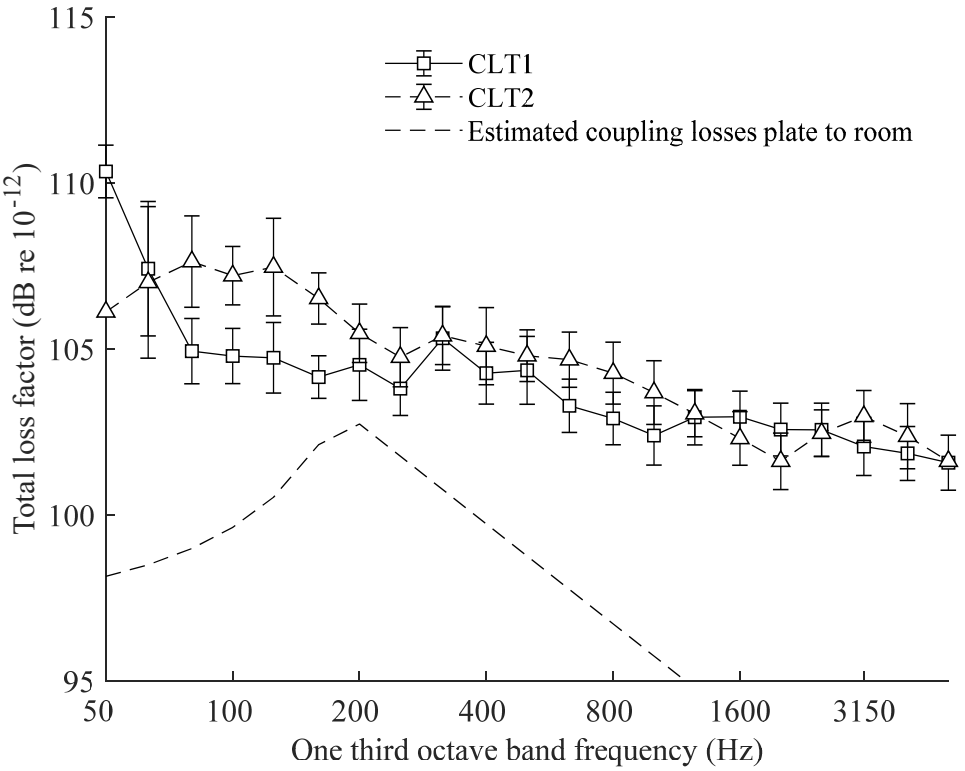

Figure 6-12 Total loss factor for the CLT walls

In this junction, the plate to room coupling losses are close enough to the measured values of loss factor to increase them by more than 2.0dB (by simply adding the loss factors) in the frequency range 200-250Hz. Unfortunately, there was no opportunity to measure the internal loss factor of the walls installed in the flanking laboratory to make a direct comparison.

A comparison of measurements of the HBV floor on the concrete and OSB sides was made at build stage (2) when the default elements were first installed but before the suspended ceiling and shielding were fully installed. The total loss factors measured on either side of the floor were similar, however meaningful values of the loss factor could not be obtained on the OSB side at high frequencies >1250Hz. This could be due to the difficulty of measuring the loss factor of layered materials. It is therefore

preferable to measure only on the concrete (upper) surface of the floor and the measurements for HBV1 were discarded. The mean loss factors for build stages (2) and (3) for the upper surface concrete floor (HBV2) are shown in Figure 6-13.

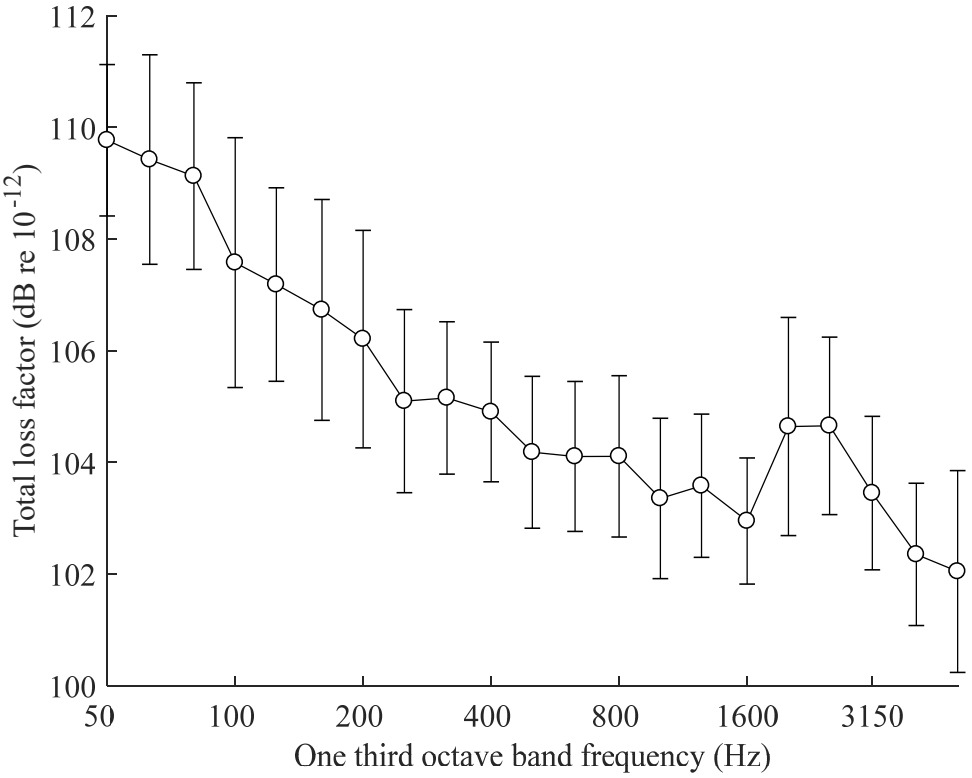

Figure 6-13 Total loss factor measurements for the HBV floor.

An increase in the total loss factor was again observed below 200Hz between build stages (1) and (2) when the default test stand walls were installed. This could be due to change in measurement methodologies (T_{20} using MLS was measured at build stage (1) and T_5 using a swept sine was measured at build stages (2) and (3)) and like the CLT the build stage may also be of influence.

The loss factors for the plasterboard forming the suspended ceiling are shown in Figure 6-14 and were higher than the expected internal loss factor of 101.0dB (for plasterboard) [8]. The plate to room coupling loss factors and the coupling losses through the suspended ceiling hangers for model 2b are also shown and are unlikely to be the cause of the increase. Measured coupling losses at the junction are also too low to be the cause. A possible cause is that the contact between the plasterboard and mineral wool in the cavity increases the radiation efficiency of the plasterboard on

the cavity side thus increasing the measured total loss factor. (The plate to room coupling loss factor shown in Figure 6-14 sums the contribution from both sides of the plate and is hence an estimate in the absence of adjacent mineral wool.)

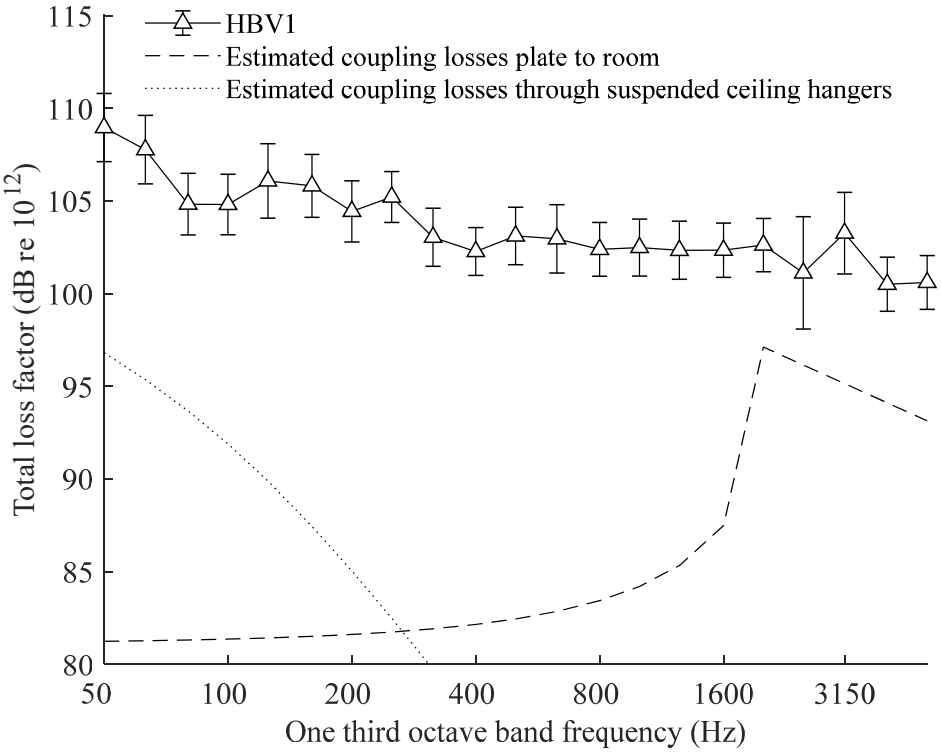

Figure 6-14 Total loss factors of the plasterboard suspended ceiling (labelled HBV1 in build stage (3)).

6.6.1.2 Velocity level differences

For the Ff path the mean velocity level difference measurements gathered at all build stages using structure-borne excitation are compared with using airborne excitation in Figure 6-15 to Figure 6-18. The mean velocity level differences between the measurements made with structure-borne and airborne excitation for the Ff path in the frequency range 80Hz to 2kHz are -1.5dB (in the CLT1 to CLT2 direction) and -0.8dB (in the CLT1 to CLT2 direction). There is overlap of 95% confidence limits at some frequencies. However, flanking outside the facility in the open laboratory space is shown to be a factor (see sections 6.3.5 and 6.6.2) this would account for the dip in the region of the critical frequency of the CLT plate which is unexpected if the measurements were solely due to structure-borne energy transfer.

The measurements for the Df path measured on the concrete side of the floor (rather than the OSB or plasterboard side) are shown in Figure 6-16. However, for this path a direct comparison between data measured with structure-borne and airborne sources can only be made with measurements from the plasterboard suspended ceiling, this comparison is shown in Figure 6-17. The mean velocity level differences between the measurements made with structure-borne and airborne excitation in the frequency range 80Hz to 2kHz are −0.2dB (in the CLT2 to HBV1 direction) and −2.5dB (in the HBV1 to CLT2 direction). In the CLT2 to HBV1 direction there is overlap of the 95% confidence limits for most of the frequency range (80-2000Hz), however for the reverse direction (HBV1 to CLT2) overlap in the 95% confidence limits is patchy.

For the Fd path the mean velocity level difference measurements gathered at all build stages using structure-borne excitation are compared with using airborne excitation in Figure 6-18. The mean velocity level differences between the measurements made with structure-borne and airborne excitation in the frequency range 80Hz to 2kHz are -2.1dB (in the CLT1 to HBV2 direction) and -2.6dB (in the HBV2 to CLT1 direction). In the CLT1 to HBV2 direction overlap in the 95% confidence limits is patchy. However, there is clear disparity at high frequencies (>1.25kHz) for the reverse direction (HBV1 to CLT2).

The differences at high frequencies (>1.25kHz) for the Fd path in the reverse direction (HBV1 to CLT2) can be almost completely accounted for by separating the velocity level measurements from the two floor slabs. The measurements were examined to see if the floor is acting as a single element or two separate slabs elements. This revealed that at build stage (1) when the test stand is open to the laboratory space the floor slabs appear to be strongly coupled whereas at build stage (3) when the suspended ceiling and shielding are fully installed the floor slabs appear more decoupled. The mean velocity levels for the twelve accelerometer positions from build stages (1) and (3) for a single source position is shown in Figure 6-19. These results are typical of each of the three source positions on the concrete floor surface. Unfortunately, it is not possible to separate the data from the two floor slabs at build stage (2) because of the data structure.

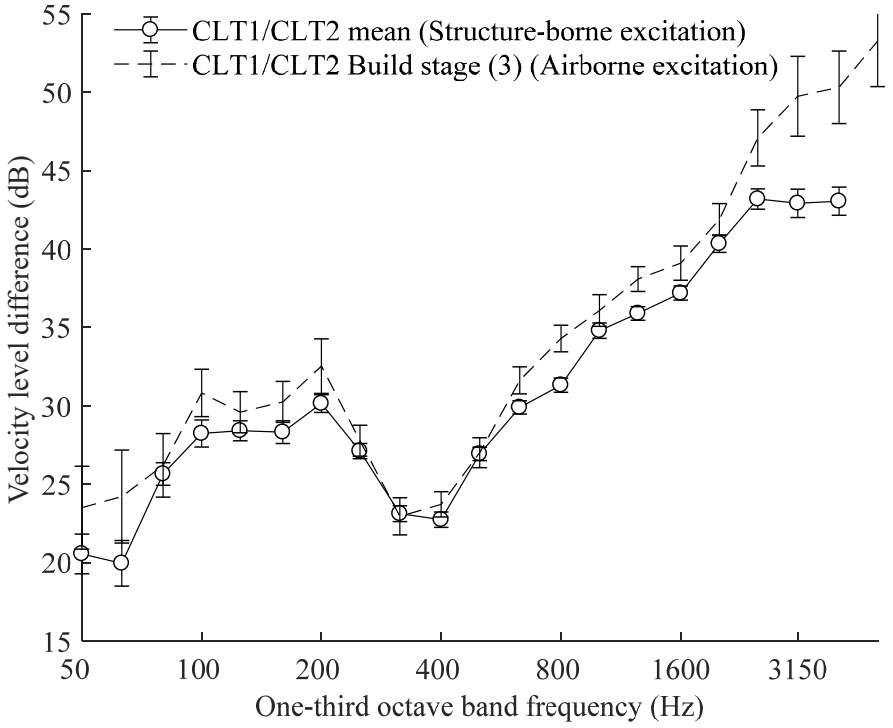

(a)

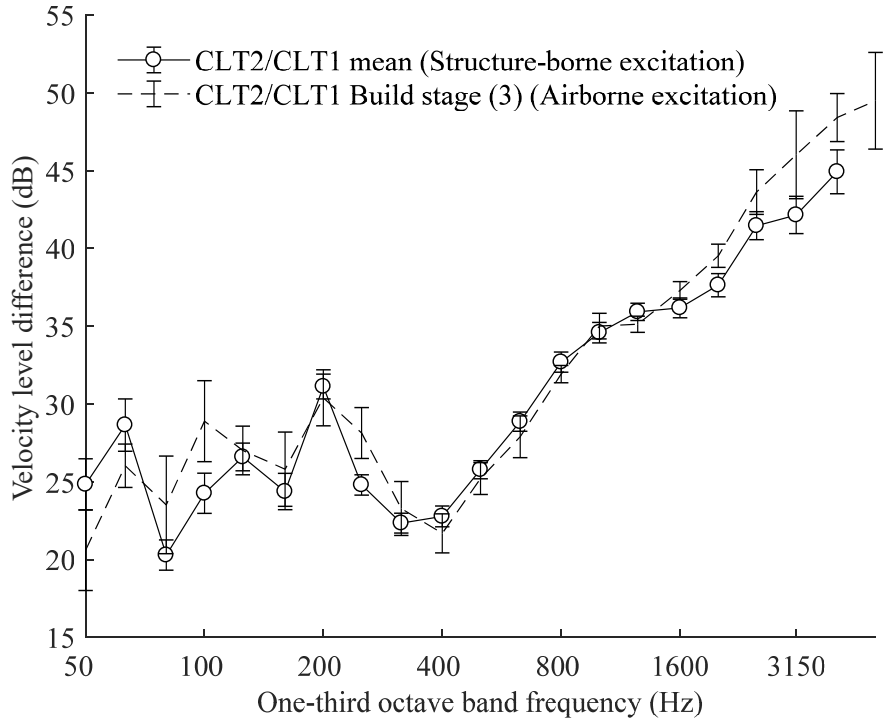

(b)

Figure 6-15 Velocity level difference measurements for the Ff path (comparison between structure-borne and airborne sources)

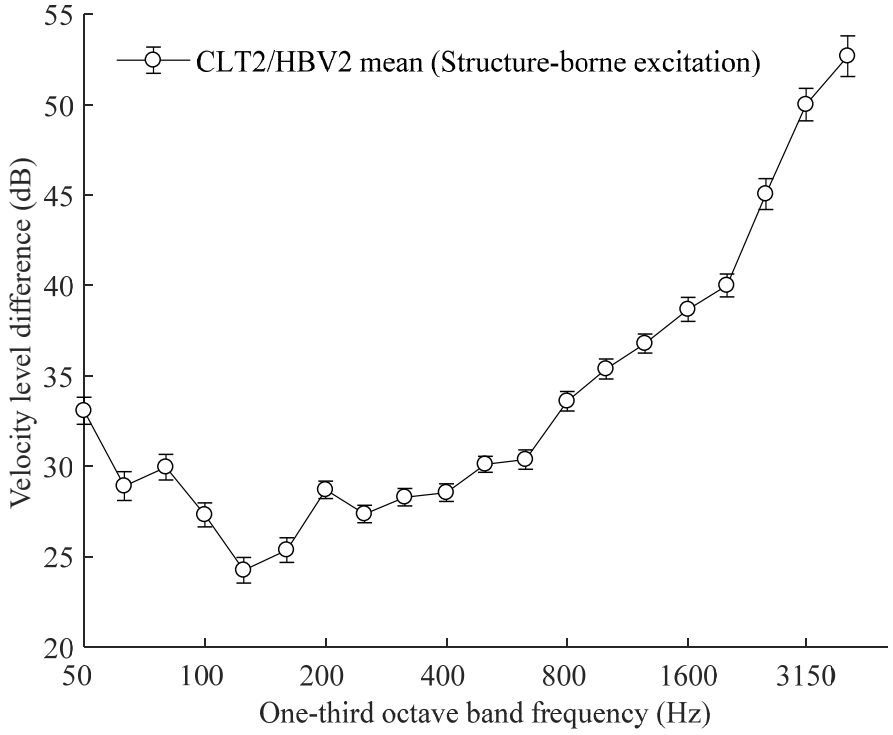

(a)

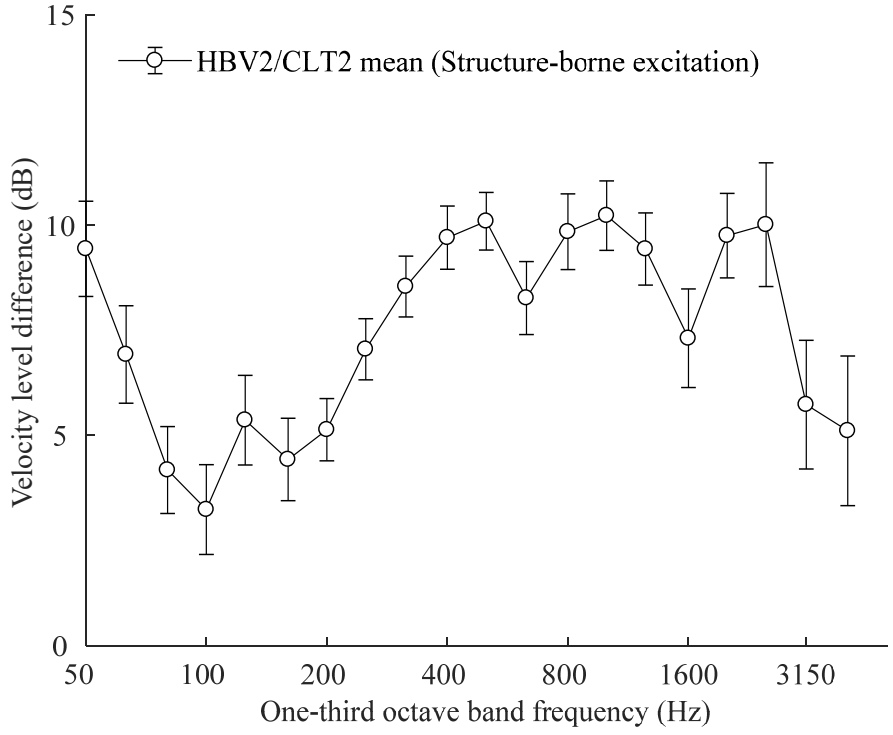

(b)

Figure 6-16 Velocity level difference measurements for the Df path (measurements made on the concrete surface)

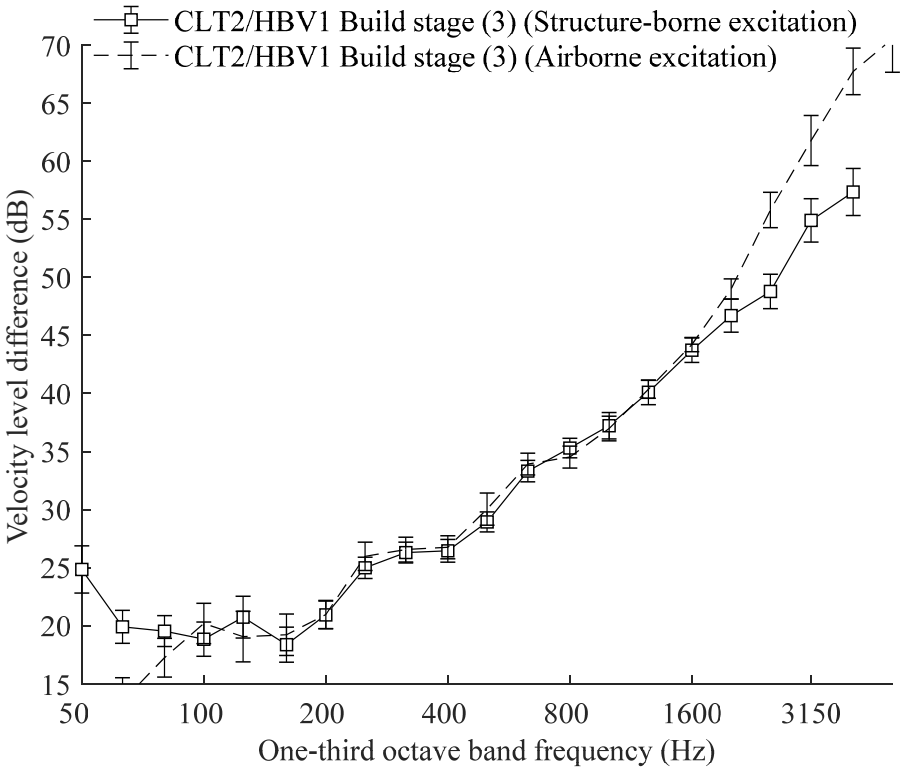

(a)

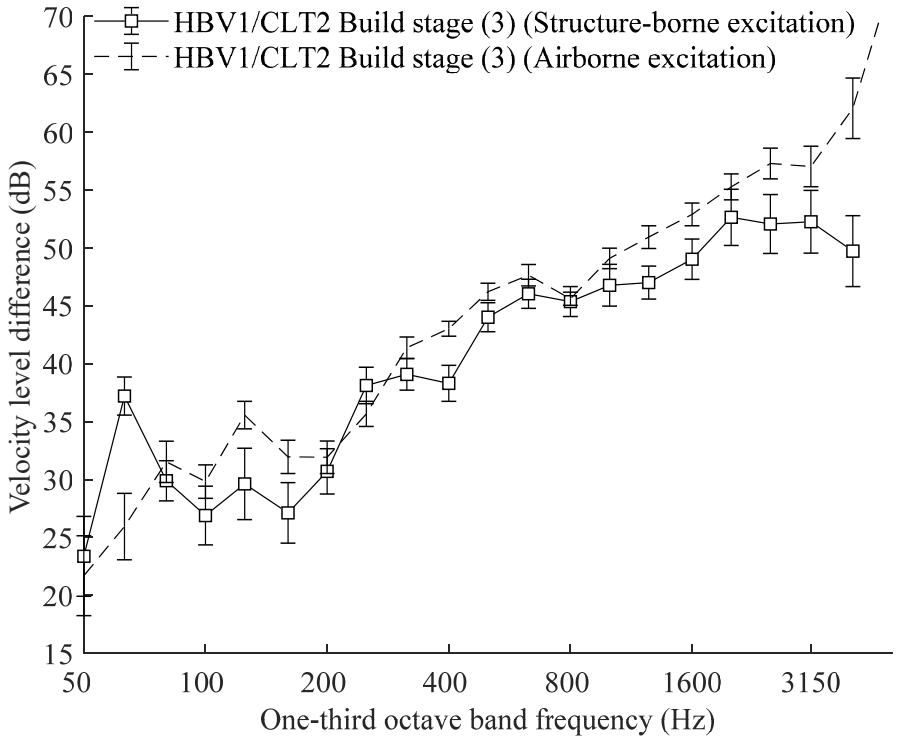

(b)

Figure 6-17 Velocity level difference measurements for the Df path (comparison between structure-borne and airborne sources)

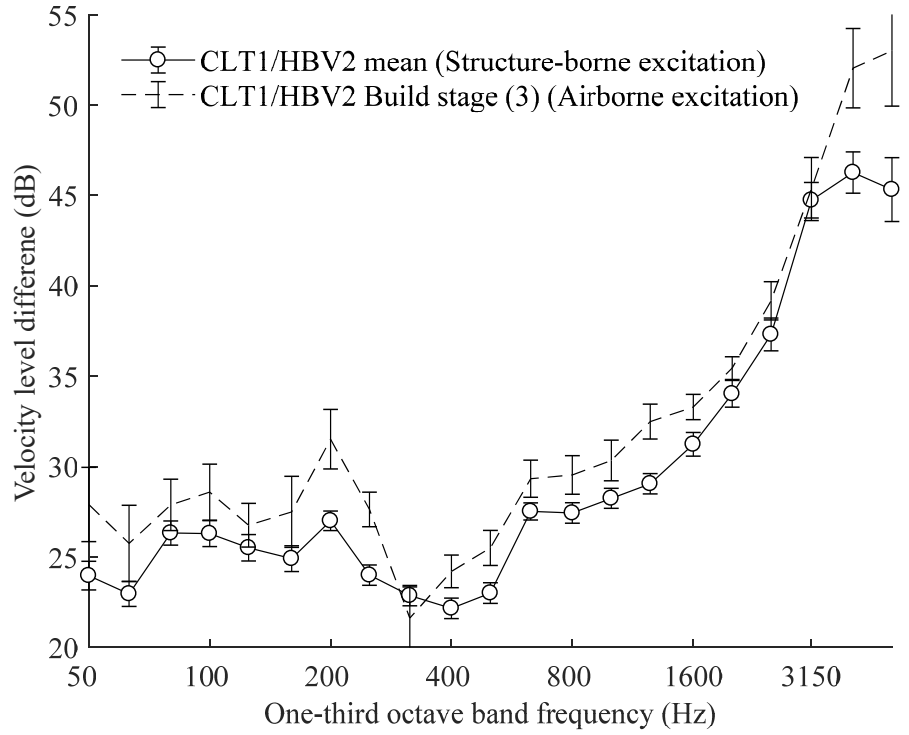

(a)

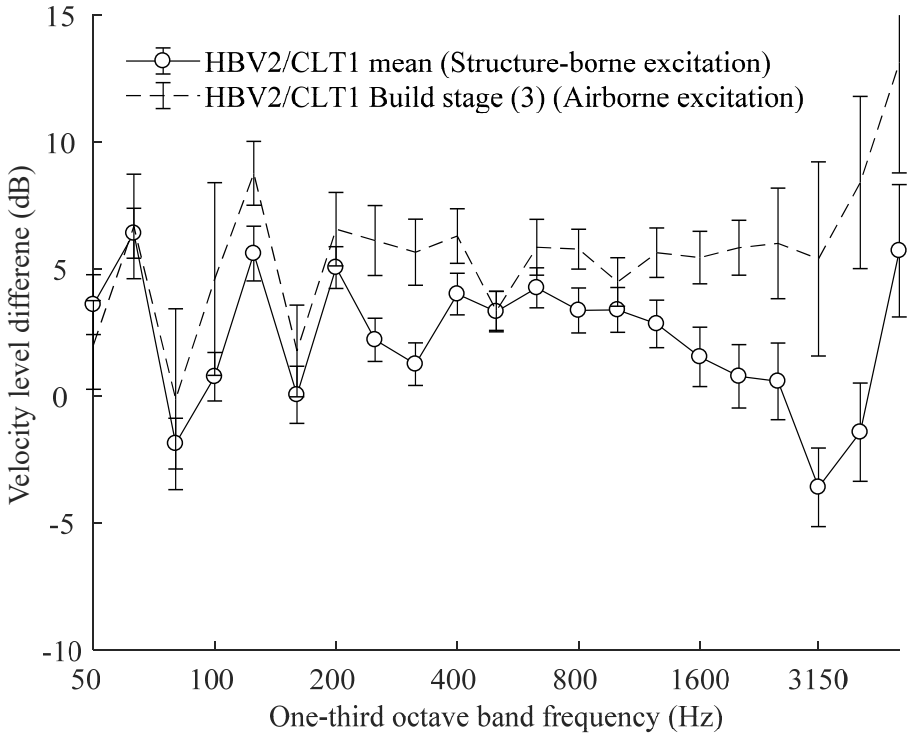

(b)

Figure 6-18 Velocity level difference measurements for the Fd path (comparison between structure-borne and airborne sources)

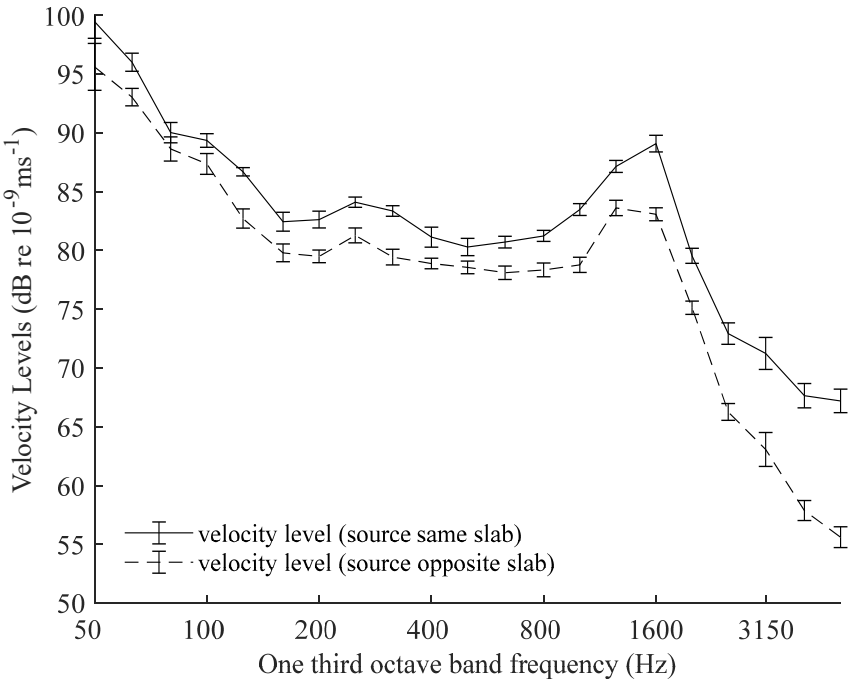

(a)

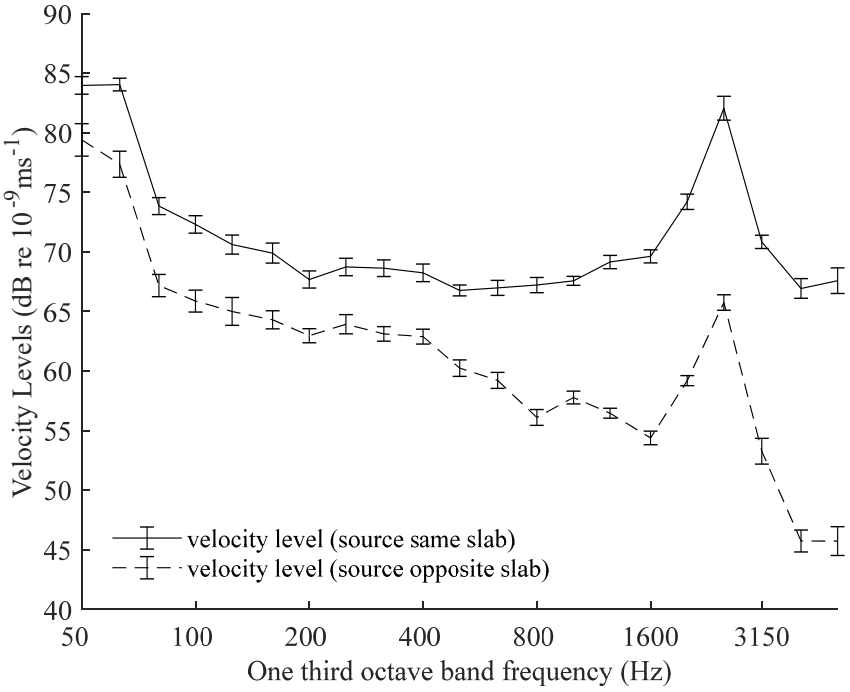

(b)

Figure 6-19 Mean velocity levels on each of the floor slabs for a single source position at (a) build stage (1) test stand open to the laboratory space and (b) build stage (3) when the suspended ceiling and shielding are fully installed. Black solid lines indicate source and measurement position on the same slab and black dashed lines indicate source and measurement position on different slabs.

There were no physical signs of wear of the concrete skim between the floors. The apparent separation of the slabs at build stage (3) is therefore likely to be due to something else. One possibility is a lower degree of coupling between the two floor slabs through the room (which masks the actual separation of the slabs), when the default walls and shielding were installed. If at build stage (1) energy radiated from the floor into the reverberant space is reabsorbed by the adjacent element; the two elements could appear to be strongly coupled. Whereas, if at build stage (3) the increased absorption due to the installation of the laboratory walls and shielding reduces the amount of energy reabsorbed by the adjacent element an apparent decoupling of the adjacent elements from build stage (1) to (3) could be observed without necessarily changing the measurements on the overall floor between build situations shown in Figure 6-15. Note that evidence for coupling through the room between junction elements and shielding at build stage (3) was also found when measuring the velocity level differences between the junction elements and the default laboratory shielding. The effect of separating the floor slabs on the velocity level difference data is shown in Figure 6-20, overlap of the 95% confidence limits is observed for much of the frequency range (50-400Hz, 630Hz, 800Hz and 1250-5000Hz).

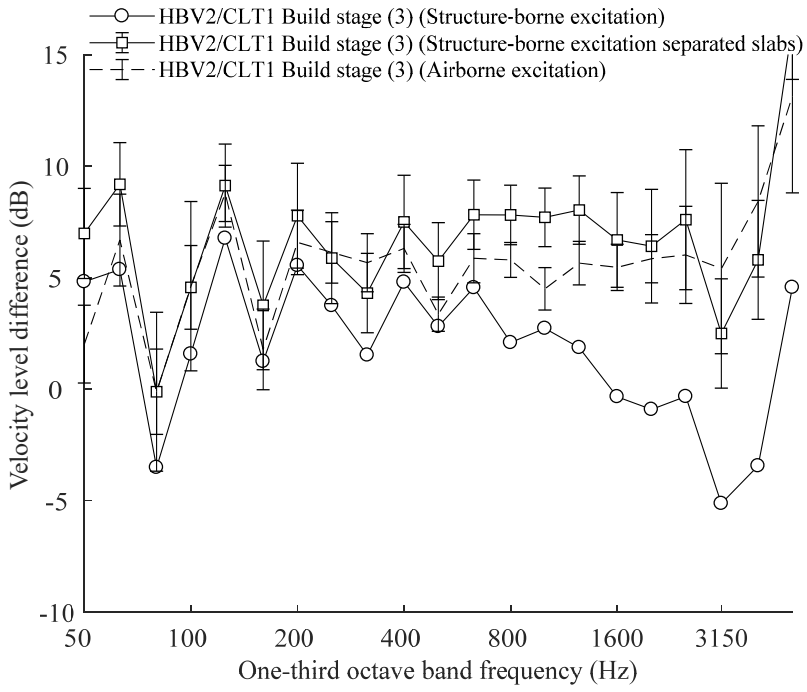

Figure 6-20 The effect of separating the floor slabs on the measured velocity levels

Problems with obtaining an appropriate velocity level difference when several structurally decoupled slabs are used to build a floor (or wall) can be overcome by acquiring the data for each slab separately; including the velocity level measurements only on the same slab as the source to determine velocity level difference. However, the closeness in agreement between velocity level differences acquired using airborne and structure-borne excitation suggests that an alternative solution to the problem could be to use airborne excitation to measure the velocity level difference in such situations.

6.6.1.3 Coupling loss factors

To compare coupling loss factors using the consistency relationship (Eqn. (2-142)) the data from build stage (3) only was used. The data from build stage (1) is discarded because of problematic reverberation time measurements (see section 6.6.1.1) and the unusual behaviour of coupling between the floor slabs (possibly through the reverberant space). The data from build stage (2) is discarded because it was not possible to separate the data measured on each plate. The remaining data from build stage (3) was used to calculate the coupling loss factors for the Fd and Df paths. Data corrected for the vibration level difference of the two slabs of the floor can therefore be included (where the total mass of the floor is halved). Note that the data from build stage (3) collected from the underside of the floor is from the suspended ceiling rather than the OSB. The Ff path is not included here as the measurements were shown to be strongly influenced by airborne flanking outside the laboratory (see sections 6.3.5 and 6.6.2). Coupling loss factors to and from the lower wall are shown in Figure 6-21 and coupling loss factors to and from the upper wall are shown in Figure 6-22.

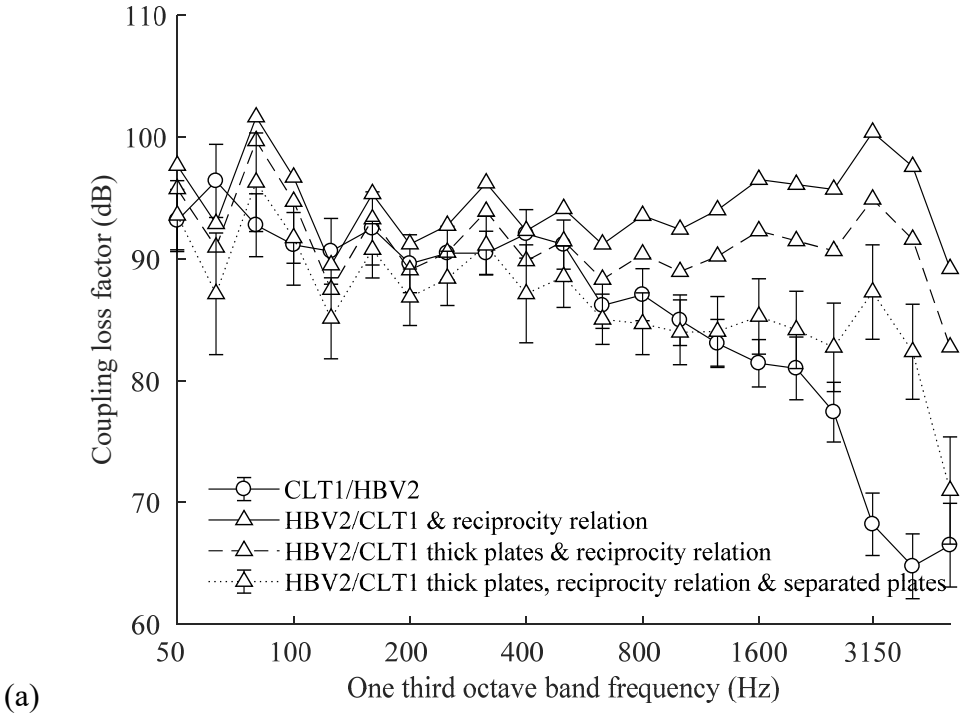

(a)

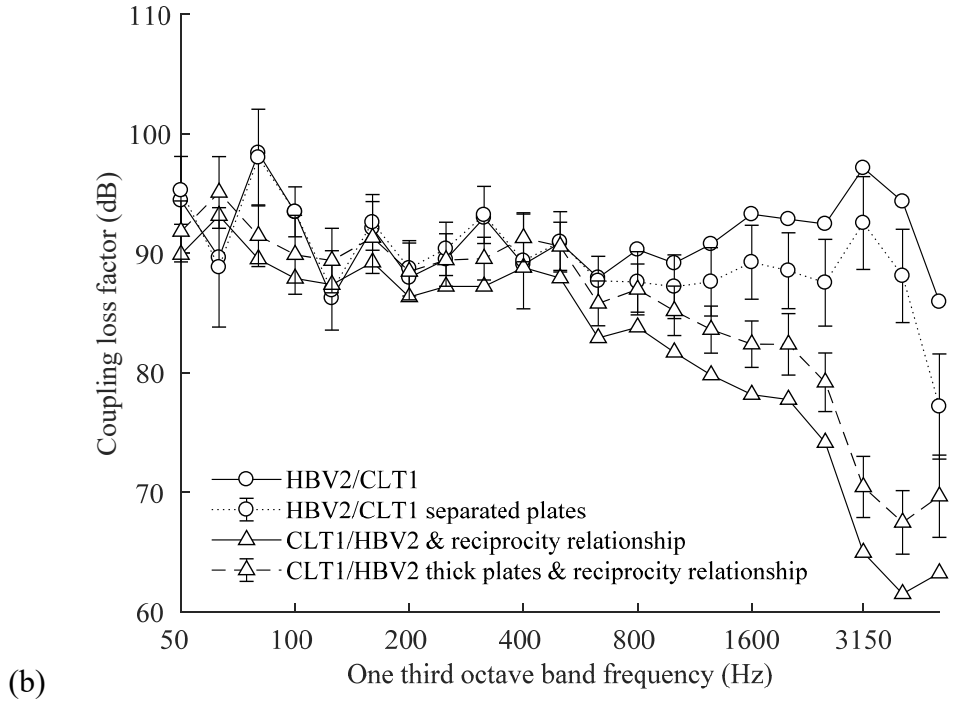

(b)

Figure 6-21 Coupling loss factors (a) CLT1 to HBV2 (b) reverse direction HBV2 to CLT1

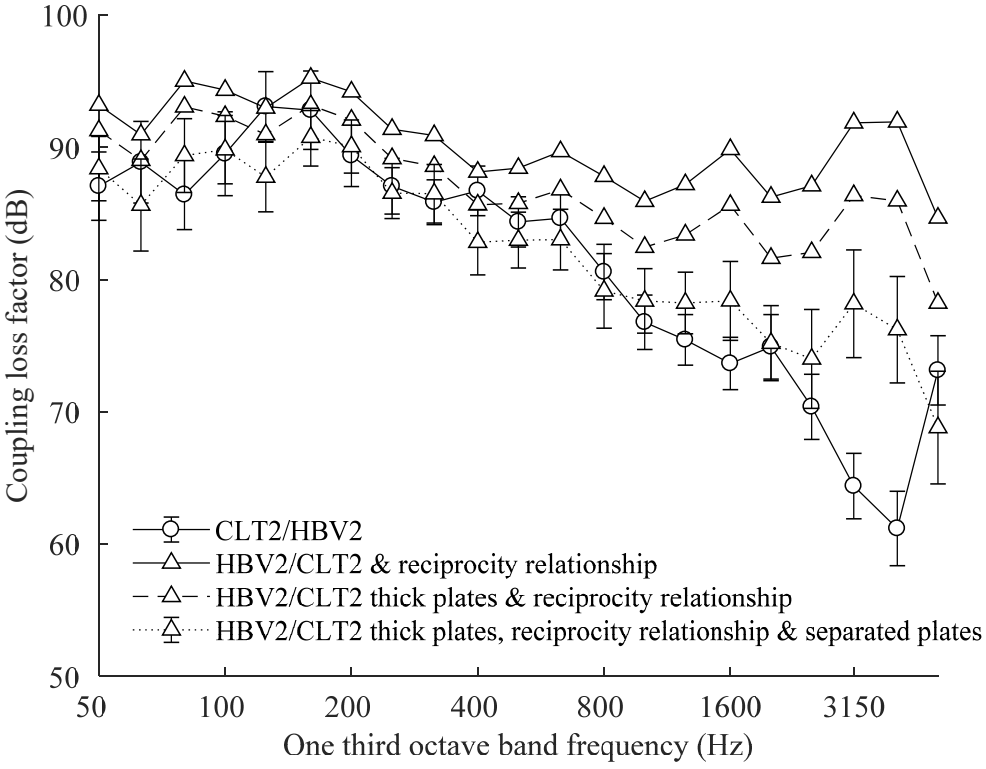

(a)

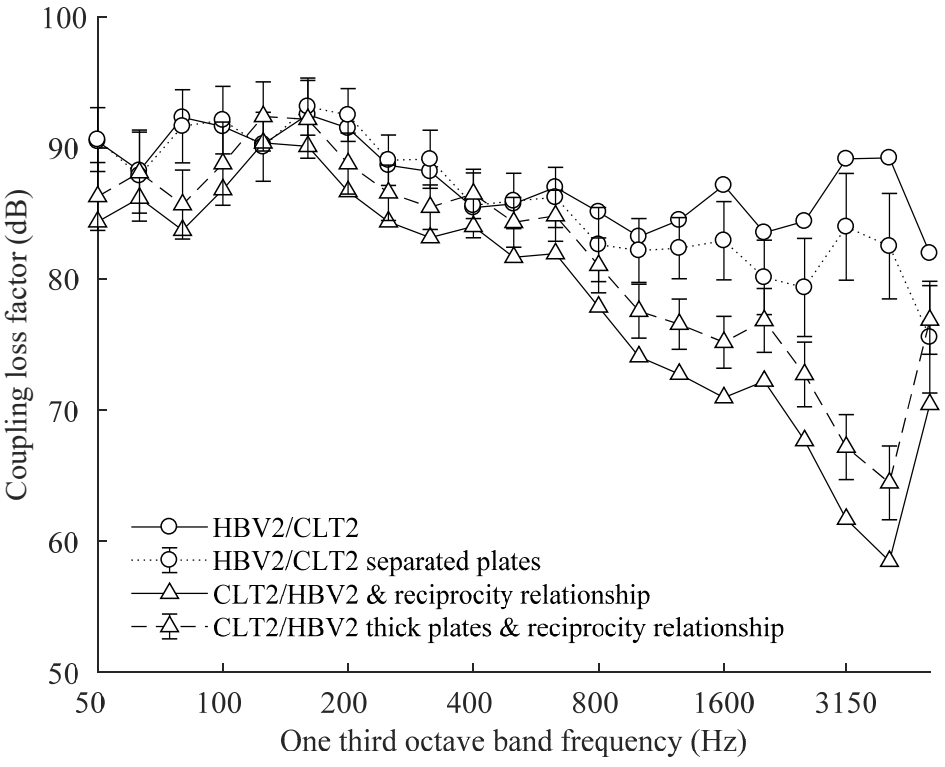

(b)

Figure 6-22 Coupling loss factors (a) CLT2 to HBV2 (b) reverse direction HBV2 to CLT2

The agreement between the data collected in the forwards and reverse directions for the Fd and Df paths is significantly improved at mid (250Hz-1000Hz) and high frequencies (1250Hz-3150Hz) by separating the data for each floor slab and by using an estimated thick plate value for the bending wave phase velocity to calculate the modal density for the consistency relationship. At low frequencies, an improvement is mostly but not always observed. For the Df and Fd paths at high frequencies (>1250Hz) there are differences in the coupling loss factors in the forwards and reverse directions (of up to 19.1dB) for which a cause is still unaccounted. It is striking when compared to measured CLT only data presented in section 5.5.6. In situations, such as this where the principle of reciprocity appears to be violated the most likely explanation is that the system is ill-defined. Therefore, at high frequencies the meaningfulness of the coupling loss factors is questionable. (The low (50Hz-200Hz), middle (250Hz-1000Hz) and high (1250Hz-3150Hz) frequency categories are adopted from the low middle and high ranges for single figure values in EN10848 [94].)

6.6.2 Method No. 2: Flanking path measurements using an airborne method

Comparisons between the measurements of airborne sound transmission and the calculated flanking using the structure-borne measurement methodology to calculate an R_{ij} from the $\overline{D_{v,ij}}$ calculated in section 6.6.1.2 for the different paths are shown in Figure 6-23, Figure 6-24 and Figure 6-25. The 95% confidence limits of the measurements are plotted for structure-borne excitation.

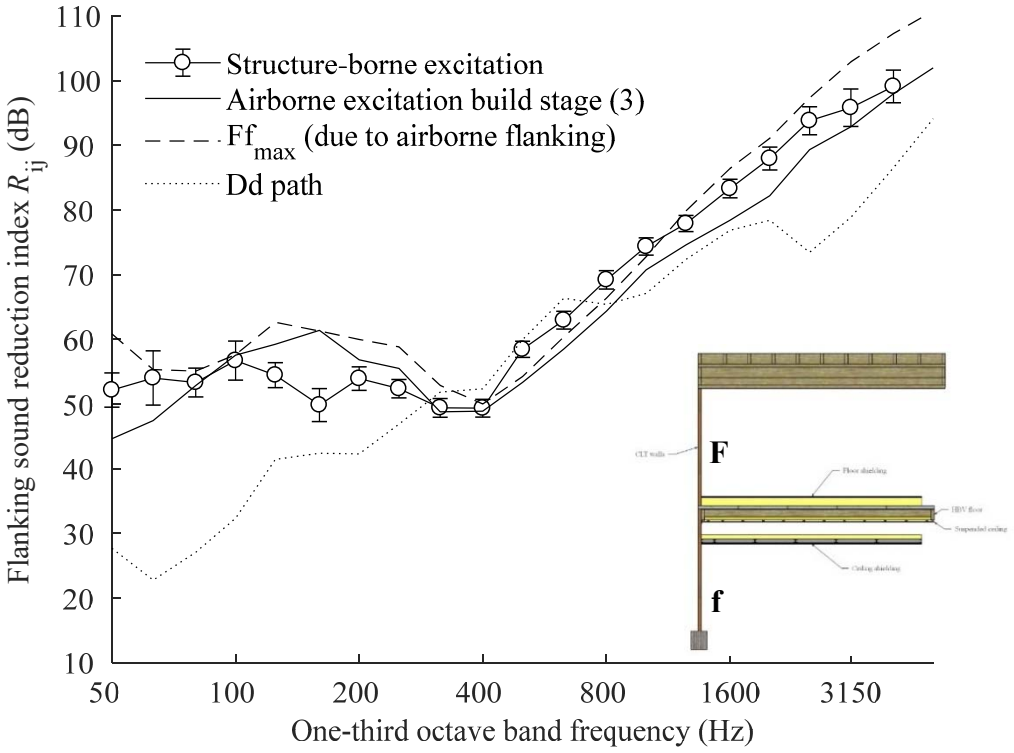

Figure 6-23 Ff path - comparison of different measurement methods.

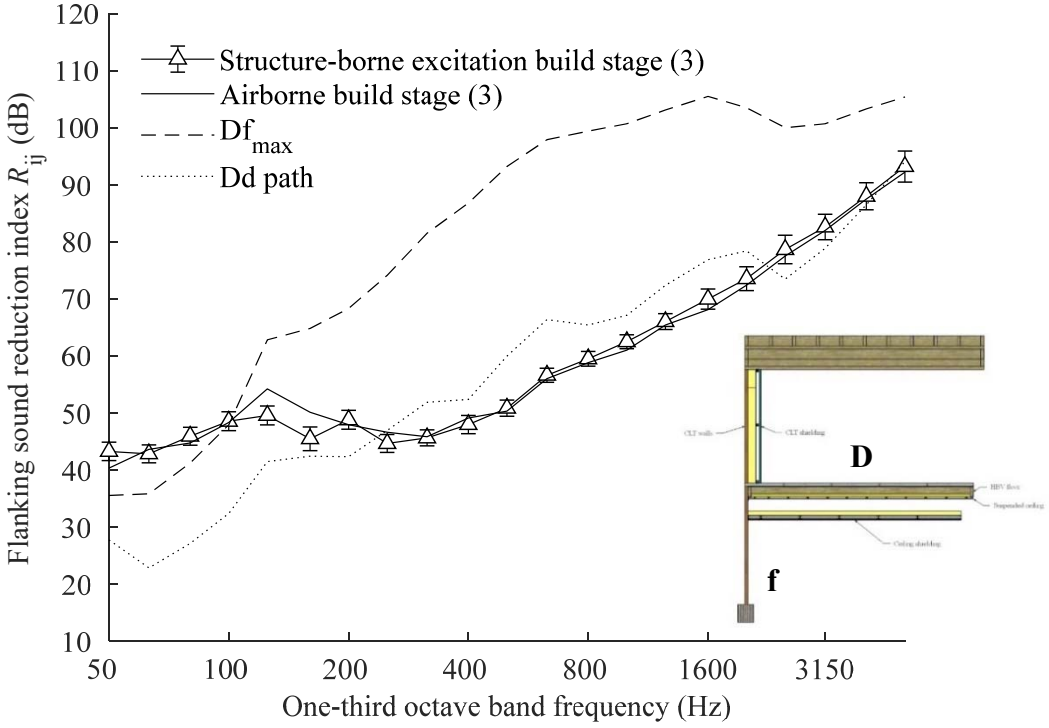

Figure 6-24 Df path - comparison of different measurement methods.

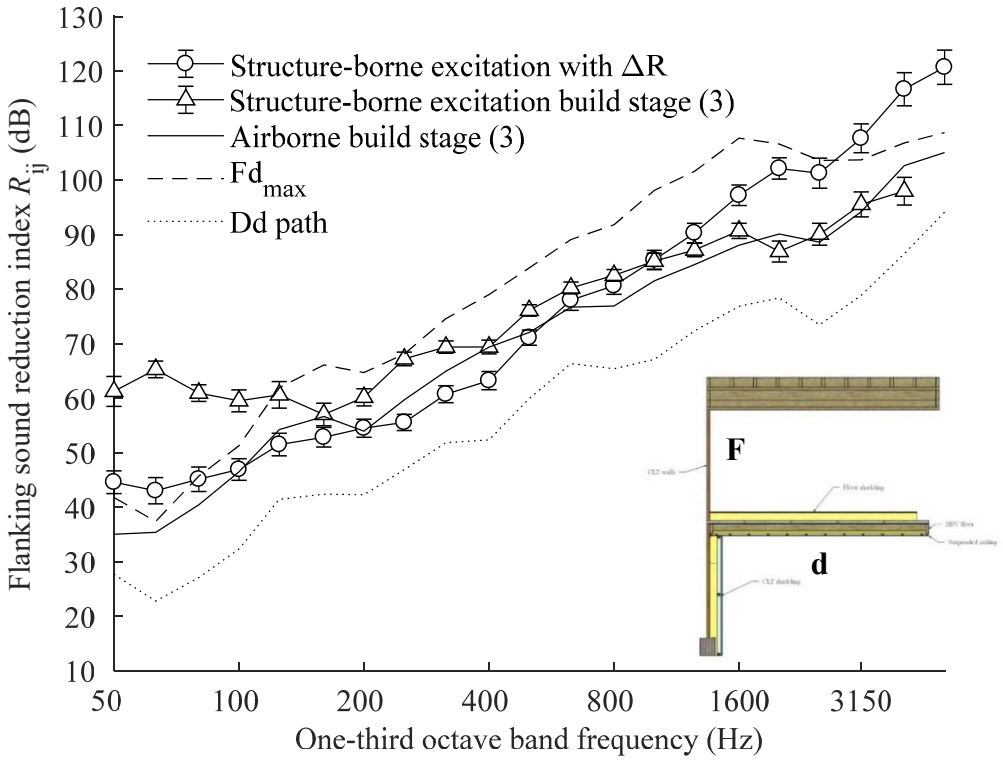

Figure 6-25 Fd path - comparison of different measurement methods.

Calculated resonant transmission indices (as described in section 6.4.2.1) were used to perform the calculations. For measurements made on the plasterboard, a calculated resonant transmission for plasterboard is used. Otherwise the *ΔR* of the plasterboard (see section 6.6.2.2 below) is used to allow comparison of airborne measurements with structure-borne measurements made on the concrete at build stages (2) and (3).

The Ff path is affected by flanking outside the laboratory for the whole frequency range. This would present a problem for many junctions as the Ff path is usually assumed to be the strongest flanking path, however, this T-junction is unusual in that regard. The problem is difficult to correct without affecting the measurement result. Remedial measures such as adding a layer of absorption to the outside of the CLT plates would have the side effect of increasing the losses on this side and hence total loss factor of the CLT plates. A more appropriate way to avoid this could be to commission the remaining two rooms of the laboratory and to remeasure the sample as a cross junction in a four room (rather than a two room) configuration. This would

block the airborne path outside the laboratory by the addition of a separating floor and rooms. (Unfortunately, there was not the opportunity to do this at the time of measurement as only two rooms of the laboratory had been commissioned.) It is potentially an advantage of a laboratory installation with the capacity to close the rooms that when high flanking coefficients must be measured (as in this case in conjunction with walls of low SRI) an appropriate laboratory configuration can be selected to eliminate any unwanted flanking paths through the surrounding laboratory space. (In this configuration where the exterior flanking walls are identical R_{max} can be approximated as $2R$ where R is the sound insulation of the exterior walls).

Df path measurements are valid in the frequency range 125-5000Hz, measurements below this range are affected by the maximum measurable Df path (Df_{max}) of the laboratory. For the Df path excellent agreement is obtained with a mean absolute difference of 2.7dB across this frequency range between the airborne and structure-borne measurement methodologies. The maximum deviations are 7.9dB and 8.6dB at 160Hz and 200Hz respectively. This is the strongest and most significant transmission path for determining apparent SRI (R') of the floor. The application of the high frequency correction term to obtain the resonant SRI works favourably to align the results of the measurement methods. With respect to the separation of the floor slabs separated data (from build stage (3) only) was used to make the comparison and this also improved the data fit. However, the full area of the floor was used to make the calculation according to Eqn. (2-189).

Fd path measurements are valid (i.e. (R_{max}-R_{ij}) >6.0dB of the Fd path of the laboratory within the frequency range 160-3150Hz.). Note that corrections for R_{max} were not applied to the data. At low frequencies 160-1250Hz the structure-borne measurements made on the concrete (using an insertion loss (ΔR) for the plasterboard) and the structure-borne measurements made on the plasterboard both show good agreement with the airborne methodology. The mean absolute difference across this frequency range between the airborne and structure-borne measurement methodologies is 6.0dB. The maximum deviations are 11.7dB and 8.7dB at 250Hz and 315Hz respectively. At high frequencies 1600-3150Hz the structure-borne

measurements made on the plasterboard show the best agreement. The mean absolute difference across this frequency range between the airborne and structure-borne measurement methodologies is 2.7dB. The Fd path has the highest R_{ij} therefore it is the least critical to calculate an accurate apparent SRI (R'). The sum of paths according to Eqn. (2-171) is shown in Figure 6-26.

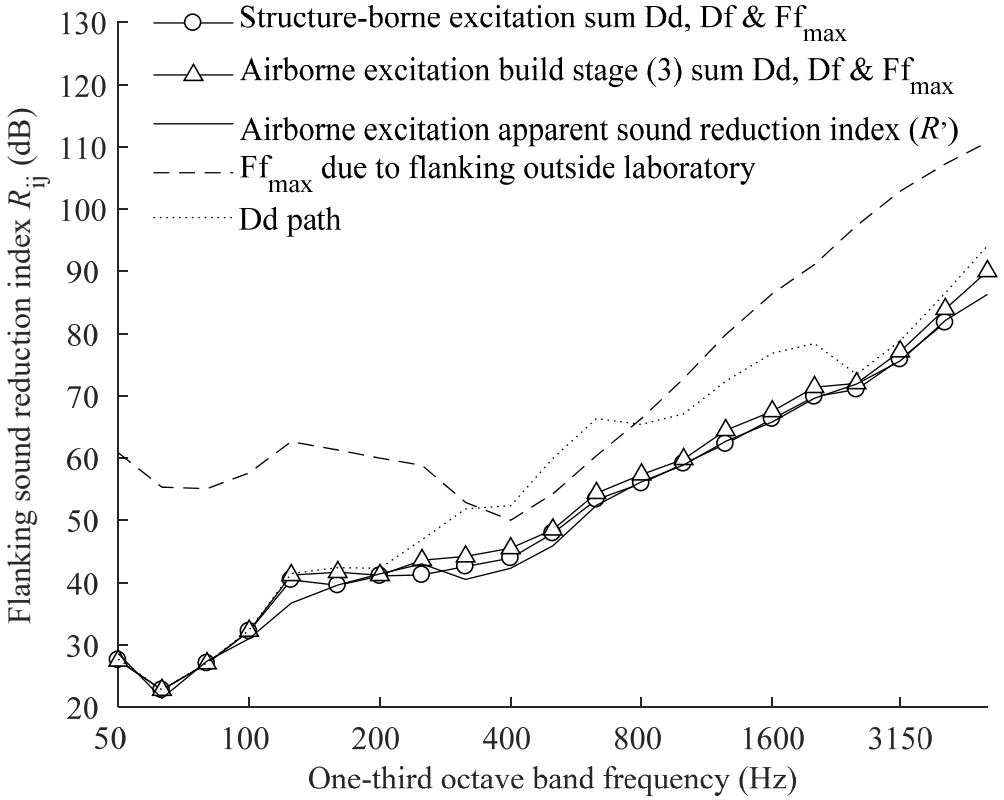

Figure 6-26 Sum of paths for each of the methods.

Only the direct path (Dd), the Df path and the flanking path outside the laboratory (Ff_{max}) are required to obtain good agreement between summed airborne or structure-borne methodologies and the measured apparent sound reduction index (R') measured with no shielding. The mean absolute difference across the whole building acoustics range (50-5000Hz) between the sums of all paths for the airborne and structure-borne measurement methodologies is 2.4dB. Up to 200Hz the weakest path is the direct path (the Dd path) through the floor, between 250-315Hz and 800-2000Hz it is the flanking Df path, (400-630Hz the measurement is affected by the flanking path outside the laboratory, Ff_{max}) and above 2000Hz it is a combination of

the direct (the Dd path) and flanking Df path. It is also shown in Figure 6-23 that when there is no shielding on the CLT the airborne flanking outside the laboratory (Ff_{max}) is stronger than the Dd path in the frequency range 315Hz-800Hz.

6.6.2.2 Sound reduction improvement index of the plasterboard

For completeness, the values measured for ΔR is shown in Figure 6-27. This is used to compare structure-borne flanking measurements on the concrete to quantify flanking to the lower room (Fd path) with the airborne made at measurements at build stage (3).

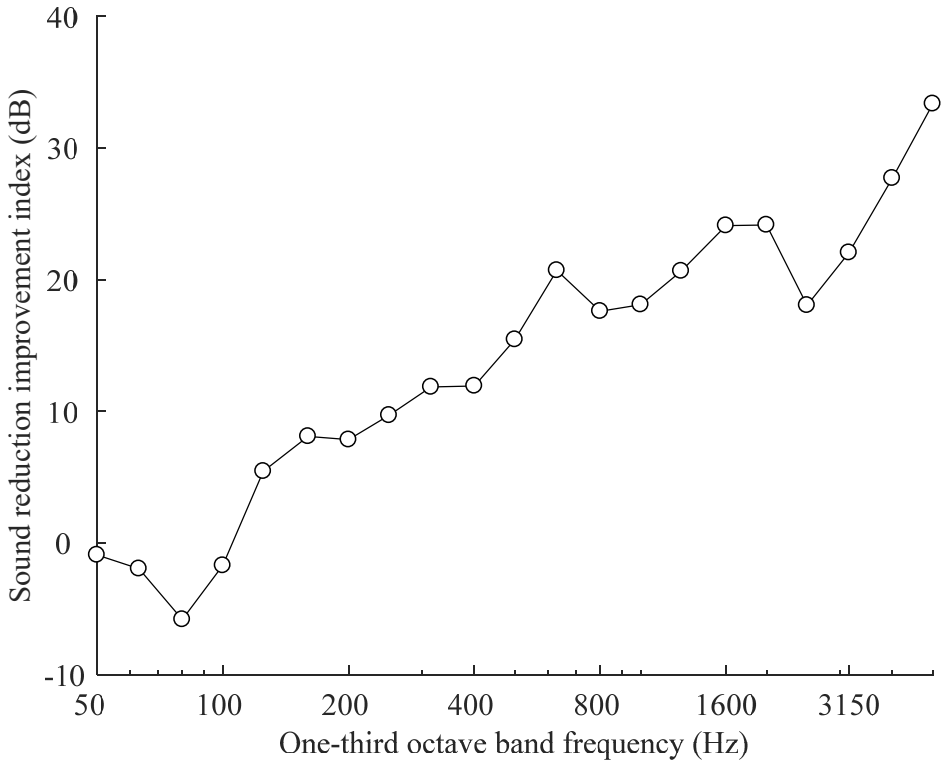

Figure 6-27 Sound reduction improvement index of the plasterboard measured for the Dd path.

6.6.3 SEA Models

Model 1 is shown (in Figure 6-28) alongside the corrected measured apparent sound reduction index (R') (which has been corrected for all values of R_{max} described in section 6.6.2). Careful application of the high frequency loss factors (>1250Hz) is required because (as shown in section 6.6.1.3) the consistency relationship cannot be

applied. The mean difference between the results across the frequency range 80-5000Hz is 2.9dB.

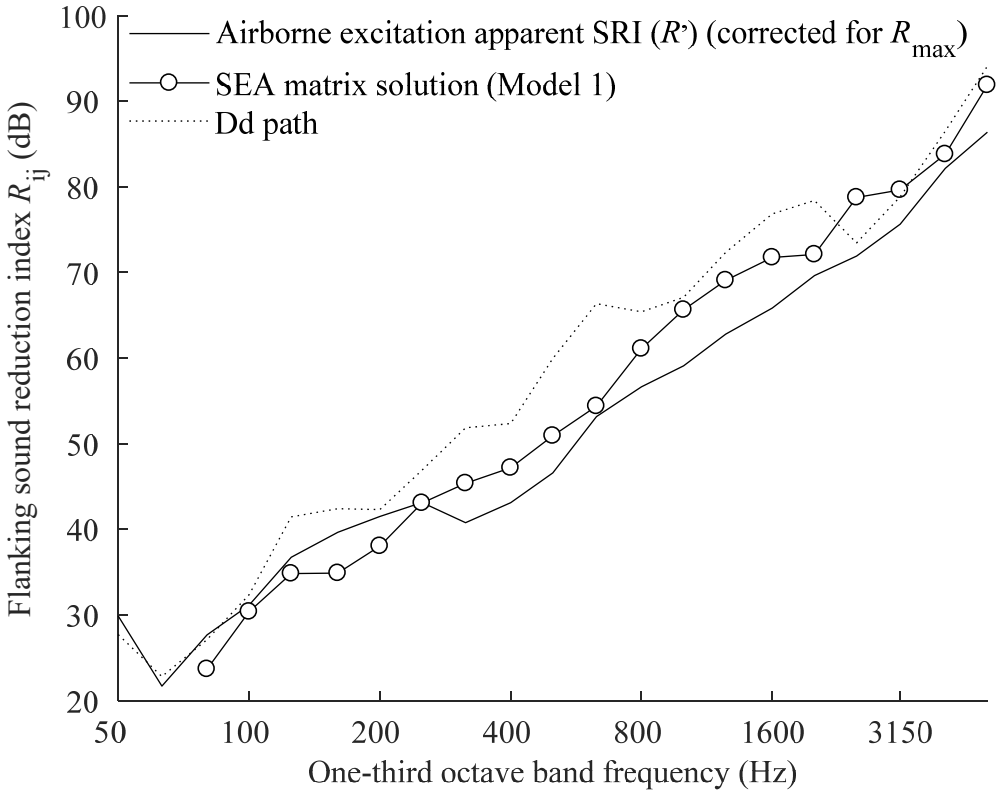

Figure 6-28 SEA matrix analysis of the T-junction.

A comparison of the SEA model and measurements of the Fd and Df paths are shown in Figure 6-29 and Figure 6-30. The flanking paths are determined by a sum of the principle paths (i.e. involving each subsystem only once). The Df path is the 1-2-7-5 path and the Fd path, at low frequencies (<2000Hz), is the 1-6-2-3-5 path and, at high frequencies (≥2000Hz), is the 1-6-2-3-4-5 path.

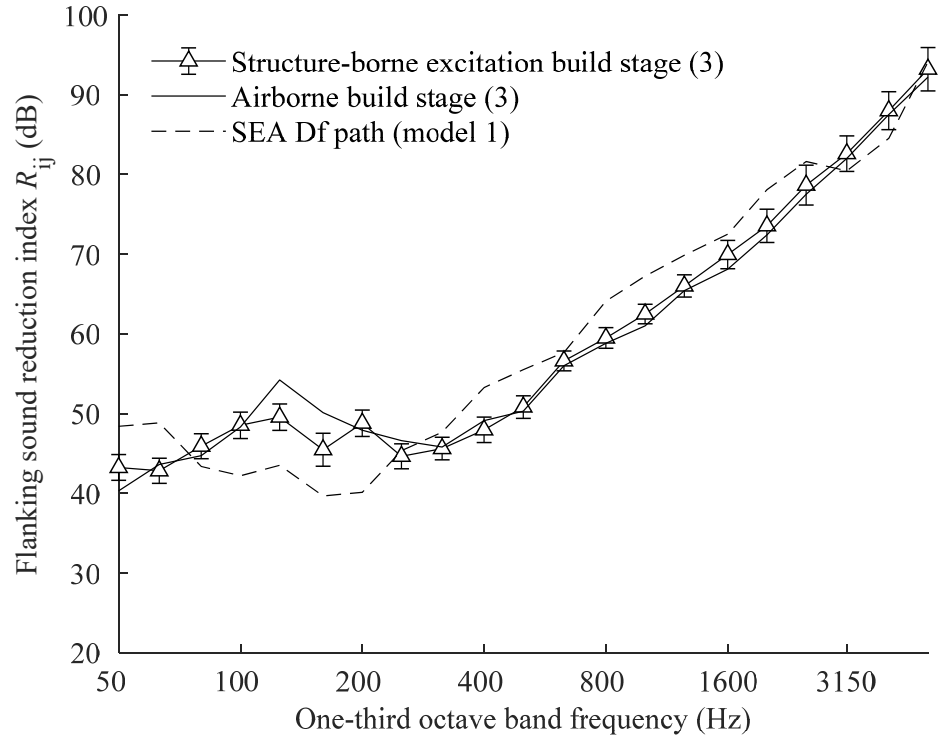

Figure 6-29 Comparison SEA path analysis and measured result (Df path)

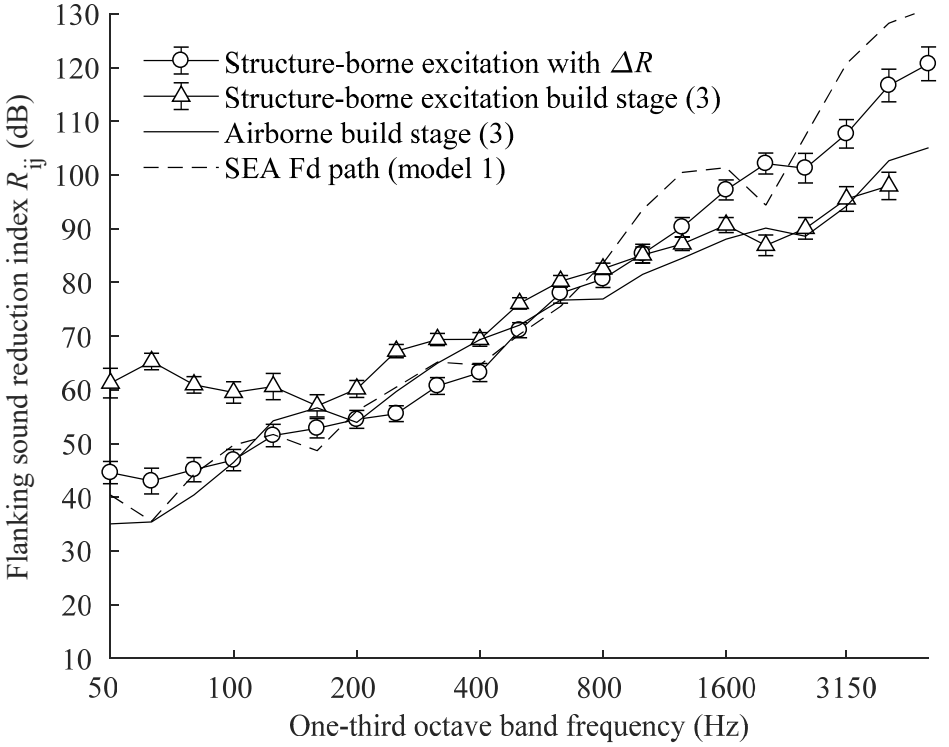

Figure 6-30 Comparison SEA path analysis and measured result (Fd path)

Unfortunately, structure-borne flanking by way of the Ff path cannot be rigorously verified by model 2 because of the contribution from the airborne flanking path outside of the laboratory. Path analysis for model 2 is shown in Figure 6-31.

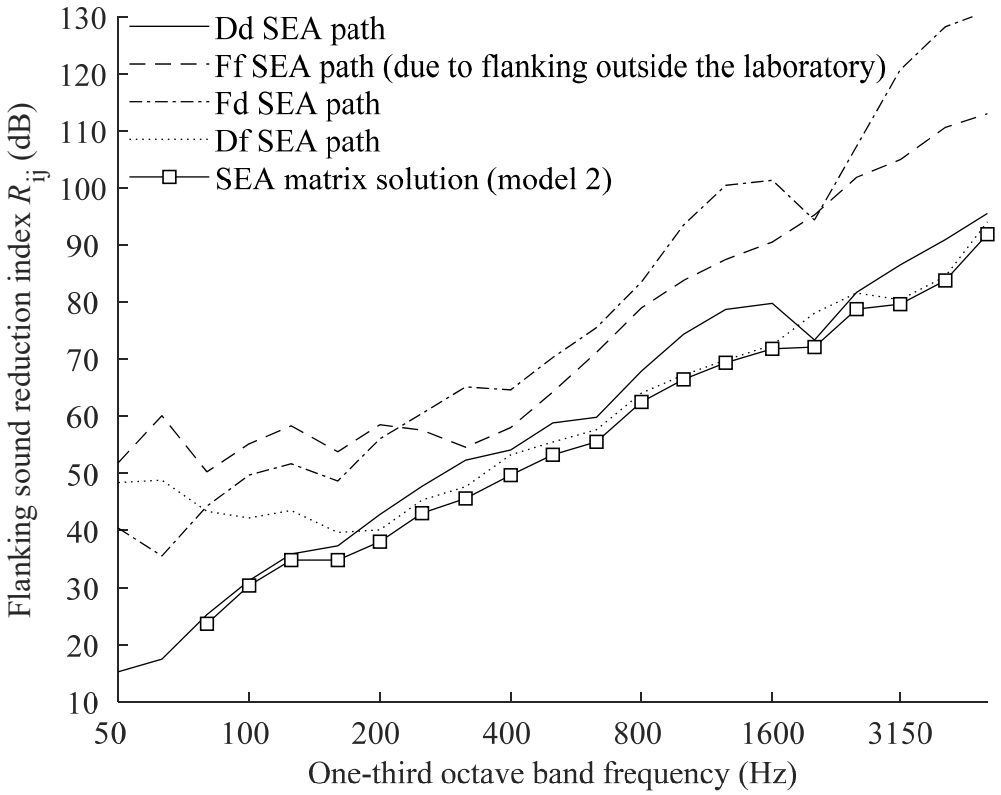

Figure 6-31 Path analysis of Model 2.

6.7 Conclusions

For both the CLT and the HBV floor the structural reverberation times were most difficult to accurately measure in the region of the critical frequency. A measurement methodology which uses a T_5 is preferred to capture structural reverberation times. In the case of the HBV floor the OSB and the concrete did not act as a single plate above 800Hz (see also section 3.7.1) and reverberation time data was acquired on the concrete side. To obtain results across the whole building acoustics range for an HBV (or similar) floor it is therefore recommended only to make measurements on the concrete.

Comparison of airborne and structure-borne methods of obtaining the velocity level difference are complicated by the fact that the HBV floor consists of two weakly attached slabs. For this reason, the airborne source methodology might be preferable (see section 6.6.1.2). Separating the velocity level difference data of the two floor slabs and using an estimated thick plate bending group velocity to calculate modal densities improves the agreement between coupling loss factors in the forwards and reverse directions for the Df and Fd flanking paths. However, it is also possible that coupling of the slabs through the airspace in the room reduces the prominence of structural decoupling in some measurements.

At frequencies >1250Hz the applicability of coupling loss factors is questionable because of large differences between coupling loss factors determined in the forwards and reverse directions. The most likely explanation is that the SEA subsystems are poorly defined at high frequencies. There are several ways in which the floor may be separated into more than one subsystem for modelling or measurement such as two separate slabs, separate concrete and OSB subsystems at high frequencies (section 3.7.1), and maybe even separate beam subsystems (section 3.4.3). No similar problem with reciprocity is found with R_{ij} measured using an airborne method or a structure-borne method provided the direction averaged velocity level difference is measured carefully considering the weak coupling between the floor slabs.

The accuracy of the comparison between the structure-borne and the airborne vibration reduction index methodologies is constrained by the assumptions made in determining a resonant SRI for each of the plates. The governing behaviour of the CLT plate requires careful attention because it is not fully described by a thin plate model. There is a lack of agreement between the two measurement methodologies for the Ff and Fd paths: In the former case, this is likely due to flanking outside the laboratory and in the latter, it is partly due to the difficulty of determining ΔR for the plasterboard suspended ceiling. The strongest transmission path (Df) is the most accurately predicted and hence it is possible to predict the apparent sound reduction index (R') by summing the paths. To obtain agreement between measurements made with a structure-borne or airborne source a resonant SRI is required for each plate.

Calculated resonant SRI, rather than measured data, for the HBV floor using models (ii)c (63Hz to 200Hz) and (ii)b (250-5000Hz) (both shown in section 3.8.3) and for the CLT walls using model 1a (shown in section 4.7.8.1) were shown to improve the agreement between calculated and measured flanking coefficients using structure-borne and airborne excitation for the Df path. This procedure is equivalent to applying a mid to high frequency correction factor (>400Hz) to measured data. For comparison, the resonant correction factors at low frequencies (see APPENDIX D) are mostly obscured by the R_{max} of the laboratory,

The analysis in this chapter indicates some characteristic problems to incorporate measured flanking data for combined lightweight and heavyweight constructions into a prediction model. In this case it was necessary to consider correcting for the two slabs of the floor or using airborne excitation, and taking velocity level measurements and structural decay times on the concrete sides of the floor slabs. For these measurements, airborne flanking outside the room is a problem for the Ff path, and the apparent sound reduction index (R'). If the measured flanking reduction indices are more than twice the sound reduction of the exterior walls of the junction ($2R$) there may be no alternative but to close off the rooms entirely to prevent (airborne) flanking through the laboratory space. All other R_{max} values were of significance in only a few third octave bands at high and low frequencies.

7 Conclusions

7.1 Main findings

There are several methods of construction using timber elements available in the market place. Partition types can be broadly categorised into three construction types: timber frame lightweight construction, timber-frame heavyweight construction and solid wood construction. Direct and flanking transmission of one wall (CLT) and floor (HBV) selected from the latter two categories were examined. These partitions can be used to build modular constructions. The building materials may be characterised by strong orthotropy, and timber products may exhibit thick plate behaviour for an extended region of the building acoustics range when compared with concrete or masonry (see chapter 4). There can also be, in some cases, strong coupling to the structural framework as shown in chapter 3 in the case of HBV floors, or alternatively, weak connections between elements (or modules), such as between the floor slabs or the connection between the concrete and OSB, as shown in chapters 3 and 6.

Isotropic and orthotropic thin plate models of an HBV floor (which consist of a thin concrete layer cast over timber beams with suspended ceiling) were experimentally validated against laboratory measurements in chapter 3 and predicted weighted SRI to within 2.0dB. The large number of nails and presence of shear connectors to prevent the cast concrete plate from sliding parallel to the structural frame strengthens the coupling between plate and framework. In this arrangement, the stiffness in the parallel and perpendicular directions are effectively modelled using an equivalent orthotropic plate approximation. The methods of Huffington and Troitsky are preferred over other methods, such as that of Kimura and Inoue,

primarily for the flexibility of the approach but also for the slightly improved accuracy. However, the theory for non-resonant transmission between the critical frequencies when they are widely spaced requires further work.

In chapter 4 the low-frequency material constants of the CLT plate were determined by comparing an experimental modal analysis with a Rayleigh-Ritz thin plate calculation of the first nine modal frequencies. E_x determined using this method is within 3% of that calculated from the material constants of the raw material and E_y is within 8-29% of that calculated from the raw material depending on the Poisson's ratio used to optimise the constants.

The high frequency material constants, which are frequency-dependant, were determined from a direct measurement of bending wavespeed. Young's moduli (E_x and E_y) obtained in this manner (before a diffuse phase correction is applied) were approximately 50% lower than those obtained from the modal frequencies and the value of G_{yz} is approximately 90% of the value in the literature [102]. These material constants, which were uncorrected for diffuse phase, give the closest results to measured airborne sound insulation when substituted into an isotropic and orthotropic model. Note that E_x and E_y for the composite CLT panel also differ significantly from the values for solid sawn lumber (e.g. E_x=1.66x10^{9}Pa and E_y=3.94x10^{9}Pa for CLT compared with E_x=6.9 x10^{8}Pa, E_y=1.59 x10^{10}Pa for sawn lumber, E_{eff} calculated using Eqn. (2-133) for the CLT plate is 77% the value of E_{eff} for sawn lumber). Understanding the mechanism by which the Young's moduli are reduced at high frequencies would mean that not every CLT panel would need to be measured individually to predict sound insulation.

The correction for diffuse phase shown in section 4.7.5 and expressed by Eqn. (4-10) was thought to be analogous to the addition of residual modes described in section 5.5.1 which added a stiffness contribution from higher modes to the mobility in the mid to high frequency range. In which case, the lowered values of the elastic constants act essentially as an empirical correction to enable accurate calculation of the SRI for the CLT. Further work with other CLT panel specifications would be required to confirm this observation and generalise these findings for application to other CLT plates.

The most problematic (though perhaps least influential) of the material constants for CLT products is Poisson's ratio (ν_{xy}). From the work presented in this thesis it seems likely that ν_{xy} or ν_{yx} differs from the values for sawn lumber (e.g. ν_{xy}=0.04 and ν_{yx}=0.07 for a composite CLT plate compared with ν_{xy}=0.036 and ν_{yx}=0.394 for sawn lumber). A value of Poisson's ratio in bending for CLT panels was determined from the values in tension provided in the literature.

Experimental modal analysis of CLT plates and junctions (including a simply supported plate, a freely hanging plate and T- and L-junctions with approximately freely supported edges) was described in chapter 5. The effect of the plateau in bending wavespeed, due to the transition to thick plate properties, on the mobility of CLT plates was considered. This transition results in a modal density that is no longer constant but which increases as a function of frequency.

Analytical models of driving point mobility were shown to require the high frequency elastic constants determined from uncorrected measured wavespeed data to give agreement with measured results. However, a convergence analysis (using FEM) to determine the effect of the stiffness contribution from modes that are higher than the frequency range of interest (residual modes) on the calculated mobility of a CLT plate showed that agreement with measurement results can be achieved using the low frequency constants, provided an adequate number of residual modes are included in the calculation.

The structure-borne flanking measurement methodology gave very consistent results and ISO 10848 seemed highly suited to measurement of the flanking of T- and L-junctions of CLT. The velocity level difference of CLT T- and L-junctions were modelled using the FEM for thick plates of linear material. The type (a) connection described in section 5.3.2 fitted well to measured data for L-junction No.1 (although less well to L-junction No.2). However, the type (c) junction gave the best fit with T-junction experimental data. Models must be constructed to correctly account for the thick plate properties of CLT. Overall the best agreement between the FEM model and measured results was obtained for the L-junction and comparatively poor agreement was obtained for the T-junction.

The junctions of combined material construction consisting of an HBV floor and CLT walls described in chapter 6 had some strong and some weak flanking paths. It is recommended that only strong flanking paths are measured in open laboratory spaces to minimise the effect of airborne flanking through the laboratory. For nominally identical wall pairs, junction measurements made in an open laboratory space have an expected R_{max} of $2R$ due to flanking through the laboratory space where R is the measured sound reduction index of the nominally identical walls. When the flanking paths approach this prescribed limit, airborne flanking through the laboratory may dominate and must be eliminated using an appropriate method. Additional room constructions may be one way to eliminate unwanted flanking. In this thesis, two of a possible four rooms were used.

The definitions of the structural coupling loss factors in Eqns. (2-178) and (2-179) were incomplete or the subsystems used in this thesis were ill-defined for the combinations of CLT and HBV plates at high frequencies (>1250Hz). Reciprocity was not demonstrated and bending waves were not necessarily the dominant wave motion. This problem resulted in large differences in coupling loss factors for connected plates between the forwards and reverse directions in section 6.6.1.3. Some possible reasons for this were the introduction of an element with two separate floor slabs and/or the substantial beams. However, there were additional hitherto undefined causes. No similar problem was observed with R_{ij} and to avoid these issues R_{ij} can be calculated directly using Eqns. (2-189) or (2-190). ISO 10848 provides suitable measurement guidance for mixed material junctions of combined HBV and CLT construction when an R_{ij} is used. Flanking (R_{ij}) may be calculated from airborne (i.e. pressure level difference) or structure-borne measurements (i.e. velocity level difference).

The materials described in this junction (except for the plasterboard) have critical frequencies in the lower end of the building acoustics range (<250Hz) and in the case of these materials it may be better to leave off a non-resonant correction factor (see APPENDIX D) for laboratory sound insulation measurements for these types of construction. In this work the calculated resonant SRI for the HBV floor using models (ii)c (63Hz to 200Hz) and (ii)b (250-5000Hz) (both shown in section 3.8.3)

and for the CLT walls using model 1a (shown in section 4.7.8.1) were necessary in the mid to high frequency range (≥400Hz) to obtain agreement between structure-borne and airborne measurement methods. This was described as the application of a mid to high frequency correction factor to the measured data. While the agreement between structure-borne and airborne results for the Df path was improved by applying this correction, only one junction was tested. Therefore, it is difficult to conclude if this procedure should be more generally applied.

7.2 Impact of the research

Timber has been used for millennia as a building material. However, aesthetic and environmental considerations have prompted architects and engineers to take a renewed look at timber construction. With modern construction methods there are many innovative ways to incorporate wood products into new builds [123] and renovations. Novel techniques are changing the way building components are fabricated and assembled on site. However, the incorporation of new building methods into the housing sector is limited not only by manufacture, assembly and running costs, but also the ability to predict building performance (e.g. fire safety, thermal and acoustic requirements) at the design stage. Innovations are sometimes showcased in large commercial buildings where safety requirements are met but the acoustic requirements for multifamily housing cannot yet be guaranteed. (Some Swiss examples include the Tamedia building, the Monte Rosa alpine hut, the elephant house at Zurich zoo and [16, 124, 125].) Improved acoustic prediction techniques for manufacturers of timber constructions would firm a share in the housing market sector.

SEA was used to model airborne transmission across a realistic cavity wall/floor construction with a high degree of accuracy in chapter 3. However, measured parameters such as: the dynamic stiffness of the resilient isolators, and the reverberation time in the cavity were required. Using SEA to model airborne transmission across a CLT wall was more problematic. Though an improved model to obtain the airborne sound insulation from measured elastic constants was achieved, an overview of all results collected for the CLT (carried out in chapters 4,

5 and 6) suggests that more work is required to correctly understand the energy transfer mechanisms. SEA can also be used to model flanking in CLT construction when used as walls and floors (investigated in chapter 5) or in combination with other floor components (investigated in chapter 6) although in the latter case a significant amount of care is required to ensure the validity of calculated coupling loss factors.

EN 12354 (parts 1 to 3) [77] prediction standards are interpreted mostly with the assumption that whole partitions are the basic subsystems of a building (exceptions include small elements, and wall shielding using ΔR) however work in this thesis and by others [9, 26, 60] suggests the methodology could be enhanced by implementing coupling loss factors between more appropriate subsystems e.g. including cavities, the battens or beams of a supporting framework, or shielding elements (instead of using ΔR). More flexible interpretation and implementation of prediction methods in this manner could allow the incorporation of new materials, construction methods (e.g. including resilient elements) or other architectural features more readily. Subsystems must be defined with careful attention to factors which might render underlying assumptions of the loss factor calculations inappropriate (e.g. separated slabs, thin/thick plates), the results from section 6.6.1.3 suggest that not all factors are yet fully known or understood.

SEA path analysis facilitates the evaluation of different transmission mechanisms, allowing architects, engineers and building component manufacturers to easily identify dominant paths for design improvements. The apparatus for measuring suspended ceiling hangers (designed by Brunskog and Hammer), for example, can be applied to many types of suspended ceiling hangers [68] enabling different coupling loss factors to be calculated for different hanger types. Continued work to quantify loss factors for other building components could result in flexible models for sound insulation prediction which would provide more guidance in the selection of new components or designs with improved sound insulation.

7.3 Further work

The theory for non-resonant transmission between widely spaced critical frequencies of an orthotropic plate requires further work. The calculations in this thesis are carried out using non-resonant transmission across a plate into and out of a 1D cavity (Eqn. (3-5)) which produces adequate results. However other partitions may exist which have strong non-resonant transmission or require expressions for transmission into and out of a 3D cavity, and further work may be required to verify the expressions. Additionally, since no expression of radiation efficiency at the lower critical frequency of an orthotropic plate was found in the literature, a measured value was applied to calculate resonant transmission. The application of Huffington and Troitsky to determine the bending stiffness for impact insulation models of orthotropic plates could also be developed.

Further work is required to collect data on many CLT panels of different specifications to confirm if the correction for diffuse phase shown in section 4.7.5 and expressed by Eqn. (4-10) is indeed analogous to the addition of a stiffness contribution from higher modes described in section 5.5.1. Also calculated resonant transmission is used to calculate coupling loss factors and R_{ij} rather than the measured SRI. The general applicability of this approach would need to be confirmed by comparing data collected from other CLT panels and to determine additional measures, if any, that would be required to incorporate this building material into modelling standards.

Further experimental work would be required to determine Poisson's ratio when the panel is subjected to a bending moment. There is much work devoted to Poisson's ratio in tension or compression. However, the influence of Poisson's ratio in layered plates specifically in bending problems deserves more attention. Several papers (e.g. Warburton [28] or Leissa [45]) observe that, for a clamped isotropic plate, the presence of curved nodal lines in bending modes are determined only by its aspect ratio, but for a freely suspended isotropic plate, the presence of curved nodal lines is dependent on both the aspect ratio and Poisson's ratio. The observation manifests physically in some modes as a transition point where a small change in the aspect

ratio of a plate by cutting or filing the plate results in a radical change of the mode shape. The effect has been observed since long ago by Waller [113] (and others) when making comparative observations of the modal patterns of vibrating rectangular and square plates. This effect could be used to make deductions about Poisson's ratio of a panel; by comparing modelled and measured panels of different aspect ratios with free edge conditions.

Also noteworthy is that during bending one face of the panel is subjected to tension and the other compression; to improve the accuracy (for some materials) different Poisson's ratios on opposing sides of the plate might also be considered in the calculation [108]. The moisture content of the panel may also be an influencing factor [112].

References

[1] L. Krajci, C. Hopkins and J. Davy, “Airborne sound transmission of a cross-laminated timber plate with orthotropic stiffness,” in *Euronoise*, 2012.

[2] J. Forssén, W. Kropp, J. Brunskog, S. Ljunggren, D. Bard, G. Sandberg, F. Ljunggren, A. Agren, O. Hallstrom, H. Dybro, K. Larsson, K. Tillberg, K. Jarnero, L. G. Sjokvist, B. Ostman, K. Hagberg, A. Bolmsvik, A. Olsson, C. G. Ekstrand and M. Johansson, “Vinnova project 2007-01653 Acoustics in wooden buildings, state of the art,” Swedish national research testing and institute, 2008.

[3] Berner Fachhochschule, Lignum, “Projekt Schallschutz im Holzbau: Bauteilkatalog (kombiniert & reduziert),” Berner Fachhochschule, Biel, 10. Mai 2011.

[4] T. R. T. Nightingale, “Application of the CEN draft building acoustics preditiona model to a lightweight double leaf construction,” *Applied Acoustics,* vol. 46, pp. 265-284, 1995.

[5] M. Villot and C. G. Carter, “Measurement methods adapted to wood frame lightweight construction,” *Journal of Building Acoustics,* vol. 13, no. 3, pp. 189-198, 2006.

[6] C. Guigou-Carter, M. Villot and R. Wetta, “Prediction method adapted to wood frame lightweight constructions,” *Journal of Buidling Acoustics,* vol. 13, no. 3, pp. 173-188, 2006.

[7] S. Schoenwald, Flanking sound transmission through lightweight framed double leaf walls - Prediction using statistical energy analysis, Eindhoven: Einhoven University Press, 2008.

[8] C. Hopkins, Sound Insulation, Butterworth-Heinemann (Elsevier), 2007.

[9] R. J. M. Craik and L. Galbrun, “Vibration transmission through a frame typical

of timber-framed buildings,," *Journal of Sound and Vibration,* vol. 281, pp. 763-782, 2005.

[10] L. Galbrun, "Vibration transmission through plate/beam structures typical of lightweight buildings: Applicability and limitations of fundamental theories," *Applied Acoustics,* vol. 71, pp. 587-596, 2010.

[11] I. Bosmans and T. R. T. Nightingale, "Structure-borne sound transmission in rib stiffened plate structures typical of wood frame buildings," *Building Acoustics,* vol. 6, no. 3, pp. 289-307, 1999.

[12] R. J. M. Craik, J. A. Steel and D. J. Evans, "Statistical energy analysis of structure-borne sound transmission at low frequencies," *Journal of Sound and Vibration,* vol. 1, no. 144, pp. 95-107, 1991.

[13] D. Wuyts, C. Crispin, B. Ingelaere and M. Van Damme, "Laboratory sound insulation measurements of improved timber floor constructions: A parametric survey," *Journal of Building Acoustics,* vol. 13, no. 4, pp. 311-325, 2006.

[14] J. Bodig and B. A. Jayne, Mechanics of Wood and Wood Composites, Malabar, Florida: Krieger Publishing Company, 1993.

[15] R. M. Jones, Mechanics of composite materials (second edition), New York: Taylor & Francis, 1999.

[16] M. Antemann, "The Tamedia building Zurich," in *Wood Build Norway*, Oslo, 2013.

[17] A. Ordubadi and R. H. Lyon, "Effect of orthotropy on the sound transmission through plywood panels," *Journal of the Acoustical Society of America,* vol. 65, no. 1, pp. 133-139, 1979.

[18] T. Augustsson, "Evaluating SEA modelling of lightweight building elements containing cross laminated timber," Chalmers University of Technology, Gothenburg, 2016.

[19] N. J. Huffington, “Bending athwart a parallel stiffened plate,” *Journal of Applied Mechanics,* vol. 34, no. 2, pp. 278-282, 1967.

[20] M. S. Troitsky, Stiffened plates: bending stability and vibrations, Elsevier, 1976.

[21] R. R. Wareing, J. L. Davy and J. R. Pearse, “The sound insulation of single leaf finite size rectangular plywood panels with orthotropic frequency dependant bending stiffness,” *Journal of the Acoustical Society of America,* vol. 139, no. 1, pp. 520-528, 2016.

[22] Dassault Systèmes, ABAQUS benchmarks guide, USA, 2014.

[23] S. Timoshenko and J. N. Goodier, Theory of elasticity (second edition), McGraw-Hill, 1951.

[24] Y. H. Pao and R. K. Kaul, “Waves and vibrations in isotropic and anisotropic plates,” in *R. D. Mindlin and applied mechanics*, Pergamon Press Inc., 1974, pp. 149-195.

[25] R. Radovitzky, “Massachusetts Institute of Technology Open Courseware: 16.21 Techniques for structural analysis and design,” 2005. [Online]. Available: https://ocw.mit.edu. [Accessed 2016].

[26] C. Hopkins, “Sound transmission across a separating and flanking cavity wall construction,” *Applied Acoustics,* vol. 52, no. (3/4), pp. 259-272, 1997.

[27] E. O. Ayorinde and R. F. Gibson, “Elastic constants of orthotropic composite materials using plate resonance frequencies, classical lamination theory and an optimised three-mode Rayleigh formulation,” *Composites Engineering,* vol. 3, no. 5, pp. 395-407, 1993.

[28] G. B. Warburton, “The vibration of rectangular plates,” *Proceedings of the Institution of Mechancal Engineers,* vol. 168, pp. 371-384, 1954.

[29] R. D. Mindlin, “Influence of rotatory Inertia and shear on flexural motions of isotropic, elastic plates,” *Journal of Applied Mechanics,* vol. 18, no. 1, pp. 31-38, 1951.

[30] R. W. Clough and J. Penzian, Dynamics of structures, USA: McGraw-Hill, 1975.

[31] G. Kurtze and B. G. Watters, “New wall design for high transmission loss or high damping,” *Journal of the Acoustical Society of America,* vol. 31, no. 6, pp. 739-748, 1959.

[32] R. J. M. Craik, Sound transmission through buildings using statistical energy analysis, Aldershot: Gower, 1996.

[33] J. H. Rindel, “Dispersion and absorption of structureborne sound in acoustically thick plates,” *Applied Acoustics,* vol. 41, pp. 97-111, 1994.

[34] Dassault Systèmes, ABAQUS theory guide, USA, 2014.

[35] Dassault Systèmes, ABAQUS analysis user's guide, United States of America, 2015.

[36] E. B. Magrab, Vibrations of elastic structural members, Alphen aan den Rijn, The Netherlands: Sijthoff & Noordhoff, 1979.

[37] R. H. Lyon and R. G. DeJong, “Chapter 8 Evaluating the mode count,” in *Theory and applications of SEA*, Butterworth-Heinemann, 1995, pp. 135-152.

[38] D. J. Gorman, Free vibration analysis of rectangular plates, North Holland: New York Elsevier, 1982.

[39] D. J. Gorman, “Accurate free vibration analysis of clamped orthotropic plates by the method of superposition,” *Journal of Sound and Vibration,* vol. 140, pp. 391-411, 1990.

[40] S. M. Dickinson and E. K. H. Li, “On the use of simply supported plate

functions in the Rayleigh-Ritz method applied to the flexural vibration of rectangular plates," *Journal of Sound and Vibration (Letters to the Editor),* vol. 80, no. 2, pp. 292-297, 1982.

[41] R. Bhat, "Natural frequencies of rectangular plates using characteristic orthogonal polynomials in Rayleigh-Ritz method," *Journal of Sound and Vibration,* vol. 102, no. 4, pp. 493-499, 1985.

[42] A. W. Leissa, "Vibration of plates," NASA, 1969.

[43] C. S. Kim and S. M. Dickinson, "Improved approximate expressions for the natural frequencies of isotropic and orthotropic rectangular plates," *Journal of Sound and Vibration,* vol. 103, no. 1, pp. 142-149, 1985.

[44] E. O. Ayorinde and L. Yu, "On the elastic characterisation of composite plates with vibration data," *Journal of Sound and Vibration,* vol. 283, pp. 243-262, 2005.

[45] A. W. Leissa, "The free vibration of rectangular plates," *Journal of Sound and Vibration,* vol. 31, no. 3, pp. 257-293, 1973.

[46] F. G. Leppington, K. H. Heron, E. Broadbent and S. M. Mead, "Resonant and non-resonant acoustic transmission of elastic panels; Part I the radiation problem," *Proceedings of the Royal Society,* pp. 309-337, 1987.

[47] F. G. Leppington, K. H. Heron, E. G. Broadent and S. M. Mead, "Resonant and non-resonant acoustic properties of elastic panels: Part II the sound transmission problem," *Proceedings of the Royal Society,* vol. 412, pp. 309-337, 1987.

[48] L. Cremer, M. Heckl and B. A. T. Pederson, Structure-Borne Sound, Springer, 2005 (third edition).

[49] K. J. Bulhert, "Driving point impedances of thick homogeneous plates in flexure," *Journal of Sound and Vibration,* vol. 78, no. 2, pp. 235-245, 1981.

[50] R. H. Lyon, “Part I: Basic Theory,” in *Statistical energy analysis of dynamical systems*, Massachusetts Institute of Technology, 1975, pp. 3-169.

[51] J. L. Davy, “Predicting the sound insulation of walls,” *Building Acoustics,* vol. 16, no. 1, pp. 1-20, 2009.

[52] M. Heckl, “Untersuchungen an Orthotropen Platten,” *Acustica,* vol. 10, pp. 109-115, 1960.

[53] J. Davy, “Predicting the sound insulation of single leaf walls: Extension of Cremer's model,” *Journal of the Acoustical Society of America,* vol. 126, no. 4, pp. 1871-1877, 2009.

[54] S. Ljunggren, “Airborne sound insulation of thick walls,” *Journal of the Acoustical Society of America,* vol. 89, no. 5, pp. 2338-2345, 1991.

[55] R. M. Jones and Klein, “Equivalence between single-layered and certain multilayered shells,” *American Institute of Aeronautics and Astronautics Journal,* vol. 6, no. 12, pp. 2295-2300, 1968.

[56] S. Kimura and K. Inoue, “Practical calculation of floor impact sound by impedance method,” *Applied Acoustics,* vol. 26, pp. 263-292, 1989.

[57] M. J. Crocker and A. J. Price, “Sound transmission using statistical energy analsis,” *Journal of Sound and Vibration,* vol. 9, no. 3, pp. 469-486, 1969.

[58] M. J. Crocker and A. J. Price, “Sound transmission through double panels using statistical energy analysis,” *Journal of the Acoustical Society of America,* vol. 47, no. 3, pp. 683-693, 1970.

[59] B. H. Sharp, “Prediction methods for the sound transmission of building elements,” *Noise Control Engineering,* vol. 11, pp. 53-63, 1978.

[60] R. J. M. Craik and R. S. Smith, “Sound transmission through double leaf lightweight partitions. Part I: airborne sound,” *Applied Acoustics,* vol. 61, pp.

223-245, 2000.

[61] V. Hongisto, “Sound insulation of double panels -Comparison of existing prediction models,” *Acta Acustica united with Acustica,* vol. 92, pp. 61-78, 2006.

[62] R. J. M. Craik and R. S. Smith, “Sound Transmission through lightweight parallel plates. Part 2: Structure-borne sound,” *Applied Acoustics,* vol. 61, pp. 247-269, 2000.

[63] R. J. M. Craik, “Non-resonant sound transmission through double walls using statistical energy analysis,” *Applied Acoustics,* vol. 64, pp. 325-341, 2003.

[64] J. D. Quirt, T. R. T. Nightingale and F. King, “NRC guide for sound insulation in wood frame construction,” 2006.

[65] S. Schoenwald, E. Wenzke, F. King and B. Zeitler, “Effect of structural changes on acoustic performance of wood frame walls,” in *Euronoise*, Prague, 2012.

[66] S. Su, F. A. Fairfield and S. Smith, “Vibration isolation properties of resilient bars in timber floors,” *Building Acoustics,* vol. 17, no. 4, pp. 249-268, 2010.

[67] S. Su, S. Smith and C. Fairfield, “An experimental study on the effects of resilient bars on plate vibration,” *Applied Acoustics,* vol. 72, pp. 241-247, 2011.

[68] J. Brunskog and P. Hammer, “Measurement of the acoustic properties of resilient statically tensile loading devices in lightweight structures,” *Building acoustics,* vol. 9, no. 2, pp. 99-137, 2002.

[69] K. J. Bathe, “Finite element procedures for solids and structures,” http://ocw.mit.edu (Accessed Feb-Mar, 2016). License: Creative Commons BY-NC-SA, Massachusetts Institute of Technology: MIT OpenCourseWare, Spring 2010.

[70] J. He and Z. F. Fu, Modal Analysis, Butterworth- Heinemann, 2001.

[71] J. A. Moore and R. H. Lyon, “Sound trasnsmission loss characteristics of sandwich panel constructions,” *Journal of the Acoustical Society of America,* vol. 89, no. 2, pp. 777-791, 1991.

[72] J. L. Guyader and C. Lesueur, “Acoustic transmission through orthotropic multilayered plates, Part I: Plate vibration modes,” *Journal of Sound and Vibration,* vol. 58, no. 1, pp. 51-68, 1978.

[73] J. L. Guyader and C. Lesueur, “Acoustic transmssion through orthotropic multilayered plates, Part II: Transmission loss,” *Journal of Sound and Vibration,* vol. 58, no. 1, pp. 69-86, 1978.

[74] J. L. Guyader and C. Lesueur, “Transmission of reverberant sound through orthotropic, viscoelastic multilayered plates,” *Journal of Sound and Vibration,* vol. 70, no. 3, pp. 319-332, 1980.

[75] C. T. Sun and J. M. Whitney, “Theories for the dynamic response of laminated plates,” *American Institute of Aeronautics and Astronautics Journal,* vol. 11, no. 2, pp. 178-183, 1973.

[76] V. N. Burlayenko, H. Altenbach and T. Sadowski, “An evaluation of displacement-based finite element models used for free vibration analysis of homogeneous and composite plates,” *Journal of Sound and Vibration,* vol. 358, pp. 152-175, 2015.

[77] “EN 12354 Building acoustics - Estimation of acoustic performance of buildings from the performance of elements,” CEN, 2000.

[78] E. Gerretsen and T. R. T. Nightingale, “Prediction models in building acoustics: Introduction in the special sessions at Forum Acusticum 1999 in Berlin,” in *Forum Acusticum*, Berlin, 1999.

[79] E. Gerretsen, “Prediction models for building performance - European need

and world wide use," in *Euronoise*, Paris, 2008.

[80] E. Gerretsen, "Possibilities to improve the modelling in EN12354 for lightweight elements," in *Internoise*, Tampere, 2006.

[81] E. Gerretsen, "Some aspects to improve sound insulation prediction models for lightweight elements," in *Internoise*, Istanbul, 2007.

[82] S. Schoenwald, E. Gerretson and H. Martin, "Measurement of flanking transmission through gypsum board walls with a modified SEA method," in *Internoise*, Istanbul, 2007.

[83] J. L. Davy, J. Mahn, C. Guigou-Carter and M. Villot, "The prediction of flanking sound transmission below the critical frequency," *Journal of the Acoustical Society of America,* vol. 132, no. 4, pp. 2359-2370, 2012.

[84] T. R. T. Nightingale and I. Bosmans, "Expressions for first-order flanking paths in homogeneous isotropic and lightly damped buildings," *Acta Acoustics united with Acoustica,* vol. 89, pp. 110-122, 2003.

[85] L. Galbrun, "The prediction of airborne sound transmission between two rooms using first-order flanking paths," *Applied Acoustics,* vol. 69, pp. 1332-1342, 2008.

[86] R. J. M. Craik, "The contribution of long flanking paths to sound transmission in buildings," *Applied Acoustics,* vol. 62, pp. 29-46, 2001.

[87] A. Neves e Sousa and B. M. Gibbs, "Low frequency impact sound transmission in dwellings through homogenous concrete floors," *Applied Acoustics,* vol. 72, no. 4, pp. 177-189, 2011.

[88] S. Maluski and B. M. Gibbs, "The effect of construction material, contents and room geometry on the sound field in dwellings at low frequencies," *Applied Acoustics,* vol. 65, no. 1, pp. 31-44, 2004.

[89] C. Hopkins and P. Turner, "Field measurements of airborne sound insulation

between rooms with non-diffuse sound fields at low frequencies," *Applied Acoustics,* vol. 66, pp. 1339-1382, 2005.

[90] J. Mahn, *Prediction of flanking noise transmission in lightweight building constructions: A theoretical and experimental evaluation of the application of EN12354-1,* University of Canterbury, Christchurch, New Zealand, 2008.

[91] "EN ISO 10140 Acoustics. Laboratory measurement of sound insulation of building elements. Part 1: Application rules for specific products," ISO, 2016.

[92] "EN ISO 10140-2 Acoustics - Laboratory measurement of sound insulation of buiding elements - Part 2: Measurement of airborne sound insulation," ISO, 2010.

[93] E. Gerretsen, "Calculation of airborne and impact sound insulation between dwellings," *Applied Acoustics,* vol. 19, pp. 245-264, 1986.

[94] "ISO 10848-1 Acoustics - Laboratory measurement of the flanking transmission of airborne and impact sound between adjoining rooms," ISO, 2006.

[95] "EN ISO 140-3 Acoustics - Measurement of sound insulation in buildings and of building elements - Part 3: Laboratory measurement of airborne sound insulation of building elements," ISO, 1995.

[96] C. Hopkins, R. Wilson and R. J. M. Craik, "Dynamic stiffness as an acoustic specification parameter for wall ties used in masonry cavity walls," *Applied Acoustics,* vol. 58, pp. 51-68, 1999.

[97] C. Churchill and C. Hopkins, "Development of SEA models of composite heavyweight-lightweight floors by incorporating measured stiffness data for suspended ceiling hangers," in *Internoise*, Innsbruck, 2013.

[98] F. G. Leppington, K. H. Heron and E. G. Broadbent, "Resonant and non-resonant transmission of random noise through complex plates," *Proceedings*

of the Royal Society, vol. 458, pp. 683-704, 2002.

[99] "ISO 717-1 Acoustics - Rating of sound insulation in buildings and of building elements - Part 1: Airborne sound insulation," ISO, 2013.

[100] B. Van Damme, S. Schoenwald, M. A. Blanco and A. Zemp, "Limitation to the use of homogenized material parameters of cross laminated timber plates for vibration and sound transmission modelling," in *International congress on sound and vibration*, Florence, 2015.

[101] A. Santoni, S. Schoenwald, B. Van Damme, H. Tröbs and P. Faustini, "Average sound radiation model for orthotropic CLT plates," in *EuroRegio*, Porto, 2016.

[102] R. Steiger, A. Gulzow, C. Czaderski, M. T. Howald and P. Neimz, "Comparison of bending stiffness of cross-laminated solid timber derived by a modal analysis of full panels and by bending tests of strip-shaped specimens," *European Journal of Wood and Wood Products,* vol. 70, pp. 141-153, 2012.

[103] L. R. Deobald and R. F. Gibson, "Determination of elastic constants of orthotropic plates by a modal analysis/ Rayleigh-Ritz technique," *Journal of Sound and Vibration,* vol. 124, no. 2, pp. 269-283, 1988.

[104] F. Moussu and M. Nivoit, "Determination of elastic constants of orthotropic plates by a modal analysis/method of superposition," *Journal of Sound and Vibration,* vol. 165, no. 1, pp. 149-163, 1993.

[105] "EN 338 Structural timber - strength classes," CEN, 2003.

[106] V. Bucur, Acoustics of wood, Springer, 2006.

[107] C. Kohlnhauser and C. Hellmich, "Determination of Poisson ratios in isotropic, transversely isotropic and orthotropic materials by means of combined ultrasonic-mechanical testing of normal stiffnesses: Application to metals and wood," *European Journal of Mechanics and Solids,* no. 33, pp. 82-

98, 2012.

[108] P. Niemz, T. Ozhar and S. Hering, “Moisture-dependent orthotropic tension compression,” *Holzforschung,* vol. 67, no. 4, pp. 395-404, 2012.

[109] B. Voichita, Acoustics of wood, Springer, 2006.

[110] C. Churchill and C. Hopkins, “Prediction of the elastic properties of a cross laminated timber plate from an investigation of the eigenmodes using a scanning laser vibrometer,” in *DAGA*, 2013.

[111] O. I. Moarcas, *The measurement and modelling of the effects of concentrated loads on particleboard floor decking,* PhD Thesis Brunal University: Brunel University, 1999.

[112] T. Ozyhar, S. Hering, S. J. Sanabria and P. Niemz, “Determining moisture-dependent elastic characteristics of beech wood by means of ultrasonic waves,” *Wood Science and Technology,* vol. 47, no. 2, pp. 329-341, 2013.

[113] M. Waller, “Vibration of free rectangular plates,” *Procedings of the Royal Physical Society of London (Series B),* vol. 62, no. 353, pp. 277-285, 1949.

[114] M. Robinson and C. Hopkins, “On the evaluation of decay curves to determine structural reverberation times for building elements,” *Acta Acustica united with Acustica,* vol. 99, pp. 226-244, 2013.

[115] R. F. S. Hearmon, “The fundamental frequency of vibration of rectangular wood and plywood plates,” *Proceedings of the Physical Society,* vol. 58, pp. 78-92, 1946.

[116] L. Roelens, F. Nuytten, I. Bosmans and G. Vermeir, “In situ measurements of the stiffness properties of building components,” *Applied Acoustics,* vol. 52, pp. 289-309, 1997.

[117] N. H. Clark and S. Thwaites, “Local phase velocity measurements in plates,” *Journal of Sound and Vibration,* vol. 187, no. 2, pp. 241-252, 1995.

[118] Mathworks, “MATLAB Documentation,” [Online]. Available: http://ch.mathworks.com/. [Accessed April 2016].

[119] K. M. Liew, Y. Xiang and S. Kitipornchai, “Research on thick plate vibration: A literature survey,” *Journal of Sound and Vibration,* vol. 180, no. 1, pp. 163-176, 1995.

[120] M. Perez and M. Fuente, “Acoustic design through predictive methods in Cross Laminated Timber (CLT) panel structures for buildings,” in *Internoise*, Innsbruck, 2013.

[121] N. C. Barford, Experimental measurements: Precision, error and truth, Addison-Wesley Publising Company, 1967.

[122] Dassault Systèmes, ABAQUS example problems guide, USA, 2014.

[123] A. Waugh, “Stadthaus, Murray Grove Tower,” in *Wood Build Norway*, Oslo, 2013.

[124] Holcim (Switzerland) AG, Director, *Monte Rose Hut.* [Film]. Switzerland: HABEGGER AG, 2015.

[125] Markus Schietsch Architecten, “Elefantenhaus Zoo Zurich,” [Online]. Available: http://www.markusschietsch.com/index.php/projekte/elefantenhaus. [Accessed 12 June 2016].

[126] Gerretsen E., “Calculation of the sound transmission between dwellings by partitions and flanking structures,” *Applied Acoustics,* vol. 12, pp. 413-433, 1979.

[127] Working Group 1: COST Action FP0702 Net - Acoustics for timber based lightweight buildings and elements, “Chapter 1 - Prediction methods for sound and vibration performances, including low frequencies,” Cost European Cooperation in Science and Technology, 2011.

[128] T. Kihlman, “Transmission of structure borne sound in buildings,” National Swedish Institute for Building Research, Stockholm, 1967.

[129] J. Mahn and J. Pearse, “Separation of resonant and non-resonant components - Part I: Sound reduction index,” *Building Acoustics,* vol. 15, no. 2, pp. 95-115, 2008.

[130] “EN ISO 10140-4 Acoustics - Laboratory measurement of sound insulation of building elements - Part 4: Measurement procedures and requirements,” ISO, 2016.

APPENDIX A: Shielding configurations

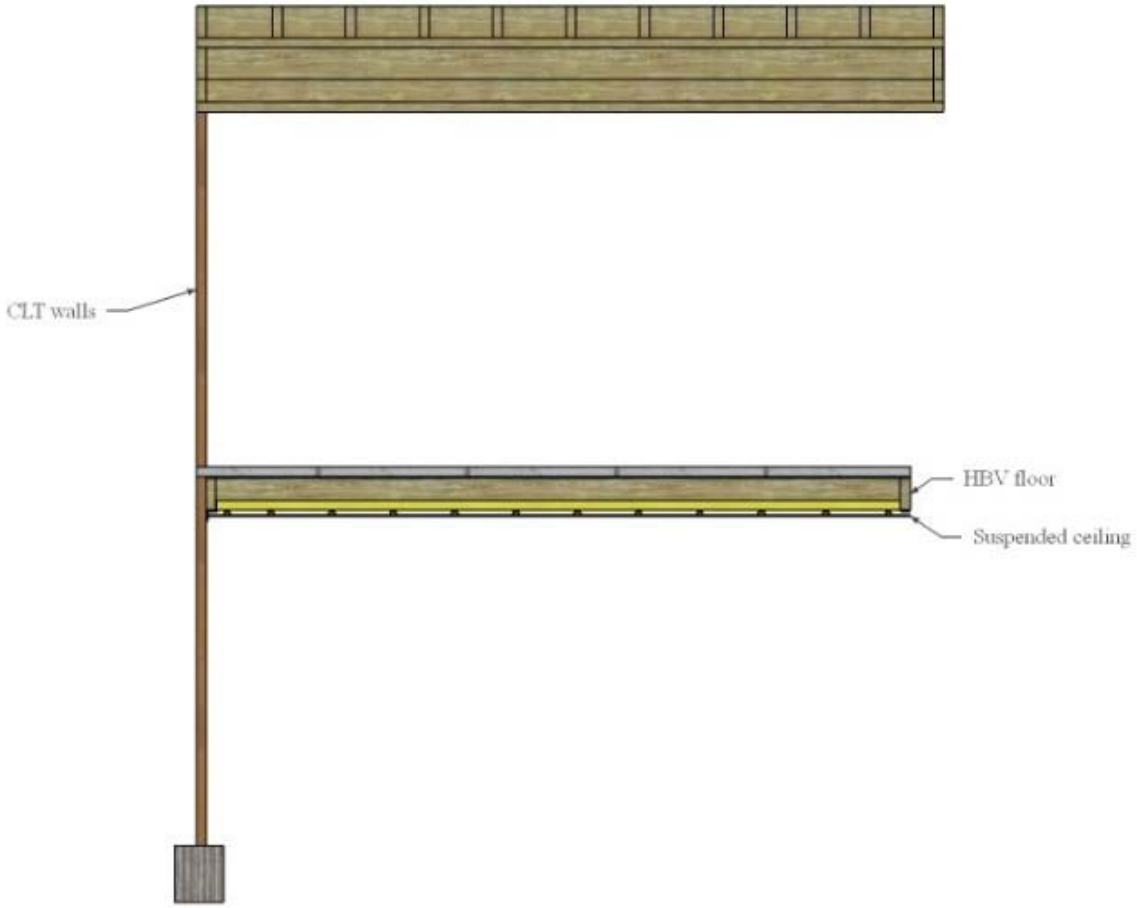

Figure A-1 Shielding configuration (a) No shielding

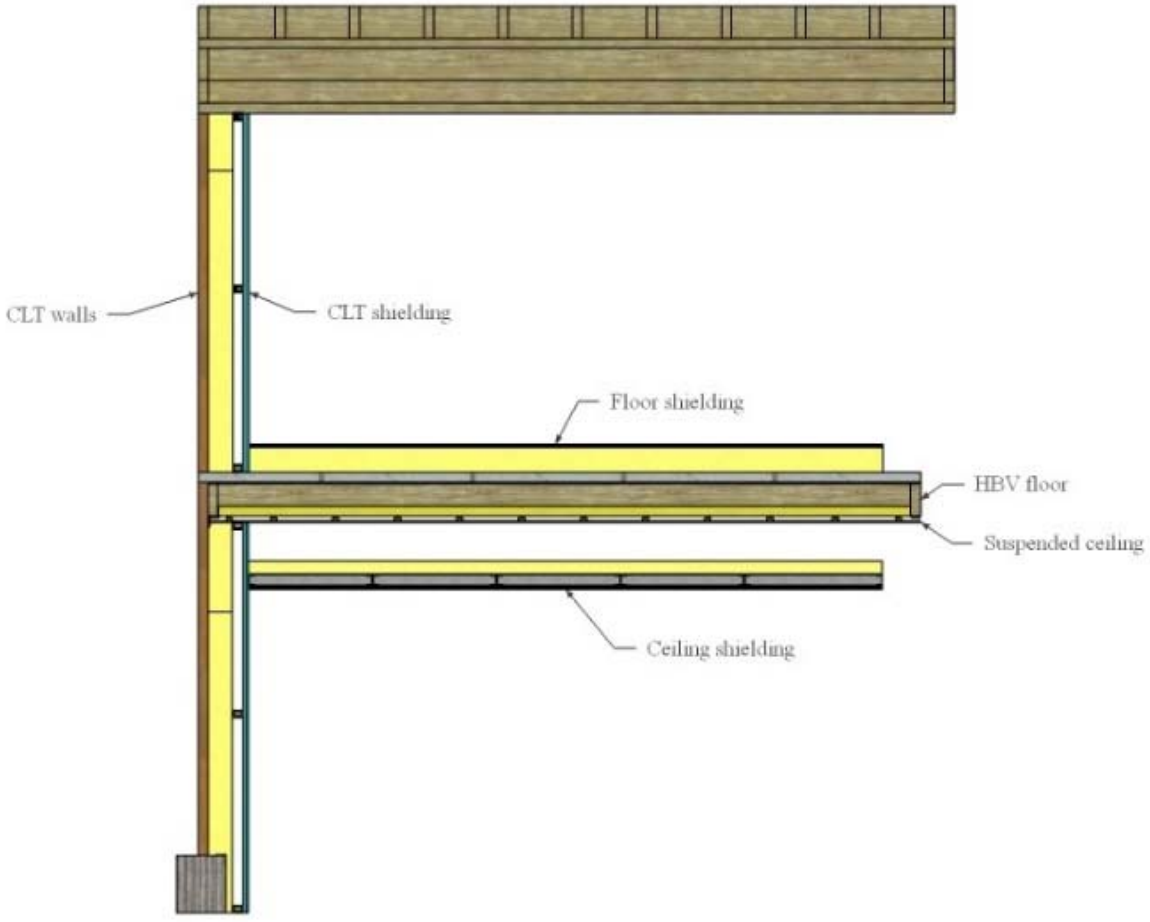

Figure A-2 Shielding configuration (b) R_{max}

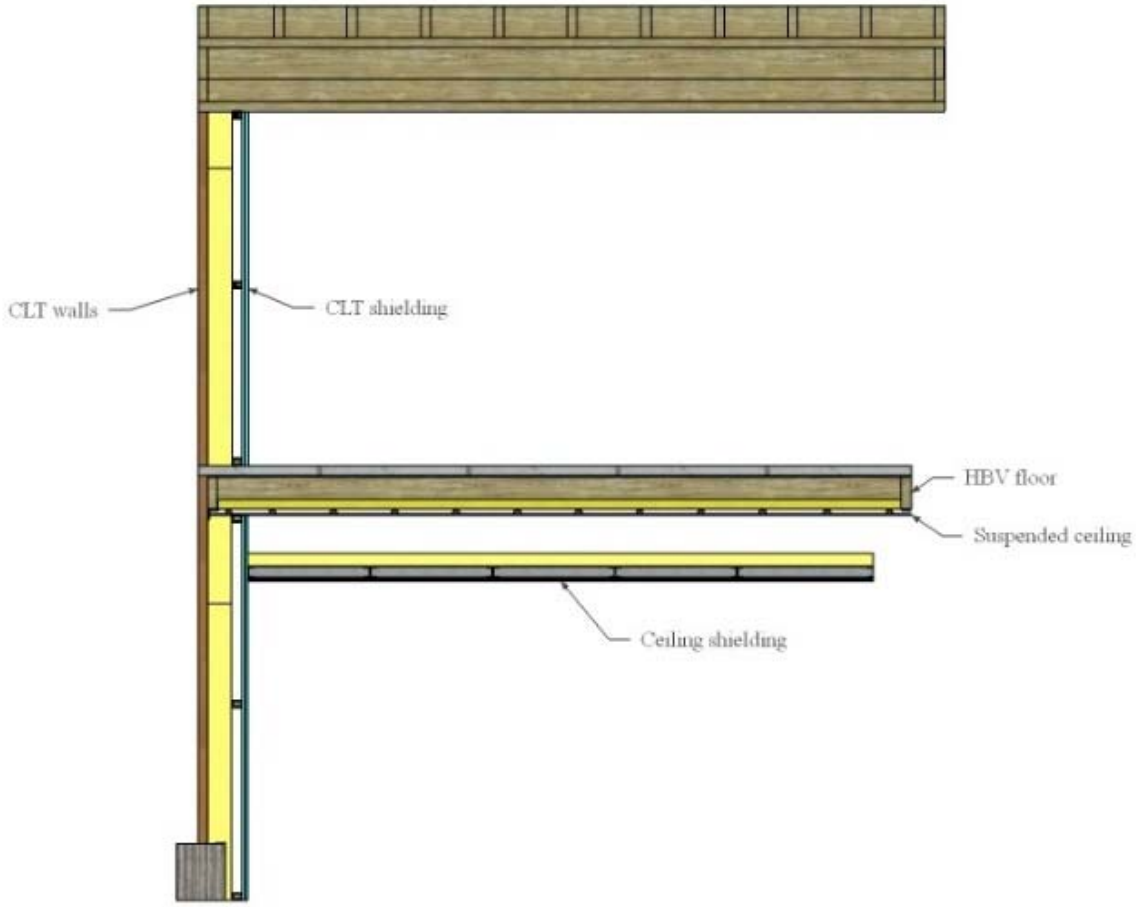

Figure A-3 Shielding configuration (c) R_{max} Df path

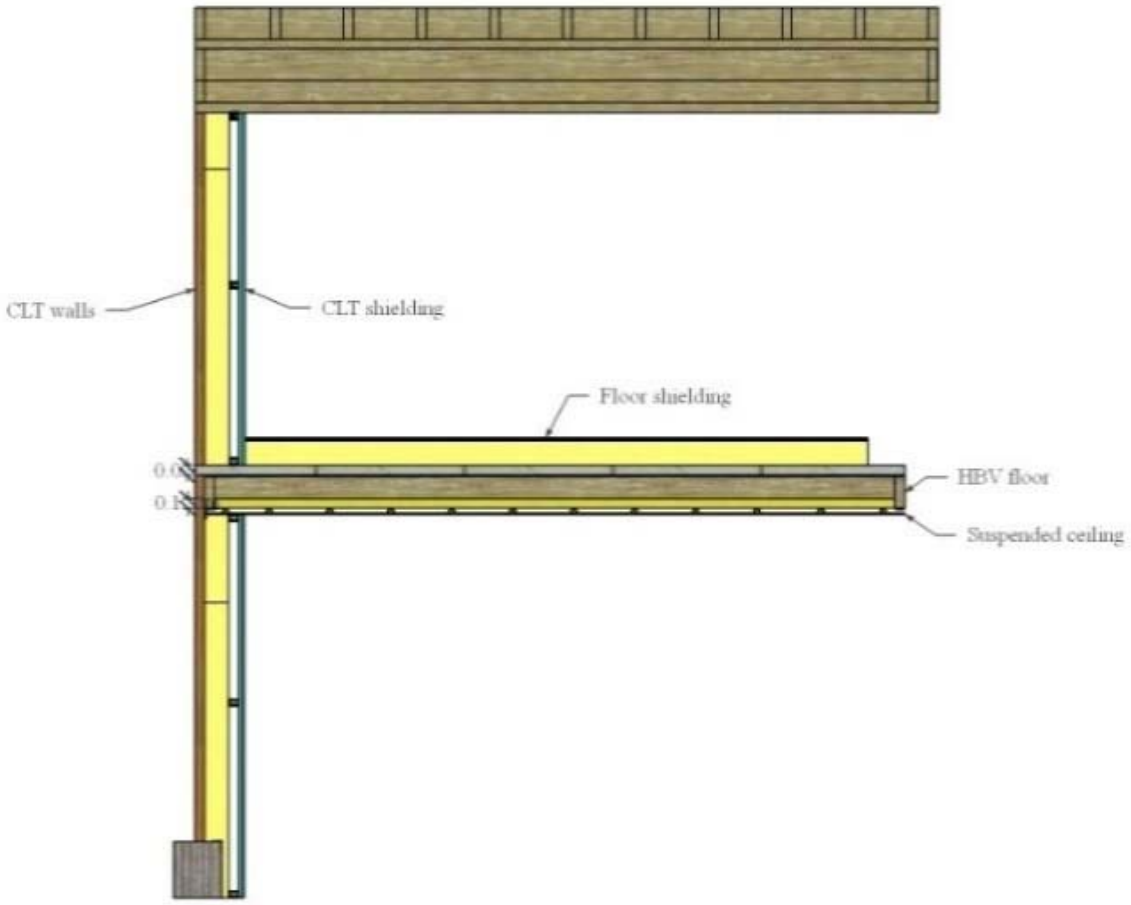

Figure A-4 Shielding configuration (d) R_{max} Fd path

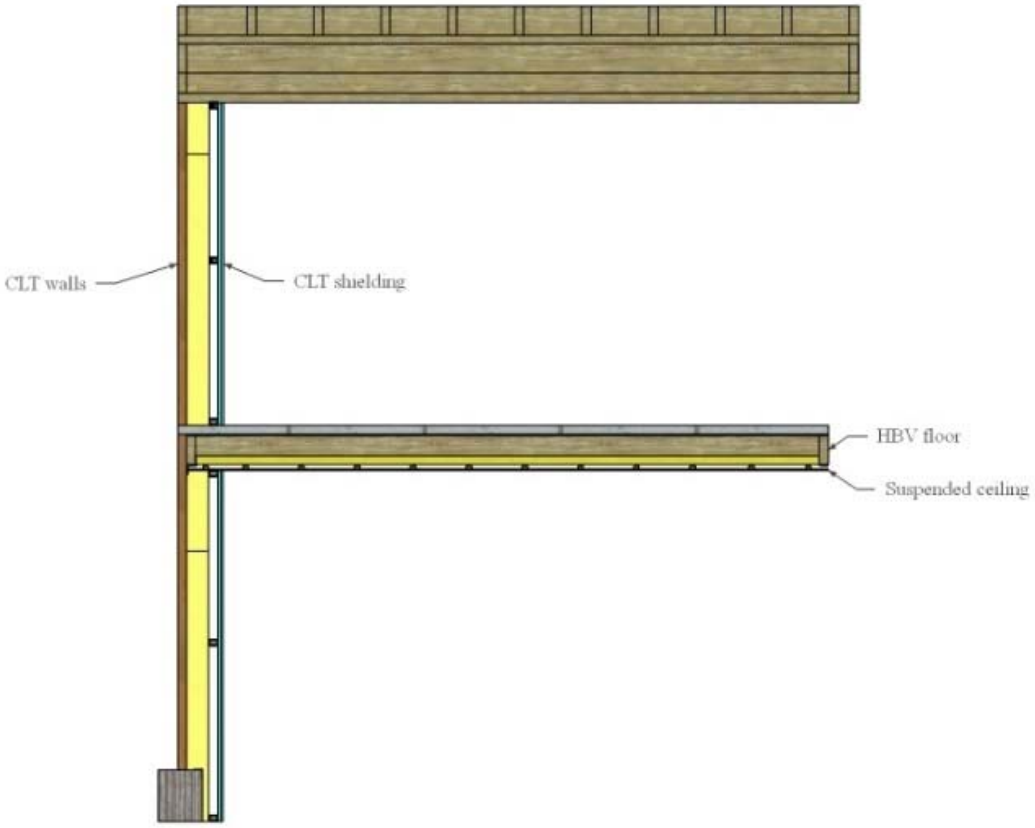

Figure A-5 Shielding configuration (e) Dd path

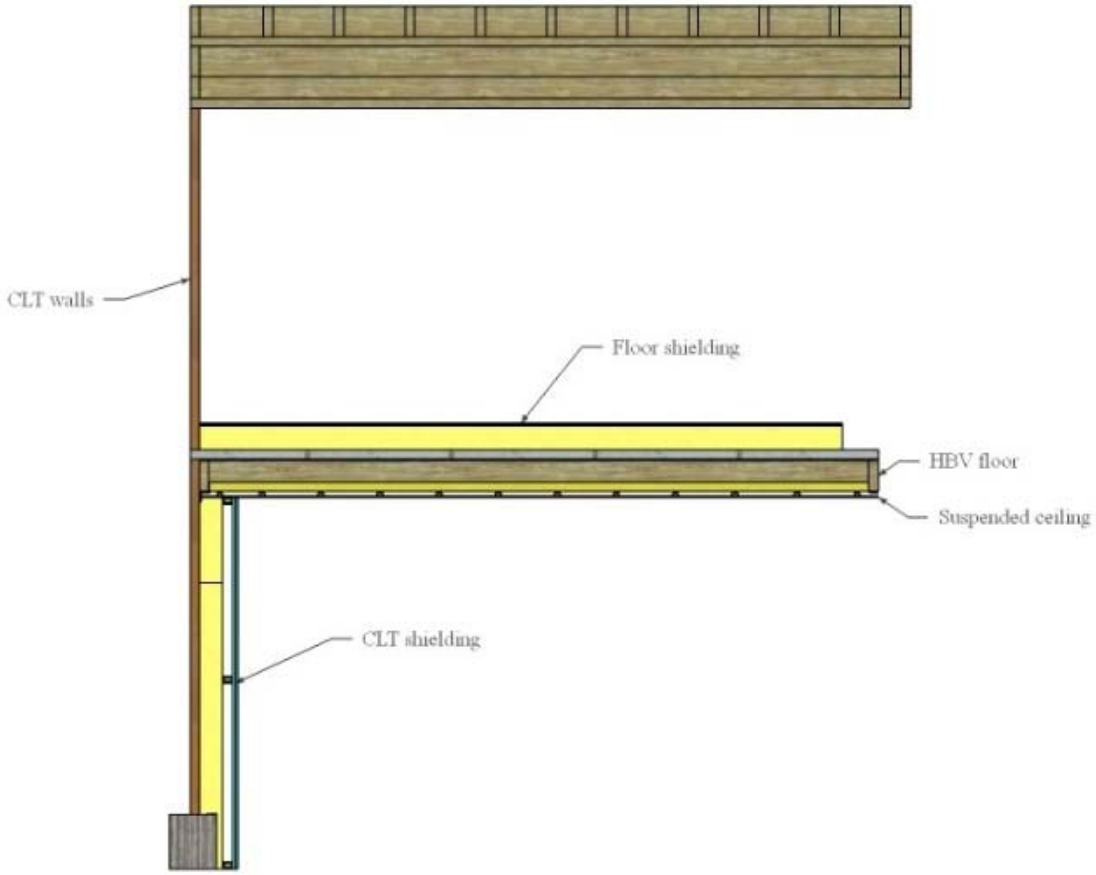

Figure A-6 Shielding configuration (f) Fd path

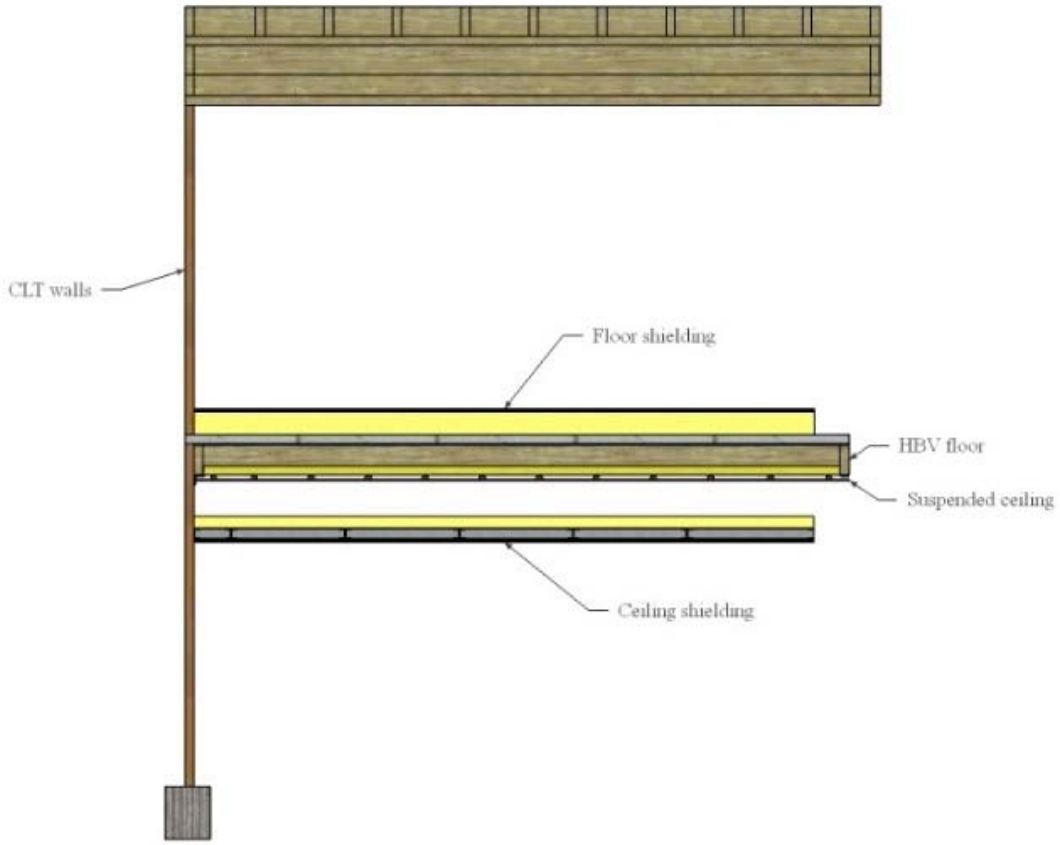

Figure A-7 Shielding configuration (g) Ff path

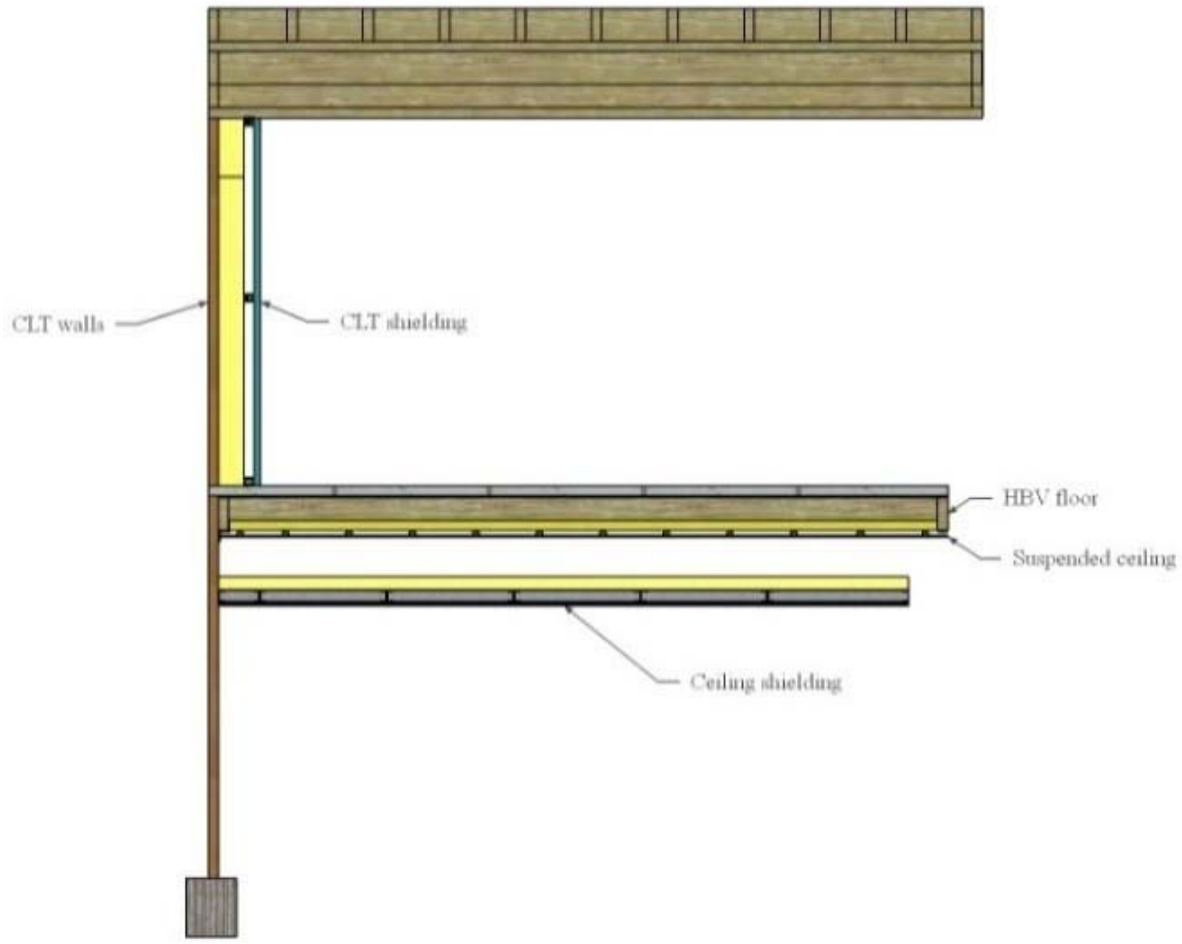

Figure A-8 Shielding configuration (h) Df path

APPENDIX B: Sketches of the test junction

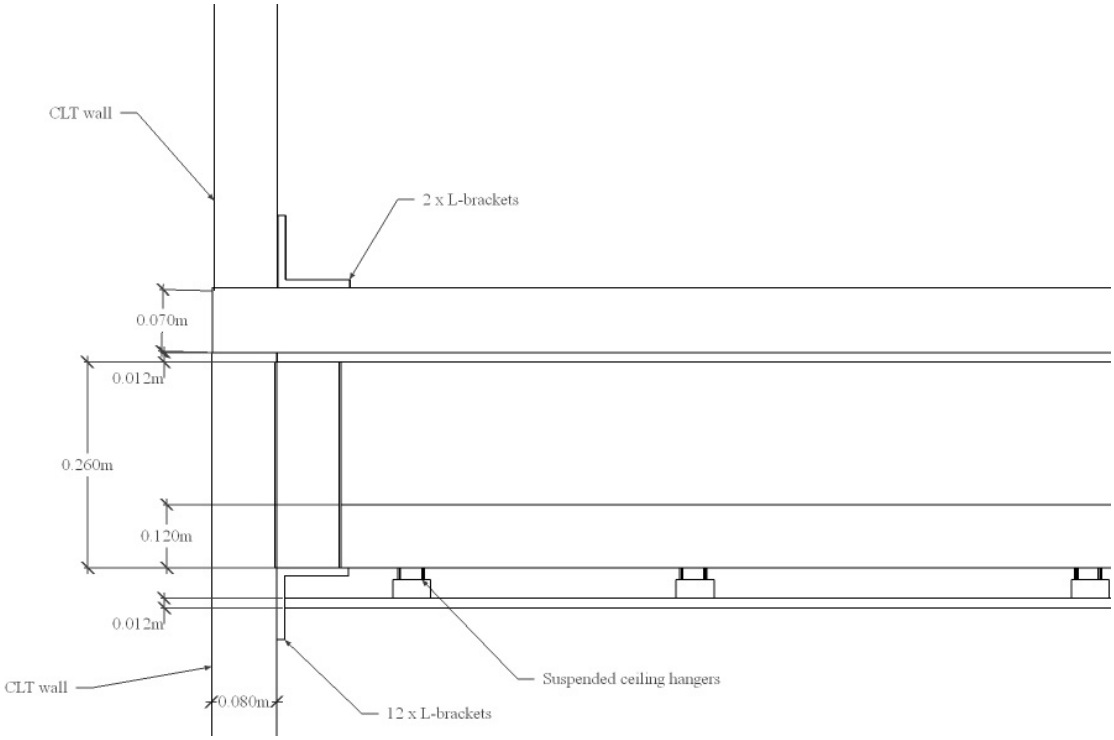

Figure B-1 Cross-section of the junction

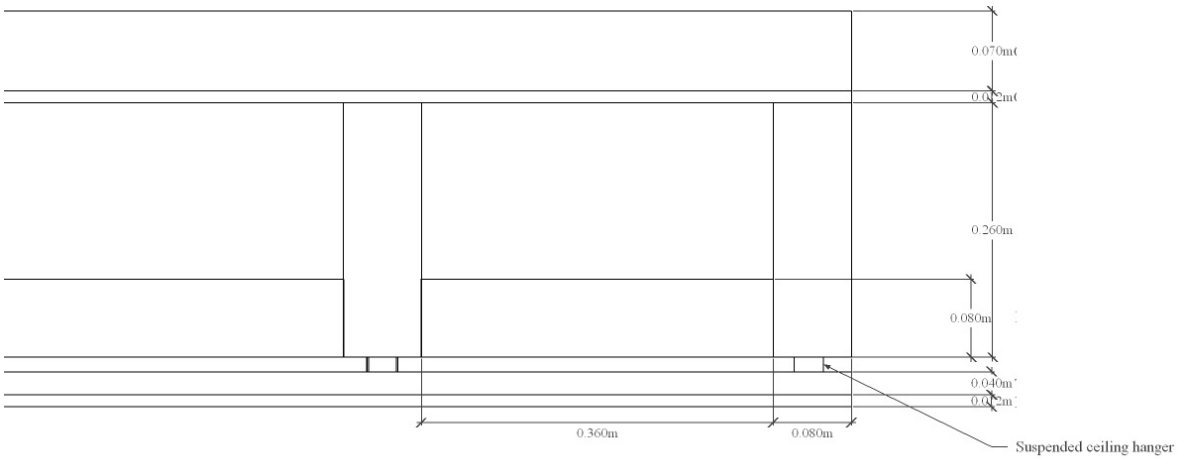

Figure B-2 Cross-section of the HBV floor and suspended ceiling

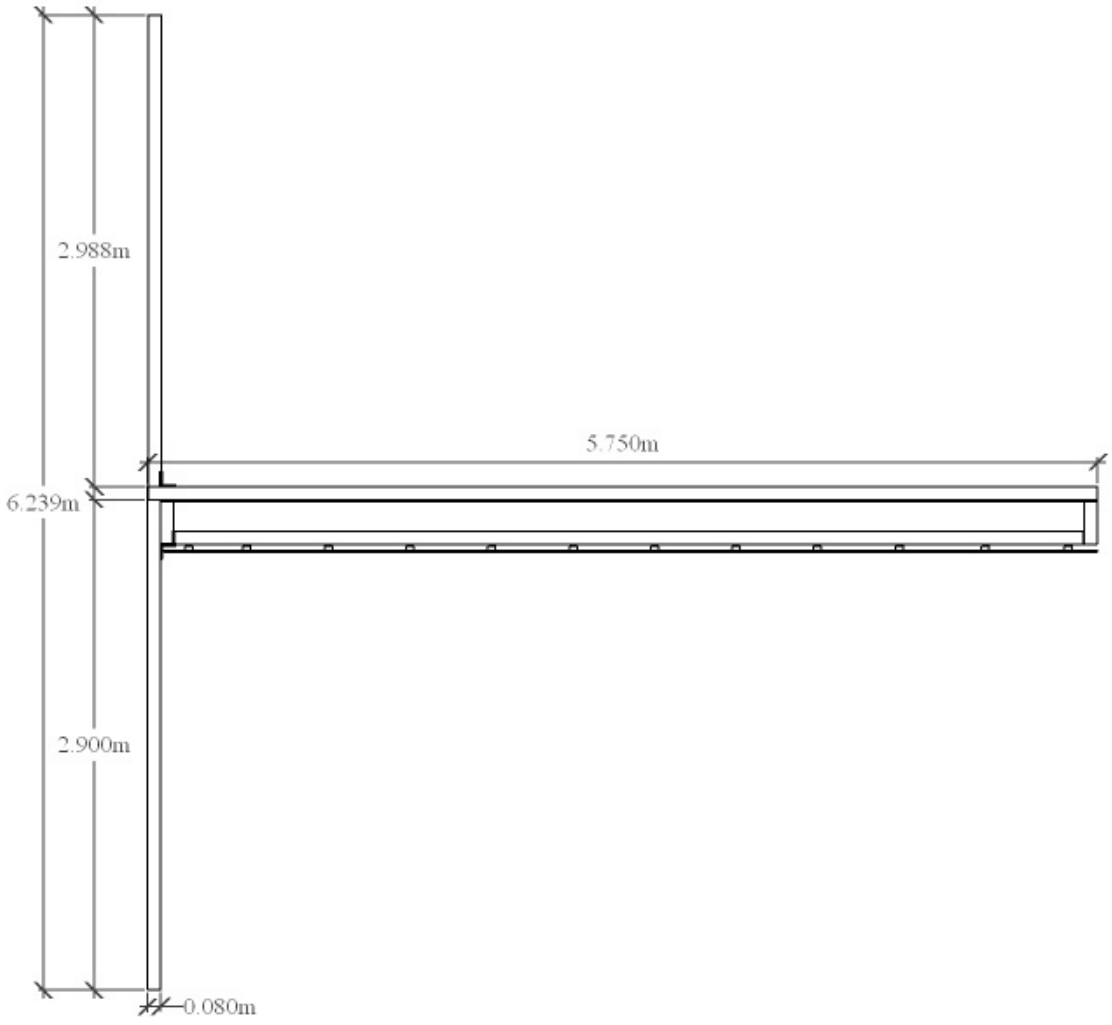

Figure B-3 Combined CLT and HBV T-junction dimensions

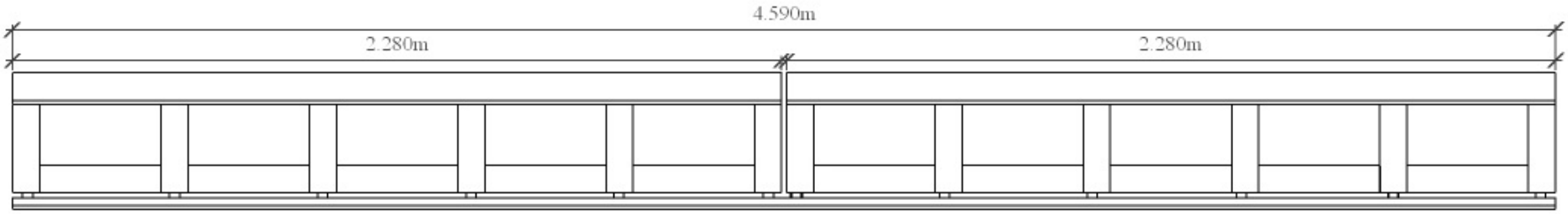

Figure B-4 HBV floor width dimension

APPENDIX C: Non-resonant transmission below the critical frequency

An early model for flanking transmission is outlined in Gerretsen [126] which was first applied to heavyweight construction. This was later revised to incorporate cavity wall constructions [93]. Standards first appeared for monolithic construction [78] which, despite using measured transmission coefficients, is well suited to an SEA methodology because of the low critical frequency and hence only resonant transmission is included in the measured transmission coefficient. These models formed the basis upon which measurement based methodologies (such as can be found in EN12354) were developed. In practice, particularly for lightweight construction, the measured SRI contains both resonant and non-resonant sound transmission; hence development was required to account for non-resonant transmission when calculating the plate vibration. The model includes the following terms:

Absorption length is analogous to the absorption area used in room acoustics. It is defined as the length of the boundary that would be totally absorbing and is calculated using [8]:

$$a_i = \frac{2.2S\pi^2}{0.5c_{\mathrm{g(B)}}T} \tag{C-1}$$

where S is the surface area of the plate, $c_{\mathrm{g(B)}}$ is the bending wave group velocity ($c_{\mathrm{g(B)}}=2c_{\mathrm{B}}$ for thin, isotropic plates).

Equivalent absorption length defined in EN 12354 [77] is given by

$$a_{eq,i} = \frac{2.2S\pi^2}{c_0 T\sqrt{\frac{f}{f_{\mathrm{ref}}}}} \tag{C-2}$$

where f_{ref}=1000Hz is the reference frequency. One advantage of this alternative definition is it requires require no knowledge of the plate properties and gives a good estimate of absorption length when the critical frequency, bending phase velocity and/or group velocity are unknown.

Vibration reduction index of a junction in a single direction is defined according to [126]:

$$\gamma_{\mathrm{ij}} = d_{\mathrm{ij}} \frac{\rho_{\mathrm{S},i} c_{\mathrm{B,p},i}}{\rho_{\mathrm{S},j} c_{\mathrm{B,p},j}} \cdot \frac{l}{a_j} \tag{C-3}$$

where $\rho_{s,\mathrm{i}}$ and $\rho_{s,\mathrm{j}}$ are the mass per unit areas of the plates, $c_{\mathrm{b,i}}$ and $c_{\mathrm{b,j}}$ are the bending phase velocity of the plates, l is the length of the junction. In logarithmic form, this is expressed as

$$10\mathrm{lg}\gamma_{\mathrm{ij}} = D_{\mathrm{v,ij}} + 10\mathrm{lg}\frac{\rho_{\mathrm{S,i}} c_{\mathrm{B,p,i}}}{\rho_{\mathrm{S,j}} c_{\mathrm{B,p,j}}} + 10\mathrm{lg}\frac{l}{a_{\mathrm{j}}} \tag{C-4}$$

where $D_{\mathrm{v,ij}}$ is the vibration level difference between the two plates (i and j). For isotropic plates of the same material and thickness this term $10\mathrm{lg}\frac{\rho_{\mathrm{S,i}} c_{\mathrm{B,p,i}}}{\rho_{S,j} c_{\mathrm{B,p,j}}} = 0$.

Transmission coefficient defines the flanking between two rooms in a building [126]

$$\tau_{\mathrm{ij}} = \frac{\langle \mathrm{p}_{\mathrm{R}}^2 \rangle}{\langle p_{\mathrm{S}}^2 \rangle} \frac{A}{S_0} = \tau_{\mathrm{i}} d_{\mathrm{ij}} \left(\frac{\rho_{\mathrm{S,i}} c_{\mathrm{B,p,i}}}{\rho_{S,j} c_{\mathrm{B,p,j}}} \right) \frac{\sigma_{\mathrm{j}}}{\sigma_{\mathrm{i}}} \frac{S_{\mathrm{j}}}{S_0} \tag{C-5}$$

Flanking reduction index expresses this in logarithmic form:

$$R_{\mathrm{ij}} = R_{\mathrm{i}} + D_{\mathrm{v,ij}} \left(+10\mathrm{lg}\frac{\rho_{\mathrm{S,i}} c_{\mathrm{B,p,i}}}{\rho_{S,j} c_{\mathrm{B,p,j}}} \right) + 10\,\mathrm{lg}\frac{S_{\mathrm{j}}}{S_{\mathrm{o}}} + 10\,\mathrm{lg}\frac{\sigma_{\mathrm{j}}}{\sigma_{\mathrm{i}}} \tag{C-6}$$

The terms in brackets are required for the more general case that the two walls i and j are not identical.

Two approaches were developed, one based on airborne excitation (the first part of Eqn. (C-5)) and the other on structure-borne excitation (the second part of Eqn. (C-5)). The airborne approach was developed by Villot *et al.* [5] and Guigou-Carter *et al.* [6] and the structure-borne approach by Gerretsen [126]. The model developed by Gerretsen was shown to underestimate the transmission coefficient of a flanking path when applied to lightweight elements if both the resonant and non-resonant

components of the sound transmission coefficients were used [4]. Villot *et al.* proposed correction factors to calculate the resonant transmission from the measured SRI. Consequently, the two approaches have been shown to be equivalent and the results transferable from one measurement regime to the other given knowledge about the resonant transmission coefficients [127].

With structure-borne excitation, the principle of reciprocity applies to the vibration reduction index with the following assumptions: (1) linear elasticity and (2) the wave impedance for the wave-types crossing the junction are real (true for the bending, longitudinal and transverse waves of thin plates) [128]. Therefore

$$\gamma_{\mathrm{ij}} c_{\mathrm{B,p,j}} = \gamma_{\mathrm{ji}} c_{\mathrm{B,p,i}} \tag{C-7}$$

Direction-averaged vibration reduction index ($\boldsymbol{K_{ij}}$) is defined according to [77]:

$$K_{\mathrm{ij}} = -10\lg\left(\frac{\gamma_{\mathrm{ij}} + \gamma_{\mathrm{ji}}}{2}\right) = \frac{D_{\mathrm{v,ij}} + D_{\mathrm{v,ji}}}{2} + 10\lg\frac{l}{\sqrt{a_{\mathrm{i}} a_{\mathrm{j}}}} \tag{C-8}$$

Also applying reciprocity to the transmission coefficient

$$\tau_{\mathrm{ij}} = \tau_{\mathrm{ji}} \tag{C-9}$$

The definition can be altered to include the geometric mean of the transmission coefficients

$$\tau_{\mathrm{ij}} = \sqrt{\tau_{\mathrm{ij}}\tau_{\mathrm{ji}}} = \left(\tau_{\mathrm{i}}\tau_{\mathrm{j}} d_{\mathrm{ij}} d_{\mathrm{ji}} \frac{\sigma_{\mathrm{j,r}}}{\sigma_{\mathrm{i,r}}} \frac{\sigma_{\mathrm{i,r}}}{\sigma_{\mathrm{j,r}}} \frac{S_i S_{\mathrm{j}}}{S_0^2}\right)^{1/2} \tag{C-10}$$

where $\sigma_{\mathrm{i,r}}$, and $\sigma_{\mathrm{j,r}}$ are the resonant radiation efficiencies of walls *i* and *j*. Here the radiation factors cancel however a resonant SRI ($\tau_{\mathrm{i}}\tau_{\mathrm{j}}$) is required for calculation.

The **correction factor (*C*)** was developed along this theoretical basis to bring into line the methodologies of Gerretsen and Villot for lightweight elements [5, 127].

$$C = \frac{\tau}{\tau_r} = 1 + \frac{\tau_{nr}}{\tau_r} = 1 + \frac{\sigma_{nr}}{\sigma_r}\frac{\sigma_a - \sigma_r}{\sigma_{nr} - \sigma_a} \approx \frac{\sigma_a}{\sigma_s}\frac{1 - \sigma_s}{1 - \sigma_a} \approx \frac{\sigma_a}{\sigma_s} \tag{C-11}$$

where τ, τ_r and τ_{nr} represent the total, resonant and non-resonant transmission coefficients respectively, and σ_a, σ_r and σ_{nr} are the airborne, resonant and non-

resonant radiation efficiencies respectively. To obtain the correction factor Eqn. (C-11) presents several possibilities. Calculated σ_r can be used, calculating σ_{nr} is somewhat more problematic. A "total" radiation efficiency σ_a can be measured using airborne excitation of the panel and it is assumed the resonant radiation efficiency σ_r is equivalent to a measurement with structure-borne excitation of the panel (assuming no additional radiation from the near field of the shaker or connectors e.g. studs). The correction factor can then be determined from appropriate combinations of calculated or measured data. Calculation methods indicate that well below the critical frequency the correction factor is 10.0dB (or more) [8, 129], although measurement methods indicate that it is probably somewhat lower [129]. Alternative methods of determining a lightweight correction factor are explored in [83, 129].

APPENDIX D: Radiation efficiency measurement

D.1 Introduction

There are currently no standardised procedures to measure radiation efficiency, although this parameter can be crucial to obtain close agreement between airborne and structure-borne methodologies [5, 6]. Measurement requires the sound power radiated by the panel to be determined, either using sound intensity or sound pressure levels. For thin plates, the governing equations are well understood (see APPENDIX C) and for lightweight elements reflects the large difference between measured resonant velocity levels on the surface of a panel and unmeasurable non-resonant velocity levels. To determine the radiation efficiency (and resonant correction factors) of other plate types (e.g. rib-stiffened, orthotropic, or thick plates), however, the physical processes are less well understood and approximations must be considered to allow modelling processes to be simplified. This means that the measurement of radiation efficiency is susceptible to error if inappropriate assumptions are used or the physical laws on which the measurement methodology is based differ from those expected.

When considering thin plates, the different measurement methodologies can be divided into two groups; those that measure resonant radiation efficiency, and those that measure "total" radiation efficiency (see APPENDIX C). However, for thick plates this division is not necessarily appropriate. A simple method to measure the radiation efficiency proposed by Villot and Carter [5], was implemented, where the velocity on the radiating surface and the sound pressure in the room are required. Radiation efficiency is determined using an airborne source (to measure "total" radiation efficiency), a structure-borne point source and excitation from an adjacent wall via the junction (which both measure resonant radiation efficiency). In each case the following formula (from [5]) is used:

$$10\lg(\sigma) = L_p - 6 - L_v + 10\lg\left(\frac{A}{S}\right) \quad \text{(D-1)}$$

where L_p is the pressure level in the receiving room, L_v is the velocity level. The absorption area, A, in the room is calculated using Eqn. (2-170) from measurements of reverberation time. Values for the total radiation efficiency (using an airborne source), the resonant radiation efficiency (using a structure-borne point source) and the radiation efficiency when excited by an adjacent wall via the junction were compared.

D.2 Method

The radiation efficiency of the HBV floor was measured in the flanking laboratory. For airborne excitation, two speaker positions were used as the sources with a continuous pink noise signal. The measurement was made in both directions, from the upper room to the lower and vice versa for comparison with excitation of the concrete and OSB surfaces. For structure-borne excitation, three shaker positions were used.

The radiation efficiency of the CLT wall (2.9m high x 3.9m wide) with airborne and point structure-borne excitation were measured on a nominally identical plate in a horizontal transmission suite. For the airborne measurement, a dodecahedron loudspeaker was placed in the source room and pink noise used as the source. Twelve measurement positions were used for velocity level on the surface of the plate and for sound pressure level in the room. For structure-borne point excitation, two shaker positions were used with a pink noise signal and twelve accelerometer positions per excitation position. A rotating microphone boom was used to obtain the sound pressure level in the room with one sound pressure level measurement for each accelerometer measurement. Reverberation times were measured to determine the absorption in the rooms according to EN ISO 10140-4 [130].

Radiation efficiency measurements using excitation via the junction were made in the transmission suite during build stage (3). Pairs of elements were exposed (shielding configurations (c, Figure A-3), (d, Figure A-4) and (f, Figure A-8) in APPENDIX A) to allow selective excitation of the source element and measurement of the receiving element. Airborne noise was used to excite the source element a

dodecahedron loudspeaker and pink noise were used as the source. Accelerometers were used to measure the velocity level, and a Müller-BBM PAK system was used to acquire the data. The sound pressure levels in the rooms were measured using a rotating boom. The absorption in the room is calculated from the reverberation time of the receiving room. Measured resonant radiation efficiencies were compared with values calculated using Leppington's model [46] (or Heckl's model [52] when radiation efficiency between the two critical frequencies were required for the HBV floor.)

D.3 Results

For the HBV plate, the measured radiation efficiency using structure-borne point excitation and excitation through the junction is shown in Figure D-1(a) alongside the calculation for Heckl using Eqn. (2-109) (all calculated values of the radiation efficiency greater than one are set to a value of one for $f \geq f_{c2}$) and the measured radiation efficiency using airborne excitation is shown in Figure D-1(b).

The structure-borne point source radiation efficiency shows at least one peak corresponding to the first critical frequency and the airborne radiation efficiency shows two peaks corresponding to the two critical frequencies calculated if the HBV floor is an orthotropic plate. The structure-borne point radiation efficiency measured (on the concrete side) and modelled curves level off at the second critical frequency (in the 250Hz third octave band) to a value of approximately 0.0dB. The radiation efficiency measured on the OSB side appears to level at a slightly lower value of ~−1.2dB. Adjusting the results by taking only the exposed area of OSB rather than the whole area of the floor corrects this problem. (The radiation from the beams is thought to be negligible.) Heckl's calculation for resonant radiation efficiency between the critical frequencies compares favourably with the structure-borne point source measurements. The radiation efficiency using junction excitation compared favourably with the structure-borne point source measurement except in the frequency range (160-250Hz) near the highest critical frequency (f_2). At very high frequencies (>3150Hz) the results drop off below 0.0dB, the reason for this was undetermined, it is not due to a high background correction at these frequencies.

The measured radiation efficiency using airborne excitation, point structure-borne excitation and line-borne excitation via the junction for the CLT plate is shown in

Figure D-2. These measurements are compared with the calculation using an equivalent isotropic model where the elastic constants from section 4.7.4 are substituted into Leppington's Eqns. (2-94), (2-95) and (2-96). All calculated values of the radiation efficiency greater than one are set to a value of one [8].

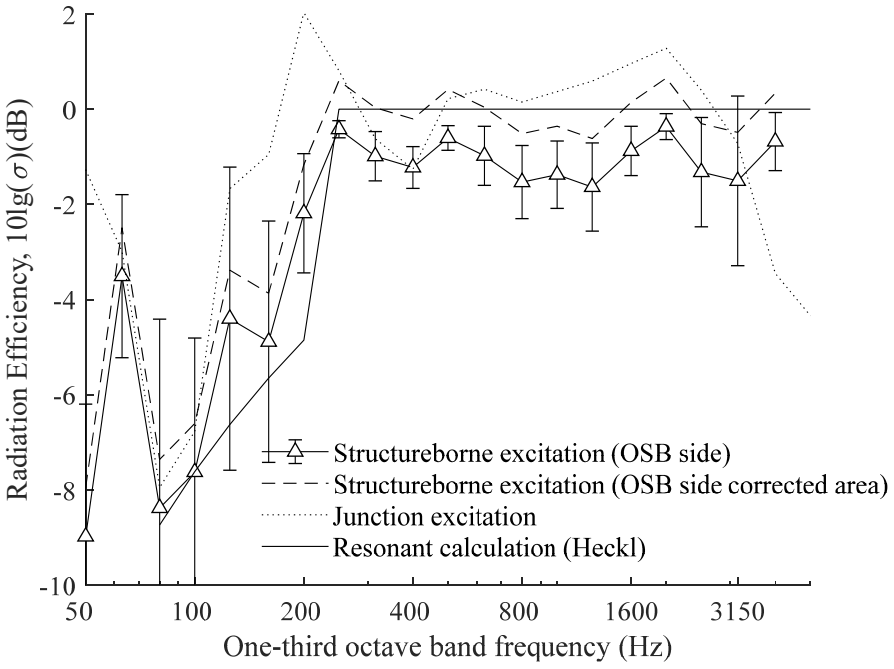

(a)

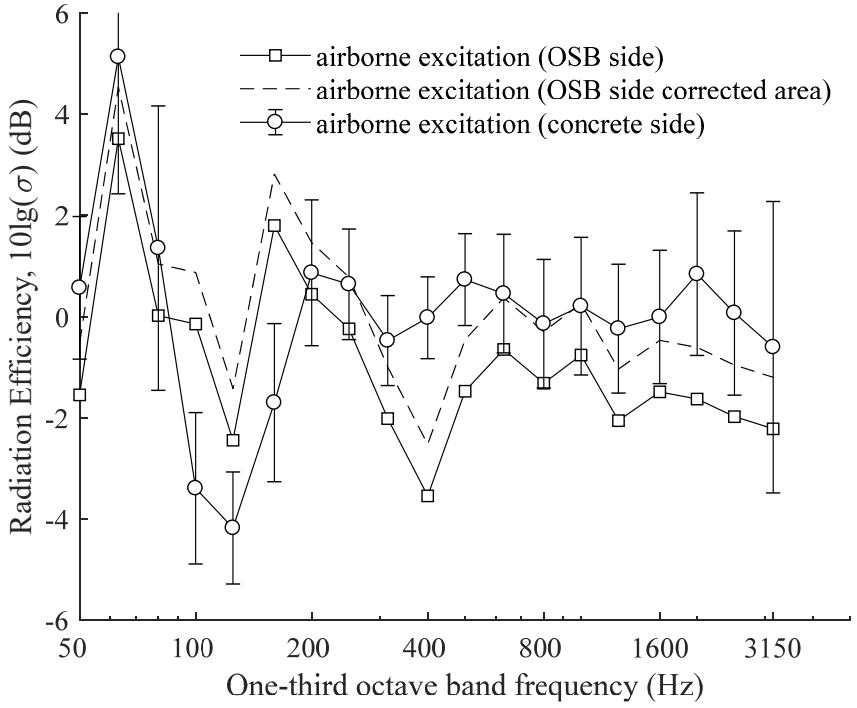

(b)

Figure D-1 Measured radiation efficiency using (a) airborne and (b) structure-borne (point) excitation for the HBV plate for comparison with Heckl's calculation for an orthotropic plate between the critical frequencies.

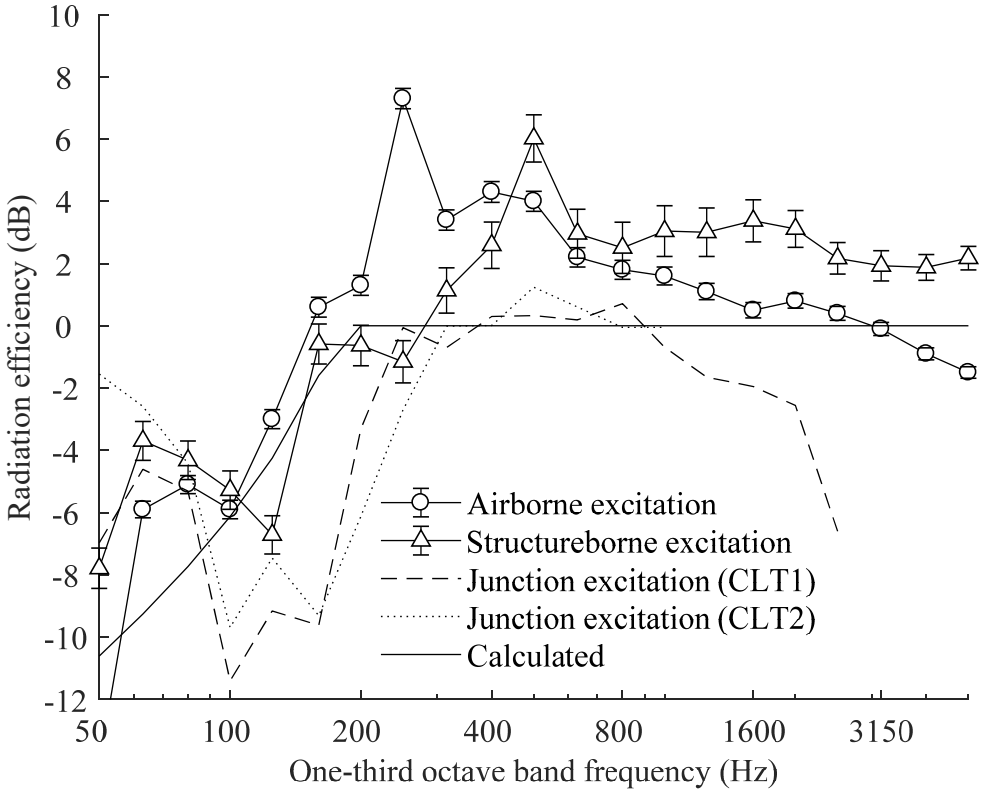

Figure D-2 Measured radiation efficiency for the CLT plate.

At low frequencies (e.g. below the critical frequency <250Hz), the plate behaviour is governed by the assumptions of a thin plate model and the measurement with the structure-borne point source does follow the trend of the calculated resonant radiation efficiency approximated by a thin isotropic plate calculation. In this frequency range when the CLT plate is excited by the junction the radiation efficiency is found to be much lower than that of the structure-borne point source. A possible explanation for this is that excitation at the bottom (or top) edge of the plate would favour excitation of vertical modes. The plate is much stiffer in the vertical direction resulting in significantly fewer vertical modes to excite (than in the horizontal direction). Therefore, the radiation efficiency is due to selected modes rather than a frequency average of all modes.

At very low frequencies for the airborne and structure-borne point sources ≤80Hz poor agreement between the methodologies and with the model is most likely to be due to systematic error in the measurement. At very low frequencies (<125Hz) the radiation efficiency due to excitation at the junction is affected by the Df_{max} and Fd_{max} values. Results for the Ff path are not available for excitation through the

junction because this path is shown to be dominated by airborne flanking outside the laboratory.

At frequencies ≥500Hz the measurement with the structure-borne point source exceeds the measurement with the airborne source and the airborne measurement does not reach a plateau but reduces to a value below 0.0dB at high frequencies. This may be indicative of thick plate effects [8]. To provide a thorough investigation measurements should be compared with other similar plates and from other laboratories. In the mid-range (250-1000Hz) for excitation at the junction the radiation efficiency levels to 0.0dB. At high frequencies (>1000Hz) for CLT1 the radiation efficiency reduces below 0.0dB the reason for this was undetermined, it is not due to a high background correction at these frequencies. However, one of the problems with this methodology is the difficulty to ensure that the sound pressure levels in the receiving room are sufficiently far above the background level to be able to characterise the flanking path.

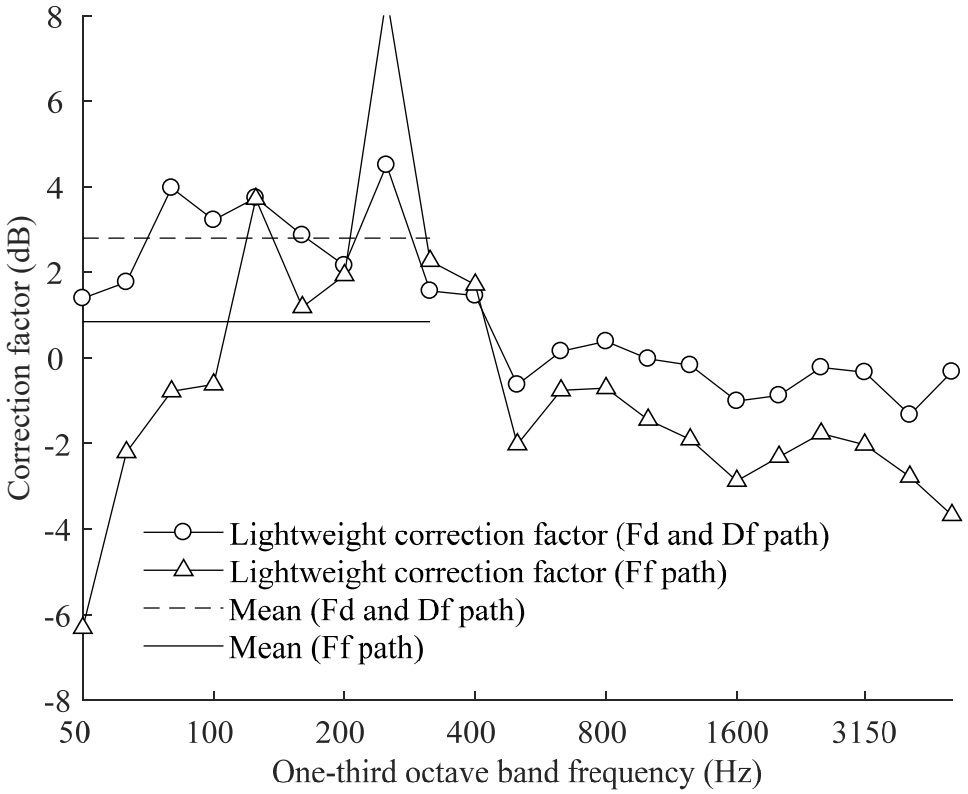

Figure D-3 Lightweight correction factors for the Ff, Df and Fd paths.

The peaks of the graphs do not coincide; it would be usual to assume that the peak in the structure-borne point source measurements corresponds to the critical frequency

however it at the high end of the anticipated values (250-500Hz depending on the methodology for measuring the elastic constants see section 4.7.5). The peak in airborne radiation is at a lower frequency. A drawback of all measurement methods is that it is most difficult to obtain meaningful results near the critical frequency.

Correction factors for lightweight plates based on the measured radiation efficiencies are shown in Figure D-3. The smoothed mean correction factors for a Ff, Fd and Df paths are low and could probably be neglected in a prediction model.

D.4 Conclusions

The comparison of measured and calculated radiation efficiency on the HBV floor provides evidence that the floor is behaving as an orthotropic plate. The calculation of resonant radiation efficiency carried out according to Heckl [52] agreed with the structure-borne point and line excitation. Below and close to the critical frequency (<250Hz) of the CLT plate, measurements using structure-borne point excitation agree well with a thin plate calculation assuming an isotropic plate, although measurements using excitation through a junction do not. In the latter case, this is thought to be because of a highly modal response of the plate rather than a frequency averaged response. However, a frequency averaged response would be expected if the panel is excited at the side edge. The measured data behaves unusually at high frequencies (>500Hz for this plate) levelling off at ~2.6dB. With airborne excitation and structure-borne line excitation the results do not reach a plateau but instead reduce to a value below 0.0dB at high frequencies. This unusual behaviour may indicate a transition to thick plate behaviour.

APPENDIX E: Drawings of the suspended ceiling hanger apparatus

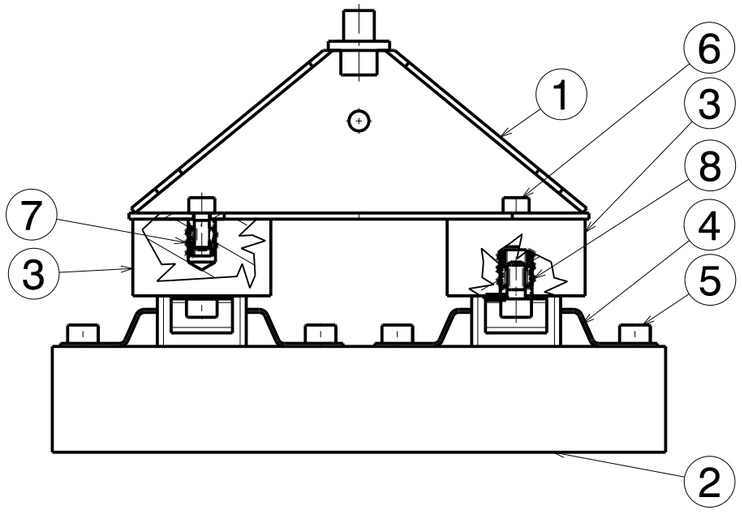

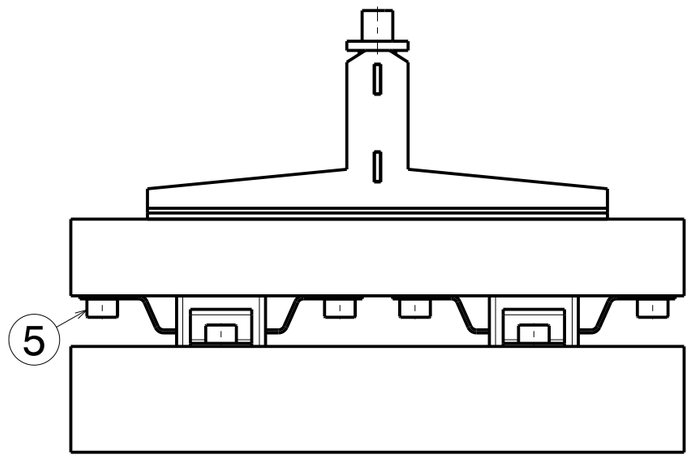

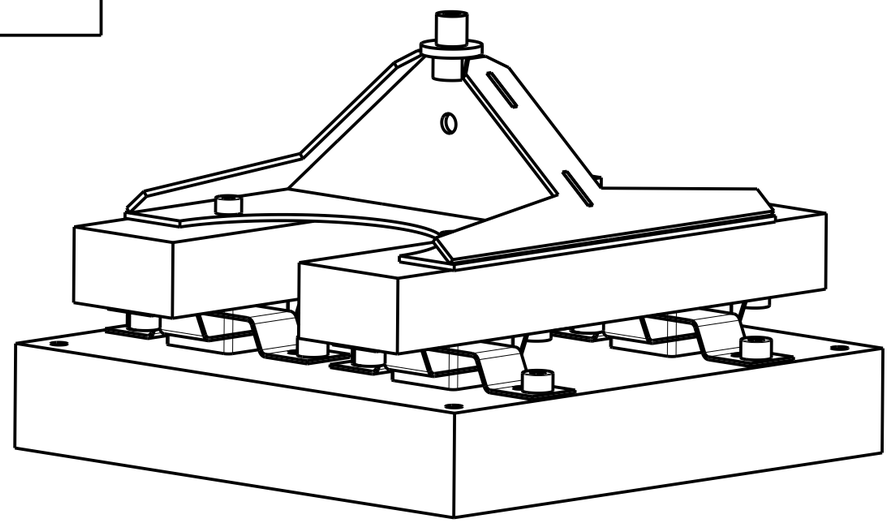

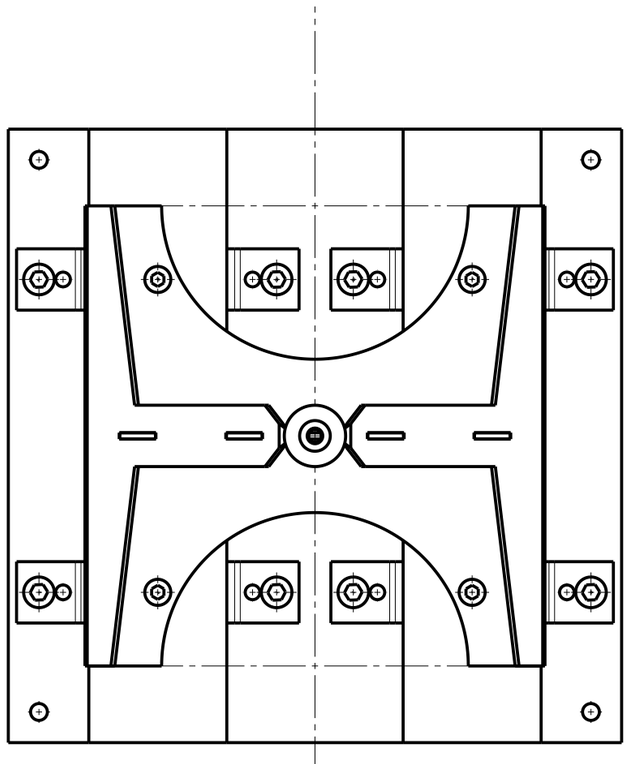

+0,3
+0,1
-0,1
-0,3
Ra 1.6

	Oberfläche	Gewicht	
	Allgemeintoleranzen ISO 2768-mK	Material	
	Projekt: Projekt-0001747	Erstelldatum: 12.06.2012	Kurzzeichen: uhi
	Baugruppe	Format: A3	Blatt: 1/1
EMPA	Benennung: Ceiling hanger measurement_1	Zeichnungs-Nr.: Drawing-0013567	Index

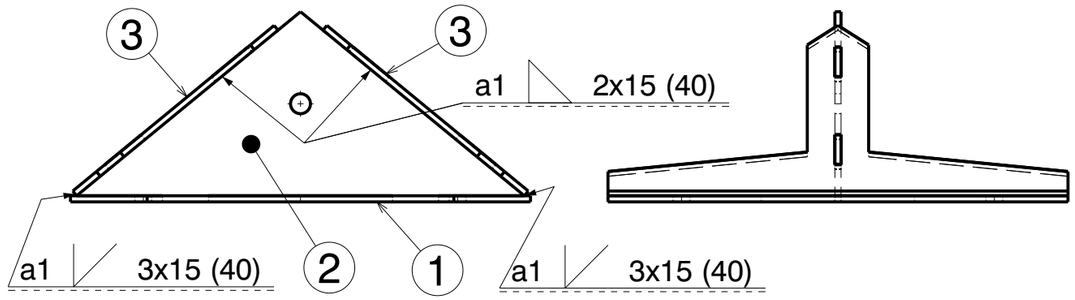

Mass 55mm nach dem Verschweissen der Blechteile bearbeiten

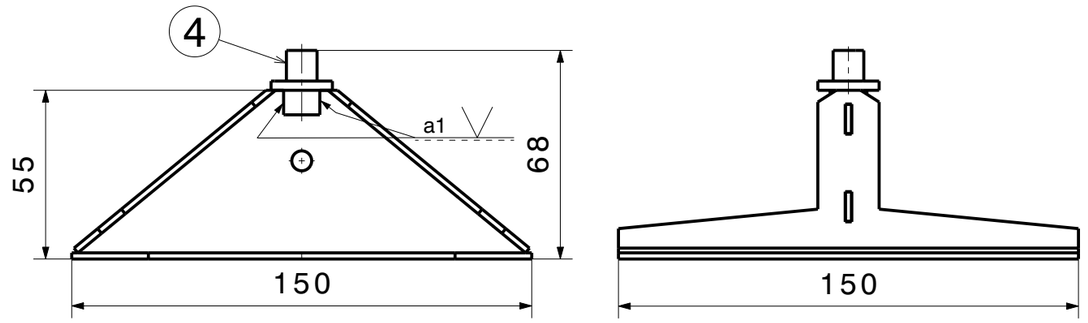

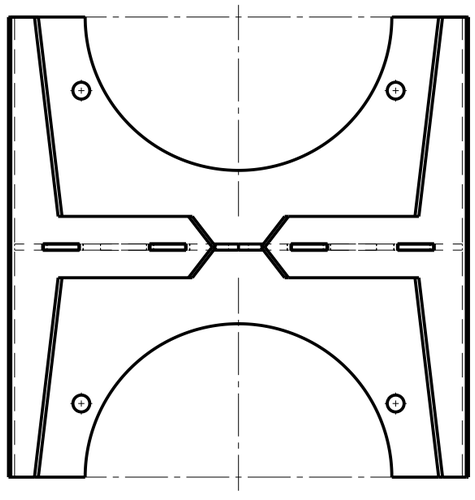

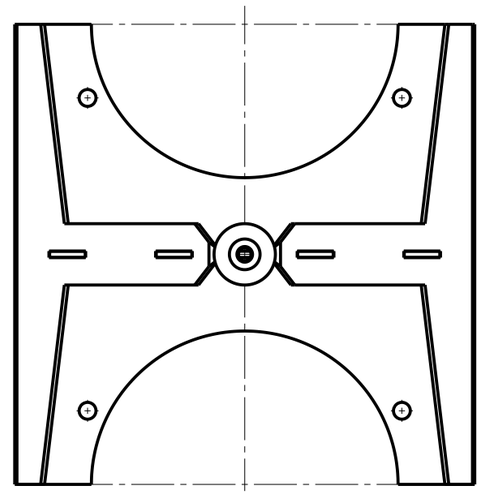

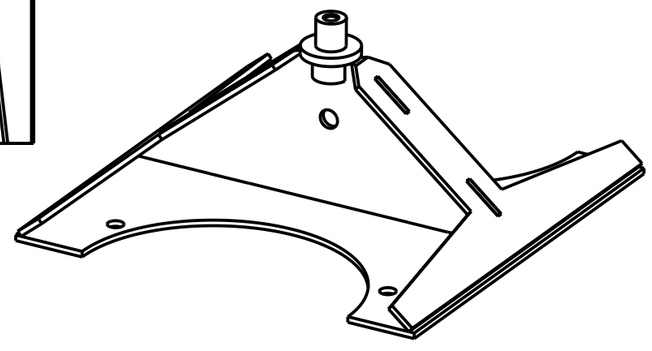

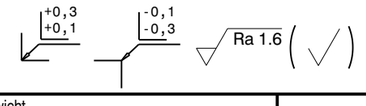

	Oberfläche	Gewicht 425 g	
	Allgemeintoleranzen ISO 2768-mK	Material S235	
	Projekt Projekt-0001747	Erstelldatum 12.06.2012	Kurzzeichen uhi
	Baugruppe Ceiling hanger measurement_1		Format A3 / Blatt 1/1
EMPA	Benennung upper mass_1	Zeichnungs-Nr. Drawing-0013570	Index

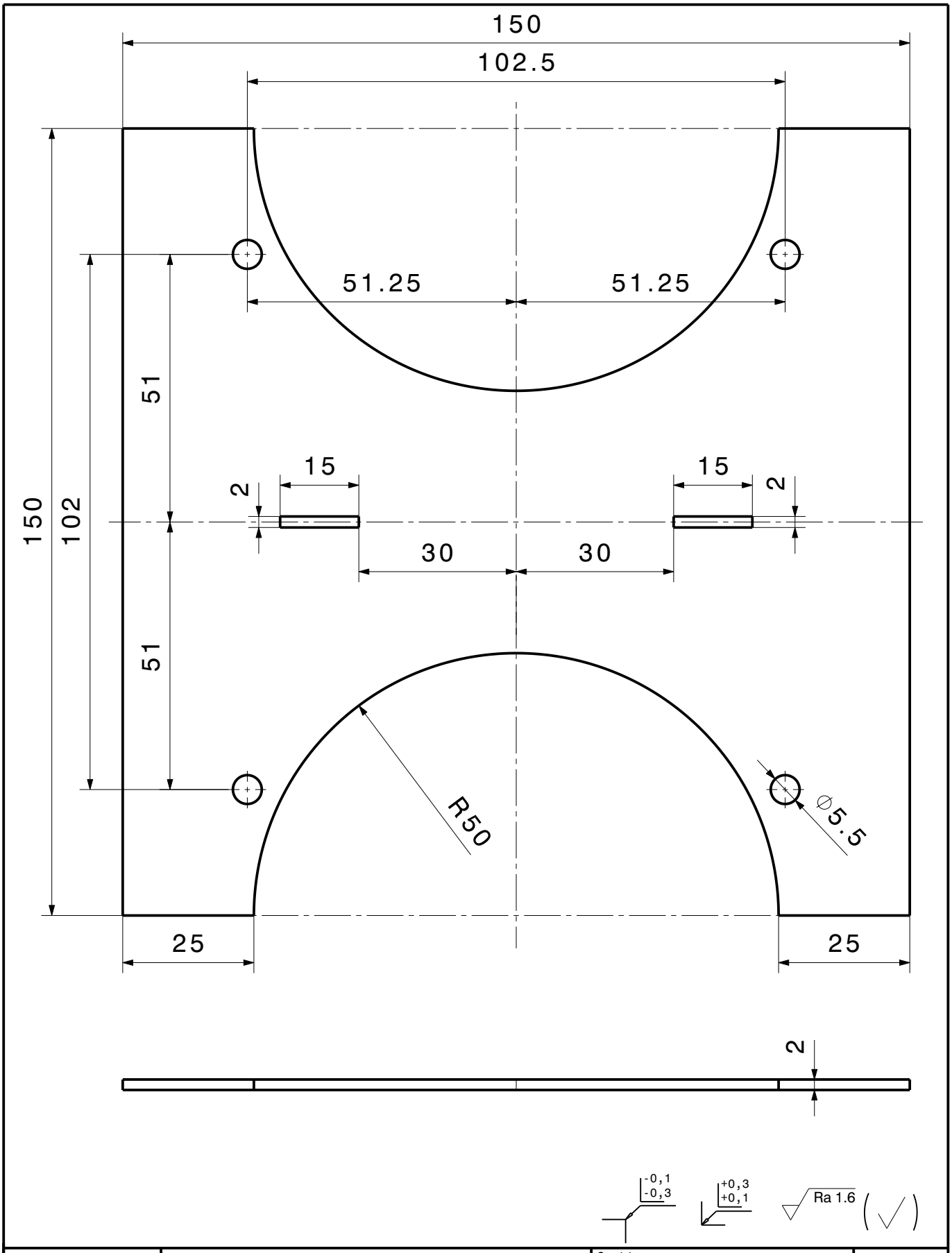

-0,1
-0,3

+0,3
+0,1

Ra 1.6

	Oberfläche	Gewicht 228 g		
	Allgemeintoleranzen ISO 2768-mK	Material S235		
	Projekt Projekt-0001747	Erstellt 12.06.2012	Kurzzeichen uhi	
	Baugruppe upper mass_1		Format A4	Blatt 1/1
EMPA	Benennung top base_1	Drawing-0013571		Index

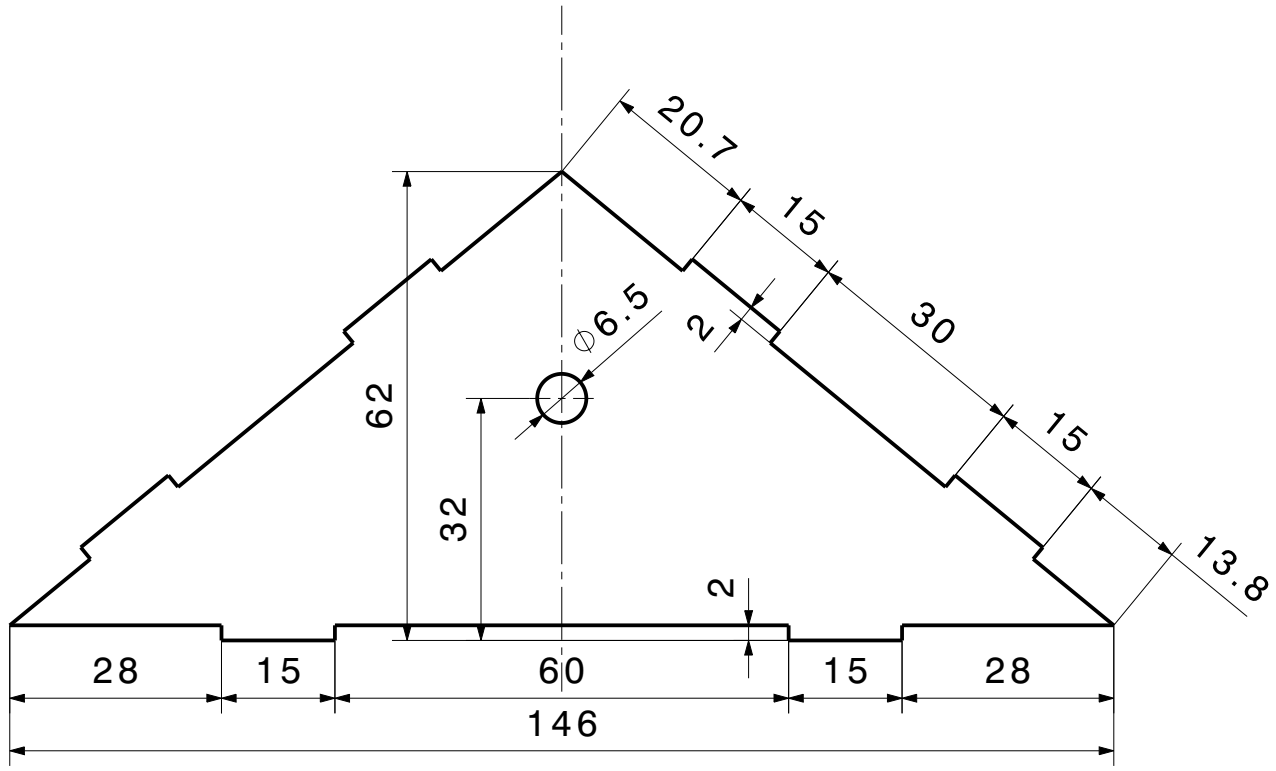

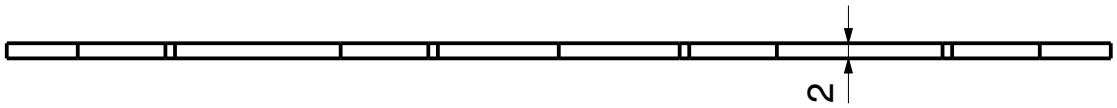

-0,1
-0,3

+0,3
+0,1

Ra 1.6

	Oberfläche	Gewicht 71 g		
	Allgemeintoleranzen ISO 2768-mK	Material S235		
	Projekt Projekt-0001747	Erstellt 12.06.2012	Kurzzeichen uhi	
	Baugruppe upper mass_1		Format A4	Blatt 1/1
EMPA	Benennung middle section	Drawing-0013572		Index

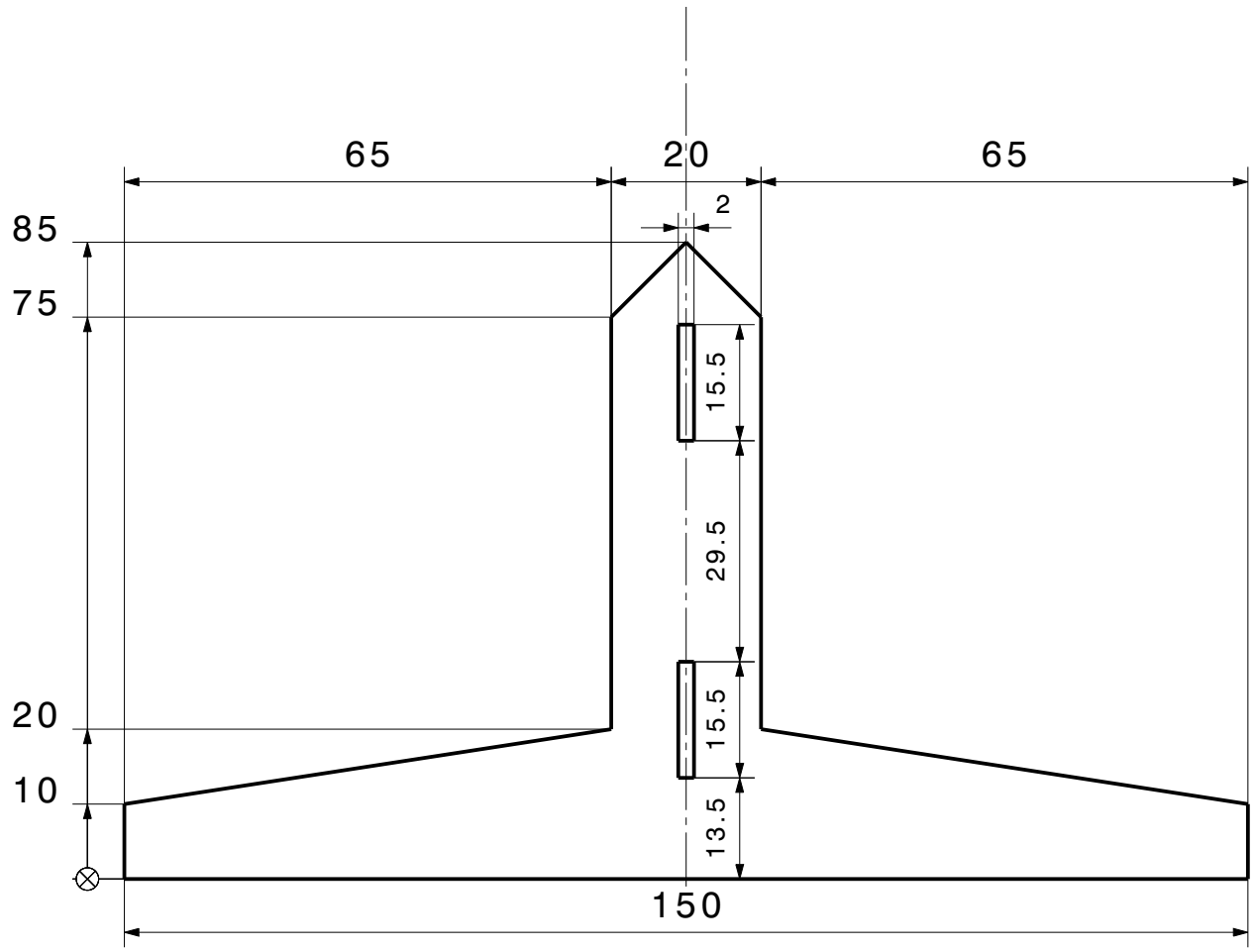

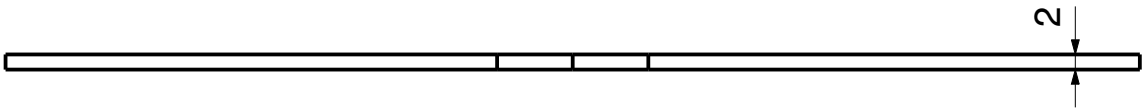

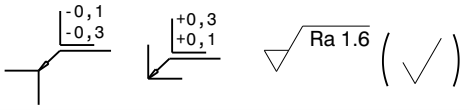

	Oberfläche	Gewicht 55 g		
	Allgemeintoleranzen ISO 2768-mK	Material S235		
	Projekt Projekt-0001747	Erstellt 14.06.2012	Kurzzeichen uhi	
	Baugruppe upper mass_1		Format A4	Blatt 1/1
EMPA	Benennung side part_1	Drawing-0013574		Index

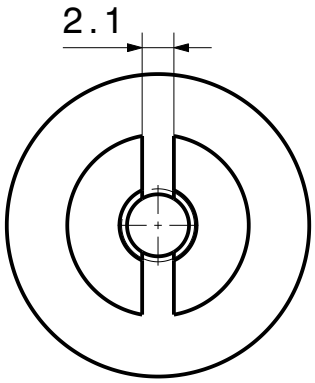

SchnittansichtA-A
Maßstab: 2:1

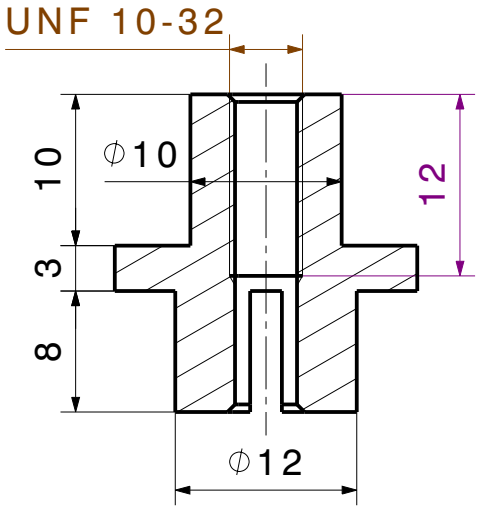

Isometrische Ansicht
Maßstab: 1:1

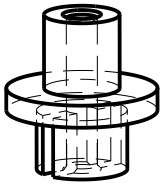

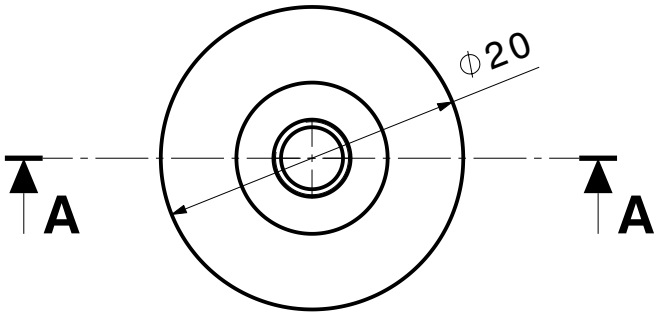

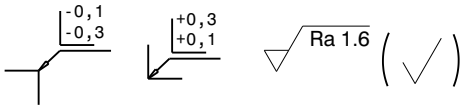

	Oberfläche	Gewicht 17 g		
	Allgemeintoleranzen ISO 2768-mK	Material S235		
	Projekt Projekt-0001747	Erstellt 14.06.2012	Kurzzeichen uhi	
	Baugruppe upper mass_1		Format A4	Blatt 1/1
EMPA	Benennung Gewindeadapter_1 UNF 10-32	Drawing-0013575		Index

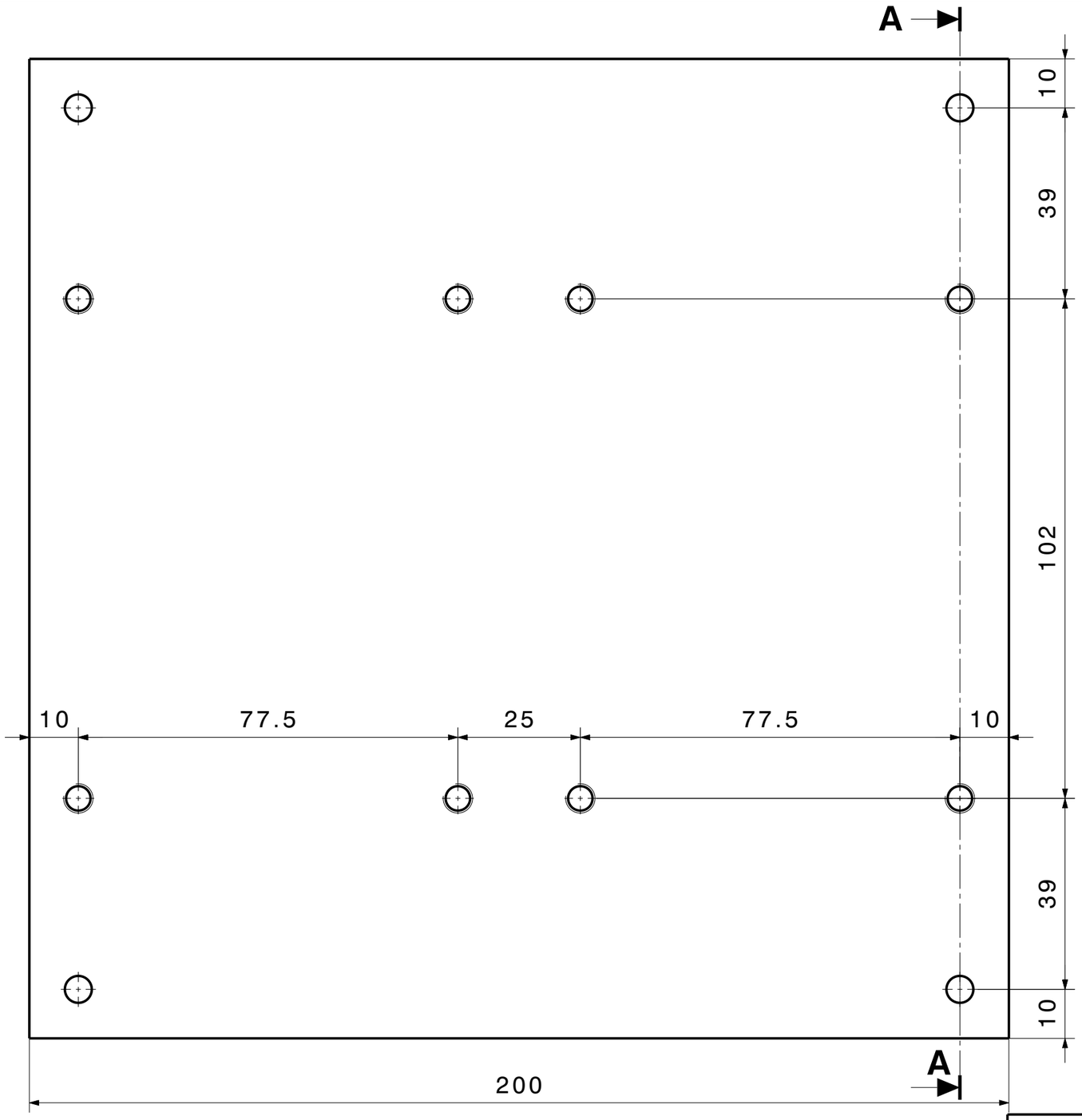

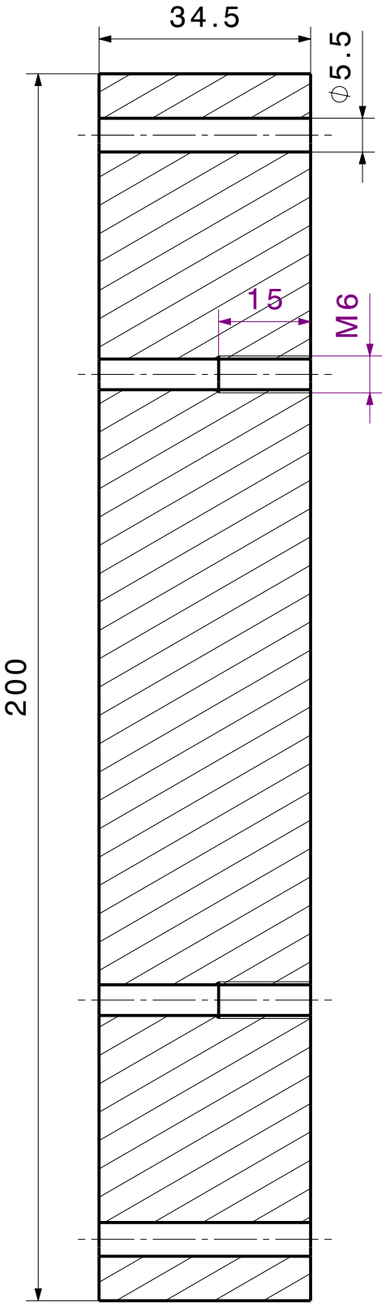

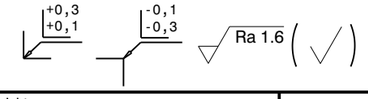

	Oberfläche	Gewicht 10.75 kg	
	Allgemeintoleranzen ISO 2768-mK	Material S235	
	Projekt Projekt-0001747	Erstelldatum 14.06.2012	Kurzzeichen uhi
	Baugruppe ceiling hanger measurement_1		Format A3 / Blatt 1/1
EMPA	Benennung lower mass_1	Zeichnungs-Nr. Drawing-0013576	Index

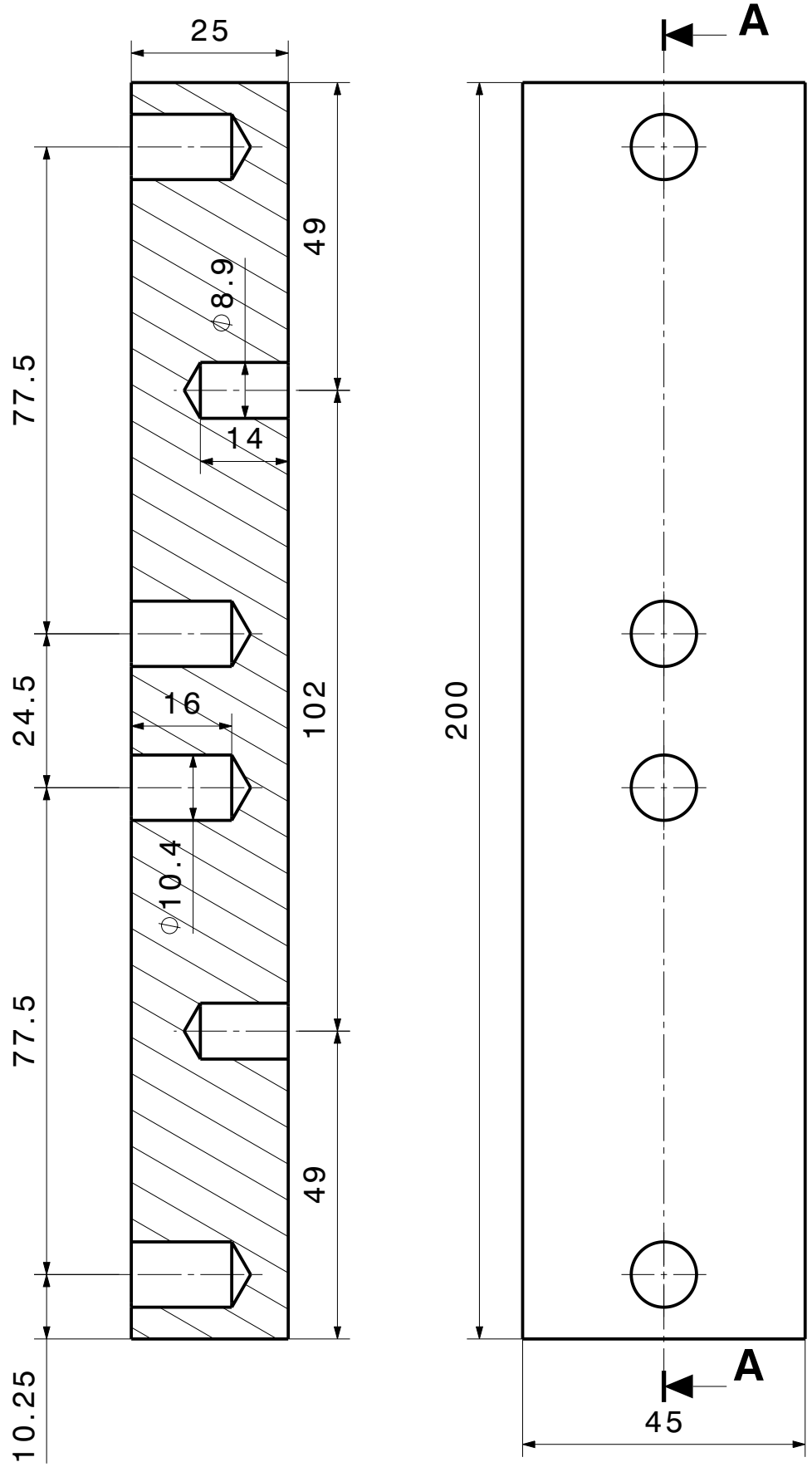

	Oberfläche	Gewicht 96 g	
	Allgemeintoleranzen ISO 2768-mK	Material Holz	
	Projekt Projekt-0001747	Erstellt 14.06.2012	Kurzzeichen uhi
	Baugruppe ceiling hanger measurement_1		Format A4 / Blatt 1/1
EMPA	Benennung Holzunterlage	Drawing-0013577	Index

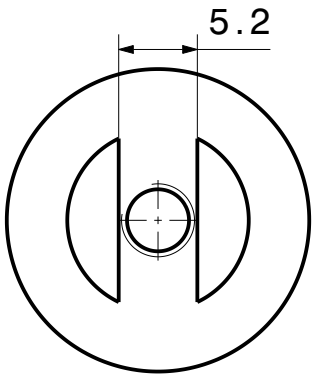

SchnittansichtA-A
Maßstab: 2:1

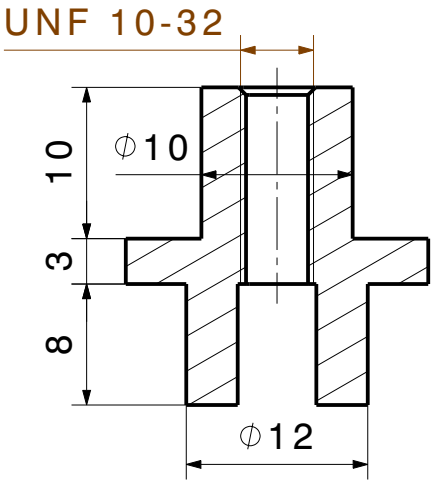

Isometrische Ansicht
Maßstab: 1:1

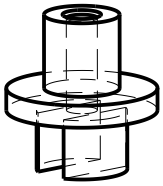

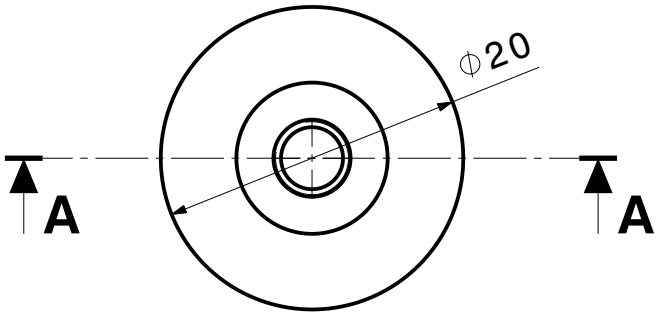

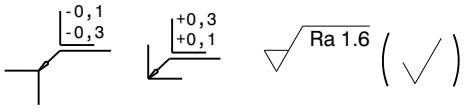

	Oberfläche	Gewicht 17 g		
	Allgemeintoleranzen ISO 2768-mK	Material S235		
	Projekt Projekt-0001747	Erstellt 15.06.2012	Kurzzeichen uhi	
	Baugruppe upper mass_2		Format A4	Blatt 1/1
EMPA	Benennung Gewindeadapter_2 UNF 10-32	Drawing-0013580		Index

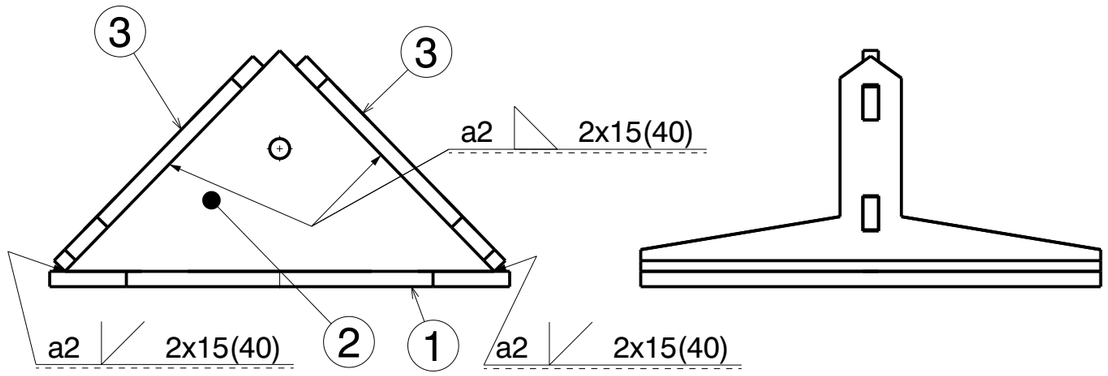

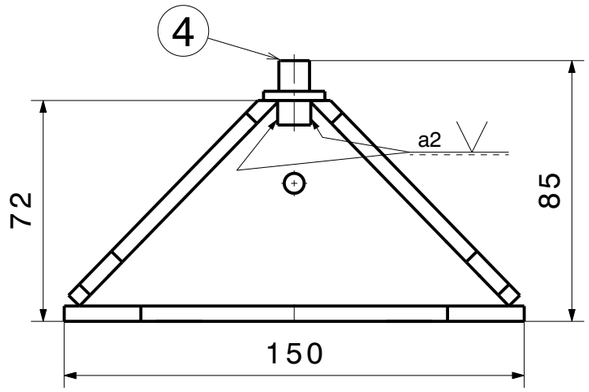

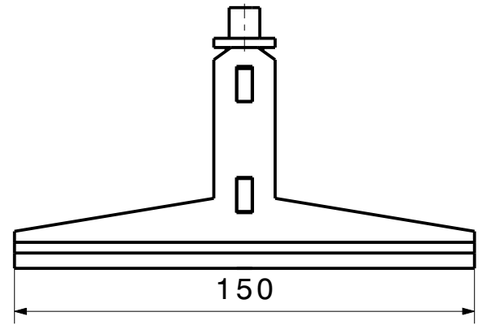

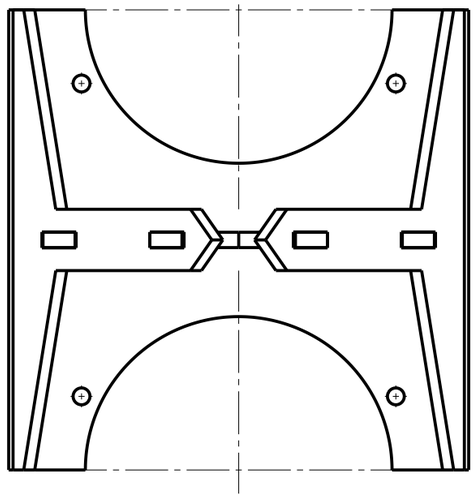

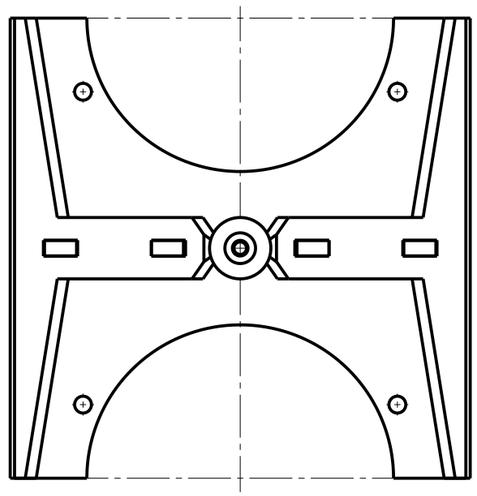

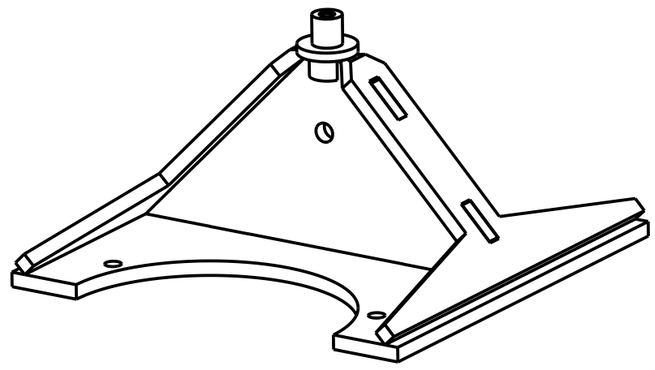

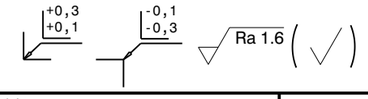

	Oberfläche	Gewicht 1.047 kg	
	Allgemeintoleranzen ISO 2768-mK	Material S235	
	Projekt Projekt-0001747	Erstelldatum 15.06.2012	Kurzzeichen uhi
	Baugruppe Ceiling hanger measurement_2	Format A3	Blatt 1/1
EMPA	Benennung upper mass_2	Zeichnungs-Nr. Drawing-0013581	Index

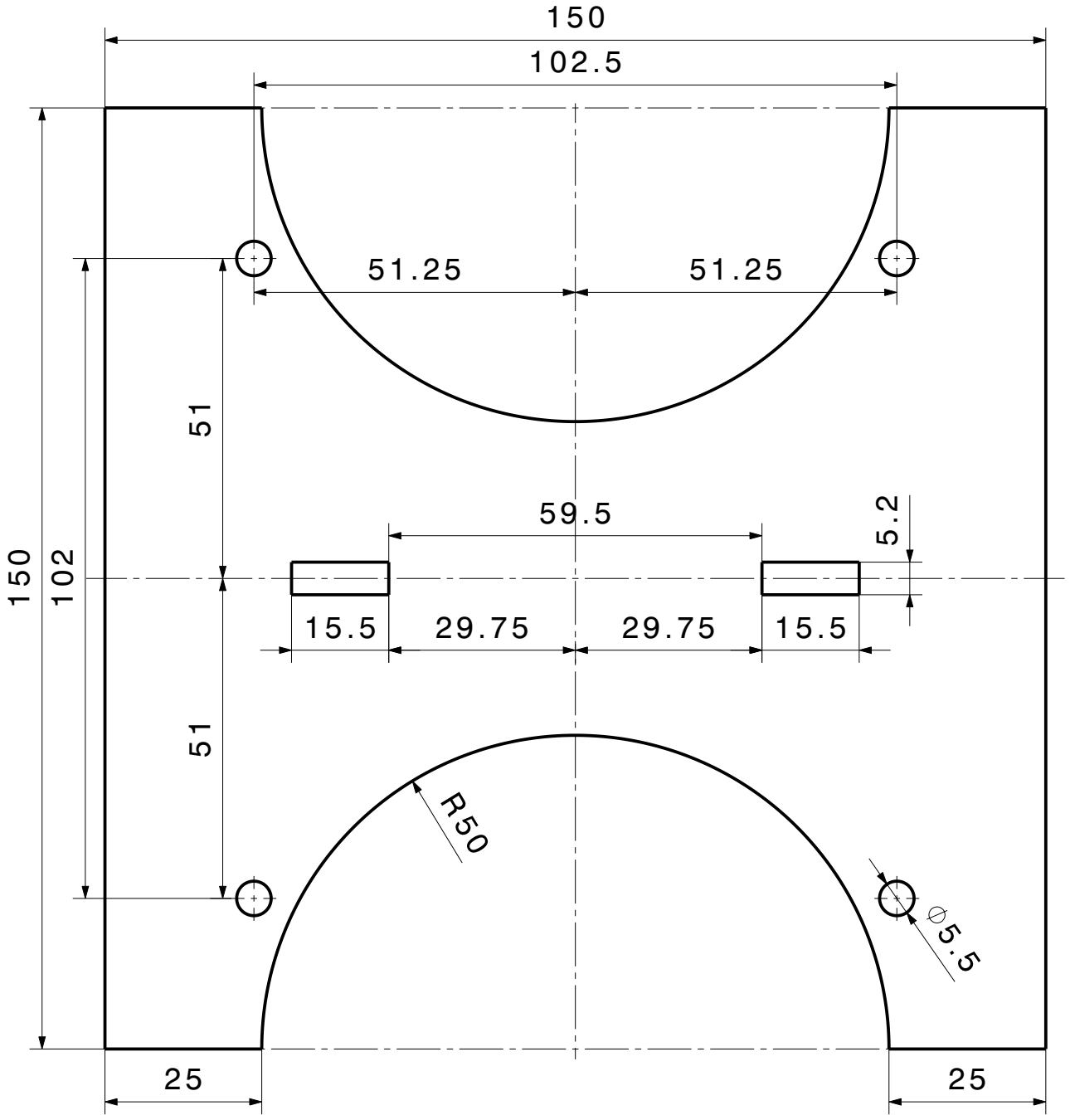

-0,1 -0,3 +0,3 +0,1 Ra 1.6

	Oberfläche	Gewicht 566 g		
	Allgemeintoleranzen ISO 2768-mK	Material S235		
	Projekt Projekt-0001747	Erstellt 15.06.2012	Kurzzeichen uhi	
	Baugruppe upper mass_2		Format A4	Blatt 1/1
EMPA	Benennung top base_2	Drawing-0013582		Index

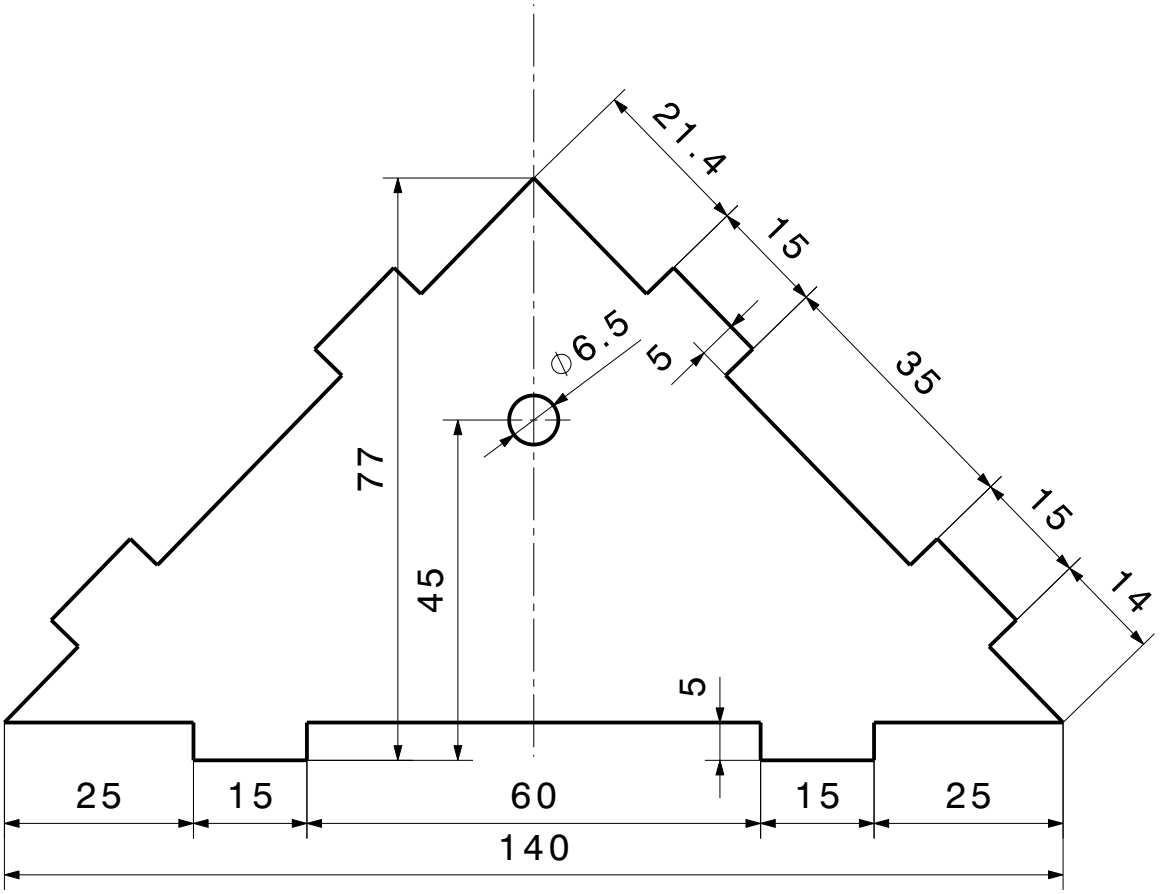

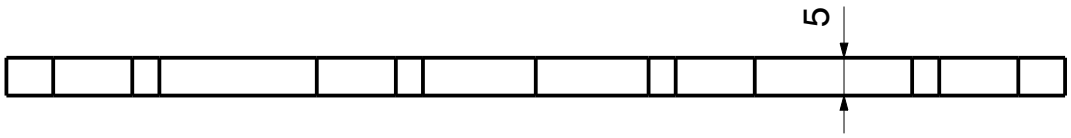

-0,1
-0,3

+0,3
+0,1

Ra 1.6

	Oberfläche	Gewicht 214 g		
	Allgemeintoleranzen ISO 2768-mK	Material S235		
	Projekt Projekt-0001747	Erstellt 15.06.2012	Kurzzeichen uhi	
	Baugruppe upper mass_2		Format A4	Blatt 1/1
EMPA	Benennung middle section_2	Drawing-0013583		Index

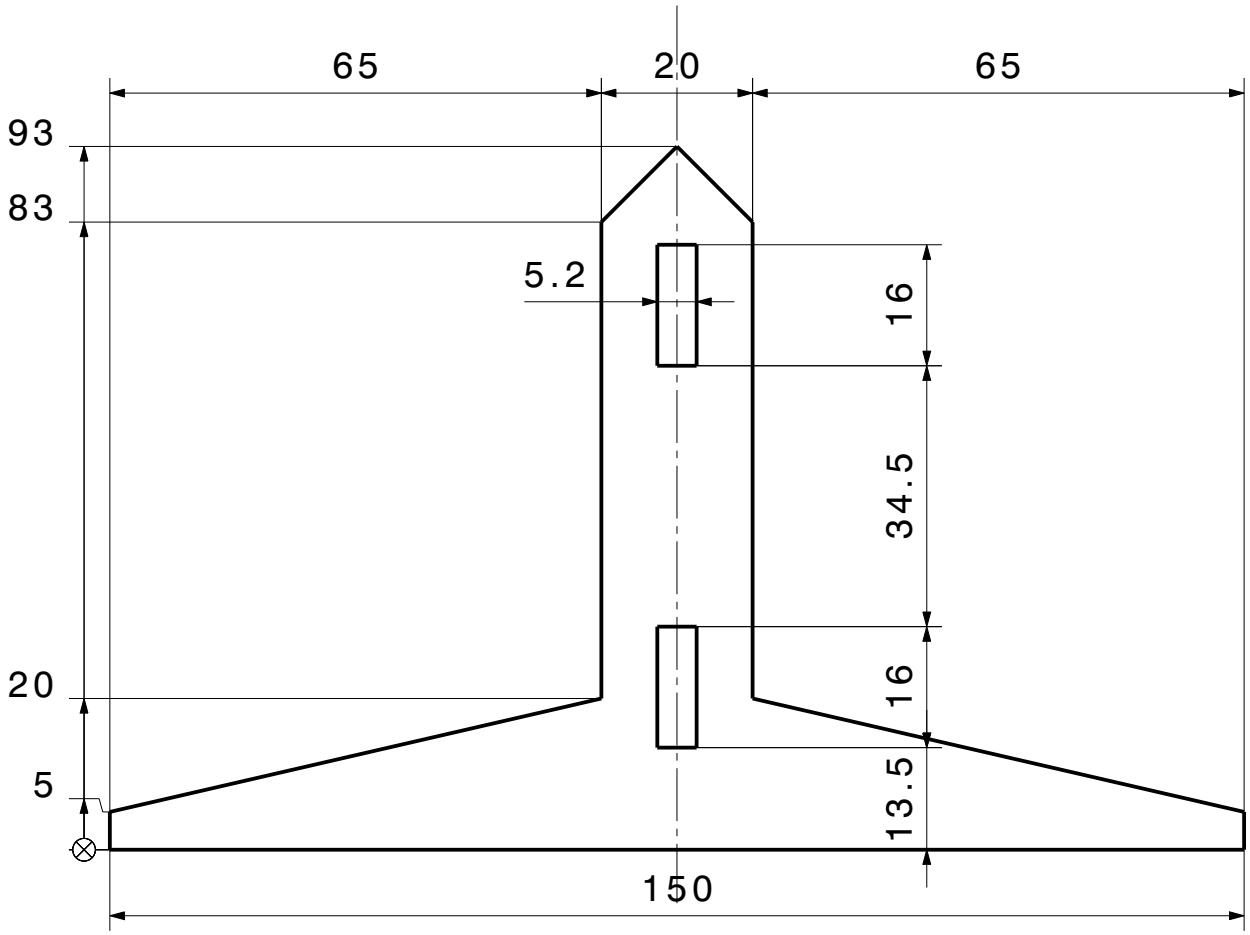

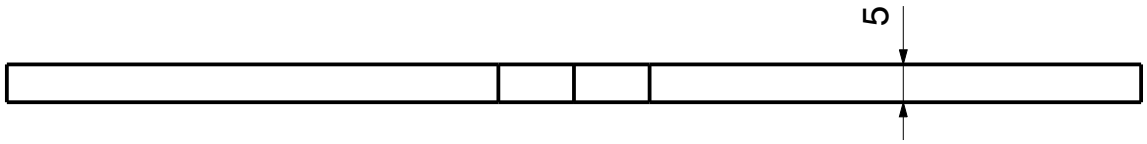

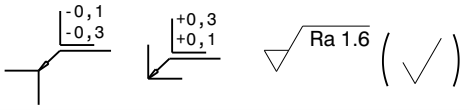

	Oberfläche	Gewicht 126 g	
	Allgemeintoleranzen ISO 2768-mK	Material S235	
	Projekt Projekt-0001747	Erstellt 15.06.2012	Kurzzeichen uhi
	Baugruppe upper mass_2	Format A4	Blatt 1/1
EMPA	Benennung side part_2	Drawing-0013584	Index

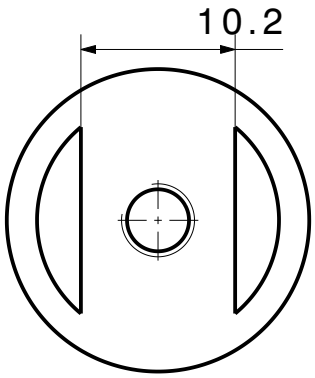

SchnittansichtA-A
Maßstab: 2:1

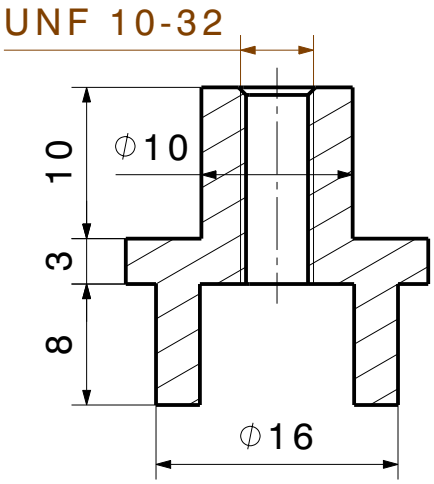

Isometrische Ansicht
Maßstab: 1:1

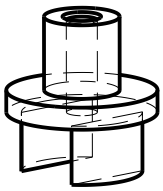

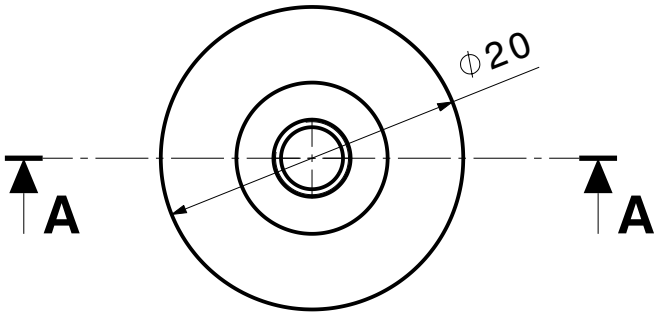

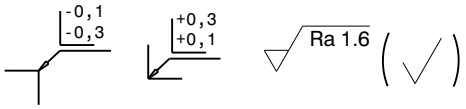

	Oberfläche	Gewicht 17 g		
	Allgemeintoleranzen ISO 2768-mK	Material S235		
	Projekt Projekt-0001747	Erstellt 15.06.2012	Kurzzeichen uhi	
	Baugruppe upper mass_2		Format A4	Blatt 1/1
EMPA	Benennung Gewindeadapter_3 UNF 10-32	Drawing-0013585		Index

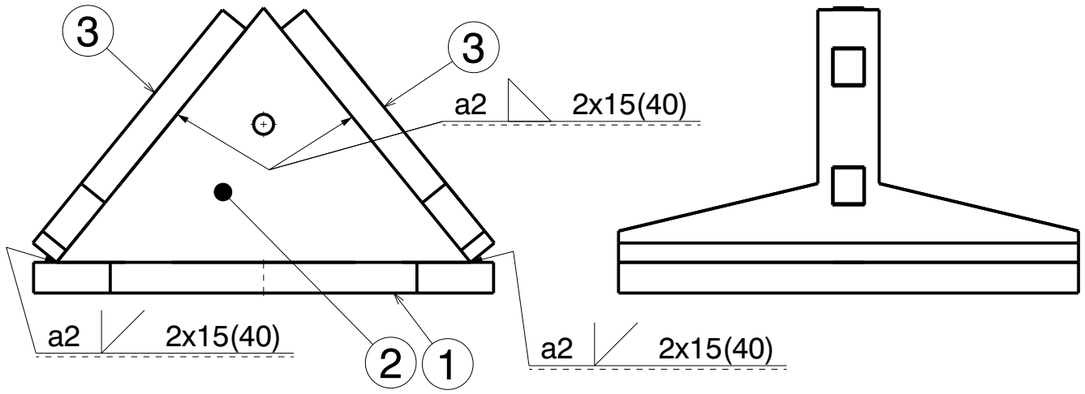

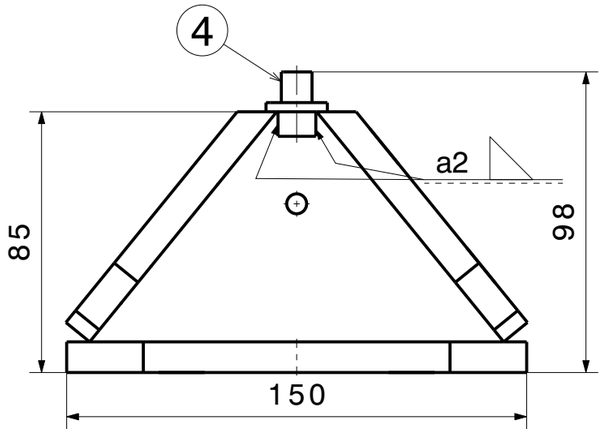

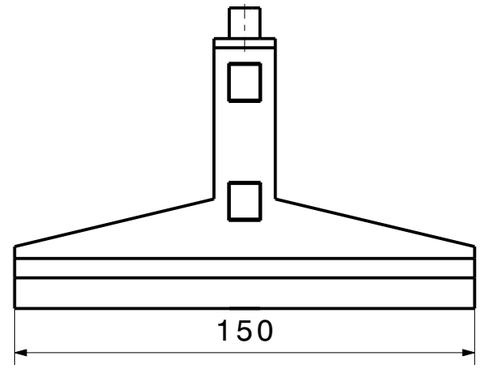

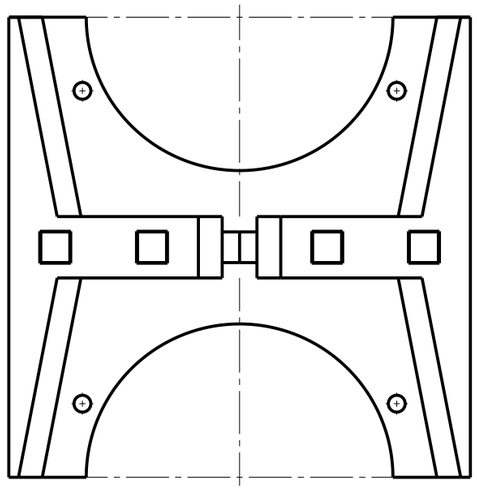

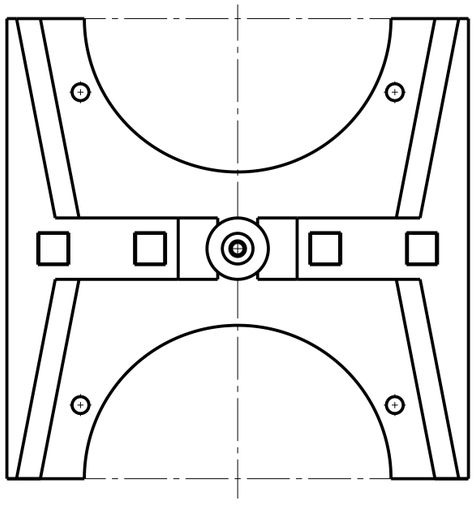

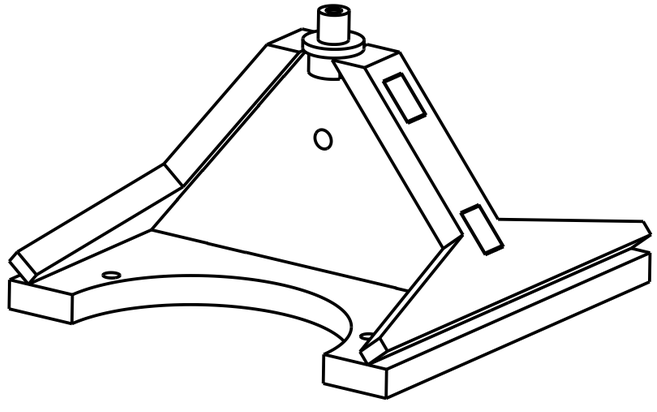

+0,3 +0,1 | -0,1 -0,3 | Ra 1.6 (√)

	Oberfläche	Gewicht 2.183 kg	
	Allgemeintoleranzen ISO 2768-mK	Material S235	
	Projekt Projekt-0001747	Erstelldatum 15.06.2012	Kurzzeichen uhi
	Baugruppe ceiling hanger measurement_3		Format A3 / Blatt 1/1
EMPA	Benennung upper mass_3	Zeichnungs-Nr. Drawing-0013586	Index

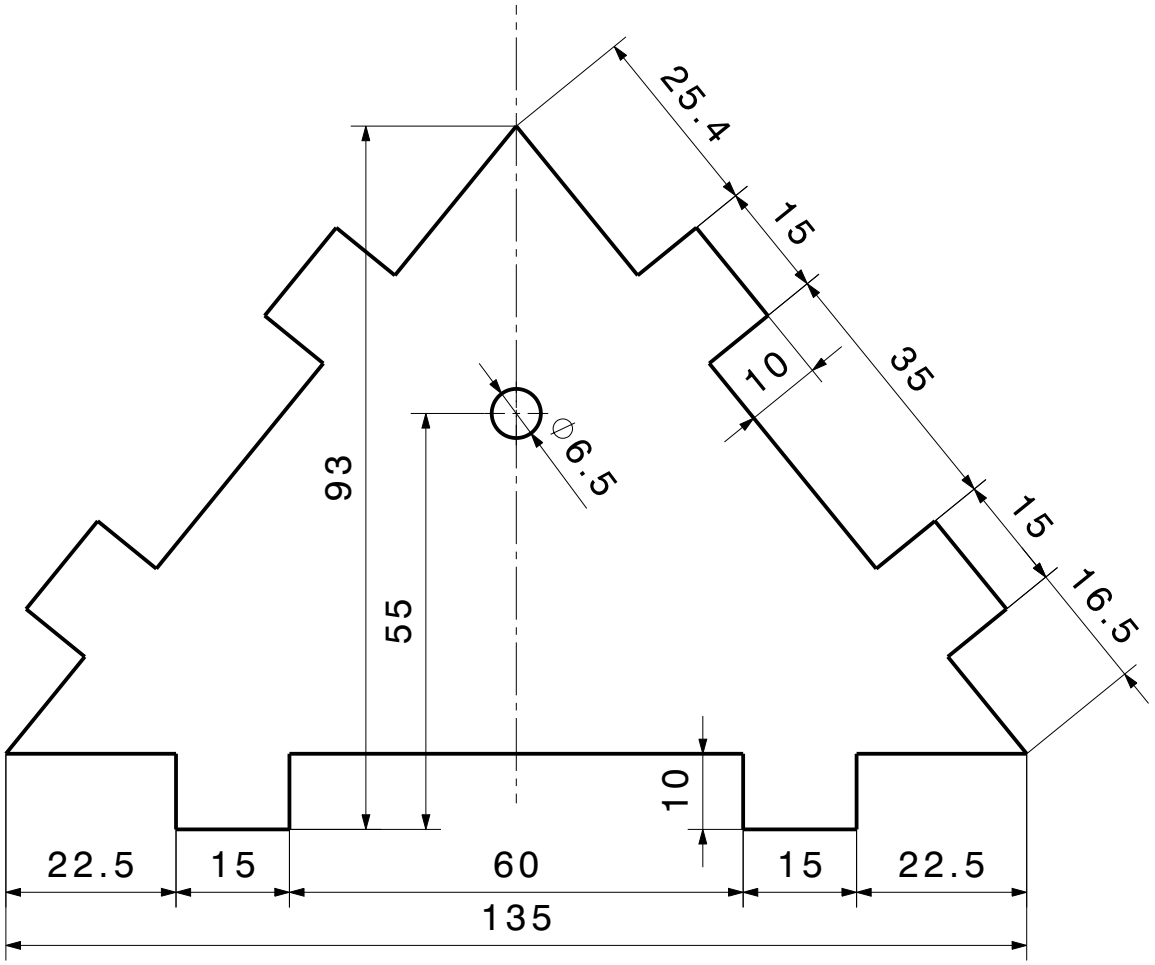

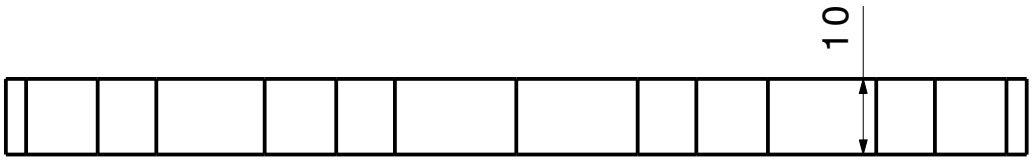

-0,1
-0,3

+0,3
+0,1

Ra 1.6

	Oberfläche	Gewicht 508 g		
	Allgemeintoleranzen ISO 2768-mK	Material S235		
	Projekt Projekt-0001747	Erstellt 15.06.2012	Kurzzeichen uhi	
	Baugruppe upper mass_3		Format A4	Blatt 1/1
EMPA	Benennung middle section_3	Drawing-0013588		Index

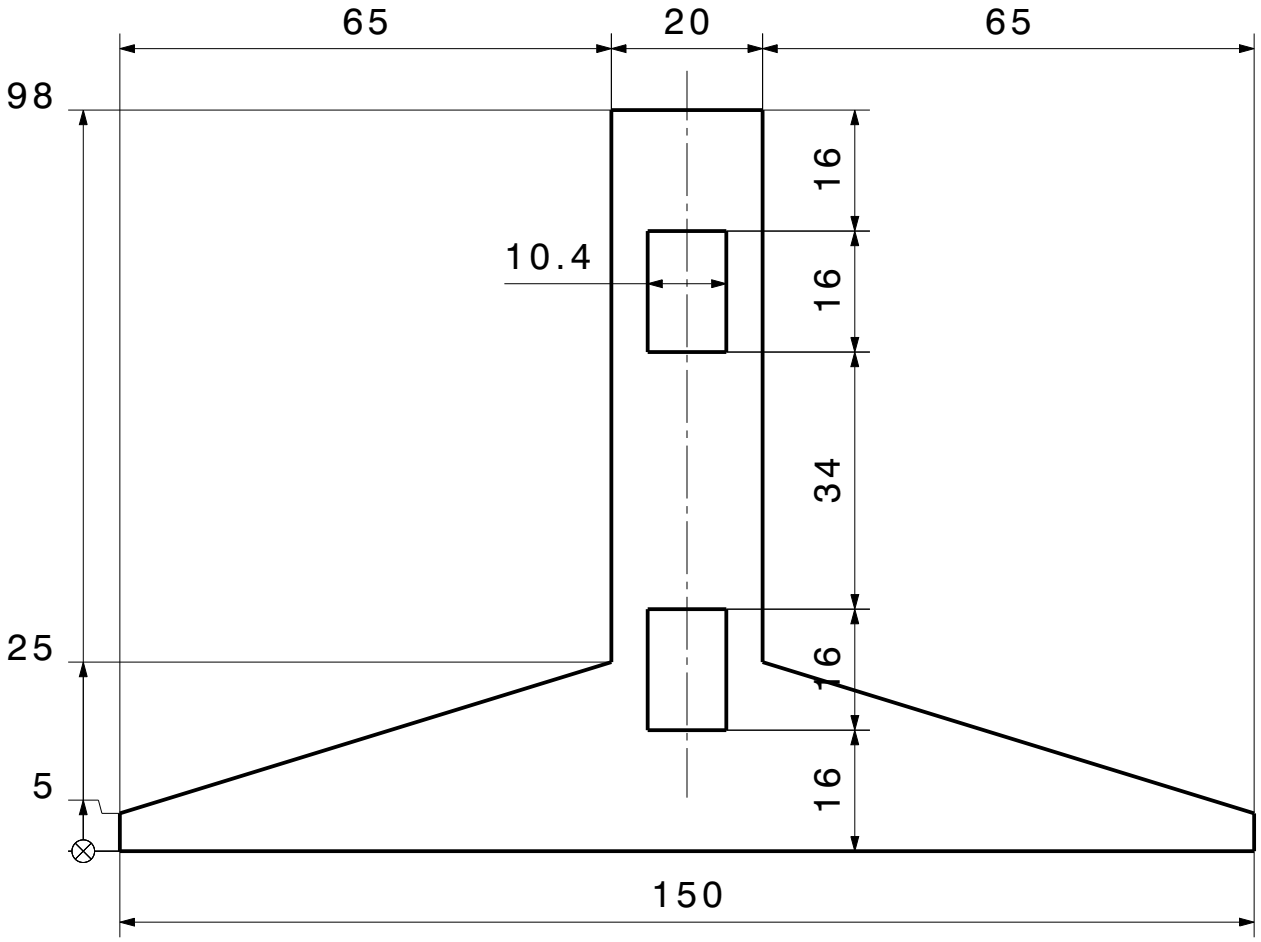

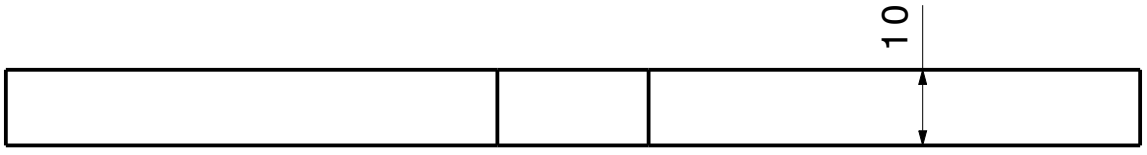

-0,1
-0,3

+0,3
+0,1

Ra 1.6

	Oberfläche	Gewicht 281 g		
	Allgemeintoleranzen ISO 2768-mK	Material S235		
	Projekt Projekt-0001747	Erstellt 15.06.2012	Kurzzeichen uhi	
	Baugruppe upper mass_3		Format A4	Blatt 1/1
EMPA	Benennung side part_3	Drawing-0013589		Index

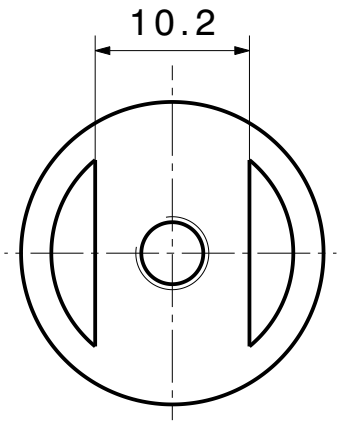

SchnittansichtA-A
Maßstab: 2:1

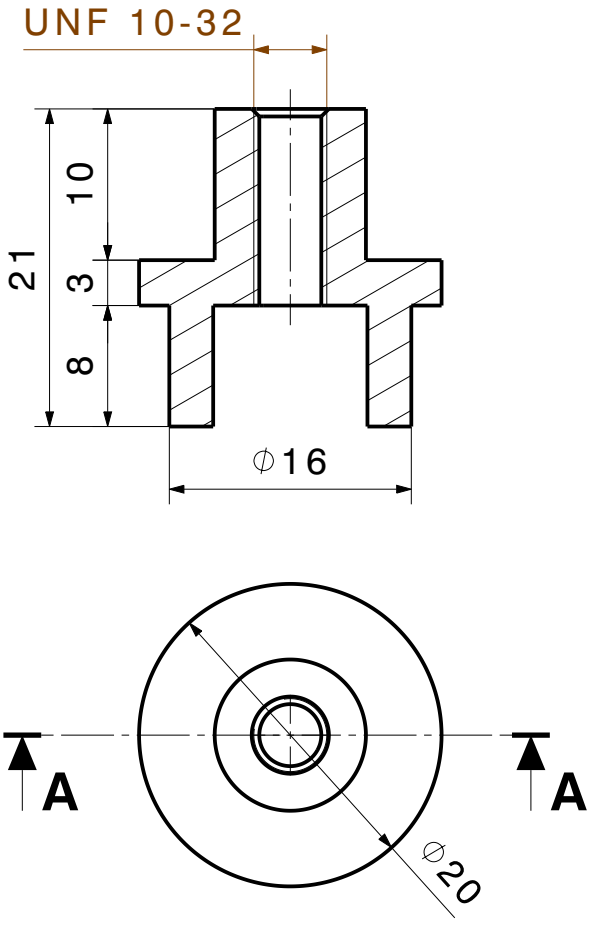

Isometrische Ansicht
Maßstab: 1:1

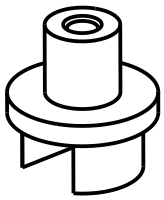

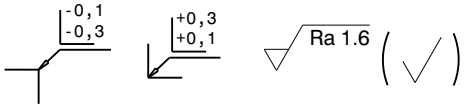

	Oberfläche	Gewicht 15 g	
	Allgemeintoleranzen ISO 2768-mK	Material S235	
	Projekt Projekt-0001747	Erstellt 15.06.2012	Kurzzeichen uhi
	Baugruppe upper mass_3		Format A4 / Blatt 1/1
EMPA	Benennung Gewindeadapter_3 UNF 10-32	Drawing-0013590	Index

APPENDIX F: Drawings of the HBV floor

Zwischendecke HBV:

von oben nach unten

Beton 70mm
OSB Typ 4 12mm formaldehydfrei
Steg BSH GL 24h, BxH 80 x260mm

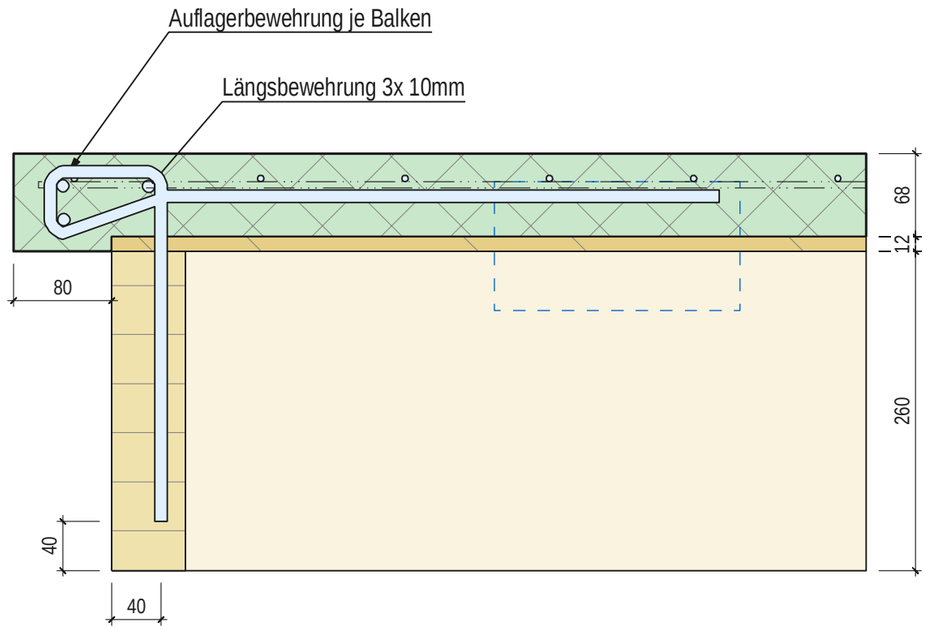

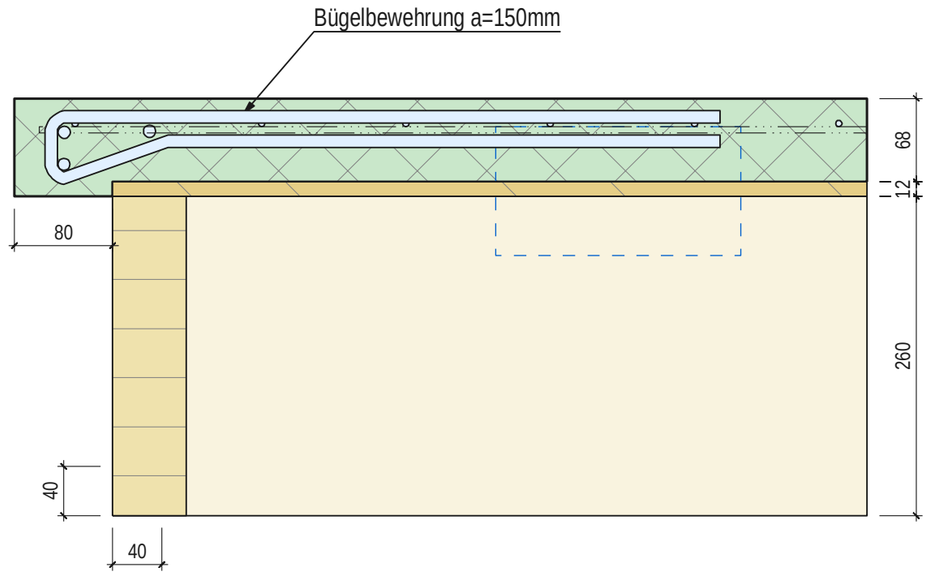

HBV Testelement Detail Auflager	Massstab 1:5 W.377440.TE .1 .0
Datum 26.11.2013 Gezeichnet LaC	

ERNE modul-technologie
CH-5080 Laufenburg
Tel. 062 869 81 81
Info@erne.net
Ein Unternehmen der ERNE - Gruppe

Schichtendarstellung BundseiteMST: 1:20

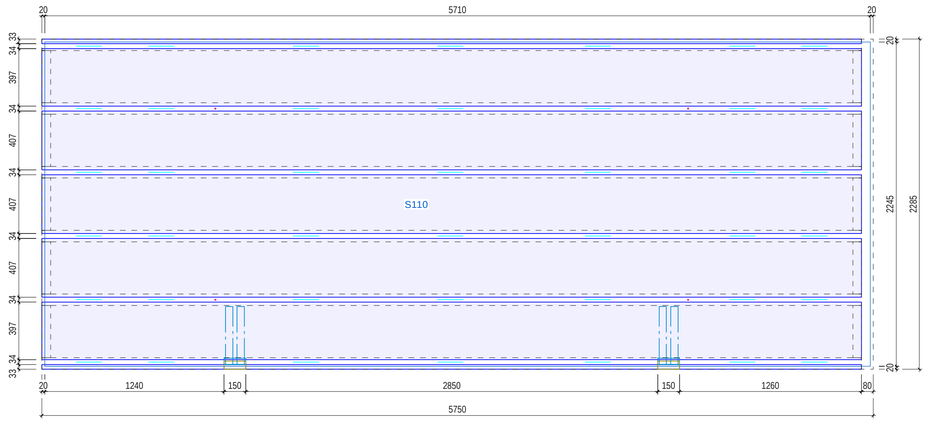

Schichtendarstellung Bundseite

Schichtendarstellung GegenseiteMST: 1:20

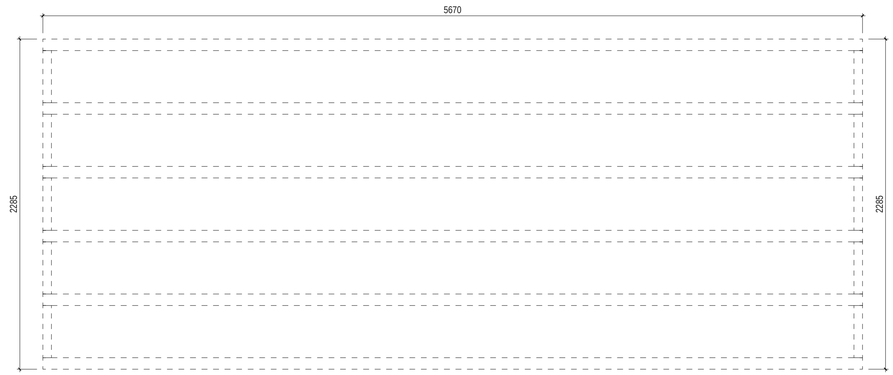

Schichtendarstellung Gegenseite

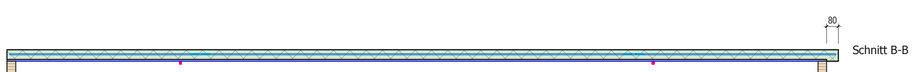

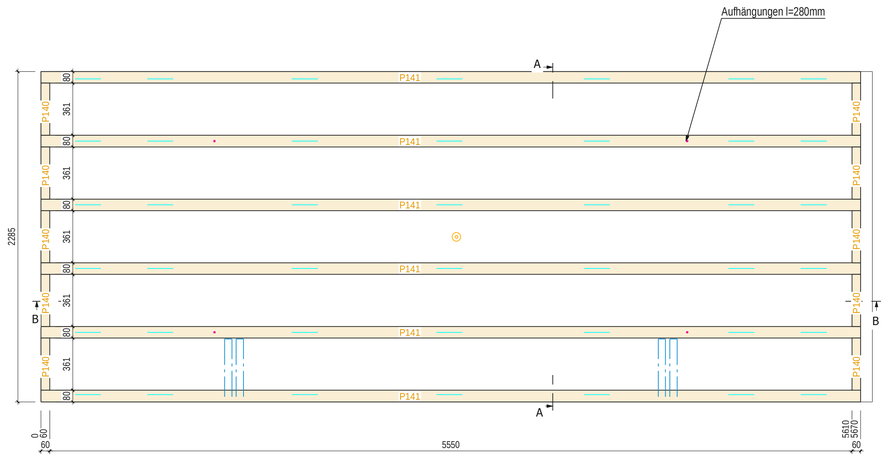

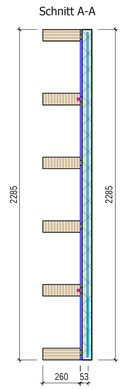

GRUNDBEDINGUNGEN FÜR BETON- UND HOLZ-BETON-VERBUNDARBEITEN:

Betonüberdeckung: 2.0 cm
Beton: SCC C30/37 XC1 0-16 F6 z.B. HOLCIM Selfpact 3716 CL
Oberflächenbehandlung: Sauber über Schalungskante abgezogen ± 5mm
Nachbehandlung: Nachbehandlungmittel (Curing) auftragen z.B. Sika Antisol-E20
Armierungskontrolle: Der Ingenieur ist mindestens 24h vor dem Betonieren zu benachrichtigen!

GRUNDBEDINGUNG ZUR VERLEIMUNG VON BODEN- UND DACHELEMENTEN:

Staubfrei
Holzfeuchte 6 - 15 %, min. Raumtemperatur 10 C^0
Leimauftragsmenge: pro 3 cm Rippenbreite Leimraupe von 4 - 5 mm d.h. 2 Raupen bei 6er Steg (250 g/m2)
Bei sichtbarer Befestigung: - Rillennägel mit Schaft
- Nagellänge = 2,5 x Plattendicke
- Nagelabstand = 1 Nagel pro 65 cm2 (< 100mm)
Element nach Verleimung 3 Stunden liegen lassen
Plattenstoss sind exakt nach Werkplanung auszuführen (Laschen min. 800 mm Lang)

HBV Testelemente Planausgabe

Nr.	PL Baugruppe	Material	Name	Anzahl	Breite PL	Höhe PL	Laenge PL
141	HBV T1	BSH GL 24h l	Balkenlage	6	80	260	5670
140	HBV T1	BSH GL 24h l	Wechsel	10	60	260	361

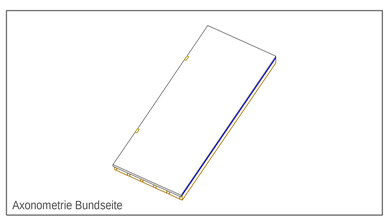
Axonometrie Bundseite

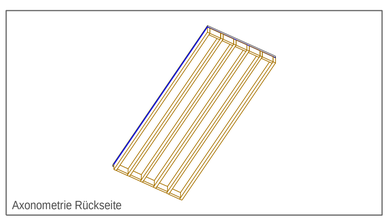
Axonometrie Rückseite

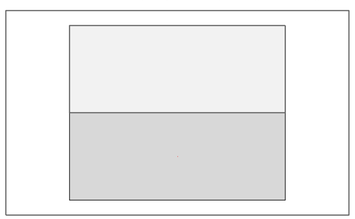

Nagelpressleimung:
Semparoc I 12 BL
RNä 2.8 x 70mm
1-Reihig
e // = 100mm ca. 20 Nägel pro m2

MST:1:20

Endkontrolle ordnungsgemäss durchgeführt	.	.	.
Beplankungen ordnungsgemäss durchgeführt	.	.	.
Rahmenzusammenbau ordnungsgemäss durchgeführt	.	.	.
.	.	.	.
Planfreigabe durch ?	?	01.01.2012	A
Bezeichnung Plangrösse **890 x 594 mm**	Gezeichnet	Datum	Index

ELEKTROROHR
○ RÜCKSEITE
• VORDERSEITE
ELEKTRODOSEN
○ RÜCKSEITE
● VORDERSEITE

Oftringen GLW
HBV T1
W.377440.HBV T1.O

Datum	26.11.2013							
Gezeichnet	LaC							

Gewicht: 2832.68 kg

ERNE modul-technologie
CH-5080 Laufenburg
Tel. 062 869 81 81
Info@erne.net

Ein Unternehmen der ERNE - Gruppe

Schichtendarstellung BundseiteMST: 1:20

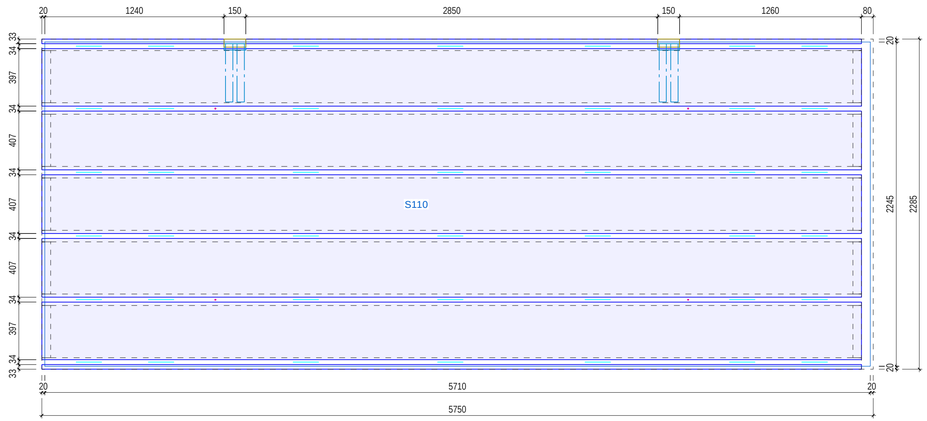

Schichtendarstellung Bundseite

Schichtendarstellung GegenseiteMST: 1:20

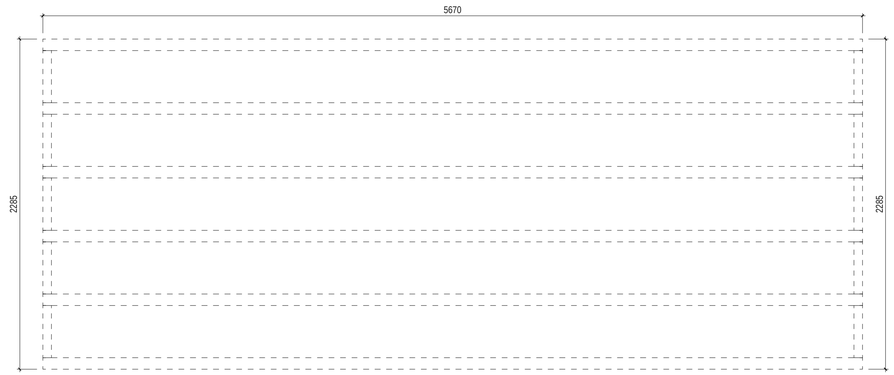

Schichtendarstellung Gegenseite

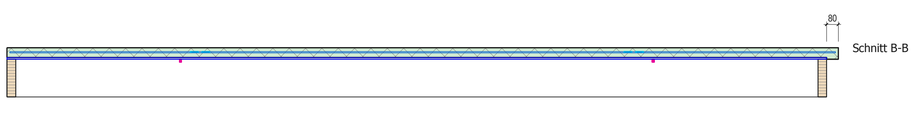

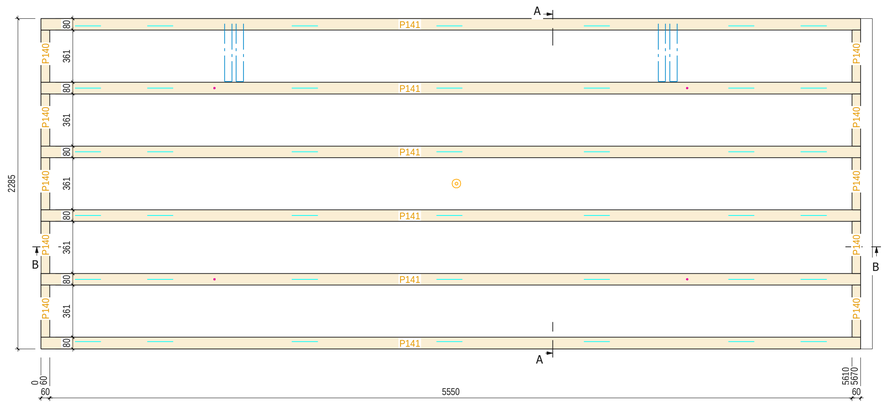

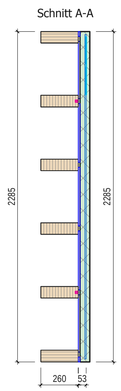

GRUNDBEDINGUNGEN FÜR BETON- UND HOLZ-BETON-VERBUNDARBEITEN:

Betonüberdeckung: 2.0 cm
Beton: SCC C30/37 XC1 0-16 F6 z.B. HOLCIM Selfpact 3716 CL
Oberflächenbehandlung: Sauber über Schalungskante abgezogen ± 5mm
Nachbehandlung: Nachbehandlungmittel (Curing) auftragen z.B. Sika Antisol-E20
Armierungskontrolle: Der Ingenieur ist mindestens 24h vor dem Betonieren zu benachrichtigen!

GRUNDBEDINGUNG ZUR VERLEIMUNG VON BODEN- UND DACHELEMENTEN:

Staubfrei
Holzfeuchte 6 - 15 %, min. Raumtemperatur 10 C^0
Leimauftragsmenge: pro 3 cm Rippenbreite Leimraupe von 4 - 5 mm d.h. 2 Raupen bei 6er Steg (250 g/m2)
Bei sichtbarer Befestigung: - Rillennägel mit Schaft
- Nagellänge = 2,5 x Plattendicke
- Nagelabstand = 1 Nagel pro 65 cm2 (< 100mm)
Element nach Verleimung 3 Stunden liegen lassen
Plattenstoss sind exakt nach Werkplanung auszuführen (Laschen min. 800 mm Lang)

Nagelpressleimung:
Semparoc I 12 BL
RNä 2.8 x 70mm
1-Reihig
e // = 100mm ca. 20 Nägel pro m2

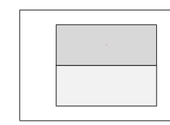

MST:1:20

Endkontrolle ordnungsgemäss durchgeführt	.	.	.
Beplankungen ordnungsgemäss durchgeführt	.	.	.
Rahmenzusammenbau ordnungsgemäss durchgeführt	.	.	.
.	.	.	.
Planfreigabe durch ?	?	01.01.2012	A
Bezeichnung Plangrösse **890 x 594 mm**	Gezeichnet	Datum	Index

HBV Testelemente Planausgabe

Nr.	PL Baugruppe	Material	Name	Anzahl	Breite PL	Höhe PL	Laenge PL
141	HBV T2	BSH GL 24h l	Balkenlage	6	80	260	5670
140	HBV T2	BSH GL 24h l	Wechsel	10	60	260	361

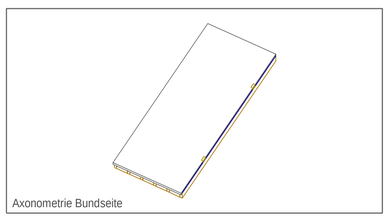

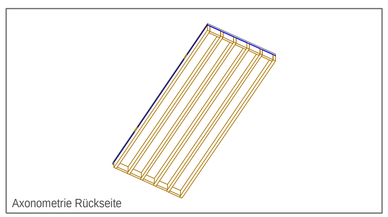

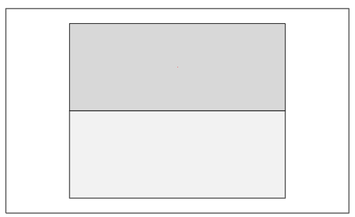

ELEKTROROHR
○ RÜCKSEITE
• VORDERSEITE
ELEKTRODOSEN
○ RÜCKSEITE
● VORDERSEITE

Oftringen GLW
HBV T2

W.377440.HBV T2.O

Datum	26.11.2013							
Gezeichnet	LaC							

Gewicht: 2832.68 kg

ERNE modul-technologie
CH-5080 Laufenburg
Tel. 062 869 81 81
Info@erne.net

Ein Unternehmen der ERNE - Gruppe